Lecture Notes in Energy 37

Nicu Bizon
Naser Mahdavi Tabatabaei
Frede Blaabjerg
Erol Kurt *Editors*

Energy Harvesting and Energy Efficiency

Technology, Methods, and Applications

Springer

Lecture Notes in Energy

Volume 37

Lecture Notes in Energy (LNE) is a series that reports on new developments in the study of energy: from science and engineering to the analysis of energy policy. The series' scope includes but is not limited to, renewable and green energy, nuclear, fossil fuels and carbon capture, energy systems, energy storage and harvesting, batteries and fuel cells, power systems, energy efficiency, energy in buildings, energy policy, as well as energy-related topics in economics, management and transportation. Books published in LNE are original and timely and bridge between advanced textbooks and the forefront of research. Readers of LNE include postgraduate students and non-specialist researchers wishing to gain an accessible introduction to a field of research as well as professionals and researchers with a need for an up-to-date reference book on a well-defined topic. The series publishes single and multi-authored volumes as well as advanced textbooks.

More information about this series at http://www.springer.com/series/8874

Nicu Bizon · Naser Mahdavi Tabatabaei
Frede Blaabjerg · Erol Kurt
Editors

Energy Harvesting and Energy Efficiency

Technology, Methods, and Applications

Springer

Editors
Nicu Bizon
Faculty of Electronics, Communication, and Computers
University of Piteşti
Piteşti
Romania

Naser Mahdavi Tabatabaei
Electrical Engineering Department, Faculty of Engineering
Seraj Higher Education Institute
Tabriz
Iran

Frede Blaabjerg
Department of Energy Technology
Aalborg University
Aalborg East
Denmark

Erol Kurt
Department of Electrical and Electronics Engineering, Faculty of Technology
Gazi University
Ankara
Turkey

ISSN 2195-1284 ISSN 2195-1292 (electronic)
Lecture Notes in Energy
ISBN 978-3-319-49874-4 ISBN 978-3-319-49875-1 (eBook)
DOI 10.1007/978-3-319-49875-1

Library of Congress Control Number: 2016959749

Printed on acid-free paper

This Springer imprint is published by Springer Nature
The registered company is Springer International Publishing AG
The registered company address is: Gewerbestrasse 11, 6330 Cham, Switzerland

Foreword

Energy efficiency has always been a major challenge for the scientist and the engineers. However, in recent years, the increased public concern for the preservation of natural resources and the protection of the environment has strongly stimulated the research and development activities in this area. More than 20,000 technical papers written in 2016 and stored in "Scopus" database have "energy efficiency" in their title, in their abstract or in their list of keywords. There were less than 4000 in 1996.

Energy harvesting is a much more recent topic. Less than 100 papers addressed it twenty years ago. More than 2500 articles were published in top-level journals from January to October 2016. The reason behind this spectacular growth is simple: Both academia and industry are interested in the design and engineering of energy-autonomous small electronic devices that can harvest the various forms of energy available in the environment (solar, eolian, and hydraulic) and convert them to electric power. The development of energy-harvesting applications is driven by the increased need of autonomous wireless electronic systems in various fields of human activities, ranging from medicine and aeronautics to civil engineering and animal tracking.

Textbooks and monographs are already available for anyone who wants to learn more on either "energy efficiency" or "energy harvesting." The merit of this book is that it brings together the two topics, which are more and more interrelated. The editors carefully selected the topics to be treated, and each chapter of this book is written by well-recognized experts in the field. This book introduces the reader to up-to-date research on nonlinearity of energy-harvesting systems, energy efficiency of hybrid power systems, and optimal design of autonomous electronic systems. It also contains instructive case studies and examples of experimental validation of the novel energy-saving or energy-harvesting techniques.

This book can be used in the classroom, to teach energy management courses to graduate students, and be suggested as further reading to undergraduate students in engineering sciences. It will also be a valuable information resource for the researchers and engineers concerned by energy efficiency issues or involved in the development and application of energy-harvesting techniques.

October 2016

Lucian Dascalescu
IEEE Fellow, Distinguished Professor
of Electrical Engineering
University of Poitiers, University Institute
of Technology, Angoulême, France

Preface

Energy harvesting and energy efficiency are two key topics for today's power community. In the development of modern society, one of the key factors is to save energy in order to become more independent of other resources. Two important approaches can be taken—one is to change behavior and thereby save energy and the second is to develop new technology which is able to save energy in different applications. Chapter 1 gives an overview of challenges and possibilities in terms of energy saving and also energy efficient use.

Initially, the first key topic—energy harvesting—becomes one of the most motivated fields of the multidisciplinary science due to the complicated features of the harvester materials, dependences on various mechanical, electrical, and magnetic parameters, rich responses on different external excitation frequencies and strength. Strictly speaking, vibrations stem from either man-made systems or natural processes can be used as an important electric resource for low-power-consuming electronic devices such as transducers and wireless sensors. That can contribute at the batteryless applications for much sustainable and renewable power generation, whereas some technical problems should be solved to achieve the expectations of the electronics society. Although conventional harvesters work on the basis of linear resonance, there exist certain parametrical limitations on their power generation. Indeed, excitation frequency, electrical load, manufacturing tolerance, and ambient temperature play important roles in order to determine the optimized energy generation. Besides, the nonlinear nature of the vibration phenomena contributes at the power, and these nonlinear effects cannot be neglected for an optimized harvester system. Thus, Part I of this book initially gives an outline to the reader on the electromagnetic and piezoelectric energy-harvesting systems and then focuses on the theoretical and experimental techniques by introducing different harvester systems.

In that context, Chap. 2 describes the harvesting sources with classical and novel types for the use of electromagnetic and piezoelectric hybrid structures. Various

experimental systems are described in detail in order to compare their output powers and their relation to the system parameters.

The batteryless applications of microscale harvesters have been explained in Chap. 3 for information technologies (IT). The importance of low-power harvesting systems for IT applications is particularly emphasized, and model systems have been discussed. One of the important practice areas of the harvesters is wireless sensor application. Therefore, a specific chapter (i.e., Chap. 4) is dedicated to the problems of electromagnetic and piezoelectric harvesters in wireless devices. This chapter gives both experimental and theoretical details on the matter. As the harvester systems have complicated equilibrium features for their time- and space-dependent nature, nonlinearity plays an important role to identify their dynamic behavior and power-generation strategy. Therefore, Chap. 5 is devoted to the nonlinear problems of the harvesters. Although the energy-harvesting issues mostly cover the systems related to the piezoelectric and electromagnetic ones in low power range, the most frequent energy-generation system—photovoltaics (PV) has been an important topic. Therefore, Chap. 6 focuses on the control phenomena of PV hybrid systems.

It can be emphasized that the chapters mentioned above provide a good background to the reader on the harvester systems and their applications. Both experimental and theoretical approaches to different harvesting problems help to understand the advanced problems and cutting-edge information, world widely, thereby the readers at different educational levels from undergraduate to the professionals can find interesting research topics in order to apply in their own studies.

Other main topic of this book is the energy efficiency. Due to the increasing population and industrial growth, energy efficiency has become a popular topic for every level of communities from ordinary to technical. There exist many attempts today that the energy efficiency itself can be counted as a new energy resource. Thus, interdisciplinary studies, which have been carried out in the fields of renewable energy, focus on different mechanisms that decrease the losses of the energy in methodological ways. In light of the present technology, the efficiency cannot be considered detached from the cost. Strictly speaking, the balance between the efficiency and system cost should be ascertained. With that respect, many energy systems such as solar, wind, and tidal can make use of good-quality materials or efficiency techniques if they are financially appropriate. Therefore, Chaps. 7–9 are devoted to the sun-tracking applications and maximal power point tracking (MPPT) techniques in PVs. In these chapters, both practices and theoretical backgrounds on the tracking mechanisms are presented including the case studies. Chapter 10 mentions the partial shading effect on the PV systems and clarifies the methodology on the solution of MPPT for those systems. The applications on solar cars are presented in Chap. 11. This chapter also sheds a light on the polymer composite materials in order to enhance the efficiency and gives some information on the charging stations.

The increasing demand for electricity supply along with higher requirements for power quality and system reliability, restrictions to use the available fossil fuels, and minimization of the environmental pollutants leads to the aggregation of clean

energy sources (renewable energy sources, fuel cell, etc.) in distributed generation systems and developing microgrids. Consequently, the energy efficiency of hybrid power system that integrates such clean energy sources must be improved through appropriate energy management strategies. Thus, the remaining parts of the book, namely II, III, and IV, analyze the energy efficiency based on fuel cell, PV, wind, and hybrid power systems.

The term "hybrid" means the use of other energy storage devices, or multiple input energy sources in hybrid power sources to sustain the load demand. Thus, the use of fuel cell system as energy source or energy storage devices in conjunction with an electrolyzer is analyzed in Chaps. 12 and 13. While Chap. 12 analyzes the possibility to use the extremum seeking control schemes for the reduction of hydrogen consumption in fuel cell hybrid power sources, Chap. 13 analyzes the efficiency of a fuel cell hybrid power source required for an automotive application. Chapter 14 proposes a stochastic model to analyze the microgrids with the goal of profit maximization and imbalance cost minimization. In this framework, a new method based on neural network theory is proposed for predicting wind speed and solar radiation. Other chapter (i.e., Chap. 15) analyzes the energy efficiency of a micro-combined cooling, heating, and power system driven by a solar dish stirling heat engine that is used for residential buildings. A novel methodology was introduced for short-term scheduling of small-scale trigeneration system, which can be used optimally and efficiently to provide cooling, heating, and power for residential applications, being environmentally friendliness, cost-cutting, and on-site applied.

The last part of this book is dedicated to some technical strategies, efficient methods, and applications in field of energy efficiency, so it will be of interest for all current researchers and specialists in that field as well as for technicians.

Chapter 16 presents wired and wireless communication systems in smart homes and buildings based on the recent developments proposed in applications. The basic principles of the smart homes and energy efficient buildings are introduced firstly in order to provide basic knowledge for readers and the chapter also gives an idea on the communication systems used for outdoor and indoor scenarios. Chapters 17 and 18 propose new flexible hybrid architecture for the power-conditioning unit for small satellites. Since the space agencies all over the world are interested today in very small satellites due to their advantages compared to heavier satellites, the advanced techniques are discussed including their converter and storage systems.

The batteries are unavoidable for any electricity system. Therefore, while making a discussion on the efficiency issues, one should also consider the storage techniques. Chapter 19 introduces a new method for determining the optimal model of batteries, puts a starting point in analyzing their discharge profiles, and employs a multicriteria analysis for processing the experimental data.

While considering the efficiency in solar, fuel cell and related hybrid systems, the energy efficiency in wind and water distribution systems should also be mentioned. In this manner, the optimal planning and operation of water distribution is presented in Chap. 20. This problem mainly involves the establishment of the operation schedule for all water hydrophore stations and uses a database of 85 urban

water hydrophore stations as a case study. Finally, the last chapter (i.e., Chap. 21) provides an overview about available knowledge, references, and investigations on the active and passive flow control devices, initially developed for aeronautical industry that are currently being investigated and introduced on wind turbines in order to improve their efficiency.

As a conclusion, a sustained research in the field of energy efficiency does not only give more chances to significant reduction of carbon dioxide, greenhouse gas emissions, and environmental pollution, but also increases the economic saving in fuel consumption and use of energy sources. Therefore, this book tries to highlight the difficulties of the basic methods on energy harvesting and energy efficiency and proposes advanced methods to solve these issues. All proposed methods were validated through simulation and experimental results. These "hot subjects" will be of interest for many decades and, at the same time, will be a challenge and hard task for the researchers all over the world, considering the new energy policies due to energy crisis.

We hope that this book will be very efficient for students and engineers who learn and wish to work in this field, because the chapters of this book cover all important and challenging subjects related to energy harvesting and energy efficiency. The book comprises the knowledgeable and up-to-date contents that present the state-of-the-art equipment and methods used for the energy harvesting and energy efficiency. Finally, the main arguments that may recommend this book to be read are the following: (1) It is the first comprehensive book on energy harvesting and energy efficiency of the power hybrid systems; (2) covers the operating principles, design methods, and real applications; (3) enables the low power for autonomous electronic system design; (4) introduces the high-power density technology and adiabatic concept to efficiently design the mission critical systems; (5) provides a much-needed system approach to hydrogen energy applications; (6) provides a comprehensive overview of the fundamentals of renewable power generation, conversion, and storage; and the last, but not the least, (7) can be used as a course text.

The editors and authors made all efforts to have a good book, and we hope interested readers to enjoy by reading this book and to be satisfied by its content.

Piteşti, Romania — Nicu Bizon
Tabriz, Iran — Naser Mahdavi Tabatabaei
Aalborg, Denmark — Frede Blaabjerg
Ankara, Turkey — Erol Kurt

Contents

Contributors

Necmi Altin Department of Electrical and Electronics Engineering, Faculty of Technology, Gazi University, Ankara, Turkey

Iñigo Aramendia Department of Nuclear Engineering and Fluid Mechanics, University of the Basque Country, Vitoria-Gasteiz, Araba, Spain

Nicu Bizon Department of Electronics, Computers and Electrical Engineering, University of Piteşti, Piteşti, Romania; University Politehnica of Bucharest, Bucharest, Romania

Frede Blaabjerg Department of Energy Technology, Center of Reliable Power Electronics (CORPE), Aalborg University, Aalborg, Denmark

Luminita-Mirela Constantinescu University of Piteşti, Piteşti, Romania

Pooya Davari Department of Energy Technology, Center of Reliable Power Electronics (CORPE), Aalborg University, Aalborg, Denmark

Mustafa Doğan Department of Electrical and Electronics Engineering, Baskent University, Ankara, Turkey

Ali Durusu Yildiz Technical University, Istanbul, Turkey

Bogdan-Adrian Enache Faculty of Electronics, Communications and Computers, University of Piteşti, Piteşti, Romania

Unai Fernandez-Gamiz Department of Nuclear Engineering and Fluid Mechanics, University of the Basque Country, Vitoria-Gasteiz, Araba, Spain

Adriana Florescu University POLITEHNICA of Bucharest, Bucharest, Romania

Gheorghe Grigoras Department of Power System, Faculty of Electrical Engineering, "Gheorghe Asachi" Technical University of Iasi, Iasi, Romania

Nazenin Gure Department of Mechanical Engineering, Faculty of Engineering, Marmara University, Istanbul, Turkey; Enhas R&D Energy Systems Ind. Co. Ltd, Istanbul, Turkey

Aytaç Gören Automatic Control and Robotics Laboratories, Department of Mechanical Engineering, Dokuz Eylul University, Izmir, Turkey

Sıtkı Çağdaş İnam Department of Electrical and Electronics Engineering, Baskent University, Ankara, Turkey

Farkhondeh Jabari Faculty of Electrical and Computer Engineering, University of Tabriz, Tabriz, Iran

Ersan Kabalci Department of Electrical and Electronics Engineering, Faculty of Engineering and Architecture, Nevsehir HBV University, Nevsehir, Turkey

Yasin Kabalci Department of Electrical and Electronics Engineering, Faculty of Engineering, Omer Halisdemir University, Nigde, Turkey

Abdulkerim Kar Department of Mechanical Engineering, Faculty of Engineering, Marmara University, Istanbul, Turkey

Fevzi Kentli Department of Mechatronics Engineering, Technology Faculty, Marmara University, Istanbul, Turkey

Erol Kurt Department of Electrical and Electronics Engineering, Technology Faculty, Gazi University, Teknikokullar, Ankara, Turkey

Adrian-Ioan Lita University Politehnica of Bucharest, Bucharest, Romania

Ioan Lita University of Piteşti, Piteşti, Romania

Jose Manuel Lopez-Guede Department of Systems Engineering and Automatics, University of the Basque Country, Vitoria-Gasteiz, Araba, Spain

Behnam Mohammadi-Ivatloo Faculty of Electrical and Computer Engineering, University of Tabriz, Tabriz, Iran

Ali Muhtaroğlu Department of Electrical and Electronics Engineering, Middle East Technical University, Northern Cyprus Campus, Güzelyurt, Mersin 10, Turkey

Ismail Nakir Yildiz Technical University, Istanbul, Turkey

Sergiu Oprea University POLITEHNICA of Bucharest, Bucharest, Romania

Mihai Oproescu University of Piteşti, Piteşti, Romania

Ö. Orkun Sürel Department of Electrical and Electronics Engineering, Baskent University, Ankara, Turkey

Saban Ozdemir Vocational School of Technical Sciences, Gazi University, Ankara, Turkey

Xiaohui Qu School of Electrical Engineering, Southeast University, Nanjing, China

Mircea Raceanu National Research and Development Institute for Cryogenics and Isotopic Technologies, Râmnicu Vâlcea, Romania; University Politehnica of Bucharest, Bucharest, Romania

Constantin Radoi University POLITEHNICA of Bucharest, Bucharest, Romania

Marian Raducu University of Piteşti, Piteşti, Romania

Jose Antonio Ramos-Hernanz Department of Electrical Engineering, University of the Basque Country, Vitoria-Gasteiz, Araba, Spain

Mohammad Rasouli Department of Electrical and Computer Engineering, School of Engineering, Penn State University, Erie, PA, USA

Javier Sancho Department of Nuclear Engineering and Fluid Mechanics, University of the Basque Country, Vitoria-Gasteiz, Araba, Spain

Andrei-Stefan Savu University POLITEHNICA of Bucharest, Bucharest, Romania

Ibrahim Sefa Department of Electrical and Electronics Engineering, Faculty of Technology, Gazi University, Ankara, Turkey

Elnaz Shahryari Department of Technical Engineering, University of Mohaghegh Ardabili, Ardabil, Iran

Hossein Shayeghi Department of Technical Engineering, University of Mohaghegh Ardabili, Ardabil, Iran

Alper Sisman Department of Electrical and Electronics Engineering, Faculty of Engineering, Marmara University, Istanbul, Turkey

Naser Mahdavi Tabatabaei Department of Electrical Engineering, Faculty of Engineering, Seraj Higher Education Institute, Tabriz, Iran

Erturul Tacgin Department of Mechanical Engineering, Faculty of Engineering, Marmara University, Istanbul, Turkey

Mugdesem Tanrioven Yildiz Technical University, Istanbul, Turkey

Yunus Uzun Department of Electrical and Electronics Engineering, Faculty of Engineering, Aksaray University, Aksaray, Turkey

Huai Wang Department of Energy Technology, Center of Reliable Power Electronics (CORPE), Aalborg University, Aalborg, Denmark

Musa Yilmaz Department of Electronics and Communications Engineering, Technology Faculty, Batman University, Batman, Turkey

Firuz Zare Power and Energy Group, The University of Queensland, Brisbane, QLD, Australia

Ekaitz Zulueta Department of Systems Engineering and Automatics, University of the Basque Country, Vitoria-Gasteiz, Araba, Spain

Abbreviations and Acronyms

AAHP	Air-to-Air Heat Pump
ABC	Artificial Bee Colony
AC	Alternative Current
ACA	Ant Colony Algorithm
AcVG	Actuator Vortex Generator
ADC	Analog-to-Digital Conversion
AES	Advanced Encryption Standard
aESC	Advanced Extremum Seeking Control
AF	Active Filtering
AFC	Active Flow Control
AFE	Active Frontend
AGS	Automatic Generating System
AI	Artificial Intelligence
AJVG	Air Jet Vortex Generator
AM	Amplitude Modulation
AMI	Advanced Metering Infrastructure
AMM	Automatic Meter Management
AMR	Automatic Meter Reading
ANN	Artificial Neural Network
AP	Access Point
ARIB	Association of Radio Industries and Businesses
ASD	Adjustable Speed Drive
ASHP	Air Source Heat Pump
a-Si	Amorphous Silicon
ASIC	Application-Specific Integrated Circuit
ASM	Assembly
BAN	Body Area Network
BB	Broadband
BCDMU	Battery Charge/Discharge Monitor Unit
BCU	Battery Charger Unit

BDR	Battery Discharge Regulator
BFV	Best Fixed Voltage
BGA	Ball Grid Array
BLDCM	Brushless Direct Current Motor
BMS	Battery Management System
BOL	(Battery's) Beginning of Life
BoP	Balance of Plant
BP	Belief Propagation
BPF	Band-Pass Filter
bpfESC	Band-Pass Filter ESC
BPSK	Binary Phase Shift Keying
BSN	Body Sensor Nod
BU	Battery Unit
CAD	Computer-Aided Design
CART	Classification and Regression Trees
CC	Constant Current
CCHP	Combined Cooling Heating and Power
CCK	Complementary Code Keying
CCM	Continuous Current Mode
CCP	Combined Cool and Power
CD	Charge Depletion
CDRG	Coulomb-Damped Resonant Generator
CFD	Computational Fluid Dynamics
CFL	Compact Fluorescent Lamp
CHP	Combined Heat and Power
CI	Charge Increasing
CMMR	Common Mode Rejection Ratio
COA	Centroid of Area
COE	Cost of Energy
COFDM	Coded OFDM
COTS	Commercial Off-the-Shelf
CP	Cyclic Prefix
CS	Charge Sustaining
CSMA	Carrier Sense Multiple Access
CSMA/CA	Carrier Sense Multiple Access/Collision Avoidance
CSMA/CD	Carrier Sense Multiple Access/Collision Detection
CST	Current Sweep Technique
CT	Copper Thickness
CU	Chargers' Unit
CV	Constant Voltage
CVaR	Conditional Value at Risk
D8PSK	Differential 8-Phase Shift Keying
DA	Day Ahead
DAQ	Data Acquisition
DBPSK	Differential Binary Phase Shift Keying

DC	Direct Current
DCM	Discontinuous Conduction Mode
DCSK	Differential Chaos Shift Keying
DET	Direct Energy Transfer
DG	Distributed Generation
DM	Damper Motor
DMS	Data Management System
DNLP	Discontinuous Nonlinear Program
DO	Disjoint Operation
DOD	Depth of Discharge
DOF	Degree of Freedom
DPE	Direct Piezoelectric Effect
DQPSK	Differential Quadrature Phase Shift Keying
DRIBA	Double-Regulated Intermediate Bus Architecture
DS	Delay Stall
DSL	Digital Subscriber Line
DTU	Denmark Technical University
DVS	Dynamic Voltage Scaling
e.i.r.p.	Equivalent Isotropic Radiated Power
EA	Evolutionary Algorithms
EH	Energy Harvester
EHing	Energy Harvesting
EM	Electromagnetic
EMF	Electromotive Force
EMHs	Electromagnetic Energy Harvesters
EMI	Electromagnetic Interference
EMP	Electromagnetic Pulse
EMS	Energy Management Strategy
EOL	(Battery's) End of Life
EP	Evolutionary Programming
EQ	Equivalence
ES	Energy Sources
ESA	European Space Agency
ESC	Extremum Seeking Control
ESR	Equivalent Series Resistance
ESS	Energy Storage System
EU	European Union
EV	Electric Vehicle
EWEA	Energy Wind Energy Association
FC	Fuel Cell
FCC	Federal Communications Commission
FCHPS	Fuel Cell Hybrid Power Source
FEA (FEM)	Finite Element Analysis (Finite Element Method)
FEC	Forward Error Correction
FEM	Finite Element Method

FFT	Fast Fourier Transform
FLC	Fuzzy Logic Controller
FSK	Frequency Shift Keying
FT	Fuzzy Techniques
FW	Freewheeling Diode
GA	Genetic Algorithm
GAMS	General Algebraic Modeling System
GaN	Gallium Nitride
GEO	Geosynchronous Earth Orbit
GFSK	Gaussian Frequency Shift Keying
GMPP	Global Maximum Power Point
GMPPT	Global Maximum Power Point Tracking
GP	Global Peak
GSTP	General Support Technology Program
GUI	Graphical User Interface
H_1	First Harmonic
HAN	Home Area Network
HAWT	Horizontal Axis Wind Turbine
HC	Hill Climbing
HEHs	Hybrid Energy Harvesters
HEO	Highly Elliptical Orbit
HF	High Frequency
HID	High Intensity Discharge
hoESC	High-Order Extremum Seeking Control
HPF	High-Pass Filter
HPS	Hybrid Power Source
HRTHs	Hybrid Rotary-Translational Harvesters
HSAT	Horizontal Single Axis Tracking
HT	Hydro-Turbines
IC	Integrated Circuit
ICE	Internal Combustion Engine
ICT	Information and Communication Technologies
IEA	International Energy Agency
IGBT	Insulated-Gate Bipolar Transistor
IncCond	Incremental Conductance
IOD	In-Orbit Demonstration
IRRWBF	Implementation-Efficient Reliability Ratio-Based Weighted Bit Flipping
ITU	International Telecommunication Union
IU	Isolation Unit
I-V	Current–Voltage
IWBF	Improved Weighted Bit Flipping
LAN	Local Area Network
LDPC	Low-Density Parity Check
LDR	Light-Dependent Resistor

LE	Leading Edge
LED	Light-Emitting Diode
LEO	Low-Earth Orbit
LET	Linear Energy Transfer
LF	Low Frequency
LFP	$LiFePO_4$ Battery
LLR	Log-Likelihood Ratio
LP	Local Peak
LPF	Low-Pass Filter
LRCM	Linear Reoriented Coordinates Method
M2M	Machine-to-Machine
MAC	Media Access Control
MAPE	Mean Absolute Percentage Error
MC	Mid-Chord
MCA	Multicriteria Analysis
MCP	Marginal Clearing Price
MCU	Microcontroller Unit
MDO	Multidisciplinary Design Optimization
MEMS	Micro-Electro-Mechanical Systems
MEO	Mid-Earth Orbit
MEP	Maximum Efficiency Point
mESC	Modified Extremum Seeking Control
MG	Microgrid
MILP	Mixed-Integer Linear Programming
MLI	Multilevel Inverter
MLP	Multilayer Perceptron
MPP	Maximum Power Point
MPPT	Maximum Power Point Tracker
MSE	Mean Square Error
MT	Micro-Turbine
MTBF	Mean Time between Failures
NB	Narrowband
NGSO	Non-Geostationary Orbit
NN	Neural Network
NOCT	Normal Operating Cell Temperature
NREL	National Renewable Energy Laboratory
NTC	Negative Temperature Coefficient
O&M	Operation and Maintenance
OC	Only Current Photovoltaic
OCC	One-Cycle Control MPPT
OCV	Open-Circuit Voltage
ODE	Ordinary Differential Equations
OFDM	Orthogonal Frequency Division Multiplexing
OOK	On–Off Keying
OPGW	Optical Power Ground Wire

O-QPSK	Offset Quadrature Phase Shift Keying
ORC	Organic Rankine Cycle
ORING	OR-ing Output Logic Function
OV	Open Voltage
P&Q	Perturb and Observe
PAGV	Power Augmentation Guide Vane
PAM	Pulse Amplitude Modulation
PAN	Personal Area Network
PASAT	Polar-Aligned Single Axis Tracking
PC	Personal Computer
PCB	Printed Circuit Board
PDE	Partial Differential Equations
PE	Piezoelectric
PEC	Packet Error Check
PEHs	Piezoelectric Energy Harvesters
PEM	Proton Exchange Membrane
PEMFCS	Proton Exchange Membrane Fuel Cell Stack
PET	Polyethylene Terephthalate
PF	Passive Filtering
PFC	Power Factor Correction
PG	Pressure Growth
PI	Proportional Integral
PID	Proportional Integral Derivative
PLC	Power Line Communication
POL	Point of Load
POL/D	Point-of-Load/Distribution
POU	Point of Use
PPM	Pulse Position Modulation
PSC	Partially Shading Condition
PSO	Particle Swarm Optimization
PV	Photovoltaic
P-V	Power-Voltage
PVGJ	Pulsed Vortex Generator Jet
PVHPS	Photovoltaic Hybrid Power Source
PWM	Pulse Width Modulation
PZT	Lead Zirconate Titanate
QAM	Quadrature Amplitude Modulation
QPSK	Quadrature Phase Shift Keying
RANS	Reynolds-Averaged Navier Stokes
RC	Resistance–Capacitor
RCC	Ripple Correlation Control
RES	Renewable Energy Sources
RF	Radio Frequency
RLP	Representative Loading Profiles
RMS	Root Mean Square

RS	Reed Solomon
RWT	Reference Wind Turbine
S3R	Sequential Switching Shunt Regulator
SAPV	Stand-Alone Photovoltaic
SAT	Single Axis Tracking
SBEMS	Smart Building Energy Management Systems
SCPB	Short-Current Pulse-Based
SCRIMP™	Seemann Composites Resin Infusion Molding Process
SDSHE	Solar Dish Stirling Heat Engine
SEB	Single Event Burnout
SEBP	Single Event Burnout Phenomenon
SECE	Synchronous Electric Charge Extraction
SEE	Single Event Phenomenon
SEGR	Single Event Gate Rupture
SEL	Single Event Latch-up
SEPIC	Single-Ended Primary Inductor Converter
SEU	Single Event Upset
S-FSK	Spread Frequency Shift Keying
SGEMP	System-Generated EMP
SGI	Silhouette Global Index
Si	Silicon
SiC	Silicon Carbide
SIDO	Single İnductor Dual Output
SM	Smart Meter
SME	Shape Memory Effect
SMPS	Switched Mode Power Supply
SoC	State of Charge
SOFC	Solid Oxide Fuel Cell
SoH	State of Health
SS	Spread Spectrum
SSPB	Single-Supply Pre-Biasing
SST	Shear Stress Transport
STAR	Space Technology and Advanced Research
STC	Standard Test Conditions
TDD	Time Division Duplexing
TDMA	Time Division Multiple Access
TE	Trailing Edge
TEG	Thermoelectric Generator
TENG	Triboelectric Nanogenerator
THD	Total Harmonic Distortion
TID	Total Ionizing Doze
TSAT	Tilted Single Axis Tracking

TT&C	Telemetry, Tracking, and Telecommand
TVAC-PSO	Time Varying Acceleration Coefficients Particle Swarm Optimization
UC	Ultracapacitor
UDDS	Urban Dynamometer Driving Schedule
VARIM	Vacuum-Assisted Resin Infusion Molding
VAWT	Vertical Axis Wind Turbine
VBRTM	Vacuum Bag Resin Transfer Molding
VDRG	Velocity-Damped Resonant Generator
VG	Vortex Generator
VRM	Voltage-Regulated Module
VSAT	Vertical Single Axis Tracking
W	Daily Electrical Energy Consumption
WAN	Wide Area Network
WAST	Warm Air Storage Tank
WBF	Weighted Bit Flipping
WBG	Wide Band-Gap
WF	Daily Water Flow
WiSH	Wind-Solar Hybrid
WLAN	Wide Local Area Network
WM-Bus	Wireless M-Bus
WPAN	Wireless Personal Area Network
WSN	Wireless Sensor Network
WT	Wind Turbine
ZCS	Zero Current Switching
ZVS	Zero Voltage Switching

Chapter 1
Energy Saving and Efficient Energy Use By Power Electronic Systems

Frede Blaabjerg, Huai Wang, Pooya Davari, Xiaohui Qu and Firuz Zare

Abstract In the development of the modern society, one of the key factors is to save energy in order to become more independent of other energy resources. Two important approaches can be taken—one is to change behavior and thereby save energy—the second one is to develop new technology which is able to save energy in different applications. This chapter will give an overview of challenges and possibilities in terms of energy saving and also energy efficient use. This includes a discussion on high efficiency power electronics devices and the systems they are used for energy loss reduction. The key enabling technologies are power electronics, Information and Communication Technology (ICT) as well as systems to carry the electrical energy through power transmission, conversion and distribution. A couple of examples will be given to demonstrate the energy saving possibilities by power electronics systems, such as in the applications of adjustable speed drives and solid-state lighting systems. Power electronics gives also a high flexibility when renewable power production is introduced to electrical energy systems. Future research opportunities and challenges will finally be discussed.

F. Blaabjerg · H. Wang · P. Davari (✉)
Department of Energy Technology, Center of Reliable Power Electronics (CORPE), Aalborg University, Aalborg, Denmark
e-mail: pda@et.aau.dk

F. Blaabjerg
e-mail: fbl@et.aau.dk

H. Wang
e-mail: hwa@et.aau.dk

X. Qu
School of Electrical Engineering, Southeast University, Nanjing, China
e-mail: xhqu@seu.edu.cn

F. Zare
Power and Energy Group, The University of Queensland, Brisbane, QLD, Australia
e-mail: f.zare@uq.edu.au

N. Bizon et al. (eds.), *Energy Harvesting and Energy Efficiency*,
Lecture Notes in Energy 37, DOI 10.1007/978-3-319-49875-1_1

Keywords Electrical energy · Power electronics · Adjustable speed drive · Wide band-gap power devices · Intelligent lighting

Abbreviation and Acronyms

AF	Active Filtering
AFE	Active Front-End
AM	Amplitude Modulation
ASD	Adjustable Speed Drive
CFL	Compact Fluorescent Lamp
GaN	Gallium Nitride
HID	High Intensity Discharge
ICT	Information and Communication Technology
IEA	International Energy Agency
LED	Light-Emitting Diode
PF	Passive Filtering
PFC	Power Factor Correction
PWM	Pulse-Width Modulation
Si	Silicon
SiC	Silicon Carbide
WBG	Wide Band-Gap

1.1 Introduction

Among the technologies that support the growth of clean energy and the improvement of energy efficiency, power electronics has been representing a major enabler. It provides efficient conversion and flexible control of electrical energy. The power electronics converters make possible the connection of renewable energy generators to the legacy power systems, as schematically shown in Fig. 1.1, and efficiency improvement of energy harvesting through dedicated controls. Furthermore, power electronics is extensively used on the consumer side and is a core technology for the new smart grid [1]. It unlocks the potentials of energy savings in motor drives, buildings (e.g., lighting, energy-efficient appliances), transportation (e.g., electric vehicles, high speed trains), consumer electronics (e.g., computers, cell phones), etc.

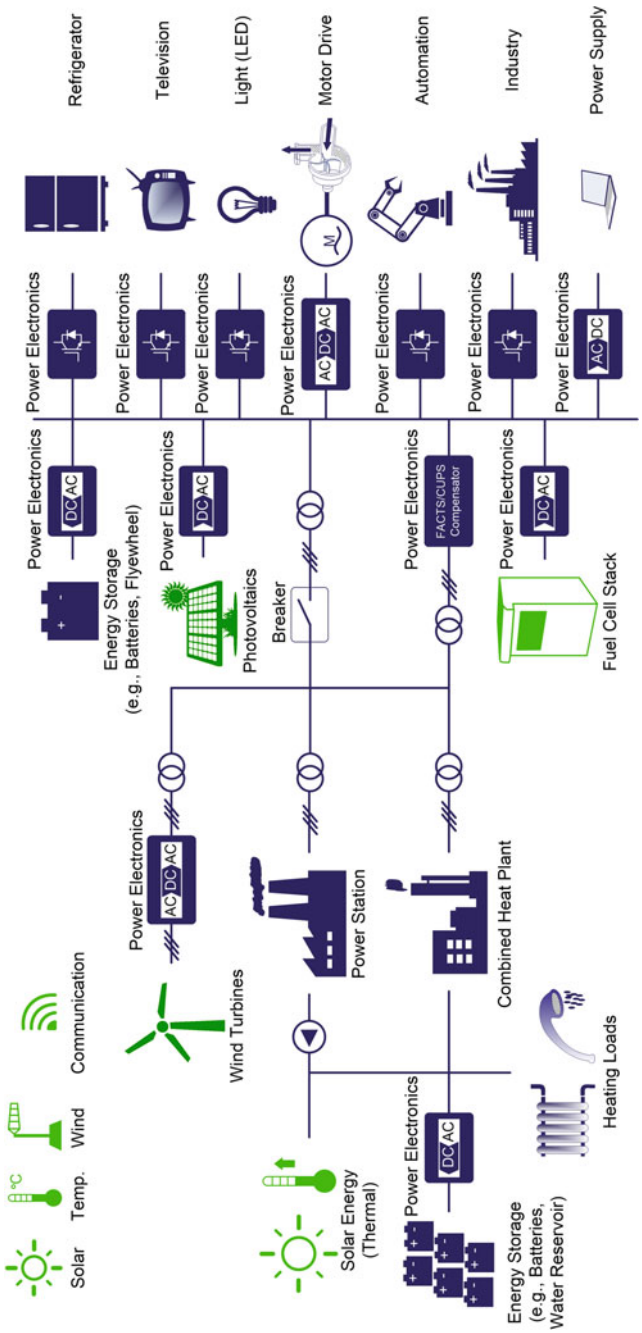

Fig. 1.1 The role of power electronics in electrical energy generation, transmission, distribution, and consumption [1]

1.2 Electrical Energy Generation and Consumption

Today more than 40% of all energy consumption is in the form of electrical energy, which is expected to grow to 60% by 2040 [2]. The generation of the electrical energy is becoming more renewable-based as shown in Fig. 1.2, which is according to the projection by the International Energy Agency (IEA) [3]. The power generation capacity worldwide is expected to increase by 80%, from 5,952 GW in 2014 to about 10,700 GW in 2040. During this period, about 2,250 GW power capacity currently in operation and about 200 GW capacity from newly commissioned renewables is expected to be retired due to the end of service life. The cost gap between electricity generated from renewable sources and fossil fuels is narrowing as discussed in [1]. Connection of the electrical energy generated from renewable energy sources (e.g., wind power and photovoltaics) to power grids is not possible without power electronics based energy conversion systems.

The generated electrical energy is consumed by different sectors, such as industry, residential, and transportation. The transportation sector sees a clear electrification both in cars and ships, and also in air-planes which is made possible by means of power electronics. In terms of applications, motor drives, and lighting

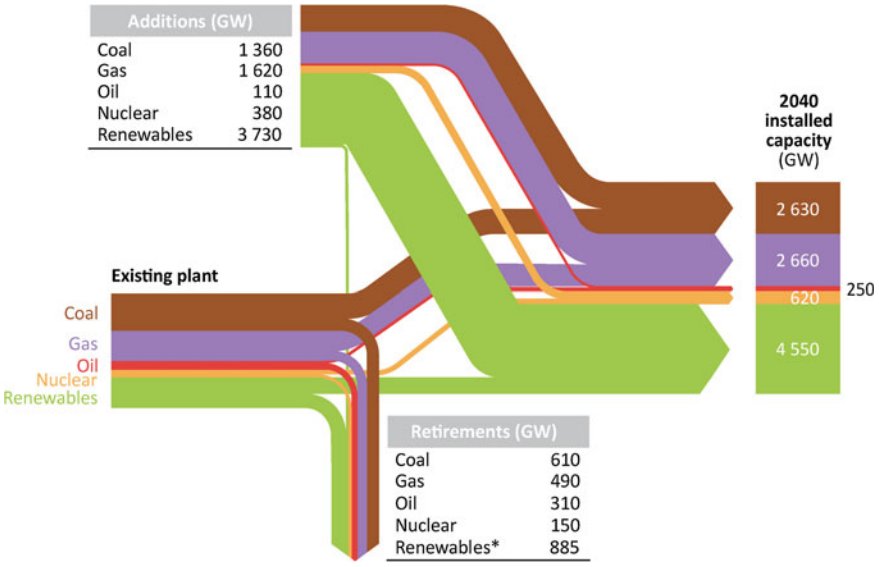

Fig. 1.2 Power generation capacity flow by source from 2014 to 2040 projected by the International Energy Agency (IEA) (*over the projection period, a portion of renewable additions is retired, with the assumption of 25 years of lifetime for wind farms and solar photovoltaics plants) [3] © OECD/IEA 2014, World Energy Outlook 2014, IEA Publishing. Licence: www.iea.org/t&c

are two of the dominant ones, which will be discussed in the next two sections, respectively. The end-use energy efficiency of these applications plays a key role in reducing CO_2 emissions as discussed in [4, 5].

1.3 Power Electronics for Adjustable Speed Drives

Electric motors consume more than 40% of global electrical energy, as shown in Fig. 1.3. This share is even higher in industrial applications, where electric motors are utilized for approximately 64% of industrial electricity consumption [6, 7].

In fact, the high demand for electric motors in different applications such as pumps, fans and conveyer systems has made them as the major source of electricity consumption. Therefore, developing energy efficient motor drive systems holds a great potential for reducing the worldwide energy consumption.

Introducing Adjustable Speed Drive (ASD) based on power electronics technology leads to more energy efficient motor drive systems. An ASD improves energy efficiency of a system by controlling the speed of motor at an optimal speed and/or torque. Hence, the energy consumption of the motor is reduced from full power to a partial power for the same performance (i.e., speed and/or torque). However, in order to achieve the maximum possible energy savings of a system, understanding the application demand and operating mode of an ASD, its system architecture and components are mandatory.

1.3.1 Motor Drive Applications

ASDs only contribute to energy saving when different speeds and/or torques are required over time. This means that adding an ASD unit to a motor which has to operate continuously at full speed and full load only result in excessive losses.

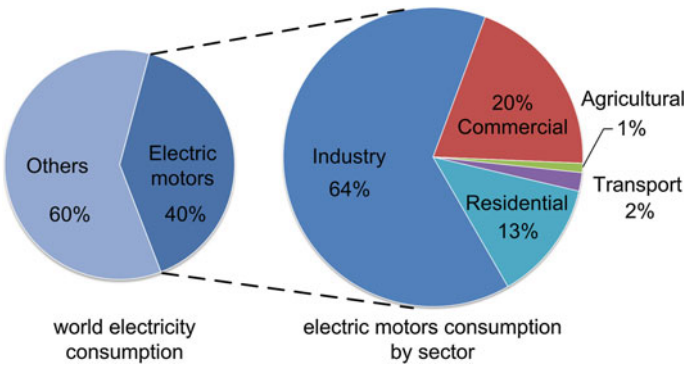

Fig. 1.3 Estimated share of electricity consumption for all electric motors [6]

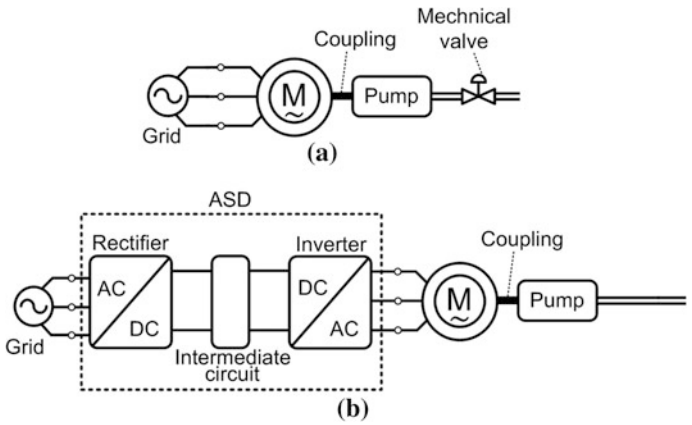

Fig. 1.4 Block diagrams of: **a** direct connected AC motor and **b** ASD

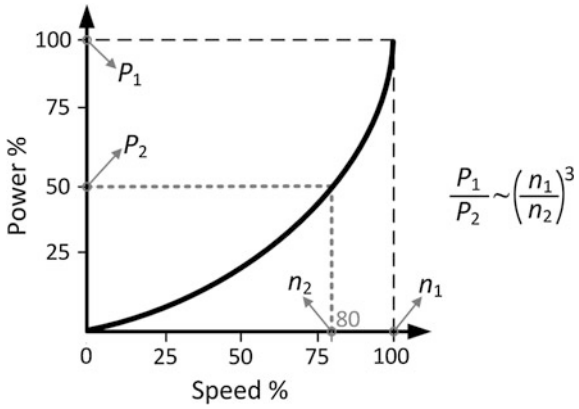

Fig. 1.5 Relation between the out power and speed in variable torque applications (for instance a reduction in speed of 20% results in an energy reduction of 50% [8])

Figure 1.4a exemplifies a direct connected AC motor to a main where a mechanical valve is used to regulate the machine's working point while in Fig. 1.4b an ASD motor drive system is utilized to adjust the speed based on the applied voltage and frequency.

In reality, in most of ASD applications, their load profiles vary over time and the systems are commonly operated in partial load conditions [8]. However, the energy saving potential is different in every application and it can be exploited by understanding the application demand (Fig. 1.5).

1.3.2 System Architecture

Electric motors can operate in generative mode when decelerating from one speed to another or during a braking mode. As illustrated in Fig. 1.6a, standard ASDs are equipped with the conventional line-commutated front-end rectifiers, which provide unidirectional power flow [9]. Therefore, the regenerated power will be dissipated in braking resistors as heat. Feeding the regenerated power back to the grid may improve the system energy efficiency to some extent [8, 10]. This requires bidirectional power flow in ASDs which is achievable by replacing the conventional front-end rectifier with a regenerative rectifier such as Active Front-End (AFE). The resulting system is known as back-to-back topology shown in Fig. 1.6b.

Although most applications generate energy during deceleration and braking, but feeding back this energy to the grid not necessarily justify the use of regenerative rectifiers in an ASD system. This is due to the fact that a regenerative rectifier accounts for more active components comparing with a standard rectifier unit.

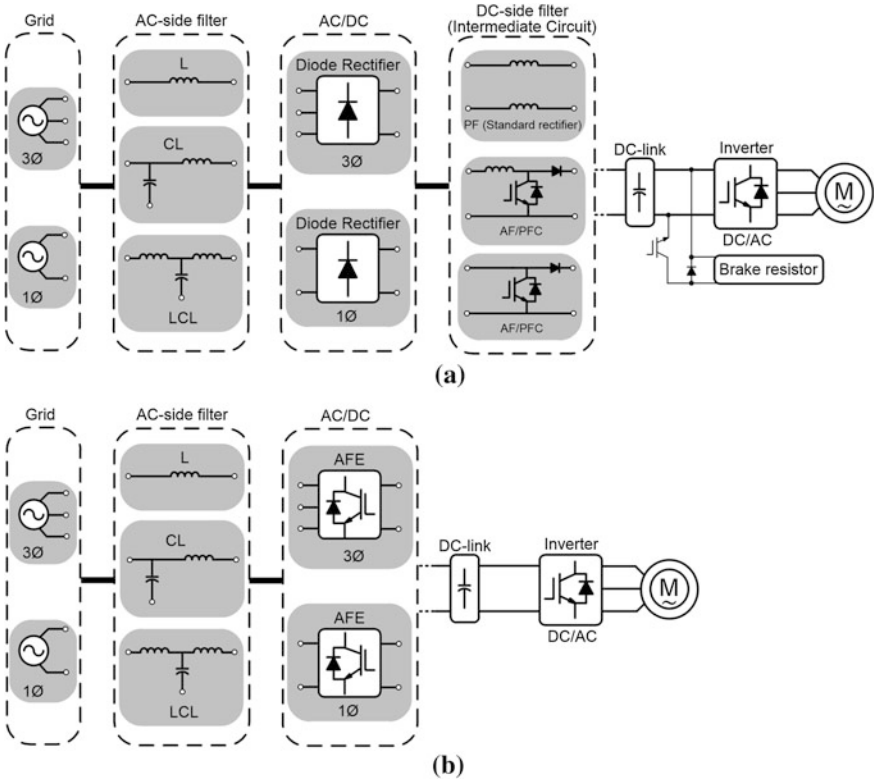

Fig. 1.6 Typical single-phase and three-phase front-end rectifier configurations in an ASD system with possible Passive Filtering (*PF*) and Active Filtering (*AF*) with **a** unidirectional rectifier and **b** regenerative rectifier system

However, despite the losses in an ASD system, to select proper system architecture the grid side efficiency needs to be accounted as well.

From power quality point of view the main concern with ASD systems is the generation of current harmonics which may lead to high losses and stability issues in the grid [11]. To cancel out the harmonics, additional passive or active filtering needs to be employed at the front-end stage of the ASD [12–14]. While such a technique has been matured in single-phase systems, known as Power Factor Correction (PFC), it still remains a big challenge in three-phase systems [7, 9, 12–14].

Notably, regenerative rectifiers such as AFE extensively improve input current quality which leads to a better power quality and lower losses from grid side point of view [7, 10]. Therefore, employing a back-to-back system can only be validated by considering the motor regenerative load cycle versus the additional costs and losses affecting both the ASD and the grid.

Another alternative approach in improving energy efficiency is employing a multi-drive or cascaded configuration (Fig. 1.7). In many applications it is a common practice to employ parallel connected drive units (e.g., multi-pump arrangement) [7, 8, 15]. In this situation the application demand is met using multiple modestly sized motor units rather than one single large unit. Hence, depending on the applied control strategy such as multi-follower or multi-master the load can be shared across the drive units evenly or unevenly, respectively [15]. This configuration can satisfy partial load conditions more efficiently by keeping majority of units in standby mode. Moreover, it allows easier system diagnosis and leads to better redundancy. More importantly, by implementing a proper interaction among the parallel connected units the input current harmonics can be significantly reduced leading to a better power quality and losses from grid side point of view [7].

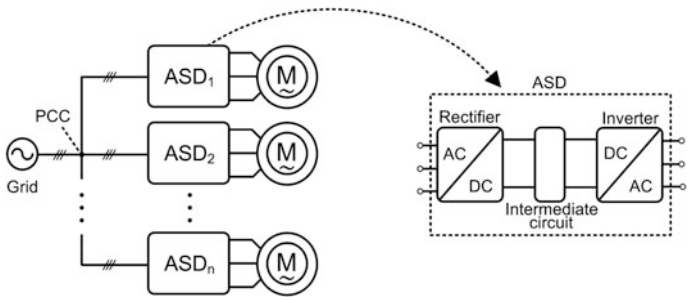

Fig. 1.7 Block diagram of a multi-drive configuration of ASD units

1.3.3 System Components

Every component contributes to system losses. In power electronics systems switching losses of power semiconductors dominate significant share of total system losses. Figure 1.8 illustrates typical structures for unidirectional and bidirectional ASD systems. It is obvious that the bidirectional topology having AFE includes larger number of active power switches. Notably, the chopper switch used for braking operation is not in continuous operation in the unidirectional topology. In fact, the introduction of additional losses, cost and size cannot justify the investment in more complex topologies such as AFE in most of the three-phase ASDs.

However, the advent of new power semiconductor devices, known as Wide Band-Gap (WBG) devices, and their continuous decreasing price due to market demand can break through many barriers and provide more degrees of freedom. Employing WBG devices at front-end stage not only significantly improve performance of single-phase systems, but also offer an opportunity to revolutionize the next generation of three-phase ASD systems.

To sum up, although each three aforementioned sections can affect energy efficiency, but the ultimate efficiency are to be made by optimizing the entire system, which can be obtained by considering a trade-off between different sections.

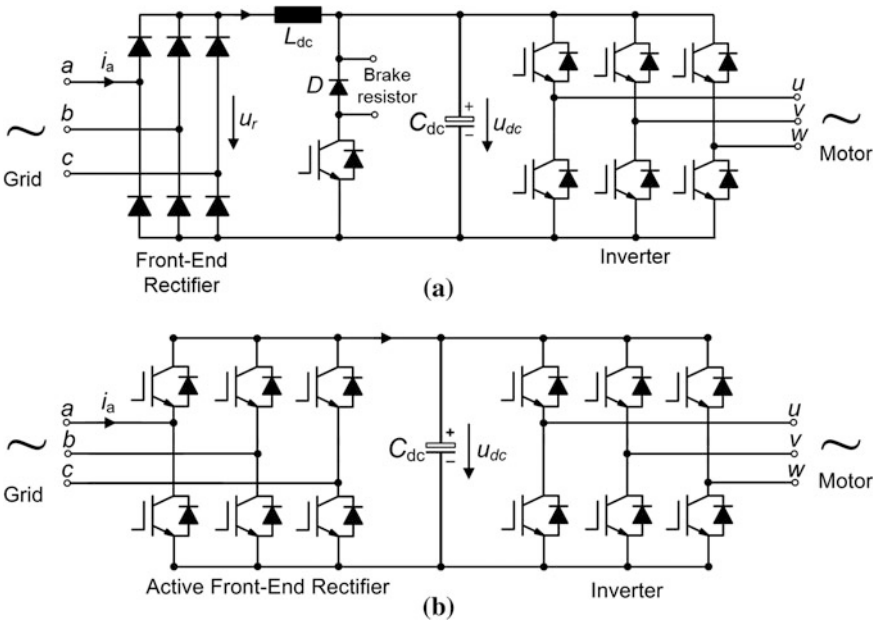

Fig. 1.8 Block diagram of typical ASD systems: **a** unidirectional structure with diode rectifier, **b** bidirectional structure with AFE

1.4 Power Electronics for Lighting

1.4.1 Evolution of Lighting Technology

Since the first incandescent light bulb was invented in 1879, lighting began to consume electrical energy. Nowadays electric lighting has accounted for 22% of the total electricity energy used in the world [16], and about 10% of the average household's energy use goes into lighting costs. Hence, energy-efficient lighting is potential to improve the global energy saving and cut users' energy cost.

In the last century, technology evolution has occurred in the lighting sources, which brings various efficient and durable lighting lamps suitable for different indoor and outdoor applications. According to the technology development, they can be classified as heated filaments (e.g., traditional incandescent and energy-saving incandescent (tungsten halogen) lamps), gas dischargers (e.g., tubular and compact fluorescent lamps (CFL), and high intensity discharge (HID) lamps), and currently most promising solid state lighting, i.e., Light-Emitting Diode (LED) lamps. Figure 1.9 compares the luminous efficacy among these different types of lamps, where the LED lighting has incomparable advantages on high luminous efficiency and also extremely long lifetime to become the dominant lighting source in the near future.

To promote more energy saving, some government in the world, such as European Union, United States, and China have introduced measures to phase out traditional incandescent lamps gradually [17]. LED lamps are the prospective successors.

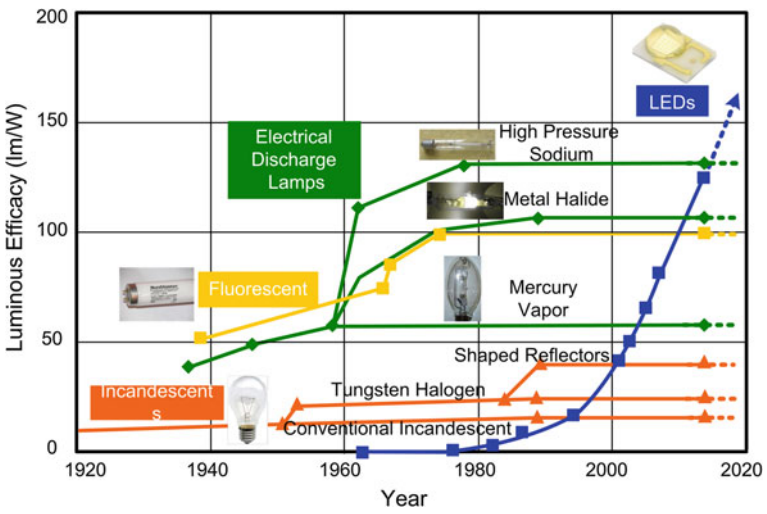

Fig. 1.9 Comparison of luminous efficacy among different types of lighting lamps

1.4.2 Energy Efficient and Intelligent Lighting Power Electronics

Due to different light emitting principles, some lamps may not operate properly or even fail without power electronic drivers. Efficient lighting power electronics can improve the efficiency by a minimum of 20%. Intelligent power electronic drivers with dimming can further save on average an additional 30%.

Filament incandescent lamps can be heated directly by AC mains. TRIAC incandescent dimmer can change the turn-on phase of input voltage to dim light. Compared to incandescent lamps, gas discharge lamps offer higher efficiency, but are more complicated to manufacture and require auxiliary electronic equipment such as high voltage initiation circuit to excite the gas atoms and driving ballast to control current flow through the gas. Thus, the frequent turning on and off for these lamps will affect the operating life and there are some rules for CFL blub dimming. As the current-driven semiconductor, LEDs have fast dynamic response and the operating life is unaffected by turning them on and off. A small increment in driving voltage will cause the current increasing dramatically. Therefore, an LED driver should provide a constant DC current for a stable light color and lumen output. Figure 1.10 shows the typical LED driving configuration with accurate current control for each LED lamp. Generally, the LED dimming have three main methods: amplitude modulation (AM), pulse-width modulation (PWM) and TRIAC dimming. AM and PWM dimming can be integrated in LED driver with smart and simple dimming control for user requirement. TRIAC dimmers are suitable for the interim lighting fixtures, which are expected to have the ability of accommodating both incandescent bulbs and LED retrofit lamps to save the cost.

For the potential solid state lighting, advanced power electronics not only improves the energy saving in the energy transformation, but also ensures a reliable and durable operation to reduce the running and maintenance cost. For example, the least reliable components in the LED driver are energy-buffering electrolytic capacitors, i.e., the main storage capacitor as shown in Fig. 1.10, most of which last below 5,000 h, far from the LED lifetime. LEDs emit heat, and 70–80% of

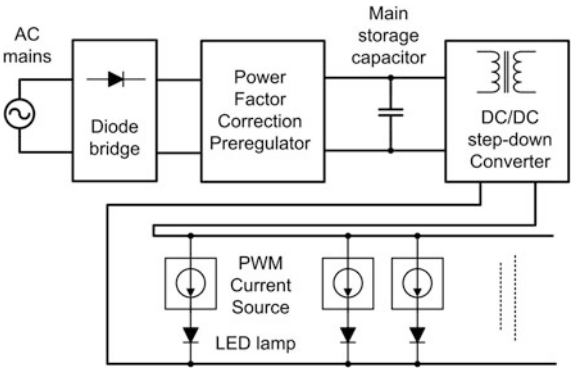

Fig. 1.10 Typical LED driving configuration for multiple lamps

electrical power are radiated as heat. Without good thermal control, heat from LEDs and driver will significantly reduce the LED output lumen efficiency and lifetime. By taking into account the electrical, thermal and optical issues, efficient and intelligent lighting power electronics should integrate sensors, actuators and dimmer control schemes to offer more functions, and develop more compact, efficient, and reliable drivers and control, leading to optimal LED lighting systems.

The future of both domestic and professional lighting is in the application of LEDs, by taking advantages of the technology's intrinsic qualities. This will lead to products that inspire designers and enable lighting to develop in ways that conventional lighting systems could never do.

1.5 Emerging Opportunities and Challenges

Power electronics technology is highly evolving and becoming more and more multi-disciplinary based, bringing new opportunities and challenges in energy saving and electrical energy conditioning. One of the promising opportunities is the commercialization of WBG semiconductor devices (e.g., SiC and GaN) in the last decade. These new devices enable further power loss reductions and extended operation ranges, which are otherwise limited by Si based devices in terms of voltage rating and maximum allowable junction temperature. Figure 1.11 shows the figure of merit of SiC, GaN, and Si devices [18]. One of the important challenges is

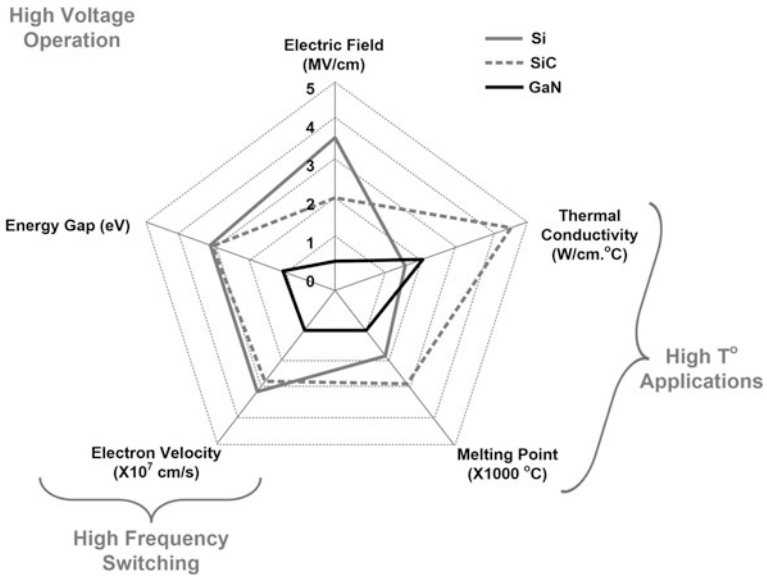

Fig. 1.11 Figure of merit of SiC, GaN and Si based power semiconductor devices [18]

Table 1.1 Typical lifetime target in different power electronics applications

Applications	Typical design target of lifetime
Aircraft	24 years (100,000 h flight operation)
Automotive	15 years (10,000 operating hours, 300,000 km)
Industry motor drives	5–20 years (60,000 h in at full load)
Railway	20–30 years (73,000–110,000 h)
Wind turbines	20 years (120,000 h)
Photovoltaic plants	5–30 years (90,000–130,000 h)

the reliability of power electronic systems, especially due to the increasing reliability requirements and more stringent cost constraints as discussed in [19–21]. Table 1.1 lists the typical lifetime targets in different applications.

1.6 Conclusions

The key role of power electronics in energy saving and highly-efficient electrical energy conditioning is discussed in this chapter. More and more power electronics systems will be used, especially as renewables are becoming the mainstreamed electrical energy sources, and the transportation sector sees a clear trend of electrification. The power electronics applications in ASDs and solid-state lighting systems are discussed. The future opportunities in WBG power semiconductor devices and the challenges in reliability aspect performance are also addressed.

References

1. Blaabjerg F, Ionel DM (2015) Renewable energy devices and systems—state-of-the-art technology, research and development, challenges and future trends. Electr Power Compon Syst 43(12):1319–1328
2. European Center for Power Electronics (ECPE) (2007) Position paper on energy efficiency—the role of power electronics, March 2007
3. IEA report (2014) world energy outlook 2014
4. IEA report (2015) Tracking clean energy progress 2015—energy technology perspectives
5. Gerber JP, Ferreira JA, van Wyk JD (2011) Quantifying the value of power electronics in sustainable electrical energy systems. IEEE Trans Power Electron 26(12):3534–3544
6. Waide P, Brunner C (2011) Energy-efficiency policy opportunities for electric motor-driven systems. In: International energy agency working paper, energy efficiency series
7. Davari P, Yang Y, Zare F, Blaabjerg F (2016) A multi-pulse pattern modulation scheme for harmonic mitigation in three-phase multi-motor drives. IEEE J Emerg Sel Topics Power Electron 4(1):174–185
8. Danfoss (2008) Facts worth knowing about frequency converters. Danfoss, Nordborg
9. Kolar JW, Friedli T (2013) The essence of three-phase PFC rectifier systems—Part I. IEEE Trans Power Electron 28(1):176–198

10. Rodriguez JR, Dixon JW, Espinoza JR, Pontt J, Lezana P (2005) PWM regenerative rectifiers: state of the art. IEEE Trans Ind Electron 52(1):5–22
11. Kumar D, Zare F (2016) Harmonic analysis of grid connected power electronic systems in low voltage distribution networks. IEEE J Emerg Sel Topics Power Electron 4(1):70–79
12. Davari P, Yang Y, Zare F, Blaabjerg F (2016) Predictive pulse pattern current modulation scheme for harmonic reduction in three-phase multi-drive systems. IEEE Trans Ind Electron 62(9):5932–5942
13. Davari P, Zare F, Blaabjerg F (2016) Pulse pattern modulated strategy for harmonic current components reduction in three-phase AC-DC converters. IEEE Trans Ind Appl 52(4):3182–3192
14. Klumpner C, Blaabjerg F, Thogersen P (2006) Alternate ASDs: evaluation of the converter topologies suited for integrated motor drives. IEEE Ind Appl Mag 2(2):71–83
15. Vacon: Multiple pumps—simple control. http://www.vacon.com/fr-FR/Vacon/media/Articles/Multiple-pumps—simple-control
16. Department of Energy. http://www.energy.gov/public-services/homes/saving-electricity/lighting
17. https://en.wikipedia.org/wiki/Phase-out_of_incandescent_light_bulbs
18. Yole Development (2015) Market and technology trends in WBG power module packaging, presentation at IEEE APEC
19. Wang H, Liserre M, Blaabjerg F (2013) Toward reliable power electronics—challenges, design tools and opportunities. IEEE Ind Electron Mag 7(2):17–26
20. Wang H, Liserre M, Blaabjerg F, de Rimmen PP, Jacobsen JB, Kvisgaard T, Landkildehus J (2014) Transitioning to physics of failure as a reliability driver in power electronics. IEEE J Emerg Sel Top Power Electron 2(1):97–114
21. Chung H, Wang H, Blaabjerg F, Pecht M (2015) Reliability of power electronic converter systems, IET. ISBN: 978-1-84919-901-8

Part I
Energy Harvesting

Chapter 2
Hybrid Energy Harvesters (HEHs)—A Review

Nazenin Gure, Abdulkerim Kar, Erturul Tacgin, Alper Sisman and Naser Mahdavi Tabatabaei

Abstract In this millennium, the methodologies to harvest existing dissipated powers not only supply input energy to our sophisticated devices, but also contribute the current technological researches and developments. Single harvester generator or harvesting single power source may remain insufficient for the energy feed into the systems like electronic devices, biosensors, human, structural and machine health monitoring, and wireless sensor nodes. To overcome this problem, hybridization of energy harvesters (EHs) takes place to increase the limited energy generation of stand-alone EHs. In this chapter, piezoelectric and electromagnetic generators are compared and classic as well as novel hybrid energy harvester (HEH) designs are reviewed by considering fixed-frequency; broadband including linear, nonlinear and tunable HEHs; multimode; and multisource powered configurations. This review covers two-, three-, four-multi source powered HEHs in micro-, meso- and large-scales. Overall comparisons of classic and novel HEHs are tabulated and discussed in detail in order to guide potential researchers. In the scope of this

N. Gure (✉) · A. Kar · E. Tacgin
Faculty of Engineering, Department of Mechanical Engineering, Marmara University, Goztepe Campus - Kadikoy, Istanbul, Turkey
e-mail: nazeningure@marun.edu.tr; nazeningure@hotmail.com

A. Kar
e-mail: akar@marmara.edu.tr

E. Tacgin
e-mail: ertugrul.tacgin@marmara.edu.tr

A. Sisman
Faculty of Engineering, Department of Electrical and Electronics Engineering, Marmara University, Goztepe Campus - Kadikoy, Istanbul, Turkey
e-mail: alper.sisman@marmara.edu.tr

N.M. Tabatabaei
Faculty of Engineering, Department of Electrical Engineering, Seraj Higher Education Institute, Tabriz, Iran
e-mail: n.m.tabatabaei@gmail.com

N. Gure
Enhas R&D Energy Systems Ind. Co. Ltd, Maltepe, 34844 Istanbul, Turkey

N. Bizon et al. (eds.), *Energy Harvesting and Energy Efficiency*,
Lecture Notes in Energy 37, DOI 10.1007/978-3-319-49875-1_2

chapter review, it is seen that HEHs generate greater power outputs than its single harvester components. The most promising power and energy generations are 315 mW by four-source powered novel HEH in meso-scale, 215 μW by tunable broadband classic HEH in microscale and 440 kW h/day by partially three-source powered HEH in large scale. This chapter indicates that HEHs not only increase the output powers and power densities, but also enables endless configurations to maximize harnessing existing power sources.

Keywords Hybrid energy harvesting · Multimode energy harvesting · Multisource energy harvesting · Novel energy harvesters · Microscale energy harvesting · Large-scale energy harvesting

Abbreviation and Acronyms

A-Si	Amorphous Silicon
AGS	Automatic Generating System
DPE	Direct Piezoelectric Effect
EM	Electromagnetic
EMHs	Electromagnetic Energy Harvesters
EHing	Energy Harvesting
HAWT	Horizontal Axis Wind Turbine
HEHs	Hybrid Energy Harvesters
HRTHs	Hybrid Rotary-Translational Harvesters
MEMs	Microelectromechanical Systems
PAGV	Power Augmentation Guide Vane
PE	Piezoelectric
PEHs	Piezoelectric Energy Harvesters
PET	Polyethylene Terephthalate
PV	Photo-voltaic
PZT	Lead Zirconate Titanate
RF	Radio Frequency
SME	Shape Memory Effect
TENG	Triboelectric Nanogenerator
VAWT	Vertical Axis Wind Turbine
WiSH	Wind-Solar Hybrid

2.1 Introduction

Ever since the beginning of the industrial age, being independent from man and animal power sources, especially at greater energy levels, was the greatest innovation. As the time passes by, the more technological improvements occur along

with wireless networks, the more devices are in our lives thus, elevating the quality of life, production and work. In spite of the efforts to decrease the energy input of the electronic devices, this ever increasing demand on energy surprisingly takes us to seek using existing power sources like human movement, known as kinesiology, similar to the energy source before industrial age [1–3]. In this millennium, the methodologies to harvest existing dissipated powers not only supply input energy to our sophisticated devices, but also contribute the current technological researches and developments. Among energy harvesting (EHing) systems, one of the innovative research trend is on hybrid energy harvesters [4, 5].

Obeying the first law of thermodynamics, conservation of energy implies that the existing and dissipated power sources can be scavenged and transduce into usable electrical energy [1]. Up until recently, energy harvester (EH) need is arose by the dominant use of electronic devices, biosensors, human, structural and machine health monitoring, and wireless sensor nodes [6–9]. Single harvester generator or harvesting single power source, also known as stand-alone EH, may produce low output powers to supply energy to the system. For sufficient energy feed to these vast varieties of applications, hybridization of EHs takes place to increase the limited energy generation of stand-alone EHs [10–23].

Harnessing multiple power sources or combining multiple generators for energy extraction in a single unit is called "hybrid energy harvesting or multimodal energy harvesting" [24–27].

In this chapter, piezoelectric (PE) and electromagnetic (EM) generators are compared in Sect. 2.2. Classic HEH designs and novel configurations are reviewed in Sects. 2.3 and 2.4, respectively. Sections 2.3 and 2.4 covers fixed-frequency, broadband HEHs, and their comparisons. Furthermore, Sect. 2.4 includes multimode vibration HEHs and multisource powered energy harvesters along with meso-, micro- and large-scale applications. In the final part, HEH performances and evaluations are compared and concluded.

2.2 Comparison of Piezoelectric and Electromagnetic Generators

EM energy harvesters (EMHs) generate power based on faraday's law of induction, which equates the time derivative of flux to the electromotive force. As the scale shrinks to microscopic level, the decreased coil area results smaller magnetic flux. On the other hand, quasi-static (ultra-low-frequency) movements increase the time intervals. Thus, both factors lead electromotive force to approach to zero. Apart from the fabrication boundaries of coil diameters and turns, theoretically EM harvesters are bound to be limited at low speeds [28]. Thus, EM harvesters perform better at high frequencies and PE harvesters outperform at low frequencies [8]. Additionally, at microscale level, EMH output voltage generally stays lower than the need to power devices [17]. As a result, piezoelectric and electrostatic harvesters

are more suitable for microscale applications, while electrostatic systems hold greater advantage due to the ease of integration to microelectromechanical systems (MEMs) [27].

Similar to EMHs, PE harvesters (PEHs) do not require voltage source while electrostatic generators require separate voltage source and more difficult in practice, and in contrast to EMHs, PEHs produce sufficient output voltage but at low current level [8, 19, 27]. Among these three types of transducers, piezoelectric generators are the simplest ones in terms of required components, transducer geometries and directly converting mechanical energy to voltage output [9]. In addition to PEHs, at macroscopic level, EMHs also provide simplicity in geometry, design and production [19].

In conclusion, PEHs are applicable for micro-, meso- and large-scales, while EMHs are easily manufactured and although they perform better at mesoscale, they are integrable to MEMs. As a result, abundant PE and EM HEH are reviewed and compared in the following sections.

2.3 Classic HEH Systems

While tremendous amounts of multimode energy harvesters (EHs) are possible, there exist such PE and EM combination that takes the greatest research and development interest and turns out to be classic. As listed in Fig. 2.1, these are composed of piezoelectric plate or patch attachment on Euler-Bernoulli beam and either magnetic or coil tip mass is surrounded by respective coil or magnets to achieve faraday law of induction [29].

In this chapter, PE unimorph and bimorph structures; comparison of rectangular and trapezoidal beams; four and two poles magnet configurations and comparisons; serial, parallel and isolated connections of PE and EM transducers in HEHs; fixed-frequency applications; and rarely studied broadband HEH designs are reviewed.

2.3.1 Fixed-Frequency Classic HEHs

Figures 2.1 and 2.2 shows the classic HEH designs and fabrications, respectively. As a brief summary, in 2008, Wischke and Woias researched PE layers on unimorph and bimorph cantilevers with rectangular and trapezoidal layouts in HEH. It is seen that trapezoidal shape is not superior in terms of power generation and its fabrication is more complicated. Since unimorph HEH has greater tip velocity, EM transducer generates greater power. In contrast to unimorph design, bimorph PE part produces greater output than EM part. Upon this contrary output, authors suggest using greater tip mass (magnet) to reduce EM coupling [11]. Becker et al.

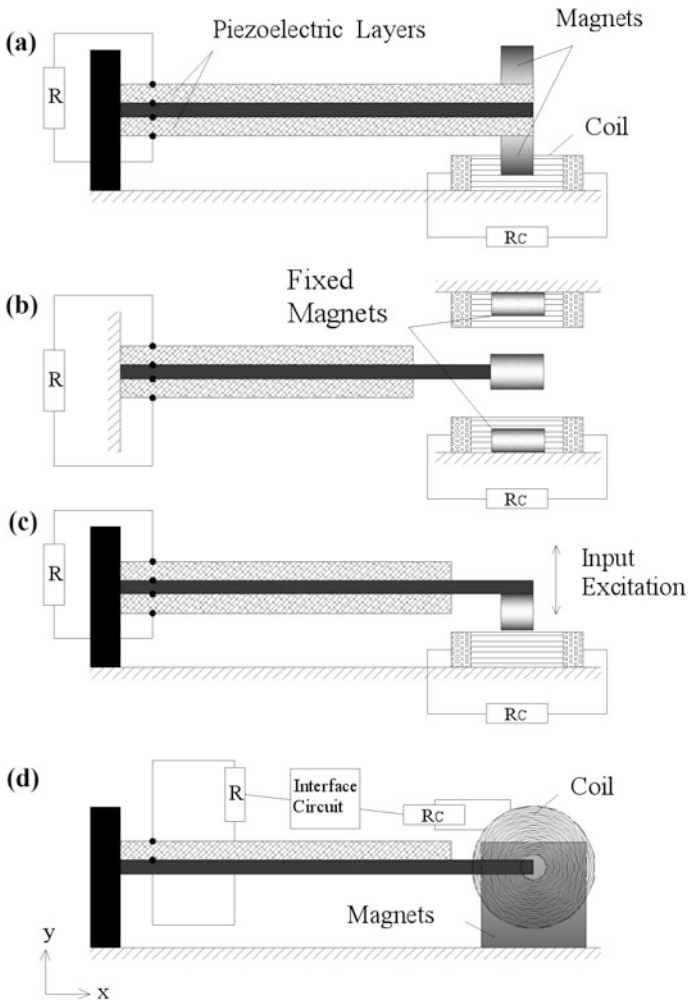

Fig. 2.1 Classic energy HEH configurations are categorized and illustrated. **a** [20, 25, 26, 33–36] and **c** [30, 32, 37] are the most common ones and the tip mass can either be two magnets as in (**a**), or single magnet surrounded by coils as in (**b**) [4, 15] and (**c**), or vertical coil surrounded by magnets as in (**d**) [20, 33, 38] as well as modified horizontal arrangement [21]. Along with varying PE length on beam, PE unimorph (**d**) and bimorph (**a**, **b** and **c**) cantilever configurations are also possible [11]. Interface circuit is schematically indicated on (**d**)

begin to test HEH prototype in Fig. 2.1c and research further for its adaptation into synchronized switch harvesting interface [30].

Xu et al., both theoretically and experimentally analyzed PE and EM HEH. Theoretical optimum output power is 1.02 mW at 77.8 Hz and experimental value is 0.845 mW at the resonance frequency of 66 Hz under the vibration acceleration of 9.8 m/s^2. Respective to single PE and EM transducer, output powers are 667 and

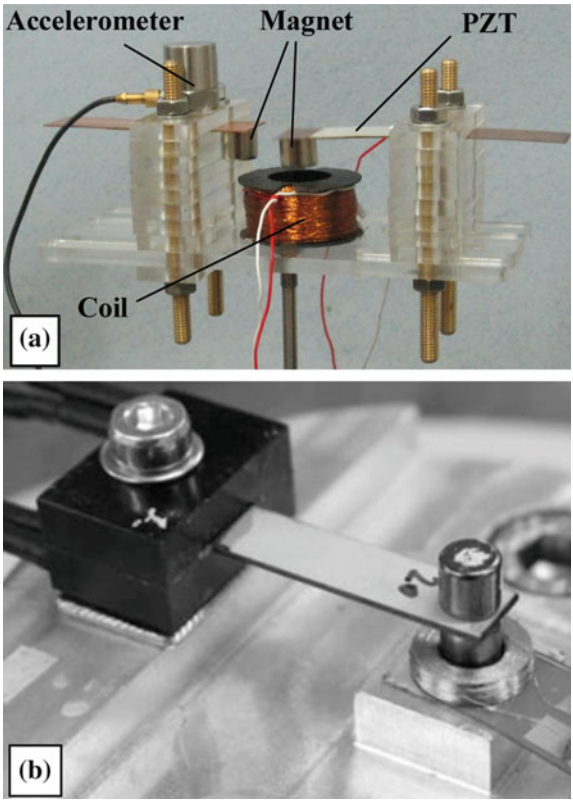

Fig. 2.2 Classic HEH prototypes in test setup [25, 39, 40]

0.32 mW at 9.8 m/s^2 and 66 Hz. Xu et al. proves that presented HEH generates greater power than single EHs [31].

Ali et al., investigated total power outputs of PE and EM harvesters in serial, parallel connection and separately. As seen in Fig. 2.1c, the HEH has approximately 1000 turns and 4 magnets (25 $\times$ 10 $\times$ 5 mm^3) with opposite polarization at cantilever tip. At the fixed input frequency of 76.2 Hz, total generated power is the highest when PE and EM transducers are isolated. While PEH generates 27.56 mW, EMH generates the lowest power output. Besides, single PEH output power is 3 times greater than serial connected HEH and parallel connected HEH generates 3 times more than single EM transducer [32].

As a recent study, Xia et al. not only investigates the classic HEH but also compared the performances of HEH and EMH (Fig. 2.1c). Throughout the experiments best HEH case generated the output power of 2.26 mW with 41% efficiency at 23.3 Hz and 0.4 g input excitation and thus, greater performance compared to EMH alone. HEH not only owns greater output power and efficiency, but also enables broadband operation [33]. In contrast to these findings, Sang and Shan et al. experiments result that HEH has the almost the same resonance frequency with the PEH. Sang et al., considered the valuable Classic HEH

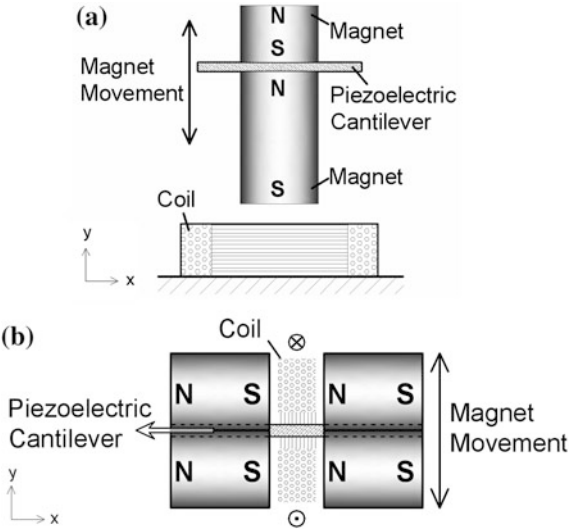

Fig. 2.3 **a** *Two-pole* and **b** *four-pole* magnet arrangements on classic HEH designs [20, 34]

configurations and yet, similar to Fig. 2.1c with only difference of having vertical coil placement on both sides of magnet is researched for four different cantilever lengths. HEH with cantilever and PE layer respective sizes of 50 × 15 × 1 mm^3 and 30 × 15 × 0.5 mm^3, generated 10.7 mW while EM alone was 5.9 mW at 50 Hz with the acceleration of 0.4 g [21]. Supportively, Shan et al. also reported that HEH produced greater output power of 4.25 mW than single PEH of 3.75 mW at 40.5 Hz and optimum loads. Their design is slightly modified version of Fig. 2.1c, d. The U-shaped magnet cage is fixed at the beam end and coil was fixed filling the gap in U-shape magnets during vibration [16].

Ab Rahman et al. studied two and four pole magnet arrangements on classic HEH in Fig. 2.1a, d, respectively (see Fig. 2.3). It is experimentally proved that each HEH transducer with four-pole magnets produce greater output voltage than two pole HEH. When the input excitation is 1 g, generated output powers of four pole type PE and EM parts were 2.3 and 3.5 mW at 15 Hz, whereas those outputs were 0.5 and 1 mW at 49 Hz for two pole HEH [20, 34]. More detailed comparison of four-, two- and single magnet novel HEH performances are studied by Castagnetti and covered in Sect. 2.4.2 [35].

2.3.2 *Broadband Classic HEHs*

The ever-demanded ideal EH efficiently performs in wide bandwidth. In order to satisfy this demand, many researches have been conducted and broadband EHing is still one of the popular EHing research subjects. These researches include passive tuning either manually or with linear, non-linear, multi-stable and band-pass harvester structures; and active tuning which may result in negative power outputs due

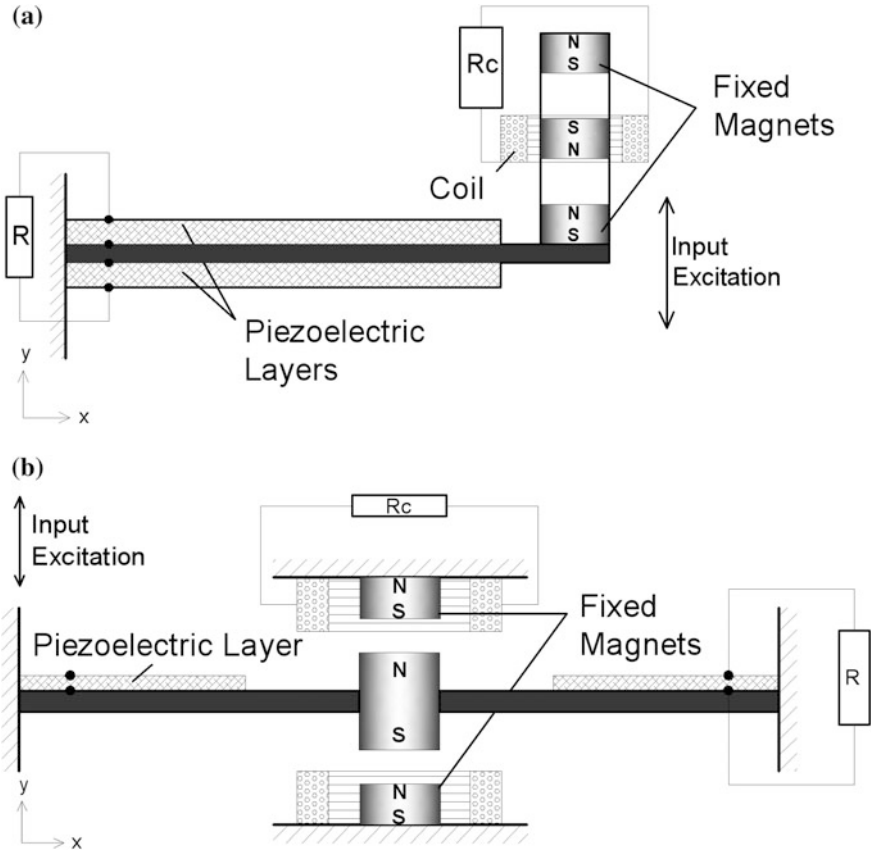

Fig. 2.4 **a** Shan et al. [15] and **b** Ping Li et al. [4] broadband HEH. NdFe35 magnet and PZT-5H ceramics are used as EM and PE transducer components on Shan et al. prototype. Mahmoudi et al. used oppositely aligned magnets and unimorph PE layers in (**b**) configuration [29]

to consumed energy by active parts and advanced electronic networks [26, 36, 37]. Among these efforts, there are some classic HEH design approaches exist. Operation of an EH within wider frequency band is a very significant advantage in EHs. A few studied novel micro scale HEHs are also mentioned in this section for being broadband.

Linear Classic HEH: In 2013, Ping Li et al. designed similar to Fig. 2.4b without fixed magnets. They analyzed their linear HEH performance under white noise excitement to model random vibration. Their sensitivity analysis indicated that the power generation of HEH dominantly affected by vibration frequency, damping ratio, coupling coefficients, which widens the bandwidth and increase power output as increases, and load resistances to achieve HEH impedance matching and maximize power generation. While PE load directly proportional to resonance

frequency of harvester, EM load has almost no effect. The most efficient performances have the mean power levels of 0.44, 1.93, 4.2 mW at 77.5 Hz [17, 38].

Tunable Classic HEH: Wischke et al. focused on frequency tuning method for HEH exactly shown in Fig. 2.1a and the picture of the prototype is on the in Fig. 2.2a. In this technique, voltage is introduced to the PE layer. Applied voltage changes the stiffness of the generator and relatedly, resonance frequency. By matching input frequency with tuned generator's resonance frequency, broadband operation is achieved. Electrode length's effect on tunability is also investigated and found that greater than 10 mm PE beam length, tunable range almost saturates between ~50 to 60 Hz. To investigate widest tunable range, fabricated HEH cantilever length was 20 mm with the width of 5 mm. Extractable output powers from EM part is 60 μW, for PE part with parallel connection is around 200 μW and with serial connection it is 215 μW. EM transducer generated minimum of 50 μW at 56 Hz wide operation band width around the range of 267–323 Hz [25, 39].

Non-linear Classic HEHs: One method to achieve broadband operation is that harvester to be nonlinear so that the frequency response range between half power outputs can be widen [35]. Li et al. summarized nonlinear broadband mechanism such that as nonlinearity increases, resonance frequency decreases and as the acceleration increases, half power bandwidth broadens, whereas resonance frequency decreases [4].

As inspired from classic HEHs in Fig. 2.1b and c, Shan et al. design and materials are illustrated in Fig. 2.4a. In magnet configuration, poles are oppositely aligned so that indirectly exerted force on the suspended magnet can yield nonlinear mono-stable HEH [15]. Two peak powers and modes of HEH are 11.4 mW at 8.373 Hz by EM and 21.6 mW at 14.83 Hz by PE transducers. At half peak power, the device band is around 7–17 Hz [15].

In Addition to HEH in Fig. 2.1c, Xu et al. used same pole magnet aligned in front of the tip magnet (Fig. 2.2a) so that HEH can be nonlinear and operate at larger frequency band. Their nonlinear HEH prototype achieved 5.66 mW power output at 1 g, this result is 247% greater than at 0.5 g and at half power level (3 dB), the frequency band is 83.3% wider than PE transducer alone [40].

Recently, HEH illustrated in Fig. 2.4b is researched by Mahmoudi et al. [29] and Ping Li et al. [4]. Their device mirrors the configuration in Fig. 2.1b; opposite pole magnet arrangement is used by Mahmoudi et al. and same pole magnet arrangement is used by Ping Li et al. While the moving magnet is shared with both symmetrically placed beams having bimorph PE layers by Mahmoudi et al. and lead zirconate titanate (PZT) patches by Ping Li et al. For Mahmoudi et al. HEH, EM and PE parts respectively produce 39 and 61% of the power output. This EM transducer can increase power density by 60% up to 1035 mW/cm^3 and bandwidth by 29% (155 to 220 Hz) at 0.9 g with respect to single EMHs [29]. Ping Li et al. deeply studied modeling, tests, effects of nonlinear factors, loads, input frequency and acceleration on amplitude, and found that their HEH design both enhance as wider band with low resonance frequency and greater power output compared to linear HEH designs. In contrast to linear EHs, optimal loads differ with excitation

acceleration. Apart from Ping Li et al. statement, their theoretical and experimental frequency responses show no significant band widening other than shifting the linear resonance frequency from 119 down to 113.5 Hz. Experimental analysis optimum results with respect to input accelerations of 0.2 and 0.45 g are 0.14 and 1.19 mW for EM generator and 0.085 and 0.5 mW for PE generator. The HEH peak power output is 3.6 mW at 0.6 g and ∼110 Hz having half-power frequency range of ∼107.5 to 112.5 Hz [4].

As a different vibration source and application on airflow harvesting system example, hybrid aeroelastic vibration EH is modeled by Dias et al. Their system includes an airfoil that is connected to fixed spring and damper at around mid-plane and starting that point, cantilever beam as seen in Fig. 2.1c is connected. Dias et al. propose 2 and 3 degree of freedom system dynamic modeling [41, 42]. Relatedly, novel aeroelastic HEH harvesting incident sunlight is proposed by Chatterjee and Bryant (Fig. 2.16), and their research is covered in Sect. 2.4.3.2. under 'Two-Multi Source Powered HEHs' title.

2.3.3 *Overall Classic HEHs Comparision*

Up to this end, classic HEHs are classified and their performances are reviewed in terms of generated powers by EM and PE parts as well as the whole HEH system. The important factors of classic HEHs are peak power generations, HEH volumes, magnet masses, input excitations, input frequencies and half power band width ranges. Comparison of reviewed performances in Sects. 2.3.1 and 2.3.2, regarding mentioned factors are listed in Table 2.1.

As seen in Table 2.1, among broadband and the whole classic HEHs, the greatest power output of total of 33 mW (21.6 mW by PEH and 11.4 mW by EMH) is achieved by Shan et al. with HEH configuration as illustrated in Fig. 2.4a [15]. Among fixed-frequency HEHs, Ali et al. reached the greatest power output of 27.56 mW [32]. It is then followed by 10.7 mW via Sang et al. HEH [21], both of HEHs share the similar configuration as in Fig. 2.1c, Sang et al. HEH has almost the half device volume of Ali et al. HEH as well as applying below half of the input excitation.

Shan et al. [16] and Ab Rahman et al. [20, 34] HEHs are around similar power generation levels of 4.25, 5.7 and 5.8 mW, respectively. For broadband HEHs to achieve similar power levels, the device volume expands approximately ten times with and exception of Xu et al. nonlinear HEH (Fig. 2.1a) having almost the same device volume with Ab Rahman et al. HEH [40]. Table 2.1 also indicates that four-pole arrangements [20, 34] are always superior to Ab Rahman et al. two-pole arrangement [20].

Finally, the lowest power outputs belongs to Xu et al. [31] and Wischke et al. (Fig. 2.2b) [25, 39]. However, Xu et al. fixed-band HEH volume is also the smallest device volume in Table 2.1, whereas Wischke et al. tunable HEH owns the second biggest device volume.

Table 2.1 The overall comparison of the reviewed classic HEH systems in Sects. 2.3.1 and 2.3.2

Type	References	Input acc.	Input frequency/bandwidth range (Hz)	Volume (mm^3)	Peak power (mW)	Mass (g)
Fixed-frequency classic HEHs						
	[30]	–	130	–	–	–
	[31]	1 g	66	187.2	0.845	–
	[32]	1 g	76.2	5992	PEH:27.56	–
	[33]	0.4 g	23.3		2.26	11
	[21]	0.4 g	50	2975	10.7	∼15
	[16]	–	40.5	760	4.25	∼21.5
Four-pole	[34]	1 g	15	2280	PEH: 2.2	–
					EMH: 3.5	
Four-pole	[20]	1 g	15	2280	PEH: 2.3	–
					EMH: 3.5	
Two-pole	[20]	1 g	49	1181	PEH: 1	–
					EMH: 0.5	
Broadband classic HEHs						
Linear	[17, 38]	***A****	77.5/∼70–80	29,810	4.2	–
Tunable	[25, 39]	1 g	299/∼267–323	31,201	215 μW	–
Nonlinear	[15]	0.5 g	8.373 for EM	20,726	PEH: 21.6	100
			14.83 for PE/7–17		EMH: 11.4	
Nonlinear	[40]	1 g	∼45.5/∼43–47	2257	5.66	9.8
Nonlinear	[29]	0.9 g	93/155–220	40,000	***B****	–
Nonlinear	[4]	0.6 g	110/∼107.5–112.5	18,437	3.6	–

(*) ***A***: random acceleration with $(0.1\ g)^2$/Hz spectral density of acceleration
(**) ***B***: Peak power density of 1035 mW/cm^3
Note: Device volumes represent the minimum volume occupied by the harvester components and do not include and remaining device parts and the air gaps in HEHs, and Mass generally stands for the only stated magnet mass in references

2.4 Novel HEH Systems

While stand-alone systems are generally bound to be limited by one power source, multimode designs offer never-ending possibilities. Especially, when multi-source powered EHing concept is included as well as multimode HEHs, designs turn out to be novel. In this section, vibrational HEH novel designs are covered along with multiple vibration source harvesting, two and three multi-source powered harvesting systems in meso, micro and large scales.

2.4.1 Fixed-Frequency Single-Source Powered HEHs

As a preliminary study, Reuschel et al. proposed axial flux and radial flux arrangements, where set of opposite pole magnets aligned radially in a radial coil house, designing EMH and PE cantilever modeling for the proposed arrangements. They announce to combine both transducers and analyze HEH as a whole system [43].

Harvesting from human motion is a demanded research subject especially to power personal electronics. Wei and Ramasamy studied harvesting kinesiology and it is shown that the HEH is suitable to feed personal electronics and charged mobile phone in experiments. The mechanical harvesting part composed of flywheel and in each footfall, it runs the shaft connected to one-third of diameter of the actual wheel. Two piezoelectric configurations researched for shoe insole and it is seen that rolled piezoelectric plate is placed in shoe sole. It is seen that though this HEH is slow to charge mobile phone for being able to charge about 10% in 30 min, it is also found that starting from half-fully charged phone. The user can end up with 70% of charge with HEH, whereas without any harvester, charge level would be 16%. Authors assume the potential over one-million personal usages of their harvester. In this case, they foreseen the total power generation of 60,000 kW h [1].

Halim et al. unique components turns classic HEH into novel one. The main harvester body is almost same with the illustration in Fig. 2.4 on the right. Novel parts are the parabolic top of the tip mass, which is intended to move vertically by the non-magnetic ball action during horizontal input excitations (see Fig. 2.5). This mechanism also leads vertical PE bimorph displacement at center and EM induction with magnet attachment. This design is aimed to harvest human motion, thus shaken manually by hand at around 5 Hz during experiments. Resulted frequency responses of EM and PE transducers show that the first mode is at 816 Hz for both parts. Optimum power generation performances are 0.64 mW for EM part and 0.98 mW for PE part of HEH system [14].

2.4.2 Broadband Single-Source Powered HEHs

Linear Novel HEHs: Castagnetti's novel HEH is one of the most innovative one as well possessing 60 Hz-bandwidth. The design concept is composed of Belleville springs (B1 and B2 in Fig. 2.6b and c) and three different case of EM part for having a single magnet as in Fig. 2.6a, 2 magnets (Fig. 2.6c) and four magnets configurations. The vertical frame in (a) is shown horizontally in (c), denoted by "F". Experiments conducted for three cases of HEHs at 1 g and 19.62 m/s^2. Input acceleration of 19.62 m/s^2 yield greater power outputs at resonance frequency. Among HEHs, the generated power of four-magnet HEH is 2 times of two-pole magnet HEH and 8 times of single magnet HEH. The four-magnet HEH

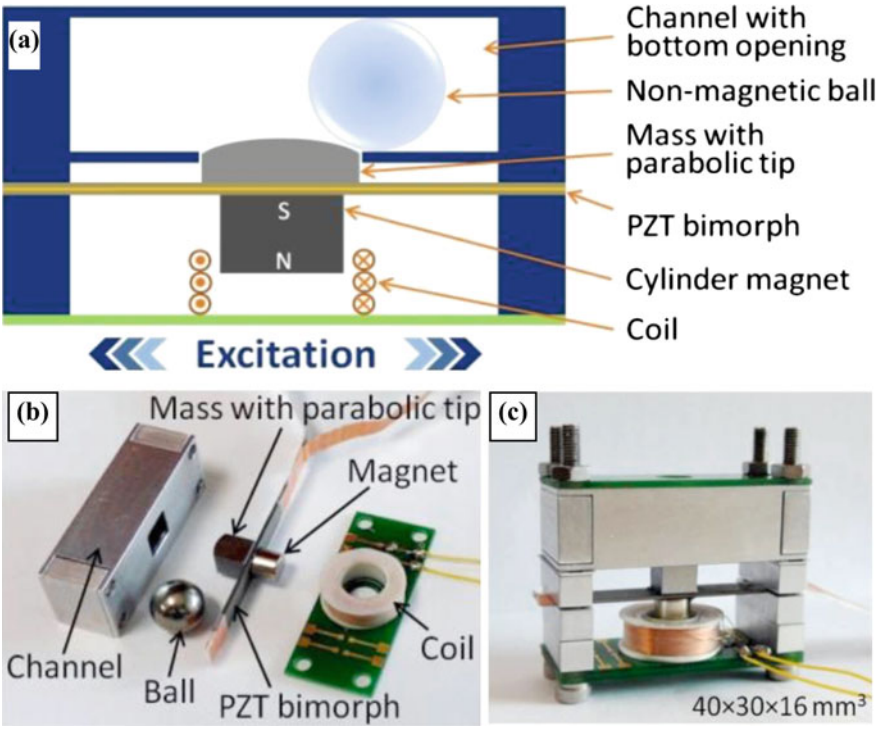

Fig. 2.5 **a** Halim et al. novel HEH design schematic representation, **b** listed fabricated components, and **c** assembled prototype [14]

configuration produced the greater power of 15.31 mW and enables broadband operation from 120 to 180 Hz at 2 g. Castagnetti also reported their HEH is superior than commercial products like Perpetuum in terms of power generation and band-width [35].

Non-linear Novel HEHs: Karami and Inman presented mono and bistable non-linear thus, broadband novel HEH, as seen in Fig. 2.7. As the horizontal input excitation is applied, then, the tip magnet moves harmonically. This oscillation yields EM and PE energy generation. HEH magnets are aligned with opposite polarization and these magnets' distance is arranged such that the HEH can perform as mono or bistable but nonlinear unless the gap is set to 50 mm in order to see linear system performance. Additionally, the system behaves as linear at low input base excitation and nonlinear at greater acceleration inputs. The best power output results are close to 35 μW for EM transducer and 1.5 mW for PE part at 1.7 m/s^2. It is worth to mentioned that linear dynamics of these HEH systems at low excitations [44, 45] are overcome by Leadenham and Erturk's M-shaped PEH design [46].

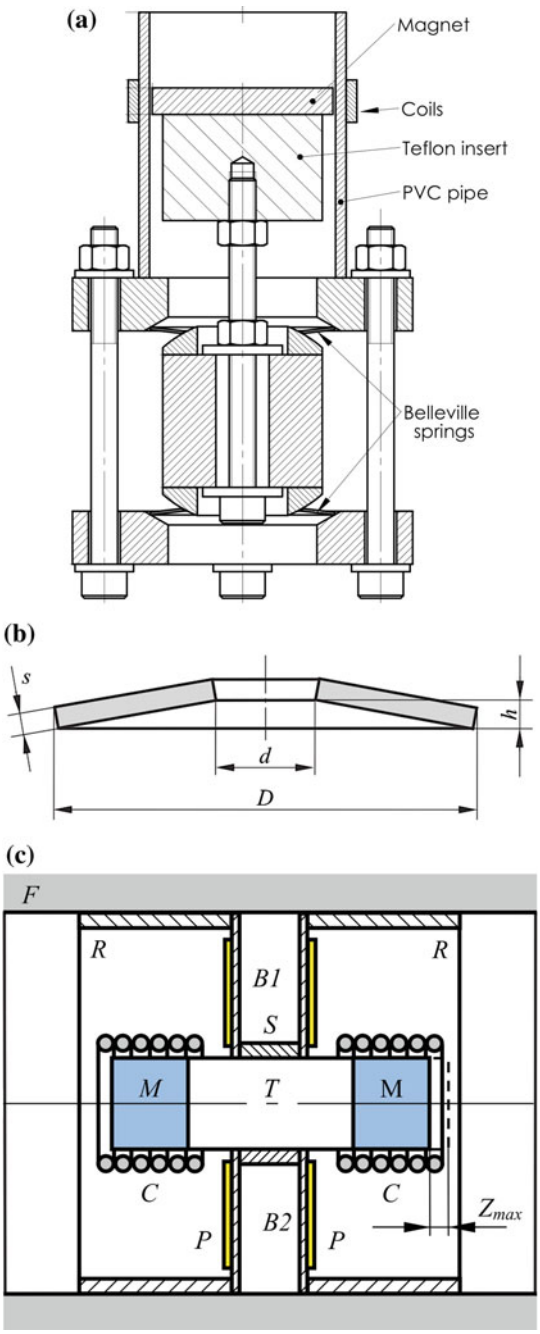

Fig. 2.6 **a** The technical drawing of the Castagnetti's HEH prototype, **b** Belleville spring scheme, and **c** HEH scheme with two magnets [35]

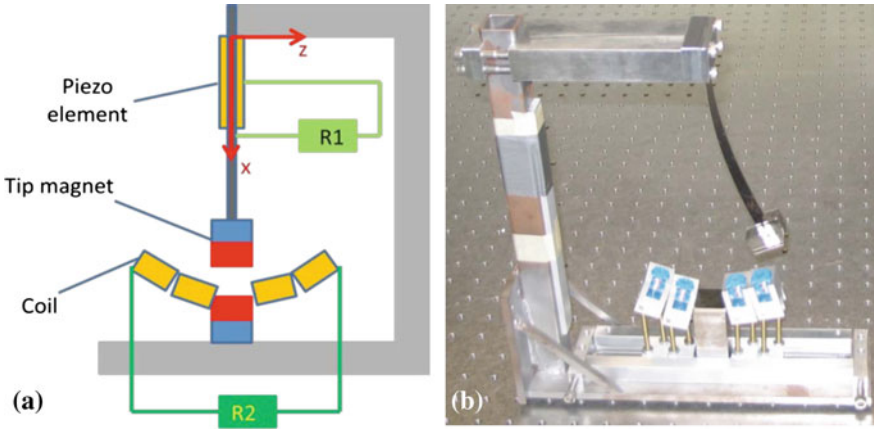

Fig. 2.7 Karami and Inman's design illustration and prototype [44, 45]

2.4.3 Multimode and Multisource Powered HEHs

The term "multimode EH" refers larger literature than "hybrid EH". Further, multimode and multisource power terms are used in title to imply that novel researches of the extreme levels of hybridization of harvesters, multi-vibrational power source types (Sect. 2.4.3.1) and multi-power source inputs (Sects. 2.4.3.2, 2.4.3.3 and 2.4.3.4) are reviewed in this part.

2.4.3.1 Hybrid Rotary-Translational Harvesters (HRTHs)

The characteristics of motion highly affect the harvester design. Unlike the excitement types so far, two axes translational and rotary motions are the realistic cases of vibration inputs as in kinesiology and rotary machines. All these and chaotic or random and varying excitations lead broadband methods, among these, manual tuning is preferably employed for simplicity. However, as an alternative, different types of random motions can be scavenged without active physical input and it is known as "automatic generating system (AGS)" under the Kinetic brand. One classic commonly known commercial example is SEIKO wristwatches. Harmonic movement of the rotor drives the gear train and eventually almost 100 times of the eccentric mass rotational speed is converted to run the EM generator (at 5–15 krpm for 50 ms). In 1988, the device average power output range was 5–10 μW and in 1996 it was 10 μW when worn, 1 mW when shaken with a maximum capacity of 10 mW [47–51]. Sasaki et al. researched this HRTH and analyzed damping, self excited rotation and swinging motions as indicated in Fig. 2.8b. Electric load connection on generator causes rotor axis damping to increase up to some limit for self-excited rotation mode. This electromechanical damping limit is a

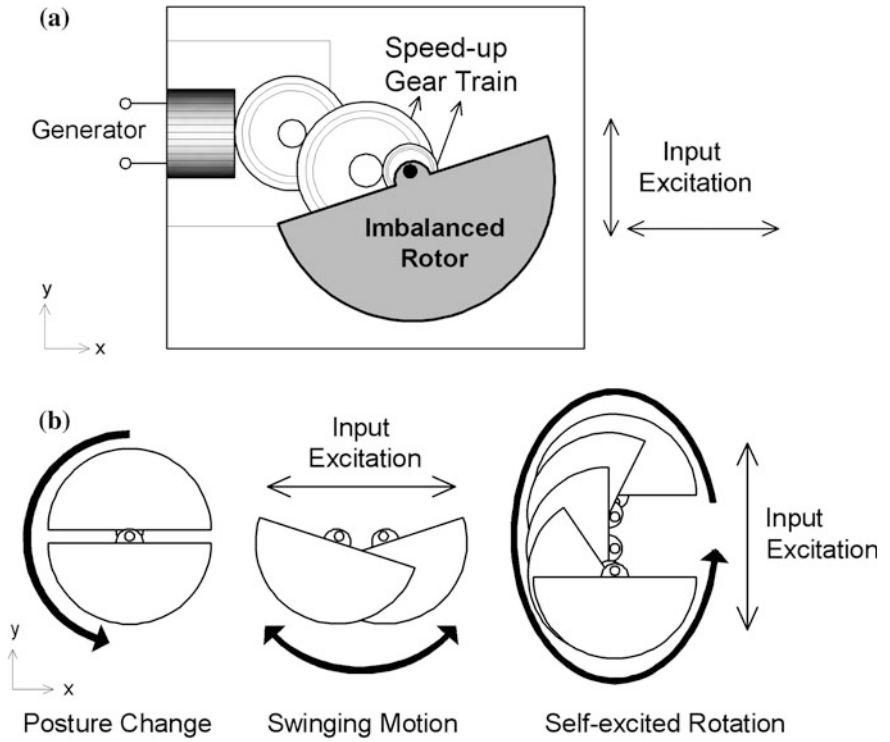

Fig. 2.8 Schematic AGS mechanism and harvested multi-motions [48, 49]

bit greater than 10^{-4} Nms/rad. Self excited rotation reaches its maximum value of 10 mW at this point and as damping increases further, sudden decline in power generation occurs down to 1 mW and the mode turns into swinging motion. This indicated that power generation in self-excited rotation is 10 times greater than swinging mode. In the light of these findings, AGS is better at low frequency and large amplitude inputs like walking or running [48].

For medical implants, this HRTH is experimentally tested on the right ventricular wall of the dog's heart. Test results are 13 μJ per heartbeat, and 80 mJ in 30 min (44 μW), yet never further tested to feed aimed application of heart-pace since less power is produced than needed 200 mJ per half an hour. This design's feasibility on pacemakers further studied: This harvester mechanism is placed on the surface of a human chest and performance tested in office activity. In 8 h, multi-mode harvester generated 0.5 μW, which is much less than peacemaker battery recharge feed [50]. Related to Sasaki et al. conclusion on AGS, high amplitude is necessary for greater power outputs. Hence, office environment does not provide this vibration input as in running. However, generated power in office is sufficient enough to run wristwatches.

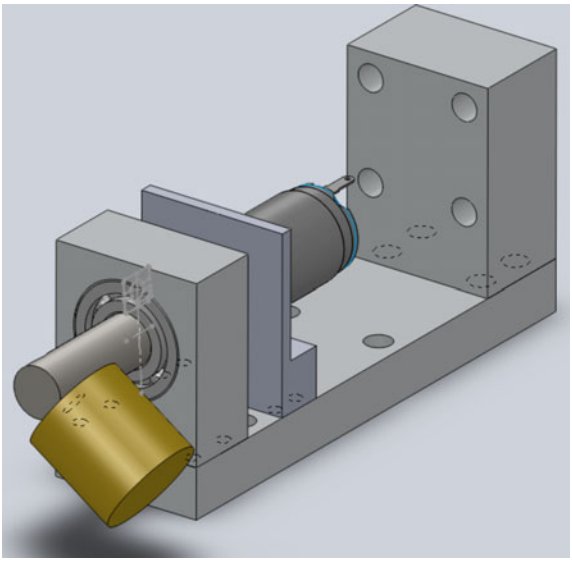

Fig. 2.9 HRTH with magnetic pendulum and DC motor components [51]

Karami and Inman, investigated, modeled and simulated nonlinear HRTH in order to enlarge operation bandwidth. This design has magnetic pendulum as an eccentric mass connected to DC motor shaft and generates power from DC motor as the magnet oscillates (Fig. 2.9). In case of full rotation is passed, the resulted vibration is either two period vibration or chaotic. As the vertical base acceleration increases from 1 g up to 1000 g, power output rises from 10 mW to 1 W. While the base frequency increases up to 10 Hz, the output power is almost the same around 1 mW, after 20 Hz, logarithmically increases maximum of 0.5 mW, which is the saturation value at 90 Hz. The multiplicity of these findings gave maximum power generation of about 70 mW. The analytic calculations of power generations are much higher than the alternative proposed HRTHs, which is highly favorable in applications like tires and wind turbine blades [51].

Jung Kim Min et al. are especially designed HRTH for low frequency and structural applications. The complete HRTH design is shown in Figs. 2.10 and 2.11c as Case 3. The whole system is separately analyzed and tested for three cases of harvester components. The first case (Fig. 2.11a) is EM transducer where same pole magnet movement results in EM induction. In case 2 (Fig. 2.11b), as the beam oscillates, it is transformed into rotational motion and similar to Karami and Inman design, this rotation input yields power generation by DC motor. When all the harvesting mechanisms are gathered, there exists another implementation for the permanent magnets to oscillate in boundary limits so that the efficiency can be increased and since the beam is not fixed or not able to complete full rotation. Therefore, In case 3, the mechanical stoppers are added to both oscillation radial clockwise and counter-clockwise directions as seen in Fig. 2.11. In experiments, all cases are tested at constant input excitation of 0.03 g and the frequency is shifted

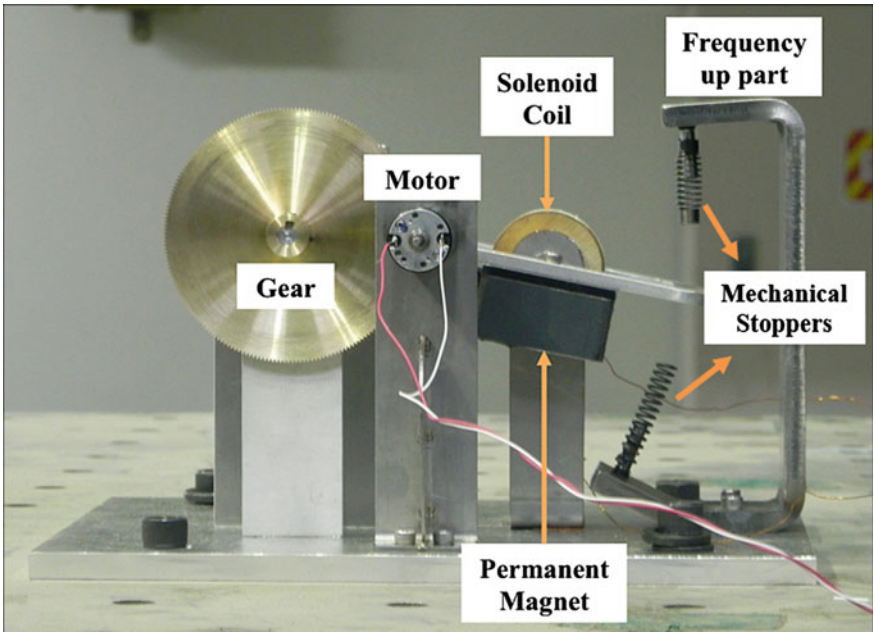

Fig. 2.10 Jung Kim Min et al. test HRTH prototype, it is analyzed in three cases [52]

from 0.5 to 5 Hz. Frequency response showed that the resonance frequency of all cases is almost at 1 Hz and output power of the system in Case 2 that is power generated by the motor with the gear ratio of 10:1, overwhelms the generation in Case 1. As a result, the harvester power generation of 37 mW is mostly contributed by the second case [52].

Larkin and Tadesse's novel design is composed of 3 HEH cantilevers in Fig. 2.1a mounted onto rotation center and a circular coil house (Fig. 2.12). The 3 HEH cantilever acts as eccentric mass and in addition to operation modes are shown at the bottom of Fig. 2.8, PE beams allow harvesting perpendicular translational forces. To sum up, the operation modes are rotational, and translational in both vertical and horizontal axes in 1–10 Hz with a maximum of 30 Hz operation range. Combined PE generator output power was 332 μW at 5 Hz and 0.8 g input excitation, and 1.25 mW at 20.6 Hz and 0.6 g vibration input. Other experiments cover testing at two body levels (wrist and ankle) when the device is placed horizontally (normal to gravitational axis, Fig. 2.12d and f) and vertically (in line with gravitational axis for walking, walk with spinning and jogging, Fig. 2.12e). The best performances respective to EM and PE generators are 17 at mW vertical placement on the wrist, and 759 μW at ankle while jogging. For both transduction mechanisms, lowest performances are observed for horizontal placement on the wrist with walking alone. The reason for vertical placement to produce greater powers is that the gravitational force effect on the eccentric mass set which increases its rotational

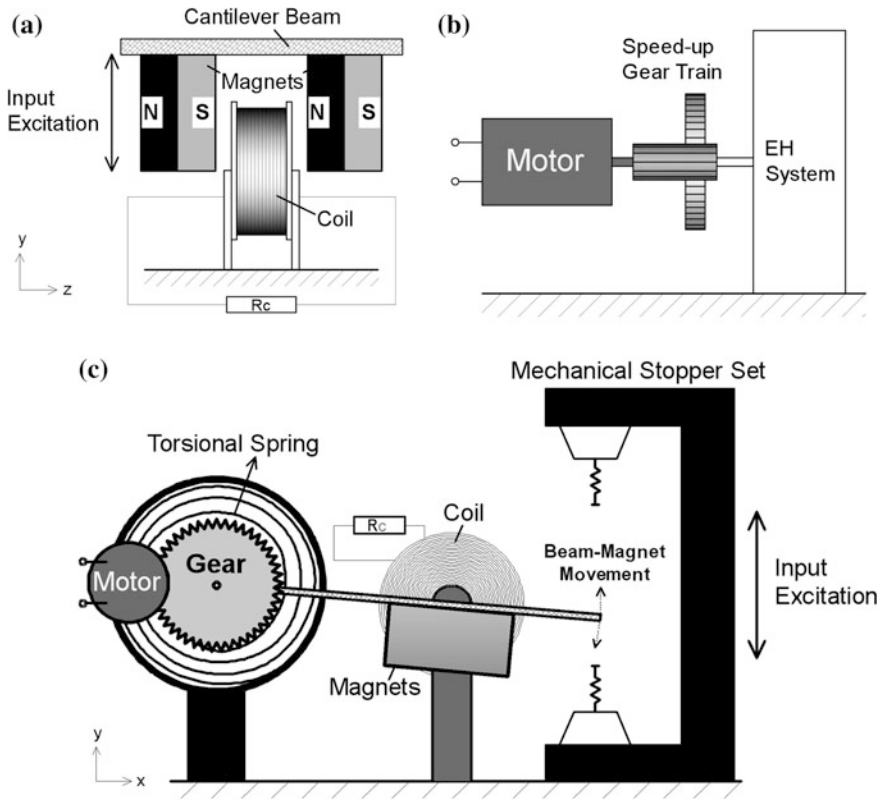

Fig. 2.11 The tested three cases of HRTH. **a** Case 1 represents EMH part, **b** Case 2 illustrates transformed beam oscillation as rotational input yields power generation by DC motor, and **c** Case 3 shows the schematic Fig. 2.2 of the whole HRTH system [52]

speed [24, 54]. Similar to AGS mechanism and Larkin and Tadesse's novel HRTH, Zhong et al. multi-source powered HEH (Figs. 2.17 and 2.18) is covered in Sect. 2.4.3.2.

In addition to combination of multiple transducers for EHing in HEHs concept, the other phenomenon is to harvest multiple power sources with either single or multiple generators and the former is known as "hybrid power systems or multi source power systems" [55]. In the following parts, multi source systems will be investigated in three parts so that the number of different power sources can be classified.

2.4.3.2 Two-Multi Source Powered HEHs

Gambier et al. presented combined solar and PE transducers as a multi-source HEH. In addition to HEH, they also investigate thermoelectric generator and suggest

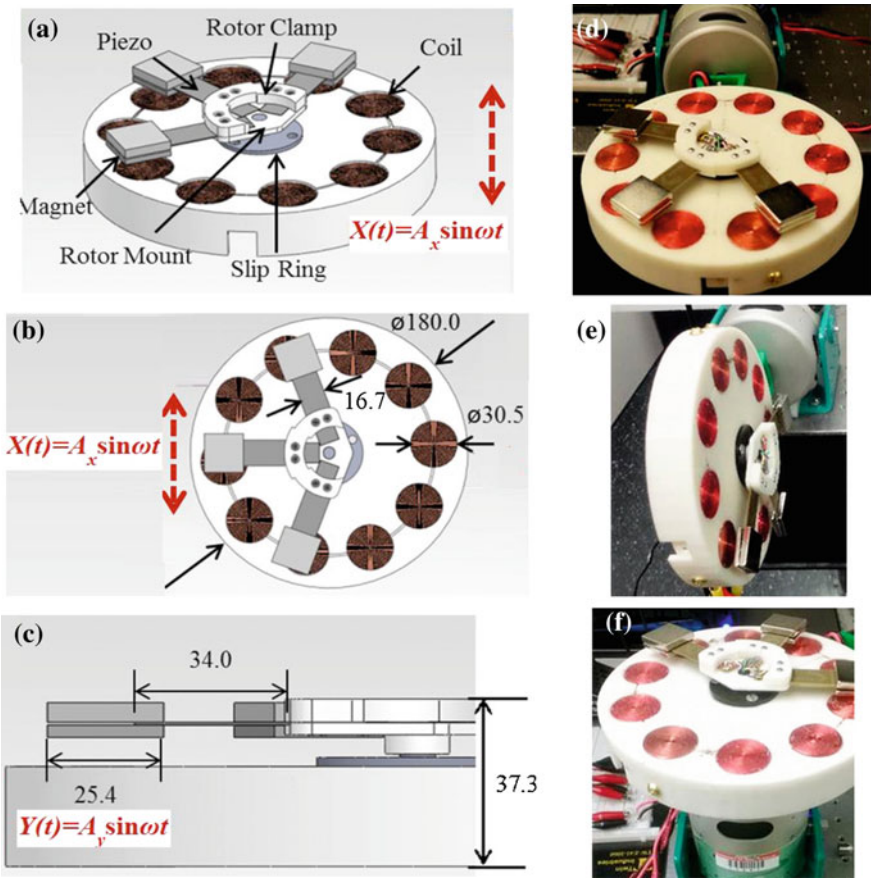

Fig. 2.12 Larkin and Tadesse's novel HRTH schematic design in (**a**), (**b**) and (**c**) [53], and the tested prototype vertical (**e**) and horizontal (**d** and **f**) arrangements [24, 54]

combining these three generators as a HEH. HEH design is composed of flexible solar (PowerFilm, Inc.), piezoceramic (QuickPack QP10n, Mide TC) generators and thin-film battery (MEC102, Infinite Power Solutions, Inc.) supported by metallic substrates, Kapton layers with implanted flexible copper electrodes for electrical isolation and epoxy layers having high-shear strength, as seen in Fig. 2.13. Single layer solar transducer dimensions are 93 × 25 × 0.178 mm^3 and cantilever volume including piezoceramic is 93 × 25 × 1.5 mm^3. Tests are conducted independently and together with solar and vibrational EHs. Three levels of illumination intensities are used as 124, 223, 311 and 437 W/m^2. As expected, highest irradiance of 437 W/m^2 resulted the maximum output power of 30 mW, while it is 12.5 mW at 223 W/m^2. Frequency swept from 0 to 500 Hz to catch the device resonance frequency and after that, measured output powers at 56.4 Hz are 0.4 and 0.49 mW with respect to the base excitations of 0.1 and 0.5 g.

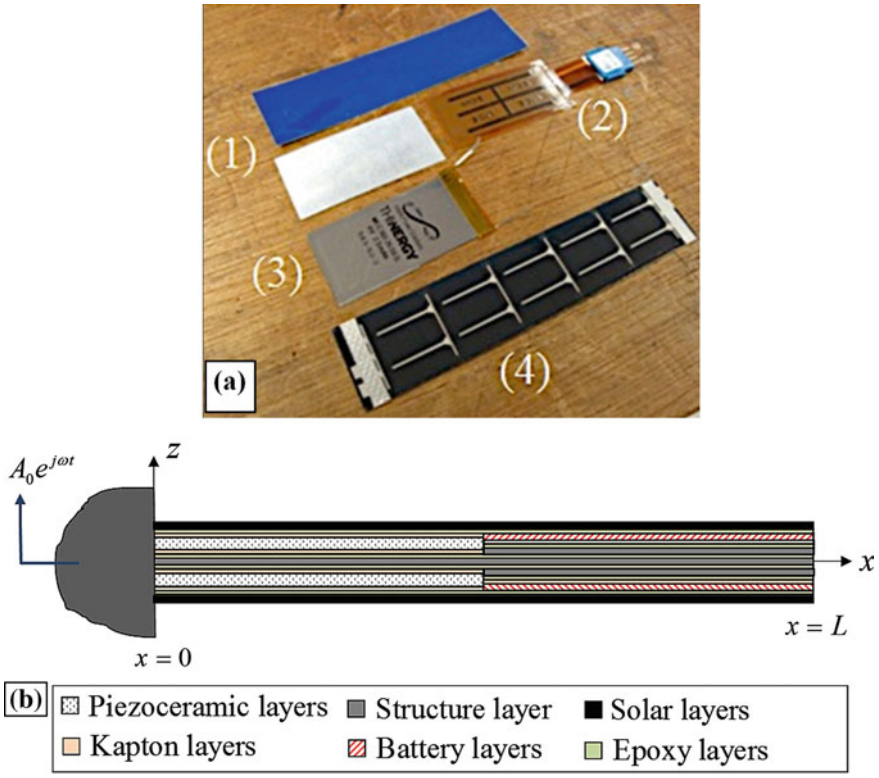

Fig. 2.13 Gambier et al. novel HEH combined with flexible thin-film batteries. **a** Aluminum structure layer (*1*), piezoceramic in Kapton material (*2*), flexible battery (*3*) and flexible solar layer (*4*), and **b** HEH scheme after integration of the layers [56]

At illumination exposure at 223 W/m^2 single solar generator charges 1 mA h of a thin-film battery in 20 min and 1.3 mA h in 26 min, whereas it takes 8 h for 1 mA h and 3 h for 0.38 mA h of capacity with PEH at base excitation of 0.5 g and 56.4 Hz [56].

Novelty of Hehr et al. research is that both vibrational and radio frequency (RF) inputs are harvested upon the same solenoid coil in EMH. As seen in Fig. 2.14, EMH dimensions are 50.8 mm diameter and 95.3 mm length with neodymium magnet of 38.1 mm diameter and 12.5 mm length. Designed harvester has the first resonance frequency of 12.5 Hz, which is experimentally validated at 3.5 and 5 g acceleration amplitudes. Coil diameter of 40.5 mm (coil set 1 and 2) is selected in order to keep the center frequency of band at 2.45 GHz and its equivalent wavelength is 122.4 mm so that HEH can function for industrial, scientific and medical radio band of 2.4 GHz. Throughout experiments, electromagnetic resonance was measured as 2.46 GHz. For the helical antenna, grounding copper ring diameter is 39 mm. For maximum voltage output, coil sets are

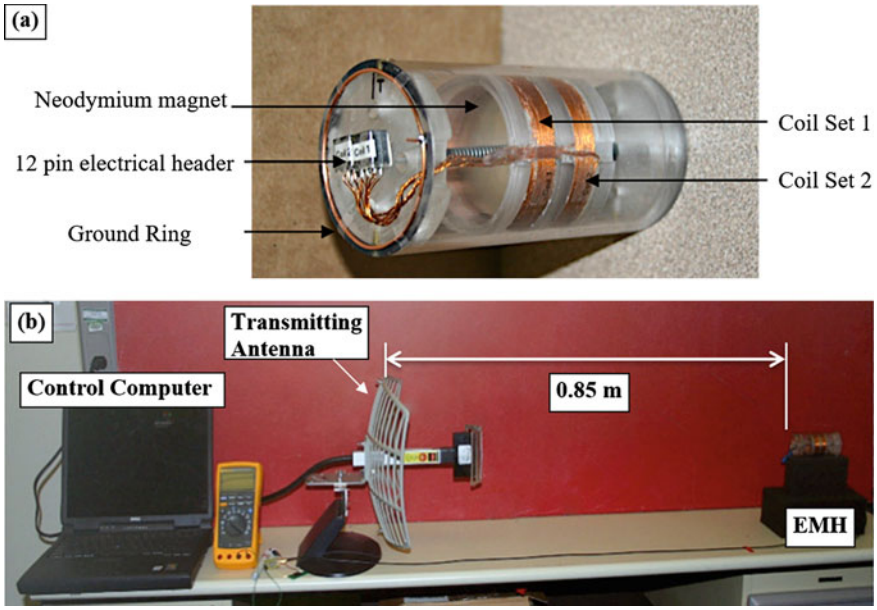

Fig. 2.14 **a** Kinetic and RF EM generator and **b** RF EHing test set-up with the same multi source powered harvester upon coil part alone [57]

connected in series for vibrational EHing and in parallel for RF EHing in the axial orientation to the source antenna as seen in the bottom in Fig. 2.14. The interesting finding was that the voltage differences between 1.52 V for coil 1 only and 1.32 V for coil 1 and 2 connected in parallel. Hehr et al. explains the reason as the indication of RF interface between the coils. At 1 g and 12.5 Hz, EM generator output energy is 1 J in ~90 s namely, ~11 mW. At 2.46 GHz, RF generator produces 70 mJ of energy in 100 s in other words, 0.7 mW [57].

Collado and Georgiadis also comprised unusual two energy sources of solar and electromagnetic waves in a single device. Novelty of their research is not limited to these harvesting sources but also include the HEH design in Fig. 2.15, developed low cost and efficient solar cells, maximized power point tracking and low power DC/DC converter to fix DC voltage. Collado and Georgiadis's novel HEH design is based on broadband monopole rectifying antenna on flexible polyethylene terephthalate (PET) substrate structure and on top of the antenna, flexible hydrogenated amorphous silicon (A-Si) solar panel is thin solar cell arrays are implemented (Fig. 2.15). The antenna alone is the copper layer of 35 μm covering a PET substrate of 75 μm. In contrast to Hehr et al., authors aimed to harvest broadband range of 800 MHz to 6 GHz so that dissipated wide range of standard communication bands can be harvested. Solar array integration was chosen such that the RF harvesting performance will not be affected. Thus the experiments conducted at a distance of 3.45 m from the transmitter, which transmits RF power less than

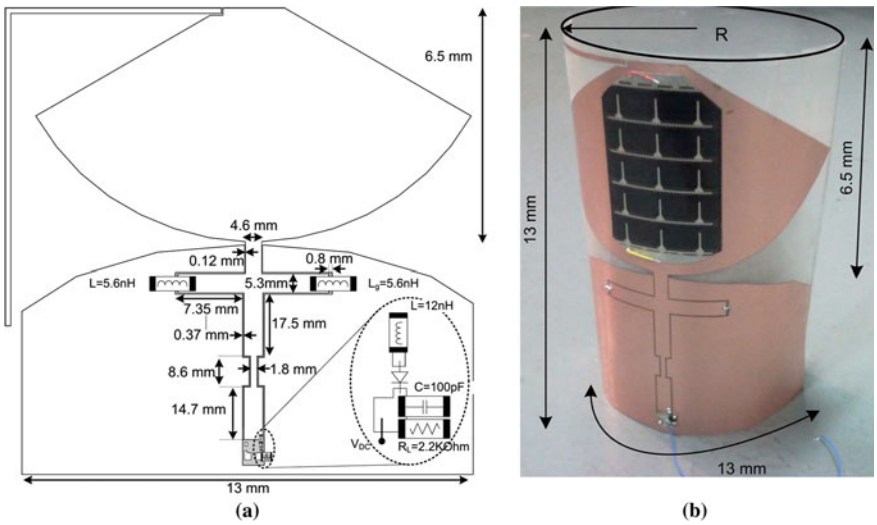

Fig. 2.15 **a** HEH design with dimensions and implemented dual band rectifier and **b** broadband rectenna on PET substrate [58, 59]

20 dBm for the rectenna of radius (R) of 70 and 100 mm and with and without the solar cell integration. For solar and RF HEH, the illumination was set almost to standard global solar irradiance of 100 and 15 mW/cm^2 for shade simulation. With respect to the stated illuminations, the voltage outputs of the solar array are 4.06 V and 3.90 mV. It is seen that EH with and without solar cells generates similar voltage trend and amount just as the radius of 10 and 7 mm prototypes resulted, yet 10 mm radii prototype generates slightly higher voltage at 850 and 1850 MHz. Collado and Georgiadis concluded that the best performance of the HEH is able to generate 56 mW [58, 59].

Resembling Gambier et al. novel multi source powered HEH [56], Chatterjee and Bryant's HEH harnesses solar and wind flow or vibration type kinetic powers. Only Chatterjee and Bryant state possible application of HEHs on mobile robots. As shown in Fig. 2.16, the PE patches are laminated underneath flexible thin film solar ribbon with very low aspect ratio. HEH is fixed in both ends and during longitudinal tension; transverse wind flow is induced to form aeroelastic vibration. In spite of setting the test set up, in Chatterjee and Bryant's paper, authors only proposed theoretical modeling and tuning via changing the longitudinal tension. They concluded that the transverse matrix methods is superior over Bokaikan method, where as the stress is reduced, the power generation of PE patches also reduces while being almost ineffective on mode shapes, yet effective on the mode shape of the structure without the PE patches [60].

Similar to AGS mechanism and Larkin and Tadesse's novel HRTH, Zhong et al. combined planar rotary disk EMH with triboelectric nanogenerator (TENG) in order to harvest hand induced rotating kinesiology (see Fig. 2.17).

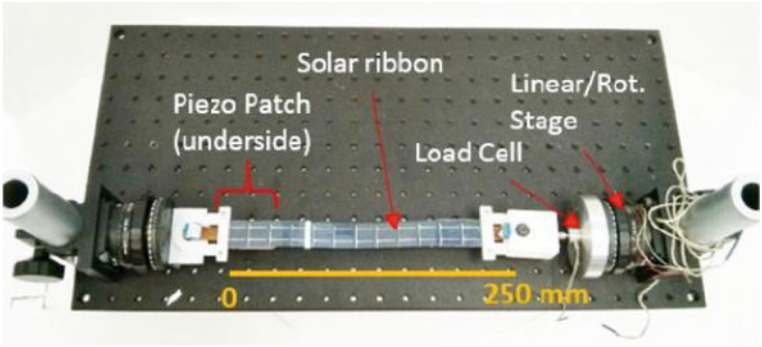

Fig. 2.16 Test setup of the solar and vibrational HEH [60]

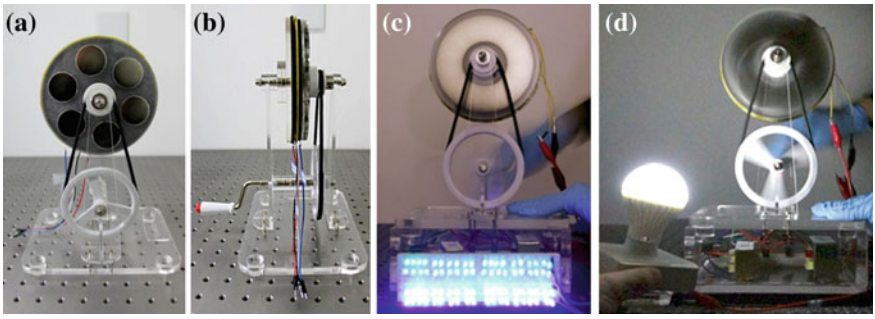

Fig. 2.17 Assembled prototype used in tests (**a** and **b**). Hand motion induced to HEH and lights 40 LEDs (**c**), and a globe light (**d**) [61]

During experiments, hand induced rotation supplied to HEH and successfully lit 40 LEDs and a globe light with a maximum illumination up to 1700 lux (Figs. 2.17 and 2.18). At a rate of 200 rpm, HEH generates ~8.4 mW by EM part and 8.4 mW by TENG part. Under optimum loads of 1 and 2 kΩ, respective power generations by EM and TENG transducers are 50 and 17 mW [61].

Microscale Examples: Yu et al. investigated the combination of solar panels for low illumination and MEM vibrational EH. Similar to Collado and Georgiadis, Yu et al. also selected A-Si solar panel with a surface area of 9.6 cm^2 since it is suitable for indoor light (fluorescent or LED). When authors' five-parameter modeling simulations of solar power generations are compared with the experiments, their modeling is closer to the experimental measurements and thus, more accurate than traditional models. The maximum power output is 110 μW at 530 lux. Microscopic scale vibrational EH is composed of five PZT beam array connected in series with a silicon proof mass (Fig. 2.19a). The peak power output is 66.75 μW at 234.5 Hz and 5 m/s^2 [62].

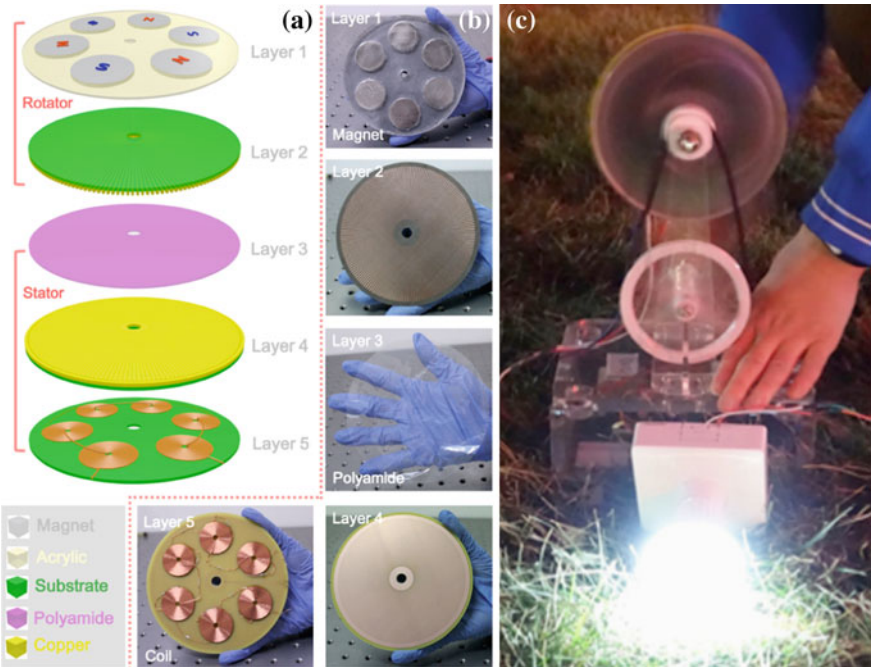

Fig. 2.18 **a** and **b** the first layer consists 6 magnets on a 5 mm *thick circular* acrylic disk with 140 mm in diameter. Likewise, 6 coil sets are aligned to the magnets on last layer. *2–4* layers are TENG parts: *second* and *fourth* layers are the combination of the copper strips that are integrated on a flexible substrate. The *third* polyamide layer is sandwiched in between these layers. **c** The prototype picture in use and HEH runs the globe light [61]

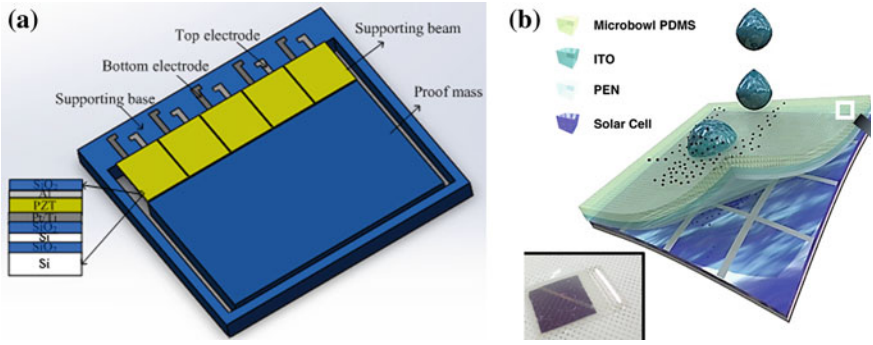

Fig. 2.19 **a** Yu et al. vibrational HEH structure without solar panels [62] and **b** Jeon et al. self cleaning rain drop and solar powered HEH [63]

Jeon et al. not only propose a novel multi source powered HEH but also solves the cleaning need of the solar cells and thus, keep its efficiency stable by the second power source of raindrops. In addition contact electrification by mechanic input, water solid interactions are also enough to harness energy via TENGs. Transparent and superhydrophobic TENGs with small contact angle allows water droplets to remove particles on the surface as well providing light to transmit and reach to the solar cells. In Fig. 2.19b, transparent superhydrophobic PDMS and ITO-PEN substrate layers on solar cells, and the prototype (below) are demonstrated. Throughout the experiments conducted with distilled water, raw tap water, actual rain, 0.01 and 1 M NaCl solutions. The resulted power generation is in the same order of the tested solutions regarding the highest to lowest power generation. While in the real rain case the output power is decreased, it is almost negligible especially the standard deviations are considered. Jeon et al. multi-function HEH generated maximum power output of 0.27 μW [63].

Novelty of Zakharov et al. study is to harness thermal energy via PE transducer due to the resulted mechanical deformation. Their design couples shape memory effect (SME) and direct piezoelectric effect (DPE). However, proposed novel harvester is partially HEH since the direct main source is thermal and the second source is indirect mechanical deformation, caused by the thermal input (Fig. 2.20) [64]. NiTi wire connected to fixed support and the tip of the cantilever shrinks during heating and bend the bulk PZT ceramic plate, and also reach the initial state as it is cooled down as shown in Fig. 2.20a. SME and DPE structure with 0.2 cm^3 of active materials energy generations are 90 μJ over a temperature increase of 35 °C and 60 μJ while cooling [64].

Large Scale Examples: Dr. Tong's research team installed HEH consists of surrounding novel power augmentation guide vane (PAGV), vertical axis wind turbine (VAWT) and solar panel at the top so that the LED outdoor light can be driven.

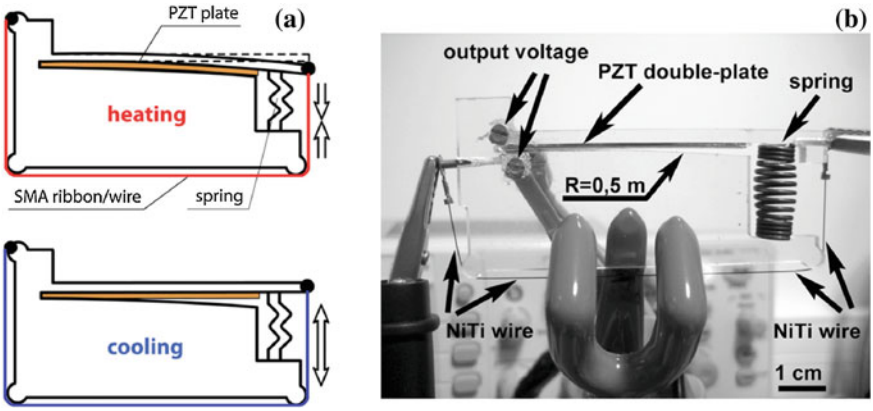

Fig. 2.20 **a** Zakharov et al. partially hybrid EH working principle scheme and **b** prototype picture along with the heat source (for the video record during operation, please visit www.youtube.com/watch?v=uS0z4ZEBeYw) [64]

Fig. 2.21 Eco-GreenergyTM Wind-Solar Outdoor Lighting System in Kuala Lumpur Campus, University of Mala [65, 66]

The developed system runs against low wind speeds due to PAGV integration (Fig. 2.21) [65, 66].

De et al. also studied wind-solar hybrid EH. Their so-called "WiSH" system consists horizontal axis wind turbine (HAWT) having 500 W rotor and solar PV panels with 250 W capacity so that the energy production can be increased during low wind speed regimes in India. HAWTs have two types; having 3 blades and 4 blades. Each blade weighs about 600 g and to achieve this low weight and high strength, they are made of carbon fiber composite. Performance curves gained from mobile testing indicated that fabricated 4-blade HAWT is more efficient than 3-bladed one. Prototypes of WiSH systems are installed in Kodihalli Campus, India for field tests (Fig. 2.22). Both 4 bladed HAWTs are parallel and 30 m-high. With the help of industrial partnership of ARES, prototypes developed up to 1–5 kW capacity and further produced 50 units of these WiSH systems [67].

2.4.3.3 Three-Multi Source Powered HEHs

In edition to Porcarelli et al. novel device comprising solar, airflow and hydrogen micro fuel cell EHs (Fig. 2.23), their [68] and Chung et al. researches [69] lie in the early studies about powering wireless sensor nodes by fuel cells.

Simulations for power generation of solar and wind EHs are compared with the experimental results. Solar cells are tested for the irradiation levels of 8000; 24,000; 40,000; and 80,000 lux. In the same order with light intensities, the photo-voltaic (PV) cell maximum output powers are 0.075, 0.13, 0.28, and 0.45 mW. Airflow energy is harvested by meso-scale plastic four bladed HAWT, 6.3 cm in diameter and 7.5 cm in length. Flow EH is tested for the flow speeds of 8.5, 15 and 16 km/h

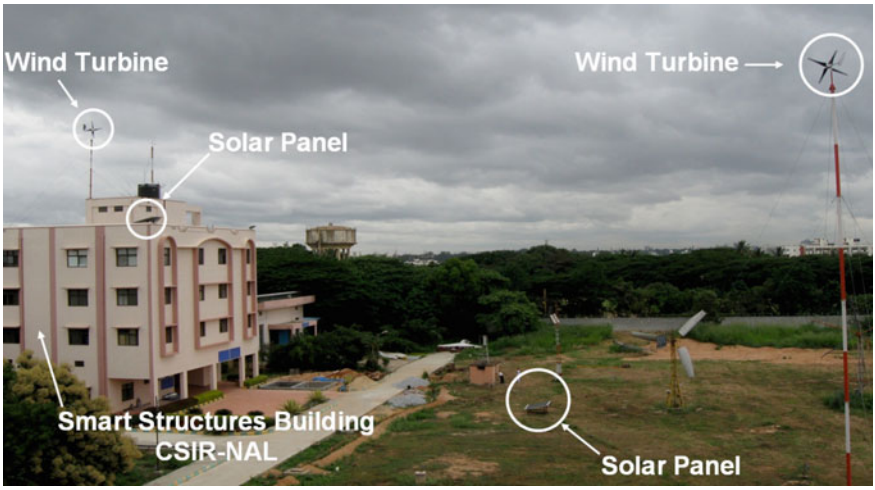

Fig. 2.22 De et al. WiSH prototypes under field test. For controlled conditions, HAWTs are 30 m above the ground level and parallel to each other [67]

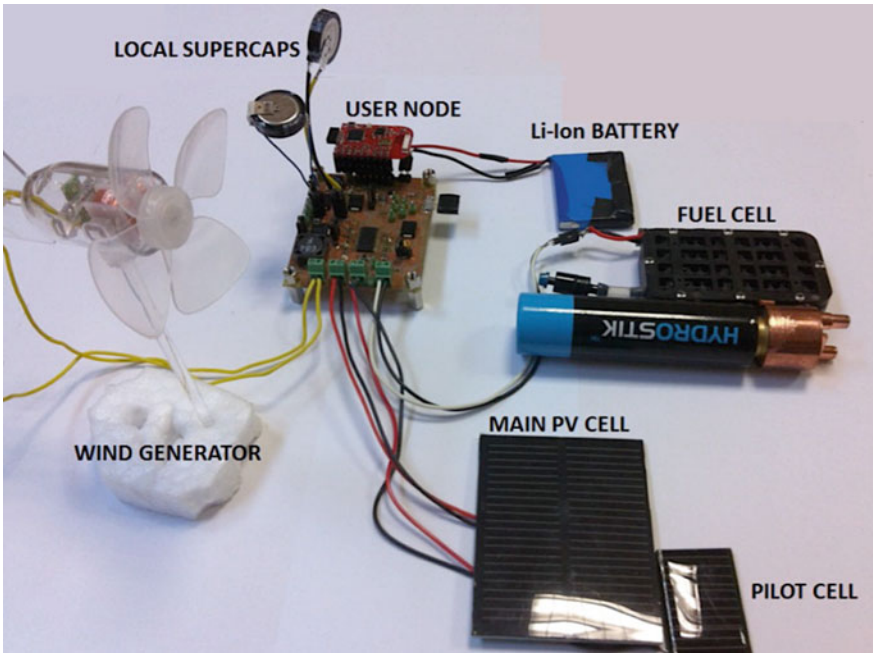

Fig. 2.23 Porcarelli et al. three-multi source powered HEH: solar, airflow and hydrogen micro fuel cell harvesters, battery and harvester circuitry are shown [68]

and the respective wind generator maximum output powers are 3.1, 5, and 7.7 mW. Solar cell and wind harvester experimental results are very close to simulation findings. As a final component, fuel cell EH with 3.61 cm^2 area, power generation is around 1 mW [68].

Zheng et al. are researched a pretty novel application of single improved dual mode TENG in such a way to harness raindrop and wind energies, and combined it with solar EHing. The very similar structure is in Jean et al. HEH as demonstrated in Fig. 2.19b. Zheng et al. also used the transparent superhydrophobic TENG with a 40 cm^2 surface area on silicon-based solar cells. TENG's transparency is validated by spectra transmittance test as being more transparent even than a 3 mm-thick commercial glass. Moreover, separation of polytetrafluoroethylene and nylon layers by PET spacer border enhances dual mode of TENG (fabrication and experiments of HEH components are given in detail in Zheng et al. article). These dual modes are: water contact TENG as rain EH and the wind contact TENG as wind EH. The tests are set as such: Rainy day conditions are considered (13.6 and 20 mL/s dripping rates) and the incident angle between raindrops and TENG surface is 45°, with a distance of 40 cm from the rain shower. Common daily wind speeds of 1.7; 2.7; 4.1 and 4.9 m/s are flowed from a faucet and the solar irradiation is set to 100 mW/cm^2. At 20 mL/s dripping rate, water TENG, water contact TENG and HEH drive 10, 20 and 50 LEDs, respectively. Experiments have shown that the dual-mode TENG (water and water contact TENGs are in series) voltage and current densities are greater than water contact TENG that is greater than water TENG alone. Generated power of the prototype is limited but since the size can be expanded, generated powers in per square meter of the HEH surface area are more representative as in current densities, thus, for HEH it is 86 mW/m^2 at a dripping rate of 13.6 mL/s and in the absence of solar and rain sources, it is 8 mW/m^2 from wind at a speed of 2.7 m/s [70].

Microscale Examples: Chung et al. combined thermal, mechanical and magnetic powers in such a novel way. As mentioned in two-multi source powered HEHs title for Zakharov et al. 2015-design, in 2012, Chung et al. also used indirect source of magnetism to harness direct thermal power source. So, Chung et al. device is partially three-source powered HEH. As seen in the prototype picture in Fig. 2.24a, main body is copper-beryllium spring and the PE cantilever is both fixed to glass frame and attached to the spring. Design has two types of magnets: Moving gadolinium soft-magnet on top of spring and fixed neodymium-iron-boron hard-magnet on frame. The working principle of this novel HEH demonstrated in Fig. 2.24b and c: As the soft magnet is cooled below Curie temperature, it gains ferromagnetic property and almost attaches to the fixed hard magnet (b), which bends the spring and PEH. Worth to mention that magnets never really touch due to the distance between them in y direction. As the topside is cooled down (15 °C) and heated (27 °C), magnetic attraction incidence and withdrawal of the magnetic attraction leads spring, thus, PE beam oscillation and power generation. Second working mode is classic vibrational spring-proof mass energy generation on PEHs. Final creative additional working mode is the oscillation of the soft magnet on spring due to the induced AC magnetic field in z direction (c) [69].

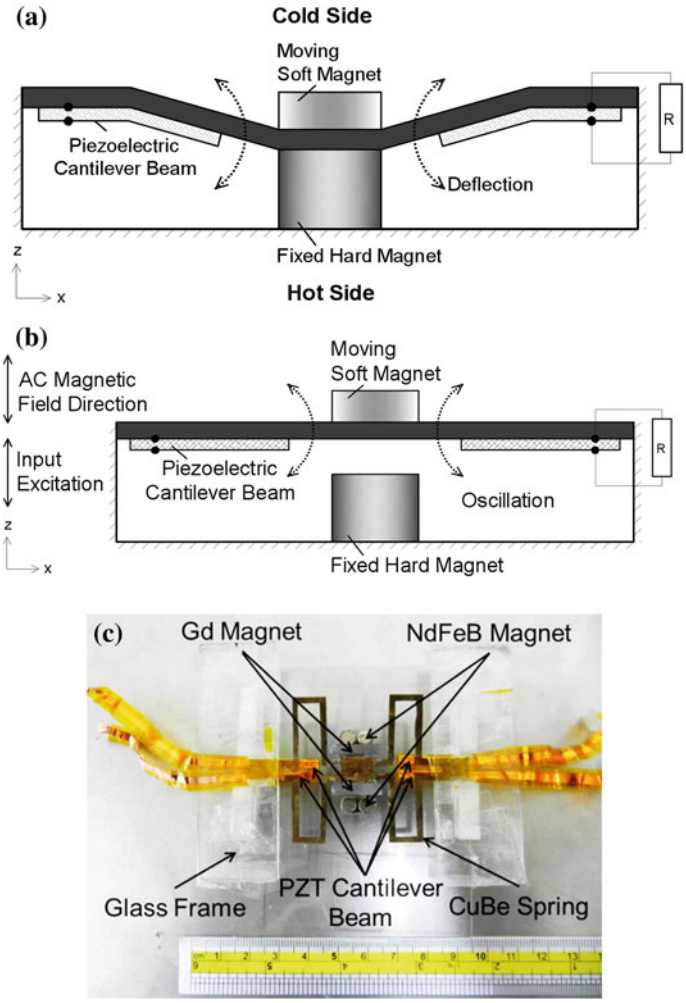

Fig. 2.24 **a** Temperature-difference-driven thermal and **b** vibrational and magnetic field induced schematic working principles. **c** Chung et al. fabricated prototype [69]

Chung et al. experiments resulted as: For temperature-difference-driven thermal EHing, a 25 °C difference lead minimum and maximum of 15 and 70 peak-to-peak voltages, respectively. Generated peak-to-peak voltage outputs are 175 and 20 mV with respect to the input excitation of 1 mm at 46 Hz, and AC magnetic field of ±3.5 Oe at 43 Hz. The preliminary results clearly indicate that the vibrational energy generation is undoubtedly greater than other working modes [69]. Almost the same research team; Chen et al. took further to analyze their novel design (Fig. 2.25) [71].

Chen et al. simplified their previous study by using gadolinium soft-magnet as a fixed beam on PZT sheet and silicon clamps and keeping the same fixed neodymium-iron-boron hard-magnet on frame. Experimental measurements are

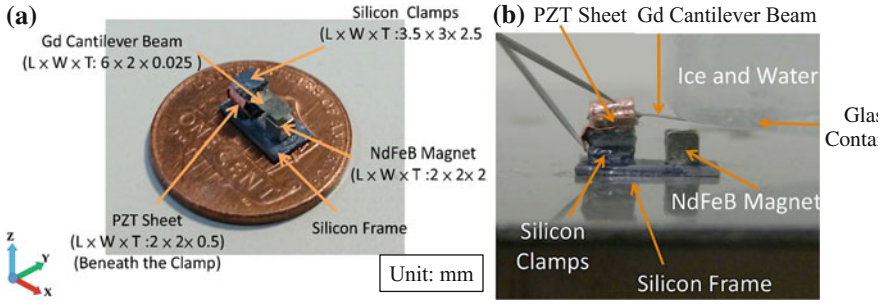

Fig. 2.25 Chen et al. simplified recent magnetic-piezoelectric thermal HEH prototype with dimensions (**a**) and during experiments with ice water (**b**) [71]

37 mV of peak-to-peak voltage and 1.98 mV RMS voltage at 20 °C temperature difference for the temperature range of 6.7 to 26.7 °C. The maximum output power is and average power density is ∼1.37 nW with an average of ∼3.96 pW with the breakthrough HEH volume of about 0.063 cm^3 [71].

Large Scale Examples: Chong et al. presented VAWT, solar energy converter and rainwater collection systems integration with PAGV. Since the rainwater collection system is not an EH, it is only for storage purpose and indirectly saving energy from the reduced pumping need [72, 73] so their design is partially three-source powered HEH. Nevertheless, as Mithra et al. suggested in their research, it is also possible to harness energy from rainwater by increasing its kinetic energy from falling and the use of turbines [55]. As seen in their patent scheme in Fig. 2.26a–c, the wind turbine 'A' is placed in the middle of the structure with rudder 'C', PAGV 'B' has sloped upper 'D' and lower 'E' wall ducts, and surrounded by the protective mesh 'M'. The upper wall duct also acts as a collector of the rain shower and at the same time, having solar energy converter (PV and/or solar thermal panel or solar concentrator system) 'F' on the upper surface. The captured rainwater after filter 'N' flows through the passage 'G' and reach to the storage 'K', which has thermal insulation at the base 'L' so that heat transfer into building can be blocked. VAWT power drive shaft 'H' is connected to the generator 'I' via mechanical drive box 'J'. Their design is open to many modifications and one is illustrated in Fig. 2.26b. Tests conducted with and without 3-blade Sistan rotor having 0.5 m diameter and 0.25 m height, surrounded by the PAGV having 30 m diameter. Pilot-scale test set up height from the PAGV to base is 12 m. It is reported that PAGV amplifies the wind speed by ∼1.8 times (46 rpm for pilot tests) and VAWT gains direct flow angle. It is seen that PAVG integration increases energy generation by 1.25 times. It is estimated that for the system on a 220 m high skyscraper, energy generations of the wind energy harvester system is approximately 157 and 58.4 MW h/year, solar panels with a 650 m^2 active area is 280 kW h/day, and monthly the energy saving for 220 m pumped domestic water is 79 kW h. Ultimately, Chong et al. research suggests the annual total saved and generated energy is 160 MW h and by

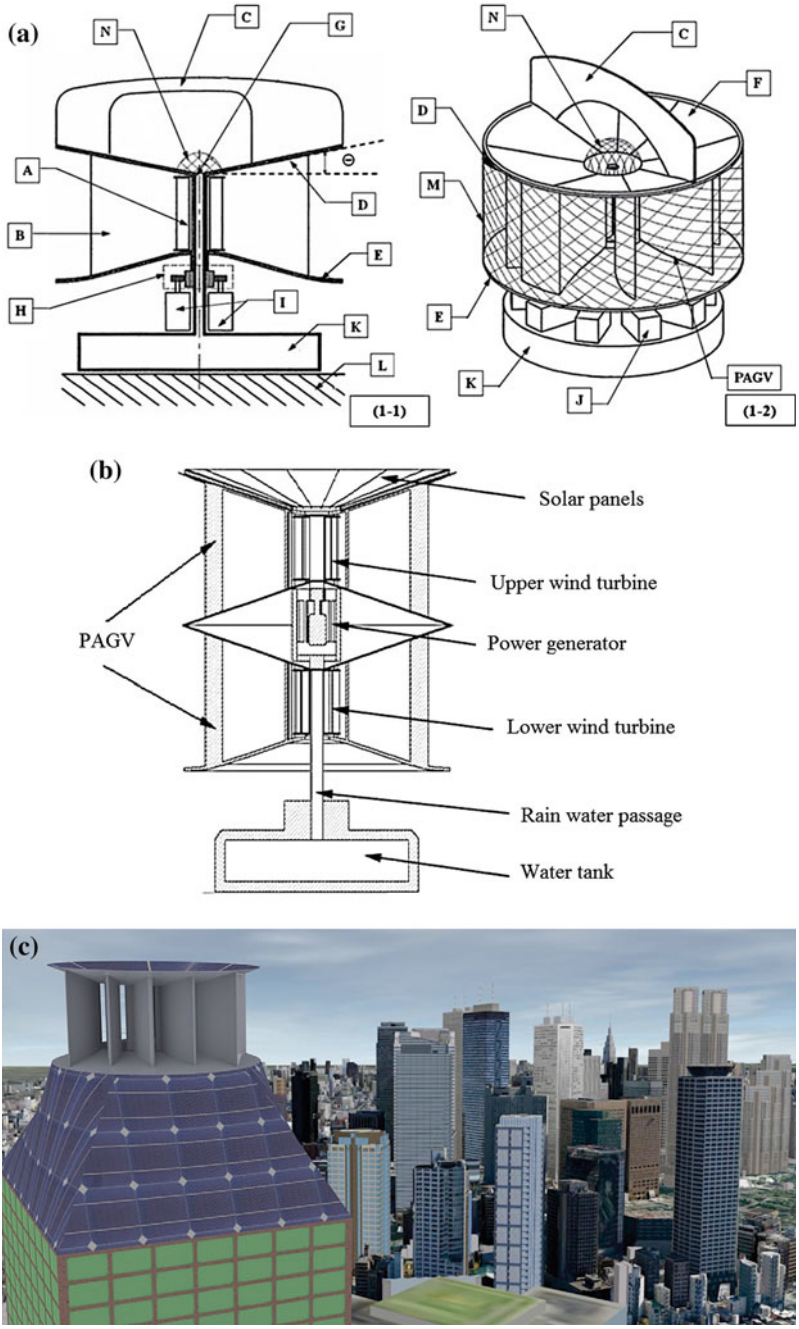

Fig. 2.26 **a** Patented and proposed design's referred figure and **b** proposed modified design, and **c** artistic demonstration of HEH on the high rise building in Tokyo, Japan [72, 73]

considering 2.8 MW h of energy consumption per house, one skyscraper application can help to supply energy for 57 houses [72, 73].

Relatedly, Donnie holds a patent of the similar HEH application. Patented HEH has solar panels on the outer rotating large blades, harvesting wind energy and the inner part has either acoustic piezoelectric or electrostatic energy harvester in order to harness entered wind's remaining kinetic energy [74].

Sathiyamoorthya and Bharathib proposed the idea of combining PEH integration roads, rotational solar panel and two-blade VAWT between two-way roads to gain turbulence, and thus, rotational motion input. This configuration aims to feed streetlights but they also suggested HEH implementation on rooftop to supply electricity for households. Proposed VAWT is applicable at low levels for energy generation, in other words, suitable for residential structures. The novelty lies on the sun-tracking module that does not require any sensor or controller. It works as a pendulum clock and as the hanging wheel oscillates, it rotates the escapement wheel and the center shaft. Gear mechanism, reduce the clockwise rotation of the shaft and reduced shaft is connected to solar panel and tracking sun's direction from east to west. PEH is selected as PZT (lead zirconium titanate) and connected in series. Measured maximum output power and peak-to-peak voltage of solar panel and PE are 10 W and 12 V, respectively. Authors propose wind turbine analytic modeling but do not mention the value of the potential power generation [75].

Mithra et al. combined the classic rainwater, solar and wind harvesting systems. Rainwater harvesting starts from the collection of the rainfall on the roof of a three-floor, $\sim$9 m high building to the header tank. The water falls from the conduits, which increase pressure thus, velocity. At the base the falling water meets the turbine and its shaft is connected to alternator's rotor. After the rainwater hits the turbine blades it is collected and stored for further use, while the generated power is used to feed first of all power electronics and then, power systems. Based on this plot scale findings, the desired real-life application's evaluated electricity production is stated as 1.53 kW h for 7 m high normal house and 290 kWh for 98 m skyscrapers. Classic Solar PV arrays and wind turbine to harvest wind energy are suggested to meet domestic power consumption. Nonetheless, Mithra et al. have not stated pilot scale tests along with rainwater system. The combination of mentioned generation systems are concluded as: The rainwater and wind power generations are rectified by AC-DC converters and the PV power alone is converted to fix DC voltage by chopper. The control unit combines these three different generated energies as a hybrid system [55].

2.4.3.4 Four-Multi Source Powered HEH

After Porcarelli et al. another attempt to research solar, wind and fuel cell EHs are studied by Saini et al. with an additional novel segment of electrolyzer (Fig. 2.27). Saini et al. uses solar, airflow, water, and produced hydrogen and oxygen as a result of electrolysis. HEH solar module is 95 $\times$ 135 $\times$ 30 mm^3 in dimension, 89 g of weight and the maximum PV power generation is $\sim$190 mW when exposed to single 75 W lamp at 90°. Six blade HAWT and the maximum output power is 400 mW.

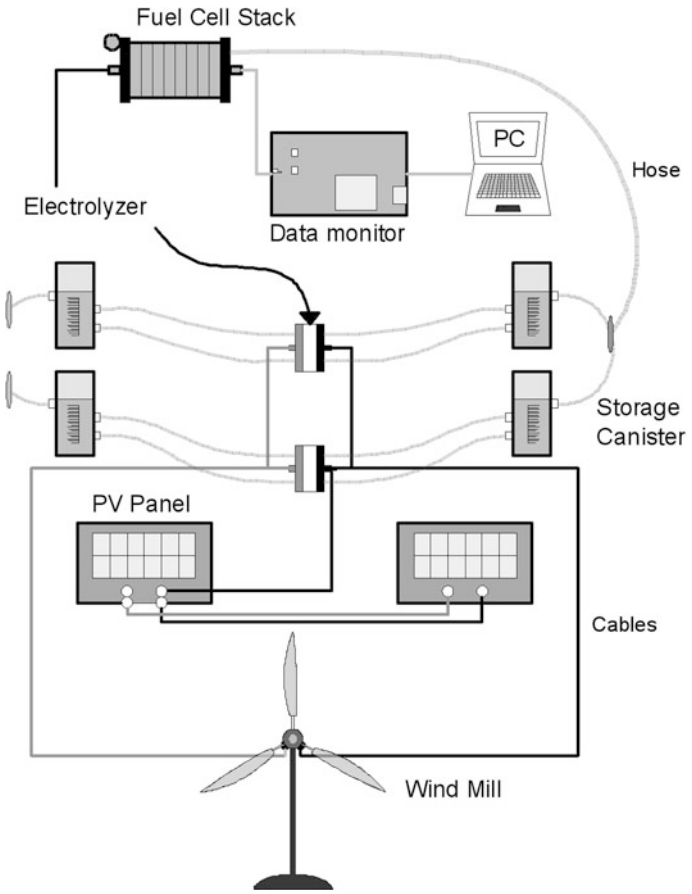

Fig. 2.27 Four-multi source powered HEH system diagram by Saini et al. [2]

Electrolyzer is the basis of fuel cell for decomposing water into hydrogen and oxygen. Afterwards, produced hydrogen and oxygen is used by fuel cell and increases the total source number up to four. Electrolyzer dimensions are $50 \times 40 \times 57$ mm^3 and the generator is 54 g in weight with a decomposition voltage of 1.5 V in practice. Final harvester component of fuel cell is selected as proton exchange membrane and as a 5-fuel cell set, it is $60 \times 70 \times 175$ mm^3 in volume and 430 g in weight. Four-multi source powered HEH maximum output power is 315 mW [2].

2.4.4 Overall Novel HEHs Comparison

The reviewed novel HEH systems peak power generations, total harvester component volumes and/or active surface areas device masses, input excitations, input frequencies and half power band width ranges are compared in Tables 2.2 and 2.3.

Table 2.2 The overall comparison of fixed-frequency and broadband single-source powered HEHs and multimode HRTHs in Sects. 2.4.1 and 2.4.2

Type	References	Input power sources/types	Working modes	Input acc.	Input properties	Volume/surface A.	Peak output power voltage, power density	Mass
Fixed-frequency single-source powered HEHs								
	[1]	Mechanical: foot fall	Rotary Generator, PEH	–	~5 Hz*	–	0.06 kW h, 10 V	–
	[14]	Mechanical: hand motion	Ball driven PEH, EMH	–	~5 Hz**	19 cm^3	PEH: 0.98 mW, 20 V	–
							EMH: 0.64 mW, 0.65 V	
							HEH: 84.4 μW/cm^3	
Broadband single-source powered HEHs								
Linear	[35]	Mechanical	PE and EM	2 g	~150/120–180 Hz	884 cm^3	4 magnet HEH: 15.31 mW, 1.75 V	–
Nonlinear	[44, 45]	Mechanical	PE and EM	1.7 m/s^2	~12 Hz	819 mm^3	PEH: 1.5 mW	48 g
							EMH: 35 mW	
Multimode: hybrid rotary-translational harvesters								
	[47–51]	Mechanical: wrist motion	Mechanical: rotary-translational AGS	–	5–15 krpm	in the wristwatch	1–10 mW	–
	[50]	Mechanical: dog's heart		–	–	–	44 μW	–
		Mechanical: on chest		–	–	–	0.5 μW	–

(continued)

Table 2.2 (continued)

Type	References	Input power sources/types	Working modes	Input acc.	Input properties	Volume/surface A.	Peak output power voltage, power density	Mass
	[51]	Mechanical	Rotary-translational generator, DC motor	1–1000 g	10–90 Hz		10 mW to 1 W, (avg: 70 mW)	–
	[52]	Mechanical	Rotary-translational DC motor, EMH	0.03 g	1 Hz	~1000 cm^3	37 mW, 0.27 V	–
	[24, 54]	Mechanical: walking, jogging	Mechanical: rotary-translational PEH and EM	–	Jogging: PEH on ankle, EMH on wrist	958 cm^3	PEH: 759 μW, EMH: 17 mW	–

(*) Standard walking and running human motion frequency value [14]

(**) Input frequency is 5 Hz in horizontal axis, but the HEH resonance frequency is 816 Hz

Table 2.3 The overall comparison of multisource powered HEHs. Classified according to micro-, meso- and large scales

# of source	References	Input power sources	Working modes	Input acc.	Input properties	Volume/ surface A.	Peak output power voltage, power density	Mass (g)
Microscale								
Two	[62]	Solar, vibration	PV, PE	0.5 g	Solar: 530 lux, PE: 234.5 Hz	1096 mm^2	Solar: 110 μW, PE: 66.75 μW	–
Two	[63]	Raindrop, solar	TENG, PV	–	Solar: 150 mW/cm^2	13.4 mm^2	0.27 μW	–
Two	[64]	Thermal, (mechanical)	Thermally-driven PE, (SME, DPE)	–	Temp increase: 35 °C	200 mm^3	Temp rise: 90 μJ Cooling: 60 μJ	–
Three	[69]	Thermal, magnetic field, vibration	Thermally-driven PE,	–	T: 25 °C,	49 cm^3	Thermally-driven PE: 35 V	–
			Magnetic field induced PE,		PE: 1 mm at 46 Hz,			
			Vibration induced PE		AC magnetic field: ±3.5 Oe at 43 Hz			
Three	[71]	Thermal, (magnetic field, vibration)	Thermally driven PE, (Magnetic Field driven PE, Vibration)	–	T: 20 °C	63 mm^3	~1.37 nW, 1.98 V, 21.7 nW/cm^3	–
Mesoscale								
Two	[56]	Solar, vibration	PV, PE	0.5 g	Solar: 437 W/m^2, PE: 56.4 Hz	3488 mm^3	Solar: 30 mW, PE: 0.49 mW	–
Two	[57]	RF, vibration	RF, EM	5 g	RF: 2.46 GHz,	773 cm^3	RF: 0.7 mW, 1.52 V, EM: 11 mW, 4.5 V	–
					RF wavelength: 122 mm, EM: 12.5 Hz			
Two	[58, 59]	RF, solar	RF, PV	–	RF: 800 MHz-6 GHz Solar: 100 mW/cm^2	4084 mm^3	HEH: 56 mW,	–
							Solar: 4.06 V	

(continued)

Table 2.3 (continued)

# of source	References	Input power sources	Working modes	Input acc.	Input properties	Volume/ surface A.	Peak output power voltage, power density	Mass (g)
Two	[61]	Mechanical: hand-induced	TENG, EM	–	200 rpm	77 cm^3	TENG: 17 mW,	–
							EM: 50 mW	
Three	[68]	Solar, airflow, fuel cell	PV, HAWT, hydrogen fuel cell	–	PV: 80,000 lux, Wind speed: 16 km/h	HAWT: 234 cm^3, Fuel cell: 361 mm^3	PV: 0.45 mW	–
							HAWT: 7.7 mW	
							Fuel cell: ~1 mW, 1.23 V, 2.5 A, 282 mW/cm^2	
Three	[70]	Solar, raindrop, airflow	A-Si Solar cells, TENG	–	Solar: 100 mW/cm^2 Rain: 13.6 mL/s Wind speed: 2.7 m/s	40 cm^2	HEH: 344 μW, 86 mW/m^2	–
Four	[2]	Solar, airflow, water, fuel cell	PV, wind mill, electrolyzer, hydrogen & Oxygen fuel cell	–	75 W lamp at 90°	1234 cm^3	Solar: 190 mW	573
							Wind: 400 mW,	
							HEH: 315 mW, 3 V, 105 mA	
Large-scale								
Two	[65, 66]	Solar, airflow	PV, HAWT	–	–	Outdoor-light Size	Enough to drive LED street-light	–
Two	[67]	Solar, wind	PV, HAWT	–	8.5 m/s	30 m-high	up to 1–5 kW	–
Three	[72, 73]	Solar, airflow, (rainwater collection)	PV or Solar Thermal Panel or Solar Concentrator System, VAWT	–	–	Pilot scale: 10,603 m^3	VAWT: 157 kW h/day PV: 280 kW h/day Saved Pumping: 2.6 kW h/day	–

(continued)

Table 2.3 (continued)

# of source	References	Input power sources	Working modes	Input acc.	Input properties	Volume/ surface A.	Peak output power voltage, power density	Mass (g)
						Actual: on 220 m high skyscraper		
Three	[75]	Solar, airflow, road traffic	PV, VAWT, PE	–	–	Actual on two-way roads and houses	Solar: 10 W, PE: 12 V	–
Three	[55]	Solar, airflow, rainwater	PV, Wind turbine, Turbine	–	–	Pilot: three-floor, ~9 m high building	290 kWh	–
						Actual: 98 m skyscrapers		

Table 2.2 covers fixed-frequency and broadband single-source powered HEHs and multimode HRTHs in Sects. 2.4.1, 2.4.2 and 2.4.3.1. Table 2.3 emphasizes micro-, meso-, and large-scale based comparisons of two-, three- and four-multisource powered HEHs in Sects. 2.4.3.2, 2.4.3.3 and 2.4.3.4. The given device volume and surface areas are the conservative values of the HEHs, and generally belong to transducer parts and active surface areas. The overall novel HEHs comparisons are evaluated in Sect. 2.5.

2.5 Conclusions

The need to achieve greater power generation leads researchers to investigate hybridization of EHing transduction mechanisms, working modes and source powers. As indicated in literature [10–23], in the scope of this chapter review, it is seen that HEHs generate greater power outputs than their single harvester components.

Among classic HEHs, Table 2.1 shows that Shan et al. HEH holds the greatest power output of 33 mW along with broadband performance in the range of 7 to 17 Hz [16]. Regarding the device volume, Ali et al. holds greater power density than Shan et al. [32]. Once PE and EM power generations are compared, generally, EM power generations are lower than PE parts with an only exception of Ab Rahman et al. HEH with four pole magnet arrangement [20, 34]. Apart from Wischke et al. microscale HEH, Xu et al. device [31] has the lowest energy generation with the minimum volume of 187.2 [31].

In novel HEH class, the most promising power generations are proposed by Yu et al. [62] in microscale, Saini et al. [2] and Karami and Inman [51] in meso-scale, and Chang et al. [72, 73] in large scale HEHs. Broadband technique significantly increases output power and density in nonlinear designs [44, 45]. In case of linear HEHs, Halim et al. novel design suppresses power density of Castagnetti's HEH [35] about 5 times, but not the bandwidth [14]. Within HRTHs, best performance is achieved by Karami and Inman with an average power output of 70 mW and maximum of 1 W when exposed to 1000 g [51]. However, Jung et al. managed to produce 37 mW at low excitation as much as 0.03 g [52]. At almost the same device size with Jung et al. Larkin and Tadesse gained more than 17 mW during jogging activity on wrist placement [24, 54] (see Table 2.2). In micro-scale HEH class, Wischke et al. managed to gain the highest output power of 215 μW via tuning in broadband operation, yet the total harvester volume is much greater [25, 39] than remaining prototypes. The closest result of 177 μW is reached by Yu et al. by solar and vibration powered HEH with a surface area of ~ 1 cm^2 [62]. The smallest size prototype with 13.4 mm^2 surface area is fabricated and tested by Jeon et al. and it produces 0.27 μW of output power [63]. Comparison of mesoscale novel HEHs emphasize that four-source powered HEH produces the greatest power output of 315 mW, whereas occupying the greatest volume [2]. It is seen that two-multisource powered HEHs produce greater power than three-multisource

powered ones without an exception. Collado and Georgiadis proved that RF and solar HEH are able to harness 56 mW of power with a small volume of 4 cm^3 [58, 59]. Regardless of the device size, Zhong et al. hand induced hybrid TENG and EM harvester generates total of 67 mW of power [61]. Lastly, large-scale HEHs result the best when implemented on high buildings such as skyscrapers. The greatest energy generation is estimated for solar and airflow harvesting along with rainwater storage, which saves pumping cost and eventually serves a total of 440 kW h of surplus energy daily [72, 73] (Table 2.3).

Among overall reviewed classic and novel HEHs, the peak power of 1 W is achieved by Karami and Inman at an extreme excitation of 1000 g, yet reasonable daily conditions are enough for the generation of 315 mW by Saini et al. four-source powered novel HEH. Regarding the size of HEHs, Collado and Georgiadis' two-source powered HEH generates the highest output power of 56 mW. The most promising power generations are achieved by Saini et al. four-source powered novel HEH in meso-scale, Wischke et al. tunable broadband classic HEH in microscale and Chong et al. proposed partially three-source powered HEH arrangement in large scale. In conclusion, HEHs not only increase the output powers and power densities, but also enable endless configurations to maximize harnessing existing power sources.

Acknowledgements Provided supports of Scientific and Technological Research Council of Turkey (TUBITAK) 2210-C Master Scholarship Program and Technological Entrepreneurship Industry Support (TGSD) by Republic of Turkey's Ministry of Science, Industry, and Technology (MoSIT) are greatly acknowledged.

References

1. Wei CK, Ramasamy G (2011) A hybrid energy harvesting system for small battery powered applications. In: 2011 IEEE conference on sustainable utilization and development in engineering and technology (student), October, pp 165–170. doi:10.1109/STUDENT.2011.6089346
2. Saini PK, Biswas A, Bhanja D (2015) Performance evaluation and simulation of solar panel, wind mill, fuel cell hybrid system for small scale energy harvesting. J Clean Energy Technol 3 (6):417–421. doi:10.7763/JOCET.2015.V3.234
3. Weddell AS, Magno M, Merrett GV, Brunelli D, Al-Hashimi BM, Benini L (2013) A survey of multi-source energy harvesting systems. In: Design, automation & test in Europe conference & exhibition (date). IEEE Conference Publications, New Jersey, pp 905–908. doi:10.7873/DATE.2013.190
4. Li P, Gao S, Cai H, Wu L (2015) Theoretical analysis and experimental study for nonlinear hybrid piezoelectric and electromagnetic energy harvester. Microsyst Technol 10(8). doi:10.1007/s00542-015-2440-8
5. Wu X, Khaligh A, Xu Y (2008) Modeling, design and optimization of hybrid electromagnetic and piezoelectric MEMS energy scavengers. In: Custom integrated circuits conference (CICC). IEEE, San Jose, CA, USA, pp 177–180
6. Energy Research Center (2015) Hybrid adaptive ambient vibration energy harvesting. University of Maryland. http://www.umerc.umd.edu/projects/harvest01. Accessed 10 Oct 2015

7. IDTechEx (2015) Multi-mode energy harvesting. Energy Harv J http://www.energyharvestingjournal.com/articles/8294/multi-mode-energy-harvesting. Accessed 10 Oct 2015
8. Yang B (2010) Hybrid energy harvester based on piezoelectric and electromagnetic mechanisms. J Micro/Nanolithogr MEMS MOEMS 9(2):023002. doi:10.1117/1.3373516
9. Cook-Chennault KA, Thambi N, Sastry AM (2008) Powering MEMS portable devices—a review of non-regenerative and regenerative power supply systems with special emphasis on piezoelectric energy harvesting systems. Smart Mater Struct 17(4):043001. doi:10.1088/0964-1726/17/4/043001
10. Challa VR, Prasad MG, Fisher FT (2009) A coupled piezoelectric–electromagnetic energy harvesting technique for achieving increased power output through damping matching. Smart Mater Struct 18(9):095029. doi:10.1088/0964-1726/18/9/095029
11. Wischke M, Woias P (2008) A multi-functional cantilever for energy scavenging from vibrations. In: Proceedings of PowerMEMS 2008. IEEE, Sendai, pp 73–76. http://cap.ee.ic.ac.uk/~pdm97/powermems/2008/pdfs/073-76%20Wischke,%20M.pdf
12. Khbeis MT (2010) Development of a simplified, mass producible hybridized ambient, low frequency, low intensity vibration energy scavenger (half-lives). University of Maryland, College Park. http://drum.lib.umd.edu/handle/1903/10778
13. Eun Y, Kwon D, Kim M, Yoo I, Sim J, Ko H-J, Cho K-H, Kim J (2015) A flexible hybrid strain energy harvester using piezoelectric and electrostatic conversion. Smart Mater Struct 23 (4):045040. doi:10.1088/0964-1726/23/4/045040
14. Halim MA, Cho HO, Park JY (2014) A handy-motion driven, frequency up-converted hybrid vibration energy harvester using PZT bimorph and nonmagnetic ball. J Phys Conf Ser 557 (1):012042. doi:10.1088/1742-6596/557/1/012042
15. Shan X, Guan S, Liu Z, Xu Z, Xie T (2013) A new energy harvester using a piezoelectric and suspension electromagnetic mechanism. Appl Phys Eng 14(12):890–897. doi:10.1631/jzus.A1300210
16. Shan X, Xu Z, Song R, Xie T (2013) A new mathematical model for a piezoelectric-electromagnetic hybrid energy harvester. Ferroelectrics 450(1):57–65. doi:10.1080/00150193.2013.838490
17. Li P, Gao S, Cai H (2013) Modeling and analysis of hybrid piezoelectric and electromagnetic energy harvesting from random vibrations. Microsyst Technol 21(2):401–414. doi:10.1007/s00542-013-2030-6
18. Chen S, Sun J, Hu J (2013) A vibration energy harvester with internal impact and hybrid transduction mechanisms. In: 13th international conference on fracture. IEEE, Beijing, pp 1–10
19. Karthik KS, Ali SF, Adhikari S, Friswell MI (2013) Base excited hybrid energy harvesting. In: 2013 IEEE international conference on control applications (CCA). IEEE, Hyderabad, pp 978–982. doi:10.1109/CCA.2013.6662878
20. Ab Rahman MF, Kok SL, Ruslan E, Dahalan AH, Salam S (2013) Comparison study between four poles and two poles magnets structure in the hybrid vibration energy harvester. In: IEEE (ed) 2013 IEEE student conference on research and development (SCOReD), Putrajaya, Malaysia Comparison, pp 16–17
21. Sang Y, Huang X, Liu H, Jin P (2012) A vibration-based hybrid energy harvester for wireless sensor systems. IEEE Trans Magn 48(11):4495–4498
22. Tadesse Y, Priya S (2008) Multimodal energy harvesting system: piezoelectric and electromagnetic. J Intell Mater Syst Struct 20(5):625–632. doi:10.1177/1045389X08099965
23. Matiko JW, Grabham NJ, Beeby SP, Tudor MJ (2014) Review of the application of energy harvesting in buildings. Meas Sci Technol 25(1):012002. doi:10.1088/0957-0233/25/1/012002
24. Larkin M, Tadesse Y (2014) HM-EH-RT: hybrid multimodal energy harvesting from rotational and translational motions. Int J Smart Nano Mater 4(4):257–285
25. Wischke M, Masur M, Goldschmidtboeing F, Woias P (2010) Electromagnetic vibration harvester with piezoelectrically tunable resonance frequency. J Micromech Microeng 20 (3):035025. doi:10.1088/0960-1317/20/3/035025

26. Tang L, Yang Y, Soh CK (2010) Toward broadband vibration-based energy harvesting. J Intell Mater Syst Struct 21(18):1867–1897. doi:10.1177/1045389X10390249
27. Khameneifar F (2011) Vibration-based piezoelectric energy harvesting system for rotary motion applications. Simon Fraser University. http://summit.sfu.ca/item/11906
28. Lafont T, Gimeno L, Delamare J, Lebedev GA, Zakharov DI, Viala B, Cugat O, Galopin N, Garbuio L, Geoffroy O (2015) Magnetostrictive—piezoelectric composite structures for energy harvesting. J Micromech Microeng 22(9):094009. doi:10.1088/0960-1317/22/9/094009
29. Mahmoudi S, Kacem N, Bouhaddi N (2014) Enhancement of the performance of a hybrid nonlinear vibration energy harvester based on piezoelectric and electromagnetic transductions. Smart Mater Struct 23(7):075024. doi:10.1088/0964-1726/23/7/075024
30. Becker P, Folkmer B, Manoli Y (2009) The hybrid vibration generator, a new approach for a high efficiency energy scavenger. In: IEEE (ed) International workshop on micro and nanotechnology for power generation and energy conversion applications. PowerMEMS, Washington, DC, pp 439–442
31. Xu ZL, Wang XX, Shan XB, Xie T (2012) Modeling and experimental verification of a hybrid energy harvester using piezoelectric and electromagnetic technologies. Adv Mater Res 569:529–532. doi:10.4028/www.scientific.net/AMR.569.529
32. Ali NM, Mustapha AA, Leong KS (2013) Investigation of hybrid energy harvesting circuits using piezoelectric and electromagnetic mechanisms. In: IEEE student conference on research and development, December, pp 16–17
33. Xia H, Chen R, Ren L (2015) Analysis of piezoelectric–electromagnetic hybrid vibration energy harvester under different electrical boundary conditions. Sens Actuators A 234:87–98. doi:10.1016/j.sna.2015.08.014
34. Ab Rahman MF, Kok SL, Ali, NM, Hamzah RA, Aziz KA (2013). Hybrid vibration energy harvester based on piezoelectric and electromagnetic transduction mechanism. In: 2013 IEEE conference on clean energy and technology (CEAT). IEEE, Langkawi TBD, pp 243–247. doi:10.1109/CEAT.2013.6775634
35. Castagnetti D (2015) A belleville-spring-based electromagnetic energy harvester. Smart Mater Struct 24(9):94009. doi:10.1088/0964-1726/24/9/094009
36. Twiefel J, Westermann H (2013) Survey on broadband techniques for vibration energy harvesting. J Intell Mater Syst Struct 24(11):1291–1302. doi:10.1177/1045389X13476149
37. Zhou S, Cao J, Inman DJ, Lin J, Liu S, Wang Z (2014) Broadband tristable energy harvester: modeling and experiment verification. Appl Energy 133:33–39. doi:10.1016/j.apenergy.2014.07.077
38. Li P, Gao S, Niu S, Liu H, Cai H (2014) An analysis of the coupling effect for a hybrid piezoelectric and electromagnetic energy harvester. Smart Mater Struct 23(6):065016. doi:10.1088/0964-1726/23/6/065016
39. Wischke M, Masur M, Goldschmidtboeing F, Woias P (2010) Piezoelectrically tunable electromagnetic vibration harvester. In: 2010 IEEE 23rd international conference on micro electro mechanical systems (MEMS). IEEE, pp 1199–1202. doi:10.1109/MEMSYS.2010.5442427
40. Xu ZL, Shan XB, Song RJ, Xie T (2014) Electromechanical modeling and experimental verification of nonlinear hybrid vibration energy harvester. In: Applications of ferroelectrics (ed) 2014 joint IEEE international symposium on the applications of ferroelectric, international workshop on acoustic transduction materials and devices & workshop on piezoresponse force microscopy. IEEE, State College, PA, USA, pp 1–4. doi:10.1109/ISAF.2014.6923018
41. Dias JAC, Marqui C De, Erturk A (2013) Hybrid piezoelectric-inductive flow energy harvesting and dimensionless electroaeroelastic analysis for scaling. Am Inst Phys 044101 (102):1–6
42. Dias JAC, De Marqui C, Erturk A (2015) Three-degree-of-freedom hybrid piezoelectric-inductive aeroelastic energy harvester exploiting a control surface. AIAA J 53 (2):394–404. doi:10.2514/1.J053108

43. Reuschel T, Salehian A, Kotsireas I, Melnik R, West B (2011) Analysis and modelling towards hybrid piezo-electromagnetic vibrating energy harvesting devices. doi:10.1063/1.3663465
44. Karami MA, Inman DJ (2011) Equivalent damping and frequency change for linear and nonlinear hybrid vibrational energy harvesting systems. J Sound Vib 330(23):5583–5597. doi:10.1016/j.jsv.2011.06.021
45. Karami M.A, Inman, DJ (2010) Nonlinear hybrid energy harvesting utilizing a piezo-magneto-elastic spring. In: Ghasemi-Nejhad MN (ed) SPIE smart structures and materials + nondestructive evaluation and health monitoring, vol 7643, p 76430U–76430U–11. doi:10.1117/12.847566
46. Leadenham S, Erturk A (2015) Nonlinear M-shaped broadband piezoelectric energy harvester for very low base accelerations: primary and secondary resonances. Smart Mater Struct 24 (5):055021. doi:10.1088/0964-1726/24/5/055021
47. Ishikuro H (2011) Energy harvesting technology, system LSI design. Tokyo, Japan
48. Sasaki K, Osaki Y, Okazaki J, Hosaka H, Itao K (2005) Vibration-based automatic power-generation system. Microsyst Technol 11(8–10):965–969. doi:10.1007/s00542-005-0506-8
49. Khaligh A, Zeng P, Zheng C (2010) Kinetic energy harvesting using piezoelectric and electromagnetic technologies—state of the art. IEEE Transduct Ind Electron 57(3):850–860
50. Romero E, Warrington RO, Neuman MR (2009) Energy scavenging sources for biomedical sensors. Physiol Meas 30(9):35–62. doi:10.1088/0967-3334/30/9/R01
51. Karami MA, Inman DJ (2013) Nonlinear dynamics of the hybrid rotary-translational energy harvester. In: ASME conference on smart materials, adaptive structures and intelligent systems (SMASIS). doi:10.1115/SMASIS2013-3110
52. Jung H-J, Kim I-H, Min DY, Sim S-H, Koo J-H (2013) A hybrid electromagnetic energy harvesting device for low frequency vibration. In: Sodano H (ed) Active and passive structures and intelligent systems 2013, SPIE, vol 8688, p 86881I. doi:10.1117/12.2010014
53 Taylor, Francis (2013) Int J Smart Nano Mater 4(4):257–285. www.tandfonline.com/doi/abs/10.1080/19475411.2014.902870
54. Larkin MR, Tadesse Y (2014) Characterization of a rotary hybrid multimodal energy harvester. In: Proceedings of SPIE, October 2015, vol 9057, p 90570U. doi:10.1117/12.2045271
55. Mithra VTV, Sharmila R, Giridhar MVSS (2014) Development of hybrid power generation model using rain water, solar and wind. In: Centre for water resources, IST, JNTUH. JNTUH, Hyderabad
56. Gambier P, Anton SR, Kong N, Erturk A, Inman DJ (2011) Piezoelectric, solar and thermal energy harvesting for hybrid low-power generator systems with thin-film batteries. Measur Sci Technol 23(1):015101. doi:10.1088/0957-0233/23/1/015101
57. Hehr A, Park G, Farinholt K (2012) Hybrid energy harvesting/transmission system for embedded devices. Proc SPIE Ind Commer Appl Smart Struct Technol 8343(07):1–6. doi:10.1117/12.915461
58. Collado A, Georgiadis A (2013) Conformal hybrid solar and electromagnetic (EM) energy harvesting rectenna. IEEE Trans Circuits Syst I Regul Pap 60(8):2225–2234. doi:10.1109/TCSI.2013.2239154
59. Georgiadis A, Collado A, Via S, Meneses C (2011) Flexible hybrid solar/EM energy harvester for autonomous sensors. In: IEEE MTT-S international microwave symposium (IMS), Baltimore, MD, USA
60. Chatterjee P, Bryant M (2015) Transfer matrix modeling of a tensioned piezo-solar hybrid energy harvesting ribbon. In: Liao W-H (ed) SPIE, vol 9431, p 94310D. doi:10.1117/12.2086138
61. Zhong X, Yang Y, Wang X, Wang ZL (2015) Rotating-disk-based hybridized electromagnetic-triboelectric nanogenerator for scavenging biomechanical energy as a mobile power source. Nano Energy 13:771–780. doi:10.1016/j.nanoen.2015.03.012

62. Yu H, Yue Q, Zhou J, Wang W (2014) A hybrid indoor ambient light and vibration energy harvester for wireless sensor nodes. Sensors 14(5):8740–8755. doi:10.3390/s140508740
63. Jeon S, Kim D, Yoon G-W, Yoon J, Choi Y-K (2015) Self-cleaning hybrid energy harvester to generate power from raindrop and sunlight. Nano Energy 12:636–645. doi:10.1016/j.nanoen.2015.01.039
64. Zakharov D, Lebedev G, Cugat O, Delamare J, Viala B, Lafont T, Gimeno L, Shelyakov A (2012) Thermal energy conversion by coupled shape memory and piezoelectric effects. J Micromech Microeng 22(9):094005. doi:10.1088/0960-1317/22/9/094005
65. Tong CW (2014) Lighting up University of Malaya—an innovative idea to provide outdoor lighting using wind-solar hybrid renewable energy sources. University of Malaya. http://www.researchsea.com/html/article.php/aid/8212/cid/1/research/science/university_of_malaya/lighting_up_university_of_malaya_____an_innovative_idea_to_provide_outdoor_lighting_using_wind-solar_hybrid_renewable_energy_sources.html. Accessed 12 Oct 2015
66. Malaya U (2014) Outdoor lighting using wind-solar hybrid renewable energy sources. ScienceDaily. http://www.sciencedaily.com/releases/2014/05/140525204734.htm. Accessed 12 Oct 2015
67. De MM, Reddy KJ, Srikanth L, Jayasankar S, Muthu K, Samiullah TH, Dayananda GN (2014) Research, design, development & demonstration (RD 3) of a wind solar hybrid (WiSH) system. In: Indian technology congress, ITC2014. NIMHANS Convention Centre, The Institution of Engineers (India), NDRF & Indian Technology Congress, Bangalore, pp 1–10
68. Porcarelli D, Brunelli D, Magno M, Benini L (2012) A multi-harvester architecture with hybrid storage devices and smart capabilities for low power systems. In: International symposium on power electronics, electrical drives, automation and motion. IEEE, Sorrento doi:10.1109/SPEEDAM.2012.6264533
69. Chung T-K, Tseng C-Y, Chen C, Wang C (2012) Design, fabrication, and testing of a thermal/mechanical/magnetic hybrid energy micro-harvester. In: ASME 2012 conference on smart materials, adaptive structures and intelligent systems, SMASIS2012-8192, vol 2. ASME, Stone Mountain, Georgia, USA, pp 1–6. doi:10.1115/SMASIS2012-8192
70. Zheng L, Cheng G, Chen J, Lin L, Wang J, Liu Y, Li H, Wang ZL (2015) A hybridized power panel to simultaneously generate electricity from sunlight, raindrops, and wind around the clock. Adv Energy Mater. doi:10.1002/aenm.201501152
71. Chen C-C, Chung T-K, Tseng C-Y, Hung C-F, Yeh P-C, Cheng C-C (2015) A miniature magnetic-piezoelectric thermal energy harvester. IEEE Trans Magn 51(7):1–9. doi:10.1109/TMAG.2015.2395385
72. Chong WT, Fazlizan A, Poh SC, Pan KC, Ping HW (2012) Early development of an innovative building integrated wind, solar and rain water harvester for Urban high rise application. Energy Build 47:201–207. doi:10.1016/j.enbuild.2011.11.041
73. Chong WT, Pan KC, Poh SC, Fazlizan A, Oon CS, Badarudin A, Nik-Ghazali N (2013) Performance investigation of a power augmented vertical axis wind turbine for urban high-rise application. Renew Energy 51:388–397. doi:10.1016/j.renene.2012.09.033
74. Donnie EJ (2014) Hybrid energy harvesting device and fixed threshold power production. United States Patent, NV (US). USOO8847425B2 (12)
75. Sathiyamoorthy S, Bharathi N (2012) Hybrid energy harvesting using piezoelectric materials, automatic rotational solar panel, vertical axis wind turbine. Procedia Eng 38:843–852. doi:10.1016/j.proeng.2012.06.106

Chapter 3
Micro-scale Energy Harvesting for Batteryless Information Technologies

Ali Muhtaroğlu

Abstract Continually growing integration levels and miniaturization in electronics has led to the enrichment of features to enable a variety of new applications with simultaneous reduction in system power consumption. The start of the 21st century is hallmarked by the emergence of small information engines (microsystems) as part of "internet of things" thrust to provide the intelligence behind the building blocks of the increasingly automated, digitized, and connected eco-system around residential, industrial, health, education, transportation, communication, and other sectors of our civilization. These engines require small amount of power to work in an embedded environment where frequent access for maintenance, and power delivery or battery refurbishment is not desirable. The focus of this chapter is batteryless operation, which is at the center-stage of microscale harvesting research efforts to enable such applications. Energy and power budgeting, and system design concerns are reviewed for batteryless operation, and system examples are provided. First part of Sect. 3.1 discusses demand for micro-scale information technologies. Section 3.1.3 provides typical power and energy budgets for sensor nodes. The motivations for batteryless operation are examined in Sect. 3.1.4. Power generation is provided as a recent power management thrust in such systems in Sect. 3.1.5. System design issues for realizing batteryless information technologies are covered in Sect. 3.2 with the review of energy harvesting techniques such as small-scale solar irradiation, environmental vibration, thermal differences, and ambient radio-frequency electromagnetic waves. Finally, the last part of the section briefly discusses upcoming trends and further efforts in enabling batteryless information technologies at a disruptive level.

Keywords Microsystems · Batteryless operation · Energy harvesting · Energy scavenging · Information technologies

A. Muhtaroğlu (✉)
Department of Electrical and Electronics Engineering, Middle East Technical University, Northern Cyprus Campus, Güzelyurt, Mersin 10, Turkey
e-mail: amuhtar@metu.edu.tr

N. Bizon et al. (eds.), *Energy Harvesting and Energy Efficiency*,
Lecture Notes in Energy 37, DOI 10.1007/978-3-319-49875-1_3

Abbreviation and Acronyms

AC	Alternating-current
ADC	Analog-to-digital conversion
ASIC	Application specific integrated circuit
BSN	Body sensor nod
COTS	Commercial off-the-shelf
DC	Direct-current
DVS	Dynamic voltage scaling (), 20
ICT	Information and communication technologies
M2M	Machine-to-machine (), 4
MCU	Microcontroller unit
MEMS	Micro-electromechanical system
MPPT	Maximum Power Point Tracking
PC	Personal Computer
PV	Photovoltaic
PZT	Piezoelectric
PCB	Printed circuit board
SECE	Synchronous electric charge extraction
TEG	Thermoelectric generator
WSN	Wireless Sensor Networks

3.1 Micro-scale Energy Harvesting

3.1.1 Introduction

The development of integrated microprocessor chip in 1971 was a key enabler for the Personal Computer (PC). Since then, Moore's Law has correctly predicted the seamless technology advancement of doubled transistor count on a chip about every two years, while the transistors themselves shrunk with every generation. Additional transistors with better power consumption characteristics were utilized by component and system architects to develop advanced features in electronic platforms, and by circuit designers to build faster circuits. More integration was achieved with every technology generation, which not only pulled down system cost through reduced number of components, but also lowered overall power dissipation due to the elimination of glue-logic between components, and the fact that each transistor could be switched on/off with less power. Computer quickly stopped being an expensive machine in a laboratory reserved for privileged scientists, and by 1990s marketing segmentation drove differentiation of computer systems to address emerging usage models, making computers available to virtually everyone.

Some computers evolved into mobile productivity tools that travel along with us. Some turned into entertainment centers with emphasis on multi-media performance. Some continued their evolution on traditional high performance computing with the goal to achieve more scientific computations per unit time. Another important segment was enabled through simple-task dedicated 'small' information engines shaping the building blocks of the progressively automated, digitized, and connected eco-system around all major application sectors such as residential, industrial, health, education, transportation, and communication. It was commonly accepted by the end of the 20th century that wireless machines and networks would have a fundamental role in intelligent system design. It has become clear ever since that 21st century is the era of internet of things (IoT) or "internet of everything", meaning everything from small sensors to large machines get connected. These "things" make our life easier, and increase our productivity. The information, available at our finger tips, contributes to our health, comfort, safety, education, professional development. This realization quickly leads to the need for embedded applications without batteries i.e. longevity with minimum maintenance.

Contemporary microsystems for handling information require features to dynamically trade off performance and power dissipation. Other simultaneously critical ingredients are long battery life, low energy operation, wireless communication, compact, low cost, light platforms. Due to the recent emphasis on intelligent environment, small embedded systems with very low power consumption and longevity have become vital to the exponentially growing number of 'miniaturized and ubiquitous' devices in the 21st century. Since good power and energy consumption characteristics have been the determinant for the success of new information engines, much engineering effort has been spent on various aspects of power management. Batteryless operation, however, continues to be a great challenge. Energy harvesting is thus introduced in this section as the means to achieve zero or close-to-zero average input power for green micro-scale IT (Information Technologies) of the future. Energy and power budgeting for such applications, the need for batteryless operation, consumption management and generation are covered in the following discussion.

3.1.2 Demand for Micro-scale Information Technologies

Use of IT has been proven to increase productivity in organizations for the last few decades [1]. Tendency for decentralized or distributed operations, mobile lifestyles has naturally increased the demand for IT. In a recent white paper by Cisco, tremendous growth in demand for smartphones, tablets, and other mobile computing devices is projected. Average number of connected devices per capita is projected to grow from 2 to 3.2 in the period between 2014 and 2019. Particularly, machine-to-machine (M2M) connection is the fastest growing category as depicted in Fig. 3.1 [2].

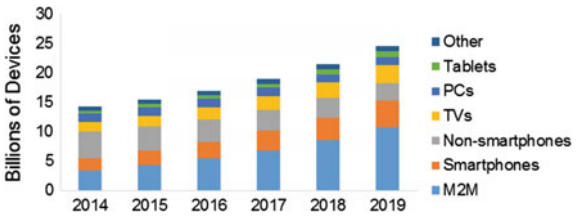

Fig. 3.1 Global projected growth of connected devices by type [2]

The reported trends further emphasize the forecasted growth in demand for smaller or micro-scale IT devices for applications with M2M connectivity to improve quality of daily services. The largest expected growth is in connected health sector, with compound annual growth rate close to 50% between 2014 and 2019 [2]. Similarly, agriculture, construction, emergency services, and transportation (cars) sectors are expected to experience a fast growth rate in the adoption of M2M connected devices. Sensing, digitization, processing, and communication are ubiquitously embedded into everyday objects, turning them into the IoT [3]. Individual devices thus collaborate in Wireless Sensor Networks (WSNs) across a variety of contexts to provide invaluable data and information on physical phenomena. The applications of such WSNs are widespread as summarized in Fig. 3.2.

The generic WSN system architecture and requirements are outlined in Fig. 3.3. Many embedded sensors attached to the system have the most stringent power dissipation and energy requirements for sensing and transmission of data to the local HUB. Microelectromechanical system (MEMS) components may be used for miniaturization of mechanical aspects of the sensor nodes. These nodes also contain some processing features implemented in application specific integrated circuit (ASIC) components in a subset of the applications of interest. Adding to these the size and cost constraints, and potentially dynamic, unfavorably out-of-touch physical environment, the sensor node system design becomes a challenging problem. The local processing and control hub follows a pre-programmed algorithm to collect data from a variety of sensors in the neighborhood (few meters to few kilometers as typical range), and may respond by activating various actuators in the intelligent system after processing the received information. A desirable feature of the WSN is the ability to communicate with cloud or servers over the internet for remote monitoring and control. This aspect further allows remote policies and user interfaces to be devised and implemented through software for a particular WSN.

Considering transportation, for example, use of WSNs in aeronautical vehicles is an emerging trend. More than one thousand sensor nodes may potentially be utilized in an aircraft, for automation of flight attendant control panels, passenger services, cabin illumination, surveillance cameras, safety sensors (smoke, temperature, humidity), passenger entertainment, signs and various other controls [7]. It has become increasingly difficult to reliably wire signals and power lines to and from the sensors and actuators through the tight space available within the structure

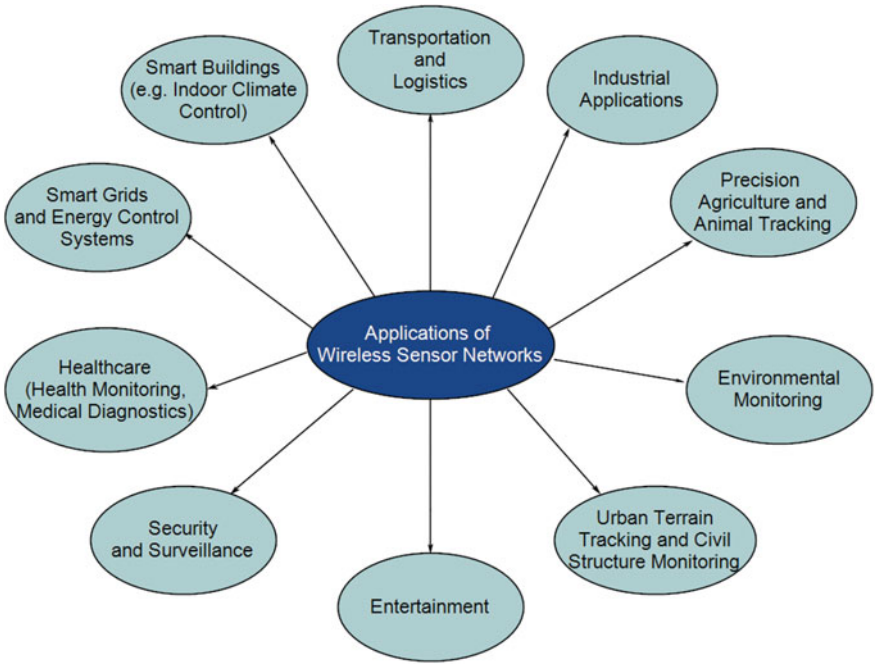

Fig. 3.2 Application of WSNs (based on [4–6])

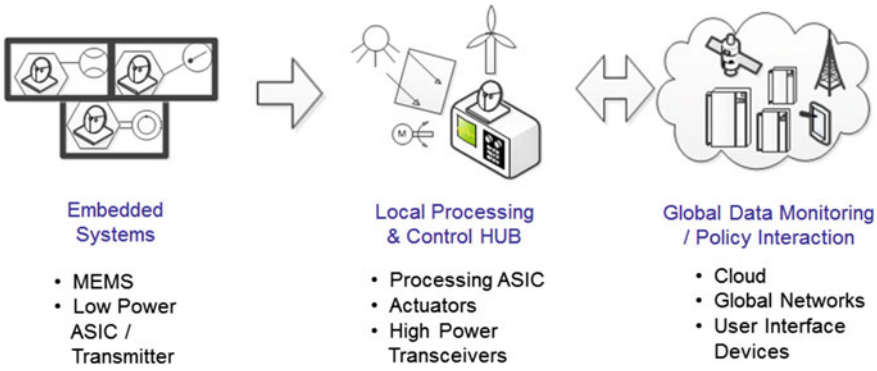

Fig. 3.3 A generic WSN system architecture and component requirements [8]

of the plane. As in the case of aircrafts, many uses of WSNs require accurate processing and delivery of data from one location to another, while at the same time satisfying strict system requirements related to power source, power consumption and size.

3.1.3 Power and Energy Budgets

Sensor nodes are either battery driven or are required to operate on energy scavenged (harvested) from the environment. Hence, the energy budget is tight. The importance of optimizing design based on application needs cannot be stressed enough. Designs using commercial off-the-shelf (COTS) components are often disadvantaged in power consumption due to redundancy of features, and interconnect. Custom integrated designs and system-on-chip (SOC) components on the other hand can potentially deliver minimum power for the application, but typically are subject to longer design, fabrication and test lead times, and higher unit costs for low volume operations.

A typical architecture for wireless sensor nodes is depicted in Fig. 3.4. The voltage from the battery is converted to one or more voltage levels by DC/DC converter(s) to supply power to sensor(s), one or more analog-to-digital converters (ADCs), microcontroller unit (MCU), a memory if storage requirement is higher than what is available in the MCU, and a radio for communication of data. Local algorithm for capturing and processing the data is programmed into the MCU. Although transceiver and/or receiver circuits in the radio module are generally accepted to be the most power-hungry of all blocks, the rest of the system components, software and hardware power management features, algorithms and protocols may potentially have far greater cumulative impact on the average power dissipation and energy consumption of the node.

Table 3.1 illustrates the power dissipation values for fundamental components and modes of the two sensor node architectures captured by a case study in 2002. Although the technology scaling in integrated circuit industry results in significant (potentially up to 2–3 orders of magnitude) reduction today in all of the provided power figures, the table is indicative of the relative spread of power consumption across modes of operation, and across different architectures. For calculation of accurate energy consumption, it is necessary to characterize the portion of the total operation time that is statistically spent in each valid sensor node power state i.e. percent residence per power state. Then the average power per sensor node can be computed for battery life estimation through weighted summation of all power levels. A comprehensive model was recently developed [10] for accurately

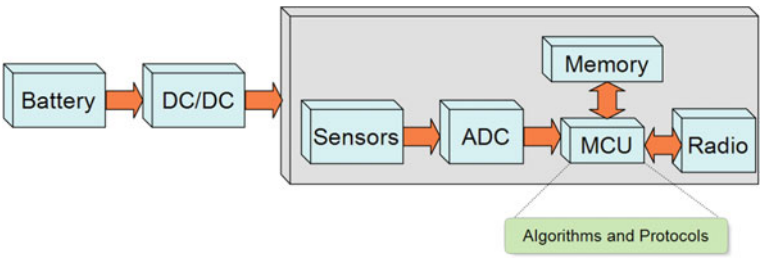

Fig. 3.4 System architecture of a typical wireless sensor node [9]

Table 3.1 Power analysis of (a) Rockwell's WINS, (b) Medusa II nodes [9]

(a) Rockwell's WINS				(b) Medusa II			
MCU mode	Sensor mode	Radio mode	Power (mW)	MCU mode	Sensor mode	Radio mode	Power (mW)
ACTIVE	ON	Tx (Power: 36.3 mW)	1080.5	ACTIVE	ON	Tx (Power: 0.7368 mW)	24.58
		Tx (Power: 19.1 mW)	986.0			Tx (Power: 0.0979 mW)	19.24
		Tx (Power: 13.8 mW)	942.6			Tx (Power: 0.7368 mW)	25.37
		Tx (Power: 3.47 mW)	815.5			Tx (Power: 0.0979 mW)	20.05
		Tx (Power: 2.51 mW)	807.5			Tx (Power: 0.7368 mW)	26.55
		Tx (Power: 0.96 mW)	787.5			Tx (Power: 0.0979 mW)	21.26
		Tx (Power: 0.30 mW)	773.9			Tx (Power: 0.7368 mW)	27.46
		Tx (Power: 0.12 mW)	771.1			Tx (Power: 0.0979 mW)	22.06
ACTIVE	ON	Rx	751.6	ACTIVE	ON	Rx	22.20
ACTIVE	ON	IDLE	727.5	ACTIVE	ON	IDLE	22.06
ACTIVE	ON	SLEEP	416.3	ACTIVE	ON	OFF	9.72
ACTIVE	ON	REMOVED	383.3	IDLE	ON	OFF	5.92
SLEEP	ON	REMOVED	64.0	SLEEP	OFF	OFF	0.02
ACTIVE	REMOVED	REMOVED	360.0	–	–	–	–

predicting the power consumption of wireless sensor nodes across a variety of usage scenarios. It can be inferred from the table that, the variation with various power modes aside, transmitter and receiver (radio) circuits in sensor nodes consume a significant portion of the total power budget. Low-power radios typically have a minimum power consumption of around 50 μW, for example, in order to provide sufficient sensitivity in body sensor networks [11]. In a recently reported bladder-pressure monitoring application [12], the concern was battery life, since the recharge frequency was not high. A custom application specific integrated circuit (ASIC) implant in this application achieved around 33 μW average power when enhanced with a special power control unit (PCU). When the unit was excluded, the average power exceeded 1 mW.

3.1.4 The Case for "Batteryless"

A viable energy source continues to be a challenge in wireless sensors that make up the IoT infrastructure. Although batteries have traditionally been used to power

small microelectronic systems, much of recent research is focused on eliminating them from future sensor networks. Historically three parallel motivations have driven this thrust:

i. Green Computing: Information and communication technologies (ICT) generate 2% of worldwide CO_2 emissions, which roughly corresponds to a quarter of the emissions generated by cars [13]. With the unprecedented growth forecasted in ICT, as outlined in Sect. 3.1.2, this trend brings on significant concerns about the contribution of computing to global warming. There have been many emerging initiatives on energy efficiency around the globe, such as the Energystar [14], which is clearly a significant component in green computing approach. The other important component is achieving a sustainable life-cycle cost in microelectronics. An undisputed problem in this regard has been the disposal of batteries or disposal of microelectronic components that contain batteries.
ii. Avoiding Invasive and Bulky: Implantable sensors are of high interest in biomedical field for monitoring various body functions, such as blood pressure [15], electrocardiogram (ECG), electroencephalogram (EEG), and electromyogram (EMG) [16]. However, their utility reduces significantly if they become invasive to the part of the body they are integrated in, or even cause additional patient anxiety due to bulkiness. Significant portion of the volume and intrusiveness of non-batteryless body sensor networks can be traced to on-board batteries.
iii. Cost Reduction: Due to the cost and inconvenience or in some cases unfeasibility of regular refurbishing of batteries, the operational expenses of the WSNs increase significantly. In many embedded applications, it may even be cheaper to install a new sensor node instead of accessing the old one for maintenance and battery replacement.

3.1.5 Consumption Management and Generation

Due to the concomitant power resource constraints, as discussed in the previous section, management of power and energy at sensor nodes takes high priority. There are many energy saving methods to improve the working model or algorithms employed by a given sensor at the data manipulation or communication layer in order to ensure different components are activated on demand whenever there is a significant "event". These techniques significantly reduce average power consumption, and hence the energy. A comprehensive tree of approaches that can be applied to the energy conservation problem for a particular system is outlined in Fig. 3.5.

Duty cycling solutions emphasize management of the radio transceiver subsystem, which traditionally consumes much more energy than the processing subsystem. Distributed sleep/wake-up scheduling algorithms are applied to the radio

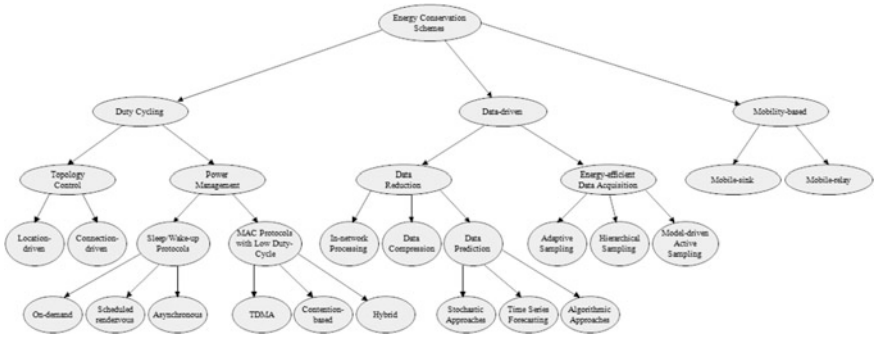

Fig. 3.5 Taxonomy of approaches for energy consumption management in sensor networks [17]

circuits in order to turn them on when there is data to send or receive. The present-day subsystem components also support multiple power management modes, depending on "how active" they need to be in any given instant. Such component power management features will be further discussed later. Excessive data sampling unnecessarily keeps both the processor(s) and the transceivers awake causing them to burn active power. Thus, *data driven* techniques shown as one of the main branches in Fig. 3.5 target diminution in the amount of sampled or transmitted data, while maintaining the minimum required sensing accuracy. When the sensor nodes are static, some nodes may be on congested data paths while others may hardly receive data 'hops' from the surroundings. Such asymmetry in WSN may require location based management schemes. In cases when sensor nodes are dynamic, data 'hops' may first detect proximity of the receiving sensors to the transmitting sensors in order to optimize power dissipated in transmission. Such algorithms are categorized under *mobility-based* approaches in the figure. Details of the individual energy conservation schemes in the tree will not be discussed further here, but can be accessed at the original publication [17].

Various hardware design and fabrication methods are utilized to reduce power consumption at component level, which all directly contribute to the power management of the sensor node. Different facets of power management in microelectronic computing systems are presented in Fig. 3.6. The balloon on the lower right represents the software design features described in the above paragraphs. As the rest of the picture exhaustively presents, the hardware power management design task is shared across different expertise areas. Process technology based features combine physical enhancements to semiconductors with fabrication methods to reduce static power consumption (leakage) per device for a targeted switching performance. Circuit designers focus on effective use of transistors in order to simultaneously achieve goals related to circuit delay, dynamic and static power dissipation through various circuit design techniques. Architects use their knowledge of hardware/software interface and how different hardware blocks are expected to "behave" to optimize power at a higher abstraction level. For example, memory blocks can be put in low-leakage (e.g. low supply voltage) mode, when not in use. Clocks may be

removed from blocks of processing units (clock gating) to reduce dynamic power dissipation, or power may be shut down to inactive blocks selectively to lower total power. Dynamic speed/power tradeoffs can be realized in real-time through the simultaneous modulation of supply voltage and operating system clock frequency. Integration of power electronics, such as DC/DC regulators, into the SOC reduces system cost, and allows elimination of losses in large power delivery networks. More importantly, processing engines can control supply voltage with better resolution to support advanced power management. Temperature, power, motion sensors incorporated into the electronic components or SOCs further provide tools for system level power/performance optimizations, while keeping within reliability constraints.

Energy scavenging (a.k.a. energy harvesting), depicted at the bottom of Fig. 3.6, has recently been a fast growing area of research and development to enhance system power management characteristics, and address the issues associated with batteries covered in Sect. 3.1.4. This trend is encouraged by the ever-diminishing power and energy dissipation requirements of IoT devices with technology scaling trends. Energy harvesting is the ultimate sustainable or green solution to powering micro-scale IT systems. It involves use of constant or continually available energy

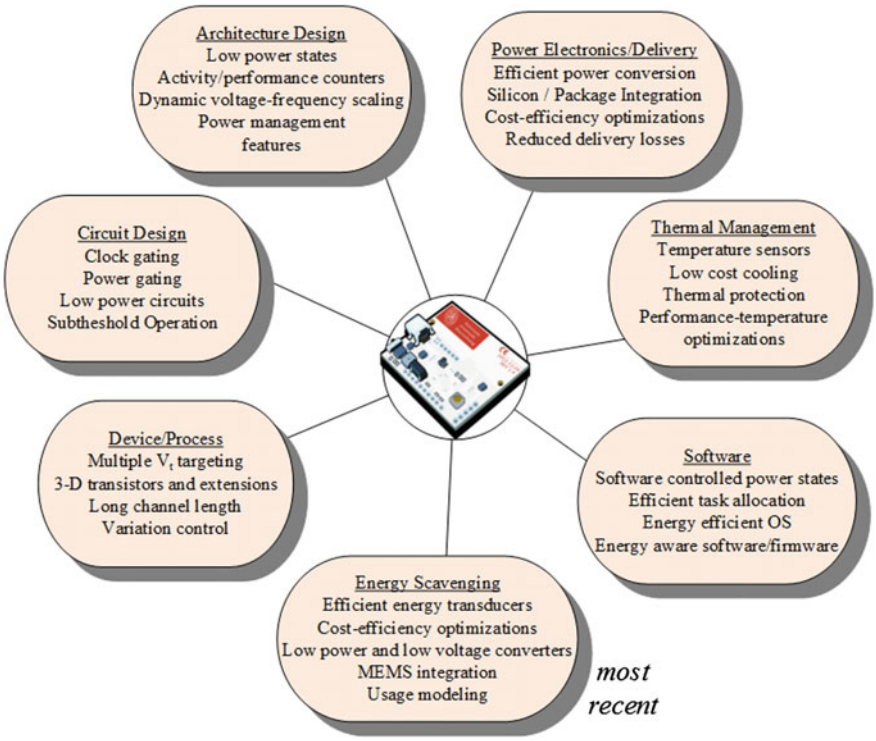

Fig. 3.6 Different facets of power management [18]

sources in the vicinity of the sensor node to generate electrical power. Since such resources practically never run out, they are referred to as "renewable". Although traditional renewable energy sources such as sunlight and wind can and should be utilized in a variety of IoT contexts when applicable, they are often non-existent in the environment of the embedded sensors. When they do get utilized, the associated transducers need to be miniaturized to satisfy the requirements of the micro-scale IT nodes. Therefore, there are multiple system design challenges involved. Examples from appealing solutions will be discussed in the next section in the context of applications.

3.2 Systems and Applications

3.2.1 Introduction

System design issues associated with incorporating and utilizing available energy sources around intelligent embedded systems are reviewed in this section. Particularly micro-scale (solar) photovoltaic, piezoelectric, vibration based electromagnetic, thermoelectric and ambient radio-frequency (RF) wave energy will receive focus. The final section of the chapter highlights examples from emerging applications to demonstrate successful technology integration, and upcoming trends.

3.2.2 System Design

The goal of an ideal energy harvester, which is often referred to as a micro-power generator, is to replace the battery previously depicted in Fig. 3.4. Availability of sufficient energy at the source is an important but an insufficient condition for energy harvesting. This is due to the fact that useful power available at the micro-scale power generators typically varies between micro-Watts to tens of milli-Watts, with voltage output between tens of milli-Volts to hundreds of milli-Volts, at most, under realistic scenarios. It may take one or more power electronics stages before the power can be safely delivered to the sensor node with acceptable voltage and current characteristics.

Each stage bears losses, and inadvertently reduces overall system efficiency by some amount. For example, if the generated voltage from the harvester is in AC (alternating-current) form, it requires rectification because typical electronic loads consume DC (direct-current) power. If the harvester output impedance or resistance characteristic is far from that of an ideal supply or varies significantly with environmental conditions, then impedance matching circuit may be required to extract maximum energy. Finally, the voltage needs to be stepped-up to suitable levels for

the load circuits in the target system. Integrated design approaches often combine a number of such circuits in one design to simultaneously reduce the cost and size of the interface electronics, and improve power conversion efficiency. It is challenging to design interface electronics with high efficiency, especially in cost and area constrained systems. Therefore, one needs to carefully analyze the target application, and evaluate solution space for energy harvester integration at minimum cost.

3.2.3 Micro-scale Harvesters

Micro-scale IT systems vary widely in volume between few cm^3 to few tens of cm^3, which sets the range for acceptable sizes for the energy harvesters. The energy sources in the vicinity also alter in magnitude and availability. Depending on use environment, some sensor nodes may experience motion and vibration, while others may be subject to temperature variations. A number of embedded applications may, by design, shield RF radiation, while others may be exposed to strong RF waves. Therefore, it is necessary to carefully analyze application environment and requirements before incorporating the correct energy harvesting mode. Common ambient energy sources for embedded sensors are outlined in Table 3.2, along with available power density and voltage levels at their output. Pros and cons have also been listed.

3.2.3.1 Photovoltaic (Solar) Energy Harvesting

In a typical photovoltaic (PV) system shown in Fig. 3.7, MPPT (Maximum Power Point Tracking) sub-system matches the input impedance of the power conditioning circuitry to the output impedance of the PV source, and the output impedance of the power conditioning circuitry to the input impedance of the load. The function of maximizing power extraction across varying temperature and irradiance conditions is also often incorporated into the MPPT. All of these features bring along the extra burden of power consumption, and only make sense when this consumption is much lower than the harvested average power. System analysis is performed on feasibility of incorporating such circuits, which often results in bare minimum power conditioning design in sensor systems without a digital controller.

One such simplified design based on COTS is presented in [19], with robust functionality, bare-bone maximum power point (MPP) support, and up to 10% divergence from the truly optimal operating point (PV current and voltage). The energy harvesting interface circuit consumes less than 1 mW. Since no MCU or DSP (Digital Signal Processor) is utilized for MPP regulation, the system can be shut down when unused for energy savings. A small (9 mm^2) pilot cell with the same characteristics as the main harvester array (112 cm^2) is used to track maximum power point based on fractional open circuit voltage method as depicted in Fig. 3.8. The governing relationship in Eq. 3.1 justifies this simple approach to

Table 3.2 Ambient energy sources and characteristics of micro-power generators

	PV Solar	Thermoelectric	Piezoelectric vibration	Electromagnetic vibration	Ambient RF
Power density	Outdoor: 100 mW/cm^2 Indoor: <100 μW/cm^2	50–100 μW/cm^2 per ^{0}C	10–200 μW/cm^3	1–2 μW/cm^3	0.0002–1 μW/cm^2
Output voltage	0.5 V max	10–100 mV	10–20 V (open ckt)	few 100 mV	3–4 V (open ckt)
Availability condition	Lighted environment	Surfaces with ΔT	Hz–kHz Vibration	Hz Vibration	Vicinity to radiation source
Pros	High power density Well developed technology	Non-intermittent/less intermittent than alternatives	High voltage Well developed technology	Well developed	Antenna can be integrated Widely available
Cons	Intermittent Highly dependent on light	Low voltage Need ΔT	Highly variable output Large area High output impedance	Bulky Low power density Low output voltage	Very sensitive to distance of the RF source

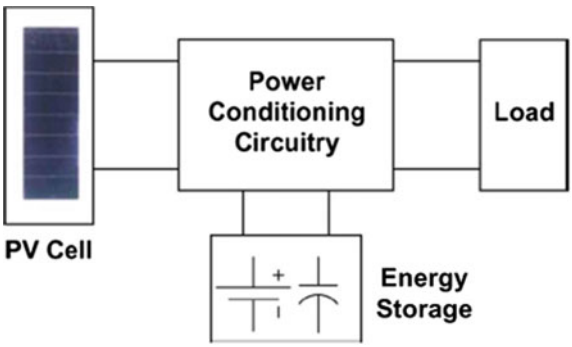

Fig. 3.7 PV harvesting system [18]

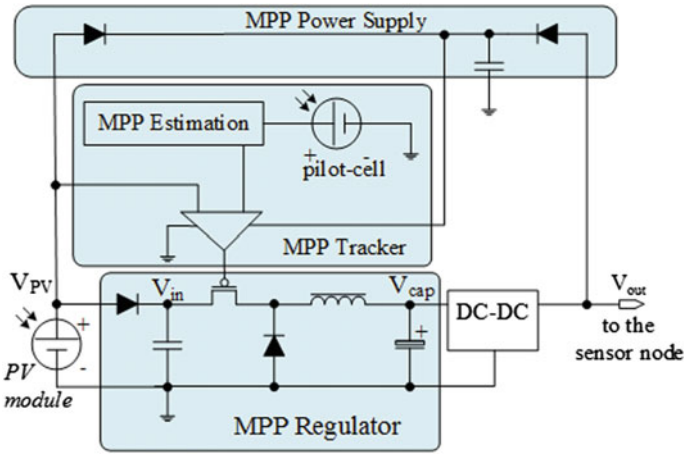

Fig. 3.8 PV harvester platform with simple pilot-cell based MPPT [19]

MPPT implementation to optimize extracted power across temperature and irradiation variations:

$$V_{MPP} \approx K_{FOC} \bullet V_{OC} \approx K_{FOC} \bullet (K_{PILOT} \bullet V_{PilotCell}) \tag{3.1}$$

where, V_{MPP} is the target voltage at maximum power point, K_{FOC} is the fractional open circuit voltage constant, and $K_{PilotCell}$ is the scaling constant associated with the pilot cell reference. A supercapacitor is deployed for storage. Power conversion efficiency, using commercial LTC3401 step-up voltage regulator in the last stage (DC-DC block in Fig. 3.8), varies between 50–80% with 50 mW of power delivered to the commercial embedded sensor platform called *Tmotesky*.

3.2.3.2 Thermoelectric (Temperature Difference) Energy Harvesting

The available voltage level from thermoelectric micro-modules is low, as noted previously in Table 3.2. Recent work on integrating TE modules into WSN nodes have thus focused on developing efficient voltage step-up circuits. An integrated interface circuit in 0.35 μm CMOS technology reported by [20] boosts 35 mV input voltage from a TE module up to regulated 1.8 V output to drive a sensor node. A motion activated switch is used to mechanically assist the starting of power generation, as depicted in Fig. 3.9. This approach avoids batteries for start-up. The interface achieves 58% efficiency using external inductors for the buck converter and start-up. The existing large inductors (not shown in the figure) cannot be integrated on-chip in this design, adding incrementally to the system cost (and size). The printed circuit board (PCB) for the thermal harvesting system only occupies 7.5 cm^2.

A 130 nm CMOS ultra-low power batteryless energy harvesting body sensor node (BSN) system-on-chip (SoC) was presented in [16], which acquires, processes, and transmits electrocardiogram (ECG), electromyogram (EMG), and electroencephalogram (EEG) data. Dynamic power management concepts, low voltage and subthreshold circuit techniques for low power design are applied to constrain average power dissipation to 19 μW, which is supplied by thermoelectric module and/or RF harvester. It operates at a minimum thermoelectric supply voltage of 30 mV. The design, depicted at high level in Fig. 3.10, is a first of its kind in multiple aspects, but certainly in the small power dissipation achieved for the number of features it supports. A 4 × 4 cm^2 COTS thermoelectric generator (TEG) module successfully delivers the required sensor node power at room temperature when attached to the back of the neck or chest of a human being. First, the boost converter and voltage regulator together step up harvested TEG input up to a regulated 1.35 V using an off-chip capacitor and an inductor for efficient

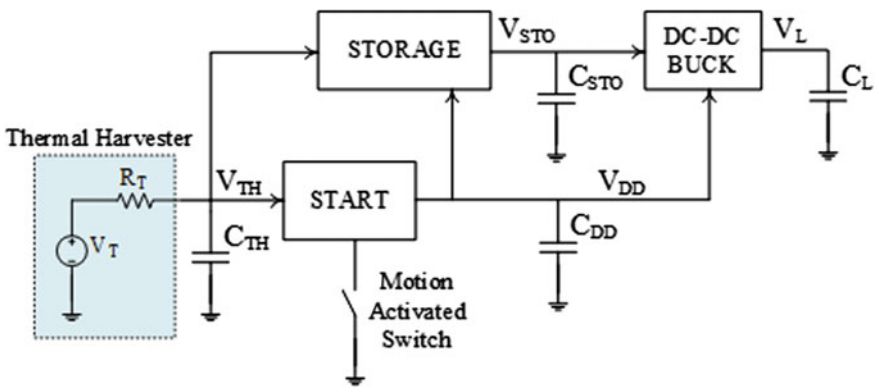

Fig. 3.9 Thermoelectric energy harvesting system block diagram [20]

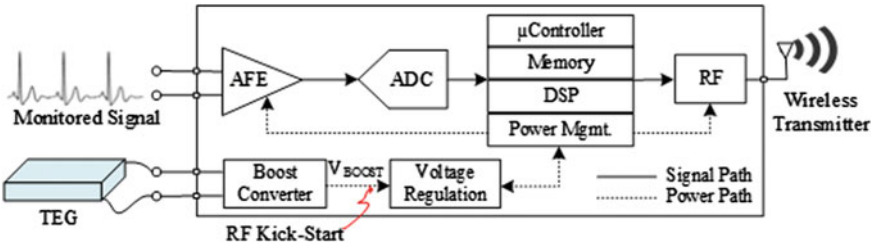

Fig. 3.10 High level block diagram of the BSN design [16]

conversion. The regulator in addition provides five regulated voltage supplies and a bandgap reference to the rest of the chip. Monitored signal is processed through an analog front-end (AFE) with programmable gain and sampling range, and converted to digital domain using the analog-to-digital conversion (ADC) block. Signals as low as a few µVs are amplified with less than 4 µW power consumption per analog channel. The digital processing system that follows is implemented using subthreshold circuit design techniques, and incorporates power and clock gating as well as dynamic voltage scaling (DVS) for optimization of power dissipation. Internal voltage regulation control circuit requires 600 mV to start up, which is not available from the TEG. Wireless RF power is therefore used for kick-starting. A short RF burst of −10 dBm completes a one-time precharge of V_{BOOST} node within few seconds after TEG output settles through a six-stage charge pump circuit. The system is able to communicate data wirelessly in 433 MHz ISM band with low (280 µW) instantaneous (burst) power consumption.

3.2.3.3 Piezoelectric (Vibration) Energy Harvesting

Piezoelectric (PZT) harvesters have high output impedance, and need an impedance matching interface in order to supply maximum power. Recent improvements to conventional full-bridge rectifier and voltage doubler interface circuits have increased the piezoelectric harvester efficiency to above 85% [21]. This is achieved through a number of circuit enhancements for efficiency. External inductor arbiter component (with value in tens of µHs), shown in Fig. 3.11, cannot be integrated on-chip in the design. On the other hand special features, such as analog multiplexers, are embodied to enable various power converters to share the same inductor for cost reduction.

A different approach for power conversion, named synchronous electric charge extraction (SECE) is currently researched by several groups. The Multi-shot SECE system (MS-SECE), depicted in Fig. 3.12 [22], can self-start and handle a wide range of piezoelectric power and voltage levels with the help of small off-chip components. It only consumes 1 µW at 5 Hz vibration frequency, and is suitable for low frequency motion available in daily human activity. The efficiency is

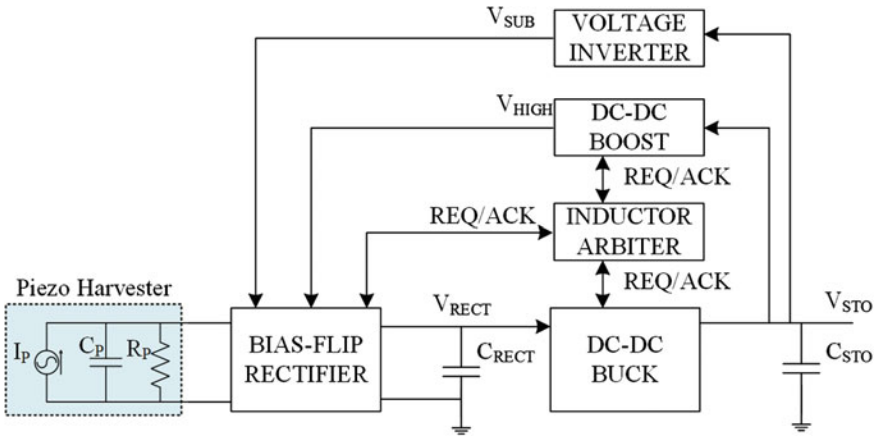

Fig. 3.11 Bias-flip rectifier based interface system for PZT harvesting with high efficiency [21]

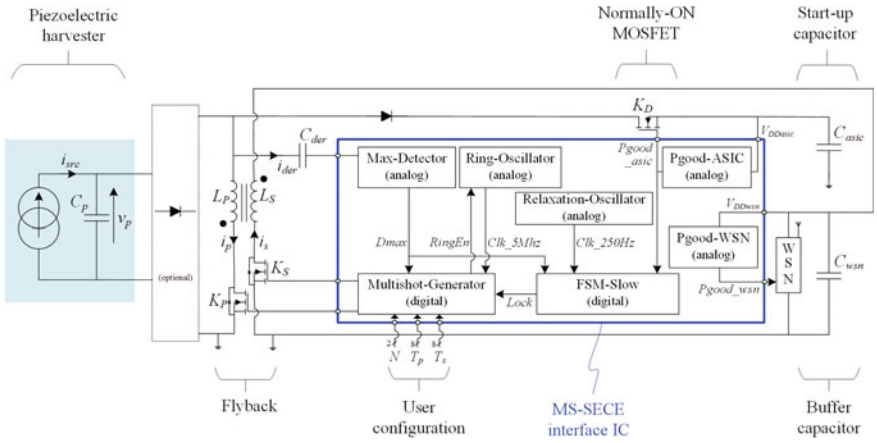

Fig. 3.12 Autonomous piezoelectric energy harvester interface schematic [22]

reported at 61% using a 125 mm^3 coupled-inductor. Storage capacitors C_{asic} and C_{wsn} in Fig. 3.12 are dedicated to the power supplies of the MS-SECE integrated circuit (IC) component and WSN device respectively. There is an "optimized path" controlled through the K_P and K_S switch transistors to implement the SECE technique. The PZT harvester is optimally discharged through the flyback circuit to C_{wsn}. The SECE technique is based on storing charge to the primary inductor (L_p) when PZT harvester voltage reaches maximum value, and then transferring charge to secondary inductor (L_s) after a predetermined period by closing K_S and opening K_P. The further optimized MS-SECE technique transfers the energy from the harvester in N successive transfers instead of a single transfer (hence the name "multi-shot"). As the maximum value of the voltage v_p is detected, multi-shot

generator and ring-oscillator turn on to precisely control K_P and K_S for charge transfer. When V_{DDwsn} reaches a predetermined threshold, *Pgood_wsn* signal triggers WSN block to perform a measurement or a RF transmission. The "non-optimized path", which is used to charge C_{asic} directly from the PZT harvester, is activated during the cold-start, and periodically when C_{asic} voltage drops below a minimum. FSM_slow block utilizes the *Pgood_asic* signal from the Pgood-ASIC block and clock from the relaxation-oscillator to manage transition between optimized and non-optimized paths.

An application oriented study [23] on potential of typing as energy source couples electromagnetic and piezoelectric energy harvesting from the computer keyboard strikes. A prototype demonstrates that 40.8 μW can be harvested from a single key using a micro-machined piezoelectric component, and 1.15 μW from an electromagnetic component. Another similar application oriented study [24] focuses on the potential to power a body sensor node (BSN) through piezoelectric and thermoelectric harvesters. Real time experiments on human body demonstrate generation of up to 20 μW at room temperature in a 9 cm^2 area of thermoelectric generator. In addition, a 0.5 cm^3 piezoelectric harvester used in this work generates 3.7 μW while running at 7 miles/h.

3.2.3.4 Electromagnetic (Vibration) Energy Harvesting

Another practical kinetic energy harvesting type relates to the electromagnetic principle of Faraday's Law. A magnet is typically actuated with low frequency environmental motion within a coil to generate current. Since the coil has low output impedance, power extraction does not typically require the type of complex interfaces described in the previous section.

A novel batteryless interface was presented in a recent study [25] to be utilized in a system with low voltage electromagnetic harvesters to supply WSN nodes. The system, shown in Fig. 3.13, has an in-house 2 cm × 3.5 cm cylindrical harvester that feeds a novel rectification circuit with a passive (less efficient) first stage that powers an active AC-DC doubler with high efficiency. The first stage AC-DC converter consists of diode-connected MOSFET transistors, and doubles the input peak voltage.

The active doubler gets powered by the passive circuit to deliver DC voltage to the final stage with high efficiency. The final stage consists of an integrated step-up converter built using a charge-pump. The minimum AC input peak voltage that can be rectified by the system is 125 mV. The output voltage range is 1–2.48 V. The compact and low cost solution is suitable for a number of low frequency applications. The combined rectifier stage can deliver 25 μW and 0.61 V with 67% efficiency, while the second stage can deliver higher voltages and few μWs with 13% efficiency. Charge-pumps in general are commonly used for fully integrated voltage step-up, but are low in efficiency as demonstrated in this work.

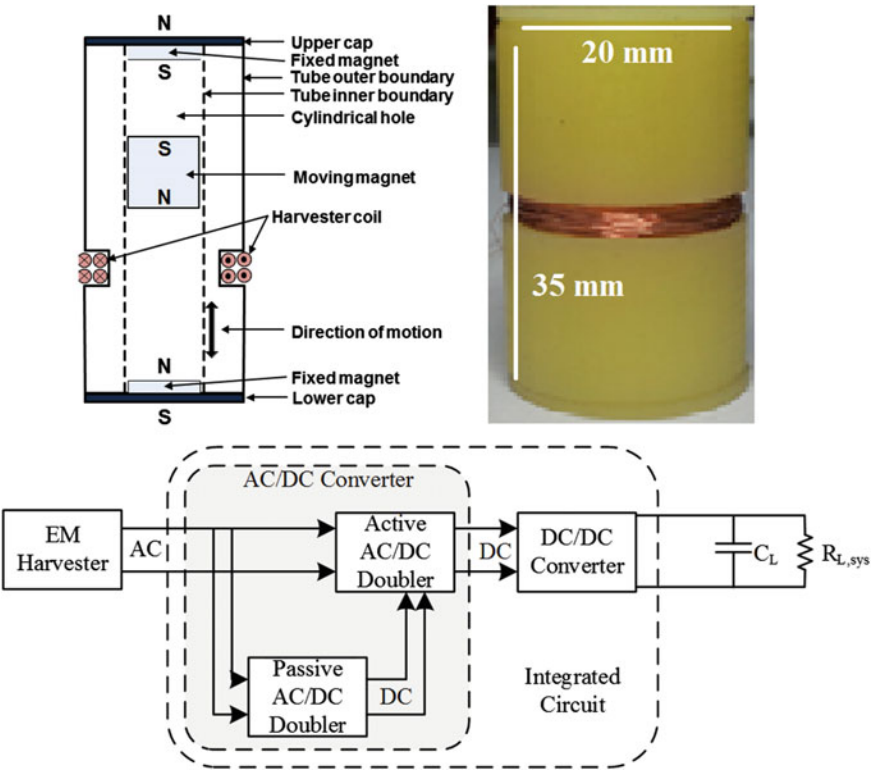

Fig. 3.13 Electromagnetic energy harvester *(top)*, and integrated interface circuit block diagram *(bottom)* [25]

3.2.3.5 Ambient RF Harvesting

Wireless digital television signals are constantly broadcasted over the air in many geographies. A wireless energy harvesting prototype, named E-WEHP [26], demonstrated harvesting of sufficient power from a TV broadcast source that is 6.3 km away to sustain a 16-bit embedded microcontroller for batteryless M2M applications. The system, depicted in Fig. 3.14, uses a log-periodic antenna designed for empirically characterized 512–566 MHz frequency spectrum. A mixed L-section matching network was designed and built using discrete components and distributed transmission line elements to match the mainly capacitive impedance of the RF-to-DC charge-pump circuit to the 50 Ω impedance of the antenna.

Energy efficiency of the system was characterized in lab by emulating a collect-first (charge/sleep) and use-later (discharge/active) mechanism through 1- and 18-MΩ resistors that represented PIC24F 16-bit embedded microcontroller power

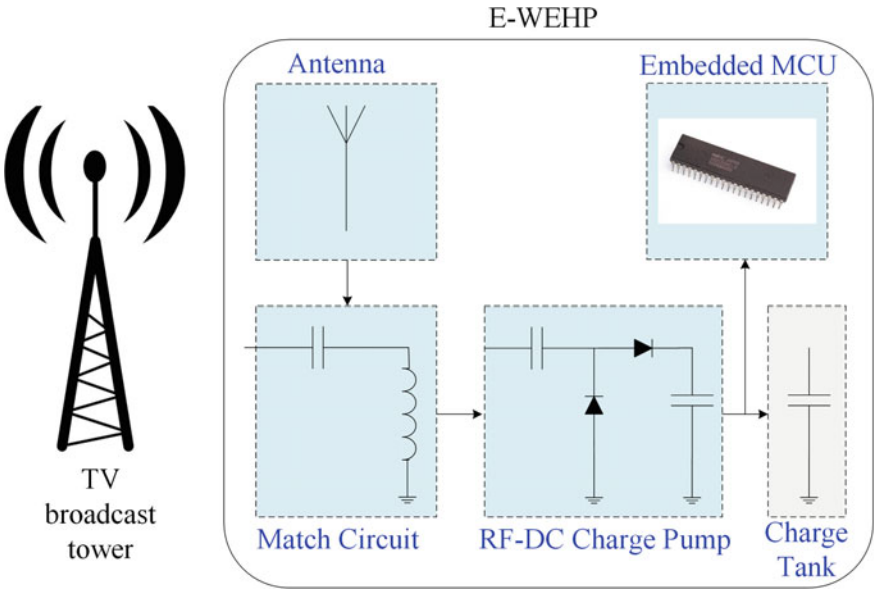

Fig. 3.14 E-WEHP system block diagram [26]

management modes. In these modes, wireless power was rectified and transferred to the charge-tank capacitor. With total channel power levels of 8.99 dBm (126 mW) that represented a location at 6.3 km from the TV source, laboratory tests on the E-WEHP yielded efficiencies between 55% and 15% for 1- and 18-M output loads across the charge-tank capacitor respectively.

3.3 Conclusion

Managing power consumption through traditional and new technologies enables smaller batteries and more compact microelectronic systems. In parallel, energy harvesting continues to be a pivotal research and development area in efforts to achieve batteryless operation in increased number of platforms. Micro-scale energy harvesting will enable many more aspects of intelligent living and working spaces. The reasons for the current trends have been presented in Sect. 3.1, and few selected examples have been provided in Sect. 3.2 from recent literature to demonstrate the state of the art. The upcoming developments are projected in the next paragraphs to conclude the chapter.

3.3.1 Upcoming Trends

A number of critical issues around sensor platforms with energy harvesting will continue to receive attention from researchers in order to enable new batteryless applications. These areas are outlined below in no particular order.

i. Hybrid mode harvesting: Wireless sensor nodes need to support multiple harvesting modes at the same time in a hybrid configuration as depicted in Fig. 3.15 in order to extend on-board features and communication range. Examples of these have recently been noted, combining thermoelectric and RF, thermoelectric and piezoelectric, piezoelectric and RF harvesting. However, seamless implementation of a single power supply with multiple sources requires further study.
ii. True self-starting operation: Efforts will continue to provide self-starting operation in all systems without batteries. Many of the more efficient systems today take advantage of small batteries, or depend on a kick-starting RF signal or motion to self-start. The system goal is to start on detection of any type and amount of energy in the surroundings without requiring any special arrangement.
iii. Integration and Efficiency: SoC integration will strive to pull in harvesters, interface circuits, and sensors into the same package, and eventually into the same semiconductor component. Elimination of all off-chip discrete components (capacitors, inductors) will receive focus. Research on integrated CMOS

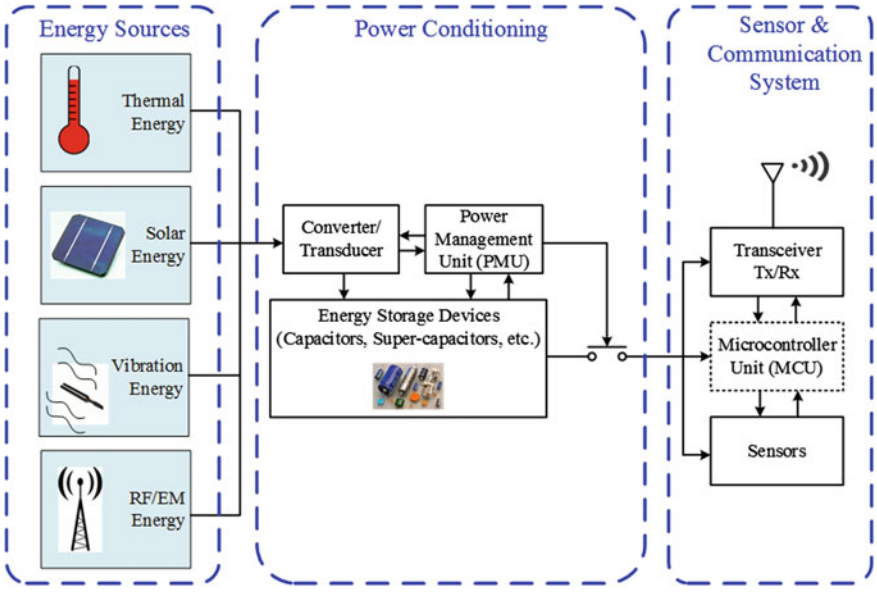

Fig. 3.15 Wireless sensor platform enabled by multiple harvesters simultaneously (based on [27])

compatible interface circuits will hence maximize power conversion efficiency without the use of discrete components. This is required not only for miniaturization of sensor nodes, but also for reduction of cost to levels that will enable massive use of sensors in disposable or semi-disposable applications.

iv. Improved materials: Material improvements will deliver transducers with higher intrinsic efficiency. This includes efficiency improvements in solar cells, thermoelectric modules, piezoelectric cantilevers, magnetic components, and RF antennas. Storage capacitors and super-capacitors with lower leakage will also be of major interest to reduce losses. New harvesters and harvesting modes will be researched in order to extend the harnessed frequency band for solar irradiation, vibrations, and RF waves without increasing the system size and cost.

References

1. Brynjolfsson E, Hitt LM (1998) Information technology and organizational design: evidence from micro data
2. Cisco Visual Networking Index: Forecast and Methodology 2014–2019 (2015) Cisco, White Paper
3. Chen YK, Wu AY, Bayoumi MA, Koushanfar F (2013) Low-power, intelligent, and secure solutions for realization of internet of things. IEEE J Emerg Sel Top Circ Syst 3:1–4
4. Culler D, Estrin D, Srivastava M (2004) Overview of sensor networks. Computer 37:41–49
5. Heppner A (2007) Sensornetzwerke - Beispiele aus der Praxis. Sensornetzwerke
6. Verdone R, Dardari D, Mazzini G, Conti A (2008) Wireless sensor and actuator networks. Academic Press/Elsevier, London
7. Blanckenstein J, Klaue J, Karl H (2015) A survey of low-power transceivers and their applications. IEEE Circ Syst Mag 15:6–17
8. Muhtaroglu A, Kulah H (2013) Micro-power generation for autonomous systems (Invited Talk). In: The 2nd Saudi international electronics, communications and photonics conference (SIECPC'13)
9. Raghunathan V, Schurgers C, Park S, Srivastava MB (2002) Energy-aware wireless microsensor networks. IEEE Sig Process Mag 19:40–50
10. Martinez MMB, Vilajosana I, Prades JD (2015) The power of models: modeling power consumption for IoT devices. IEEE Sens J 15:5777–5789
11. Calhoun BH, Lach J, Stankovic J, Wentzloff DD, Whitehouse K, Barth AT et al (2012) Body sensor networks: a holistic approach from silicon to users. Proc IEEE 100:91–106
12. Majerus SJA, Fletter PC, Damaser MS, Garverick SL (2011) Low-power wireless micromanometer system for acute and chronic bladder-pressure monitoring. IEEE Trans Biomed Eng 58:763–767
13. Karmokar A, Anpalagan A (2013) Green computing and communication techniques for future wireless systems and networks. IEEE Potentials 32:38–42
14. E. P. A. (EPA) (2005) Energy star program requirements for computers, eligibility criteria preliminary draft
15. Cong P, Ko WH, Young DJ (2010) Integrated electronic system design for an implantable wireless batteryless blood pressure sensing microsystem. IEEE Commun Mag 48:98–104
16. Zhang Y, Zhang F, Shakhsheer Y, Silver JD, Klinefelter A, Nagaraju M et al (2013) A batteryless 19 μW MICS/ISM-band energy harvesting body sensor node SoC for ExG applications. IEEE J Solid-State Circ 48:199–213

17. Anastasi G, Conti M, Di Francesco M, Passarella A (2009) Energy conservation in wireless sensor networks: a survey. Ad Hoc Netw 7:537–568
18. Muhtaroglu A (2012) Power management and energy scavenging. In: Kaabouch N, Hu W-C (eds) Energy-aware systems and networking for sustainable initiatives. IGI Global, Hershey
19. Brunelli D, Moser C, Thiele L, Benini L (2009) Design of a solar-harvesting circuit for batteryless embedded systems. IEEE Trans Circ Syst I 56:2519–2528
20. Ramadass YK, Chandrakasan AP (2011) A battery-less thermoelectric energy harvesting interface circuit with 35 mV startup voltage. IEEE J Solid State Circ 46:333–341
21. Ramadass YK, Chandrakasan AP (2010) An efficient piezoelectric energy harvesting interface circuit using a Bias-flip rectifier and shared inductor. IEEE J Solid-State Circ 45:189–204
22. Gasnier P, Willemin J, Boisseau S, Despesse G, Condemine C, Gouvernet G, Chaillout J (2014) An autonomous piezoelectric energy harvesting IC based on a synchronous multi-shot technique. IEEE J Solid-State Circ 49:1561–1570
23. Wacharasindhu T, Kwon JW (2008) A micromachined energy harvester from a keyboard using combined electromagnetic and piezoelectric conversion. J Micromech Microeng 18:055017
24. Wahbah M, Alhawari M, Mohammad B, Saleh H, Ismail M (2014) Characterization of human body-based thermal and vibration energy harvesting for wearable devices. IEEE J Emerg Sel Top Circ Syst 4:354–363
25. Ulusan H, Gharehbaghi K, Zorlu O, Muhtaroglu A, Kulah H (2015) A fully integrated and battery-free interface for low-voltage electromagnetic energy harvesters. IEEE Trans Power Electron 30:3712–3719
26. Vyas RJ, Cook BB, Kawahara Y, Tentzeris MM (2013) E-WEHP: a batteryless embedded sensor-platform wirelessly powered from ambient digital-TV signals. IEEE Trans Microw Theory Tech 61(June):2491–2505
27. Kim S, Vyas R, Bito J, Niotaki K, Collado A, Georgiadis A, Tentzeris MM (2014) Ambient rf energy-harvesting technologies for self-sustainable standalone wireless sensor platforms. Proc IEEE 102:1649–1666

Chapter 4
Efficient Energy Harvesting Systems for Vibration and Wireless Sensor Applications

Mustafa Doğan, Sıtkı Çağdaş İnam and Ö. Orkun Sürel

Abstract In the first part of the research, we present the design of a vibration-based energy harvesting system. Robotic flexible arm having variable cross-section is investigated to overcome serious problems, e.g. insufficient bandwidth and model inaccuracies. Most of the energy harvesting systems are linear with unimodal characteristics. On the other hand, real vibrations can be modeled as random, multi-modal and time varying systems. Hence, unimodal linear systems can give highly unsatisfactory results under certain circumstances. However, non-linear systems can have multi-modal character with increased performance in real and practical situations. In this work, tapered links are preferred with nonlinear coupling setup to provide sufficient bandwidth and output power requirements for modern applications. Thus, the proposed scheme has been proven by simulated and experimental results successfully. In the second part of the research, we present design and experimental results of an electromagnetic harvester, energy source of which is single-phase household AC power with a nominal voltage of 220 V and a frequency of 50 Hz. In this case, energy harvesting is based on the induced electromotive force (EMF) as a result of the periodic variations of the magnetic field around the AC power cord. In this part, we also discuss basic principles of a wireless sensor network design powered by electromagnetically harvested energy obtained from household alternating current.

Keywords Energy harvesting · Multi-modal vibrations · Piezoelectric · PDE modelling · Tapered beam · Flexible arm · Wireless sensors · Electro-magnetic radiation · Self-powered

M. Doğan (✉) · S.Ç. İnam · Ö. Orkun Sürel
Department of Electrical and Electronics Engineering, Baskent University, Bağlıca Kampüsü Eskişehir Yolu 20. Km Bağlıca, 06810 Ankara, Turkey
e-mail: mudogan@baskent.edu.tr

S.Ç. İnam
e-mail: inam@baskent.edu.tr

Ö. Orkun Sürel
e-mail: orkunsurel@gmail.com

N. Bizon et al. (eds.), *Energy Harvesting and Energy Efficiency*,
Lecture Notes in Energy 37, DOI 10.1007/978-3-319-49875-1_4

Nomenclature

a_1	Linear slope for tapering
$b_i(x)$	Variable height of the links due to tapering
E	Young's modulus
$I_i(x_i)$	Variable beam cross-section moment about the z-axis at the location x_i
I_{hi}	Inertia of ith hub
I_{ti}	Tip inertia of ith beam
l_i	Length of ith link
m_{hi}	Mass of ith hub
m_{ti}	Tip mass of ith beam
t	Time ($t \geq 0$)
$w_i(x_i, t)$	Flexural deflection of point i at the location x_i of ith beam
$w_{ix}(x_i, t)$	Flexural slope of point i at the location x_i where the subscript in w_{ix} denotes spatial derivative w.r.t. x
$w_{ixx}(x_i, t)$	Bending strain of point i at the location x_i
x_i	Coordinate along the axial centre of the ith beam ($0 \leq xi \leq li$)
θ_1	Angular position of the first link
θ_2	Angular position of the second link
$\rho_i(x_i)$	Variable density of the ith link depends on the cross-sectional area
τ_i	Input torque at ith motor

Abbreviation and Acronym

FEM	Finite element method
MEMS	Micro-electro-mechanical systems
ODE	Ordinary differential equations
PDE	Partial differential equations
FFT	Fast Fourier transform
EMF	Electromotive force

4.1 Introduction

Portable devices cannot be maintained steadily by limited power sources, e.g. batteries. This idea improved and motivated the research in energy harvesting area. Harvesting by vibrating resources, e.g. trains, buildings, bridges, cars, aircraft, machinery, is well-studied. One of the harvesting methods is based on piezoelectric materials that can transform electrical energy into mechanical strain or force and vice versa [1–4]. Recently, remote sensors/actuators are usually hard to reach as they are hidden in inaccessible locations such as bridges, civil buildings, even human body. Thus, energy harvesting is the only way to keep them alive [5–7].

As the first case study, e.g. [8], we consider a vibration-based harvesting system including beams with piezoelectric layers and proof mass. Most of the energy harvesting systems are linear with unimodal characteristics. On the other hand, real vibrations can be modeled as random, multi-modal and time varying systems. Hence, unimodal linear systems can give highly unsatisfactory results under certain circumstances. However, non-linear systems can have multi-modal character with increased performance in real and practical situations. In this work, tapered links are preferred with nonlinear coupling setup to provide sufficiently bandwidth and output power requirements for modern applications. Thus, the proposed scheme has been proven by simulated and experimental results successfully.

The flexible beams with piezoelectric layers can capture the environmental vibrations. The partial differential equations (PDE) are used to model such a challenging system due to nonlinear coupling for producing accurate and consistent results, compare with finite-dimensional models, e.g. ordinary differential equations (ODE) or finite element method (FEM), approaches, refer to [9, 10]. Thus, we will use the infinite-dimensional model in [9] for the energy harvesting system.

Optimal geometry of flexible links can be investigated to improve some features, e.g. low mass, low moments of inertia and high natural frequencies, e.g. see [11]. Besides, large bandwidth is required for fast and stable motion, can be achieved with high fundamental frequency, e.g. refer to [12]. Therefore, non-uniform cross-section is implemented for the links in this research.

The tapered beam structure and inherent non-linearity of the flexible arm model are indispensable to improve the bandwidth and output power. Thus, different from the literature, e.g. cantilever beams with permanent magnets, see [13–18], we do not use magnets, multiple beam-mass systems and lumped parameter models to increase the bandwidth and/or to introduce the non-linearity. One of main contributions is that the proposed structure is simple enough to catch multi-modality and nonlinearity.

As the second case study, we will deal with an energy harvesting case for wireless network sensors. Wireless sensor nodes typically have power requirements as low as microwatts, and as the batteries suitable for wireless sensor have limited lifetimes of the order of a few years, powering such systems by energy scavenging is an interesting and practical alternative since sensor nodes will no longer require the occasional battery replacement [19].

We consider a household power consumption detector for real time monitoring. Real time power consumption monitoring helps customers be more informed about their energy consumption and have greater control of their monthly costs. Our detector is based on a sensor with a current sense transformer which is powered by electromagnetically harvested energy originated from the AC source and is capable of wireless communication [20]. The detector transmits its readings wirelessly to a computer or a mobile terminal.

4.2 Vibration-Based Energy Scavenger

The power spectrum of the proposed system is significantly improved by non-uniform geometry of the links, especially for low frequency band that covers the most of practical ambient vibrations. The flexible robot arm configuration and equations of motion for the system are obtained with the extended Hamilton's principle, see extensive work in [8, 9].

4.2.1 Energy Harvester Design

Usual vibration sources have random, multi-modal and time varying characteristics. Hence, unimodal linear systems could be rather inefficient compared to non-linear systems that are capable of responding over a broad frequency range, thus performing better in realistic vibration spectrum.

The proposed novel energy harvesting system with tapered geometry of the flexible arm, covered with thin piezoelectric materials. The analytic model which is developed in [8, 9], are modified with damping terms and external excitation. Two kinds of damping mechanisms are added to the model in [9]: viscous damping and Kelvin–Voigt (or strain-rate) damping. This will be helpful for modelling due to its extreme sensitivity to mechanical damping for the power output under resonance excitation. Therefore designing the energy harvester beam to have less damping can be more important than choosing the right piezoelectric material [21]. Modified equations (PDE) of motion that includes damping terms are given in [8]. The vibration modes will be distributed over rich spectrum content due to non-linear coupling as rigorously proven in [8]. On the other hand, tapered beam geometry provides uniform strain field, e.g., trapezoidal geometry can supply efficiently more than twice the energy per unit volume than the rectangular one [22]. Besides, increasing the slope of tapering improves bandwidth [23, 24]. The proposed energy harvesting system can be easily implemented due to its simple geometry and structure.

4.2.2 Simulation Results

The proposed harvesting system is simulated using a MATLAB code. The PDEs are discretized in both spatial and time domains using finite difference method. In order to avoid complexity of the fourth-order derivative approximation, the second-order derivative approximation has been managed by using intermediate states that corresponds to physical variables such as deflections, velocity and bending moments, e.g. refer to [25]. The same method was also applied successfully and proven in [26]. The model parameters for the system, partially given in

Table 4.1 Simulation parameters of the flexible arm

Parameter	Value
Length of links	$l_1 = 0.1$ m, $l_2 = 0.024$ m
Time step	$\Delta t = 10^{-5}$ s
Spatial steps	$\Delta x_1 = l_1/100$, $\Delta x_2 = l_2/100$
Young's modulus, E	70 GPa
Density, ρ	2742 kg/m^3
Thickness of links, m	$c_1 = 0.003175$, $c_2 = 0.00238$
Maximum height for tapering at the root of the link	$b_o = 0.0654$ m
Linear slope for tapering	$a_1 = 0.12$, and 0.28
Hub inertias, kg m^2	$I_{h1} = 0.0055$, $I_{h2} = 0.0068$
Tip inertias, kg m^2	$I_{t1} = 0.0139$, $I_{t2} = 0.00024$
Hub mass, kg	$m_{h2} = 0.678$
Tip mass, kg	$m_{t1} = 0.800$, $m_{t2} = 0.0204$
Structural damping coef., S_f	2×10^5
Viscous damping coef., V_f	1.5
Attenuation factor, a_{tt}	0.5

[9], are listed in Table 4.1. A white noise of certain power amplitudes of which peak near ±2 is applied as external base excitation [8].

The simulations are summarized in Figs. 4.1 and 4.2. The tapered beam structure and inherent non-linearity of the flexible arm model are indispensable to improve the bandwidth and output power. Increasing the slope of the beam result in robust vibrations with increased amplitudes, see Fig. 4.2.

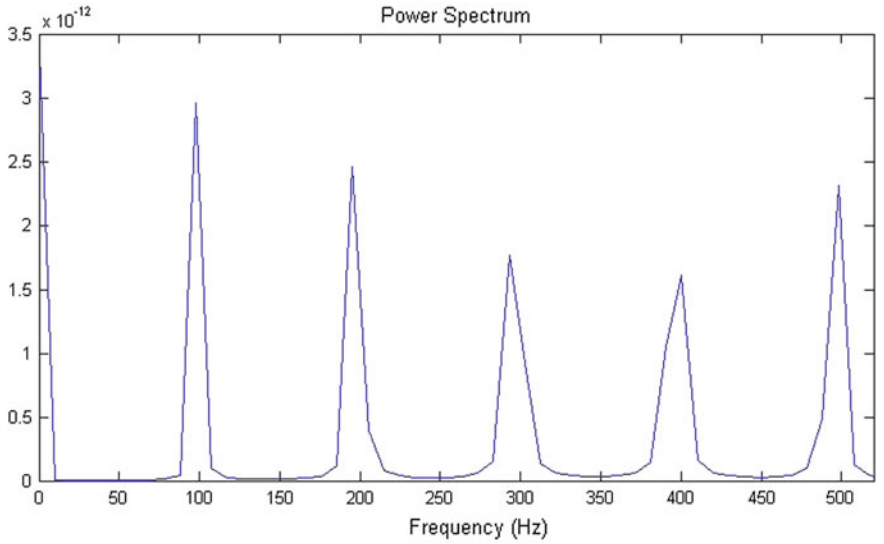

Fig. 4.1 Multi-modal character, slope = 0.12, duration = 0.1 s

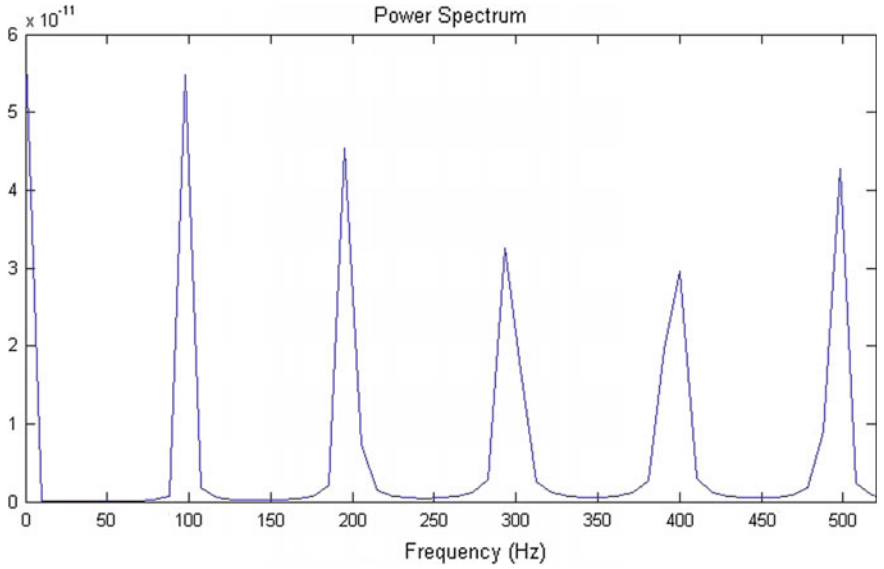

Fig. 4.2 Multi-modal character, slope = 0.28, duration = 0.1 s

Although, any kind of nonuniform cross-section can be implemented; in this particular simulation, rectangular cross-sections of given uniform thickness are examined. For small values of tip mass and tip inertia moment relative to the ones for beam, the optimum shape is approximately a linearly 'tapered' beam, see for example [12]. Consequently, the height $b_i(x)$, density, $\rho_i(x)$ and cross-section area moment $I_i(x)$ at any point can be calculated using parameters listed in Table 4.1, e.g. see [8].

4.2.3 Experimental Results

Having simple structure, stable performance and high reliability; common piezoelectric diaphragms (buzzers) are utilized as basic electronic sound components. Besides, these buzzers are also used in many sensitive equipment as shock sensors.

The main benefits of piezoelectric materials are their large power densities and ease of use. Two-link flexible arm, made of aluminum alloy, are supported by PZT buzzers. For efficient configuration, these piezoelectric materials are resided on two opposite sides of the links. The experimental setup used for measurements is shown in Fig. 4.3. Random vibration is obtained by using adjustable electronic shaker (MIKROTEK Dental Shaker RC—402) and measured by digital storage oscilloscope (RIGOL DS 5202MA, Two Channel, 200 MHz, 1 GS/s). Two-link arm are clamped to the shaker frame for robust base excitation. The second link is adjusted to freely rotate with tip mass (0.02 kg). Unamplified oscilloscope signals are

Fig. 4.3 Experiment, *1* oscilloscope, *2* data acquisition system, *3* flexible arm, *4* electronic shaker

transferred to a personal computer (PC). Built-in fast Fourier transform (FFT) utility of the digital oscilloscope are used to obtain power spectrum. All figures in this section are oscilloscope images.

Time response of the single link has expected unimodal spectrum, see Fig. 4.4 and this linear system behavior is observed for different levels of external vibrations. However, time responses of the flexible arm in Figs. 4.5, 4.6 and 4.7 are similar to that of white noise. This broadband multi-peak behavior of the harvested signal can also be observed at frequency spectrum in Figs. 4.8, 4.9, 4.10, 4.11 and 4.12 as well. The frequency value at upper right of all related figures is just an estimation of dominant frequency by oscilloscope. Change in this value throughout the all figures and also rich content of the frequency spectrum in Figs. 4.8, 4.9, 4.10, 4.11 and 4.12 show that wide bandwidth with multiple peaks have been obtained by non-linear-coupled design. Note that estimated frequency value in Fig. 4.12 is quite high as expected due to removed proof mass [8].

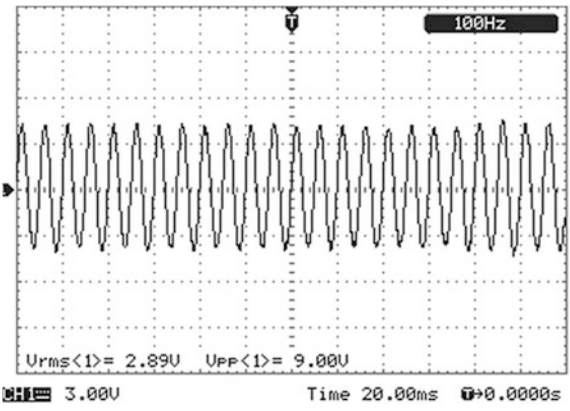

Fig. 4.4 Temporal response of the single link with tip mass

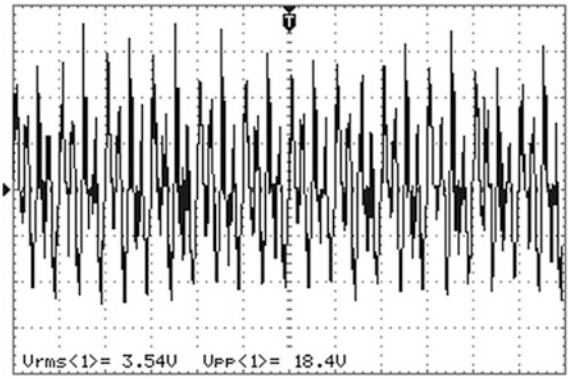

Fig. 4.5 Temporal response of the two links with tip mass with rms voltage of 3.54 V

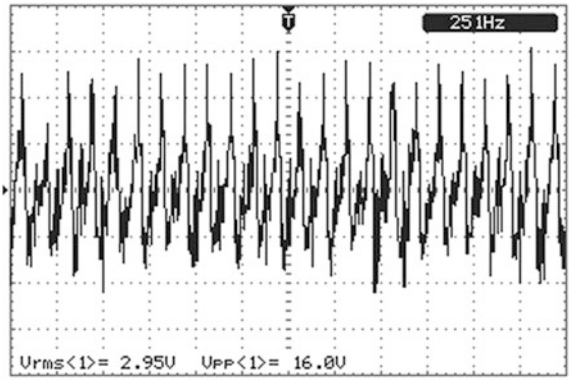

Fig. 4.6 Temporal response of the two links with tip mass with rms voltage of 2.95 V

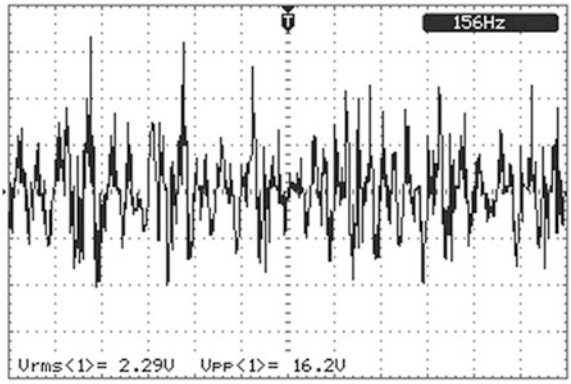

Fig. 4.7 Temporal response of the two links with tip mass with rms voltage 2.29 V

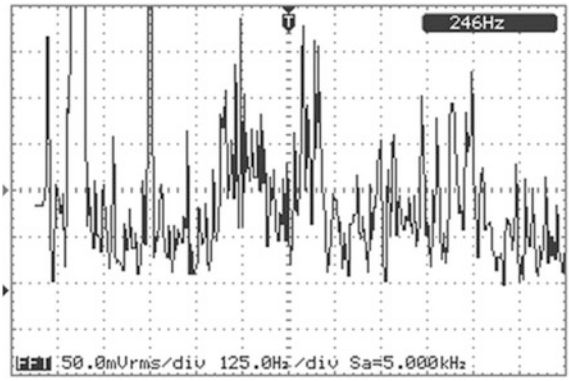

Fig. 4.8 Frequency response of the two links with tip mass with an estimated dominant frequency of 246 Hz

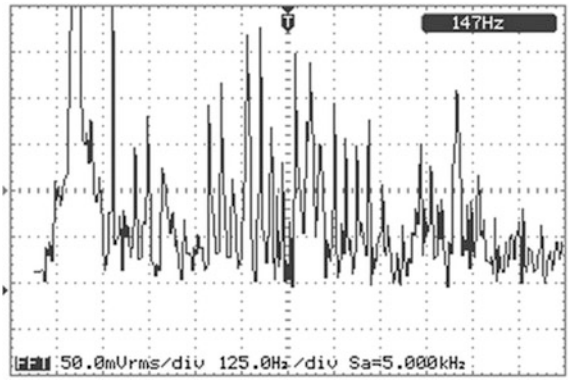

Fig. 4.9 Frequency response of the two links with tip mass with an estimated dominant frequency of 147 Hz

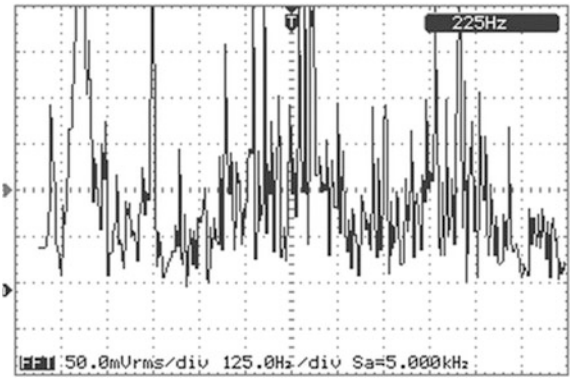

Fig. 4.10 Frequency response of the two links with tip mass with an estimated dominant frequency of 225 Hz

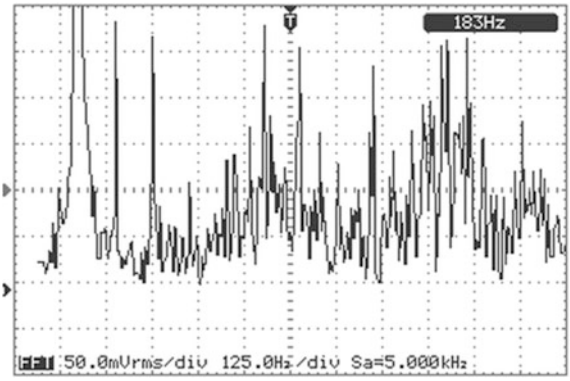

Fig. 4.11 Frequency response of the two links without tip mass with an estimated dominant frequency of183 Hz

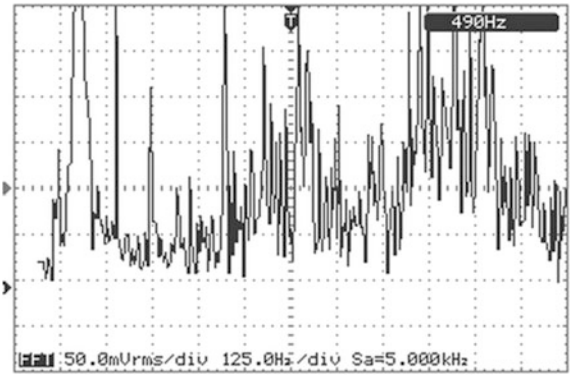

Fig. 4.12 Frequency response of the two links without tip mass with an estimated dominant frequency of 490 Hz

4.3 Wireless Sensor Network Powered by Electromagnetically Harvested Energy

In this section, we present design and the experimental results of an electromagnetic energy harvester. The source of harvested energy is single-phase household AC power with a nominal voltage of 220 V and a frequency of 50 Hz. We also discuss the use of harvested energy to power a wireless sensor network.

4.3.1 Energy Harvester Design

Energy harvesting is based on the induced electromotive force (EMF) due to change in the magnetic flux as a result of the periodic variations of the magnetic field around the AC power cord. Using Faraday's Law of Induction, it is seen that amplitude of induced EMF is proportional to four quantities: Frequency of the alternating current (AC), amplitude of the alternating current, number of turns of the

coil and the area enclosed by the coil. We are interested in harvesting power from a sub-kHz frequency and our typical current amplitude are at most of the order of a few 10 Amperes. Moreover, we have to restrict the area enclosed by the coil due to two reasons: Firstly, both magnetic field strength falls dramatically around a wire with distance. It typically changes with 1/r for very long straight wires, but in real life problems where the length of the straight part of the wire is of the order the geometric dimensions of the coil this decrease might be more substantial. Secondly, we seek for a harvesting solution that is as compact as possible. Thus, we try to increase the number of turns of the coil as much as possible without significantly extending the size of the coil. We also choose the type of the wire to ensure that it is not too thin to limit the total resistance and it is not too thick to limit the overall size of the coin.

Properties of the coil used as the energy harvester are listed in Table 4.2. Figure 4.13 shows geometry of the coil.

To harvest energy from the AC wire, we work on three different experimental setups. For the first and second setups (see top left and top right panels of Fig. 4.14), we separated the phase wire from the neutral wire so that they are more than 30 cm away. Then, as for the first setup, we place the phase wire close to the coil to enhance the magnetic flux and thus the amplitude of induced EMF. Similarly to test the amount of decrease in the harvested energy with increasing distance from the phase wire, we increase the distance between the phase wire and the coil. Thirdly, to increase the magnetic flux even further, we place both phase and neutral wires in the opposite edges of the coil (see bottom panel of Fig. 4.14). For all of these setups, the wire (or wires) are carefully held on the same plane with the area enclosing the coil.

Table 4.2 Properties of the coil used as the energy harvester

External dimensions	315 mm(L) × 75 mm(W) × 25 mm(D)
Internal dimensions	260 mm(L) × 35 mm(W) × 25 mm(D)
Number of turns	1,260 turns
Wire type	25AWG (cross-sectional area 0.45 mm^2)
Total resistance	94 Ω

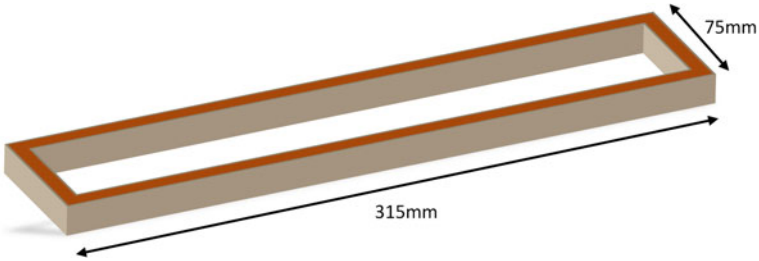

Fig. 4.13 Geometry of the coil used as the energy harvester

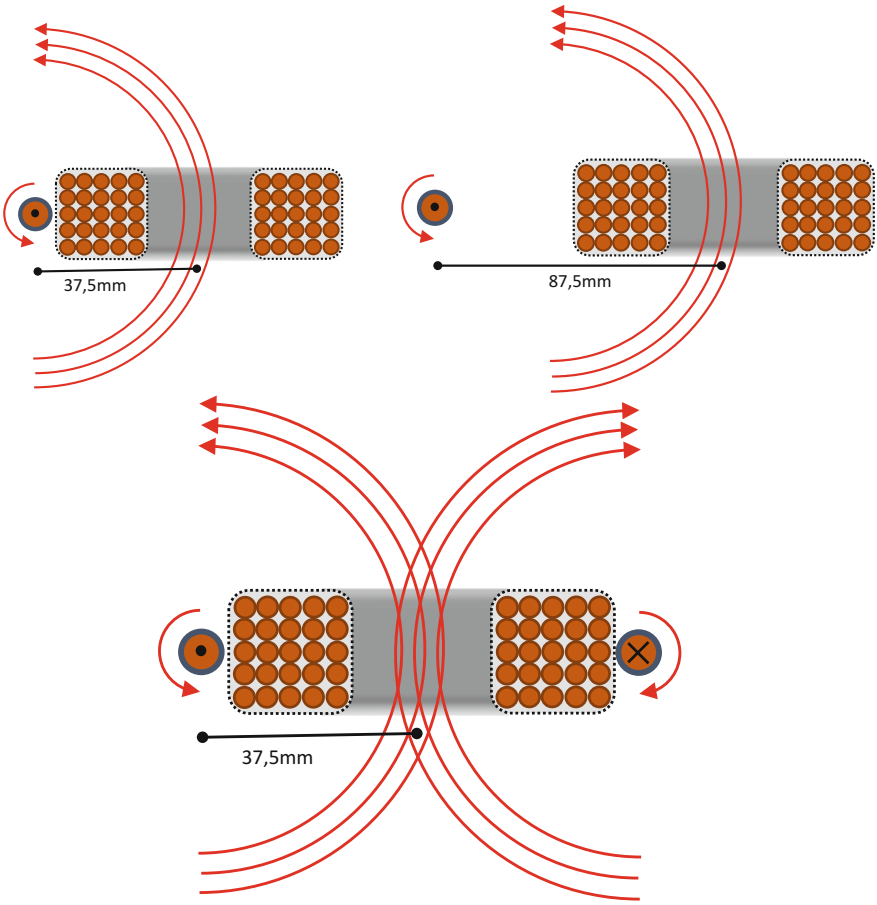

Fig. 4.14 Edge-on views of the coil corresponding to three different experimental setups. For all setups, the wires and the area enclosed by the coil lie on the same plane to maximize magnetic flux passing through the area (*red arrows* denote magnetic field line directions). *(Top left)* phase wire (separated from neutral wire) is placed close to the coil. *(Top right)* phase wire (separated from neutral wire) is placed farther away from the coil. *(Bottom)* phase and neutral wires are placed close to the coil to further enhance the magnetic flux

4.3.2 Experimental Results

In Fig. 4.15, a sample oscilloscope view obtained by measuring the voltage across the ends of the coil when it is placed close the phase wire is shown.

For the three setups shown in Fig. 4.14, we study two cases: Either AC power cord is connected to a 1000 W heater or a 2000 W heater. We measure current as a function of voltage (see left panels of Figs. 4.16, 4.17, 4.18, 4.19, 4.20 and 4.21).

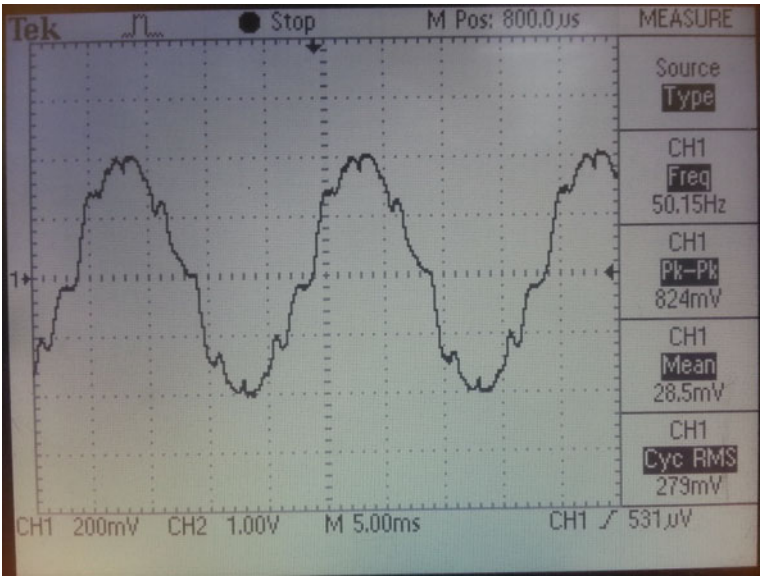

Fig. 4.15 A sample oscilloscope view obtained by measuring the voltage across the ends of the coil when it is placed close to the phase wire

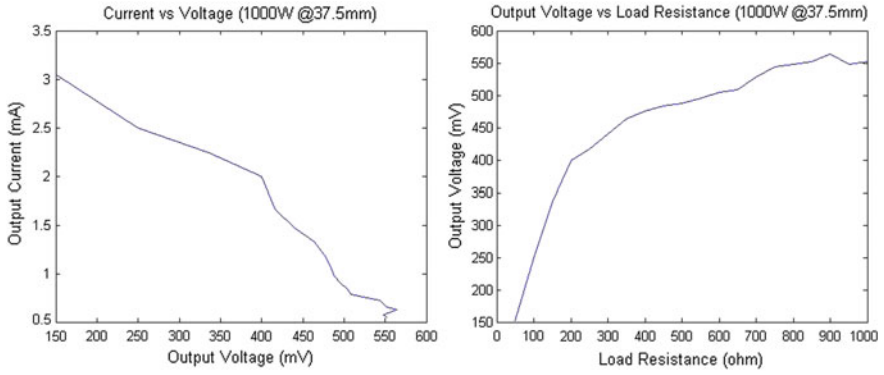

Fig. 4.16 *(Left)* current versus voltage and *(right)* output voltage versus load resistance plots for the first experimental setup and a cord connected to a 1000 W heater

We also alter the load resistance and measure corresponding voltages (see right panels of Figs. 4.16, 4.17, 4.18, 4.19, 4.20 and 4.21).

We also measure harvested and dissipated power as a function of load resistance for three experimental setups for the cases of AC power cord connected to a 1000 and a 2000 W heater (see Figs. 4.22, 4.23, 4.24, 4.25, 4.26 and 4.27).

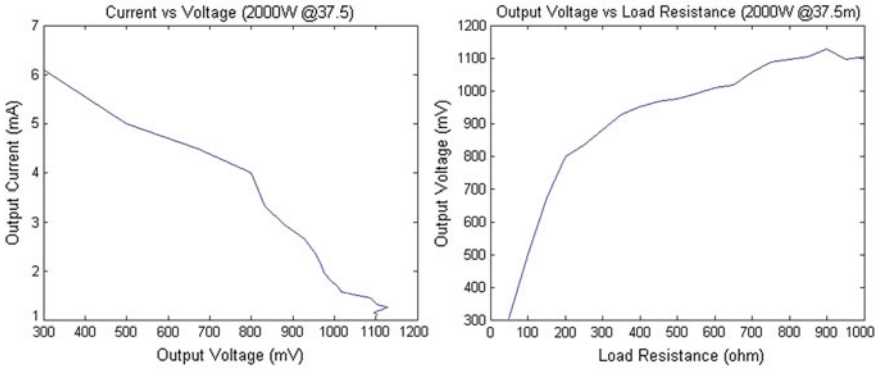

Fig. 4.17 *(Left)* current versus voltage and *(right)* output voltage versus load resistance plots for the first experimental setup and a cord connected to a 2000 W heater

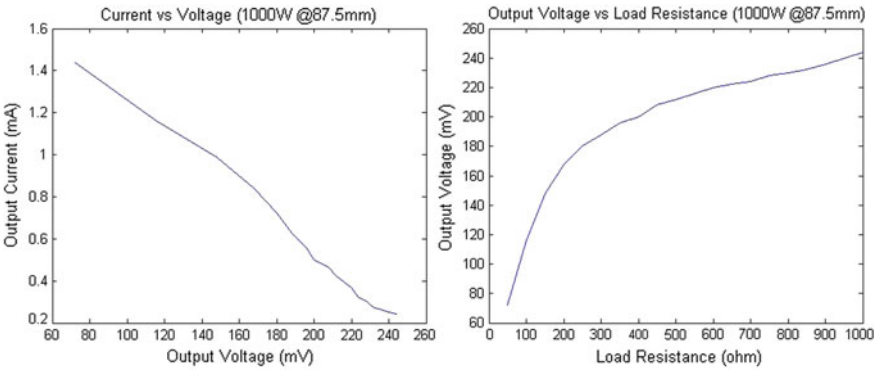

Fig. 4.18 *(Left)* current versus voltage and *(right)* output voltage versus load resistance plots for the second experimental setup and a cord connected to a 1000 W heater

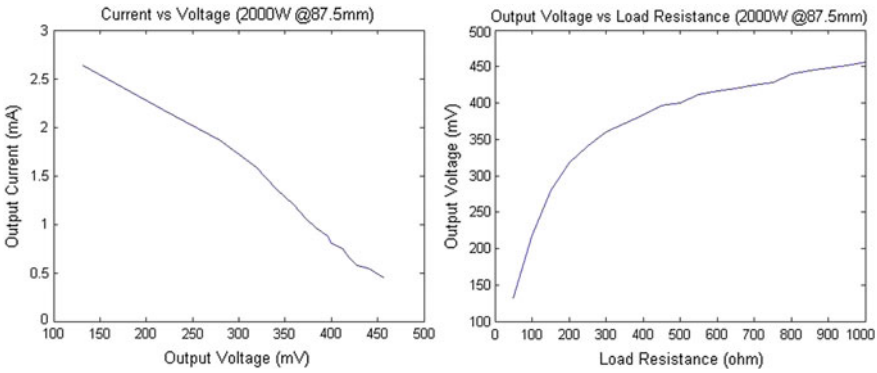

Fig. 4.19 *(Left)* current versus voltage and *(right)* output voltage versus load resistance plots for the second experimental setup and a cord connected to a 2000 W heater

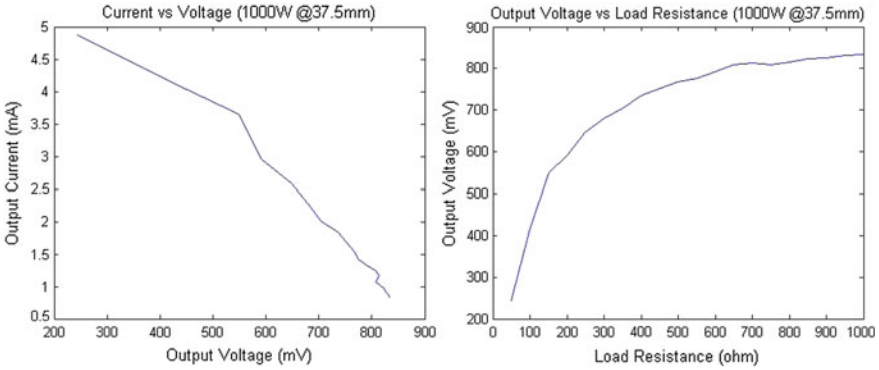

Fig. 4.20 *(Left)* current versus voltage and *(right)* output voltage versus load resistance plots for the third experimental setup and a cord connected to a 1000 W heater

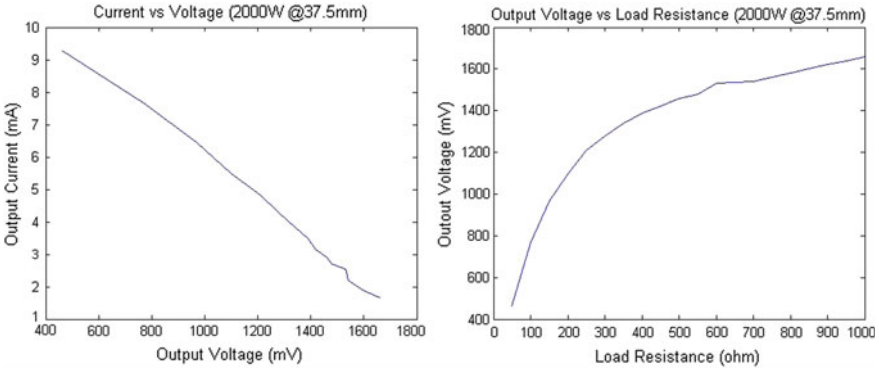

Fig. 4.21 *(Left)* current versus voltage and *(right)* output voltage versus load resistance plots for the third experimental setup and a cord connected to a 2000 W heater

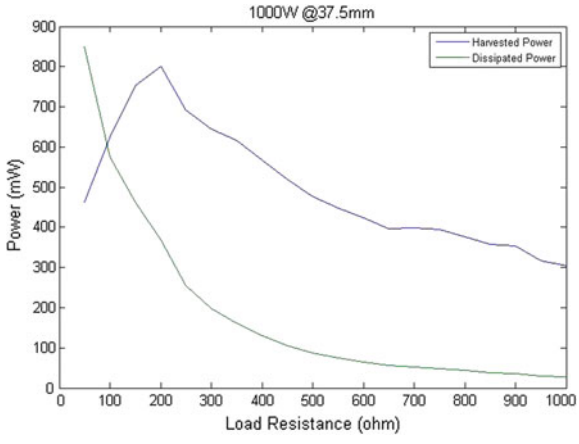

Fig. 4.22 Harvested and dissipated power as a function of load resistance plot for the first experimental setup and a cord connected to a 1000 W heater

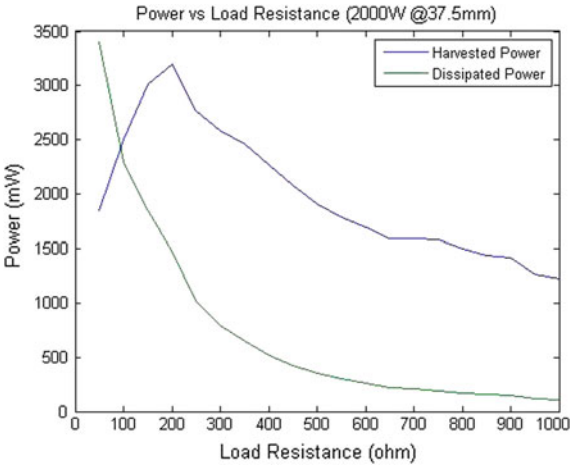

Fig. 4.23 Harvested and dissipated power as a function of load resistance plot for the first experimental setup and a cord connected to a 2000 W heater

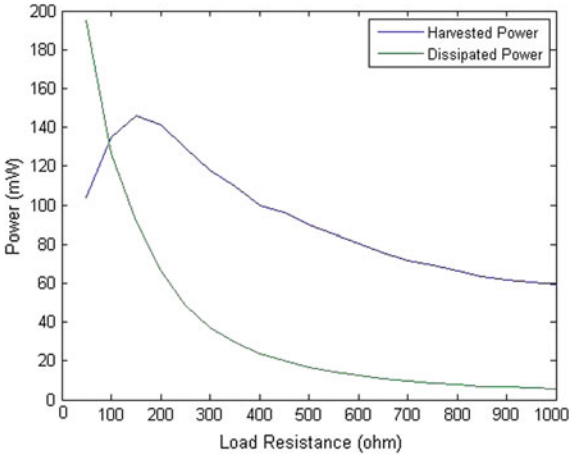

Fig. 4.24 Harvested and dissipated power as a function of load resistance plot for the second experimental setup and a cord connected to a 1000 W heater

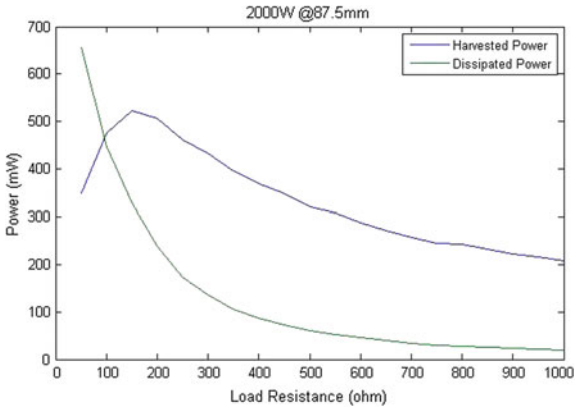

Fig. 4.25 Harvested and dissipated power as a function of load resistance plot for the second experimental setup and a cord connected to a 2000 W heater

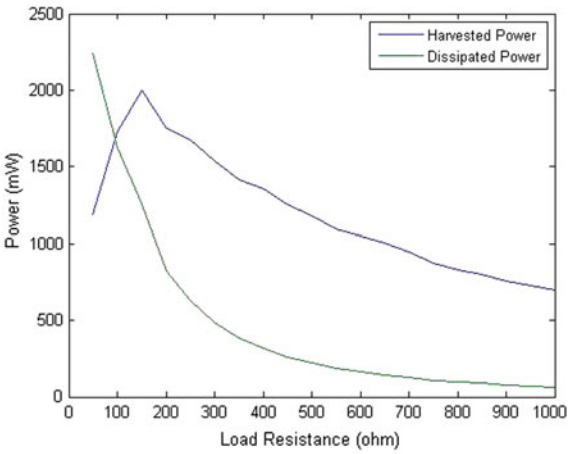

Fig. 4.26 Harvested and dissipated power as a function of load resistance plot for the third experimental setup and a cord connected to a 1000 W heater

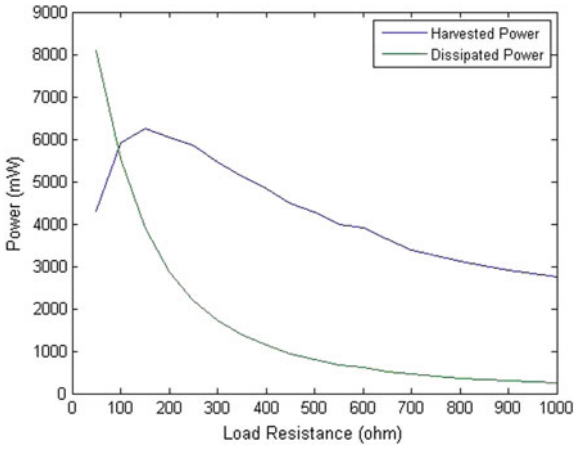

Fig. 4.27 Harvested and dissipated power as a function of load resistance plot for the third experimental setup and a cord connected to a 2000 W heater

4.3.3 Design of a Wireless Sensor Network Powered by Electromagnetically Harvested Energy Obtained from Household Alternating Current

Energy harvesting from household alternating current requires more diligent designs compared to energy harvesting from an RF field due to the fact that frequencies involved are orders of smaller compared to RF frequencies, see e.g. [27–29]. As seen from Figs. 4.16, 4.17, 4.18, 4.19, 4.20, 4.21, 4.22, 4.23, 4.24, 4.25, 4.26 and 4.27, harvested energy input from an AC power cord can be obtained very efficiently using a harvester design presented as the third experimental setup as shown in bottom panel of Fig. 4.14. For such a design, harvested powers can reach up to a few Watts for loads up to 1 kΩ in case of household currents of ≈5–10 A.

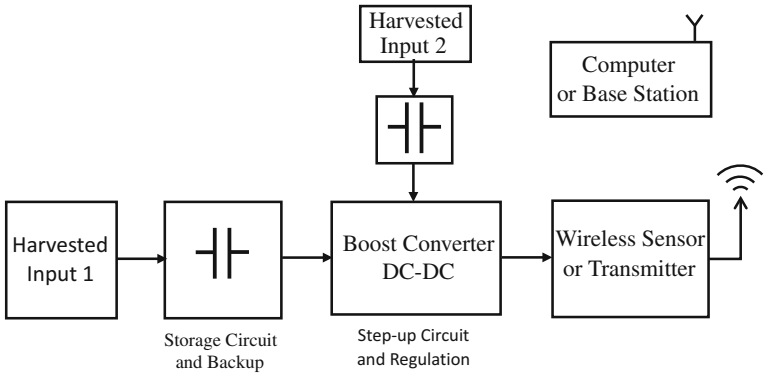

Fig. 4.28 Block diagram of a wireless sensor network powered by electromagnetically harvested energy. A single node and a computer or base station are shown only

This harvested energy can efficiently be used by a sensor network illustrated in Fig. 4.28. Such a sensor network might be used to track detailed household energy usage.

4.4 Conclusion

In this chapter, firstly we investigated the design of energy harvester by a flexible arm with non-uniform cross-section. It is proven by the simulation results that the new design method can provide efficient energy harvesting without complex structures, e.g. magnets and separated links. Coupled non-linear systems can have multi-modal character with increased performance in real and practical situations. The shape of the power spectrum is retained effectively even with some geometry and mass changes. This proves the robustness of the proposed scheme.

The tapered beam structure and inherent non-linearity of the flexible robot arm are indispensable to improve the frequency response and maximum output power. Thus, different from the literature, e.g. cantilever beams with permanent magnets, we do not use magnets, multiple beam-mass systems and lumped parameter models to increase the bandwidth and/or to introduce the non-linearity. One of main contributions is that the proposed structure is simple enough to catch multi-modality and nonlinearity.

In this work, variable cross-section links are preferred with rigorous nonlinear coupling setup to provide sufficiently bandwidth and output power requirements for modern applications. Thus, the proposed scheme has been proven by simulated and experimental results successfully.

Secondly, we design and realize an efficient energy harvester which makes use of both phase and neutral wires of a household alternating current. Having

presented our experimental results, we show that harvested powers can reach up to a few Watts for loads up to 1 kΩ for three different configurations.

We also discuss design of a wireless sensor network powered by electromagnetically harvested energy obtained from household alternating current. To power such a wireless network, it is discussed that storage/back-up and step-up/regulating circuits can be developed to feed the wireless sensors or transmitter.

References

1. Shahruz SM (2006) Limits of performance of mechanical band-pass filters used in energy scavenging. J Sound Vib 293(1–2):449–461
2. Shahruz SM (2006) Design of mechanical band-pass filters with large frequency bands for energy scavenging. Mechatronics 16(9):523–531
3. Shahruz SM (2008) Design of mechanical band-pass filters for energy scavenging: multi-degree-of-freedom models. J Vib Control 14(5):753–768
4. Shahruz SM (2008) Performance of mechanical bandpass filters used in energy scavenging in the presence of fabrication errors and coupling. J Vib Acoust 130(5):054505(9 pp). doi:10.1115/1.2950056
5. Chennault KAC, Thambi N, Sastry AM (2008) Topical review powering MEMS portable devices: a review of non-regenerative and regenerative power supply systems with special emphasis on piezoelectric energy harvesting systems. Smart Mater Struct 17(4):043001(33 pp). doi:10.1088/0964-1726/17/4/043001
6. Beeby SP, Tudor MJ, White NM (2006) Review article energy harvesting vibration sources for microsystems applications. Meas Sci Technol 17:R175–R195
7. Paradiso JA, Starner T (2005) Energy scavenging for mobile and wireless electronics. Pervasive Comput 1:18–27
8. Dogan M (2012) Efficient energy scavengers by flexible robot arm with non-uniform cross-section. IET Control Theor Appl 6(7):935–942. doi:10.1049/iet-cta.2011.0173
9. Doğan M, Morgül Ö (2010) On the control of two-link flexible Robot arm with nonuniform cross section. J Vib Control 16(5):619–646. doi:10.1177/1077546309340994
10. Luo ZH (1993) Direct strain feedback control of flexible Robot arms: new theoretical and experimental results. IEEE Trans Autom Control 38(11):1610–1622
11. Moallem M, Patel RV, Khorasani K (2000) Optimization of an actuated flexible arm for improved control properties. In: Proceedings of IEEE international conference control application, pp 709–714, Anchorage
12. Wang FY, Russell JL (1992) Optimum shape construction of flexible manipulators with tip loads. In: Proceedings of the 31st IEEE conference decision and control, Tucson, pp 311–316
13. Shahruz SM (2008) Increasing the efficiency of energy scavengers by magnets. J Comput Nonlinear Dyn 3(4):041001(12 pp). doi:10.1115/1.2960486
14. Stanton SC, McGehee CC, Mann BP (2010) Nonlinear dynamics for broadband energy harvesting: investigation of a bistable piezoelectric inertial generator. Phys D Nonlinear Phenom 239(10):640–653
15. Külah H, Najafi K (2008) Energy scavenging from low-frequency vibrations by using frequency up-conversion for wireless sensor applications. IEEE Sens J 8(3):261–268. doi:10.1109/JSEN.2008.917125
16. Sarı I, Balkan T, Külah H (2010) An electromagnetic micro power generator for low-frequency environmental vibrations based on the frequency upconversion technique. J Microelectromech Syst 19(1):14–27. doi:10.1109/JMEMS.2009.2037245

17. Ferrari M, Ferrari V, Guizzetti M, Andò B, Baglio S, Trigona C (2009) Improved energy harvesting from wideband vibrations by nonlinear piezoelectric converters. Proc Chem 1:1203–1206. doi:10.1016/j.proche.2009.07.300
18. Lin J-T, Lee B, Alphenaar B (2010) The magnetic coupling of a piezoelectric cantilever for enhanced energy harvesting efficiency. Smart Mater Struct 19:045012(7 pp). doi:10.1088/0964-1726/19/4/045012
19. Yeatman, EM (2004) Advances in power sources for wireless sensor nodes. In: Proceedings of international workshop wearable and implantable body sensor networks, pp 20–21
20. Lee V (2012) Energy harvesting for wireless sensor networks. M.S. project in Engineering—Electrical Engineering and Computer Sciences, UC, Berkeley
21. Erturk A (2009) Electromechanical modeling of piezoelectric energy harvesters. Ph D thesis, Virginia Polytechnic Institute and State University, Blacksburg, November 2009
22. Roundy S, Leland ES, Baker J et al (2005) Improving power output for vibration-based energy scavengers. Pervas Comput 1:28–36
23. Goldschmidtboeing F, Woias P (2008) Characterization of different beam shapes for piezoelectric energy harvesting. J Micromech Microeng 18(10):104013. doi:10.1088/0960-1317/18/10/104013
24. Özdemir Ö, Kaya MO (2006) Flapwise bending vibration analysis of a rotating tapered cantilever Bernoulli-Euler beam by differential transform method. J Sound Vib 289:413–420
25. Abhyankar NS, Hall EK II, Hanagud SV (1993) Chaotic vibrations of beams: numerical solution of partial differential equations. ASME J Appl Mech 60:167–174
26. Dogan M, Morgül Ö (2011) Boundary control of a rotating shear beam with observer feedback. J Vib Control 18(14):2257–2265. doi:10.1177/1077546311429145
27. Chang K-S et al (2012) Electric field energy harvesting powered wireless sensors for smart grid. J Electr Eng Technol 7(1):75–80
28. Tsunoda Y et al (2015) A small-size energy-harvesting electric power sensor for implementing existing electrical appliances into HEMS. IEEE Sens J 16(2):457–463
29. Moghe R et al (2014) A low-cost electric field energy harvester for an MV/HV asset-monitoring smart sensor. IEEE Trans Ind Appl 51(2):1828–1836

Chapter 5
Nonlinear Problems in Piezoelectric Harvesters Under Magnetic Field

Erol Kurt and Yunus Uzun

Abstract This chapter focuses on the nonlinear problems in the piezoelectric harvester systems under the magnetic field. In this manner, the chapter initially mentions an introductory section on the studies of piezoelectric harvester dynamics. After the introductory section, the basic properties of the piezoelectric systems and their energy harvester applications will be presented. Since the harvesters have a complicated structure under the magnetic field, the electromagnetic design, modeling and algebraic studies of a novel harvester study will be pointed out. After the presentation of a theoretical outline on the harvester systems, the experimental setups will be explained in detail. Thus, a complete picture of the problem will be produced in order to sustain a comparable study on the theory and experiment. The main dynamic quantities such as displacement and velocity of the vibrating piezoelectric layer as function of the system parameters will be explored. According to results, the effect of periodic magnetic flux can give varieties of responses from regular dynamics to chaotic one. Phase space constructions, Poincare sections and FFTs are evaluated depending on the parameter sets including the excitation frequency f, amplitude Uc of electromagnet and the distance d. It is proven that the periodic magnetic flux can exert high frequency velocity fluctuations nearby the minimal and maximal values of the velocity, whereas the situation differs for the position. Therefore it will be pointed out that the magnetic field mostly governs the velocity by yielding complicated vibrations. According to the detailed analyses, the FFTs prove the high frequency responses in addition to the main frequency. When f differs from the natural frequency of the system f_0, the responses become chaotic. It is proven that lower and higher frequency fluctuations in displacement and velocity, which are different from f_0 decrease the electrical power harvested by the

E. Kurt (✉)
Technology Faculty, Department of Electrical and Electronics Engineering,
Gazi University, 06500 Teknikokullar, Ankara, Turkey
e-mail: ekurt52tr@yahoo.com

Y. Uzun
Faculty of Engineering, Department of Electrical and Electronics Engineering,
Aksaray University, Aksaray, Turkey
e-mail: yunusuzun@aksaray.edu.tr

N. Bizon et al. (eds.), *Energy Harvesting and Energy Efficiency*,
Lecture Notes in Energy 37, DOI 10.1007/978-3-319-49875-1_5

piezoelectric pendulum. Indeed, it is remarkable to get a relation between the rms values of displacement/velocity and the harvested power according to the measurements. Thus this relation can be used to estimate the power output in harvester systems. The piezoelectric harvester generates much energy when f is closed to f_0 and the distance to the magnetic device should be closer in order to decrease the nonlinearities in displacement and velocity. The pendulum-like harvesters as the most preferable ones can be applied to many devices or units as a power source. The maximal power for these magnetically-excited structures can be estimated by the system parameters. At the end of the chapter, the recent techniques of maximal power point tracking (MPPT) and proposed controller units are explained for the piezoelectric harvester systems in order to optimize the harvested power.

Keywords Piezoelectric harvester · Magnetic field · Nonlinearity · Attractor · Maximal power point tracking

Abbreviations and Acronyms

MEMS	Micro-electro-mechanical system
CDRG	Coulomb-damped resonant generator
DAQ	Data acquisition
FEM	Finite element method
FFT	Fast Fourier transform
MPPT	Maximal power point tracking
RMS	Root mean square
SIDO	Single inductor dual output
SSPB	Single-supply pre-biasing
THD	Total harmonic distortion
VDRG	Velocity-damped resonant generator

5.1 Introduction

In parallel with the improvements on the fields of smart material and energy material technologies, there exists a growing interest on the harvester systems, world-widely [1–3]. The energy harvesting studies mainly focus on three types of harvester systems: Piezoelectric, electromagnetic, and electrostatic [4–7]. Although the piezoelectric materials have a complicated material production procedure (which makes the piezo-structures much expensive than the others in any induction system), higher energy densities from the piezo-systems can be available [8–10]. Table 5.1 gives brief information on the energy densities of three harvesting types.

Piezoelectric systems are more convenient than electromagnetic ones for MEMS applications, because of the problems in magnets miniaturization with current state-of-the-art microfabrication processes [12]. Piezoelectric materials can

Table 5.1 Maximum energy density of three types of energy harvesting [11]

Type	Power equation	Practical maximum (mJ/cm^3)	Theoretical maximum (mJ/cm^3)
Electromagnetic	$E = B^2/2\mu_0$	4	400
Electrostatic	$E = 1/2\varepsilon\ E^2$	4	44
Piezoelectric	$E = \sigma_y^2\ k^2/2Y$	17.7	335

efficiently convert vibrations to electrical energy with relatively high output voltage but without any other voltage source [5]. In addition to above-mentioned superiorities of piezoelectrics, the advances in solid material behavior shed a light to combine the dynamical aspects of solids and the piezoelectric features in order to explain the energy harvesting mechanism behind the solid/piezo structures. At this point, there is very thin separation between a piezoelectric dynamical system and a piezoelectric harvester system: Mainly if a piezoelectric system can harvest energy from any ambient effect such as wind, human movement, seismic forces, water flow, and traffic, etc. [13–16], it is classified as a piezoelectric harvester, otherwise any other systems related to the piezo-structures can be acceptable as piezoelectric dynamic system. From this point, any piezoelectric harvester system is also a piezoelectric dynamic system, thereby the dynamical tools to explain the physics and engineering of energy production and fluctuation phenomena can be used to determine the amplitude/power or velocity/power relations [17, 18].

According to the dynamics of a fluctuating beam, there exists a wide literature, which has been mostly studied by physicists and mechanical engineers [19–21]. According to their approach, a spring-mass model can be used to understand the dynamics of a fluctuating beam under an external stress and damping effect. Equivalently, a basic pendulum model has also been used to identify the dynamical features of the fluctuating beam in some other researches [22–24]. According to these two models, the basic harmonic motion is described by the restoring force of spring or gravitation.

The piezoelectric beams have certain force-voltage relation. Indeed, when the beam is buckled by an external stress (i.e. mechanical, magnetic, electrical, magnetic, etc.), the beam terminals induce a voltage. Note that if the buckled beam then becomes static in any position, it does not induce any potential difference since there is no certain electrical dipole moment inside the crystal structure of piezo-material. Note also that the polarization direction also plays an important role to have an efficient voltage production. Strictly speaking the force should be in the polarization direction of the electrical dipoles. In the case of magnetic stress, the magnetic flux should be oriented in such a way that the permanent magnet(s) should buckle the piezoelectric beam in the polarization direction. Therefore the poles of the magnet(s) and the external magnetic flux direction should be well-simulated [25].

In the following section, initially some basic information on the electromagnetic design, modeling and simulation will be given. Next section will handle the experimental techniques on the piezoelectric systems. Section 5.4 explains the methods of nonlinear analyses, which are used in the fluctuation studies of

piezoelectric systems. Section 5.5 introduces some piezoelectric systems and explains their nonlinear analyzes. While the nonlinear analyzes are discussed in the next section, Sect. 5.7 explains the dependence of dynamics and power to the system parameters. Section 5.8 presents MPPT techniques for piezoelectric harvester systems. Finally the conclusions give the main results of the chapter and some clues on the future perspectives.

5.2 Electromagnetic Design, Modeling and Simulation

The electromagnetic (EM) design is very important for a piezoelectric system in order to estimate the experimental results and the optimization of the system. If the EM design is made in a proper way, it helps to decrease the time consumption in the construction of the setup and the experimental researches. According to the literature there exists some tools to make electromagnetic design and simulation. However, all of them use the finite element method (FEM) because of its reliability and solution speed. Before starting any solution, the geometry and material assignment should be made correctly. Since the magnetic force depends on the distance between the magnetic sources and ferromagnetic bodies strictly, especially the magnetic bodies in the model should be positioned in the correct position in order to estimate the correct magnetic force f_m. In Fig. 5.1, a representative mesh structure is shown. Note that the number of mesh elements can be useful for the FEM simulation. Extremely large elements yield to long runs of computer and the results cannot be obtained in the proper time duration, whereas an optimized number of elements yield to both correct and faster solution.

In order to determine the number of mesh elements, one can assign different numbers to FEM programme and look for the simulation results. If there is a valley in the graph of a quantity (i.e. magnetic flux Φ, magnetic flux density B, field

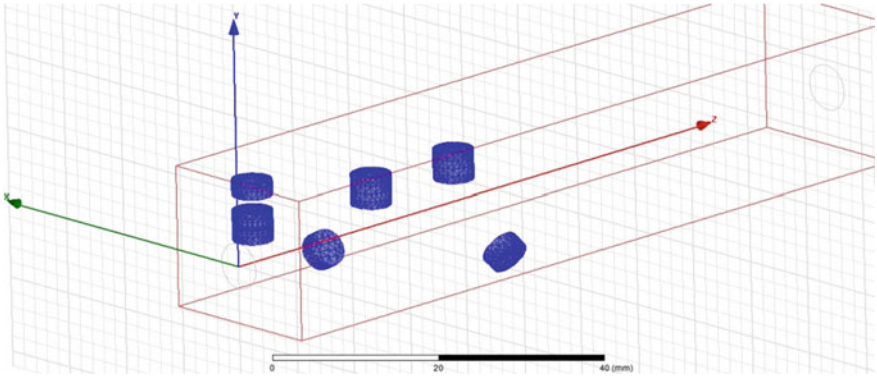

Fig. 5.1 A representative mesh structure

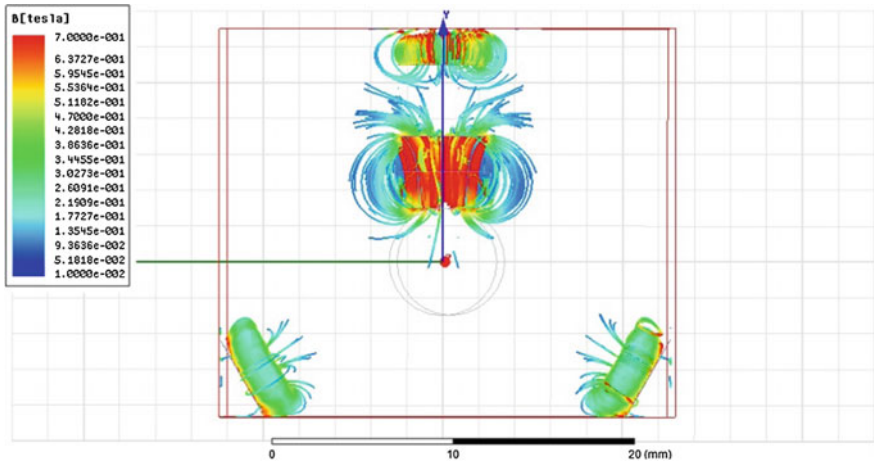

Fig. 5.2 A sample magnetostatic solution of a magnetic piezoelectric harvester

strength H, etc.) as function of number of mesh, then the left edge of this valley can be used for a proper mesh number [26].

The modeling of piezoelectric systems can be made as function of time by using Runge-Kutta time integration technique. It is a proper technique, since the fourth order term addiction gives good sensitivity for the estimation of quantities such as position, velocity, voltage, current, etc. [18]. In addition, the findings of Runge-Kutta technique can be directly used for the dynamic analyzes as in [18, 19]. In the following chapters, the applications of this technique will be given.

After the initial drawings of the model harvester system, magnetostatic analyses can be carried out. From magnetostatic solutions, the effects of magnetic sources, magnetic fields can be found in detail in 3D media (see for instance Fig. 5.2).

Note that the fields may increase at the vicinities of magnetic sources such as magnets up to $B = 1.1$ T. The advantage of the 3D magnetostatic solution is that it can give the field values at every solution region. Therefore the model can be re-drawn easily for the best result. While the distance to a magnetic source is adjusted, one should keep in mind that the piezoelectric beam should not be put closer to the source. Since the magnetic force extremely increases, it can break the beam. Thus the simulations can also give the resulting magnetic force in order to estimate the optimal distance and save the laboratory materials with that respect.

5.3 Experimental Techniques

The setups in the piezoelectric energy harvester labs can include different equipments from various research fields. Therefore experimental techniques may require scientists from different fields such as acoustics, physics, electrical and computer

engineering. The equipments, which are frequently used in the harvester studies can be summarized as follows: Shaker, amplifier, laser displacement sensor and controller, data acquation card, PC, oscilloscope, signal generator, magnets.

Figure 5.3a–c shows the setup of piezoelectric shaker test. The shakers operate with an amplifier in order to boost the amplitude of the vibration as in Fig. 5.3a. The amplifier and the signal generator are used to excite the shaker for piezoelectric tests. In some setups, a special package programme is used to excite the shaker. It can be operated under a laptop and a specific frequency and amplitude can easily be

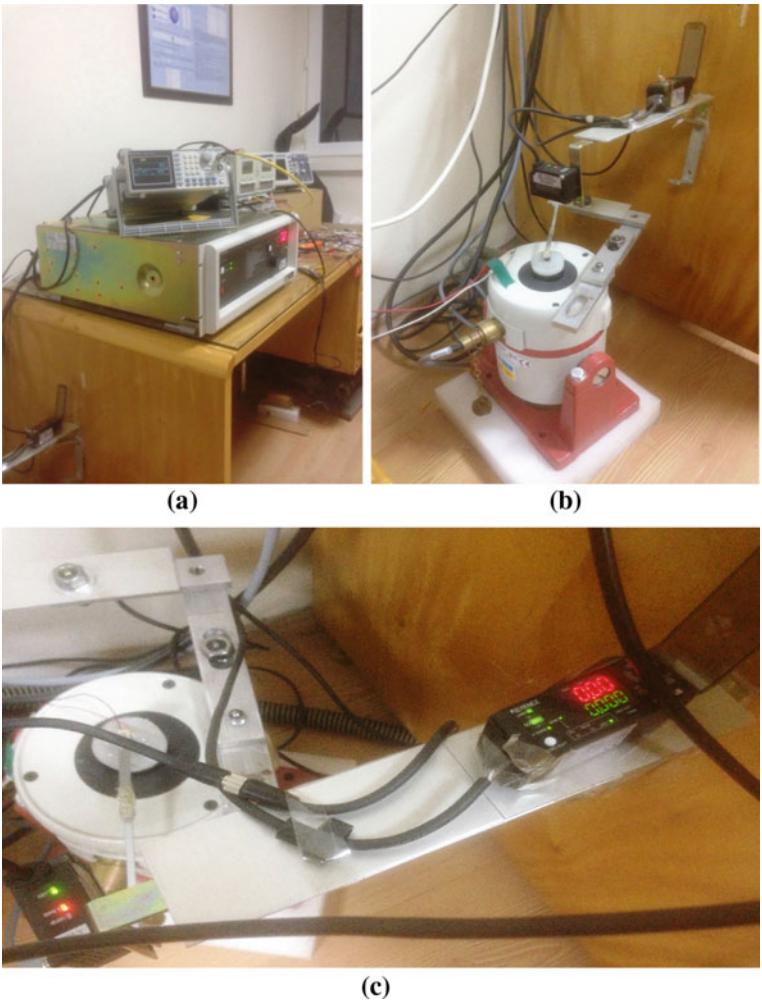

Fig. 5.3 **a** The signal generator (*top*) and connected amplifier (*bottom*) for the excitation of shaker. **b** *Side view* of a shaker. **c** *Top view* of test equipment including a piezoelectric beam and the laser displacement sensor

adjusted via the package and it does not require any signal generator. However it can increase the expenditures for such a setup. In Fig. 5.3b, c, the piezoelectric mounted shaker and the laser displacement sensor (black coloured) are seen on top of the system.

Indeed the excitation signal which comes from a signal generator with a certain frequency (generally 1–50 Hz) and amplitude (lower than 1 V peak to peak) is increased in amplitude and directed to the shaker to produce certain displacements at the tip of the piezoelectric beam. The vibration displacement can be adjusted by the amplifier just by increasing the output amplitude. However, if a certain frequency region will be sweeped, the amplitude should be constant for the experimental sensitivity. Because any small increase or decrease in displacement at the beam tip yields to different results, since the piezoelectrics are very sensitive to the buckling. The shaker setup can be used for the testing of frequency responses of the piezoelectric beams. When it vibrates the beam tip at certain frequencies f, the beam would produce fluctuations between the negative and positive sides of the equilibrium point. Figure 5.4 gives such a fluctuation on the laptop screen, if the fluctuations are read by the laser displacement sensor and send via a DAQ card.

For the interface of the laptop a LabView or other DAQ softwares can be used efficiently. It is possible with recent equipments that the laser displacement sensor and DAQ card can measure the vibrations with the sampling rate of 1 ms. This is a good accuracy in order to measure the higher frequencies of these kind of systems.

Figure 5.5 represents the results of a shaker test for three piezoelectric beams with various lengths. While the vibration amplitude of the long beam becomes large, the short one has small amplitude. In addition, the maximal amplitude, which

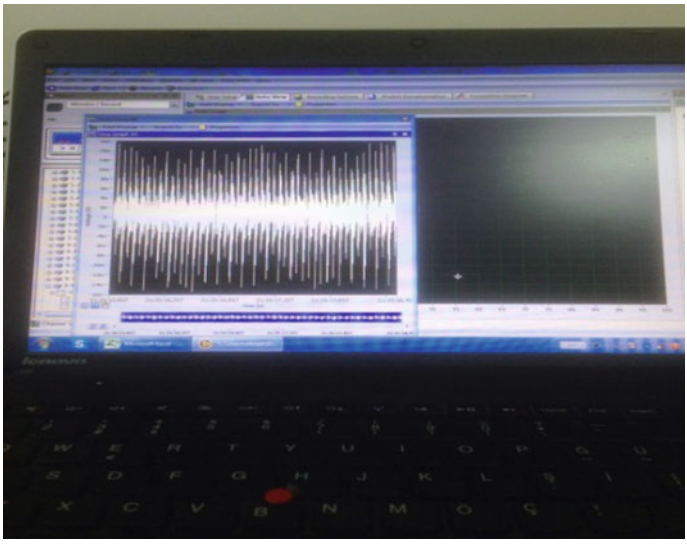

Fig. 5.4 Fluctuations of the piezoelectric beam at the shaker test

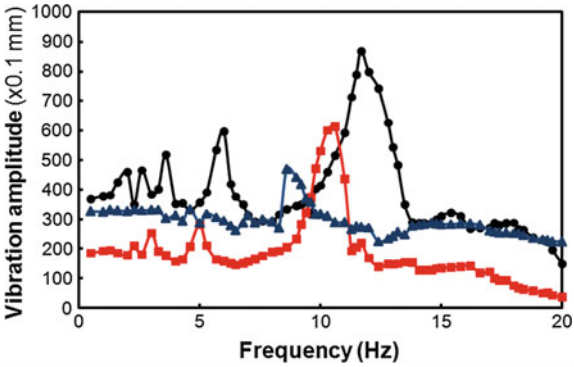

Fig. 5.5 Representative vibration amplitudes for three piezoelectric beams with various lengths: Long (*circle*), moderate (*square*) and short (*triangle*) from a shaker test

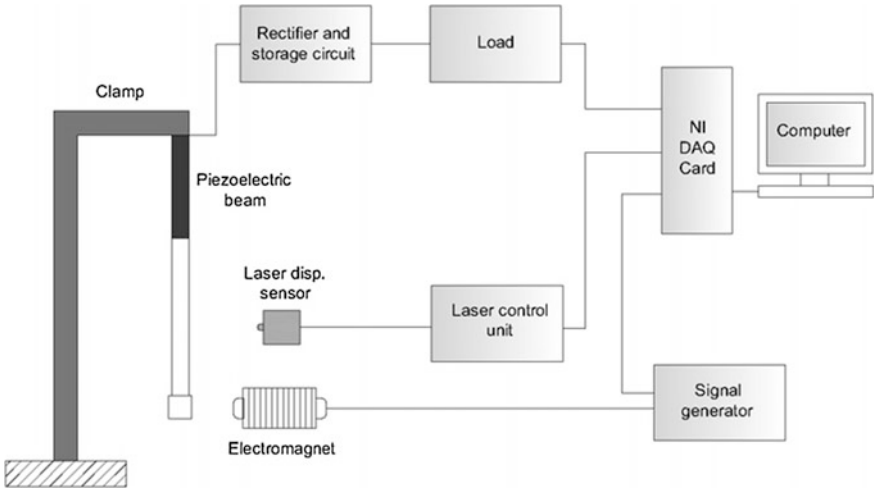

Fig. 5.6 The experimental diagram for the magnetic test system of a piezoelectric beam (*from* [27])

refers to the maximum power, is obtained for different frequencies. The reason is the difference in the natural frequencies of the beams due to their lengths. Similar to pendulums, the length will increase the period of the vibration and the f is decreased.

In order to test the harvesters in a magnetic media, the following setup has been proposed (Fig. 5.6). This system is different than the previous one, since there exists magnetic excitation in place of a mechanical one.

In this system, the response of the piezoelectric beam is tested for different magnetic excitation. The setup can give opportunity to adjust the strenght and the frequency of the magnetic field $\boldsymbol{B}$. The electromagnet is responsible to generate the

Table 5.2 The experimental parameters

Parameter	Symbol	Value
Force/voltage ratio	α	0.0001 N/V
Pendulum mass	m	27.4 g
Piezoelastic layer mass	m_p	10 g
Magnetic force coefficient	F_0	2750
Magnetic force coefficient	F_1	1500
Elastic stiffness coefficient	k	33.435 N/m
Piezoelastic layer capacitance	C	232 nF
Damping ratio	γ	1.48
Inductance of electromagnet coil	L	125 mH
Resistance of electromagnet coil	R_c	5.9 Ω

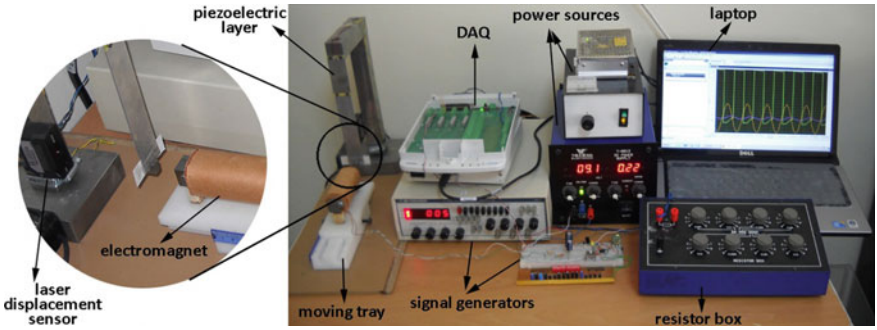

Fig. 5.7 The test setup under periodic field. From *left* to *right*, piezoelectric and non-ferromagnetic beam, laser displacement sensor, electromagnet, DAQ card, signal generator, electromagnet and LDS feeding sources, laptop and variable resistive loads

periodic $\boldsymbol{B}$. The distance of electromagnet to the tip of the beam is important, because the magnetic force strictly depends on the distance. The laser displacement sensor, DAQ Card, rectifier and storage circuit and signal generator are the main test equipments. Table 5.2 gives the experimental parameters of the equipments. In order to create a mathematical expression on the magnetic field effect, the waveform of the applied signal to the electromagnet is important. Such a problem will be introduced in Sect. 5.5. The vibration amplitude and the distance are given by $x(t)$ and d, respectively. Note also that a non-ferromagnetic beam is adhered to the piezoelectric beam tip in order to construct the desired length. The overall setup is shown in Fig. 5.7.

More than 500 thousand data points can be captured per second by the card in this setup. All experimental outputs are gathered by the LabView software. To determine the responses of harvester at different distances d to electromagnet, an adjustable slide mechanism is utilized, thereby the electromagnet can be moved forward and backward with respect to the beam tip. Throught the tests, input voltages for the electromagnet can be sweeped between 6 and 10 V in order to

change the magnetic force $F_m(t)$. Note that the voltage directly influences the current on the electromagnet. Since the electromagnet is an inductive load (X_L), the resulting waveform can change (see Sect. 5.5). The magnetic periodic force is characterized as function of current I_c and the position of the piezoelectric layer tip u.

According to the test system, piezoelectric beam (sizes of 70 × 32 × 1.5 mm and the weight of 10 g) produced by Piezo System Inc is used. The capacitance and stiffness values of piezo-material are 232 nF and 188 N/m, respectively. The laser displacement sensor has a IL-065 type head and a IL-1000 control unit made by Keyence Inc. A rectifier and a storage circuit, a square pulse signal generating circuit, and an NI USB-6250 DAQ unit are also included. The magnetic excitation unit- the electromagnet has 1050 turns with 0.7 cm diameter copper wire. A ferromagnetic core (sizes of 120 × 20 × 20 mm and the relative permeability of μ_r = 10,000) is used to increase the field density. The laser displacement sensor which measures the vibration amplitude of the tip has a sensitivity of 4 μm. It is possible to get multiple records of different physical parameters such as vibration amplitude and harvested voltages in the experiments, synchronously.

5.4 Basic Methods of Nonlinear Analyses

The nonlinearity in engineering systems is important in the sense that the time-dependent systems can be out of stability by slight change in system parameters. Thus the estimated behavior cannot be observed and even it may affect the overall results. Even in many systems such as converters [28, 29], RL-diode circuits [30, 31], beams [19] the system can come out the controlled state and the behavior of the physical quantities such as position, velocity, voltage, amplitude, current, etc. becomes of randomized. Indeed the time-dependent change in these quantities may lead to unpredictable values or periodic states with higher harmonics. At that point, one requires a brief explanation on what the nonlinearity is. Figure 5.8 shows some quantities as function of a variable.

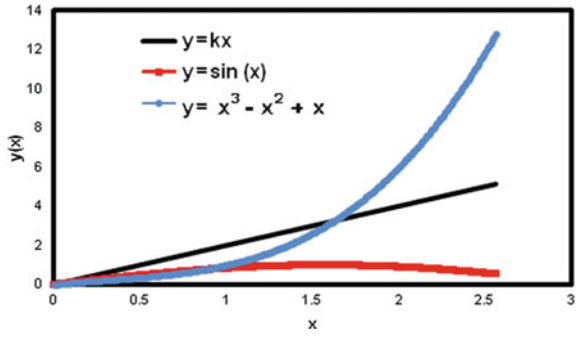

Fig. 5.8 Linearity and nonlinearity of the quantities

While the line gives a linear behavior with respect to the variable (i.e. x-axis), other two curves show complicated responses. Strictly speaking, the increase of x-axis does not yield to simple linear formula (i.e. $f(x) = ax$), indeed it may have higher order dependences to variable x such as x^2, $-x^3$, e^x, $Sin(x)$, etc. A small increase can yield to different results in $f(x)$ function, thereby all these functions are called as *nonlinear* [19, 32]. In many harvester systems, the quantities such as force, voltage, magnetic field indicate such a behavior.

There exist many tools to examine the results of a dynamic piezoelectric system. The following parts give explanations on these tools:

(a) **Phase Space Construction (Attractor Formation)**: In any higher dimensional system (i.e. higher than 1 variable), one can create a graph by putting one of the variables to the x-axis and the other to the y-axis. This representation simply gives the relation between these two variables (i.e. quantities) simultaneously. Thus, if these variables have a closed well-defined curve in the phase space representation, then one can identify the dynamics as "periodic". Indeed a periodic variable can have 2, 3 or more closed curves, then the periodicity is called such as 2P, 3P, etc. by giving a few different frequency in the variable. Figure 5.9 shows such an example.

If the phase space has no well-defined trajectory, indeed the output is assigned as "irregular". In such an attractor, the phase space fulls of many points and their position always changes by time by filling the certain region of the phase space. Beyond the quasi-periodic regime, these kinds of attractors are encountered frequently and those are the indicator of strong unpredictability. On the other hand, this irregular change in the variable is called as "chaotic". A representative example of such an attractor is shown in Fig. 5.10.

At first glance, the response of a dynamical system can be interpreted by forming the attractors, easily. It is easy since there exists a fundamental difference between Figs. 5.9 and 5.10 and it really helps to get an idea on the dynamic regimes.

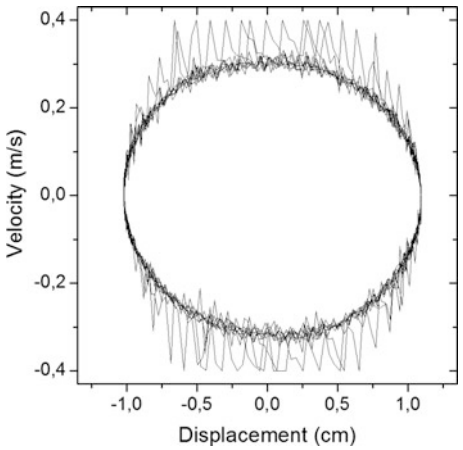

Fig. 5.9 Periodic phase space attractor from the regular motion of a piezoelectric beam

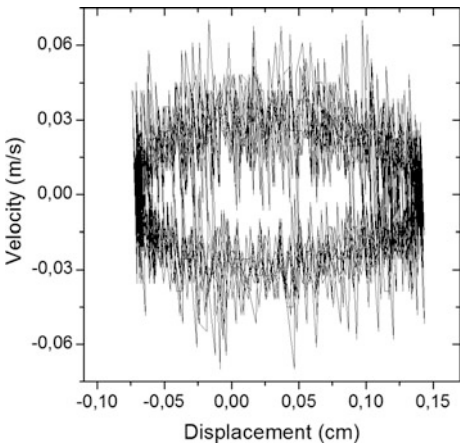

Fig. 5.10 Chaotic phase space attractor from the irregular motion of a piezoelectric beam

(b) **FFT Analysis**: Fast Fourier Transform (FFT) is very-well known process on the signal or image processing problems. It also finds broad application area in power electronics, since the harmonics, sub-harmonics and super-harmonics have importance on the design of a power electronics device. Indeed the dynamics of an output from any system variable can be analyzed by FFT and the frequency spectra can be identified in detail. From the analyses on the piezoelectric beams, periodic, quasi-periodic or chaotic spectrum can be easily understood. Mainly a chaotic output yields to a wide frequency spectra. It means that the output has the combination of many individual frequencies. Some of them can be larger than the main frequency f_0, some others can be smaller than f_0. Many peaks in the FFT indicate the chaotic output of the studied variables. On the other hand, the periodic output gives a basic FFT. A main peak and a few frequencies (they can be sub- or super- harmonics). Note that the peaks in a periodic FFT form can easily be identified, indeed it does not become complicated. Figure 5.11a, b shows two experimental examples on the FFTs from a piezoelectric beam.

(c) **Estimation of Lyapunov Exponents**: Lyapunov exponents determine the distance of the successive trajectories for a certain time evaluation in the phase space [33]. It mainly considers the exponential difference from an initial state for the system variables. Therefore the exponential change may increase the distances of future successive trajectories or it may decrease it. Therefore the logarithm of the ratio of the distances gives an idea how the variables improve in the phase space. The expression,

$$\lambda = \frac{1}{t_n - t_0} \sum_{i=1}^{n} \log_2 \frac{d(t_i)}{d(t_{i-1})} \tag{5.1}$$

gives the fastest growing exponential from the previous state. Indeed, there exist same numbers of exponential with the system variables. If the harvester

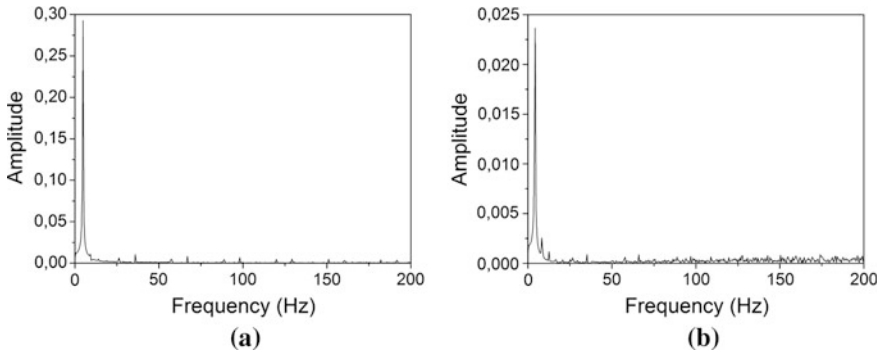

Fig. 5.11 Representative FFT analysis of a regular (**a**) and a chaotic (**b**) output

system has for instance, a coupled model of position, velocity and current as function of time, it means that it has 3 exponentials for each variable. However, the maximal exponential, which drives the overall system, is accepted as the maximal Lyapunov exponent and it is responsible for the future of the system trajectories. Note that if λ becomes negative, the trajectories get closer by time, however if it is positive, the trajectories move away.

5.5 Nonlinear Analysis of the Piezoelectric Harvester Systems

In this section, the nonlinear modeling procedure of some piezoelectric pendulum system under the changeable magnetic field is explained. In our previous study (see [19]), it was found that the vibrations of pendulum structures yield to many complicated responses. Indeed, the elasticity, the magnetic field strength, distance to the field source play important role to identify the dynamics. Initially, the pendulum model under the periodic external field is considered. The model of the setup in is given in Fig. 5.12.

In this model, it is considered that the electromagnet generates a pulsed magnetic field near the tip of beam. It has been known [19, 32] that the electromagnet can create a static and inhomogeneous magnetic field near the tip of the beam. Therefore, dynamics of the beam tip would include the elastic, gravitational and magnetic forces. In the considered system, the elastic force is much higher than the gravitational force since the mass of the system is small. With that respect, the effects of elastic and magnetic forces can be considered dominantly [19, 32, 34]. All forces which affect the tip can be summarized as in Fig. 5.13.

Following our studies [19, 27, 32] the forces in Fig. 5.13 gives the system equations. When the displacement $x(t)$ occurs at the tip of the pendulum, it produces

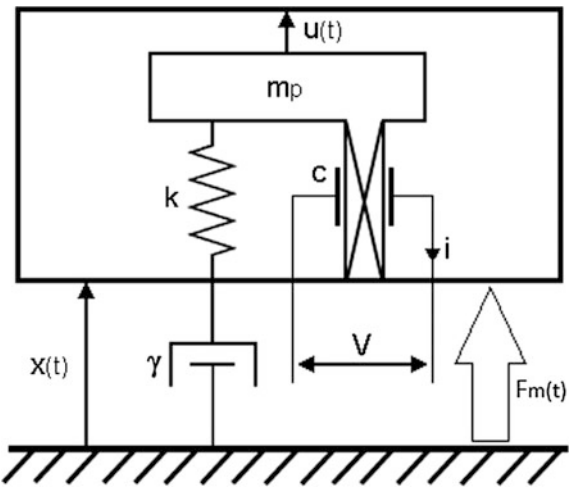

Fig. 5.12 The model of the piezoelectric pendulum in Fig. 5.7 (*from* [27])

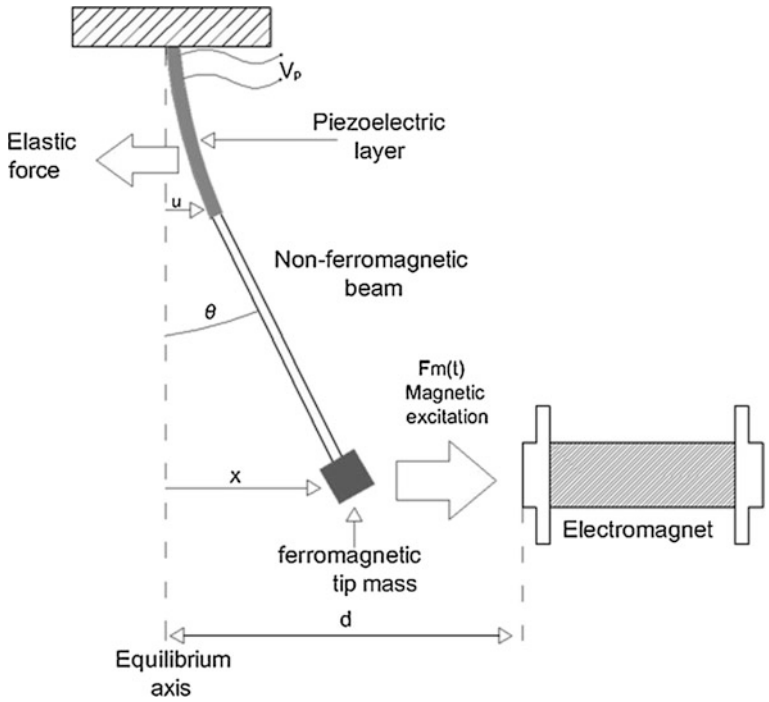

Fig. 5.13 The forces acting on the beam near the electromagnet

and internal mass displacement $u(t)$ inside the piezoelectric material. Here, Figs. 5.12 and 5.13 describe the system as a mass-spring, a damper and a capacitor. In this system, the rigid mass m_p and the stiffness constant k defines the mechanical property under a damper γ which denotes the mechanical losses. When the mass displacement u occurs in the layer, current I and voltage V are generated. In this case, the system equations is given by,

$$\begin{aligned} F_{total}(t) &= ku(t) + \alpha V(t) + F_m(t) \\ I(t) &= \alpha \frac{du(t)}{dt} - C\frac{dV(t)}{dt} \end{aligned} \tag{5.2}$$

Note that the equations include the mechanical and electrical parts. Here, the backward piezoelectric coupling is also included in addition to the mechanical effects. While C is the clamped capacitance, α denotes the force factor. If the displacement of mass inside the piezoelectrics u'(t) and the pendulum tip displacement x'(t) are used before the dimensionless form,

$$(m+m_p)\frac{d^2x'(t)}{dt'^2} = -\gamma\frac{du'(t)}{dt'} - m_p\frac{d^2u'(t)}{dt'^2} - ku'(t) - \alpha V(t) - F_m(t) \tag{5.3}$$

Here, the pendulum and piezoelectric beam masses are denoted by m and m_p, respectively. Considering the periodic magnetic force F_m(t), the equations can be written explicitly as follows:

$$\begin{aligned} \frac{d^2x'(t)}{dt'^2} &= -\frac{\gamma}{(m+m_p)}\frac{du'(t)}{dt'} - \frac{m_p}{(m+m_p)}\frac{d^2u'(t)}{dt'^2} - \frac{ku'(t)}{(m+m_p)} - \frac{\alpha V(t)}{(m+m_p)} - \frac{F_m(t)}{(m+m_p)} \\ \frac{dV'(t)}{dt'} &= \frac{\alpha}{C}\frac{du'(t)}{dt'} - \frac{I(t)}{C} \end{aligned} \tag{5.4}$$

Since x' is measured as 3 times of the displacement u', experimentally (see in Fig. 5.8), $u' = 0.33x'$ can be written. Then one arrives at,

$$\begin{aligned} \frac{d^2u'(t)}{dt'^2} &= -\frac{\gamma}{3m+4m_p}\frac{du'(t)}{dt'} - \frac{k\,u'(t)}{3m+4m_p} - \frac{\alpha\, V(t)}{3m+4m_p} - \frac{F_m(t)}{3m+4m_p} \\ \frac{dV'(t)}{dt'} &= \frac{\alpha}{C}\frac{du'(t)}{dt'} - \frac{I(t)}{C} \end{aligned} \tag{5.5}$$

The dimensionless form can be obtained when $t' = \tau t$, $y' = yd/\tau$, $u' = ud$ and $V' = V_0V$ are introduced for time, velocity, position and voltage scaling, respectively. Note that τ determines the natural period of the pendulum and cannot be confused by the excitation period of the magnetic field T. Besides, to avoid the misunderstandings, d in later two expressions refers to the distance between the

equilibrium point of pendulum and the tip of electromagnet. Then the dimensionless form can be written as;

$$\begin{aligned}
\frac{du}{dt} &= y \\
\frac{dy}{dt} &= -\frac{\gamma\tau}{3m+4m_p}y - \frac{k\tau^2}{3m+4m_p}u - \frac{(m+m_p)\tau^2 F_m(t)}{(3m+4m_p)d} - V\frac{\alpha\tau^2 V_0}{(3m+4m_p)d} \\
\frac{dV}{dt} &= \frac{\alpha d}{CV_0}\frac{du}{dt} - \frac{\tau\, V}{V_0 C R_L}
\end{aligned} \tag{5.6}$$

In above expression, d transfers the coordinate system into the equilibrium point of the beam. The vibration amplitude of the tip is represented by u.

The main problem is to find out the expression of magnetic force. The best way to find out the magnetic force expression, a magnetostatic analysis as similar to the case in Ref. [27] should be realized. The field lines are shown in Fig. 5.14 at the vicinity of the tip. Here, the *Poisson SuperFish* simulation package is used with FEM. The magnetic force F_m increases near the electromagnet and affects the ferromagnetic tip, dominantly. Flux density B decreases with the distance, thereby the 2D simulation can find the effect of the distance.

Figure 5.15 presents the results of the magnetostatic simulations. It has been found that these variations can be fitted to a combined function depending on the variables of u, U_c (i.e. I_c) and t. By considering Fig. 5.16, the overall nonlinear expression can be considered as the functions of electromagnet voltage U_c and the distance u,

$$F_m(t) = f_m(u) f_m(U_c, t) \tag{5.7}$$

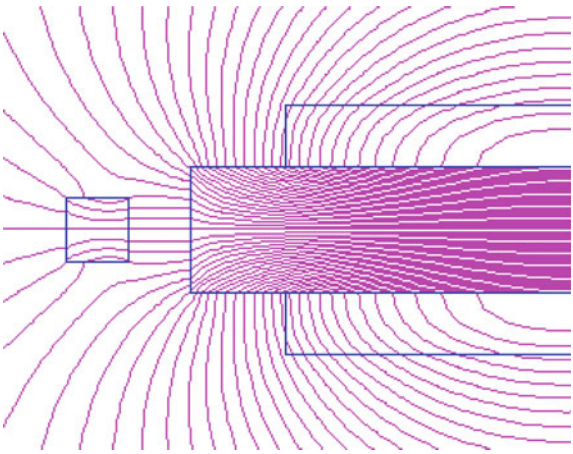

Fig. 5.14 The field lines at the vicinity of beam tip

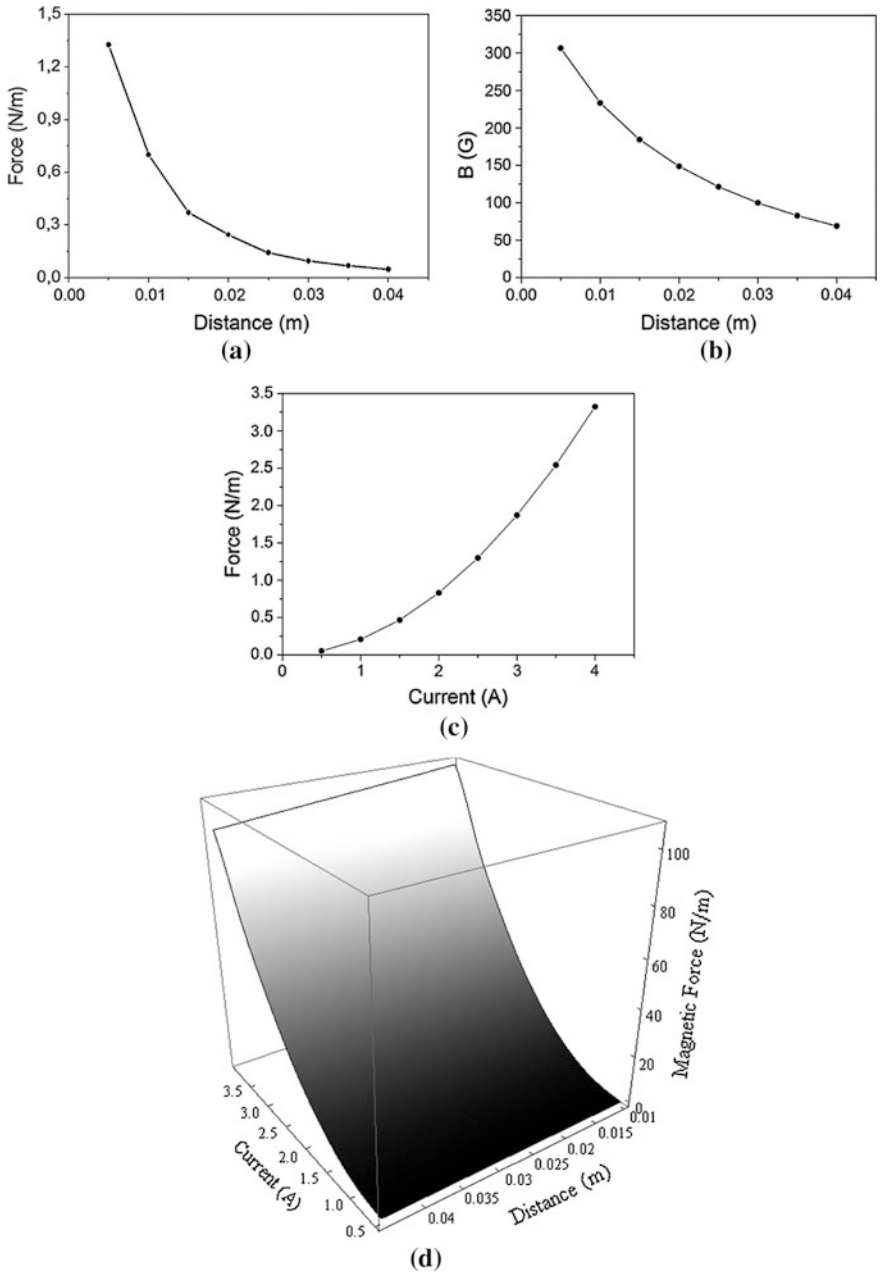

Fig. 5.15 Results of magnetostatic simulations: **a** Force, **b** magnetic flux density *B,* **c** force as function of the distance between the pendulum tip and electromagnet and **d** force on the plane of current and distance

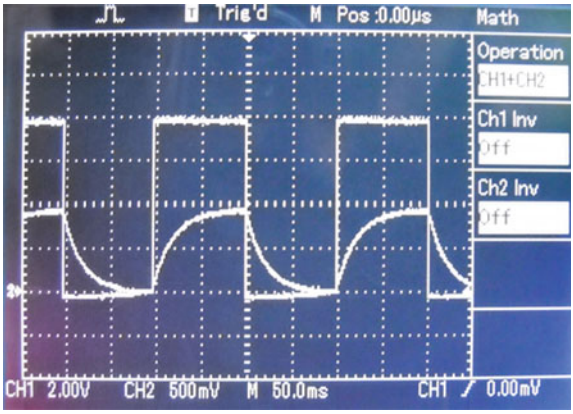

Fig. 5.16 Applied voltage to electromagnet terminals and the electromagnet current waveform which exerts the magnetic force

Note that the third-order polynomial function can fit better as in Ref. [18]. Since $f_m(U_c,t)$ is the function of time due to the periodic excitation as seen in Fig. 5.16, the exponential functions appear as follows:

$$F_m(x) = \begin{cases} \left\{(1-0.7056/d)+0.0623(1-3u)+28026d(1-3u)^2-10^6d^2(1-3u)^3\right\} & \\ \left\{\alpha\left(\frac{U_c}{R_c}(1-e^{-R_c t/L})\right)^2-\beta\frac{U_c}{R_c}(1-e^{-R_c t/L})\right\} & 0<t\le\frac{T}{2} \\ \left\{(1-0.7056/d)+0.0623(1-3u)+28026d(1-3u)^2-10^6d^2(1-3u)^3\right\} & \\ \left\{\alpha\left(\frac{U_c}{R_c}e^{-R_c t/L}\right)^2-\beta\frac{U_c}{R_c}e^{-R_c t/L}\right\} & \frac{T}{2}<t\le T \end{cases} \tag{5.8}$$

Here, d, U_c, R_c, L indicate the distance from the electromagnet to the pendulum equilibrium, voltage, resistance and inductance of the electromagnet coil, respectively. In the expression, the electromagnet force constants are defined as $\alpha = 8 \times 10^{-8}$ and $\beta = 10^{-9}$ from the electromagnetic simulation.

In order to simulate Eq. 5.6, the fourth order Runge-Kutta method can be used efficiently in the MatLab media. In that case, the time dependent results for position, velocity and voltage can be obtained. The main task is to fit the parameters of model and experiment. For this reason, the responses of simulation should be compared by the experimental findings. Therefore the damped results (without the magnetic excitation) can be compared at first step to estimate the best parameter fit.

From these graphs (Fig. 5.17), the natural period and frequency are found as $\tau = 0.210$ s and $f_0 = 4.76$ Hz. In addition, the damping constant is $\gamma = 1.48$ and the ratio of elastic constant to mass is $k/m = 894$. With the help of these parameters, the simulations and experiments fit well. Moreover, this model can be used for finite field values with the excitation frequencies.

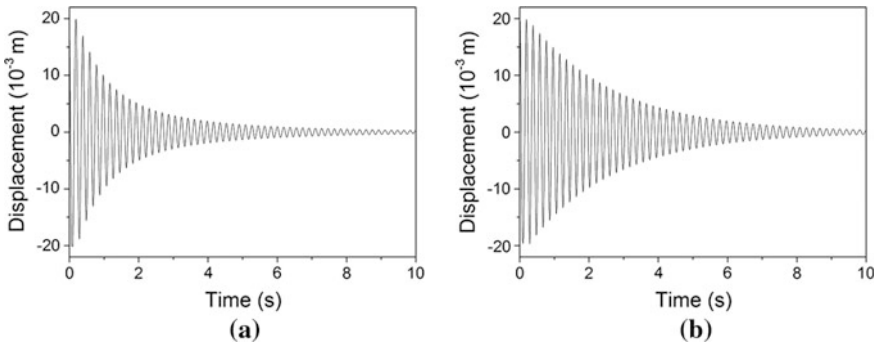

Fig. 5.17 **a** Experimental and **b** Theoretical vibration amplitudes u for non-magnetic case

In order to perform the averaged power output <P>, Eq. 5.6 is considered in frequency domain. While the second equation in Eq. 5.6 is written as,

$$V = \frac{jR_L\alpha\omega_m u}{1+jCR_L\omega_m} \tag{5.9}$$

$$V = \frac{uR_L\alpha j\omega_m\left\{(m+m_p)\,\omega_m^2 - F_0 < I_c^2 > + F_1 < I_c > \right\}}{(-\gamma j\omega_m - m_p\omega_m^2 - k)\,(1+R_L Cj\omega_m) - \alpha^2 R_L j\omega_m} + h.o.t. \tag{5.10}$$

Here the frequency ω_m is determined by the field. Note that the linear terms of the piezoelectric amplitude u is used in order to have an expression on power. Here <I_c> and <I_c^2> indicates the time-averaged values as below:

$$\begin{aligned} < I_c > &= \frac{V_c}{2R_c} + \frac{V_c L\omega_m}{2\pi R_c^2}\left(2e^{-\frac{R_c\pi}{L\omega_m}} - 1 - e^{-\frac{R_c 2\pi}{L\omega_m}}\right) \\ < I_c^2 > &= \frac{V_c^2}{2R_c^2} + \frac{V_c^2 L\omega_m}{4\pi R_c^3}\left(1 - e^{-\frac{R_c 4\pi}{L\omega_m}}\right) + \frac{L\omega_m}{\pi R_c}\left(e^{-\frac{R_c\pi}{L\omega_m}} - 1\right) \end{aligned} \tag{5.11}$$

Here, the electrical parameters belong to the electromagnet coil. A certain voltage V_c with an excitation frequency of $\omega_m = 2\pi f$ is applied to the coil. Then, the power relation is found as follows:

$$< P > = \frac{u^2 R_L\alpha^2\omega_m^2\left\{(m+m_p)\omega_m^2 - F_0 < I_c^2 > + F_1 < I_c > \right\}^2}{k^2(1+C^2R_L^2\omega_m^2) + 2k\omega_m^2(m_p + \alpha^2 CR_L^2 + C^2 m_p R_L^2\omega_m^2) + \omega_m^2\left\{2\alpha^2\gamma R_L + \alpha^4 R_L^2 + 2\alpha^2 Cm_p R_L^2\omega_m^2 + \gamma^2(1+C^2R_L^2\omega_m^2) + m_p^2\omega_m^2(1+C^2R_L^2\omega_m^2)\right\}} \tag{5.12}$$

The linear part of Eq. 5.8 as function of u and its complex conjugate divided by load resistance R_L, one arrives at $< P > \; = \; < VV^* > /R_L$. Equation 5.12 gives the relation between the output power and the electrical/mechanical parameters of the system. By using this formula, it is also possible to find out the optimal load resistance. If one gets the derivative of this equation with respect to R_L, the optimal

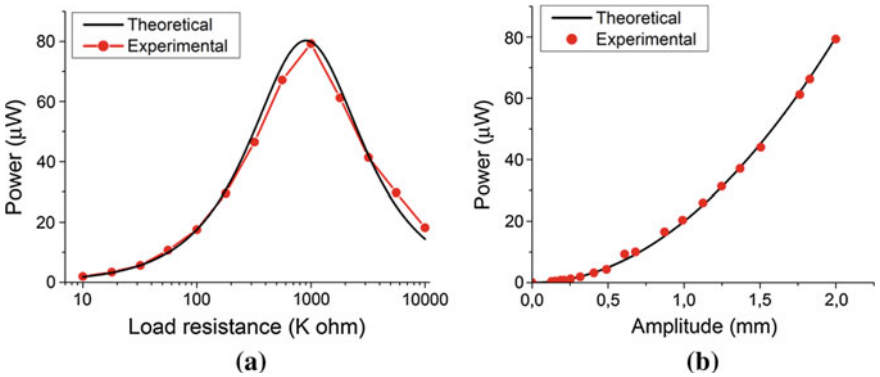

Fig. 5.18 The load resistance (**a**) and vibration amplitude (**b**) dependences of power. d = 2 cm and the voltage applied to the electromagnet terminals is 8 V [27]

load resistance is found as $(\omega C)^{-1}$. Here, ω and C give the frequency of magnetic field and the capacitance of the piezoelectric material, respectively.

Figure 5.18 gives the experimental and theoretical results of the averaged power. The resistive load about 1 MΩ gives the optimum power of the piezoelectric beam. As in other electrical systems, the piezoelectric beam gives the maximal power output when the load resistance equals to its internal empedance.

It is obvious that the theoretical and experimental explorations give the same value. In addition, power depends on the vibration amplitude with a higher order polynomial function (see in Fig. 5.18b). With higher deflactions, much power is obtained.

5.6 Experimental and Theoretical Results of Nonlinearity

In this part, the test results with respect to vibration amplitude, tip velocity and output voltage are discussed. Figure 5.19a–c presents the dynamic responses of the beam tip. It is understood that velocity has some ripples at the maximal values when the tip is at the equilibrium point. The output voltage is not ideal sinusoidal, however it has the same phase with the velocity. In Fig. 5.19d the phase plane trajectories give ripples at minimal and maximal points of velocity as stated before. This phase space representation shows these ripples much clear. Since an ideal periodic motion yields to a simple circle or ellipse in the phase space, the ripples here point out a non-regular dynamics even at the natural frequency of the system.

It has been proven that these ripples are resulted by the magnetic field [27]. The ripples cannot be related to any noisy data, because the external magnetic excitation is very strong for the adjusted parameter set. Even in the theoretical formulation, it yields to similar ripples. The spectral analysis shows that there exist some high frequencies but low amplitude effects in the velocity data. It can have 88 Hz

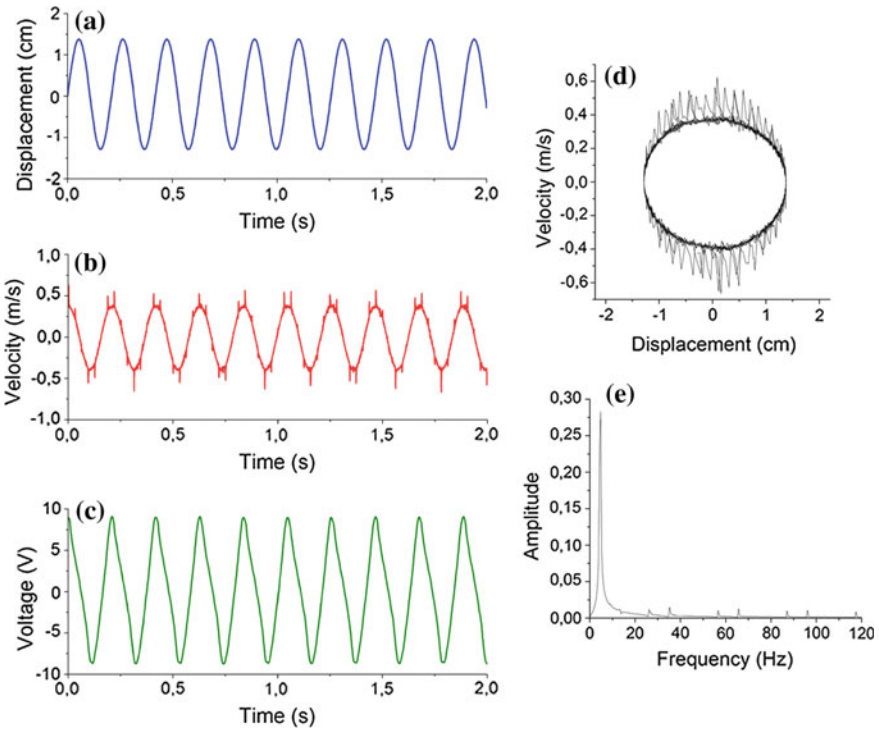

Fig. 5.19 Observation of **a** harvester tip displacement, **b** tip velocity, **c** voltage, **d** phase space portrait and **e** power spectrum of the velocity in the case $d = 2$ cm, $\omega_m = 4.76$ Hz, $R_L = 500$ kΩ

component and that explains the ripples occurring in a very short time scale. Strictly speaking, the main frequency 4.7 Hz and other high frequency components such as 14.6, 26.3, 34.9 and 56.3 Hz are clearly seen in the spectrum (Fig. 5.19e).

When the field frequency ω_m is increased to 6.09 Hz, the dynamics becomes much complicated (Fig. 5.20a). Both the velocity and voltage shows ripples as in Fig. 5.20b, c, however the vibration amplitude has still a sinusoidal character. In addition to the main frequency 6.09 Hz, there exist infinite numbers of frequencies in the spectrum as shown the inset of Fig. 5.20e. Some frequencies with larger amplitudes can be summarized as follows: 24, 36, 54, 156, 256, 425, 452 Hz etc.. These frequencies produce many ripples as in Fig. 5.20d and dominate the phase space. Thus the nonlinearity governs the dynamics for non-natural frequencies. On the other hand, these high frequencies such as 425 and 452 Hz in the velocity data are observed first time, experimentally in such a large-scale piezoelectric system to our knowledge. This result proves how the nonlinearity is important for such harvester systems and encourages us to obtain better power solutions for magnetically excited systems. Although the vibration amplitude becomes sinusoidal, the wide-band structure in velocity causes smooth power decay for different excitation frequencies as will be shown later.

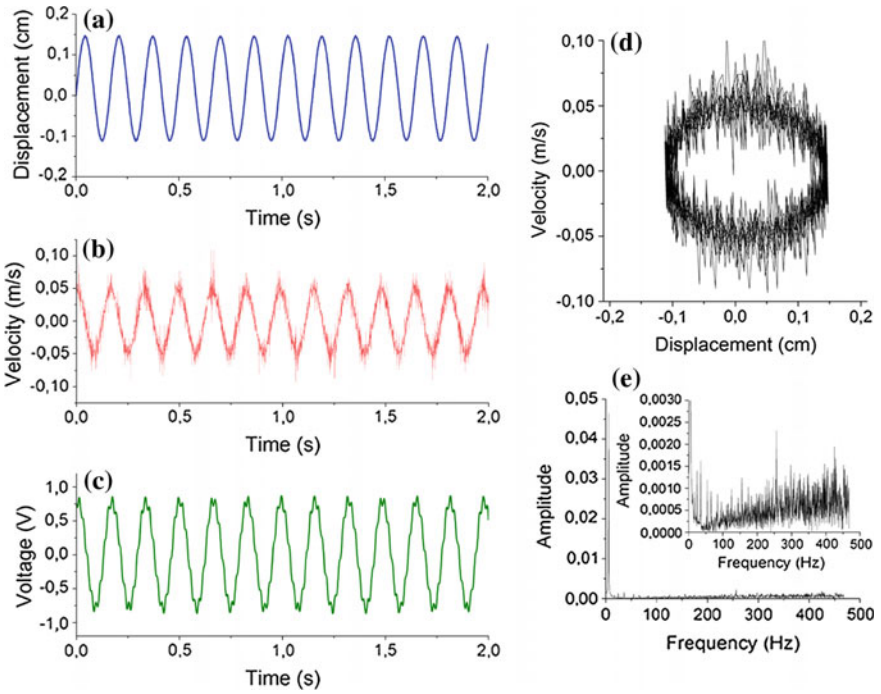

Fig. 5.20 The experimental results of **a** harvester tip displacement, **b** tip velocity, **c** voltage, **d** phase space portrait and **e** power spectrum of the velocity in the case $d = 2$ cm, $\omega_m = 6.09$ Hz, $R_L = 500$ kΩ

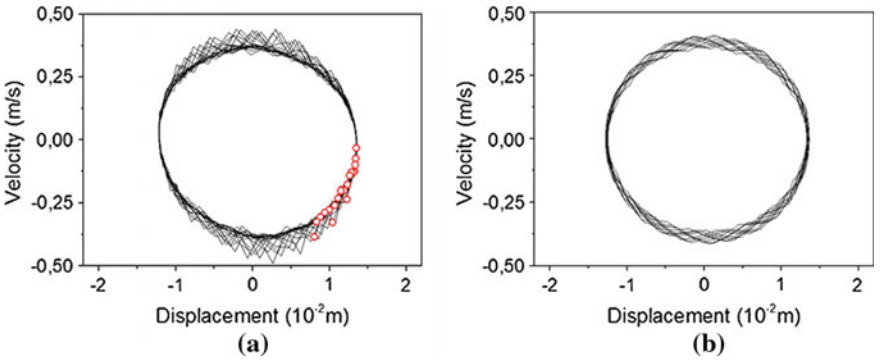

Fig. 5.21 Experimental (**a**) and theoretical (**b**) attractors for $\omega_m = 4.76$ Hz and $d = 2$ cm. The points represent Poincare sections

Figure 5.21 represents the experimental and theoretical attractors for another experimental set. Note that the only change in this parameter set is the current over the electromagnet (i.e. lower magnetic force). The ripples still exist, however their

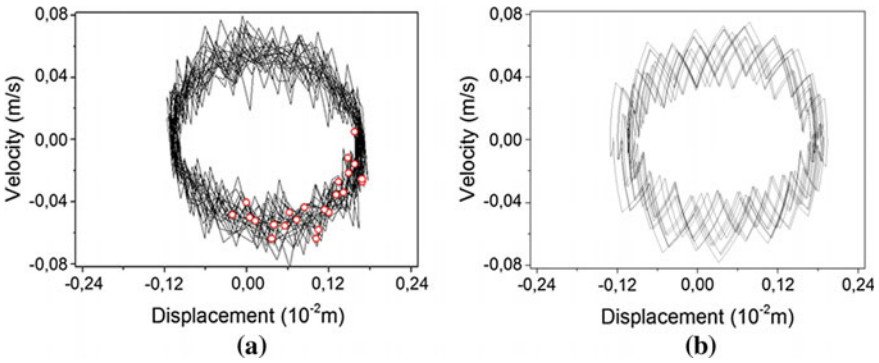

Fig. 5.22 Experimental (**a**) and theoretical (**b**) attractors for ω_m = 6.02 Hz. The points represent Poincare sections [18]

lengths are low compared to the case in Fig. 5.19. The open circles on the experimental data gives the Poincare section data, which is separated on the phase space after the same time interval. The theoretical attractor, which was calculated from Eq. 5.6 is shown in Fig. 5.21b and gives a good similarity to the experimental one.

The vibration amplitude of the beam tip becomes larger, when the field frequency approaches to the natural frequency of the system (i.e. $\omega_m = \omega_0$ = 4.76 Hz). Thus the frequencies near the natural frequency of the system are better to harvest much energy from the system, since the voltage generated by the piezoelectric layer is found to be dependent on the vibration amplitude. In Fig. 5.22, the attractors of another parameter (i.e. ω_m = 6.02 Hz) are compared. The changeable character of the magnetic flux can be seen in velocity fluctuations dominantly, whereas the vibration amplitude gets smaller values compared to the earlier cases. The similarity persists again between the theoretical and experimental findings. Note also the distributed Poincare section points on the attractor in Fig. 5.22a.

In addition to the similarities between the model system and the experimental one, the harvester systems show another interesting phenomena called hardening and softening effects. In Fig. 5.23, an example of this strange hysteresis bahaviour is presented. Here, while the blue plot gives the maximal voltage when the excitation field frequency is increased up step by step, the red plot gives the maximal voltage when the frequency is decreased gradually.

The frequency increase causes a harvesting effect with small amplitudes around 5 V (as in sweep up case) as in Fig. 5.23. But the frequency lowering beyond the natural frequency causes three-fold voltage harvest in the softening effect. This behavior is the result of the piezoelectric layer type. While some layers indicate softening effect, others give hardening effect, where increasing frequency yields to high amplitudes. As a result of these hysteresis effects, the excitation frequency

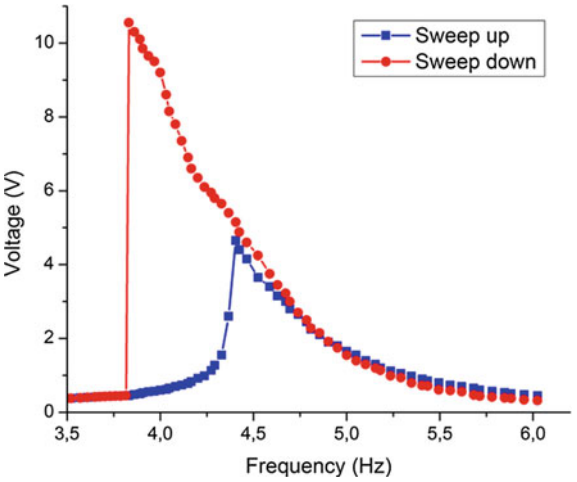

Fig. 5.23 Peak voltage as function of the excitation frequency ω_m. Softening effect is observed for the sweep up/down cases. The parameters are d = 2 cm, the load resistance R_L = 820 kΩ and the maximum voltage over electromagnet U_c = 8 V

should always change at the vicinity of natural frequency, where jumps in amplitudes can be observed.

5.7 The Dependence of Dynamics and Power to the System Parameters

In this section, the parametrical dependence of power in pendulum-like harvesters will be explained. For this aim, the dynamic feature of such a system can be summarized by an intuitive bifurcation diagram (Fig. 5.24). Indeed, such diagram can be produced by adjusting a parameter or two parameters on a plane. If one parameter dependency is studied, it is called one-dimensional bifurcation diagram, whereas two parameters are studied together on a parameter plane, it would be a two-dimensional bifurcation diagram. The bifurcation data can be produced by displacement, velocity or harvested voltage for successive parameter changes. Therefore it is nothing else than the collection of many Poincare sections. According to Fig. 5.24, the frequency values less than 4.8 Hz give regular displacement values and a periodic behavior is observed. However beyond this value, displacement values fluctuate between 0.4 and 1.4 cm till the excitation frequency becomes 5.1 Hz. The displacement vibrations become regular (i.e. periodic) for larger values. In the case of velocity (i.e. filled circles), the motion is much complicated since the fluctuations does not decay to a certain velocity value for any excitation frequency.

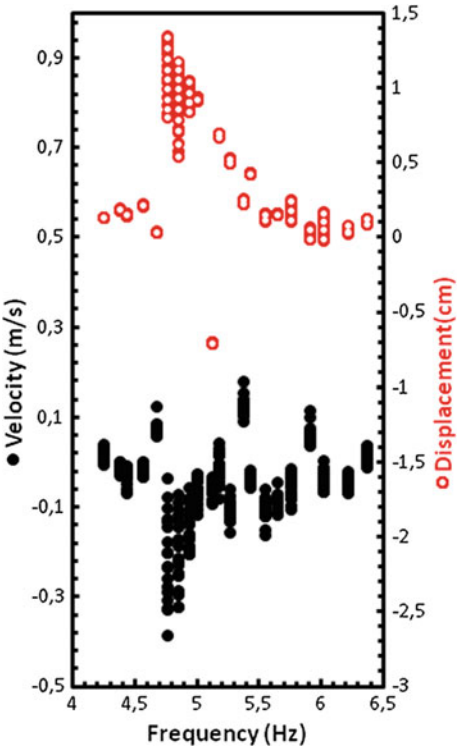

Fig. 5.24 The experimental bifurcation diagram (d = 2 cm, U_c = 8 V). The bifurcation parameter is magnetic field excitation frequency

The parametrical dependencies can also be found by root mean square (RMS) data, which is given by [35]:

$$x_{rms} = \sqrt{\frac{1}{n}\left(x_1^2 + x_2^2 + \cdots + x_n^2\right)} \tag{5.13}$$

Displacement and velocity data are represented by x_n, and n gives the total data point. It is interesting that there exist a good relation between RMS values of data and the corresponding output power as in Fig. 5.25. Indeed, this relation can be found for both experimental and theoretical data. All data can be fitted to a second order formula, which states that power increases parabolically as function of displacement and velocity rms data.

This invention of this relation is new for magnetically-excited systems and it gives a very clear result, which enables one to estimate output power just by looking at rms data of displacement and velocity [18]. In Fig. 5.26, another interesting result is given. The RMS values of displacement and velocity enables us to determine the natural frequency of the harvester system. Both RMS displacement and velocity data jumps at natural frequency. In this experiment, the natural frequency is 4.76 Hz.

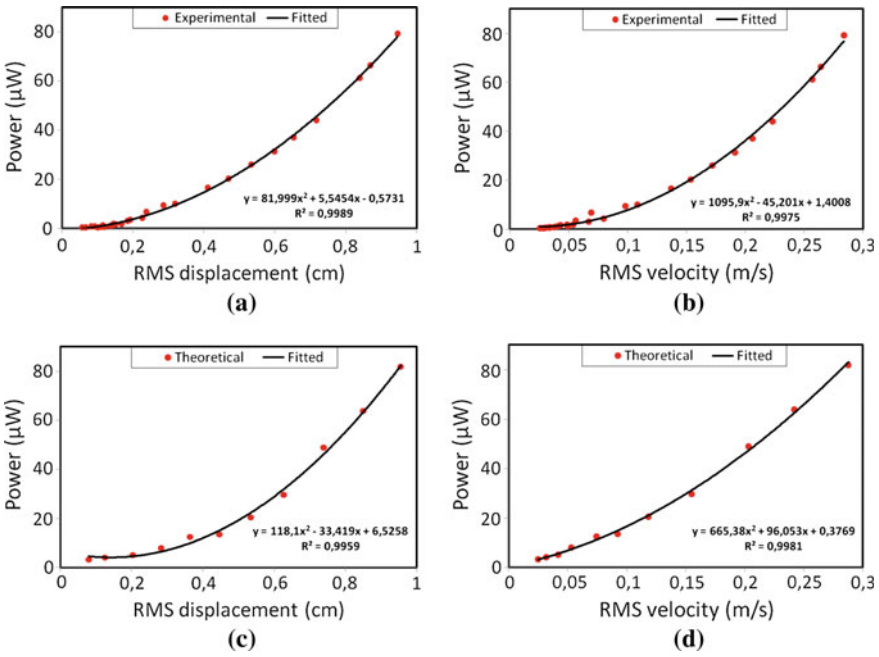

Fig. 5.25 Experimental (**a, b**) and theoretical (**c, d**) relation between displacement/velocity and output power. (d = 2 cm, U_c = 8 V and the frequency changes between 4.25 and 6.53 Hz.)

One of the important concepts to measure the nonlinearity of time-dependent data is the fluctuation amount. The nonlinearity of any fluctuation increases, when different frequencies are included in the data. When one gets the amplitudes of individual frequencies from the FFT result, a quantitative scaling can be obtained for the data. This process is mainly described with the concept of total harmonic distortion (THD) [17, 36]:

$$THD = \frac{\sqrt{\sum_{i=1}^{N_f} A_i^2}}{A_0} \tag{5.14}$$

where A_0 denotes the main frequency of the displacement or velocity data. A_i and N_f denote other frequencies and the number of total frequencies in the FFT, respectively.

In Fig. 5.27a, b, the THD results of the data are presented as function of excitation frequency. It is obvious that displacement fluctuations are smoother than velocity fluctuations in Fig. 5.27b. The nonlinearity becomes 5 times powerful in velocity fluctuations for some f values compared to the displacement fluctuations.

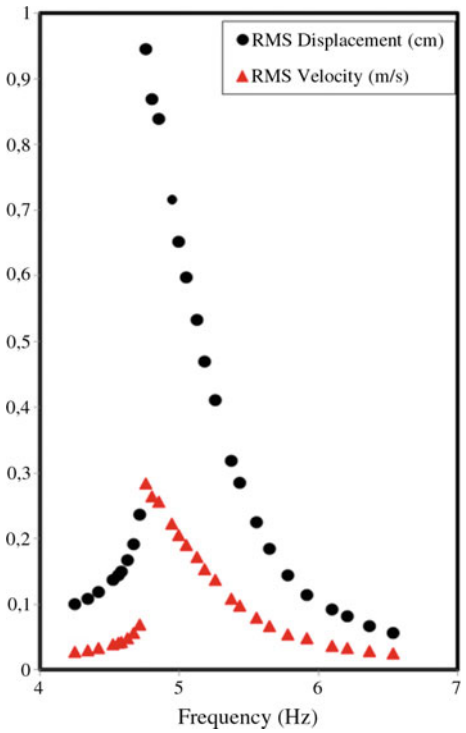

Fig. 5.26 The dependence of rms position and velocity to the excitation frequency

While the maximal distortions are obtained at lower f for both displacement and velocity, a contradiction occurs at the vicinity of natural frequency.

Because the distortion in displacement increases up to 6 at the vicinity of f_o, the distortion in velocity stays lower near 15 at the same frequency. Note also that there is a slightly decreasing character in THD of displacement (Fig. 5.27a). However, in the case of velocity, THD increases for higher frequencies as seen in Fig. 5.27b. Thus, these results prove that while the nonlinearity of displacement is generally higher for the frequencies lower than natural frequency of the system, the nonlinearity of the velocity stays higher for lower and higher frequencies and becomes lower at relatively medium frequencies. In order to find a relation between displacement/velocity THD values and output power, Fig. 5.28 is depicted. While the output power maximizes at $f = 4.8$ Hz, THD of velocity minimizes. Thus, it proves that the power decreases when irregularity increase in the velocity data. Whereas there is no significant correlation or anti-correlation between displacement and power.

From the electrical point of view, the resistive load R_L and excitation frequency f are important. In order to show this combined effect, Fig. 5.29 is presented.

There exists a certain maximum for specific resistance and magnetic excitation frequency. The output power of harvester becomes maximal, when f gets closer to the natural frequency. While the dependence on the frequency is much strict in

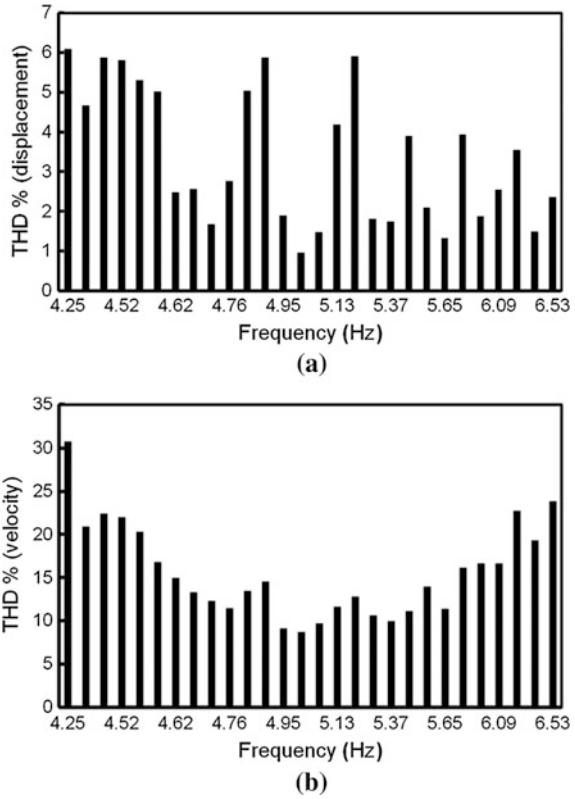

Fig. 5.27 The total harmonic distortion percentages (THD %) of **a** displacements and **b** velocities for excitation frequency

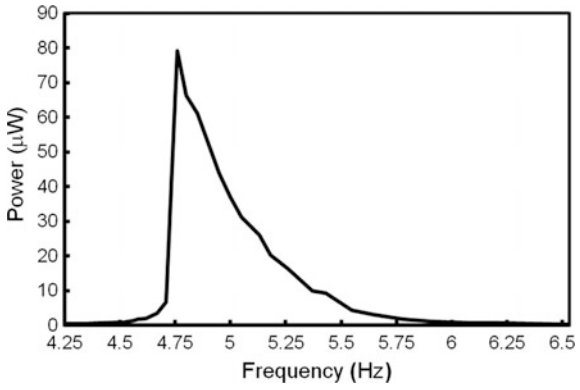

Fig. 5.28 The corresponding output power as function of excitation frequency

order to get the maximal output, the resistance dependence affects the output power relatively low. Note that the resistance axis is in the logarithmic scale. Another important result is that the harvester power shows the wider frequency region at its same value for the resistive loads of 1 MΩ. Thus if one requires much stable output for a wider range of excitation frequencies from the harvester, the load should be adjusted at that value otherwise the maximal output can be generated at certain parameters.

5.8 Maximal Power Point Tracking Techniques for Piezoelectric Harvesters

Parallel to the findings of previous section, a harvester gives the maximal power generation for a specific vibration frequency and load (see in Fig. 5.29). Therefore an efficient maximal power point tracking (MPPT) technique should be applied in order to get the optimized energy. In the literature there exist various techniques for the MPPT techniques [37–39]. Initially, it should be pointed out that surface mounted devices (SMD) can be preferable to decrease the power loss in the circuit

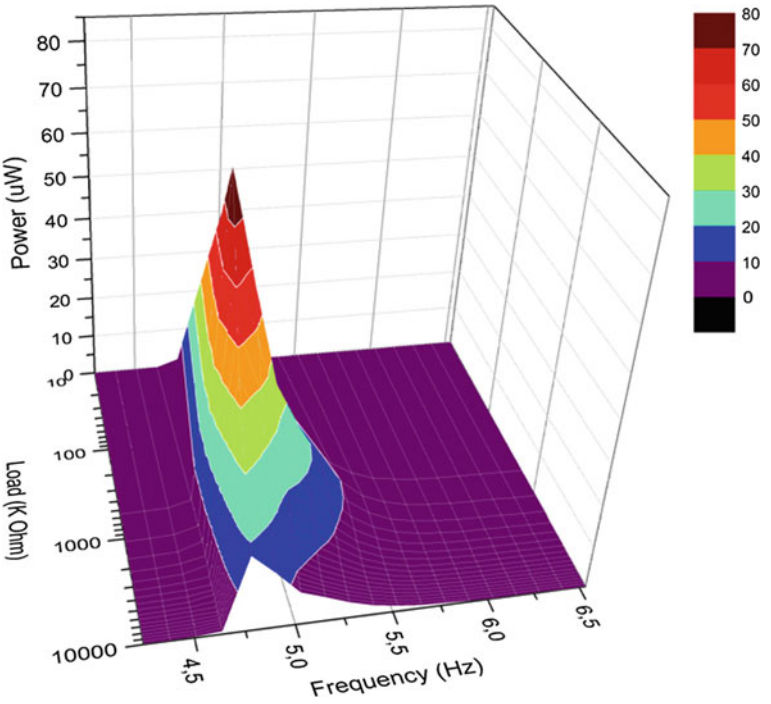

Fig. 5.29 Harvested power on the plane of resistive load and excitation frequency ω_m

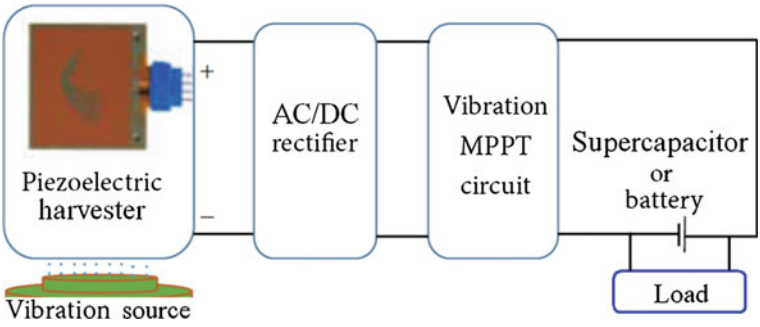

Fig. 5.30 The circuit diagram which enables to use of the harvested power: Rectification, storage and MPPT

elements since they generate μW or mW scale powers. Figure 5.30 shows a general circuit model with rectification, storage, MPPT and electrical load.

The harvested signal is initially rectified and transferred to an MPPT circuit just before the storage unit. Two recent MPPT techniques are mentioned below:

1. DC/DC single inductor dual output (SIDO) control technique,
2. The single-supply pre-biasing (SSPB) technique.

The SIDO control equipments and MPPT circuit diagram which are introduced by Ramond et al. [37] is shown in Fig. 5.31. After the harvester part in the left hand-side an AC/DC recitifier is first used as also refered in Fig. 5.30. Later, the MPPT and controller part is added to the system for an optimized power control.

In the MPPT part of Fig. 5.31, there is a certain voltage value called VMPP for which the power PMPP is delivered maximal from the harvester. After this MPP, the power decreases by the voltage increase until it reaches a value VOC, the Open Circuit voltage of the harvester for which the harvested power is null. The main

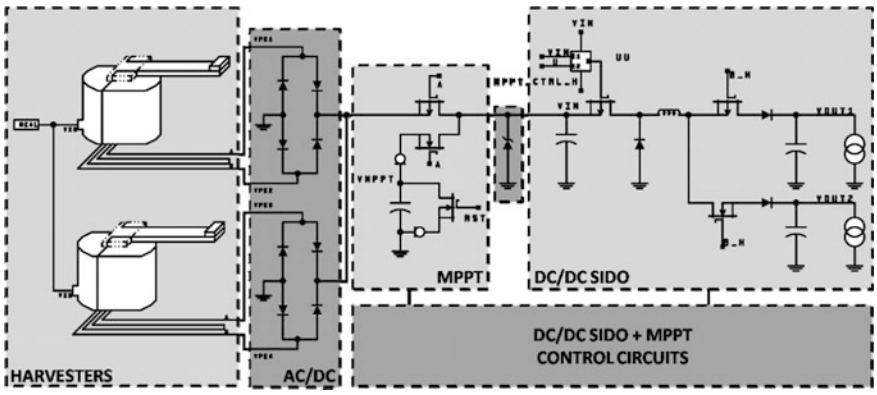

Fig. 5.31 The detailed connection of MPPT and DC/DC SIDO control circuit (*from* [37])

Table 5.3 Harvester characterization summary with SIDO control technique (*from* [37])

Vibration level (g)	$\|P_{MPP}\|$ [W]	$\|V_{MPP}\|$ [V]	$\|V_{OC}\|$ [V]	$\|V_{OC}\|/\|V_{MPP}\|$
0.1	3.5×10^{-6}	1.26	2.10	0.6
0.3	35.5×10^{-6}	4.02	6.77	0.59
0.5	103×10^{-6}	6.83	11.48	0.59

function of this MPPT technique is to sample the open circuit voltage of the harvester, periodically in order to provide a reference voltage to the DC/DC converter. Indeed as shown in Table 5.3, the ratio VMPP/VOC is constant over the whole vibration level range (0.1–0.5 g). Thus the DC/DC converter regulates the harvester polarization voltage around VMPP leading to a maximal power emission with an average efficiency of 95%.

Consequently in order to achieve an optimal power, the micropower management system should regulate the voltage of the harvester and place it close to the MPP. According to literature, this kind of MPPT problem has been solved using the charge pump or inductive DC/DC converters in order to isolate the piezoelectric layer from heavy electrical load and enable to control the polarization of the source independently of the load voltage (Fig. 5.32a). The solutions proposed by Yi et al. [40] and Simjee and Chou [41] are interesting but all the power consumed by the

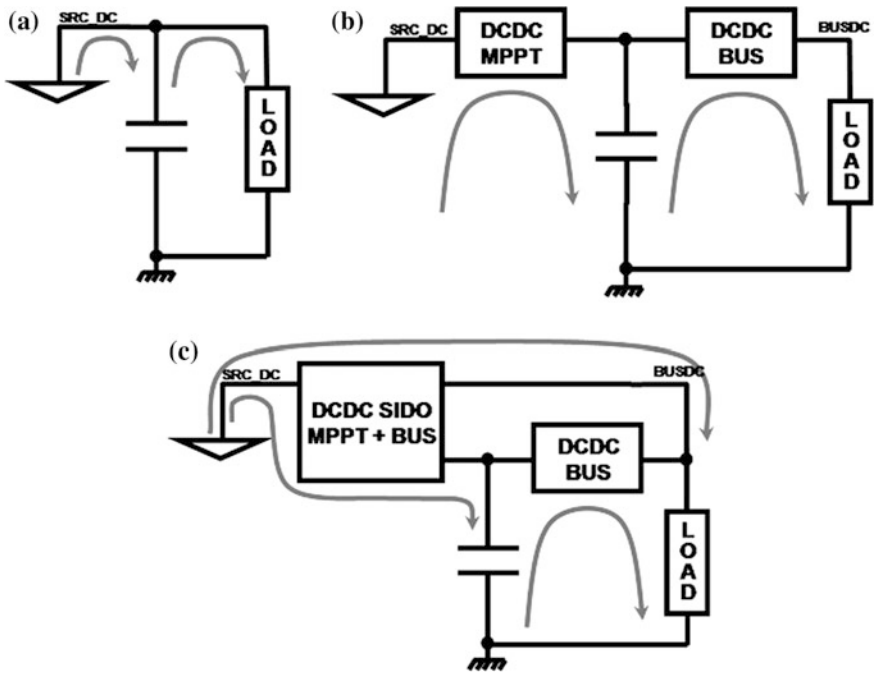

Fig. 5.32 Various MPPT management systems in the literature (*from* [37])

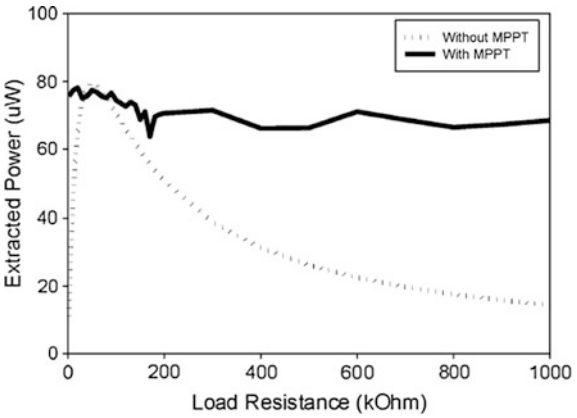

Fig. 5.33 The harvested power with/without MPPT from a piezoelectric layer (*from* [42])

load passes through the storage element and two converters (see in Fig. 5.32b), which decrease the overall efficiency of the system.

Figure 5.32c proposes another MPPT solution by providing a high efficiency direct power path from the source to the load in addition to the MPPT scheme by using a Single Inductor Dual Output (SIDO) DC/DC converter. The MPPT system operates with the control circuit as in Fig. 5.31 as well. According to the findings of Do et al. [42], the effect of an MPPT system can be seen in Fig. 5.33.

The bell-shaped dotted curve shows the harvested power after the rectifier for various ohmic loads. For the high loads then 200 kΩ, there exists a drametical decrease in power as also shown in Fig. 5.29 in the previous section. However, the MPPT system produces a much rough output for high loads and the output power is nearly fixed around 70 μW.

Other recently proposed MPPT technique is called as single-supply pre-biasing (SSPB). According to Elliott and Mitcheson [39], their technique enables the damping force to be set by a fixed voltage and by varying that voltage, real-time adaptation to variations in the mechanical force can be implemented.

Every half cycle of vibration, charge is placed on the piezoelectric material which will induce a force opposing the motion of the piezoelectric material. This tries to dampen the beam's motion, causing an increase in the harvested power. SSPB changes the circuit from a velocity-damped resonant generator (VDRG) to a Coulomb-damped resonant generator (CDRG) [43], enabling the level of damping applied to be readily set by the pre-bias voltage, V_{cc}. At the piezoelectric beam's extreme points, charge from the pre-biasing capacitor, C_{bias}, is transferred on to the beam. This generates a Coulomb force to oppose the beam's vibration until it reaches the opposite extreme position. The energy on the beam is then discharged back into C_{bias}, and the process repeats. Similarly to the bridge rectifier, the damping force can be optimally set by setting the voltage on the storage device in order to achieve maximum power extraction,

$$P_{\max} = \frac{8Q}{\pi} V_{po}^2 f_0 C_p \quad \text{and it is applied when} \quad V_{opt} = 2V_{po} \frac{\gamma}{1-\gamma^2} \tag{5.15}$$

Here Q is the Q-factor of the resonant current discharge path through the inductor and is the fraction of the magnitude of the voltage conserved on the capacitor of an RLC oscillator with Q-factor after a half-cycle of the oscillator. The system must detect a change in the piezoelectric induced voltage, quantify the magnitude of the change, and operate an appropriate response. Since both the bridge rectifier and SSPB techniques use a voltage on a bias capacitor to apply the optimal conduction angle and damping force respectively, adding a buck converter with battery enables the bias capacitor voltage to be independently set. The MPPT scheme operates by adjusting the off-time of the buck converter causing the energy on the bias capacitor to be more or less frequently transferred, resulting in a decrease or increase in voltage respectively. Figure 5.34 shows the suggested topology to adjust the voltage applied for the SSPB circuit. The voltage on the biasing capacitor, C_{bias}, is controlled by varying the power transferred through the buck converter. If the time between energy transfers is increased, C_{bias} voltage would rise and a greater damping force is applied to the piezoelectric material. For the implementation of the SSPB technique, the system requires three elements [39]: A circuit to measure the harvested power, a controller to decide whether the power has increased or decreased object to the previous measurement and a buck converter to transfer the energy. In the design of these circuits, power consumption should be minimised for the highest efficiency. Figure 5.35 gives the implementation to demonstrate the MPPT technique.

The measurement and control circuitry should operate at the lowest voltage possible, but the voltage on the biasing capacitor maybe several times larger than this. A potential divider can also be used by switching in across the biasing capacitor during the operation (see in Fig. 5.35). The switch can be an n-type MOSFET (BSS138), which can be driven by a low power FPGA (Igloo Nano). It can also be used to implement the SSPB scheme [39]. A low power Analog-to-Digital Converter (ADC AD7468) can be used to measure the voltage and a Booth Multiplier algorithm [44] on the FPGA can square the value.

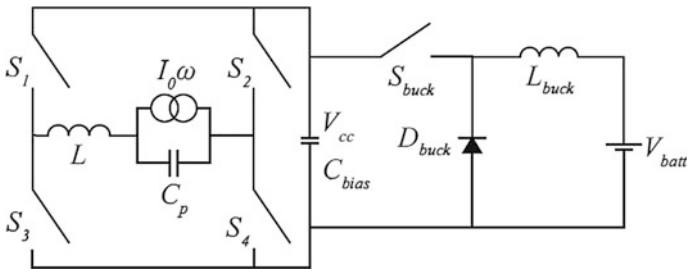

Fig. 5.34 The SSPB unit attached to a buck converter and battery (*from* [39])

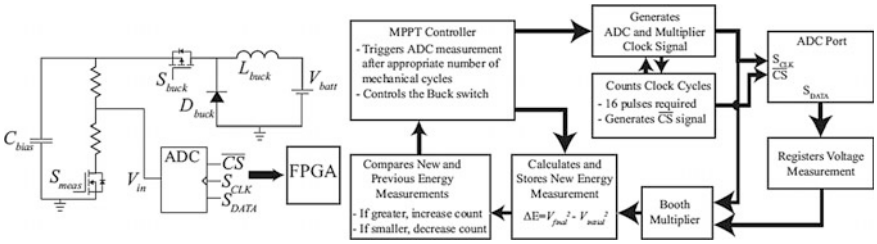

Fig. 5.35 SSPB MPPT implementation and controller (*from* [39])

5.9 Conclusions

In this chapter, the outlines of the dynamic explorations of the harvester systems have been explained. Mainly, the 3D system modeling, electromagnetic analyses and time-dependent simulations have been defined for the widely worked pendulum system. While the 3D modeling of the system gives a clue on the electromagnetic effects, especially the magnetic force steming from the permanent magnets or a stable curring carrying winding play an important role to determine the dynamics. It has been also proven that the distance between the magnetic or electrical souce contributes to the nonlinear force term as well as the current flowing the electromagnet. The other parameters such as resistive load, electromagnet excitation frequency and strength (i.e. current) dominate the dynamics and affect the harvested power in the system. In parallel with the other systems in literature, the natural frequency of the harvester causes maximum power generation. In fact, the nonlinearities in the velocity data for such periodic magnetic excited system subject to decrease the power generation obviously, whereas there exists no remarkable effect of the vibration amplitude on the output power. Considering the methodology of dynamics, many applications of the pendulum-like harvester systems should be realized and both theoretical and experimental explorations should be carried out together in order to draw a complete picture of the applications. The chapter ends with the recent proposed MPPT techniques in order to optimize the harvested power from the piezoelectric systems.

Acknowledgements The supports from Gazi University Research Development Unit under Grant Nos. BAP 07/2010-01, BAP 07/2012-12, Turkey Ministry for EU Affairs—National Agency under Grant No. 2015-1-TR01-KA203-021342 and The Scientific and Technological Research Council of Turkey (TUBITAK) under grant EEEAG-114E017 are acknowledged.

References

1. Tufekcioglu E, Dogan A (2014) A flextensional piezo-composite structure for energy harvesting applications. Sens Actuators A Phys 216:355–363
2. Saha CR, O'Donnell T, Wang N, McCloskey P (2008) Electromagnetic generator for harvesting energy from human motion. Sens Actuators A Phys 147:248–253

3. Ferrari M, Ferrari V, Guizzetti M, Andò B, Baglio S, Trigona C (2010) Improved energy harvesting from wideband vibrations by nonlinear piezoelectric converters. Sens Actuators A Phys 162:425–431
4. Erturk A, Inman DJ (2008) Issues in mathematical modeling of piezoelectric energy harvesters. Smart Mater Struct 17:065016 (14 pp)
5. Lin JH, Wu XM, Ren TL, Liu LT (2007) Modeling and simulation of piezoelectric MEMS energy harvesting device. Integr Ferroelectr 95:128–141
6. Wang L, Yuan FG (2008) Vibration energy harvesting by magnetostrictive material. Smart Mater Struct 17:045009 (14 pp)
7. Poulin G, Sarraute E, Costa F (2004) Generation of electrical energy for portable devices: comparative study of an electromagnetic and a piezoelectric system. Sens Actuators A Phys 116:461–471
8. Rocha JG, Gonçalves LM, Rocha PF, Silva MP, Lanceros-Méndez S (2010) Energy harvesting from piezoelectric materials fully integrated in footwear. IEEE Trans Ind Electron 57:813–819
9. Al-Ashtari W, Hunstig M, Hemsel T, Sextro W (2013) Enhanced energy harvesting using multiple piezoelectric elements: theory and experiments. Sens Actuators A Phys 200:138–146
10. Muralt P, Marzencki M, Belgacema B, Calamea F, Basrourb S (2009) Vibration energy harvesting with PZT micro device. In: Proceedings of the eurosensors XXIII conference, pp 1191–1194
11. Roundy S, Wright PK, Rabaey JM (2004) Energy scavenging for wireless sensor networks. Springer, New York, pp 49–50
12. Caliò R, Rongala UB, Camboni D, Milazzo M, Stefanini C, Petris G, Oddo CM (2014) Piezoelectric energy harvesting solutions. Sensors 14:4755–4790
13. Ward JK, Behrens S (2008) Adaptive learning algorithms for vibration energy harvesting. Smart Mater Struct 17:035025 (9 pp)
14. Priya S (2007) Advances in energy harvesting using low profile piezoelectric transducers. J Electroceram 19:165–182
15. Cho JH, Richards RF, Bahr DF, Richards CD (2006) Efficiency of energy conversion by piezoelectrics. Appl Phys Lett 89:104107 (3 pp)
16. Cottone F, Vocca H, Gammaitoni L (2009) Nonlinear energy harvesting. Phys Rev Lett 102:080601 (4pp)
17. Uzun Y, Kurt E (2013) Power-vibration relation for a piezoelectric harvester under magnetic excitation. In: 13th international conference on electric power system, high voltages, electric mach, Chania, Crete Island, Greece, pp 59–64
18. Uzun Y, Kurt E, Kurt HH (2015) Explorations of displacement and velocity nonlinearities and their effects to power of a magnetically-excited piezoelectric pendulum. Sens Actuators A Phys 224:119–130
19. Kurt E (2006) Nonlinear responses of a magnetoelastic beam in a step-pulsed magnetic field. Nonlinear Dynam 45:171–182
20. Tseng WY, Dugundji J (1970) Nonlinear vibrations of a beam under harmonic excitation. J Appl Mech 37:292–297
21. Tseng WY, Dugundji J (1971) Nonlinear vibrations of a buckled beam under harmonicexcitation. J Appl Mech 38:467–476
22. Poddar B, Moon FC, Mukherjee S (1988) Chaotic motion of an elastic–plastic beam. J Appl Mech 55:185–189
23. Emam SA, Nayfeh AH (2004) Nonlinear responses of buckled beams tosubharmonic-resonance excitations. Nonlinear Dyn 35:105–122
24. Saymonds PS, Yu TX (1985) Counterintuitive behavior in a problem of elastic–plasticbeam dynamics. J Appl Mech 52:517–522
25. Uzun Y, Demirbas S, Kurt E (2014) Implementation of a new contactless piezoelectric wind energy harvester to a wireless weather station. Elektron Elektrotech 20:35–39

26. Uzun Y, Kurt E (2012) Implementation and modeling of a piezoelastic pendulum under a harmonic magnetic excitation. In: 11th international conference on applications of electrical engineering, Athens, Greece, pp 1–6
27. Uzun Y, Kurt E (2013) The effect of periodic magnetic force on a piezoelectric energy harvester. Sens Actuators A Phys 192:58–68
28. Bizon N, Oproescu M (2007) Power converters for energy generation systems (Convertoare de Putere utilizate in Sistemele de Generare a Energiei). Publishing House of the University of Piteşti, Piteşti
29. Bouzelata Y, Kurt E, Altın N, Chenni R (2015) Design and simulation of a solar supplied multifunctional active power filter and a comparative study on the current-detection algorithms. Renew Sust Energ Rev 43:1114–1126
30. Kurt E, Ciylan B, Taskan OO, Kurt HH (2014) Bifurcation analysis of a resistor-double inductor and double diode circuit and a comparison with a resistor-inductor-diode circuit in phase space and parametrical responses. Sci Iran 21:935–944
31. Linsay PS (1981) Period doubling and chaotic behaviour in a driven anharmonic oscillator. Phys Rev Lett 47:1349–1352
32. Kurt E, Kasap R, Acar S (2003) Effects of periodic magnetic field to the dynamics of vibrating beam. J Math Comput Appl 9:275–284
33. Kurt E, Böyükata M, Güvenç ZB (2006) Lyapunov exponent as an indicator of phase transition in melting Pd13 clusters. Phys Scripta 74:353–361
34. Kurt E, Uzun Y (2010) Design and bifurcation analysis of a piezoelectric energy harvester under a changeable magnetic field. In: 2nd international conference on nuclear and renewable energy resources, Ankara, Turkey, pp 877–884
35. Moser RD, Kim J, Mansour NN (1999) Direct numerical simulation of turbulentchannel flow up to Re = 590. Phys Fluids 11:943–945
36. Morris DJ, Youngsman JM, Anderson MJ, Bahr DF (2008) A resonant frequency tunable extensional mode piezoelectric vibration harvesting mechanism. Smart Mater Struct 17:065021 (9 pp)
37. Ramond A, Ardila Rodríguez GA, Durou H, Jammes B, Rossi CA (2009) SIDO buck converter with ultra low power MPPT scheme for optimized vibrational energy harvesting and management. In: PowerMEMS, Washington DC, USA, pp 415–418
38. Kong N, Cochran T, Ha DS, Lin HC, Inman DJ (2010) A self-powered power management circuit for energy harvested by a piezoelectric cantilever. In: 25th applied power electronics conference and exposition (APEC), CA, USA, pp 2154–2160
39. Elliott ADT, Mitcheson PD (2014) Piezoelectric energy harvester interface with real-time MPPT. J Phys Conf Ser 557:012125(5 pp)
40. Yi J, Su F, Lam YH, Ki WH, Tsui CY (2008) An energy-adaptive MPPT power management unit for micro-power vibration energy harvesting. In: IEEE international symposium on circuits and systems, Seattle, WA, USA, pp 2570–2573
41. Simjee F, Chou PH (2006) Everlast: long-life, supercapacitor-operated wireless sensor node. In: Proceedings of the ISLPED, pp 197–202
42. Do XD, Han SK, Lee SG (2014) Optimization of piezoelectric energy harvesting systems by using a MPPT method. In: IEEE 5th international conference on communications and electronics, Danang, Vietnam, pp 309–312
43. Miller LM, Mitcheson PD, Halvorsen E, Wright PK (2012) Coulomb-damped resonant generators using piezoelectric transduction. Appl Phys Lett 100:233901(4 pp)
44. Booth AD (1951) A signed binary multiplication technique. Q J Mech Appl Math 4:236–240

Chapter 6
Energy Harvesting from the Photovoltaic Hybrid Power Source Based on Extremum Seeking Control Schemes

Nicu Bizon, Marian Raducu, Luminita-Mirela Constantinescu and Mihai Oproescu

Abstract The energy harvesting is known as the conversion process of ambient energy into usable electrical energy. The energy of the renewable and green Energy Sources (ES) is free and available without territorial restrictions. In this chapter the possibility to use the Extremum Seeking Control schemes for harvesting the solar energy via a Photovoltaic Hybrid Power Source is presented. The new ESC schemes based on a band-pass filter instead of the series combination of high-pass and low-pass filters are analyzed in order to evaluate their performance. The performance indicators used are the search speed and the tracking accuracy. The simulations performed highlight the advantages of the Extremum Seeking Control schemes based on a band-pass filter in comparison with the classical Extremum Seeking Control schemes. A Maximum Power Point tracking technique based on a modified Extremum Seeking Control slightly improves the energy efficiency of the Photovoltaic Hybrid Power Source. The advanced Extremum Seeking Control scheme reduces the power ripple, so the energy efficiency of the Photovoltaic Hybrid Power Source increases as well. The analysis of the dither persistence in the Extremum Seeking Control loop scheme shows the relations between the search speed and the derivatives of the Photovoltaic power. The ratio of these search speeds is also used as the performance indicator. Finally, the dynamical operation of the Photovoltaic Hybrid Power Source under variable irradiance profile is shown.

N. Bizon (✉) · M. Raducu · L.-M. Constantinescu · M. Oproescu
University of Pitesti, Targu din Vale Street no. 1, 110040 Pitesti, Romania
e-mail: nicu.bizon@upit.ro; nicubizon@yahoo.com

M. Raducu
e-mail: marian.raducu@upit.ro

L.-M. Constantinescu
e-mail: luminita.constantinescu@upit.ro

M. Oproescu
e-mail: mihai.oproescu@upit.ro

N. Bizon
University Politehnica of Bucharest, Splaiul Independentei Street no. 313, 060042 Bucharest, Romania

N. Bizon et al. (eds.), *Energy Harvesting and Energy Efficiency*,
Lecture Notes in Energy 37, DOI 10.1007/978-3-319-49875-1_6

Keywords Photovoltaic Hybrid Power Source (PVHPS) · Extremum Seeking Control (ESC) · Maximum Power Point (MPP) · Search speed · Tracking accuracy · Energy harvesting · Harmonics analysis

Abbreviations and Acronyms

aESC	Advanced ESC
BPF	Band-pass filter
CS	Charge-sustaining
CI	Charge-increasing
CD	Charge-depletion
DG	Distributed generation
EMS	Energy management strategy
ESC	Extremum seeking control
ESS	Energy storage system
ES	Energy source
EQ	Equivalence
FW	Freewheeling diode
FC	Fuel cell
GMPP	Global MPP
HPS	Hybrid power source
HT	Hydro-turbines
HF	High frequency
hoESC	High-order ESC
HPF	High-pass filter
IC	Incremental conductance
IGBT	Insulated-gate bipolar transistor
LF	Low frequency
LPF	Low-pass filter
MEP	Maximum efficiency point
MPP	Maximum power point
MPPT	MPP tracking
mESC	Modified ESC
P&O	Perturb & observe
PV	Photovoltaic
PVHPS	Photovoltaic hybrid power source
WT	Wind turbine

6.1 Introduction

In the last decades the solar energy is widely used as ambient energy that can be efficiently harvested and converted into electrical energy. The solar, wind and water energy are all ambient green energy resources without territorial restrictions, which can generate electrical energy via the Photovoltaic (PV) panels' array, Wind Turbines' (WT) farm and Hydro-Turbines (HT). The Energy Source (ES) shown in Fig. 6.1 can represent a single source or a mix of renewable energy sources (such as PV array, WT farm, and HTs). The Fuel Cell (FC) stack can be used as an auxiliary energy source of the Hybrid Power Source (HPS) in order to minimize the Energy Storage System (ESS) if the HPS operates under high dynamic load. The DC loads will be connected on the ESS bus (directly or via a DC-DC converter) and the AC load via a DC-AC converter.

The HPS architecture which will be analyzed in this chapter (see Sect. 6.2) is based on the generic HPS architecture shown in Fig. 6.1. Note that each ES will be connected to the ESS bus by an unidirectional DC-DC converter that is controlled using a Maximum Power Point (MPP) tracking algorithm [1]. The MPP tracking (MPPT) controller can control sequentially all ESs acquiring the samples of each ES current (i_{ES}) and the common ES voltage (v_{ES}) [2]. The MPP of each ES will be tracked using the Extremum Seeking Control (ESC) scheme that obtains the searching gradient based on the dithering action of the control loop [3].

Both searching gradient and dither signals are parts of the reference current, i_{ref}. The reference current (i_{ref}) is compared with the ES current (i_{ES}) using an appropriate current-mode control strategy to generate the switching pulses [4].

If the HPS supplies a load that has a sharp and dynamic profile, then the ESS is necessary to assure the power flow balance on the ESS bus:

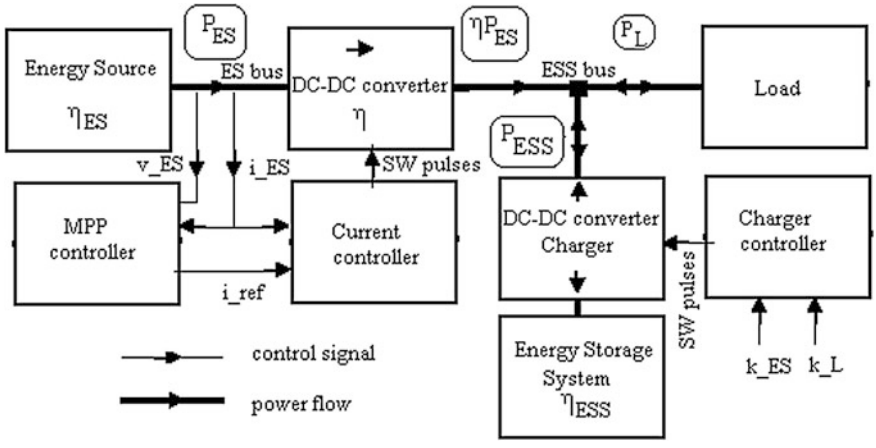

Fig. 6.1 Architecture of the Hybrid Power Source [26]

$$p_L = \eta \cdot p_{ES} + p_{ESS} \tag{6.1}$$

The ESS power is given by (6.2):

$$p_{ESS} = p_L - \eta \cdot p_{ES} \tag{6.2}$$

The ES power depends on the environmental and weather conditions, so it is difficult to dynamically compensate the power flow balance by controlling the fuel flow rates of the FC stack [5, 6]. Consequently, a hybrid ESS (of batteries and ultracapacitors connected with DC-DC converters to the ESS bus [7]) must be designed to minimize the cost of the HPS. The ESS will be charged and discharged during a load cycle and the average ESS power, $P_{ESS(AV)}$, can be zero, positive or negative if the ESS operates in charge-sustaining (CS), charge-increasing (CI) or charge-depletion (CD) mode, respectively [8, 9].

The Energy Management Strategies (EMSs) proposed in the literature are dependent to HPS application. For example, the EMS is applied to the HPS used as the Distributed Generation (DG) unit in the smart grids [10] or as the energy source for the power-train of the hybrid vehicles [8]. The EMS of the load-following type [9] will operate the ESS in CS mode based on the FC power controlled to assure the averaged power flow balance:

$$P_{FC(AV)} = P_{L(AV)} - \eta \cdot P_{ES(AV)} \tag{6.3}$$

The FC stack is efficiently operated based on the efficiency map [11] or the Maximum Efficiency Point (MEP) tracking algorithm [12, 13].

If the EMS is not of load-following control type, then the ESS will operate in CI or CD mode by controlling the ESS charger (the bidirectional DC-DC converter) based on the charging ES factor (k_{ES}) and the regenerative load factor (k_L) defined as following [9]:

$$k_{ES} = P_{ES \to ESS(AV)} / P_{ES(AV)} \tag{6.4}$$

$$k_L = P_{L \to ESS(AV)} / P_{L(AV)} \tag{6.5}$$

where

$P_{ES \to ESS(AV)}$ is the part of the ES power flow that charge the ESS;
$P_{L \to ESS(AV)}$ is the reverse power flow from the regenerative load that charge the ESS.

The ESS charger usually has the plug-in feature, so choosing between the CI mode or CD mode will depend by the price of the energy offered at the plug-in units during the route [9].

The energy must be harvested from each ES and the FC stack must be operated at MEP in order to optimize the HPS operation. In this chapter the PV HPS optimization based on an ESC scheme is analyzed. The perturbed ESC scheme will

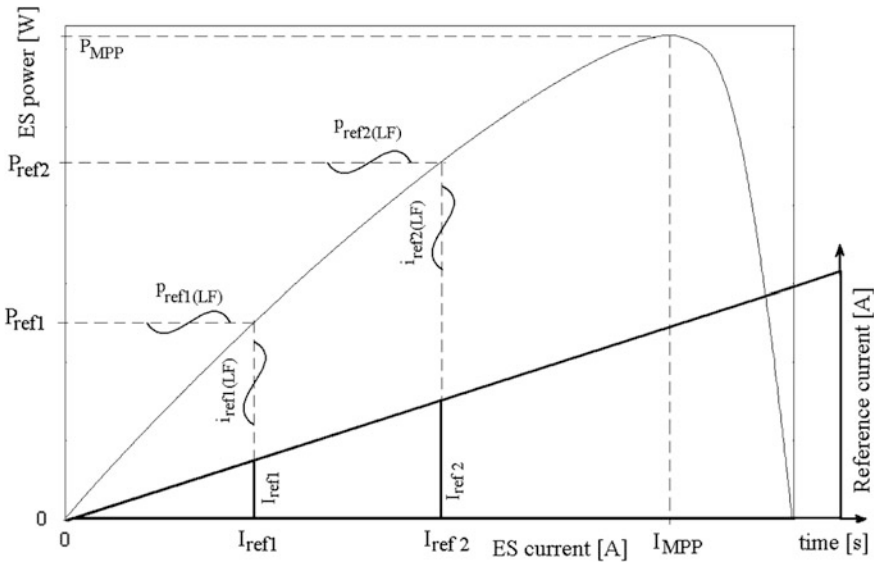

Fig. 6.2 Searching of the MPP on the power characteristic [26]

track the MPP of the PV panel (see Fig. 6.2) or the Global MPP (GMPP) of the PV array.

Besides the ESC scheme, different MPPT techniques have been proposed during the last decades. These techniques can be categorized as direct and indirect methods to maximize the power generated by an energy source that has a power characteristic with one maximum [1, 14]. The power characteristic of the solar cells is modeled using mathematical equations [15] or numerical approximations [16]. The MPP tracking performance is dependent on the resolution of the analog-to-digital converter [17] and the cut-off frequencies of the low-pass filter (LPF) [18]. The Perturb & Observe (P&O) and Incremental Conductance (IC) methods are the most used MPPT algorithms implemented in the commercial controllers [19]. The P&O method uses a perturbation of the PV voltage or PV current to search the MPP by observing the sense of the variation of the PV power. The step size of the perturbation must be carefully designed to balance the tradeoffs between the performance indicators (the search speed and tracking accuracy), assuring in meantime the robustness to variability of the irradiance [20, 21]. The irradiance profile during a sunny-cloudy day has a dynamic shape in reality, so a model of this profile is usually used in simulation [21].

This chapter analyzes three ESC schemes to compare the performance of the MPPT process. The modified ESC (mESC) scheme (see Fig. 6.3) has improved performance in comparison with the high-order ESC (hoESC) scheme (see Fig. 6.4) related to the search speed if high cut-off frequency of the band-pass filter (BPF) is higher than that of the LPF. The low cut-off frequency of the BPF may be the same with that of the high-pass filter (HPF). It can be noted that the tracking

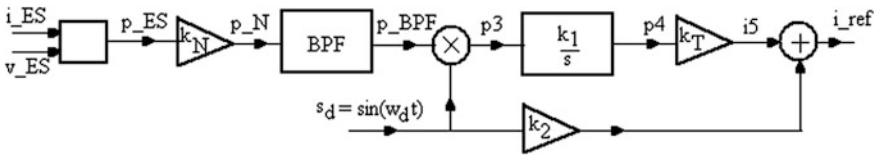

Fig. 6.3 The mESC scheme [26]

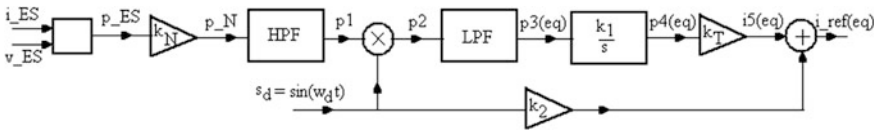

Fig. 6.4 The hoESC scheme (or equivalent (EQ) mESC scheme) [26]

accuracy remains almost the same [22], where the MPP tracking accuracy is defined as $100 \cdot (P_{PV} / P_{MPP})$ [%], P_{MPP} being the power of the PV panel operating at the MPP and P_{PV} the power harvested from the PV panel via DC-DC converter under the MPPT controller. The 99.8% tracking accuracy could be obtained with advanced MPPT algorithms (which decrease the level of perturbation close to MPP). An adaptive decrease of the perturbation is used in the advanced ESC (aESC) scheme proposed in [21]. The 99.99% tracking accuracy could be obtained without reducing the search speed and response time to irradiance changes.

The generic topologies of the mESC and hoESC schemes will be detailed in the next sections for the Photovoltaic Hybrid Power Source (PVHPS) application. It is obvious that the performance inherited from the basic hoESC scheme (such as a guaranteed convergence and an internal robustness) is taken up as well [23]. The ESC schemes can be used to search the unknown maximum of the PV power characteristic because it is a control method of adaptive type [24, 25].

Also, it is easy to show that the mESC and hoESC schemes are functionally equivalent if the cut-off frequencies of the BPF are the same with those of the HPF and LPF (see Fig. 6.5). This will be briefly shown in next section based on the specific ESC schemes for the PVHPS [5, 26].

The chapter is organized as follows. Section 6.2 briefly presents the architecture of the PVHPS. The modeling of the PVHPS is presented in Sect. 6.3, where the models of the solar cell, PV panel, boost converter, and ESC schemes used in simulation are shown. Section 6.4 deals with the performance analysis of the ESC schemes. The analysis in frequency domain of the ESC loop is performed here in order to evaluate the performance of the ESC schemes under step-up in the irradiance profile. The dither persistence on the ESC loop is also approached here. The PVHPS behavior under variable irradiance profile is shown in Sect. 6.4 using the mESC and aESC schemes in Sect. 6.6.

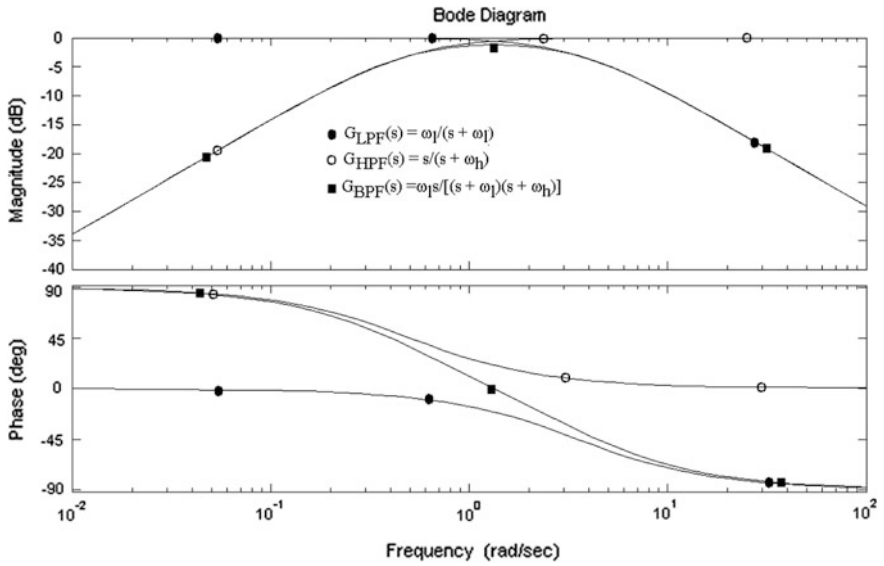

Fig. 6.5 Bode diagrams for the LPF (●), HPF (○), and BPF (■) [26]

6.2 Architecture of the Photovoltaic Hybrid Power Source

The Photovoltaic Hybrid Power Source (PVHPS) architecture is shown in Fig. 6.6, where the main subsystems are detailed by the diagram implemented in Matlab-Simulink®. The dynamic load is connected on the ESS DC bus and the ESS is implemented using a passive topology [7]. A simple current-mode hysteretic controller is used here to generate the switching command for the boost converter.

The boost converter is usually used as a DC-DC power interface between the low DC voltage of the ES (here the PV voltage) and the high DC voltage (V_{DC}) of the common DC bus for ESS and inverter system [14, 27]. If the voltage inverter system is grid connected, then the switching command must be synchronized with the grid frequency and the harmonics of the inverter and the grid voltages must have the same magnitude [28]. Thus, the low frequency (LF) and high frequency (HF) ripple having harmonics at multiples of the grid frequency and switching frequency will appear on the DC bus. The LF ripple by three harmonics is considered in the load model because only these are important to analyze the ESC control loop. It is known that the ripple correlation method can use both LF and HF ripple of the PV power signal (P_{PV}) [29], but the natural inverter ripple is usually utilized by the perturbed MPPT algorithms based on the P&O methods [30] or the ESS schemes [31].

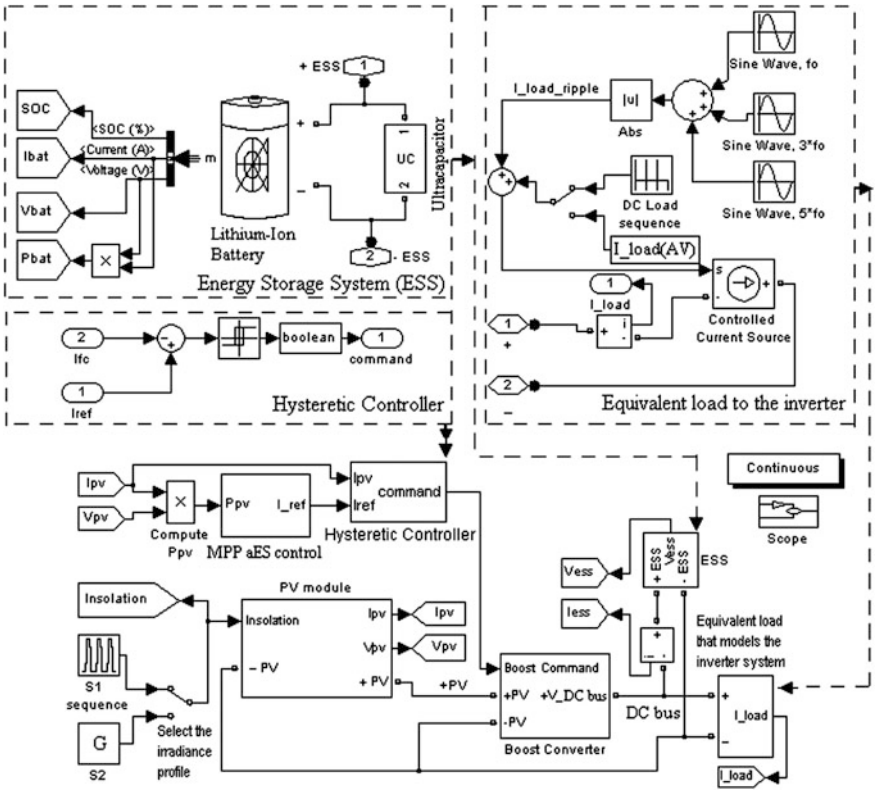

Fig. 6.6 The diagram of PV/ESS HPS operating at MPP under aESC [21]

6.3 Modeling the Photovoltaic Hybrid Power Source

6.3.1 Solar Cell and PV Panel Models

6.3.1.1 Solar Cell Model

The one-diode model of the solar cell contains a current source (I_L), a diode, a shunt resistor (R_p) and a series resistor (R_s) with the output current ($I_{PV(cell)}$) given by the (6.6) [1]:

$$I_{PV(cell)} = I_{L(cell)} - I_{0S} \cdot \left[\exp\frac{q(V_{PV(cell)} + R_s I_{PV(cell)})}{nk_B T} - 1\right] - \frac{V_{PV(cell)} + R_s I_{PV(cell)}}{R_p} \tag{6.6}$$

where $V_{PV(cell)}$ represents the solar cell voltage and T is the temperature.

The light-generated current, $I_{L(cell)}$, and the cell reverse saturation current, I_{0S}, are given by (6.7) and (6.8):

$$I_{L(cell)} = \frac{G}{G_R} \cdot I_{sc(cell)} \cdot [1 + \alpha \cdot (T - T_R)] \tag{6.7}$$

$$I_{0S} = I_{0R} \cdot \left(\frac{T}{T_R}\right)^3 \cdot \exp\left[\frac{V_G}{nV_T}\left(1 - \frac{T_R}{T}\right)\right] \tag{6.8}$$

where $V_T = k_B T_R/q$.

If the parallel resistance R_p will be neglected and the temperature is assumed to be constant, $T = T_R = 298$ K, then relations (6.6)–(6.8) can be further simplified as:

$$I_{PV(cell)} = I_{L(cell)} - I_{0S} \cdot \left[\exp\frac{q(V_{PV(cell)} + R_s I_{PV(cell)})}{nk_B T} - 1\right] \tag{6.6'}$$

$$I_{L(cell)} = \frac{G}{G_R} \cdot I_{sc(cell)} = K_{IG(cell)} G \tag{6.7'}$$

$$I_{0S} = I_{0R} \tag{6.8'}$$

where $K_{IG(cell)} = I_{sc(cell)}/G_R$ is irradiation Irradiation to short-circuit current gain.

Consequently, the simplified model of the solar cell is given by (6.9):

$$I_{PV(cell)} = K_{IG(cell)} \cdot G - I_{0R} \cdot \left[\exp\left(\frac{V_{PV(cell)} + R_s I_{PV(cell)}}{nV_T}\right) - 1\right] \tag{6.9}$$

where:

$V_{PV(cell)}$—represents the solar cell voltage;
$I_{PV(cell)}$—the solar cell current;
R_s—the series resistance of the solar cell;
$K_{IG(cell)} = I_{sc(cell)}/G_R$—the irradiation to short-circuit current gain;
$I_{L(cell)} = I_{sc(cell)} \cdot G/G_R$—the light-generated current;
G—the level of instantaneous irradiation

Other parameters are mentioned in Table 6.1.

6.3.1.2 PV Panel

The PV panel used 34 cells connected in series. Thus, the open-circuit voltage, V_{oc}, and the short-circuit current, I_{sc}, of the PV panel will be about 21 V and 3.8 A under standard test conditions: irradiation intensity of 500 W/m^2, AM1.5 G, and temperature of 25 °C. Also, the MPP of about 51.2 W is obtained for 3.5 A and 14.63 V under the same test conditions.

Table 6.1 Parameters of solar cell model [21]

Parameter	Description	Value (unit)
G_R	Reference irradiation	1,000 (W/m^2)
T_R	Reference temperature	298 (K)
q	Electron charge	$1.6e^{-19}$ (C)
k_B	Boltzmann's constant	$1.38e^{-23}$ (JK^{-1})
n	Diode ideality factor	1.3 (-)
V_G	Silicon band-gap energy	1.12 (eV)
$V_T = k_B T_R/q$	Thermic voltage	26 (mV)
I_{OR}	Reverse saturation current at $T = T_R$	$2e^{-9}$ (A)
α	Short-circuit current temperature coefficient	0.0025 (AK^{-1})
R_s	Cell series resistor	3 (mΩ)
R_p	Cell shunt resistor	10 (Ω)
$V_{oc(cell)}$	Cell open-circuit voltage	0.61 (V)
$I_{sc(cell)}$	Cell short-circuit current	(A)

6.3.2 Boost Converter Model

The basic boost converter is implemented using power devices from the SimPowerSystem® toolbox.

If the both insulated-gate bipolar transistor (IGBT) and freewheeling (FW) diode are in on-state, then the operating relationships are [10]:

$$\begin{aligned} v_{PV} &= (r_L + R_{DS(on)}) \cdot i_{PV} + L\frac{di_{PV}}{dt} + V_{DS(on)} \\ v_{PV} &= (r_L + R_{D(on)}) \cdot i_{PV} + L\frac{di_{PV}}{dt} + V_{D(on)} + v_{DC} \end{aligned} \tag{6.10}$$

where the on-state parameters, ($R_{DS(on)}$, $V_{DS(on)}$) and ($R_{D(on)}$ and $V_{D(on)}$), use the preset values.

The value of boost inductance is designed based on the magnitude of the HF components of the PV current, ΔI, and hysteretic band:

$$L = DV_{FC(MPP)} / (2f_{sw}\Delta I) \tag{6.11}$$

where $V_{FC(MPP)}$ is the maximum PV voltage that can be obtained during a sunny day, $f_{sw} = 1/T_{sw}$ is the switching frequency and D is the duty cycle estimated with (6.12):

$$D = 1 - V_{FC(MPP)} / V_{DC} \tag{6.12}$$

The switching frequency may be chosen to be about 100-times higher than the dither frequency (100 Hz) to be better tracked by the LF shape of the PV current by the reference current. Thus:

$$i_{ref(LF)} \cong i_{PV(LF)} \tag{6.13}$$

6.3.3 The ESC Schemes

The ESC schemes used in this chapter will be briefly presented here.

6.3.3.1 The hoESC Scheme

The hoESC scheme shown in Fig. 6.1 is adapted for PVHPS as in Fig. 6.7. The HPF is necessary to extract the useful LF harmonics from the PV power signal and the LPF to reduce the HF noise [32].

The information about the searching gradient is obtained by using a dither signal, $k_A \cdot \sin(2\pi f_d t)$ (k_A being the amplitude, f_d the dither frequency and t the time), injected in the ESC control loop. A compromise must to be made between the choosing of the design parameters (k_1 and k_1 gains) to obtain good performance for both indicators: the search speed and the tracking accuracy. The search speed can be increased if the cut-off frequency of the LPF is set about 5-times higher than the dither frequency. If the series connection of the HPF and LPF is replaced with an equivalent BPF, then the modified ESC (mESC) scheme will be obtained (see Fig. 6.8).

Note that the cut-off frequencies of the LPF and HPF used in hoESC scheme are usually set as $\omega_{l(ho)} = \beta_{l(ho)}\omega$, $0 < \beta_{l(ho)} < 1$, and $\omega_{h(ho)} = \beta_{h(ho)}\omega$, $0 < \beta_{h(ho)} < 1$.

6.3.3.2 The Modified ESC Scheme

The modified ESC scheme is shown in Fig. 6.8. The search speed of the mESC scheme increases about 2-times in comparison with the hoESC scheme if the same

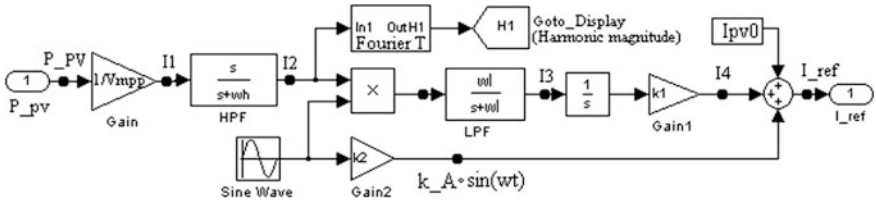

Fig. 6.7 The hoESC scheme [22]

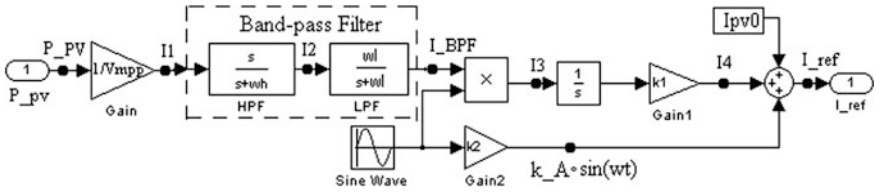

Fig. 6.8 The mESC scheme [22]

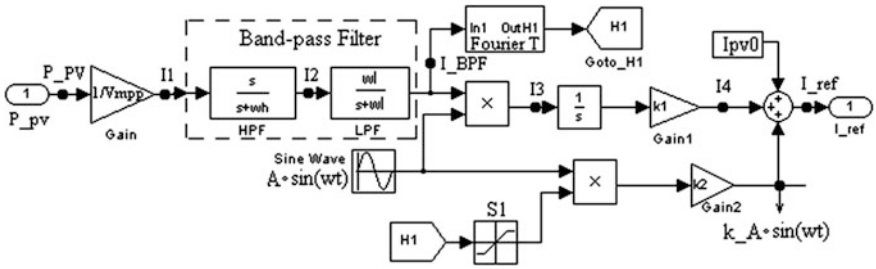

Fig. 6.9 Advanced ESC (aESC) scheme [21]

k_1 and k_1 gains are used for both mESC and hoESC schemes, but the cut-off frequency of BPF high is set $\beta_{l(m)}$-times higher than dither frequency ($\omega_{l(m)} = \beta_{l(m)}\omega$, $3 < \beta_{l(m)} < 6$) [26].

The HPF removes the average value of the PV power, so the low cut-off frequency of the HPF and BPF can be set the same for the both ESC schemes: $\omega_h = \beta_h\omega$, $0 < \beta_h < 1$.

It is known that a large value of the k_2 gain will increase the search speed, but the tracking accuracy is depreciated. A high power ripple will appear even during the stationary phase (constant irradiance). Thus, the k_1 gain must be higher during the transitory phase (change of the irradiance level) and very small during the stationary phase. This can be obtained by using the advanced ESC (aESC) scheme, where the dither injected has the amplitude modulated with the first harmonic (H_1) of the PV power: $k_A = A \cdot k_2 \cdot H_1$ (see Fig. 6.9).

6.3.3.3 The Advanced ESC Scheme

The advanced ESC (aESC) scheme is shown in Fig. 6.9, and its equivalent (EQaESC) topology based on HPF and LPF in series is shown in Fig. 6.10.

It is obvious that all the ESC schemes (hoESC, mESC, and aESC schemes) will have the same equivalent operating equations (see for example [21, 26]):

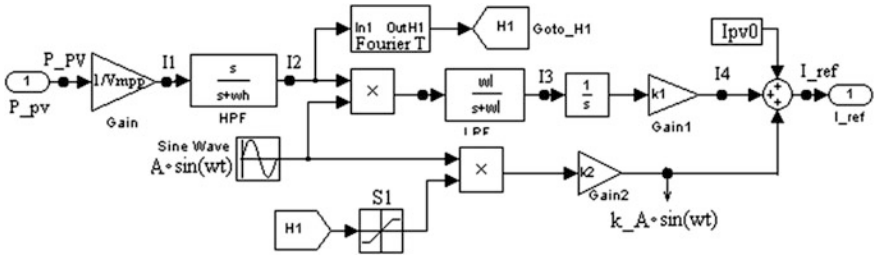

Fig. 6.10 Equivalent aESC (EQaESC) scheme [21]

$$p_{PV} = p_{PV}(i_{PV}),\ i_1 = i_{PV} / V_{MPP} \tag{6.14}$$

$$\begin{gathered} \dot{i}_{HPF} = -\omega_h i_{HPF} + \omega_h i_1, \\ i_2 = i_1 - i_{HPF},\ \dot{i}_{BPF} = -\omega_l i_{BPF} + \omega_l i_2,\ i_3 = i_{BPF} A \sin(\omega t) \end{gathered} \tag{6.15}$$

$$\dot{i}_{HPF} = -\omega_h i_{HPF} + \omega_h i_1,\ i_2 = i_1 - i_{HPF},\ \dot{i}_3 = -\omega_l i_3 + \omega_l i_2 A \sin(\omega t) \tag{6.16}$$

$$\dot{i}_4 = k_1 i_3 \tag{6.17}$$

$$i_{PV} \cong i_{ref},\ i_{ref} = i_4 + k_A \sin(\omega t) + I_{PV0} \tag{6.18}$$

where Eqs. (6.14), (6.17), and (6.18) represent the PV power characteristic, integrator, current—mode controller based on the current reference, i_{ref}, and Eqs. (6.15) and (6.16) represent the signal processing in aESC and EQaESC schemes based on BPF and series connection of HPF and LPF, respectively.

The following notations are used for all ESC schemes (see Figs. 6.7, 6.8, 6.9 and 6.10):

- k_1 is the loop gain;
- k_A is the dither's amplitude ($k_A = A \cdot k_2$ for the hoESC and mESC schemes, and $k_A = H_1 \cdot A \cdot k_2$ for the aESC scheme);
- H_1 is the magnitude of the first harmonic of the PV power;
- $\omega_l = \beta_l \omega$ is the cut-off frequency of the LPF ($0 < \beta_{l(ho)} < 1$ for hoESC scheme, and $1 < \beta_{l(m)} < 6$ for the mESC and aESC schemes);
- $\omega_h = \beta_h \omega$, $0 < \beta_h < 1$, is the cut-off frequency of the HPF for all ESC schemes;
- A and $f_d = \omega/2\pi$ are the amplitude and frequency of the dither signal;
- i_1, i_2, and i_3 are the signals after normalization block, HPF, and LPF blocks (see Fig. 6.9 and the Eqs. (6.14)–(6.16));
- i_{HPF} is an intermediate variable related to the HPF operating;
- i_{BPF} is the output signal from the BPF;

- i_4 is the signal that estimates the unknown parameter;
- V_{MPP} is voltage on the MPP;
- I_{PV0} is the initial value for the PV current.

Note that A = 1 and $I_{PV0} = 0$ for all simulations presented in this chapter.

So, the k_1 gain can be set higher (up to the stability limit) in order to have search speed up to the save value of HPS operating, without affecting the tracking accuracy. It was shown in [26] that the performance of the aESC scheme is better than that obtained with the extended Kalman-filter used for gradient estimation [32]. Thus, the main feature of the aESC scheme is related to its capability to set independently the performance indicators for each HPS application. The ESC schemes will be analyzed in next section.

6.4 Performance Analysis of the ESC Schemes

The comparative performance is performed in this section based on the analysis in the frequency domain of the ESC loop. The analytical results will be validate by a simulation using the testing diagram shown in Fig. 6.11.

6.4.1 The Analysis in Frequency Domain of the ESC Loop

The searching of the MPP on the power characteristic is mainly the same for all the ESC schemes considered here, being based on dither-pertubed search (see Fig. 6.2).

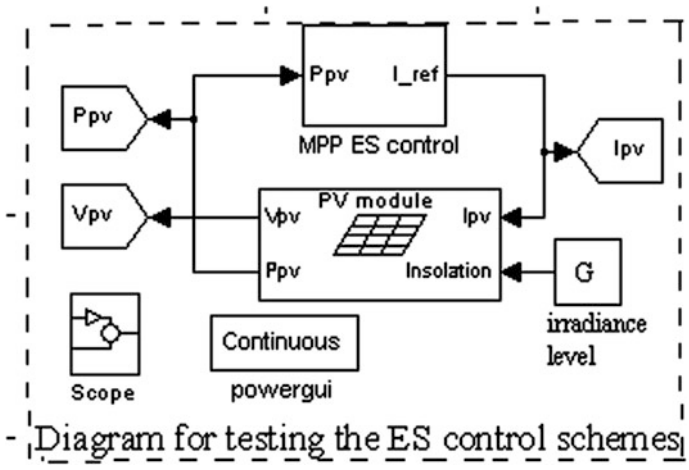

Fig. 6.11 The diagram for testing the ESC scheme [22]

The PV power can be approximated by the Taylor series:

$$p_{PV} = P_{PV} + \dot{p}_{PV}\, i_{ref} + \ddot{p}_{PV}\, i_{ref}^2 / 2! + \dddot{p}_{PV}\, i_{ref}^3 / 3! + \ldots \tag{6.19}$$

where $i_{ref} = I_{PV} + k_A \sin(\omega t)$ is the reference current, (I_{PV}, P_{PV}) is one point on static power map, and $\dot{p}_{PV}$, $\ddot{p}_{PV}$, $\dddot{p}_{PV}$, and so on are derivatives of the PV power to i_{ref} current. The i_{ref} current is linear variable in time (see Fig. 6.2), so the derivatives of the PV power will be related to time as well.

The PV power signal (p_{PV}) will become a current signal (i_1) after normalization to V_{MPP}:

$$i_1 = p_{PV} / V_{MPP} = I_1 + i_{LF1} + i_{HF1} \tag{6.20}$$

where I_1, i_{LF1} and i_{HF1} are the DC, LF and HF components of i_1 signal.

The first order HPF (with transfer function $G_{HPF}(s) = s/(s + \omega_h)$, where $\omega_h = {}_h\omega$, $0 < \beta_h < 1$) will remove the DC component of i_1 signal, so the i_2 signal will be given by (6.21):

$$i_2 = (i_{LF1} + i_{HF1}) * L^{-1}\{G_{HPF}(s)\} = i_{LF2} + i_{HF2} = i_{2(1)} + i^*_{LF2} + i_{HF2} \tag{6.21}$$

where L^{-1} is the inverse Laplace transform, * is the convolution operator, i_{LF2} and i_{HF2} are the LF and HF components of i_2, $i_{2(1)}$ is the fundamental harmonic of i_2, and i^*_{LF2} is remaining LF component of $i_2 - i_{2(1)}$ signal.

The first order LPF (with transfer function $G_{LPF}(s) = \omega_l/(s + \omega_l)$, where $\omega_l = {}_l\omega$, $0 < \beta_l < 6$) will remove the HF component of the i_2 signal, so the i_3 signal will be given by the (6.22):

$$\begin{aligned} i_3 &= [(i_{LF2} + i_{HF2}) \cdot \sin(\omega t)] * L^{-1}\{G_{LPF}(s)\} \cong [i_{LF2} \cdot \sin(\omega t)] * L^{-1}\{G_{LPF}(s)\} \\ &= I_3 + i_{LF3} \end{aligned} \tag{6.22}$$

where I_3 and i_{LF3} are the DC components and LF component of i_3 signal.

The information about the gradient $\left(\dot{p}_{PV}\right)$ is obtained by multiplying the fundamental harmonic of the i_2 signal, $i_{2(1)} = \dot{p}_{PV}|G_{HPF}| \cdot \sin(\omega t + \phi_{HPF})$, with the dither, $A \cdot \sin(\omega t)$, i.e., performing a demodulation:

$$\begin{aligned} i_{2(1)} \cdot A \sin(\omega t) &= \dot{p}_{PV}|G_{HPF}|A \cdot \sin(\omega t + \phi_{HPF}) \cdot \sin(\omega t) \\ &= (\dot{p}_{PV}|G_{HPF}|A / 2) \cdot [\cos(\phi_{HPF}) - \cos(2\omega t + \phi_{HPF})] \end{aligned} \tag{23}$$

where

$$|G_{HPF}| = 1 / \sqrt{1 + (\omega_h / \omega)^2}, \quad \phi_{HPF} = \arg(G_{HPF}) = \arctan(\omega_h / \omega) \tag{6.24}$$

The following values of the searching gradient (I_3) are obtained:

$$I_3 = \dot{p}_{PV} A |G_{HPF}||G_{LPF}| \cos(\phi_{HPF}) / (2V_{MPP}) \tag{6.25}$$

where

$$|G_{LPF}| = 1 / \sqrt{(\omega / \omega_l)^2 + 1}, \quad \phi_{LPF} = \arg(G_{LPF}) = -\arctan(\omega / \omega_l) \tag{6.26}$$

If the mESC and aESC schemes are based on BPF, then the searching gradient ($I_{3(BPF)}$) are obtained as:

$$I_{3(BPF)} = \dot{p}_{PV} A |G_{BPF}| \cos(\phi_{BPF}) / (2V_{MPP}) \tag{6.27}$$

where

$$|G_{BPF}| = |G_{HPF}||G_{LPF}|, \quad \phi_{BPF} = \arg(G_{BPF}) = \phi_{HPF} + \phi_{LPF} \tag{6.28}$$

Consequently, if the same parameters are set for the HPF and LPF in series, and equivalent BPF, then the searching gradient will almost be obtained. The simulations shown below will validate this result.

The next signal processing block for all ESC schemes is the integration block, which contains the k_1 gain as well:

$$i_4 = k_1 \int i_3 dt = k_1 \int (I_3 + i_{LF3}) dt = k_1 I_3 t + k_1 \int i_{LF3} dt = K_{SS} t + i_{LF4} \tag{6.29}$$

where i_{LF4} represents the LF components of i_4 and K_{SS} [A/s] is the search speed that is specifically computed for all ESC schemes.

Finally, the reference current, i_{ref}, is given by (6.30):

$$i_{ref} = I_{PV0} + K_{SS} t + i_{LF4} + k_A \cdot \sin(\omega t) = I_{PV0} + K_{SS} t + i_{LF(ref)} \tag{6.30}$$

where I_{PV0} and $i_{LF(ref)}$ are the initial value and the LF component of i_{ref}.

The MPP tracking process on the P-I phases plane is shown in Fig. 6.12 using the aESC scheme. The PV power spectrum is shown in three points of the PV power characteristic versus PV current.

A zoom of the tracking accuracy is shown in the lower right corner. The high power ripple during the searching phase and negligible ripple during the stationary phase (constant irradiance) can be observed.

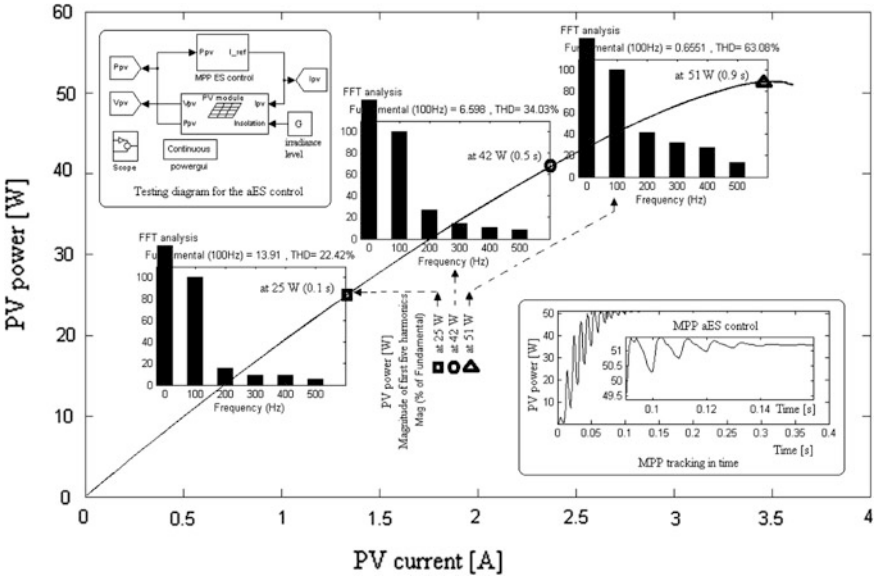

Fig. 6.12 The MPP tracking process using aESC [21]

6.4.2 *On the Equivalence of the mESC and EQmESC Schemes*

The LF equivalence (EQ) of search speed for the EQmESC and mESC schemes computed based on (6.29) is given by (6.31) and (6.32):

$$K_{SS(EQm)} = \dot{p_{PV}}\, k_1 A \left|G_{HPF(EQm)}\right| \left|G_{LPF(EQm)}\right| \cos(\phi_{HPF(EQm)}) \,/\, (2V_{MPP}) \tag{6.31}$$

$$K_{SS(m)} = \dot{p_{PV}}\, k_1 A \left|G_{BPF(m)}\right| \cos(\phi_{BPF(m)}) \,/\, (2V_{MPP}) \tag{6.32}$$

Thus, the ratio of the searching speeds ($K_{SS(m)}$ and $K_{SS(EQm)}$, respectively) is:

$$R_{SS} = \left|K_{SS(m)} \,/\, K_{SS(EQm)}\right| = \left|\cos(\phi_{HPF(m)} + \phi_{LPF(m)})\right| \,/\, \cos(\phi_{HPF(EQm)}) \tag{6.33}$$

If

$$0 < \beta_{h(m)} < 1 < 3 < \beta_{l(m)} \tag{6.34}$$

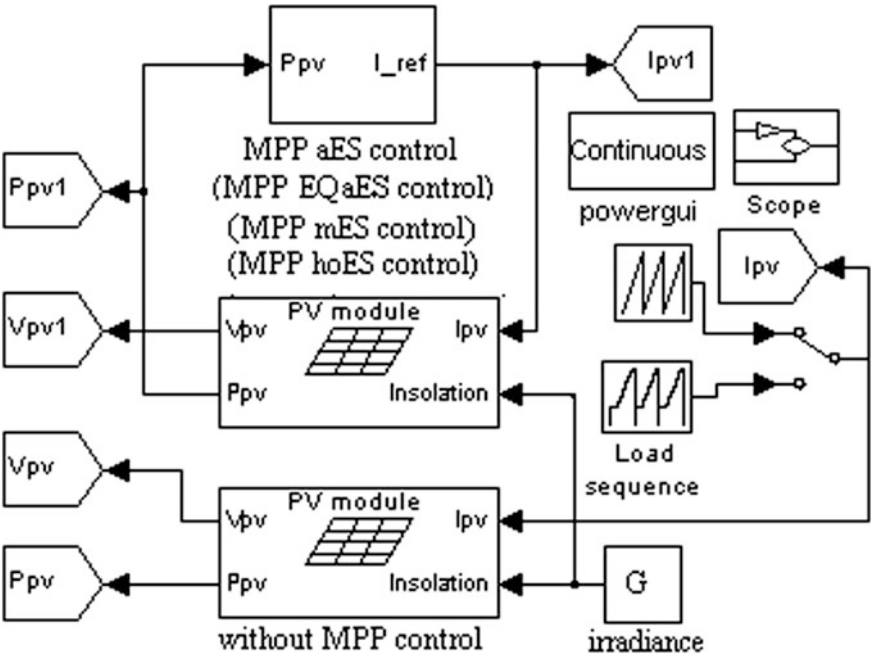

Fig. 6.13 The diagram for comparative tests using as reference the PV panel without MPP control [21]

Then

$$1 < R_{SS} \leq 1 / \cos(\phi_{HPF(ho)}) \leq 1.0541 \tag{6.35}$$

the equality being obtained when:

$$\phi_{HPF(ho)} = \left|\phi_{LPF(ho)}\right| \Leftrightarrow \beta_{l(ho)} \cdot \beta_{h(ho)} = 1 \tag{6.36}$$

The diagram from Fig. 6.13 will be used to validate the equivalence of mESC and EQmESC schemes, and aESC and EQaESC schemes.

In conclusion, based on (6.35), the mESC and EQmESC schemes have almost the same search speed if $G_{BPF(m)}(s) = G_{HPF(EQm)}(s) \cdot G_{LPF(EQm)}(s)$. The simulation results are shown in Fig. 6.14 for the following parameters set for the both mESC and EQmESC schemes: $k_1 = 400$, $k_A = 0.1$ ($k_2 = 1$, and $A = 0.1$), $f_d = 100$ Hz, $\beta_{l(m)} = 5.5$, and $\beta_{h(m)} = 0.5$ (so $\beta_{l(m)} \cdot \beta_{h(m)} = 2.75$).

Some differences in the searching process are shown in zooms for $\beta_{l(m)} \cdot \beta_{h(m)} = 1$ case, when $\beta_{l(m)} = 5.5$ and $\beta_{h(m)} = 1/\beta_{l(m)} \cong 0.18$.

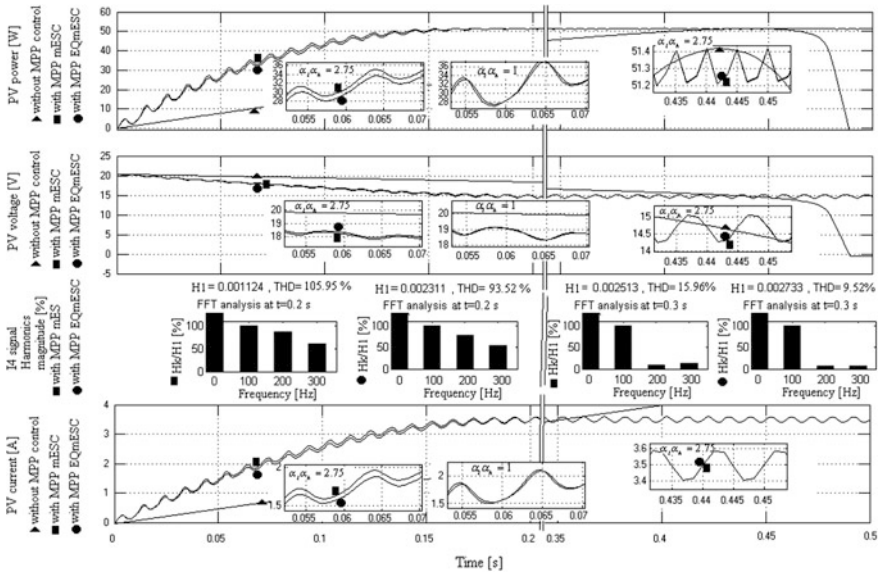

Fig. 6.14 Simulation results for mESC and EQmESC schemes [22]

The simulation results validate the analytical results presented above:

- Both the mESC and EQmESC schemes almost have the same search speed. For example, at 0.05 s it can be observed that the DC components are about I_{PV} = 1.5A, V_{PV} = 18 V, so P_{PV} = 27 W, resulting on this point the search rates: $\dot{i}_{PV} = 1A/0.04\,s = 25\,As^{-1}$, and $\dot{p}_{PV} \cong V_{PV} \cdot \dot{i}_{PV} \cong 450\,Ws^{-1}$. This power rate is verified considering the result shown on the top plot of Fig. 6.14.
- The LF harmonics content of the i_4 signal is almost the same for both mESC and EQmESC schemes.
- The power ripple is the same for both mESC and EQmESC schemes, being about $0.2W_{p\text{-}p}$ Thus, the normalized power ripple is 0.2/51.4 ≅ 0.004 = 0.4%.
- The tracking accuracy is the same for both mESC and EQmESC schemes, being about 51.3/51.4 ≅ 0.998 = 99.8% (see the zoom on right of top plot of the Fig. 6.14).

6.4.3 *On the Performance of the mESC and hoESC Schemes*

The search speed for mESC and hoESC schemes computed based on (6.29) is given by the (6.37) and (6.38):

$$K_{SS(m)} = \dot{p}_{PV}\, k_1 A \left|G_{BPF(m)}\right| \cos(\phi_{BPF(m)}) \,/\, (2V_{MPP}) \tag{6.37}$$

$$K_{SS(ho)} = \dot{p}_{PV}\, k_1 A \left|G_{HPF(ho)}\right| \left|G_{LPF(ho)}\right| \cos(\phi_{HPF(ho)}) \,/\, (2V_{MPP}) \tag{6.38}$$

Thus, the ratio of the searching speeds ($K_{SS(m)}$ and $K_{SS(ho)}$, respectively) is:

$$R_{SS} = \left|K_{SS(m)} \,/\, K_{SS(EQm)}\right| = \left|\cos(\phi_{HPF(m)} + \phi_{LPF(m)})\right| \,/\, \cos(\phi_{HPF(ho)}) \tag{6.39}$$

This ratio can be approximated by (6.40):

$$R_{SS} \cong \sqrt{1 + 1 \,/\, \beta_{l(ho)}^2} \tag{6.40}$$

because $\left(\beta_{l(m)} \,/\, \sqrt{\beta_{l(m)}^2 + 1}\right) \geq 0.95$ for $0 < \beta_{l(ho)} < 1 < 3 < \beta_{l(m)}$.

The simulation results are shown in Fig. 6.15 for the following parameters set for the both mESC and hoESC schemes: $k_1 = 400$, $k_A = 0.1$ ($k_2 = 1$, and $A = 0.1$), $f_d = 100$ Hz, $\beta_{l(m)} = 5.5$, $\beta_{l(ho)} = 0.5$, and $\beta_{h(m)} = \beta_{h(ho)} = 0.5$.

The simulation results validate the analytical results presented above:

- The search speed at t = 0.05 s is about 450 and 300 Ws^{-1} for the mES and hoESC schemes, so the ratio is 450/300 = 1.5. The theoretical value given by (6.40) is about 2.2. This difference could be explained based on simple assumptions considered in obtaining the relationship (6.40), which estimates this

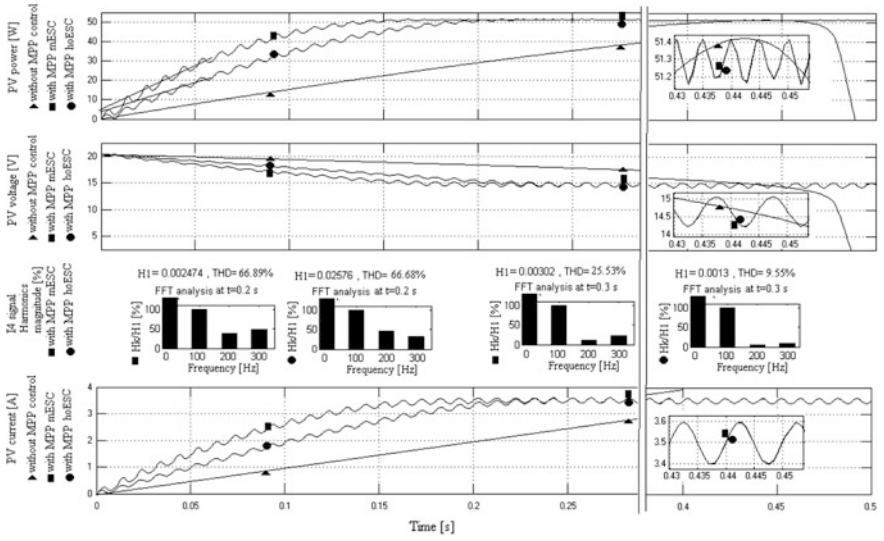

Fig. 6.15 Simulation results for the mESC and hoESC schemes [22]

rate at the dither frequency. It can be observed that the LF spectrum of the i_4 signal is different for the mESC and hoESC scheme (see plot 3 in Fig. 6.15). The dither persistence is improved for the mESC scheme [26]. This aspect will be briefly analyzed in Sect. 6.4.5 to clearly highlight the role of harmonics in the ESC loop.

- The difference between the shapes of the PV power during the searching phase (see Fig. 6.15, top plot) is about 5 J, which means an additional power harvested of about 5 J/0.2 s = 25 W from the PV module (SX60 type having $P_{MPP} \cong 51.2$ W) if the mESC scheme is used.

6.4.4 On the Performance of the aESC and mESC Schemes

The main difference between the mESC scheme and the aESC scheme is related to the dither gain, which is constant, $k_{A(m)} = A \cdot k_2$, and time variable, $k_{A(a)} = A \cdot k_2 \cdot H_1$, respectively, where H_1 is the magnitude of first harmonic of the PV power. So, the searching speed for aESC and mESC schemes are given by (6.41) and (6.42) [21]:

$$K_{SS(m)} = \dot{p}_{PV} k_{1(m)} A \left| G_{BPF(m)} \right| \cos(\phi_{BPF(m)}) / (2V_{MPP}) \tag{6.41}$$

$$K_{SS(a)} = \dot{p}_{PV} k_{1(a)} H_1 A \left| G_{BPF(a)} \right| \cos(\phi_{BPF(a)}) / (2V_{MPP}) \tag{6.42}$$

If the same design parameters will be used for the aESC and mESC schemes ($k_{1(a)} = k_{2(m)}$ and $G_{BPF(a)} = G_{BPF(m)}$), then the ratio of searching speeds will be:

$$R_{SS} = \left| K_{SS(aESC)} / K_{SS(mESC)} \right| \cong H_1 \tag{6.43}$$

If the S1 saturation block has the limits 0 and 1, then $k_{A(a)} = k_{A(m)}$ during the searching phase (when $H_1 > 1$) and $k_{A(a)} = H_1 k_{A(m)}$ if the MPP was located and $H_1 < 1$. The H_1 magnitude is very small close to MPP, so the PV power ripple is negligible during the stationary phase and the MPP is found accurately (see Fig. 6.16, where the magnitudes of the first three harmonics (H_1, H_2, and H_3) of the PV power are shown).

Note that the searching speed will be H_1-times higher for the aESC scheme in comparison with the mES scheme if the S1 saturation block has the upper limit set to infinit.

The magnitude of H_1 and its mean value are shown in the first plot of Fig. 6.16.

The magnitude of H_2 and H_3 is shown in next plots. The PV power during the MPP searching process is shown in plot 4 of Fig. 6.16 and the zoom shows the tracking accuracy. The search speed is about 200 W/s (see plot 4 of Fig. 6.16) if the values used for the k_1 and k_2 gains are set to 400 and 0.8, and A = 0.2.

The effect of amplitude limitation of the dither used for the aESC scheme is shown in Fig. 6.17.

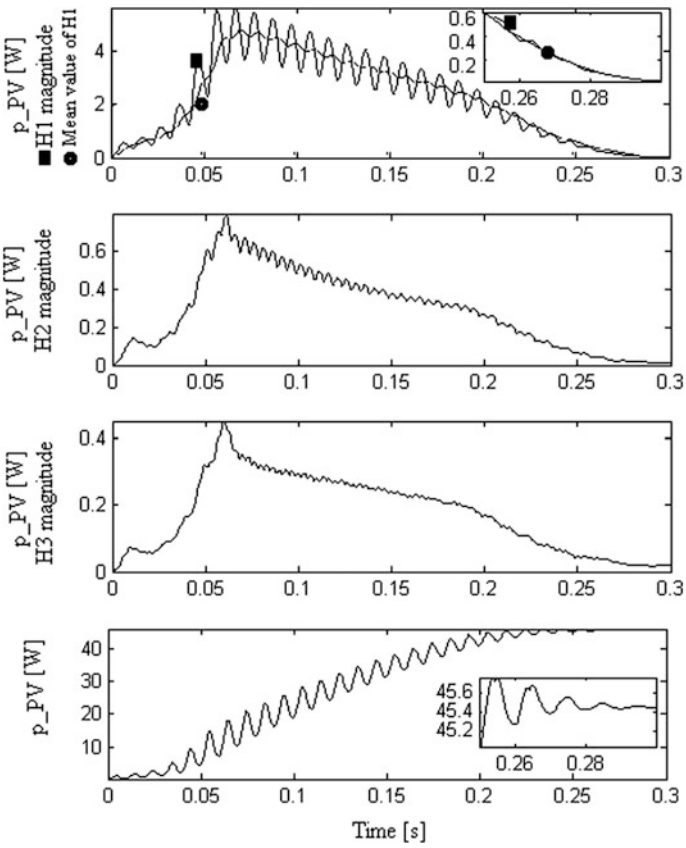

Fig. 6.16 The PV power signal and magnitude of its harmonics [21]

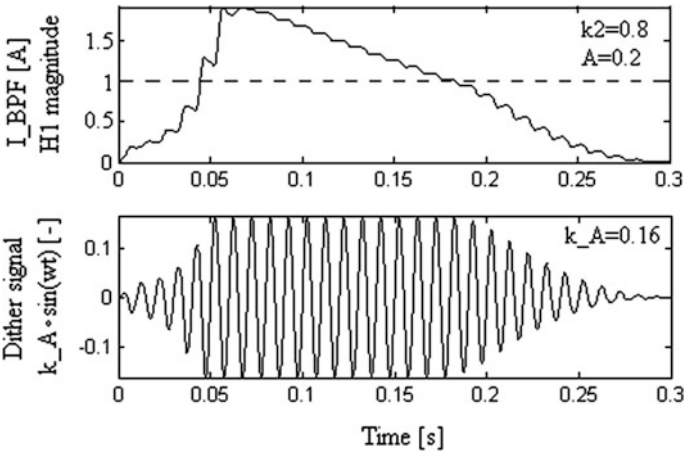

Fig. 6.17 The dither signal for the aESC scheme [21]

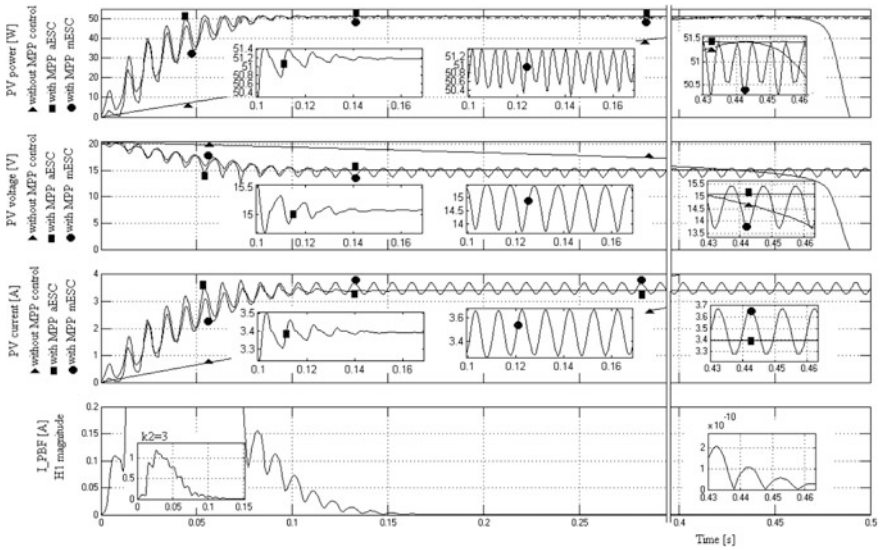

Fig. 6.18 The MPP searching for 500 W/m^2 irradiance level using the aESC (■) and mESC (●) schemes; the reference is set by the PV panel without MPP control (▲) [21]

If this type of limited dither is used for the aESC scheme, then the ratio of the searching speeds (6.43) will be 1 during the searching phase. This result is validated by simulation (see first plot in Fig. 6.18, where almost the same search speed is obtained for both mESC and aESC schemes). The search speed is about 800 W/s because k_1 = 1,600 is 4-times higher than the previous value used in Fig. 6.16, and the saturation block (S1) is used to limit the H_1 magnitude of the i_{BPF} signal at 0.2 (which is also the amplitude of the dither used in both ESC schemes), then the search speed will be the same for the both ESC techniques (about 800 W/s; see Fig. 6.10).

The MPP tracking accuracy for the both control schemes is highlighted in the zooms from the right side of Fig. 6.18. The power ripple has a decreasing and constant magnitude of ripple for the aESC and mESC schemes. This validates the ratio of the searching speeds (6.43) that is H_1 during the stationary phase. Note that the H_1 magnitude decreases to a very small value during the stationary phase (see the last plot in Fig. 6.16).

The PV panel without control (see Fig. 6.13) is used as reference to compute the MPP value for 500 W/m^2 irradiance level, the zooms are used to evaluate the performance indicators for both ESC schemes. The performance evaluated based on Fig. 6.18 are the following:

- The search speed is almost the same for both ESC techniques if H_1 magnitude is limited at 1; the search speed using the aESC scheme is H_1—times higer than that using the mESC scheme (see simulations shown in Sect. 6.5).

- The MPP tracking accuracy using the mESC scheme is about 99% (because 1% ≅100% (51.4 − 50.9)/2 × 51.4) and lower than 0.1% if the aESC scheme is used;
- The power ripple during stationary phase is about 0.5 $W_{p\text{-}p}$ (= 51.4 − 50.9) and negligible for mESC scheme and aESC scheme;

6.4.5 *On the Dither Persistence on the ESC Loop*

The dither persistence on the ESC loop will be analyzed using the following simplifying assumptions:

- Ideal HPF and LPF;
- Unitary value for k_N and k_T gains;
- Initial value for the ϕ_k is set to zero;
- $\omega_d \gg \omega_{h(ES)}$, where $\omega_{h(ES)}$ is the cut-off frequency of the Energy Source (ES) transfer function.

The dither will not interact with the ES dynamic based on last assumption, so the ES power signal will result as harmonics' superposition based on the ES static characteristic (see Fig. 6.2) and, for example, the EQmESC scheme (Fig. 6.3). The first three harmonics will be considered for the $i_{ref(LF)}$ signal:

$$i_{ref(LF)} = \sum_{k=1}^{3} I_{ref(k)} \sin(k\omega_d t + \phi_k) \tag{6.44}$$

So, the reference current, i_{ref}, will be given by (6.45):

$$\begin{aligned} i_{ref}(t) = I_{ref} + i_{ref(LF)}(t) \cong I_{ref} + a_1 \cdot \sin(\omega_d t) \\ + a_2 \cdot \sin(2\omega_d t) + a_3 \cdot \sin(3\omega_d t) \end{aligned} \tag{6.45}$$

The power response, p_{ES}, to one harmonic can be approximated by the Taylor series:

$$\begin{aligned} p_{ES}(i_{ref}) = P_{ES}|_{I_{ref}} + \dot{p}_{ES}(i_{ref}) \cdot \left(I_{ref} + a_k \cdot \sin(k \cdot \omega_d \cdot t)\right) \\ + \frac{\ddot{p}_{ES}(i_{ref})}{2!} \cdot \left(I_{ref} + a_k \cdot \sin(k \cdot \omega_d \cdot t)\right)^2 \\ + \frac{\dddot{p}_{ES}(i_{ref})}{3!} \cdot \left(I_{ref} + a_k \cdot \sin(k \cdot \omega_d \cdot t)\right)^3 + \cdots \end{aligned} \tag{6.46}$$

So, the small signal (SS) components of the p_{ES} signal are:

$$\begin{aligned} p_{ES(SS)}(t) \cong\ & \dot{p}_{ES}(t) \cdot a_k \cdot \sin(k \cdot \omega_d \cdot t) + \frac{\ddot{p}_{ES}(t)}{2} \cdot a_k^2 \cdot \sin^2(k \cdot \omega_d \cdot t) \\ & + \frac{\dddot{p}_{ES}(t)}{6} \cdot a_k^3 \cdot \sin^3(k \cdot \omega_d \cdot t) + \cdots \end{aligned} \tag{6.47}$$

or

$$\begin{aligned} p_{ES(LF)}(t) \cong\ & \dot{p}_{ES}(t) \cdot a_k \cdot \sin(k \cdot \omega_d \cdot t) - \frac{\ddot{p}_{ES}(t)}{2} \cdot \frac{a_k^2}{2} \cdot \cos(2 \cdot k \cdot \omega_d \cdot t) \\ & + \frac{\dddot{p}_{ES}(t)}{6} \cdot \frac{a_k^3}{4} \cdot [3 \cdot \sin(k \cdot \omega_d \cdot t) - \sin(3 \cdot k \cdot \omega_d \cdot t)] \end{aligned} \tag{6.48}$$

If the HPF is ideal and $k_{N=}1$, then the $p_{1(LF)}$ signal will be given by (6.49):

$$p_{1(LF)}(t) = p_{ES(LF)}(t) \tag{6.49}$$

Thus, the signal after the demodulation is:

$$\begin{aligned} p_{2(LF)}(t) = p_{1(LF)}(t) \cdot \sin(\omega_d \cdot t) =\ & \dot{p}_{ES}(t) \cdot a_k \cdot \sin(\omega_d \cdot t) \cdot \sin(k \cdot \omega_d \cdot t) \\ & - \ddot{p}_{ES}(t) \cdot \frac{a_k^2}{4} \cdot \sin(\omega_d \cdot t) \cdot \cos(2 \cdot k \cdot \omega_d \cdot t) \\ & + \dddot{p}_{ES}(t) \cdot \frac{a_k^3}{8} \cdot \sin(k \cdot \omega_d \cdot t) \cdot \sin(\omega_d \cdot t) \\ & + \dddot{p}_{ES}(t) \cdot \frac{a_k^3}{24} \cdot \sin(3 \cdot k \cdot \omega_d \cdot t) \cdot \sin(\omega_d \cdot t) \end{aligned} \tag{6.50}$$

Considering all harmonics (k = 1, 2, 3), the $p_{2(LF)}$ signal is given based on the superposition techniques as:

$$\begin{aligned} p_{2(LF)}(t) = \dot{p}_{ES} \big[& a_1 \cdot \sin^2(\omega_d \cdot t) + a_2 \cdot \sin(2 \cdot \omega_d \cdot t) \cdot \sin(\omega_d \cdot t) \\ & + a_3 \cdot \sin(3 \cdot \omega_d \cdot t) \cdot \sin(\omega_d \cdot t)] \\ & - \frac{\ddot{p}_{ES}}{4} \big[a_1^2 \cdot \sin(\omega_d \cdot t) \cdot \cos(2 \cdot \omega_d \cdot t) + a_2^2 \cdot \sin(\omega_d \cdot t) \cdot \cos(4 \cdot \omega_d \cdot t) \\ & + a_3^2 \cdot \sin(\omega_d \cdot t) \cdot \cos(6 \cdot \omega_d \cdot t) \big] \\ & + \frac{\dddot{p}_{ES}}{8} \big[a_1^3 \cdot \sin^2(\omega_d \cdot t) + a_2^3 \cdot \sin(2 \cdot \omega_d \cdot t) \cdot \sin(\omega_d \cdot t) \\ & + a_3^3 \cdot \sin(3 \cdot \omega_d \cdot t) \cdot \sin(\omega_d \cdot t) \big] \\ & - \frac{\dddot{p}_{ES}}{24} \big[a_1^3 \cdot \sin(3 \cdot \omega_d \cdot t) \cdot \sin(\omega_d \cdot t) + a_2^3 \cdot \sin(6 \cdot \omega_d \cdot t) \cdot \sin(\omega_d \cdot t) \\ & + a_3^3 \cdot \sin(9 \cdot \omega_d \cdot t) \cdot \sin(\omega_d \cdot t) \big] \end{aligned} \tag{6.51}$$

or (after simple trigonometric manipulations)

$$
\begin{aligned}
p_{2(LF)}(t) = {} & \frac{\dot{p}_{ES}}{2}\cdot a_1[1-\cos(2\cdot\omega_d\cdot t)] + \frac{\dot{p}_{ES}}{2}\cdot a_2[\cos(\omega_d\cdot t)-\cos(3\cdot\omega_d\cdot t)] \\
& + \frac{\dot{p}_{ES}}{2}\cdot a_3[\cos(2\cdot\omega_d\cdot t)-\cos(4\cdot\omega_d\cdot t)] - \frac{\ddot{p}_{ES}}{8}\cdot a_1^2[-\sin(\omega_d\cdot t)+\sin(3\cdot\omega_d\cdot t)] \\
& - \frac{\ddot{p}_{ES}}{8}\cdot a_2^2[-\sin(3\cdot\omega_d\cdot t)+\sin(5\cdot\omega_d\cdot t)] - \frac{\ddot{p}_{ES}}{8}\cdot a_3^2[-\sin(5\cdot\omega_d\cdot t)+\sin(7\cdot\omega_d\cdot t)] \\
& + \frac{\dddot{p}_{ES}}{16}\cdot a_1^3[1-\cos(2\cdot\omega_d\cdot t)] + \frac{\dddot{p}_{ES}}{16}\cdot a_2^3[\cos(\omega_d\cdot t)-\cos(3\cdot\omega_d\cdot t)] \\
& + \frac{\dddot{p}_{ES}}{16}\cdot a_3^3[\cos(2\cdot\omega_d\cdot t)-\cos(4\cdot\omega_d\cdot t)] - \frac{\dddot{p}_{ES}}{48}\cdot a_1^3[\cos(2\cdot\omega_d\cdot t)-\cos(4\cdot\omega_d\cdot t)] \\
& - \frac{\dddot{p}_{ES}}{48}\cdot a_2^3[\cos(5\cdot\omega_d\cdot t)-\cos(7\cdot\omega_d\cdot t)] - \frac{\dddot{p}_{ES}}{48}\cdot a_3^3[\cos(8\cdot\omega_d\cdot t)-\cos(10\cdot\omega_d\cdot t)]
\end{aligned}
\tag{6.52}
$$

If the LPF is ideal, then the $p_{3eq(LF)}$ signal is given by (6.53):

$$
\begin{aligned}
p_{3eq(LF)}(t) \cong p_{2(LF)}(t) = {} & \frac{\dot{p}_{ES}\cdot a_1}{2} + \frac{\dddot{p}_{ES}\cdot a_1^3}{16} + \sin(\omega_d\cdot t) \\
& \cdot\left[\frac{\ddot{p}_{ES}\cdot a_1^2}{8}\right] + \cos(\omega_d\cdot t)\left[\frac{\dot{p}_{ES}\cdot a_2}{2} + \frac{\dddot{p}_{ES}\cdot a_2^3}{16}\right] + \sin(2\cdot\omega_d\cdot t)[0] \\
& + \cos(2\cdot\omega_d\cdot t)\left[-\frac{\dot{p}_{ES}\cdot a_1}{2} + \frac{\dot{p}_{ES}\cdot a_3}{2} - \frac{\dddot{p}_{ES}\cdot a_1^3}{16} + \frac{\dddot{p}_{ES}\cdot a_3^3}{16} - \frac{\dddot{p}_{ES}\cdot a_1^3}{48} + \frac{\dddot{p}_{ES}\cdot a_1^3}{48}\right] \\
& + \sin(3\cdot\omega_d\cdot t)\left[-\frac{\ddot{p}_{ES}\cdot a_1^2}{8} + \frac{\ddot{p}_{ES}\cdot a_2^2}{8}\right] + \cos(3\cdot\omega_d\cdot t)\left[-\frac{\dot{p}_{ES}\cdot a_2}{2} - \frac{\dddot{p}_{ES}\cdot a_2^3}{16}\right]
\end{aligned}
\tag{6.53}
$$

Thus, the $p_{4eq(LF)}$ signal (after the integrator block) is:

$$
\begin{aligned}
\frac{1}{k_1}\cdot p_{4eq(LF)}(t) = {} & \left[\frac{\dot{p}_{ES}\cdot a_1}{2} + \frac{\dddot{p}_{ES}\cdot a_1^3}{16}\right]\cdot t - \cos(\omega_d\cdot t)\cdot\frac{1}{\omega_d}\cdot\left[\frac{\ddot{p}_{ES}\cdot a_1^2}{8}\right] \\
& + \sin(\omega_d\cdot t)\cdot\frac{1}{\omega_d}\cdot\left[\frac{\dot{p}_{ES}\cdot a_2}{2} + \frac{\dddot{p}_{ES}\cdot a_2^3}{16}\right] - \cos(2\cdot\omega_d\cdot t)\cdot\frac{1}{2\cdot\omega_d}\cdot[0] \\
& + \sin(2\cdot\omega_d\cdot t)\cdot\frac{1}{2\cdot\omega_d}\cdot\left[\frac{\dot{p}_{ES}\cdot(a_3-a_1)}{2} + \frac{\dddot{p}_{ES}\cdot\left(3\cdot a_3^3-4\cdot a_1^3\right)}{48}\right] \\
& - \cos(3\cdot\omega_d\cdot t)\cdot\frac{1}{3\cdot\omega_d}\cdot\left[\frac{\ddot{p}_{ES}\cdot\left(a_2^2-a_1^2\right)}{8}\right] \\
& - \sin(3\cdot\omega_d\cdot t)\cdot\frac{1}{3\cdot\omega_d}\cdot\frac{\left[8\cdot\dot{p}_{ES}\cdot a_2 + \dddot{p}_{ES}\cdot a_2^3\right]}{16}
\end{aligned}
\tag{6.54}
$$

If $k_T = 1$, then the $i_{5eq(LF)}$ signal is:

$$i_{5eq(LF)}(t) \cong k_T \cdot p_{4eq(LF)}(t) = K_{SS(EQm)} \cdot t + b_1 \cdot \sin(\omega_d t) - c_1 \cdot \cos(\omega_d t) + b_2 \cdot \sin(2\omega_d t) - c_2 \cdot \cos(2\omega_d t) - b_3 \cdot \sin(3\omega_d t) + c_3 \cdot \cos(3\omega_d t) \tag{6.55}$$

where:

$$K_{SS(EQm)} = k_1 \cdot \left[\frac{\dot{p}_{ES} \cdot a_1}{2} + \frac{\dddot{p}_{ES} \cdot a_1^3}{16} \right] \tag{6.56}$$

and

$$\begin{aligned} b_1 &= k_1 \cdot \frac{1}{\omega_d} \cdot \left[\frac{\dot{p}_{ES} \cdot a_2}{2} + \frac{\dddot{p}_{ES} \cdot a_2^3}{16} \right], \\ c_1 &= k_1 \cdot \frac{1}{\omega_d} \cdot \left[\frac{\ddot{p}_{ES} \cdot a_1^2}{8} \right], \\ b_2 &= k_1 \cdot \frac{1}{2 \cdot \omega_d} \cdot \left[\frac{\dot{p}_{ES} \cdot (a_3 - a_1)}{2} + \frac{\dddot{p}_{ES} \cdot \left(3 \cdot a_3^3 - 4 \cdot a_1^3\right)}{48} \right], \\ c_2 &= 0, \\ b_3 &= k_1 \cdot \frac{1}{3 \cdot \omega_d} \cdot \frac{\left[8 \cdot \dot{p}_{ES} \cdot a_2 + \dddot{p}_{ES} \cdot a_2^3\right]}{16}, \\ c_3 &= k_1 \cdot \frac{1}{3 \cdot \omega_d} \cdot \left[\frac{\ddot{p}_{ES} \cdot \left(a_2^2 - a_1^2\right)}{8} \right] \end{aligned} \tag{6.57}$$

Thus, the harmonics of the $i_{5(LF)}$ signal are:

$$\begin{aligned} I_{5(1)} &= \sqrt{b_1^2 + c_1^2}, \\ I_{5(2)} &= \sqrt{b_2^2 + c_2^2} = b_2, \\ I_{5(1)} &= \sqrt{b_3^2 + c_3^2} \end{aligned} \tag{6.58}$$

Consequently, besides the gradient and the gained dither, the $i_{ref(eq)}$ signal has three harmonics:

$$i_{ref(eq)} = K_{SS(EQm)} \cdot t + \sum_{k=1}^{3} I_{5(k)} \cdot \sin(k\omega_d t + \phi_{5(k)}) + k_2 \cdot A \sin(\omega_d t) \tag{6.59}$$

The better approximation of the gradient by (6.56) in comparison with (6.37), where only first derivative appears can be observed.

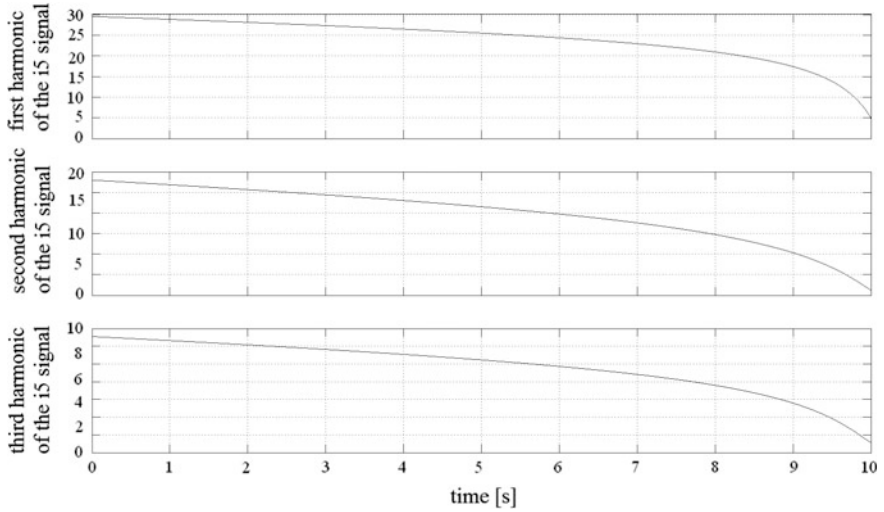

Fig. 6.19 Harmonics of the i5 signal computed based on (6.58) [26]

The $i_{5(LF)}$ harmonics will be estimated based on (6.58) using the power derivatives computed at a given I_{ref} value:

$$\dot{p}_{ES}(t)\big|_{I_{ES}=I_{ref}}, \quad \ddot{p}_{ES}(t)\big|_{I_{ES}=I_{ref}}, \quad \dddot{p}_{ES}(t)\big|_{I_{ES}=I_{ref}} \tag{6.60}$$

The shape of the $i_{5(LF)}$ harmonics is shown in Fig. 6.19.

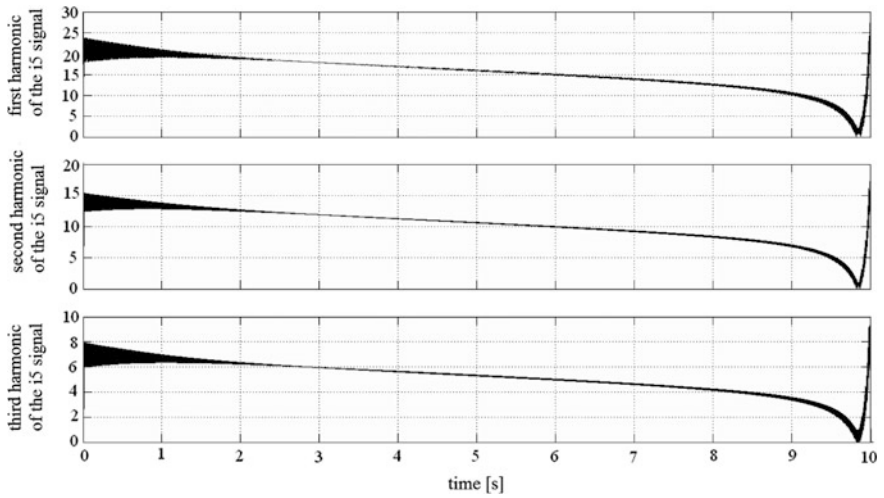

Fig. 6.20 Harmonics of the i5 signal computed based on the simulation of the signal processing in the ESC loop [26]

Also, the $i_{5(LF)}$ harmonics will be evaluated based on signal processing related to ESC loop considering the reference current given by (6.45) as dither. The shapes of $i_{5(LF)}$ harmonics are shown in Fig. 6.20. The minor differences appear close to the MPP due to high distortion of the dither (which means more harmonics in the simulated ESC loop.

The conclusion is that the searching speed is proportional to a linear combination of the first and third derivative of the p_{ES} power, besides the ESC loop gain (k_1) and the dither amplitude (A). Consequently, the search speed is dependent to the pass band set for the BPF of the mESC and aESC schemes.

The performance of the PVHPS under variable irradiance profile and constant load will be analyzed below for both mESC and aESC schemes.

6.5 The PVHPS Using the ESC Schemes

6.5.1 Testing the mESC Scheme

The variable irradiance profile (■) of step-up stairs type is shown in Fig. 6.21.

The MPP searching process is also shown in P-I phase plane (see Fig. 6.21). The simulation diagram was that from Fig. 6.6. The MPPs are tracked with a small ripple by using the mESC scheme (see the zooms on Fig. 6.22).

The MPPs tracking is also shown in the first plot of Fig. 6.21, where the PV power (●) has the same MPPs as in Fig. 6.22. The ESS voltage (■) and the ESS power (●) are shown in the second plot of Fig. 6.21. The ESS power is given by (6.2). So for a constant load of 50 W and variable PV power, the ESS will compensate the power flow balance on the DC bus.

The power ripple is about 2 $W_{p\text{-}p}$ (see zooms on Fig. 6.22), which means a normalized ripple of about 2/51 ≅ 4%, but this can be reduce further if the aESC scheme will be used instead of mESC scheme.

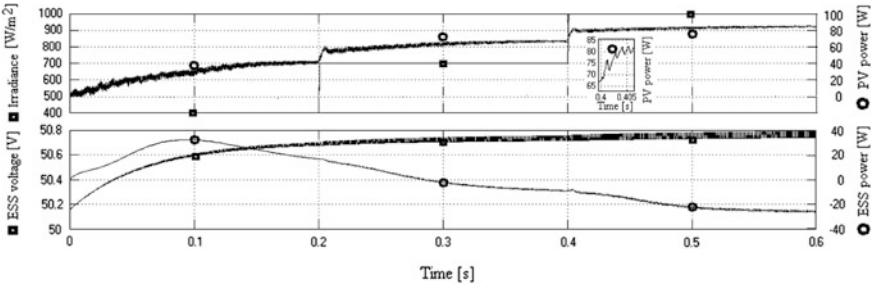

Fig. 6.21 The PVHPS behavior under a irradiance profile [22]

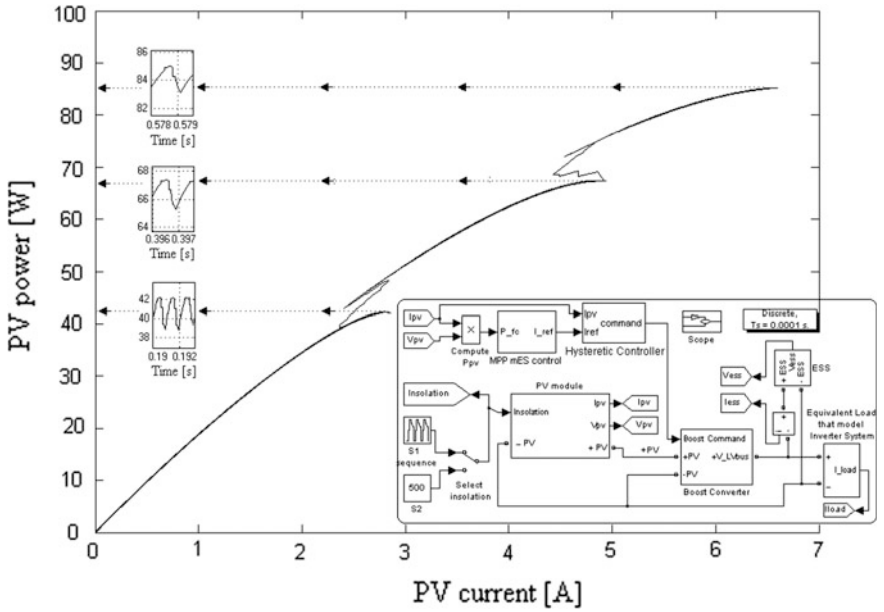

Fig. 6.22 The MPP searching process [22]

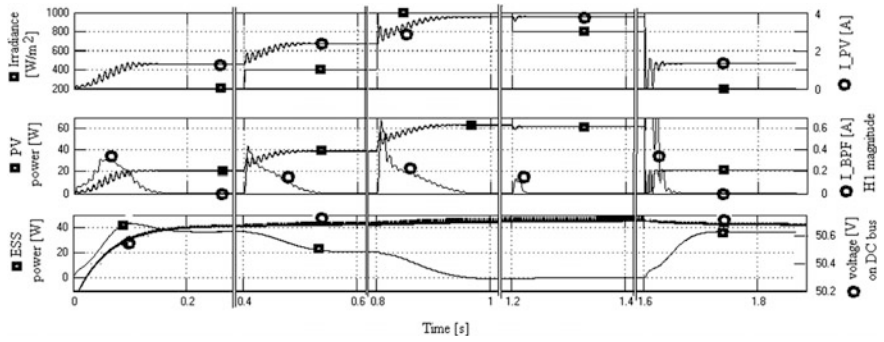

Fig. 6.23 The PVHPS behavior under aESC scheme and step up-down profile of the irradiance [21]

6.5.2 *Testing the aESC Scheme*

The irradiance profile is step-up and -down type (see Fig. 6.23, plot 1). The following plots are shown in Fig. 6.23:

- Plot 1: the irradiance sequence (■) and the PV current, i_{PV} (●);

Table 6.2 Performance of the mESC and aESC schemes

Performance indicator	mESC scheme	aESC scheme
Search speed (kW/s)	Maximum 0.8 kW/s; higher search speed means lower tracking accuracy	Higher than kW/s; H_1—times higher that mESC search speed; can be set independently to the tracking accuracy
Tracking accuracy (%)	Lower than 99.8%	Higher than 99.99%
Normalized p-p power ripple (%)	About 4%	Negligible
Robustness	High	High
Control complexity	Simple	A bit complex than mESC
Global MPP feature	No	Yes (see [33–36])

- Plot 2: the PV power (■) and the H1 magnitude of the first harmonic of the i_{BPF} signal(●);
- Plot 3: the ESS power (■) and the voltage on DC bus (●).

It can be observed that the search speed under aESC scheme is H_1-times higher than the search speed under mESC scheme. The H1 magnitude increases quickly to any variation in the irradiance level (see Fig. 6.23, plot 2). The power ripple is also negligible during the stationary phase, after the MPP is located (see Fig. 6.23, plot 2). Consequently, the performance of the aESC scheme is better than that of the mESS scheme.

The ESS will operate in charge depletion mode to assure the power flow balance on the DC bus when the PV power is lower than the load (see Fig. 6.23, plot 3—the period when the irradiance level is lower that 500 W/m^2). The DC bus remain almost constant around 50 V set by the ESS battery voltage (see Fig. 6.23, plot 3).

The PVHPS behavior under the aESC scheme was tested in Matlab-Simulink® for different irradiance and load profiles. The following performance may be highlighted (see Table 6.2): (1) the robust tracking of the MPP under irradiance profile as in reality; (2) the search speed could be set higher than 1 kW/s; (3) the tracking accuracy is higher than 99.99%; (4) a negligible ripple during the stationary phase.

6.6 Conclusion

In this chapter some analytical results related to the new ESC schemes are highlighted. The mESC scheme based on BPF was proposed to improve the search speed: this is about twice in comparison with that obtained with the hoESC scheme.

Anyway, the PV power ripple remains the same for the both mESC and hoESC schemes analyzed. The PV power ripple can be reduced by using the aESC scheme that has the following performance (see Sect. 6.4.5): (1) the tracking accuracy is higher than 99.99%, (2) the PV power ripple is negligible during the stationary phase after the MPP is located; the aESC search speed is H_1—times higher that mESC search speed; (3) the aESC search speed can be set independently (up to a safe value of PVHPS operation) in order to obtain high tracking accuracy during the transitory phase as well; (4) the aESC-based MPPT control is robust to irradiance profiles such as in reality; (5) the aESC-based MPPT control is simple to be implemented.

In conclusion, the aESC scheme slightly outperforms the mESC scheme in total power efficiency of the PVHPS.

Acknowledgements The research that led to the results shown here has received funding from the project "Cost-Efficient Data Collection for Smart Grid and Revenue Assurance (CERA-SG)", ID: 77594, 2016-19, ERA-Net Smart Grids Plus. Some figures, tables and text are reproduced from [21, 22, 26] here with kind permission from Elsevier Limited, UK, WCST, UK, and APPEL, CZ [September 13, 2016].

References

1. Salas V, Olías E, Barrado A, Lázaro A (2016) Review of the maximum power point tracking algorithms for stand-alone photovoltaic systems. Sol Energ Mat Sol C 90(11):1555–1578
2. Azar FE, Perrier M, Srinivasan B (2011) A global optimization method based on multi–unit extremum–seeking for scalar nonlinear systems. Comput Chem Eng 35:456–463
3. Tan Y, Nesic D, Mareels I (2008) On the choice of dither in extremum seeking systems: a case study. Automatica 44:1446–1450
4. Esram T, Chapman PL (2007) Comparison of photovoltaic array maximum power point tracking techniques. IEEE Trans Energ Conv 22(2):439–449
5. Bizon N, Radut M, Oproescu M (2015) Energy control strategies for the Fuel Cell Hybrid Power Source under unknown load profile. Energy 86:31–41
6. Bizon N (2014) Load-following mode control of a standalone renewable/fuel cell hybrid power source. Energ Convers Manage 77:763–772
7. Kuperman A, Aharon I (2011) Battery–ultracapacitor hybrids for pulsed current loads: a review. Renew Sust Energ Rev 15:981–992
8. Mehrdad E, Yimin G, Ali E (2010) Modern electric, hybrid electric, and fuel cell vehicles. CRC Press (15)
9. Bizon N (2012) Energy efficiency of multiport power converters used in plug-in/v2g fuel cell vehicles. Appl Energ 96:431–443
10. Bizon N (2012) Distributed generation systems integrating renewable energy resources. Nova Science Publishers Inc., New York
11. Feroldi D, Serra M, Riera J (2009) Energy Management Strategies based on efficiency map for Fuel Cell Hybrid Vehicles. J Pow Sour 190:387–401
12. Bizon N, Oproescu M, Raceanu M (2015) Efficient energy control strategies for a standalone renewable/fuel cell hybrid power source. Energ Convers Manage 77:768–772

13. Bizon N (2014) Improving the PEMFC energy efficiency by optimizing the fuelling rates based on extremum seeking algorithm. Int J Hydrogen Energ 39(20):10641–10654
14. Patel H, Agarwal V (2009) MPPT scheme for a PV-fed single-phase single-stage grid-connected inverter operating in CCM with only one current sensor. IEEE Trans Energ Convers 24:256–263
15. Wang J-C, Su Y-L, Shieh J-C, Jiang J-A (2011) High-accuracy maximum power point estimation for photovoltaic arrays. Sol Energ Mat Sol C 95:843–851
16. Toledo FJ, Blanes JM, Garrigós A, Martínez JA (2012) Analytical resolution of the electrical four-parameters model of a photovoltaic module using small perturbation around the operating point. Renew Energ 43:83–89
17. Kimball JW, Krein PT (2008) Discrete-time ripple correlation control for maximum power point tracking. IEEE Trans Power Electron 23:2353–2362
18. Leyva R, Artillan P, Cabal C, Estibals B, Alonso C (2011) Dynamic performance of maximum power point tracking circuits using sinusoidal extremum seeking control for photovoltaic generation. Int J Electron 98(4):529–542
19. Reisi AR, Moradi MH, Jamasb S (2013) Classification and comparison of maximum power point tracking techniques for photovoltaic system: a review. Renew Sust Energ Rev 19:433–443
20. Qiang M, Mingwei S, Liying L, Guerrero JMA (2011) Novel improved variable step- size incremental-resistance MPPT method for PV systems. IEEE Trans Ind Electron 58:2427–2434
21. Bizon N (2013) Energy harvesting from the PV Hybrid Power Source. Energy 52:297–307
22. Bizon N, Raducu M, Oproescu M, Constantinescu LM (2014) Energy efficiency of the PV panels using a MPPT controller with improved search speed—Part I & II. In: APPEL'14—international conference on applied electronics. http://ieeexplore.ieee.org/xpl/articleDetails.jsp?arnumber=7011666&sortType%3Dasc_p_Sequence%26filter%3DAND%28p_IS_Number%3A7011649%29
23. Krstić M (2000) Performance improvement and limitations in extremum seeking. Syst Control Lett 39(5):313–326
24. Krstić M, Wang H-H (2000) Design and stability analysis of extremum seeking feedback for general nonlinear systems. Automatica 36(2):595–601
25. Ariyur KB, Krstić M (2003) Real-time optimization by extremum-seeking control. Wiley-interscience edition, Wiley Inc.
26. Bizon N, Oproescu M, Raducu M (2012) On the dither persistence in the extremum seeking control—Part I & II, WCST-2012—World Congress on Sustainable Technologies, pp 104–114. http://ieeexplore.ieee.org/xpl/login.jsp?tp=&arnumber=6482927&url=http%3A%2F%2Fieeexplore.ieee.org%2Fxpls%2Fabs_all.jsp%3Farnumber%3D6482927
27. Harada K, Zhao G (1993) Controlled power interface between solar cells and AC source. IEEE Trans Power Electron 8:654–662
28. Subudhi B, Pradhan R (2013) A comparative study on maximum power point tracking techniques for photovoltaic power systems. IEEE Trans Sustain Energ 4:89–98
29. Brunton SL, Rowley CW, Kulkarni SR, Clarkson C (2010) Maximum power point tracking for photovoltaic optimization using ripple-based extremum seeking control. IEEE T Power Electr 25(10):2531–2540
30. Midya P, Krein PT, Turnbull R (1996) Dynamic maximum power point tracker for photovoltaic applications. In: IEEE 27th annual power electronics specialists conference, pp 1710–1716
31. Gelbert G, Moeck JP, Paschereit CO, King R (2012) Advanced algorithms for gradient estimation in one- and two-parameter extremum seeking controllers. J Process Contr 22:700–709

32. Bizon N (2010) On tracking robustness in adaptive extremum seeking control of the fuel cell power plants. Appl Energ 87(10):3115–3130
33. Bizon N (2013) Energy harvesting from the FC stack that operates using the MPP tracking based on modified extremum seeking control. Appl Energ 104:326–336
34. Lim YH, Hamill D (2000) Simple maximum power point tracker for photovoltaic arrays. Electron Lett 36(11):997–999
35. Bizon N (2013) FC energy harvesting using the MPP tracking based on advanced extremum seeking control. Int J Hydrogen Energ 38(4):1952–1966
36. Bizon N (2015) Global maximum power point tracking based on new extremum seeking control scheme, progress in photovoltaics: research and applications. http://onlinelibrary.wiley.com/doi/10.1002/pip.2700/full

Part II
Energy Efficiency of the Photovoltaic Systems

Chapter 7
Improving Tracking Efficiency of Two-Axis Sun Tracking Systems

Fevzi Kentli and Musa Yilmaz

Abstract Due to both reduction and insufficient of fossil fuel to supply current growing energy needs, investigation and employing of renewable resources has been accelerated. Besides, using fossil fuel affected the environment negatively. Therefore, renewable energy resources in the most studies are solar, wind and geothermal. In this study, electrical energy production methods from solar energy have been examined, a fixed and a two axis tracking system have been designed. Both systems are compared each other regarding to several factors by performing annual measurements. Energy consumption of the system is minimized by employing actuator motor in two axis solar tracking system. According to the efficiency of two-axis tracking system, the annual average has been calculated as 31.67% more. This efficiency has been calculated as 70% in winter, 11% in summer. As a result of these measurements several graphics of a year empirically daily, monthly and annual data have been contributed to the literature for Diyarbakir, one of the prominent cities of Southern east, having the most solar energy of Turkey. In the first section, literature review will be indicated. In the second section, solar angles, photovoltaic panels and systems, sample designs and solar tracking systems are examined. In the third section, photovoltaic two-axis solar tracking system and qualifications, work and advantages of fixed system which we designed are stated. In following section, obtained results will be given and in last section, financial analysis of fixed and tracking photovoltaic systems has been performed. Also, recommendations for increasing their efficiency have been noted.

Keywords Solar energy · Photovoltaic · Two-axis sun tracking

F. Kentli (✉)
Department of Mechatronics Engineering, Technology Faculty,
Marmara University, 34722 Istanbul, Turkey
e-mail: fkentli@marmara.edu.tr

M. Yilmaz
Department of Electronics and Communications Engineering, Technology Faculty,
Batman University, Batman, Turkey
e-mail: musa.yilmaz@batman.edu.tr

N. Bizon et al. (eds.), *Energy Harvesting and Energy Efficiency*,
Lecture Notes in Energy 37, DOI 10.1007/978-3-319-49875-1_7

7.1 Introduction

Importance of energy needed today in every area of life becomes increasing. Energy is the main input for our civilization and its production and consumption is one of the reliable merits to measure the improvement and development of the country.

Studies on finding and developing alternative energy resources have been accelerated as a result of insufficiency of existing resources to provide constantly increasing energy need. Yet, traditional energy production and consumption methods, especially fossil fuel based ones, lead to unrecoverable environmental damages. Saving the living environment on earth and decreasing the environmental damage caused by energy production and consumption beneath the damage caused by climate change give responsibility to all humankind. As a result of this responsibility; preparing national and international legal regulations, prioritizing the environmental effects in selection of energy production technology and resources and giving maximum effort in efficiently using energy are gaining much more importance by the time.

As a consequence, instead of using traditional and fossil fuel based energy production systems which are causing worldwide environmental pollution and climate change, finding energy resources and developing new technologies providing sustainability and renewability and causing less environmental damage and climate change became necessary. Both of the facts that fossil fuel resources are limited and their production and consumption systems cause environmental damage led to investigate renewable, unlimited and environmental friendly energy resources and technologies. So, renewable energy resources including solar energy gained importance [1, 2].

Solar energy with the characteristics such as its potential, cleanliness, renewability, easy-to-use and being environmental friendly features has much more probability to become widespread when compared with other renewable energy resources. Overcoming it limitations such as having higher setup cost, having less efficiency and capacity will make it more attractive at the future. Unfortunately, Turkey could not use today all its potential even though it has a favorable position from solar energy perspective.

Solar energy is vast and also does not damage environment. This makes it a good choice in this consumption era as most known energy sources have becoming exhausted and some complications are occurred such as corrosion in living world and climate changes. However, there are different opportunities which allow us fix the situation. One of these opportunities and also the most convenient one is to find out the new and clean energy sources. Another opportunity is to reduce the amount of consumed energy.

Nuclear energy has first considered as sharp cut solution but having high hazard risk and changing nearby habitat made it less preferable. On the other hand, sun has much more potential as it has not such kind of disadvantages. Available energy on

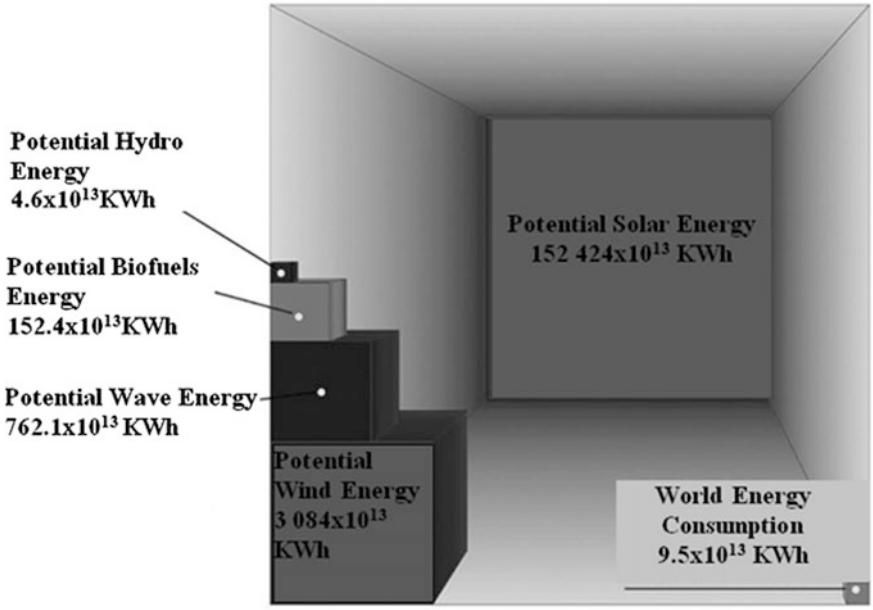

Fig. 7.1 World energy consumption and production status

the world produced by sun is in 152,424 $\times$ 10^{13} kWh while total energy produced by power plants is 100 thousand times less and produced solar energy on earth is 15 thousand times less as seen in Fig. 7.1. Thus, today solar energy systems have begun to be used in every part of life even though solar energy is intended to use after the second half of our century [1–12].

At the present time, utilization of solar energy becomes significant in almost every country as there are many different application areas. It is used in providing hot water or heating house. Also, it is converted into electrical energy and then used in lighting of buildings, for propulsion of cars and even for assisting to grow crops by the help of solar water pumps. In last 20 years, new technologies are improved on solar panels and studies are focused on making them cheaper [2, 3].

Optimal usage of photovoltaic (PV) panels for different cases is an important problem because the efficiency of the panels is changing as the weather changes. To solve this problem, panels are used in rural area or away from city centers where there are plenty of empty spaces letting get much more sunlight onto panel surface. But even in these conditions it is needed to maximize obtained solar energy by determining appropriate declination angle. That is why so many studies on declination angle have been done [1, 2].

Output power of any photovoltaic system depends on amount of obtained solar irradiance. To provide more sunlight as an input to system, it is required to track the sun. Main concern of these systems is first cost of system and cost of consumed

energy during sun tracking. In this study, consumed energy of the system during sun tracking is minimized and it is compared with the other studies [11–15]. Applications brought out different sun tracking systems [16–20].

7.2 Maximizing Sunlight on Panels

Easiest way to maximize sunlight in most system is to mount panels onto a horizontal tracking system. Sun takes highest place in sky according to horizontal axis at noon, so it is the time that sun has minimum distance in atmosphere and air has the minimum density during day. At other times, incident radiation flux becomes less since mass density is increasing and the angle between sunlight and normal of panel surface is increasing. Consequently, tracking at two axes is needed to increase the efficiency by decreasing this angle.

In summer, even with a dry weather, approximately 12% more energy could be produced by using dynamic photovoltaic panels. During winter, 70% more energy and as an annual average 31% more energy could be produced. Figure 7.2 shows the comparison of stationary and dynamic photovoltaic panels at different months [2].

To select the type of PV system (single axis or two axes) is a difficult decision as two-axis systems are much more expensive even though they are much more efficient. Slope will be changed during the year if it is decided to use one-axis tracking system. Inclination of panel changes depending one semester. For example, inclination of the system used during summer is different than others (Fig. 7.2).

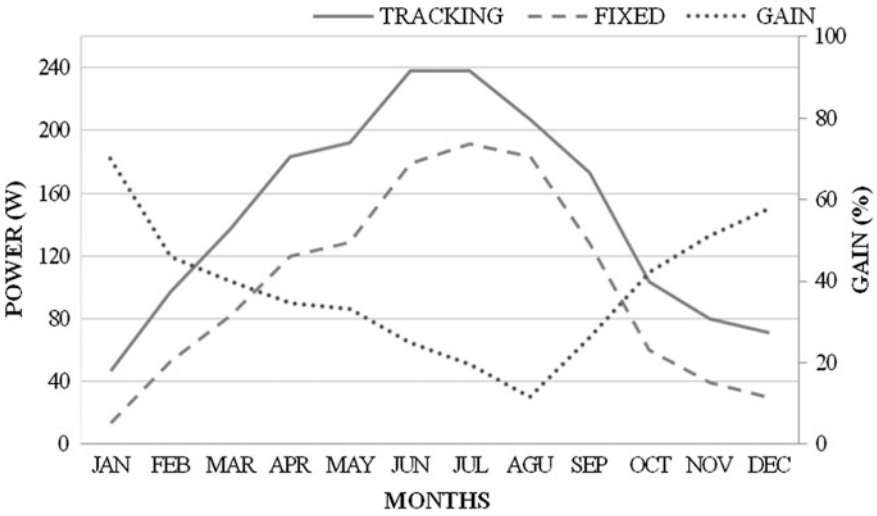

Fig. 7.2 Comparison of fixed and dynamic photovoltaic panels at different months for Diyarbakır (Turkey) in 2012 [2] [Gain = ($Power_{tracking}$ – $Power_{fixed}$) * 100/$Power_{tracking}$]

7.3 Sun Tracking Systems

Solar cells produce electrical energy using photon energy of sunlight. Output electrical energy is directly related with the amount of sunlight hitting onto the panel surface. Sunlight reaches earth with different angles during the day. So, to obtain maximum electrical energy by solar cells, PV systems should track the sun. This system aiming to maximize sunlight by tracking sun is called Sun Tracking System. Sun tracking systems are designed to track through West-East direction (one axis), West-East and North-South directions (two-axis) [3, 4]. Main aim of the all studies on photovoltaics is to decrease payback time of the system. It becomes possible only by increasing its efficiency. And efficiency could only be increased by increasing amount of solar radiation hitting on to the panel surface (Fig. 7.3).

Amount of radiation hitting on to panel surface is related with cosine of the angle between the sunlight and the normal of the surface. It means that efficiency is maximized when sunlight goes through the normal of the panel surface. This situation brings the need of a system to provide sunlight always normal to the panel surface by tracking the sun.

Finsten has developed the first tracker in 1962. Later Saavedra has added an automatic control unit to this mechanical system in 1963. This unit inspired to build Eppley pyrheliometer. Maldonado designed and constructed a sun tracker system at Technical University Federico Santa Maria [5, 6].

Main function of all tracking systems is to provide 1 or 2 degree of freedom to motion. In other words, main function is to supply sunlight at desired direction. There are many applications of single (one) axis tracking systems (SAT) as they provide power gain: Horizontal (HSAT), Vertical (VSAT), Tilted (TSAT) and Polar Aligned (PASAT). But studies on these systems are seen rarely in literature except one study which has concerned these systems. It is mentioned in this study that TSAT with 5 has collected 10% more radiation than HSAT where HSAT 15% more than VSAT. Also, it is found that PASAT collected 10% more than HSAT [3, 4].

Sun tracking systems are classified considering number of degree of freedom, position of turning axis or the systematic for sun tracking.

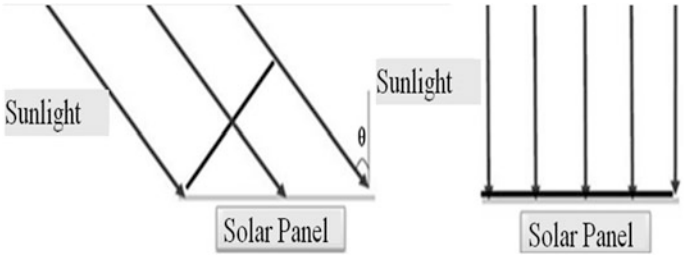

Fig. 7.3 Radiation hitting on to the panel (To provide maximum sunlight, θ should be equal to zero)

Fig. 7.4 One axis tracker system

7.3.1 *Classification Considering Number of Degree of Freedom*

One Axis Sun Tracking, Two Axis Sun Tracking.

One axis sun tracking systems: One axis tracking systems performs movement in either azimuth or vertical axis (Fig. 7.4). Reason to prefer single axis tracking system is to have free area where it is mounted [11]. For example, parabolic trough systems tracks using azimuth and most of the roof application of photovoltaic systems track using only height angle due to limited space. SAT is direct and cheaper way to get better efficiency. By using a simpler system, efficiency is increased. RayTracker, a tracking system manufacturer, implied that they improved the performance 23 and 38% when compared respectively with fixed angle modules and outer flat modules.

Two axis tracking systems: Two-axis tracking systems let movement in two axes (vertical and azimuth) which maximizes the efficiency of the tracking process. But SAT developers are questioning the efficiency as two axis tracking systems have additional installation, permitting and ongoing maintenance costs. Also higher defect risk related to having more moving parts compared to SATs is another concern. Moreover, two-axis systems need bigger spaces to place and consequently, to receive planning permits is much more difficult for them [3, 4].

7.3.2 *Classification Considering Position of Turning Axis*

Sun tracking systems are also classified considering joint axis. One axis tracking systems are classified as polar (Fig. 7.5), azimuth (Fig. 7.6) and horizontal (Fig. 7.7). On the other hand, two axis tracking systems are divided into two groups: azimuth and polar (Fig. 7.8).

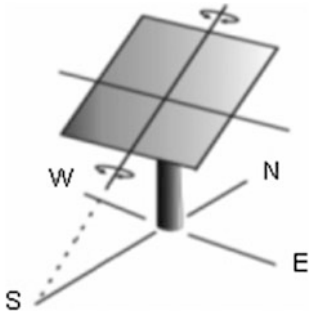

Fig. 7.5 Polar one axis tracking system

Fig. 7.6 Azimuth one axis tracking system

Panel surface of polar one axis tracking systems is tilted through south direction and azimuth angle is tracked by turning around the axis goes through weight center of panel surface. While panel is tracking azimuth angle, it also tracks height angle in the meantime due to its geometry. Thus, polar one axis tracking systems have higher performance values when compared with other one axis tracking systems from energy production perspective. Azimuth one axis tracking systems (Fig. 7.6), turns on a structure with tilted panels around the axis normal to ground. This kind of one axis tracking systems are preferred when there are big areas for the panels.

Horizontal one axis tracking systems turns on an axis parallel to ground (Fig. 7.7). This kind of tracking systems is generally used where height angle is approximately 90° like equatorial region (0°–±30°). Structure is compatible to move as groups. One motor could run many photovoltaic arrays at the same time. On the other hand, two axis systems are separated as polar and azimuth angles. Polar two axis systems only completes turning around its axis in a day. During the year it moves complying with sun movements and the issuing the commands comes from control system or sensor by the time.

On the other hand, two axis azimuth moves both around its axis and along two axis during a day and so its control is much more complex (Fig. 7.8).

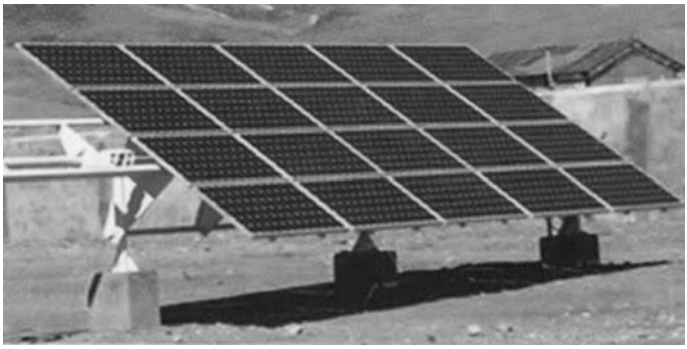

Fig. 7.7 Horizontal one axis tracking system

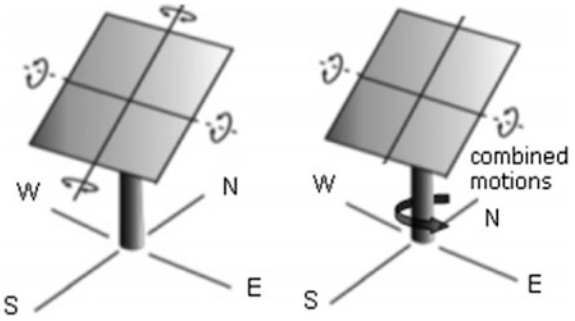

Fig. 7.8 Polar and Azimuth two axis tracking system

Setup and maintenance costs of sun tracking systems are higher than the fixed systems having certain angle. Thus, this kind of systems needs being robust, less maintenance required and high capacity to redeem their costs in long term. Also, this kind of systems should be built at rural areas and at the places where sunlight will be present from sunrise to sunset as the performance of sun tracking systems will be lowered in city centers and in the places where intense building shadows occurred (Fig. 7.9). At these places, costs related with sun tracking system and its sensors will be decreased as sun tracking will be able to be accomplished from one center for whole system. Any battery will not be needed as the system will be on grid and its cost will be removed.

7.3.3 Classification Considering Sun Tracking Systematic

Generally control circuits consisting of electronic sensor systems, controller, microprocessor and GPS are used to position the system to where it is required to be.

Fig. 7.9 A high capacity solar farm tracking sun in two axes

Passive sensor tracking: Some companies have tried to develop more energy efficient and cheaper tracking systems. For example, Portasol tracking systems—Australia—developed a hydraulic passive tracking system working according to thermal changes during the day to track the sun. Company states that electrical energy is not needed as tracking system does not include any electronic equipment, motor or gearbox. Figure 7.10 shows (a) panel stopped at night through west, at morning sun heats more the bottom part of tube and liquid expands through top, (b) panel turns until sun heats both tube equally, (c) panel tracks the sun with a certain angle by the time sun moves, (d) as a last step panel stopped at night through west [3, 4].

First decision that should be taken is to choose whether passive or active tracking system will be used. While low boiling point of compressed gas is used to move in passive tracking systems, motor, gearbox or hydraulic components are used in active tracking systems and they consume energy. Passive systems using gas pressure produced by sun does not consume energy but they are more insufficient to track the sun [3, 4].

Active sensor tracking: Two photoresistances and photovoltaic cell are used as a sensor for one axis tracking systems. These sensors place next to each other. So, both sensors are at same conditions. Sensor are directly connected to motor, generally direct current (DC) motors are used. The angle between panel surface and sunlight changes when sun moves. This leads to occur a difference between sensor outputs. Control circuit runs the motor and turns the system considering where more sunlight has come. Control circuit adjusts as panel surface is always normal to sunlight using this difference. The example by Poulek and Libra claimed their system was able to collect 95% of the energy with a $\pm 5^{\circ}$ tolerance. Figure 7.11 shows a sample structure [3, 4].

Chronological tracking: Systematic of chronological tracking is based on determining the movement positions before for every day during the year. Calculations are done for the related geographical region. System includes a pressor

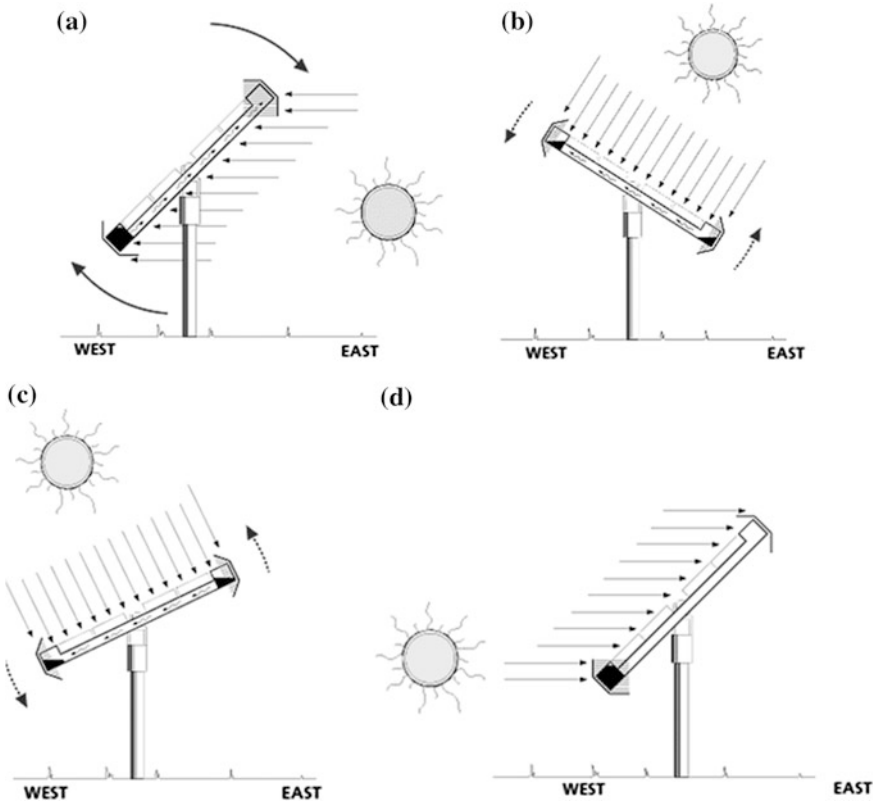

Fig. 7.10 Running of passive sensor tracking system. **a** Morning **b** Before noon **c** After noon **d** Night

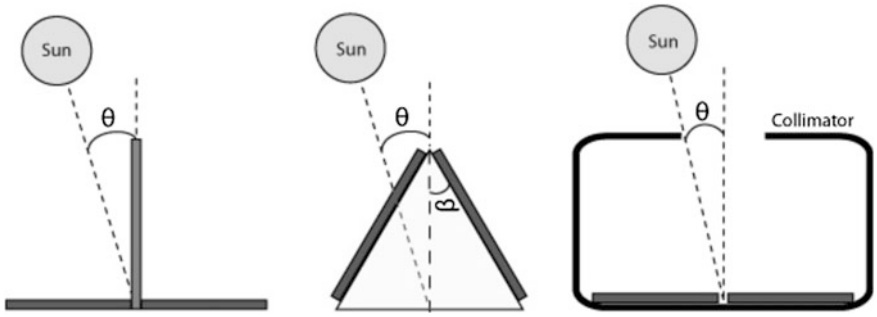

Fig. 7.11 Tracker sensor setups from *left* to *right*: divider, tilted mount, and collimator [4]

(microprocessor, PLC, computer etc.) making calculations. Latitude and longitude values of the region are given as constant input to the processor. Variable time value is taken from Real Time Clock. For the current date and time, position of sun

is calculated and system is turned as panel surface is normal to sunlight. Disadvantage of this system is that system continues to track and consume energy even during overcast sky.

7.4 Application

In this section, design and comparison of fixed and two axis photovoltaic panel system applications are given. Energy consumption is an important factor in two axis systems differing from one axis systems. It affects the system efficiency. To minimize this effect, literature is investigated and a low energy consumed DC motor having gearbox (Damper motor) is selected to use. Both used motors are identical. To be able to compare rightfully, both systems are used in same circumstances and panels having same trademark and model are used. Also, disturbing environmental factors (shadows, reflections etc.) are minimized as much as possible. Thus, a location where sunlight reached the panel all day during the whole year is chosen.

7.4.1 Fixed Photovoltaic Panel Systems

Widely used systems are fixed panel systems having low efficiency. Block scheme of fixed system is shown in Fig. 7.12 and picture of the used system is shown in Fig. 7.13. This system contains panel, measurement system, battery, inverter and load. Photovoltaic panel is placed as fixed considering geographical and meteorological data. Obtained power from panels are stored in batteries optimally.

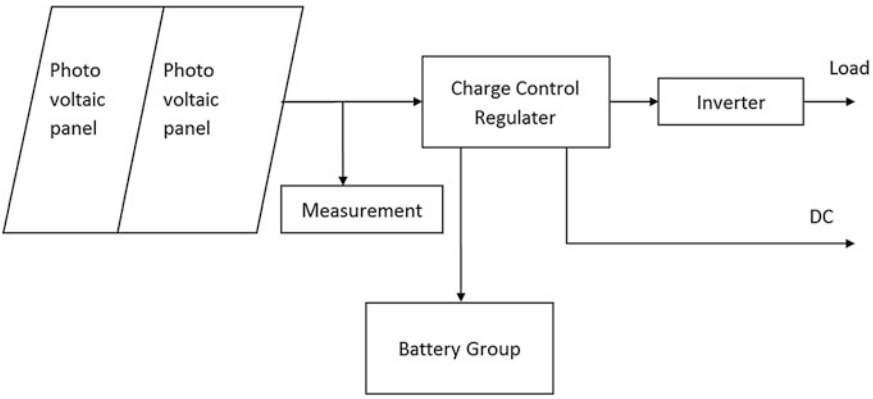

Fig. 7.12 Block scheme of fixed photovoltaic panel system

Fig. 7.13 Picture of the fixed photovoltaic panel system

Fig. 7.14 Picture of the used two-axis dynamic system [2]

7.4.2 Two Axis Photovoltaic Panel System (Sun Tracking System)

In this section, proposed two axis PV (sun tracking) system will be detailed. Consumed energy by the system has a higher priority in designing dynamic systems as it is related with the system performance. To minimize the consumed energy, literature is investigated and a new motor type (DC motor with gear unit) is found as a solution. Figure 7.14 shows the application of proposed system.

This dynamic system moves in two axes. East-West direction is defined as horizontal axis and North-South direction is defined as vertical axis. System is able to move in both axes at the same time as shown in Figs. 7.14 and 7.15. Two roller bearings are used as supports in the system. Wind load data of the last 10 years for

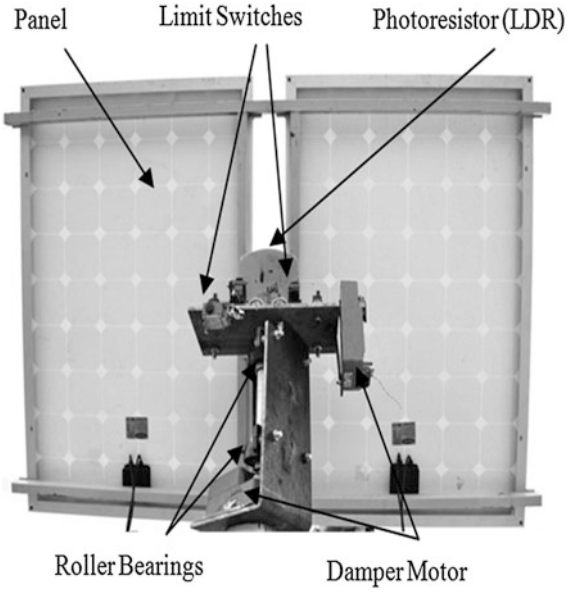

Fig. 7.15 Improved two-axis sun tracking system [2]

the application area is acquired from meteorology are so low that no need to be taken into account in design stage eventhough system is capable of resisting the loads over average [1].

Designed system consists of 2 Damper Motor (DM), 4 gel batteries (12 V–100 Ah), 2 PV panel (120 W), power inverter, solar battery charger, Maximum Power Point Tracker (MPPT), data acquisition card, Light-Dependent Resistors (LDR)s and mechanical system (Fig. 7.16).

Required energy to track the sun is provided from batteries. System tracks sun continuously at vertical and horizontal axis in sunny weather conditions. System is stopped by a LDR in cloudy weather conditions and at nights. Produced energy just after sun rise is enough to start the motor even if all energy in batteries is consumed. Because total need power for panels is 240 W while it is only 12 W for motors.

Two axes photovoltaic system contains solar panel moving through North-South and East-West directions. Solar panel is moved by the help of motor tracking sun by photoresistances (LDRs) and control system. So, it is profited from sun efficiently. Efficiency of photovoltaic panel is maximized when sunlight comes normal to panel surface. For this reason, control circuits need to command motor at certain points to provide panel angle as 90° to sunlight. This task is accomplished by control circuit by the help of photoresistances. Control system has electronic and electromechanical components. Suns movement is determined by 5 LDRs in control circuit to provide being normal to surface (Fig. 7.17). Also, time delay relays arranged with 3 s time difference are used to prevent PCBs work at the same time. 2 LDRs are used to measure movement in horizontal axis (East-West). 2 LDRs are used to measure movement in vertical axis (North-South) and one is to know whether being

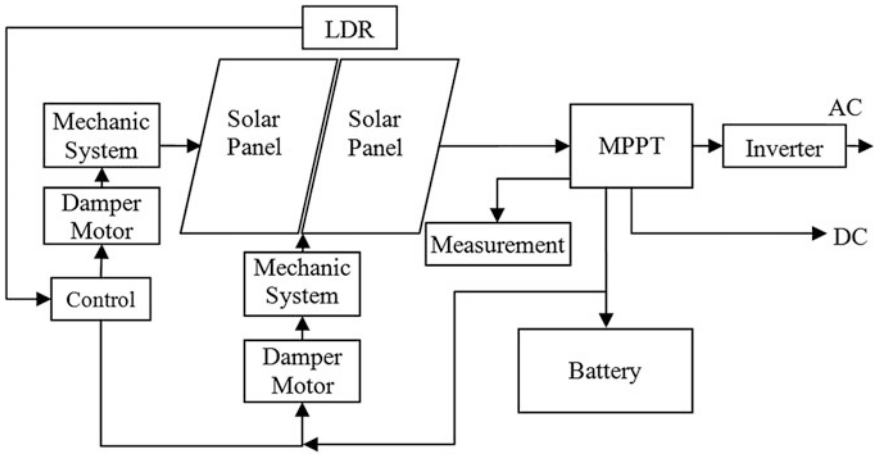

Fig. 7.16 Schematic view of two axis photovoltaic system (sun tracking system)

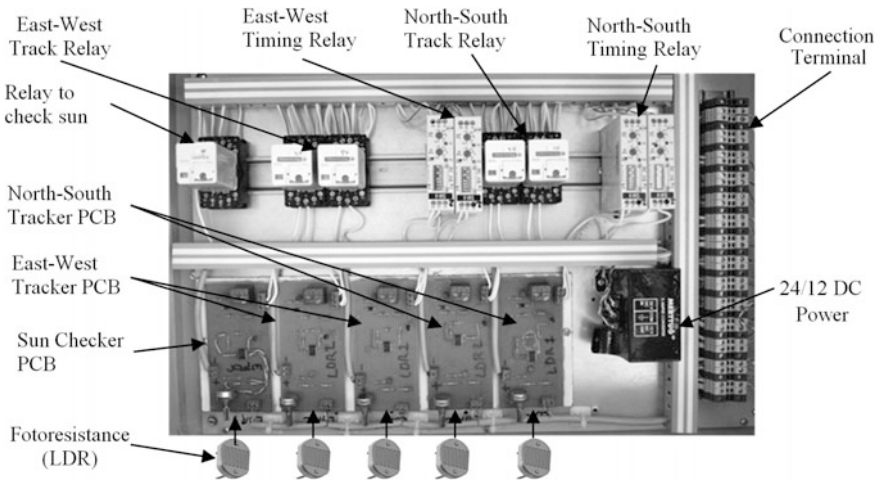

Fig. 7.17 Picture of the used control unit

sunny or not. Scheme of the sun checker PCB is shown in Fig. 7.18. So, damper motors are able to move panel to provide being normal to surface [1]. To determine the position of sun, several variables (irradiance, declination angle, azimuth angle, zenith angle etc.) should be defined or calculated. Control unit calculates these variables and then adjust the position of the system. Calculation of some important variables will be given in next sections.

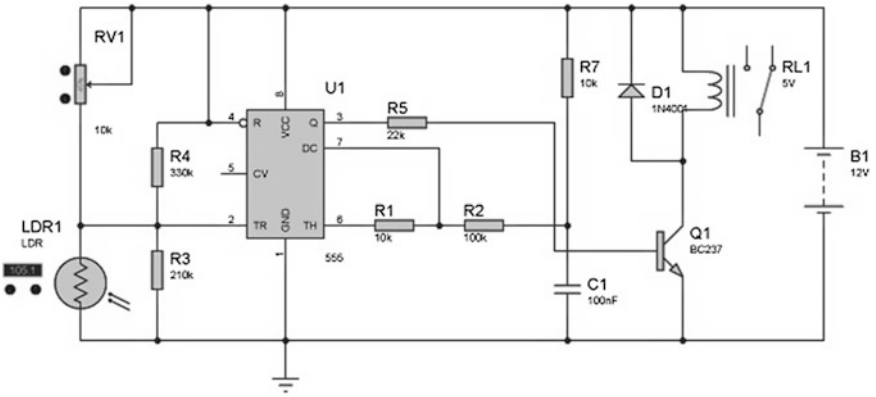

Fig. 7.18 Control circuit of sun checker PCB

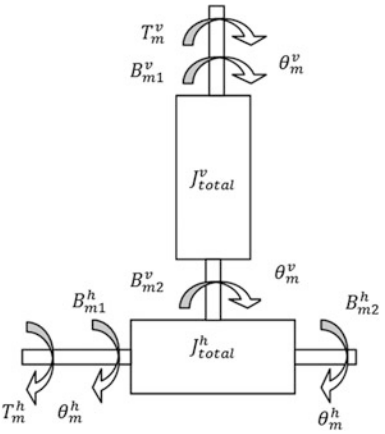

Fig. 7.19 Mechanical model of two-axis dynamic system [2, 10]

7.4.3 *Mathematical Modeling of Two Axis Photovoltaic System*

This system tracks in two axis. Even horizontal (East-west) and vertical (North-south) axis seems together, they are moving independently. System freely moves in horizontal and vertical as shown in Fig. 7.19. Two roller bearings ease movement in both axes. Wind load is omitted as it is seen low in Diyarbakır's last 10 year data (<3.5 m/s). But system is designed for overloads. Mathematical modelling of system for horizontal and vertical axis is done as seen below [2, 10].

In modeling the system, Eqs. (7.1)–(7.5) (derived for system shown in Fig. 7.20) are used for horizontal (East-West) and vertical (North-South) axis [2, 10].

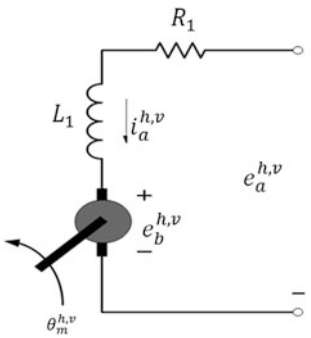

Fig. 7.20 Electric circuit of DC motor for horizontal and vertical axis [2, 10]

For vertical (North-South) axis of the system;

$$e_a^{vertical} = i_a^v R_1 + L_1 \frac{di_a^v}{dt} + e_b^v \tag{7.1}$$

$$e_b^{vertical} = K_b^v \frac{d\theta_m^v}{dt} \tag{7.2}$$

Torque constant → K_T^v
Electromotive force constant → K_b^v

$$e_a^v = i_a^v R_1 + L_1 \frac{di_a^v}{dt} + K_b^v \frac{d\theta_m^v}{dt} \tag{7.3}$$

Mathematical modeling of vertical axis of mechanical systems is (Fig. 7.19);
$B_t^v = B_{m1}^v + B_{m2}^v$ → Viscous damper coefficient of bearing

$$T_m^v = J_t^v \frac{d^2\theta_m^2}{dt^2} + B_t^v \frac{d\theta_m^v}{dt} \tag{7.4}$$

$$T_m^v = K_T^v . i_a^v \tag{7.5}$$

$J_t^v = 1$. Equivalent moment of inertia for torque of motors (kg · mm^2)

$$K_T^v \cdot i_a^v = J_t^v \frac{d^2\theta_m^2}{dt^2} + B_t^v \frac{d\theta_m^v}{dt} \tag{7.6}$$

Laplace transform of equation;

$$E_a^v(s) = I_a^v(s) R_1 + L_1 s I_a^v(s) + K_b^v s \theta_m^v(s) \tag{7.7}$$

$$K_T^v I_a^v(s) = J_t^v s^2 \theta_m^v + B_t^v s \theta_m^v(s) \tag{7.8}$$

Equation (7.7) is shortened as;

$$I_a^v(s) = \frac{E_a^v(s) - K_b^v s\theta_m^v(s)}{R_1 + L_1 s} \tag{7.9}$$

When Eq. (7.9) is substituted into Eq. (7.8);

$$K_T^v\left(\frac{E_a^v(s) - K_b^v s\theta_m^v(s)}{R_1 + L_1 s}\right) = J_t^v s^2\theta_m^v(s) + B_t^v s\theta_m^v(s) \tag{7.10}$$

$$K_T^v E_a^v(s) - K_T^v K_b^v s\theta_m^v(s) = [J_t^v s^2\theta_m^v(s) + B_t^v s\theta_m^v(s)](R_1 + L_1 s) \tag{7.11}$$

$$\begin{aligned} K_T^v E_a^v(s) = {} & J_t^v s^2\theta_m^v(s)R_1 + J_t^v s^3 L_1\theta_m^v(s) + B_t^v sR_1\theta_m^v(s) \\ & + B_t^v s^2 L_1\theta_m^v(s) + K_T^v K_b^v s\theta_m^v(s) \end{aligned} \tag{7.12}$$

$$K_T^v E_a^v(s) = \theta_m^v(s)[J_t^v s^3 L_1 + (J_t^v R_1 + B_t^v L_1)s^2 + (B_t^v R_1 + K_T^v K_b^v)s] \tag{7.13}$$

$$\frac{\theta_m^v(s)}{E_a^v(s)} = \frac{K_T^v}{J_t^v L_1 s^3 (J_t^v R_1 + B_t^v L_1)s^2 + (B_t^v R_1 + K_T^v K_b^v)s} \tag{7.14}$$

It is not needed to derive the equations for horizontal axis because both axes have same situation [2–10].

7.5 Modeling of Sun Tracking

As same principles are valid for both axes, modelling for one axis will be enough in designing system. Working principle of system is shown in Fig. 7.21. Four LDRs helped to direct panel into the right direction by giving correct angle (between normal and coming sunlight). Location of LDRs are adjusted as every LDR has the same amount of sunlight when sunlight comes as normal to panel surface. The current produced by LDRs are amplified by an operational amplifier and measured change in current is accepted as error which shows that sunlight doesn't come to surface normal. Then control unit drives the motor to turn the system into position here error value becomes zero.

Coordinate System: Center of coordinate system is assumed to be on output gear. When reference axis is accepted as the stationary body of DC motor, all rotations are measured around this axis. Sun axis (line connecting center of output gear with sun) states $\theta_r(t)$ reference angle (Fig. 7.22). Purpose of control system is to minimize the angle difference, $\alpha(t)$, between B_t^v and $\theta_0(t)$ where $\theta_0(t)$ represents the angle between reference axis and tracking axis [10].

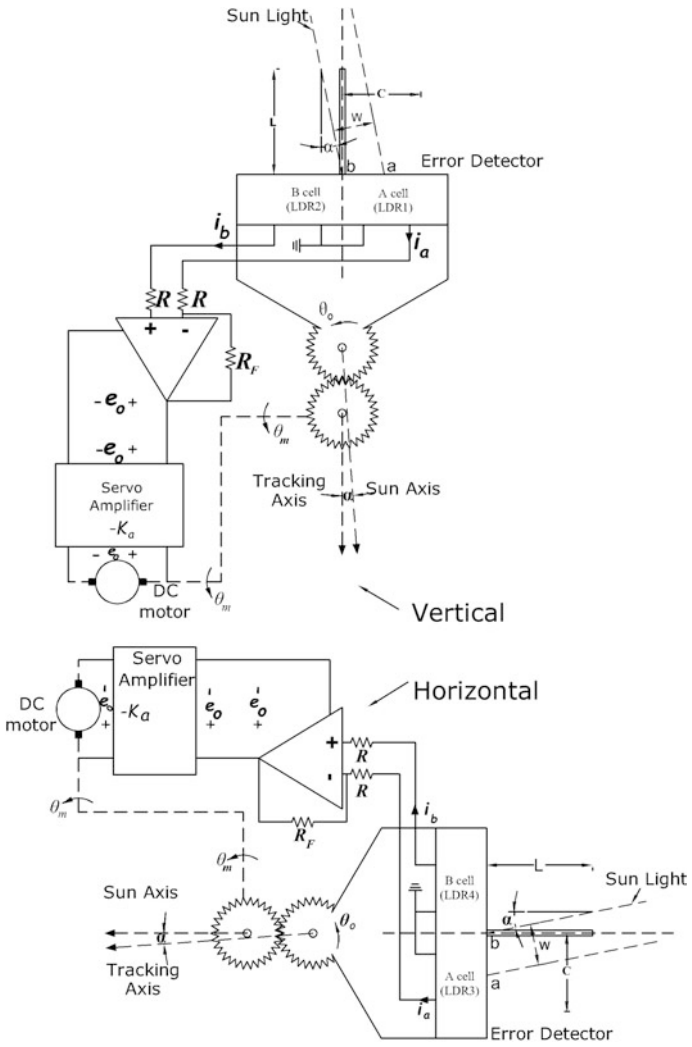

Fig. 7.21 Working principle scheme of improved two-axis solar tracking system [2, 10]

$$\alpha(t) = \theta_r(t) - \theta_0(t) \tag{7.15}$$

Error Detector: When tracking axis overlaps with sun axis: $\alpha(t) = 0$ and $i_a(t) = i_b(t) = I$ or $i_a(t) - i_b(t) = 0$. As shown in Fig. 7.21, sunlight having W width reaches at certain α angle to A cell with oa width and to B cell with ob width [10].

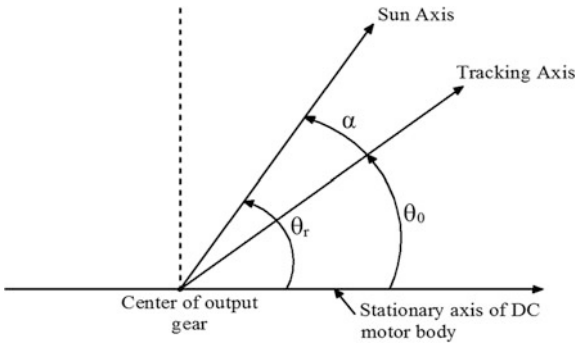

Fig. 7.22 Coordinate system of sun tracking system

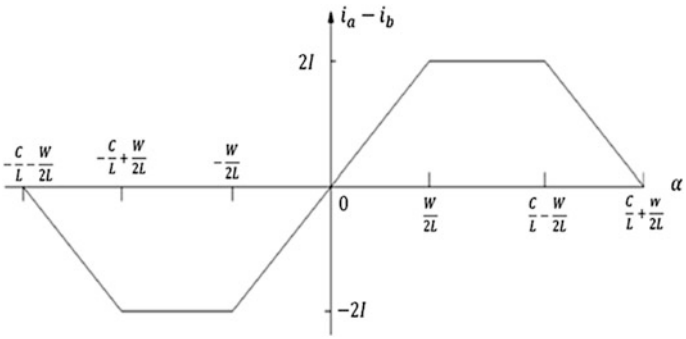

Fig. 7.23 Nonlinear characteristic of error detector

$$oa = \frac{W}{2} L \tan \alpha(t) \tag{7.16}$$

$$ob = \frac{W}{2} - L \tan \alpha(t) \tag{7.17}$$

On the other hand, when 2I is the maximum current of a LDR and $0 \leq \tan \alpha(t) \leq W/2L$ as $i_a(t)$ current is related with oa and $i_b(t)$ current is related with ob;

$$i_a(t) = I + \frac{2LI}{W} + \tan \alpha(t) \tag{7.18}$$

$$i_b(t) = I - \frac{2LI}{W} + \tan \alpha(t) \tag{7.19}$$

Sunlight goes only onto A cell (LDR1) and $i_a(t) = 2I$, $i_b(t) = 0$ when $W/2L \leq \tan \alpha(t) \leq (C - W/2)L$. When $(C - W/2)L \leq \tan \alpha(t) \leq (C + W/2)L$, $i_a(t)$ current goes through zero from 2I. When $\tan \alpha(t) \leq (C + W/2)L$, $i_a(t) - i_b(t) = 0$. Nonlinear characteristic shown in Fig. 7.23 can be used to define error detector. As $\alpha(t)$ angle is very small, $\alpha(t)$ is used instead of $\tan \alpha(t)$ [10].

Operational Amplifier: There is following relation between $i_a(t)$ and $i_b(t)$ and operational amplifier:

$$e_o(t) = -R_F[i_a(t) - i_b(t)] \tag{7.20}$$

Servo Amplifier: Gain of servo amplifier is –K. Output of servo amplifier as shown in Fig. 7.21 could be written as;

$$e_a(t) = -Ke_o(t) \tag{7.21}$$

Damper Motor: The systems using solar panels produce DC power and it is preferred to use DC motors and devices working with DC power in the system. As a matter of fact that an inverter will be needed for alternative current (AC) systems and both cost of inverter and losses of inverter will decrease the efficiency of system.

Damper motors are the AC motor types which can easily control under varying loads. Easiness to control and to start running at desired speed makes DC motors preferred in tracking systems. Moment could be changed by changing armature current and speed could be changed by changing voltage in motors by the help of electronic circuits. The motor used in the system is a brushed permanent magnet DC motor. DM consists of DC motor and a coupled gear unit (having 15 gears). Moment of DM is increased by the help of gearbox (16 Nm). For both axes, same motor is used. Movements through North-South and East-West of panels in the system are performed slowly considering movement of sun. Selected DC motor with a gear unit is shown in Fig. 7.24 and its specifications are given in Table 7.1 [1, 2].

Damper motor consists of two components. First is gear unit and second is DC motor. Angular position θ_0 of output gear is related with angular position of motor θ_m and 1/n gear ratio.

$$\theta_o = \frac{1}{n}\theta_m \tag{7.22}$$

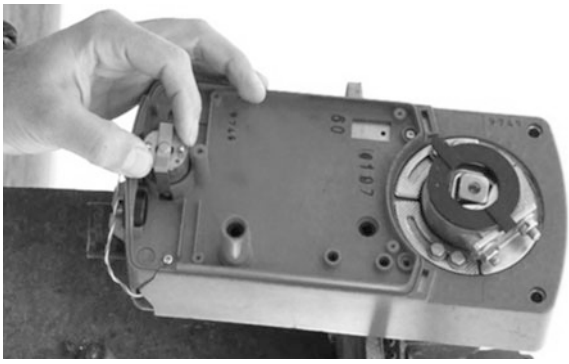

Fig. 7.24 Picture of used DC motor with gearbox (Damper motor)

Table 7.1 Specification of the motor used in the study

Parameter	Unit	Value
Voltage	V	24 DA/220 AA
Current	A	0, 5
Power	VA	12
Moment	Nm	16
Rotation angle	°	360
Rotation time	s	320
Weight	g	1200

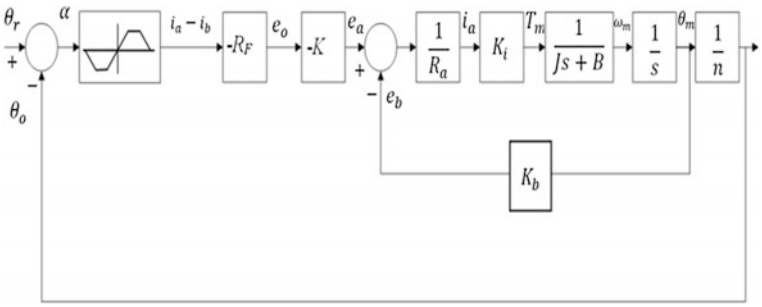

Fig. 7.25 Block diagram of sun tracking system [2, 10]

While J and B represents inertia and friction coefficient of motor shaft of DC motor;

$$e_a(t) = R_a i_a(t) + e_b(t) \tag{7.23}$$

$$e_b(t) = K_b \omega_m(t) \tag{7.24}$$

$$T_m(t) = K_i i_a(t) \tag{7.25}$$

$$T_m(t) = J\frac{d\omega_m(t)}{dt} + B\omega_m(t) \tag{7.26}$$

Block diagram showing functional relations of system is given in Fig. 7.25. It is not needed to derive equations for vertical axis as both axes has same situation.

7.6 Experimental Results

In this section, data obtained from fixed and two axis systems are compared. Diyarbakır is chosen as the location where the area of highest solar radiation potential in Turkey is and experiments are run on the roof of Engineering Faculty of Dicle University in this city. Efficiency of the designed sun tracking system is observed

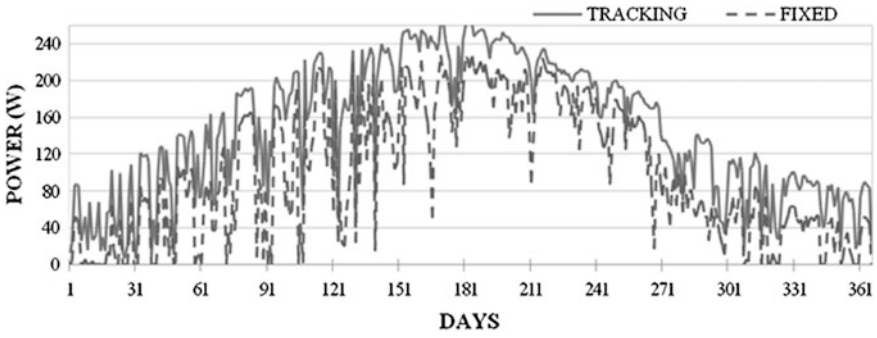

Fig. 7.26 Obtained output power of fixed and two axis systems during 2012 in Diyarbakır [2]

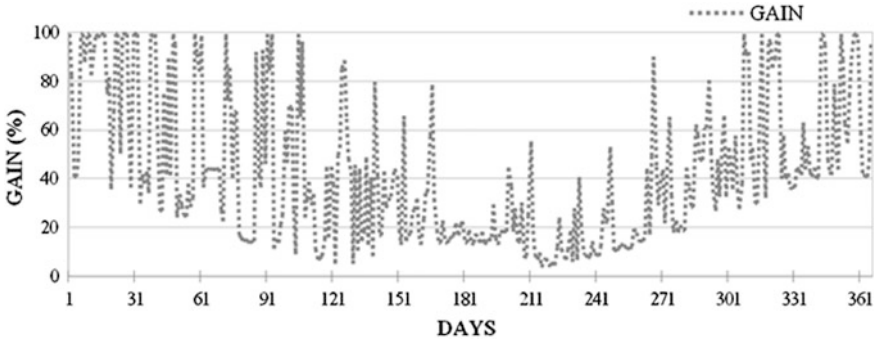

Fig. 7.27 Gain of two axis system during 2012 in Diyarbakır compared to fixed system [2] [Gain = ($Power_{tracking}$ – $Power_{fixed}$) * 100/$Power_{tracking}$]

under different weather conditions during the year [2]. To be able to compare the designed tracking system with the fixed system placed at the same location, panels having same trademark and model are used under same conditions. Comparison is done for the whole year data. Also, measurements are compared with the meteorological data. These data belong to the interval between 01.01.2012 and 30.12.2012. Measurements are done at each 10 min daily. Then, hourly and daily data are calculated using minute measurement data and also monthly and annual data are derived from daily data. Obtained data are shown in Figs. 7.26 and 7.27.

Energy consumption of two-axis sun tracking system is seen as low as not to take into consideration to calculate. As seen in Fig. 7.28, the permanent magnet DC motor of 12 W has a small structure and total consumed power during a day doesn't exceed 3 Wh. As sun tracking system stop at west position at sunset, at sunrise system turns to east for 3 min and most of the energy consumption occurs at this stage (0.6 Wh) as shown in Fig. 7.28. Then, until sunset energy is consumed at small values (as an average 0.1 Wh) according to movement of sun at horizontal and vertical axis.

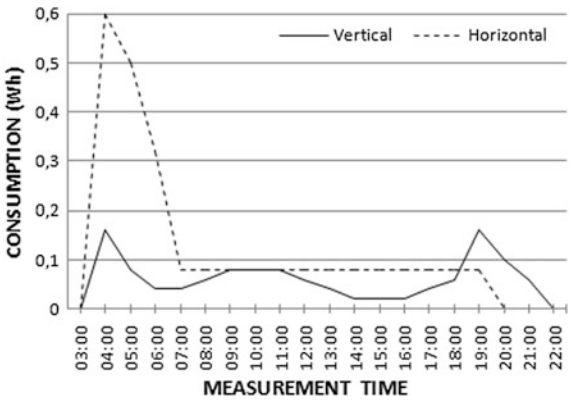

Fig. 7.28 Daily energy consumption of the used motor

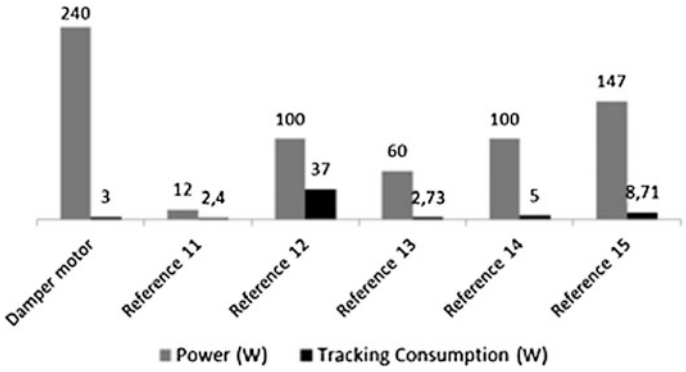

Fig. 7.29 Comparison of produced and consumed energies of tracking systems [2, 11–15]

Disadvantage of sun tracking systems is its cost and consumed energy during tracking. Damper motor, used firstly in this system, has decreased both cost and also the consumed energy during tracking. Power of used motor is equal to 12 W. Daily power consumption even for the longest day (21 June) didn't exceed 3 Wh. DC motor is generally used in sun tracking system. Asynchronous motor is also used in several studies [1–3]. Obtained power is converted to AC by the help of an inverter in these studies. In this case, inverter losses decrease energy efficiency. Comparison with previous studies has shown that the system using damper motor consumed less energy as shown in Fig. 7.29 [1–4]. There are two reasons that damper motor consumes less energy. First reason is to have less power (12 W) and second reason is to have many gears (15 gears). To use these motors is recommended in tracking systems as sun moves slowly.

7.7 Conclusions

Energy production from sun by using panels is related with their cost and efficiency. Having high cost (1 W = 1$) and low efficiency (10–25%) of panels led to develop sun tracking systems. The feasible way to reduce the cost and produce more energy in a unit panel area is to use sun tracking systems. Even setup cost is higher than fixed systems; they are more advantageous when produced energy and occupied area is considered. Today it is inevitable to use these systems.

Efficiency of photovoltaic systems used to produce electrical energy directly from sun energy is still low. Most difficult task for sun tracking system which is one of the methods applied to increase efficiency is to minimize the consumed energy and cost. Panel cost is much higher than design and consume energy costs of tracking system. Also, need surface area will be low as power obtained from a unit panel area is higher [2, 17].

Disadvantages of the sun tracking systems are setup cost and the consumed energy during tracking. Using damper motor, contrary to general application, in designed system and having more basic control circuit made possible to decrease both cost and consumed energy during tracking. In the mentioned study 12 W damper motor is used and daily consumed power is not reaching even 3 W/h during the longest day (21 June). Design of control circuit is critical as it provides tracking at both horizontal (West-East) and vertical (North-South) direction during the day. Developed circuit stops the system at cloudy weather and night and so it helps saving energy.

Obtained data showed that efficiency of newly designed two axis sun tracking system is 70% higher during winter, 11% higher during summer and 31.67% higher as an average during the year when compared with fixed system. Figure 7.2 shows that fixed system is also producing high power during summer where sun is generous even two axis system is given better results. So, power difference is becoming low during summer. But this difference changes during winter and efficiency of two axis system becomes higher.

Another important factor for tracking system is how much cheaper and light mechanical components are built. This factor affects directly payback time. New studies on minimizing its effect will make tracking system cheaper and advantageous and sun as a clean and renewable energy resource will continue to heat and give energy to next generations.

Acknowledgements We would like to thank the Research Council of Scientific Projects Coordinator—Dicle University.

References

1. Kentli F, Yilmaz M (2015) Mathematical modelling of two-axis photovoltaic system with improved efficiency. Elektron Elektrotech 21:40–43
2. Yılmaz M (2013) Determination of methods deriving electrical energy from solar energy and optimum efficiency by solar tracking system, PhD thesis, Department of Electrical Education, Marmara University, Istanbul
3. Yilmaz M, Kentli F (2015) Increasing of electrical energy with solar tracking system at the region which has Turkey's most solar energy potential. J Clean Energy Technol 3:287–291
4. Catarius A, Christiner M (2010) Azimuth-altitude dual axis solar tracker, Graduate thesis, W. P.I, Engineering, Massachusetts
5. Roth P, Georgiev A, Boudinov H (2005) Cheap two axis sun following device. Energy Convers Manag 46:1179–1192
6. Samimi J, Soleimani EA, Zabihi MS (1997) Optimal sizing of photovoltaic systems in varied climates. Sol Energy 60:97–107
7. Helwa NH, Bahgat ABG, El Shafee AMR, El Shenawy ET (2000) Maximum collectable solar energy by different solar tracking systems. Energy Source 22:23–34
8. Akkilic K, Ocak YS, Yilmaz M (2015) Analysing enhancement of electricity generating capacity with solar tracking system of the most sunning region of Turkey. J Clean Energy Technol 3:291–295
9. Appleyard D (2012) Solar trackers: facing the sun, renewable energy world
10. Kho CB (2002) Otomatik Kontrol Sistemleri, Yedinci Baskı, Literatür Yayıncılık, İstanbul, pp 207–209
11. Drury E, Lopez A, Denholm P, Margolis R (2014) Relative performance of tracking versus fixed tilt photovoltaic systems in the USA. Prog Photovolt Res 22:1302–1315
12. Şenpinar A, Cebeci M (2012) Evaluation of power output for fixed and two-axis tracking PVarrays. Appl Energy 92:677–685
13. Mecasolar Products Inc. (2014) Mecasolar two-axis 60P, Spain
14. Huang BJ, Ding WL, Huang YC (2011) Long-term field test of solar PV power generation using one-axis 3-position sun tracker. Sol Energy 85:1935–1944
15. Salsabila A, Suhaidi S, Mohd ZAAK (2013) Power feasibility of a low power consumption solar tracker. Procedia Environ Sci 17:494–502
16. Tarabsheh A, Etier I, Nimrat A (2012) Energy yield of tracking PV systems in Jordan. Int J Photoenergy 2012:1–5
17. Burduhos BG, Visa I, Neagoe M, Badea M (2015) Modeling and optimization of the global solar irradiance collecting efficiency. Int J Green Energy 12:743–755
18. Lee CY, Chou PC, Chiang CM, Lin CF (2009) Sun tracking systems: a review. Sensors 9:3875–3890
19. Reisi AR, Moradi MH, Jamas S (2013) Classification and comparison of maximum power point tracking techniques for photovoltaic system: a review. Renew Sust Energy Rev 19:433–443
20. Mousazadeh H, Keyhani A, Javadi A, Mobli H, Abrinia K, Sharifi A (2009) A review of principle and sun-tracking methods for maximizing solar systems output. Renew Sust Energy Rev 13:1800–1818

Chapter 8
Maximum Power Point Tracking (MPPT) Algorithms for Photovoltaic Systems

Ersan Kabalci

Abstract The solar energy have become a challenging area among other renewable energy sources (RESs) since the photovoltaic (PV) systems have the advantages of not causing pollution, having low maintenance, and long-lasting operation life. Besides these advantages, a PV system has several drawbacks such as considerably higher installation cost comparing some other RESs, and limited efficiency ranges between 9–18%. The feasibility analyses have a great role in order to determine the most appropriate plant site before installation. On the other hand, the operating analyses and improvements based on maximum power point tracking (MPPT) are quite important to increase the harvested total energy. The intermittent characteristic and perturbing power curve of a PV module is one of the most important defects that should be tackled to increase the generation efficiency. The power-voltage (P-V) and current-voltage (I-V) curves are main efficiency indicators of a PV system that exhibit nonlinear characteristics in its natural structure. Furthermore, the generated maximum power with a PV panel depends on two main quantities of temperature and irradiation. However, it is possible to increase the generated power up to maximum rates by MPPT algorithms. This chapter introduces most widely used algorithms respecting to their implementation and utilization properties. The indirect, direct, and computational methods are presented considering their advantages and disadvantages. The conventional and novel algorithms are explained with flowcharts and analytical details in order to provide clear comparison. The artificial methods are expressed in the last section where fuzzy logic, artificial intelligence, and optimization-based approaches are discussed.

Keywords Maximum power point tracking (MPPT) · Perturb and observe · Incremental conductance · Fuzzy logic controller · Artificial neural network · Particle swarm optimization

E. Kabalci (✉)
Faculty of Engineering and Architecture, Department of Electrical and Electronics Engineering, Nevsehir HBV University, Nevsehir, Turkey
e-mail: kabalci@nevsehir.edu.tr

N. Bizon et al. (eds.), *Energy Harvesting and Energy Efficiency*,
Lecture Notes in Energy 37, DOI 10.1007/978-3-319-49875-1_8

Abbreviation and Acronyms

ABC	Artificial Bee Colony
AF	Activation Function
ANN	Artificial Neural Network
COA	Centroid of Area
CV	Constant Voltage
EMI	Electromagnetic Interference
ESS	Energy Storage System
FLC	Fuzzy Logic Controller
GA	Genetic Algorithm
HC	Hill Climbing
IncCond	Incremental Conductance
I-V	Current-Voltage
MLI	Multilevel Inverter
MLP	Multilayer Perceptron
MPPT	Maximum Power Point Tracking
OV	Open Voltage
P&O	Perturb and Observe
PSO	Particle Swarm Optimization
PV	Photovoltaic
P-V	Power-Voltage
RES	Renewable Energy Source
SCPB	Short-Current Pulse-Based
THD	Total Harmonic Distortion

8.1 Chapter Overview

The maximum power point tracking (MPPT) is an algorithm that is associated with dc-dc power converters and inverters to track maximum power point during energy conversion process. Thus, the generated energy is maximized in this way. Although there are several methods proposed to implement an MPPT system, there are two algorithms known as "perturb and observe" (P&O) and the "incremental conductance" (IncCond methods are widely used since they are commercially preferred. However, simpler algorithms lack to provide the anticipated performance on the output power. The recent researches on MPPT algorithms exhibited that more sophisticated algorithms yield better outputs comparing to widely known basic methods. Therefore, a wide variety of numerical methods including fuzzy logic, neural networks and other computational methods are proposed. Although these recent algorithms require increased complexity, they easily compete with malfunctions of previous methods in terms of partial shading, misdirection during tracking, power fluctuations around MPP, and inadequate performance at low irradiance.

In this chapter, the MPPT algorithms have been analyzed in there groups where the first group includes indirect algorithms while others are described as direct algorithms, and numerical algorithms. The groups have been allocated considering the progress on methods and approaches where the indirect and direct algorithms are known as conventional MPPT techniques. The most recent computational algorithms including genetic algorithms, particle swarm optimization (PSO) algorithms, and artificial bee colony algorithms (ABC) are the hottest topics in MPPT algorithms. The trade-off between conventional MPPT methods and recent algorithms are related to complexity in algorithm and to cost in application.

This chapter is dedicated to these widely used MPPT algorithms of PV systems. Therefore, the initial sections introduce analytical background of a PV panel at a glance, and power curves of any PV panel in brief. Afterwards, the power conversion system of a PV plant with power converters is described to emphasize the application of a generic MPPT block in power conversion issues in the following section. The MPPT algorithms have been presented in three sections including indirect algorithms, direct algorithms, and numerical algorithms with their application examples.

8.2 Basic Principles of Photovoltaic Energy Conversion

Edmund Becquerel, a French physicist, firstly discovered the photovoltaic (PV) energy by generating electricity when he illuminated an electrode in electrolyte solution in 1839. However, Adams and Day made the first practical application of PV by applying the PV energy to solid materials about 40 years later. The primary PV cells made of selenium were performing almost 1 or 2% efficiency. Probably Einstein was the most important contributor of PV by explaining theoretical PV effect in 1904 that brought a Nobel Prize to him in 1923. The first generation silicon PV cells were produced by 1940s and 1950s by Czochralski, a Polish scientist. The solar panels constituted with numerous PV cells were commercially available in 1963 when Sharp Corporation succeeded in producing practical silicon photovoltaic modules. Although there were several applications of solar cells seen in Vanguard I space satellite in 1958, Explorer III, Vanguard II, and Sputnik-3 in 1959. World's first largest PV array was built in Japan with 242 Wp rated power in 1963 [1–4].

A PV energy conversion system is composed of a PV module, a dc-dc converter, an inverter, and preferably an energy storage system (ESS). The PV module is constituted by PV cells that are series and parallel connected to generate the desired rated power. The cells are produced in monocrystalline or polycrystalline structure depending to the purity of semiconductor [5–7]. The polycrystalline cells that provide limited efficiency around 13–14% are less efficient comparing to the monocrystalline that the efficiency increases up to 20%.

The analytical model of a PV cell is designed referring to one-diode electrical equivalent as shown in Fig. 8.1. This circuit includes a photocurrent source, a diode, and serial and shunt resistors that are known as *one-diode* or *five-parameter* model [8]. The calculations of the one-diode model seen in Fig. 8.1 are depended to the output current;

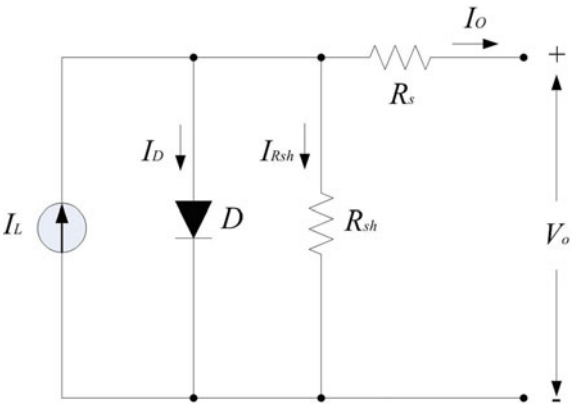

Fig. 8.1 Single-diode electrical equivalent of a mono or polycrystalline PV cell

$$I_o = I_{PV} - I_D(V) - I_{sh}(V) \tag{8.1}$$

where (V) depicts the dependency of diode and resistor currents to terminal voltage while they are independent from irradiation value.

The Shockley equation is called to express the semiconductor diode behavior to define I_D as given in Eq. (8.2);

$$I_D = I_R(e^{\frac{V_D}{\eta V_T}} - 1) \tag{8.2}$$

where I_D is current and V_D is voltage of the diode, I_R is reverse blocking current, V_D is thermal voltage, and η is the ideality factor of the diode [9, 10]. The current of shunt resistor I_{sh} is rearranged regarding to its dependence to terminal voltage as seen in (8.3);

$$I_{sh} = \frac{V_O + I_O R_S}{R_{sh}} \tag{8.3}$$

where the equivalence shown in Eq. (8.1) is achieved as seen in Eq. (8.4) referring to irradiation current I_{PV}, thermal voltage V_T, and other parameters denoted above [8–10];

$$I_O = I_{PV} - I_R\left(e^{\frac{V_O + I_O R_S}{\eta_I V_T}} - 1\right) - \frac{V_O + I_O R_S}{R_{sh}} \tag{8.4}$$

There are several other equivalent circuit models presented in the literature to increase the reliability of the PV cell design. The implementation structure of the cell is expressed by additional electrical elements in the improved models. One of these models that is being extensively studied one, amorphous silicon PV cell is illustrated in Fig. 8.2. The polymer and amorphous silicon based PV cell is constituted with an additional dependent current source controlled by photocurrent and terminal voltage.

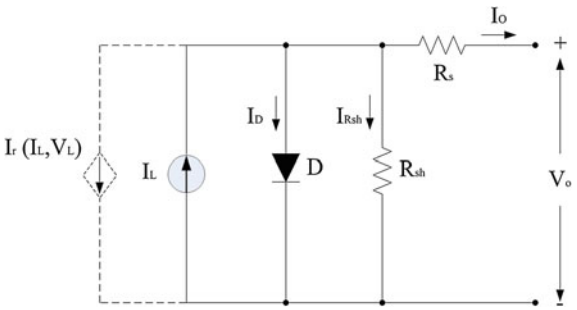

Fig. 8.2 Single-diode electrical equivalent of an amorphous silicon PV cell

This equivalent circuit is obtained by modifying the well-known five-parameter model, and the calculations are rearranged considering the dependent current source. The output current equation is rearranged by taking into account the additional dependent current source as seen in Eq. (8.5);

$$I_O = I_{PV} - I_D(V) - I_{sh}(V) - I_r(I_{PV}, V_L) \tag{8.5}$$

The photocurrent I_{PV} is proportional to the irradiation ψ where the dependent source current can be converted to $I_r(I_{PV}, V_L) = I_r(\psi, V_L)$. Since the output current of amorphous silicon PV cell is calculated regarding to the Eq. (8.6) that depicts the dependency of diode and shunt current to the irradiation and terminal voltage;

$$I_O = I_{PV} - I_D(\psi, V) - I_{sh}(\psi, V) \tag{8.6}$$

A PV module is composed of a number of series cells N_S as 36, 60, or 72 while the cells are connected in series and parallel N_P in PV arrays as shown in Fig. 8.3 where the arrangement defines the maximum output voltage V_M and maximum output current I_M. The maximum output currents of a module I_M and an array I_A are calculated regarding to Eq. (8.4) as follows [10–12];

$$I_M = I_{PV} - I_O\left(e^{\frac{V_M + I_M N_S R_S}{\eta_I N_S V_T}} - 1\right) - \frac{V_M + I_M N_S R_S}{N_S R_{sh}} \tag{8.7}$$

$$I_A = N_P I_{PV} - N_P I_O\left(e^{\frac{q\left(V_A + I_A \frac{N_S}{N_P} R_S\right)}{\eta_I N_S V_T}} - 1\right) - \frac{V_A + I_A \frac{N_S}{N_P} R_S}{\frac{N_S}{N_P} R_{sh}} \tag{8.8}$$

The basic open-circuit and short-circuit currents of a PV cell can be derived referring to Eq. (8.4) as given by respectively;

$$0 = I_{PV} - I_O\left(e^{\frac{V_{OC}}{\eta_I N_S V_T}} - 1\right) - \frac{V_{OC}}{R_{sh}} \tag{8.9}$$

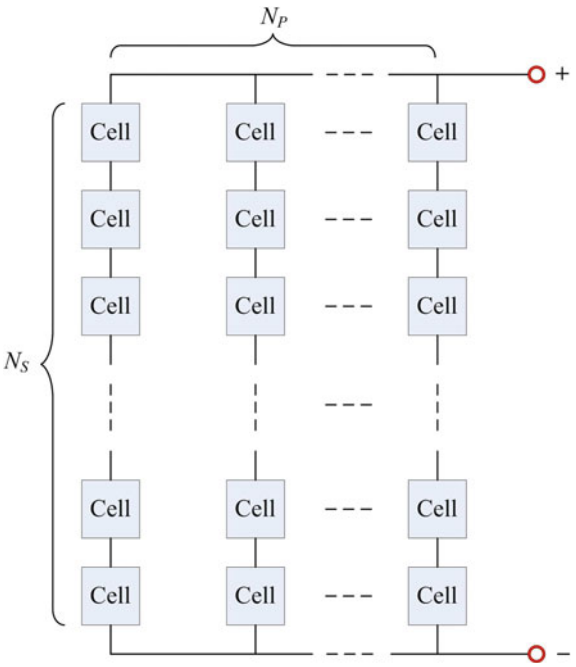

Fig. 8.3 Electrical connection diagram of a PV array

$$I_{SC} = I_{PV} - I_O\left(e^{\frac{I_{SC}R_S}{\eta_I N_S V_T}} - 1\right) - \frac{I_{SC}R_S}{R_{sh}} \tag{8.10}$$

The verification of a PV model is performed by measuring the current-voltage *I-V* and power-voltage *P-V* curves against various irradiation values. It is clear that the basic maximum power current–voltage pair belongs to the *I–V* characteristic that Eq. (8.4) is recalled to define the following maximum power relation;

$$I_M = I_{PV} - I_O\left(e^{\frac{V_M + I_M R_S}{\eta_I N_S V_T}} - 1\right) - \frac{V_M + I_M R_S}{R_{sh}} \tag{8.11}$$

A PV module is modeled referring to the relations given above that define the effect of R_s, R_{sh}, I_o, I_{PV}, and η. The curves shown in Fig. 8.4 are produced by changing the irradiation value from 200 W/m^2 to 1000 W/m^2. The axis on the left-hand side of figure represents the current variation I-V curve, while the right-hand side illustrates the output power of PV panel in terms of P-V curve. The effect of irradiation on current, power, and voltage can be easily seen from the graphic. The curves generated by the modelled PV panel are verified by comparing to datasheet of commercial PV modules at 240 Wp power [13].

The parameters of the modeled PV module are given in Table 8.1 where each parameter is verified in the simulation studies. The values are provided for 25 °C cell temperature and 1000 W/m^2 irradiation level.

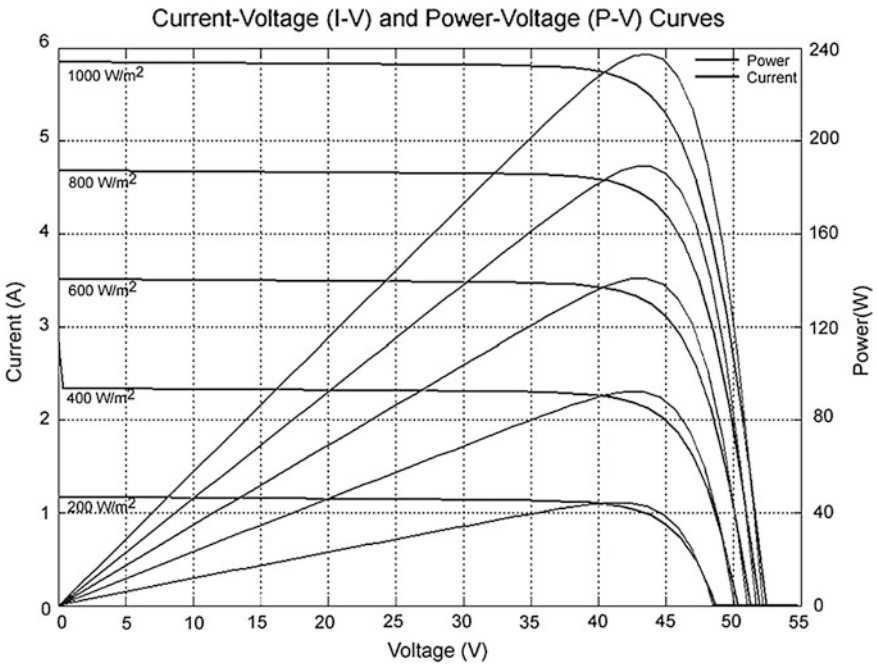

Fig. 8.4 I-V and P-V characteristics of a 240 Wp PV module at various irradiation conditions

Table 8.1 Electrical parameters of the modeled PV module [13]

Quantity	Value
Rated power (Pmax)	240 W
Open circuit voltage (V_{OC})	52.4 V
Maximum power voltage (V_{MPP})	43.7 V
Short circuit current (I_{SC})	5.85 A
Maximum power current (I_{MPP})	5.51 A
Temperature coefficient (P_{Max})	–0.30%/°C
Temperature coefficient (V_{OC})	–0.126 V/°C
Temperature coefficient (V_{SC})	1.76 mA/°C
Module efficiency	19%
Nominal operating cell temperature	48.3 °C

8.3 Power Conversion and MPPT

The solar power generation systems have attracted extensive attention in several application areas such as agricultural, residential, and even industrial sites. Furthermore, the sensations related to greenhouse emissions and carbon footprints are key factors to promote the utilization of solar power systems. Nowadays, the installation costs are decreased and overall efficiency of a PV system is increased

comparing to a few decades ago. The decreased costs allow redeeming earlier by ranging five years to seven years that accelerate the usage of solar energy in distribution systems. The solar power generation systems are constructed in two types; either standalone or grid-tied [14–17].

The standalone systems are attractive for remote sites where the distribution lines are unavailable. The standalone plants are composed of solar arrays, dc-dc converter, ESS, and inverter. On the other hand, the grid-tied systems eliminates ESS requirement and requires a grid-tie inverter instead of classical inverters. The complete block diagram of a solar power generation system with grid-connection is depicted in Fig. 8.5. The solar array is a combination of PV modules in series and parallel to generate the required power in various voltage and current ratings. The power conversion stage consists of dc power interface and its ac conversion pairs. The dc-dc converters are used to stabilize the intermittent characteristic of solar array that is considerably depended to solar irradiation and ambient temperature. The power conversion structure can be in single-stage or double-stage interface where the single-stage includes just a dc-ac inverter while the double-stage is composed of dc-dc converter and dc-ac inverter as seen in Fig. 8.5. The single-stage interface lacks in the stabilizing the dc bus voltage against rapidly varying dc output of solar array. However, the inverter requires operating an algorithm to track the maximum power point in order to match dc bus voltage of solar array.

However, it is not possible to sustain optimum matching at all radiation levels since the maximum power point rapidly fluctuates depending to the radiation and temperature. This operation can be performed in large-scale solar plants where the generated dc bus voltage excesses the required supply voltage of inverter. Therefore, the most proper way is to use double-stage power interface in any case [4, 16, 18–20].

A dc-dc converter is connected between solar array and inverter to match the required dc bus voltage in the double-stage power conversion system. The dc-dc converter handles the MPPT operation and the dc bus voltage is matched at this first stage. The MPPT algorithm of converter increases or decreases the dc bus voltage

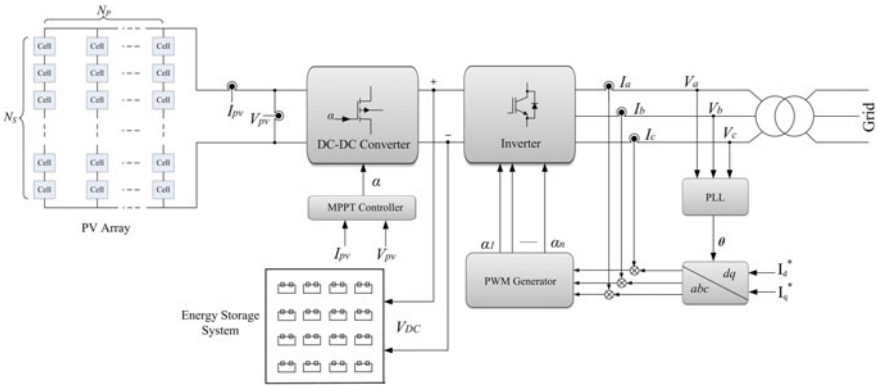

Fig. 8.5 The detailed block diagram of a solar power generation system

according to varied climatic conditions and maintains the match between dc supply limits of inverter. The MPPT algorithm controls the duty cycle of dc-dc converter where it changes the converted dc voltage level by adjusting the operation period of semiconductor switch in the topology. Thus, the maximum power is extracted from solar array by appropriately matching I-V balance of solar modules. The widely used dc-dc converter topologies are Buck-Boost and Cuk besides classical buck or boost topologies in solar power generation systems. It is not placed in this section since the converter topologies can be found in several textbooks [4, 20, 21].

The second interface used in double-stage is inverter that converts the dc bus voltage to ac power where the converted ac power is either supplied to the standalone loads or is injected to the utility grid. The inverter topology to be used in this interface depends to the power level where two-level or multilevel topologies can be selected. The multilevel topologies that were firstly introduced by Nabae generate the third voltage level with the neutral point of dc bus. The most widely used multilevel inverter (MLI) topologies are diode clamped, flying capacitor, and cascaded H-bridge in renewable energy. The diode clamped and cascaded H-bridge topologies provide the most proper involvement in high power applications where megavolt-ampere MVA power handling is desired. The flying capacitor arrangement eliminates filtering requirement comparing to diode clamped topology. However, this circuit is not accepted as robust as cascaded H-bridge to obviate the harmonic contents and the cost issues. Furthermore, several other MLI topologies such as grid-tied or string structures are implemented depending to the power ratings in solar energy application [4, 20].

The efficiency of a power conversion system is related to several factors such as conduction losses, switching losses, electromagnetic interference (EMI), and total harmonic distortion (THD) rates. The power efficiency is primarily decreased by power loss that are caused by active devices while the EMI and THD losses induce to defects on power quality and efficiency. The power losses increase proportionally to the switched voltage and current rates. The MLI topologies decrease the switched voltage and current rates at each cycle owing to its staircase output waveforms. Consequently, the power losses are also decreased comparing to regular two-level inverter topologies. The harmonic contents, THD ratios, and EMI rates are reduced by this way. The MLI output waveforms, either voltage or current depending to the topology, are increased to several levels, are particularly presented in odd numbers such as 3-level, 5-level, 7-level etc. In addition to these, the asymmetrical MLI topologies allow generating more increased output voltage levels by using same power stages as cascaded topologies [4, 19–21].

The rated power of a solar power generation system is increased by several string connections of power modules where the series-connected PV modules comprise the strings. Furthermore, several strings can be connected in parallel to achieve higher power ranges. The grid connection of PV plants that are constructed by using such strings is performed with various converter infrastructures. The most widely used power conversion schemes are illustrated in Fig. 8.6 where the connection diagrams of central converter, multi-string converter, string converter, and micro-converter are exhibited from Fig. 8.6a–d, respectively. Central converters are

constituted of inverters that convert the dc voltage achieved from PV strings ac voltage. They are widely used in residential, commercial, and utility scale systems with a power level of 1 kW or higher. The MPPT operation of the PV panels is performed centrally at the dc-ac inverter stage as shown in Fig. 8.6a. The main advantages of this scheme are decreased cost of inverter and decreased switching losses owing to unique converter structure. However, the central converter usage causes to a main drawback in acquired energy level since it is controlled by a single MPPT where the individual MPPT support is not available for each PV strings. Thus, the acquired maximum power level is limited under shading, thermal variations, aging or disorientation of PV strings. The multi-string converter seen in Fig. 8.6b is comprised of several individual dc-dc converters usually managing two

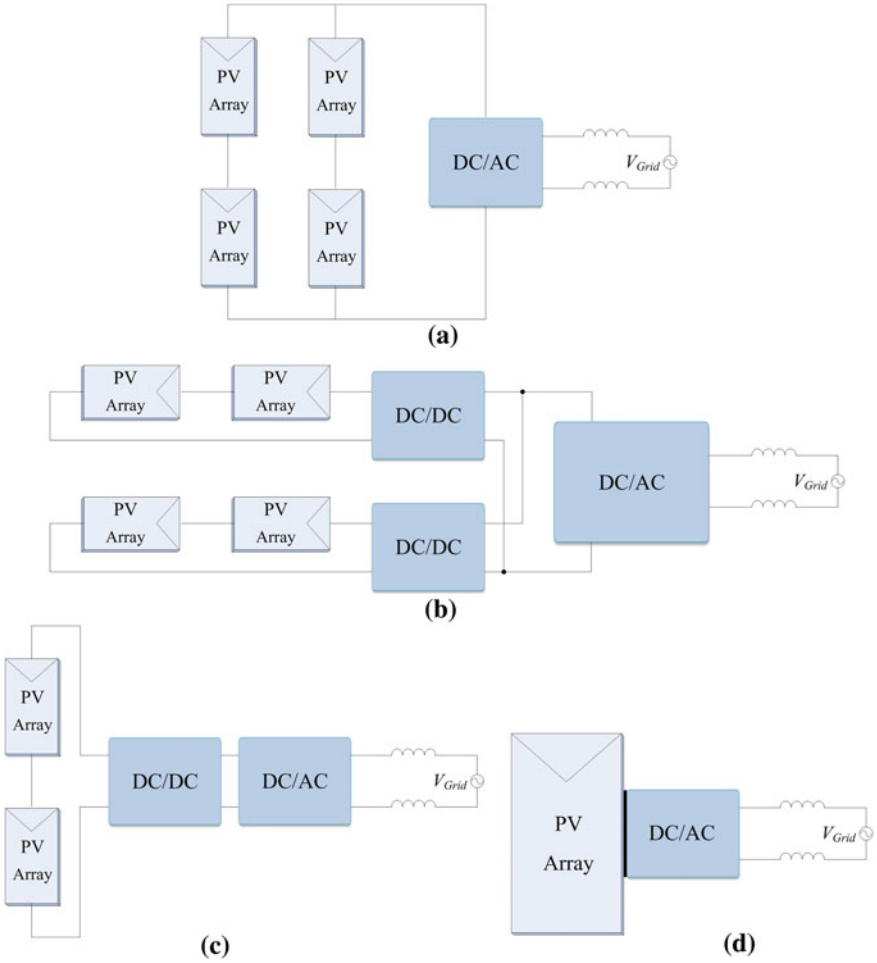

Fig. 8.6 Power conversion schemes in grid-tied PV systems, **a** central converter, **b** multi-string converter, **c** string converter, **d** micro-converter

PV strings or three PV strings at most. In this case, the double-stage interface is compulsory. The most important contribution of the double-stage interface is additional dc-dc converters that allow increasing the dc input voltage in a wide range. The PV plant can be freely constructed by arranging several dc-dc converter connections of strings. The dc-ac conversion is configured by using a central inverter that eliminates the drawbacks of the previous converter structure since the MPPT operations are handled by dc-dc converters.

The string converter that is shown in Fig. 8.6c is configured with individual MPPT controllers that do not allow parallel connection of strings. This option provides to locate each PV string in any direction or orientation. Furthermore, it is freely possible to care shading conditions and to determine PV module number in a string. The prominent feature of string converter is relevant to its power level that is widely designed at low power levels to be used in single-phase applications. In addition to this, its common topology includes full-bridge inverter with lien frequency transformer at the output stage. Thus, this configuration causes to a drawback of higher cost per kW. The micro-inverter is constituted with a dc-ac converter for each PV module where individual MPPT and power conversion features are acquired by this way. The configuration seen in Fig. 8.6d enables each PV module to connect to the ac grid without any dc wiring. Although this configuration provides simpler usage and installation, the cost per kW is higher than string converters.

Also, the operation cycle of the converter is lower than of a PV module [20, 21]. Although the utilization of PV systems are increased day by day, two main drawbacks are being extensively studied to overcome which are high installation costs, and low conversion efficiency. The acquired output power of a PV system is increased by using several mathematical algorithms. The MPPT is a fundamental method that eliminates the mismatch along the load characteristic and maximum power output of a PV module. MPPT algorithms ensure the optimal usage of PV modules against several defective conditions such as disorientation, shading or partial shading. Furthermore, the intermittent characteristic of solar power is sustained in a reliable way by using MPPT methods. Many MPPT methods have been proposed for single-stage and double-stage systems to cope with performance limitations. The most prominent classifications of MPPT methods are indirect and direct methods. The indirect methods include several algorithms such as open-circuit, constant voltage, short-circuit, and pulse method where some of them requires former knowledge on the PV array characteristics while some requires mathematical calculations. These requirements limit the efficiency of the algorithm at any case of irradiance and temperature variations.

The alternative MPPT methods are classified under direct methods where the most widely known ones are perturb and observe (P&O), hill climbing (HC), and incremental conductance (IncCon). These methods are competitor to indirect methods in terms of simplicity, easy implementation with limited prior information, and efficiency The commercial applications of MPPT methods are performed with P&O algorithm where the algorithm instantly measures voltage value at the maximum power point and tracks the variation. The MPPT algorithm is used to determine the switching angle of power converters depicted in Fig. 8.6. The algorithm detects and

tracks the reference voltage to change the duty cycle, and consequently the output voltage of converter [4, 22–25]. The most recent improvement of MPPT algorithms are performed by using intelligence based methods such as fuzzy logic controllers (FLCs), artificial neural networks (ANNs), particle swarm optimization (PSO) algorithms, and several genetic algorithm (GA)methods [23, 26]. The soft computing methods provide better efficiency and faster response comparing to indirect and direct methods. However, they lack on simplicity. The MPPT methods and outstanding properties are presented in the following sections.

8.4 Indirect MPPT Algorithms

The indirect MPPT algorithms differ from direct MPPT methods by calculations to determine the PV cell voltage and current at MPP. However, the direct MPPT methods are based on measurements instead of calculations. The indirect algorithms are based on several calculation methods including system voltage adjustment, temperature measurement, open-circuit voltage VOC calculation, and azimuth and angle calculation sometimes. The system voltage or operating voltage adjustment is performed to detect the MPP voltage according to seasonal variations where it should be higher in winters. The operating voltage depends on the PV module temperature. The MPP voltage is calculated regarding to VOC that is instantly measured. The main advantage of indirect MPPT methods including constant voltage, open-circuit voltage, and short-current pulse-based is their simplicity. However, they lack against aging and pollution of PV cells [26–29].

8.4.1 Constant Voltage MPPT Method

The constant voltage (CV) method is the plainest MPPT algorithm that is based on regulating the array voltage to track the MPP voltage V_{MPP} as seen in Table 8.1. The PV array voltage is adjusted around V_{MPP} regarding to the reference voltage V_{Ref} that is the regulated array voltage. It is intended to match the V_{Ref} to V_{MPP} in the most proper adjustment. If this is not the case, then the algorithm tries to acquire the most adequate adjustment around the V_{MPP}. The CV algorithm assumes that the irradiance and temperature variations on the cells do not cause to meaningful changes on V_{MPP} and therefore, the V_{Ref} can be kept constant during the operation of algorithm. The flowchart of the CV MPPT operation is illustrated in Fig. 8.7 where the PV array voltage is required to be measured at the beginning of the algorithm. The algorithm does not involve any other input data. The measured array voltage V_{PV} is used to set up the duty-cycle of dc-dc converter. Then the duty cycle is updated at each turn by comparing the array voltage to reference voltage [26, 28]. When the array voltage is greater than reference, the duty cycle is decreased in the next step or vice versa.

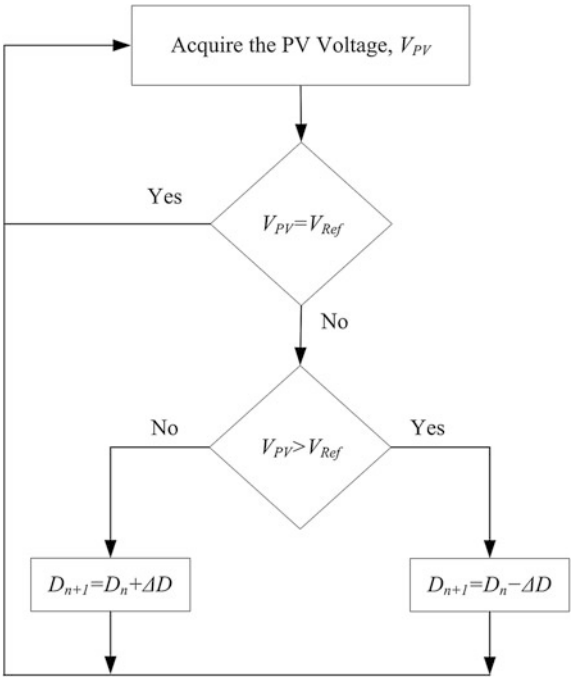

Fig. 8.7 Flowchart of the constant voltage MPPT method

It should be noted that CV method is more efficient comparing to regular P&O technique during the lower irradiance conditions. Therefore, it may be integrated other MPPT methods.

8.4.2 Open Voltage MPPT Method

The open voltage (OV) method is based on the assumption of that V_{MPP} is ever around a fixed percentage of the open-circuit voltage V_{OV}. It is also assumed that the production variations of cells, temperature, and solar irradiance rates change the MPP around 2% of its regular value. Therefore, this method defines a reference voltage V_{Ref} at the 76% of V_{OV}, which is quite near to V_{MPP}.

The flowchart of OV method is depicted in Fig. 8.8 where open-circuit voltage V_{OV} measurement is required to determine the reference voltage. This measurement is performed by opening the circuit, and a series static switch is used to carry out this action. This operation causes to zero PV current that prevents the power generation at this stage. In the next step, the measured PV voltage V_{PV} is compared to the reference voltage V_{Ref} to determine the exact duty-cycle of dc-dc converter. The pre-defined duty-cycle D_n is increased in the next step, if V_{Ref} is greater than V_{PV} [26, 28, 30, 31].

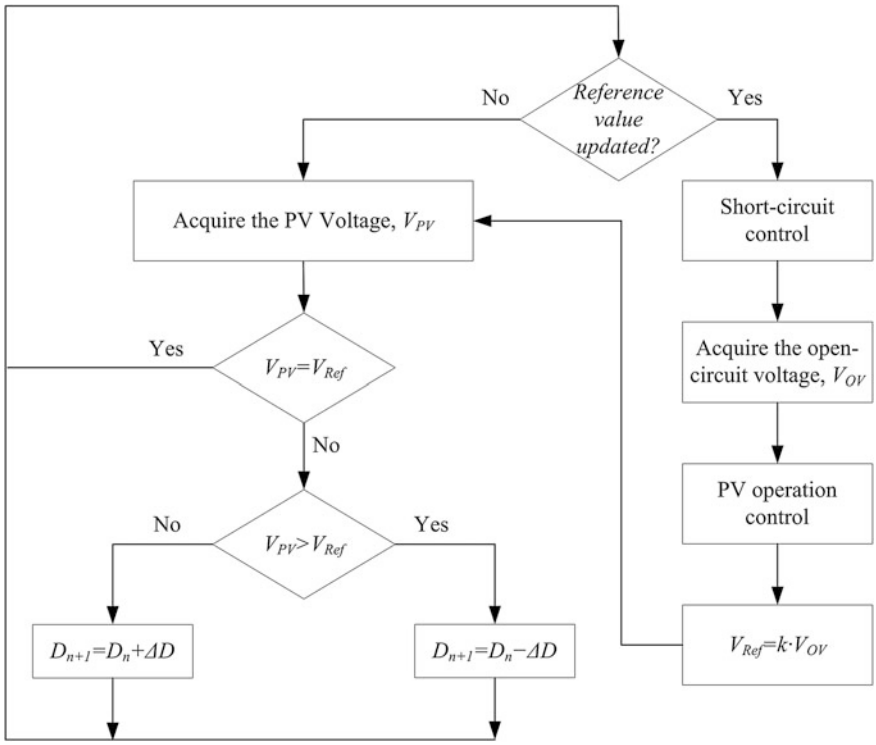

Fig. 8.8 Flowchart of the open-voltage MPPT method

If the V_{PV} is greater than V_{Ref} then the D_n is decreased by varied value for the next duty-cycle calculation D_{n+1}. The regulated dc output voltage is controlled by PI block at each cycle to track the V_{MPP}.

8.4.3 Short-Current Pulse-Based MPPT Method

The short-current pulse-based (SCPB) MPPT method determines V_{Ref} that is required to generate the optimum operating current I_{OP}. In the ideal conditions, I_{OP} is proportional to the short-circuit current I_{SC} by a coefficient k and irradiance level of S as seen in Eq. (8.12);

$$I_{OP}(S) = k \cdot I_{SC}(S) \tag{8.12}$$

The equation exhibits that the operating current is defined by irradiance level and ISC where it is also temperature dependent that varies between 0 and 60 °C. On the other hand, the coefficient is assumed to be around 92%. It is obvious that this

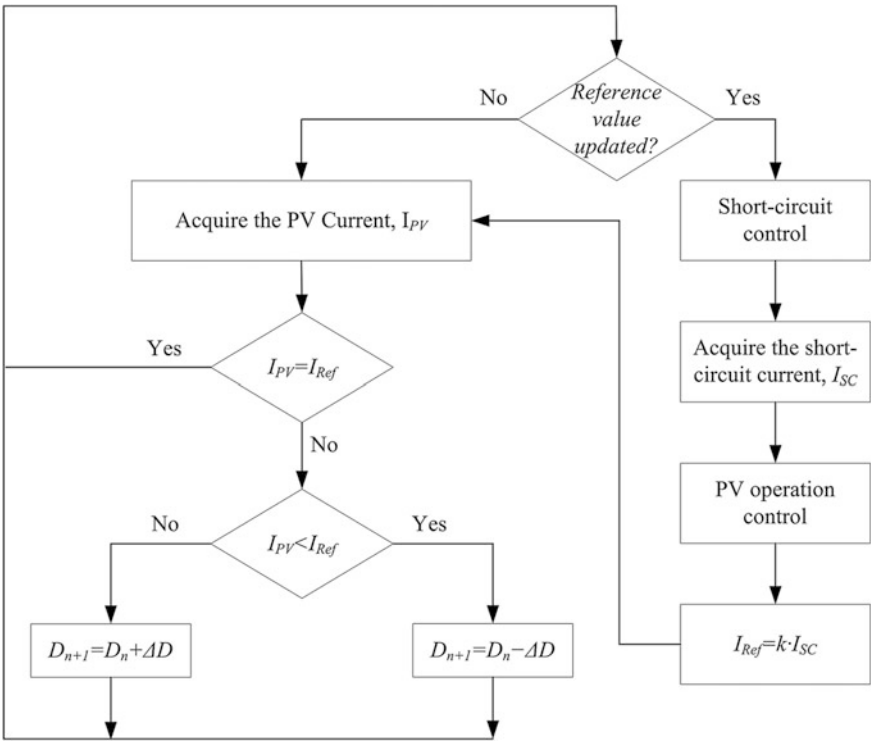

Fig. 8.9 Flowchart of the short-current pulse-based MPPT method

algorithm is based on short-circuit current measurement and that is performed by a parallel static switch similar to previous method. The parallel switch provides the short circuit conditions where the array voltage is zero and power generation is prevented. The flowchart of this control method is shown in Fig. 8.9 that the preliminary measurements and comparisons are depicted similar to OV MPPT algorithm with a difference where the measured and compared parameters are current in this method [27, 28, 30, 31].

The PI regulator requires the array voltage as in the OV method to generate the operating current where the reference voltage is also acquired at this stage.

8.5 Direct MPPT Algorithms

The direct MPPT algorithms are based on measurement of PV module voltage, current, or instant power where the performance variations are rapidly detected and more accurate tracking is performed. The basic principles of direct MPPT

algorithms are related to periodic tuning of I-V and P-V curves, and adjusting the operating voltage in small steps to increase the accuracy. The first principle is used to determine the maximum output power of PV module that is tracked at each turn of duty-cycle calculation of the dc-dc converter. The second principle is performed by a method known as hill climbing that is based on detecting the power or current direction either increasing or decreasing. In case the measured value increased depending on the operating voltage, the tracking direction is set to forward, otherwise it is set to backward. The MPP is detected by this principle and the operating point track the real MPP with little oscillations regarding to step size [24, 25, 29, 32]. The characteristics of a typical PV cell under regular irradiance and partial shading conditions are illustrated in Fig. 8.10 where the MPP dot depicts the current source and voltage source operation of PV module. If the operating point of the load is on the left-hand side of MPP, it means the module operates as a current source and the error signal M required by Hill-Climbing HC MPPT is calculated as given in (8.14);

If the operating point of the load is on the right-hand side of MPP, then PV module acts as a voltage source, and M is calculated as follows;

$$\frac{\partial P_{PV}}{\partial V_{PV}} > 0 \Rightarrow M = M + \Delta M \tag{8.13}$$

$$\frac{\partial P_{PV}}{\partial V_{PV}} < 0 \Rightarrow M = M - \Delta M \tag{8.14}$$

Apparently, the error signal will be zero at the MPP that yield $\Delta M = 0$. This approach is applied at several direct MPPT methods where the most outstanding algorithms are P&O and Incremental Conductance (IncCon) [29, 31, 32].

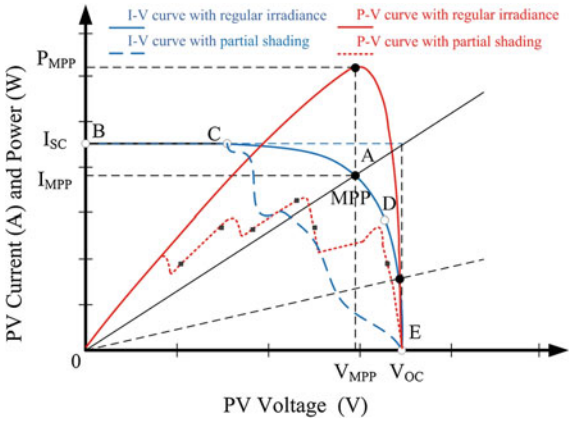

Fig. 8.10 Characteristics of a typical PV cell under regular irradiance and partial shading

8.5.1 Perturb and Observe MPPT Algorithm

The P&O algorithm is one of the most widely used and studied method owing to its simplicity and practical implementation. It perturbs the terminal voltage, as its name implies, and compares the actual PV power to previous value. The algorithm decides to track the MPP in one direction or in the opposite direction by comparing the terminal voltage change and output power increment. In case the output power is increased against the voltage change, the algorithm keeps on tracking the MPP in the same direction. Otherwise, it shifts the tracking direction [4, 26, 32, 33].

There are several textbooks and papers can be found on regular P&O algorithm in the literature. However, the main attention should be directed to improve instead of applying the regular P&O. The flowchart of an improved algorithm proposed by Dolara et al. [26] is shown in Fig. 8.11 where the power and voltage perturbations are detected in the progress, and then the voltage difference is detected to operate the algorithm. In the proposed method, the array power is sampled to generate an

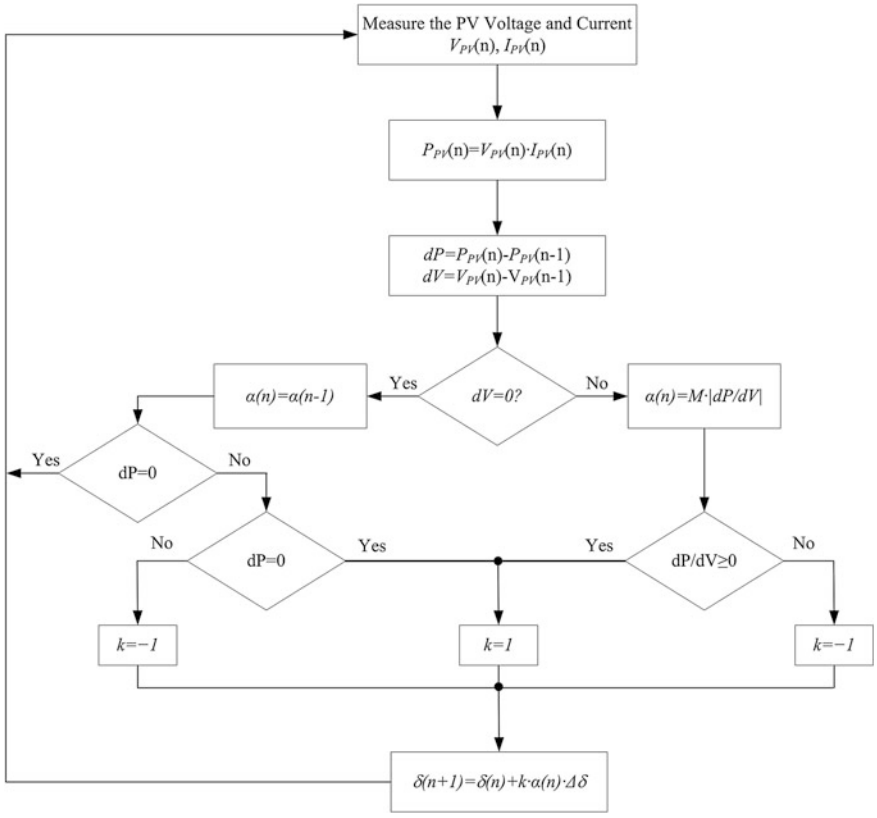

Fig. 8.11 Flowchart of optimized P&O MPPT method [26]

average value, and is used for arranging the magnitude of perturbation $\Delta\delta$ at the MPP operating point.

The arrangement is performed by calculating the $\alpha(n)$ regarding to voltage error signal M and power to voltage ratios as shown on the right-hand side of flowchart. The duty cycle is varied around 0.5% for each regular P&O methods. However, the proposed algorithm in [26] tries to adjust the duty cycle variation between 0.5% and 2.7% in the next turn regarding to k coefficient, α (n), and $\Delta\delta$ where it is equated as follows;

$$\delta(n+1) = \delta(n) \; + \; \mathrm{k} \cdot \alpha(n) \cdot \Delta\delta \tag{8.15}$$

An improved P&O MPPT method with PI control is proposed by Kabalci et al. [34, 35] where the schematic diagram of combined controller is illustrated in Fig. 8.12. The MPPT control of converters are improved with additional PI to regular P&O algorithm where measurements of solar array, dc converter, and control diagram of PI controller are shown on the left-hand side of Fig. 8.12. The flowchart of the improved PI controlled MPPT algorithm is depicted in Fig. 8.13 where additional PI calculation is managed by the error calculation segment on the flowchart.

The flowchart of MPPT algorithm is depended on voltage and power calculations that are based on current and voltage values acquired from sensors [34].

Once the actual power is calculated, then the next cycle of the measurement is compared to previous value to track the reference voltage V_{ref}. The implemented control section that the upper and lower parts of detailed PI controller block exhibit P&O detection part while the middle part on the left hand side of figure illustrates the PI control added to MPPT algorithm considering K_p and K_i parameters of the

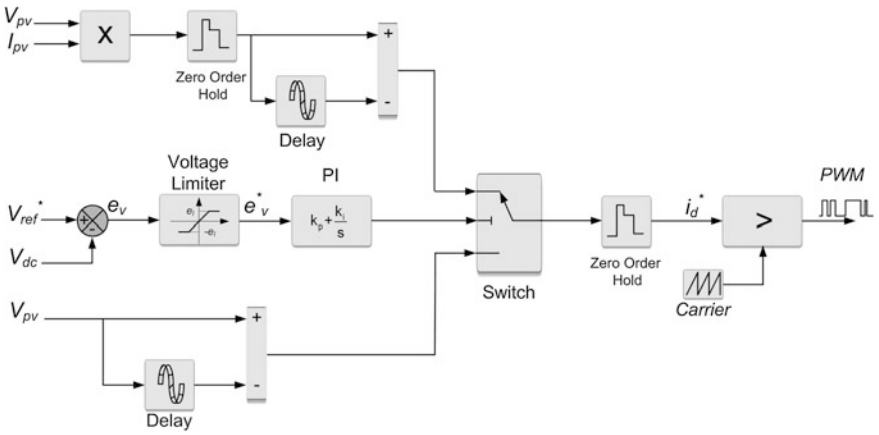

Fig. 8.12 Schematic diagram of the PI assisted MPPT [34]

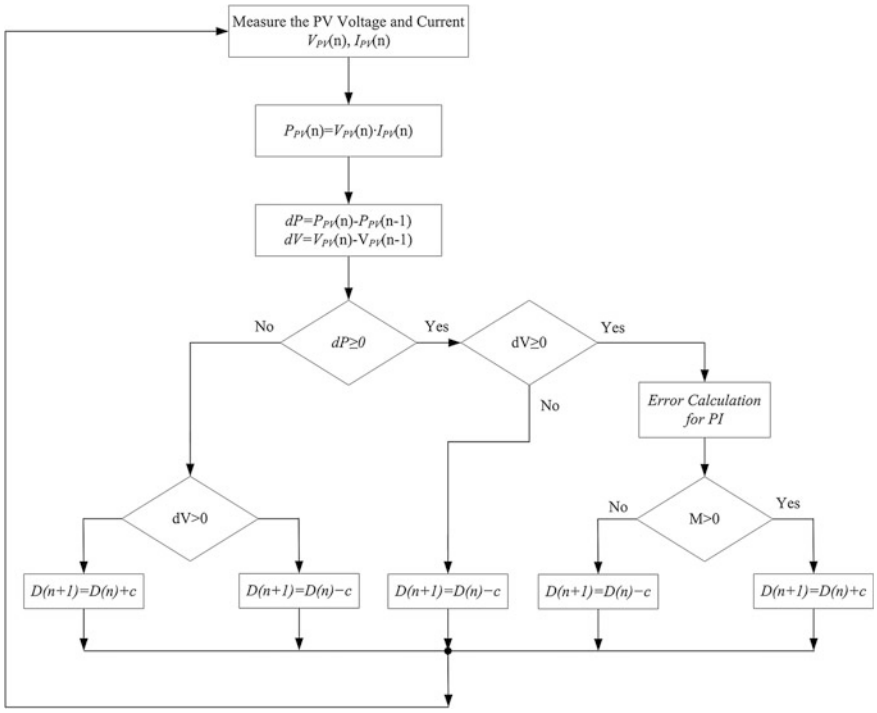

Fig. 8.13 Flowchart of optimized PI assisted P&O MPPT method [34]

system. The actual inputs and reference outputs are switched as seen in the center of PI controller block and modulating signal is conditioned by the zero-order sample and hold block. The logical comparator compares the triangular carrier signal and modulating signals to generate the PWM at each interval where the actual power measurement is repeated [34].

In order to determine duty ratio the latest observation of the obtained power is compared to the previous observation. Afterwards, ensured difference is used to specify the next PWM duty cycle. The implemented P&O algorithm looks for the increment of power perturbation and attempts to keep the duty cycle in the same way in order to achieve the MPP of PV array, also PI control is activated to reduce oscillation on the output voltage. The algorithm can reverse the perturbation when there is a decrement occurs in the power observation. The algorithm repeats this process for reach to MPP of PV array, if the system reaches to the MPP; the algorithm produces steady duty cycle value. The oscillation at the MPP of PV array is demanded to be reduced in order to increase the stability [35, 36]. The PI function, which is used to reduce oscillation on the output voltage is calculated as given in short code of Eq. (8.16) [35];

$$\left.\begin{array}{l} Void\_PI() \\ \{ \\ Error = Vref - Vo; \\ Error\_in = Error\_in + Error * dt; \\ duty = Error * Kp + Error\_in * Ki; \\ \} \end{array}\right\} \tag{8.16}$$

8.5.2 Incremental Conductance MPPT Algorithm

The incremental conductance *InCon* algorithm depends on the detection of the slope occurred in the PV curve. The slope is zero when the MPP of the curve is reached as shown in Fig. 8.10. The movement direction of operating point is detected by tracking the change occurred in the *I/V* ratio comparing to the MPP point. The operating point increases the slope when it is moving towards to the MPP, while it turns negative on the right side of MPP. This situation can be expressed as follows [25, 37–39];

$$\begin{array}{l} \dfrac{dI}{dV} = -\dfrac{I}{V}; \left(\dfrac{dP}{dV} = 0\right); \text{at MPP} \\ \dfrac{dI}{dV} > -\dfrac{I}{V}; \left(\dfrac{dP}{dV} > 0\right); \text{at left of MPP} \\ \dfrac{dI}{dV} < -\dfrac{I}{V}; \left(\dfrac{dP}{dV} < 0\right); \text{at right of MPP} \end{array} \tag{8.17}$$

The Eq. (8.17) and flowchart given in Fig. 8.14 are based on the instant conductance (*I/V*) and the incremental conductance (*dI/dV*) of PV array where the reference voltage is calculated regarding to incremental value in an iteration that is repeated until MPP is reached. Once the V_{Ref} acquired at the MPP, the algorithm maintains to track this value in order to ensure maximum output power. In case a change occurs in PV current *dI*, algorithm starts a new iteration at the beginning of the flowchart to track V_{Ref} by increasing or decreasing the previous value.

When the irradiance increases on the PV array, the array voltage is increased and the MPP moves to the right-hand side as can be seen on Fig. 8.10. The algorithm increases the operating voltage of PV array for compensating this increment. On the other hand, the decrement on irradiance triggers the algorithm to decrease the operating voltage of array in order to compensate the change. That is the way that InCon algorithm track the slope value to detect the change on irradiance and react against the cases. The easier way to determine the change is comparing previous and actual values of voltage and current that are depicted as *dV* and *dI* in the

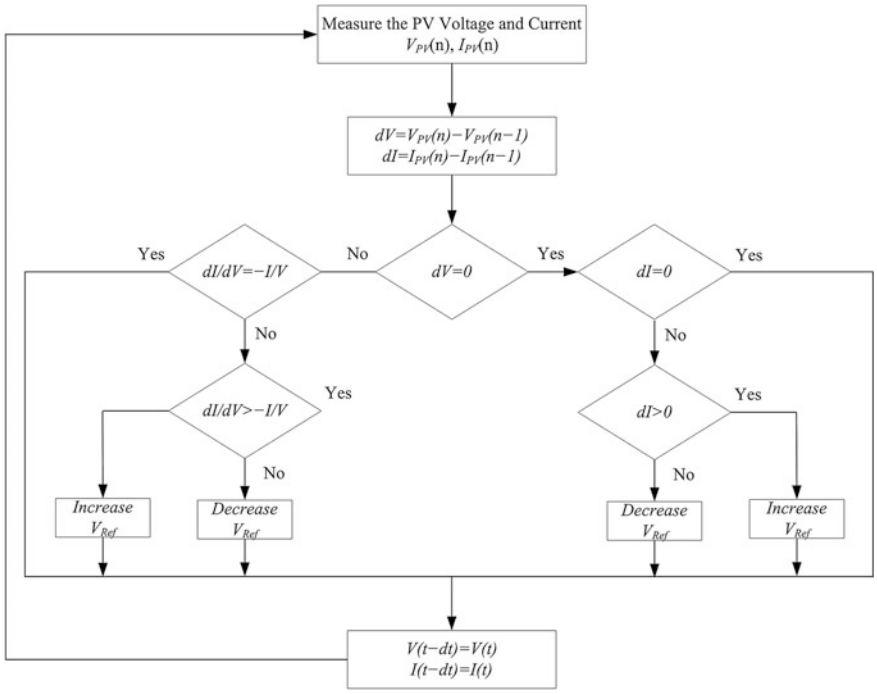

Fig. 8.14 Flowchart of incremental conductance MPPT method

algorithm. The *dV* and *dI* are zero when the irradiance and temperature are stable, and algorithm maintains to operate at MPP.

If the irradiance increases, it causes an increment on *dI* ($dI > 0$) while $dV = 0$ that also means the MPP is being increased by irradiance. The algorithm decides to increase the operating voltage at this stage. On the other hand, the decrement on irradiance causes to $dI < 0$ that requires to decrease the operating voltage. The rapidly changing cases are easily detected by InCon algorithm since it depends on tracking the operating point towards MPP. This approach prevents misleading in tracking as seen in P&O algorithm, and that makes InCon more reliable by decreasing the perturbation around MPP. However, there are several drawbacks of this algorithm related to MPP as others. Tey and Mekhilef [40] proposed an optimized alternative to regular incremental conductance method by increasing the step size that is named as variable step size InCon. The algorithm is based on defining a step size to compensate the variations on MPP change and increasing or decreasing the duty cycle considering this step size additional to previous duty cycle. Thus, an error rate is permitted by algorithm and the step size is adjusted to maintain the error control in the limit. There are several methods are proposed to optimize regular MPPT methods. However, the numerical methods including FLCs, Neural network controlled

algorithms, and some other soft computing methods are applied to improve existing methods. The rapidly adapting structures, complexity, and sophisticated approaches of these algorithms increase the reliability of regular MPPT methods.

8.6 Artificial MPPT Algorithms

The most widely used MPPT methods are introduced in 4th and 5th sections. There are several other methods are also proposed in the literature including non-linear and sliding mode control methods in order to improve the stability and efficiency of regular MPPT algorithms such as perturb and observer or incremental conductance. However, the main drawbacks seen in the proposed methods are caused by irradiation and cell temperature that are not robustly handled by existing algorithms. The widely known methods are based on discontinuous control strategy where the intersection tracking is performed around the MPP. The tracking approach of the previously introduced algorithms lack in efficiency since they are not supported by intelligent controls and are less efficient against the rapidly changing conditions [41–44]. Furthermore, the existing methods do not pay attention to measurement noises of voltage and current that has significant effect on the algorithm decisions.

These drawbacks require fast time response and increased stability comparing to widely known methods. The oscillations occurred in the acquired power output should be decreased in order to decrease power losses. The latest improvements in MPPT methods are performed by using several numerical and artificial methods including FLC, neural network, neuro-fuzzy, genetic algorithm, and some optimization algorithms such as particle swarm optimization, artificial bee colony etc. The FLC is one of the simplest algorithms among other artificial methods. Recently, an increasing attention paid to FLC based MPPT algorithms owing to its robust response against unpredictable air conditions and its simple structure not requiring complex mathematical arrangements. The neural networks are also being extensively studied owing to their high level control structure and sophisticated management features [42, 43]. The following subsections are dedicated to artificial methods used in MPPT algorithms with analyses.

8.6.1 Fuzzy Logic Control MPPT

The combining artificial intelligence with regular MPPT algorithms is a new trend of research and application in renewable energy sources. FLC is the most widely researched artificial method in MPPT applications since it provides better performance comparing the conventional methods, and involves simpler requirements comparing to sophisticate neural or estimation algorithms. These advantages of FLC are integrated to overall system by combining it to existing MPPT controller that provides to acquire maximum power transfer to the loads.

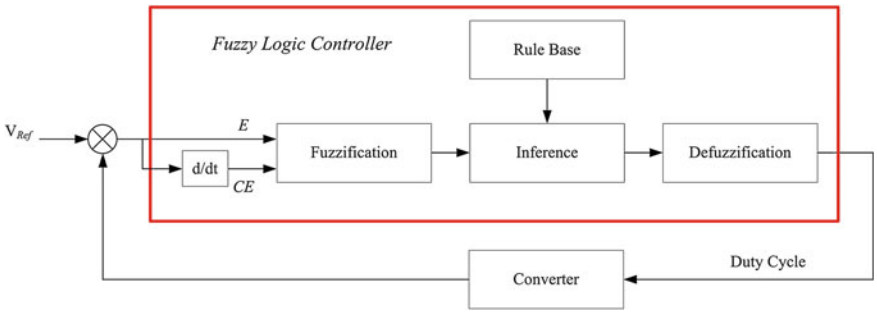

Fig. 8.15 Block diagram of a FLC MPPT controller

The block diagram of a FLC based MPPT controller is depicted in Fig. 8.15 where the contents of a regular FLC are also shown in a significant block. The reference input of FLC is used to determine the error signal *E* and change rate of the error *CE* where it is shown on the left-hand side of figure. The output of FLC is the duty cycle that is applied to converter where it is generated by the four sections of FLC. These sections are fuzzification where the numerical inputs are converted to lexical variables that are defined by rule base and depended to membership functions. The levels of membership functions can be increased to present better resolution in the calculations. The analyzed inputs are weighted according to several methods, namely modus ponens, Takagi-Sugeno or Mamdani, in the inference section, and then the lexical outputs of FLC are converted to numbers in the defuzzification section in order to generate the duty cycle. The most widely used defuzzification method is the is the centroid of area (COA) owing to its successful averaging properties and more accurate results [41, 42, 44]. The integration of FLC to the regular P&O algorithm is illustrated in Fig. 8.16 where the decision making against output power is performed regarding to the power and voltage perturbation by FLC controller that generates the adaptive duty cycle.

8.6.2 Neural Network MPPT

The most recent researches on computational MPPT methods include ANN studies that are significantly effective on wide disruptive conditions such as partial shading [45, 46]. The ANN based MPPT provides rapid and reliable estimations against quickly varying irradiance and temperature parameters. An ANN is composed of several layers in multilayer perceptron (MLP) structure as shown in Fig. 8.17. In a model as shown in figure, the neural-like organization is comprised of neurons seen in the lower part of figure where the inputs are linearly weighted and summed in a function. The sum of weighted input are transferred to a nonlinear function called

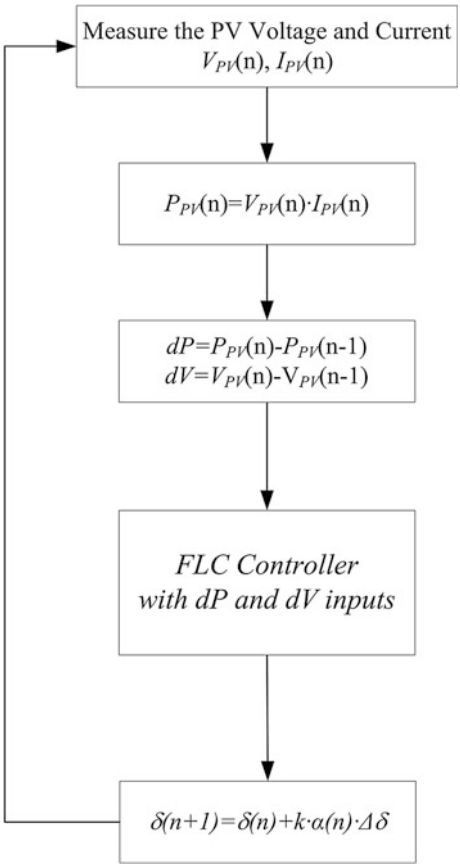

Fig. 8.16 Flowchart of a FLC P&O MPPT algorithm

activation function (AF), and lastly are sent to the following neurons. The definition of input function in AF is depicted as given in Eq. (8.18);

$$x = \sum_{m=1}^{M} w_m x_m + \alpha \tag{8.18}$$

where $x_1, x_2, \ldots, x_m$ are input signals, and $w_1, w_2, \ldots, w_m$ are the weights of each input signal [45].

The weights define the significance of each input data and the learning operation of the network is performed regarding to continuously varying weights. The training set of the ANN is composed with several different input and output data where they are voltage and current in inputs and MPP voltage at the output as seen in Fig. 8.17. There are several ANN based MPPT operation approaches are proposed. In one hand, some ANN algorithms integrated to regular MPPT methods use irradiance and temperature measurement acquired from separate sensors and

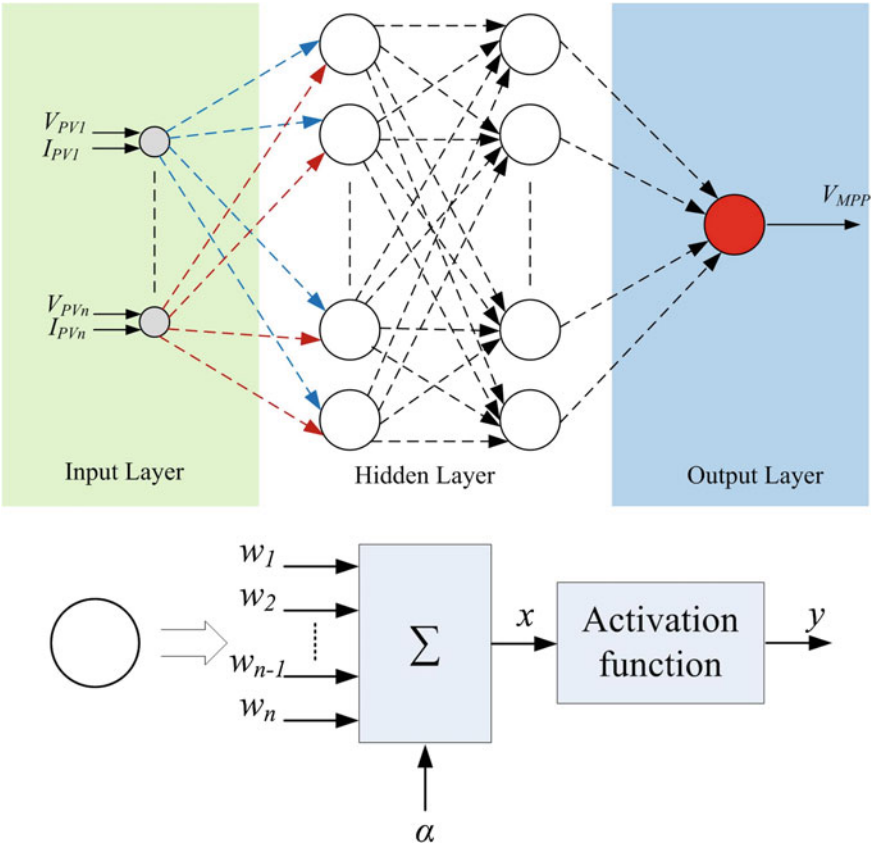

Fig. 8.17 Block diagram of an ANN controlled MPPT algorithm

directly generates variable duty cycle. On the other hand, the measured irradiation and temperature data are used to detect the voltage and current of PV module in other ANN MPPT group. The second group is widely used rather than first one and it is constructed with MLP structure [46–48].

8.6.3 Particle Swarm Optimization MPPT Algorithm

Particle swarm optimization *PSO* is a novel swarm optimization algorithm that is firstly proposed by Kennedy as an evolutionary algorithm based on behavior of birds [49, 50]. PSO uses a set of particles that each one suggests a solution to the optimization problem. It is based on the success of all particles that emulates a population where the position of each particle depends to the agent position to

detect the best solution P_{best} by using current particles in the population G. The position of any particle x_i is adjusted by

$$x_i^{k+1} = x_i^k + v_i \tag{8.19}$$

where the velocity component v_i represents the step size and is calculated by using the Eq. (8.20);

$$v_i^{k+1} = \omega v_i^k + c_1 r_1 (P_{best\_i} - x_i^k) + c_2 r_2 (G - x_i^k) \tag{8.20}$$

where ω is the inertial weight, c_1 and c_2 are the acceleration coefficients, r_1 and r_2 are random values that belong to the interval of [0, 1], P_{best_i} is the best position of particle i, and G is the best position in the entire population [50].

A typical MPPT method should be used to integrate PSO algorithm to controller. Most widely used integration is based on hill-climbing or P&O algorithm to PSO. The flowchart of a PSO MPPT algorithm is depicted in Fig. 8.18. The operation given in flowchart can be analyzed in five steps that are *initialization, fitness evaluation, updating the individual and global best value, updating the velocity and position of each particle,* and *convergence determination* [51]. In the first step, particles are randomly initialized in the distribution space, or are initialized on

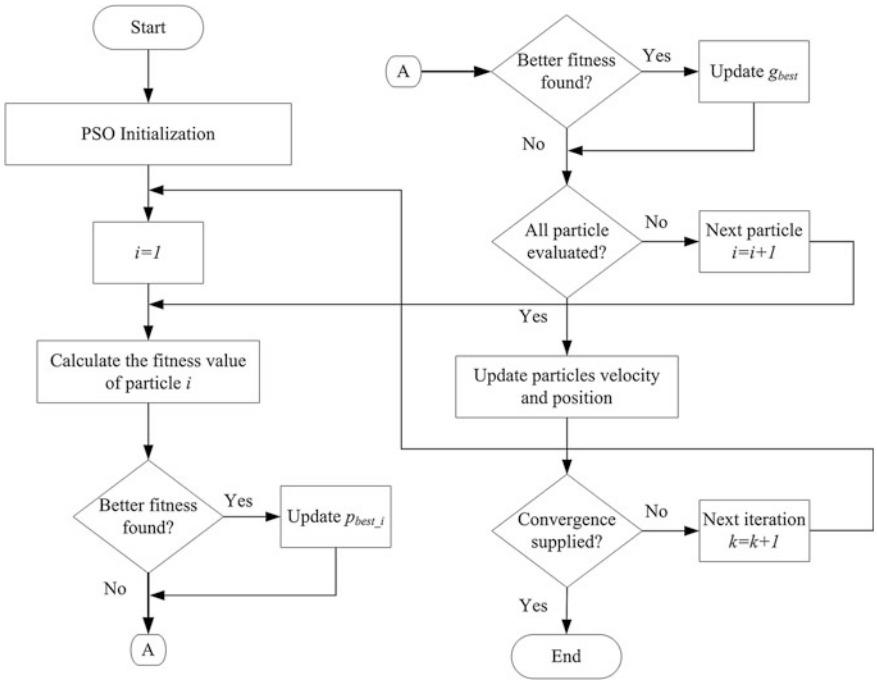

Fig. 8.18 Flowchart of PSO MPPT algorithm

described grid nodes covering the search space. Similarly, the initial velocity values are defined randomly. The fitness value of each particle is evaluated in the second step where the fitness evaluation is leaded to provide candidate solution to the objective function.

The individual and global best fitness values are determined in the third step where p_{best_i} and g_{best} are respectively determined. Then the positions are updated and replaced with better fitness values if they are found. The velocity and position of each particle are updated in the fourth step respecting to Eqs. (8.19) and (8.20). The last step of the flowchart checks the convergence criterion. If the criterion is met, the process is finished. Otherwise, the iteration number is increased and procedure returns to step 2 [51–53].

The application of PSO MPPT in a PV system is depended to the matching definitions of both systems. The particle positions are used to define the duty cycle of dc converter, and the fitness value evaluation function stands for the output power of PV array. The success of algorithm is performed by increasing the number of particles that provides more accurate MPP tracking operation, even for shading problems. On the other hand, increased number of particles causes to longer computation times. The particle number is usually selected as the number of series connected cells in a PV array in order to obtain the most exact operation time.

The particles are placed either on fixed positions or on random places in the PSO initialization step. It depends on the information about global MPP since the particles can be placed around the point, if there is any information about it. The PV voltage and current are measured and digitally filtered by using finite impulse response filters in order to calculate the fitness value, P_{PV} of particle i. The calculated fitness value is compare to the best fitness value in order to keep p_{best_i} or to update it with the new p_{best_i} in case of better fitness value. The velocity and positions of all particles are updated and convergence criteria are controlled to generate the best control signal [51–53].

The dependency to $p_{\text{best\_i}}$ and g_{best} is the main problem of conventional PSO algorithm under nonlinear shading conditions. Since there are several PSO methods proposed in the literature. The outstanding alternative to classical PSO are deterministic and dormant PSOs [52, 53].

8.7 Conclusions

This chapter deals with most widely used and recent trends in MPPT algorithms. The literature reviews show that several methods are proposed to track the MPP in a PV power system. The main concerns of all the proposed algorithms are fast response, reliable tracking, and easy implementation. The power conversion devices and configurations are improved to increase acquired energy level of a solar plant. Although there are various structures proposed in literature, double-stage power conversion holds the great share of usage in residential and industrial plants. The first stage is comprised of dc-dc converters while the second stage performs

dc-ac conversion by using inverters. The dc interface requires robust control methods to increase converted energy under heavily or partially shaded conditions. The MPPT algorithms are focused on coping with irradiance and temperature variations to balance the acquired total output power.

The preliminary algorithms classified as indirect algorithms are based on several calculation methods including system voltage adjustment, temperature measurement, open-circuit voltage V_{OC} calculation, and azimuth and angle calculation sometimes. These methods lack on responding against rapidly changing weather conditions. The direct methods that includes hill-climbing, P&O, and indirect conductance are proposed to tackle this situation. The basic operation principles of direct MPPT algorithms are based on periodic tuning of *I-V* and *P-V* curves, and adjusting the operating voltage in small steps to increase the accuracy. The decreased step size and effective measurement methods increased the reliability of direct MPPT methods. However, the researches exhibited the perturbation issue seen around the MPP can be overcome with computational methods. Their simple analytical background led the main drawback of direct methods. Therefore, more sophisticated and complex algorithms were researched to prevent the perturbations occurred in power curve of PV arrays.

A wide variety of numerical methods including fuzzy logic, neural networks and other computational methods are proposed. The most recent computational algorithms including GAs, PSO algorithms, and ABC are prominent topics in MPPT algorithms. The trade-off between conventional MPPT methods and recent algorithms are related to complexity in algorithm and increased cost in application. However, improved efficiency and fast response leads to extensive researches.

References

1. Twidell J, Weir T (2006) Renewable energy sources. Taylor & Francis, London ISBN 0-419-25330-0
2. Kabalcı E, Kabalcı Y, Develi I (2012) Int J Electr Power Energy Syst 34:19–28
3. Masters GM (2004) Renewable and efficient electric power systems. Wiley-IEEE Press. ISBN: 13: 978-0471280606
4. Colak I, Kabalci E (2014) Chapter 7-Control methods applied in renewable energy, use, operation and maintenance of renewable energy systems. Springer, pp 205–246. doi:10.1007/978-3-319-03224-5_7. ISBN: 978-3-319-03224-5
5. Zeman M (2014) Chapter 9-Photovoltaic systems, Delft University of Technology
6. Hersch P, Zweibel K (1982) Basic photovoltaic principles and methods, SERI/SP-290-1448 solar information module 6213. Golden, Colorado
7. Gray JL (2003) In: Luque A, Hegedus S (eds) Handbook of photovoltaic science and engineering. Wiley, West Sussex, pp 61–112
8. Kabalcı E, Gokkus G, Gorgun A (2015) 7th international conference electronics, computers and artificial intelligence, Bucharest, Romania, 25–27 June 2015, pp SG23–SG28
9. Lineykin S, Averbukh M, Kuperman A (2014) IEEE Trans Ind Electron 61:6785–6793
10. Kadri R, Gaubert JP, Champenois G (2012) IEEE Trans Power Electron 27:1249–1258
11. d'Alessandro V, Guerriero P, Daliento S, Gargiulo M (2011) Solid State Electron 63:130–136
12. Tian H, David F, Ellis K, Muljadi E, Jenkins P (2012) Sol Energy 86:2695–2706

13. Panasonic HIT Photovoltaic Module, HIT Power 240S. http://www.panasonic.com/business/pesna/includes/pdf/eco-construction-solution/HIT_Power_SA06_Series_(240W)_Data_sheet-v2.pdf
14. Radjai T, Rahmani L, Mekhilef S, Gaubert JP (2014) Sol Energy 110:325–337
15. Pradhan R, Subudhi B (2015) Int J Electr Power Energy Syst 64:792–803
16. Mohanty P, Bhuvaneswari G, Balasubramanian R, Dhaliwal NK (2014) Renew Sustain Energy Rev 38:581–593
17. Bendib B, Krim F, Belmili H, Almi MF, Boulouma S (2014) Energy Procedia 50:383–392
18. Wu JC, Wu K, Jou HL, Chang SK (2014) IET Power Electron 7:2717–2725
19. Jiang J, Su YL, Shieh J, Kuo K, Lin T, Lin T, Fang W, Chou J, Wang J (2014) Appl Energy 124:309–324
20. Zheng H (2013) Solar photovoltaic energy generation and conversion—from devices to grid integration. PhD dissertation, Department of Electrical and Computer Engineering, Graduate School of The University of Alabama, Tuscaloosa, Alabama
21. Lorenzani E, Franceschini G, Bellini A, Tassoni C (2014) Chapter 6-Single-phase grid connected converters for photovoltaic plants, renewable energy. In: Hammons TJ (ed) InTech. ISBN: 978-953-7619-52-7
22. Rezk H, Eltamaly A (2015) Sol Energy 112:1–11
23. Bendib B, Belmili H, Krim F (2015) Renew Sustain Energy Rev 45:637–648
24. Sivakumar P, Kader AA, Kaliavaradhan Y, Arutchelvi M (2015) Renew Energy 81:543–550
25. Eltawil MA, Zhao Z (2013) Renew Sustain Energy Rev 25:793–813
26. Dolara A, Faranda R, Leva SJ (2009) Electromagn Anal Appl 3:152–162
27. Faranda R, Leva S; Maugeri V (2008) Power and energy society general meeting—conversion and delivery of electrical energy in the 21st century, 20–24 July 2008, pp 1–6
28. Faranda R, Leva S (2008) WSEAS Trans Power Syst 3:446–455
29. Onat N (2010) Recent developments in maximum power point tracking technologies for photovoltaic systems. Int J Photoenergy 1:1–11
30. Park M, Yu K (2004) In: 30th annual conference of IEEE industrial electronics society, pp 2040–2045
31. Coelho RF, Concer FM, Martins DC (2010) 2010 IEEE international conference on sustainable energy technologies (ICSET), pp 1–6
32. Rújula AA, Abián JA (2014) Sol Energy 109:95–104
33. Ahmed J, Salam Z (2015) Appl Energy 150:97–108
34. Kabalci E, Kabalci Y, Canbaz R, Gokkus G (2015) 4th international conference on renewable energy research and applications (ICRERA 2015), Palermo, Italy, 22–25 November 2015
35. Kabalci E, Gokkus G, Gorgun A (2015) ECAI 2015 7th international conference electronics, computers and artificial intelligence, Bucharest, Romania, 25–27 June 2015, pp SG23–SG28
36. Sea TY, Ka JS, Lee, CU, Chung DH (2013) 13th international conference on control, automation and systems (ICCAS 2013). IEEE
37. Hohm DP, Ropp ME (2003) Prog Photovolt Res Appl 11:47–62
38. Hsieh GC, Hsieh H, Tsai CY, Wang CH (2013) IEEE Trans Power Electron 28:2895–2911
39. Sera D, Mathe L, Kerekes T, Spataru SV, Teodorescu R (2013) IEEE J Photovoltaics 3:1070–1078
40. Tey KS, Mekhilef S (2014) Sol Energy 101:333–342
41. Mohd Zainuri MAA, Mohd Radzi MA, Soh AC, Rahim NA (2014) IET Renew Power Gener 8:183–194
42. Chiu C (2010) IEEE Trans Energy Convers 25:1123–1132
43. Chiu C, Ouyang Y (2011) IEEE Trans Control Syst Technol 19:1516–1526
44. El Khateb A, Abd Rahim N, Selvaraj J, Uddin MN (2014) IEEE Trans Ind Appl 50:2349–2358
45. Rizzo SA, Scelba G (2015) Appl Energy 145:124–132
46. Kofinas P, Dounis AI, Papadakis G, Assimakopoulos MN (2015) Energy Build 90:51–64
47. Khanaki R, Radzi MAM, Marhaban MH (2013) In: IEEE conference on clean energy and technology (CEAT 2013), pp 287–292

48. Messalti S, Harrag AG, Loukriz AE (2015) In: 6th international renewable energy congress (IREC 2015), pp 1–6
49. Shi J, Zhang W, Zhang Y, Xue F, Yang T (2015) Electr Power Syst Res 123:100–107
50. Mirhassani SM, Golroodbari SZM, Mekhilef S (2015) Int J Electr Power Energy Syst 64:761–770
51. Liu Y, Huang S, Huang J, Liang W (2012) IEEE Trans Energy Convers 27:1027–1035
52. Lian KL, Jhang JH, Tian IS (2014) IEEE J Photovoltaics 4:626–633
53. Ishaque K, Salam Z (2013) IEEE Trans Industr Electron 60:3195–3206

Chapter 9
Photovoltaic System: Case Studies

Ali Durusu, Ismail Nakir and Mugdesem Tanrioven

Abstract Solar energy is one of the most important energy, which is environmentally friendly such as clean, inexhaustible and free, among the renewable energy sources. Studies on solar photovoltaic (PV) energy generation system were promoted in last two decades. The main application of PV systems are in stand-alone (water pumping, lighting, electrical vehicle, etc.), hybrid and grid-connected (PV power plants) configuration. Stand-alone PV power generation system is considered as good alternative for places that are far from conventional power generation/transmission/distribution system. PV generation systems have two big problems; PV conversion efficiency is very low and PV electricity generation is effected from changing of weather condition. PV output varies periodically in a year and in a day, and is not stable due to environmental condition. Accordingly, in order to increase PV output and PV efficiency, it is crucial to analyze PV output considering solar radiation, temperature, wind speed, shadow, etc. Maximum power point trackers (MPPTs) are employed for extracting power from photovoltaic (PV) panels. MPPTs enforce the solar modules to operate at maximum power point (MPP) under the fluctuations of ambient conditions. Therefore, they take a vital role for increasing of PV system efficiency. In this part, the case studies of MPPT system, which includes stand-alone and hybrid PV systems, will be briefly reviewed, followed by discussion of the MPPT modeling, design, etc. Several stand-alone and hybrid MPPT application will be presented. Latest developments in MPPT methods will be summarized. Finally some of the present challenges facing the MPPT techniques will be explored.

Keywords Photovoltaic systems · Case studies · MPPT algorithms · MPPT algorithm modeling

A. Durusu (✉) · I. Nakir · M. Tanrioven
Yildiz Technical University, Davutpasa Campus, 34220 Istanbul, Turkey
e-mail: adurusu@yildiz.edu.tr

I. Nakir
e-mail: inakir@yildiz.edu.tr

M. Tanrioven
e-mail: mtanrioven@gmail.com

N. Bizon et al. (eds.), *Energy Harvesting and Energy Efficiency*,
Lecture Notes in Energy 37, DOI 10.1007/978-3-319-49875-1_9

Abbreviation and Acronyms

IC	Incremental Conductance
MPP	Maximum Power Point
MPPT	Maximum Power Point Tracker
OC	Only Current Photovoltaic
P&O	Perturbation and Observe
PV	Photovoltaic
SC	Short Circuit Current
THD	Total Harmonic Distortion

9.1 Introduction

Solar energy is one of the most important energy, which is environmentally friendly such as clean, inexhaustible and free, among the renewable energy sources [1]. Studies on solar photovoltaic (PV) energy generation system were promoted in last two decades. The main application of PV systems are in stand-alone (water pumping, lighting, electrical vehicle, etc.), hybrid and grid-connected (PV power plants) configuration. Stand-alone PV power generation system is considered as good alternative for places that are far from conventional power generation/transmission/distribution system. Such systems applications presented in two scale: application at a small scale from 1 to 10 kW and stand-alone PV system in size, from 10 to 100 kW [2]. In hybrid PV systems, more than one type of electricity generator, such as wind turbine, fuel cell, diesel generator, etc., is employed. In grid-connected PV systems, it is usual practice to connect PV system to the electricity grid [3]. A grid-connected PV system provides parallel work with the already established electricity grid and number of PV system features are determined by this connection to the utility grid [4]. PV capacity in the world, including stand-alone, hybrid and grid connected, is rapidly increasing. Figure 9.1 shows the global PV total capacity from 2004 to 2014.

It is clear from the Fig. 9.1 that, 40 GW capacity added in 2014 and also more than 60% of all PV capacity in operation worldwide at the end of 2014 was added over the past 3 years [5].

PV generation systems have two big problems; PV conversion efficiency is very low and PV electricity generation is effected from changing of weather condition [6]. PV output varies periodically in a year and in a day, and is not stable due to environmental condition. Accordingly, in order to increase PV output and PV efficiency, it is crucial to analyze PV output considering solar radiation, temperature, wind speed, shadow, etc.

Maximum power point trackers (MPPTs) are employed for extracting power from photovoltaic (PV) panels. MPPTs enforce the solar modules to operate at MPP under the fluctuations of ambient conditions. Therefore, they take a vital role for

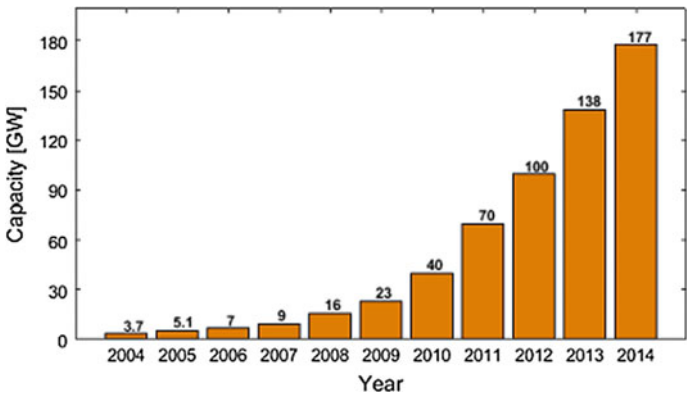

Fig. 9.1 PV total installed capacity from 2004 to 2014 in the world [5]

increasing of PV system efficiency. Different MPPT algorithms are used for the determination of MPP. These algorithms are divided into two groups: direct and indirect. In indirect algorithms, the operating point, where PV generator operates with maximum power, is estimated either measuring current, voltage and radiation values or with numerical approximations-mathematical expressions using experimental data. In direct algorithms, the maximum power point is not obtained by procedures on the contrary to indirect algorithms; the system is forced to operate at MPP. Direct and indirect methods used for determination of maximum power point are examined in the literature. A detailed review of these algorithms is done by Salas et al. [2] and advantages and disadvantages of the algorithms are given. In a study conducted by Berrera et al. [1], seven commonly used MPPT algorithms' MPP tracking performance are compared for two different radiation profiles under standard test conditions. Among the seven generally adopted algorithms, Perturbation and Observe (P&O) algorithm shows the best performance for two different radiation profiles. M. Berrera also states that, Incremental Conductance (IC) algorithm can be a good alternative to P&O algorithm under rapid and continuous irradiance variations. Esram et al. [7], made a comparison of nineteen different MPPT methods according to their cost and performance. The authors state that different algorithms can be suitable for different practice areas. Hohm et al. [8] focus on comparison of three MPPT methods i.e., P&O, IC and Constant Voltage (CV) algorithms, using a PV array simulator. Their performance comparison results show that P&O algorithm is very competitive against other MPP tracking algorithms and can have a better performance in excess of 97%. The study carried out by Hua et al. [9] shows the performance comparison of voltage feedback control, power feedback control and widely used P&O and IC MPPT methods for two different radiation condition. In result of their comparison, among three algorithms IC method shows best performance under two radiation conditions. Reisi et al. [10] compares different MPPT methods with simulation models under Matlab/Simulink.

Their study introduces a classification for MPPT methods based on three categories: hybrid, online and offline methods. As a result of their study, they provide a selection guide of appropriate MPPT methods. Subudhi et al. [11] makes a comprehensive comparison study based on features, like control variables, control strategies, circuitry and approximate costs. Their comparison results offer a useful tool not only for the MPPT users but also the designers and manufacturers of the PV systems. Brito et al. [12] performs the comparison of usual MPPT methods using solar array simulator. They made a comparison between twelve methods with respect to the amount of energy obtained from PV. The authors state that performance differences among the best MPPTs are very slight, and these algorithms must be evaluated according to each situation.

In this part, the case studies of MPPT system, which includes stand-alone and hybrid PV systems, will be briefly reviewed, followed by discussion of the MPPT modeling, design, etc. Several stand-alone and hybrid MPPT application will be presented. Latest developments in MPPT methods will be summarized. Finally some of the present challenges facing the MPPT techniques will be explored. This chapter structured as follows: Sect. 9.2 describes the MPPT techniques and MPPT algorithms modeling; Sect. 9.3 presents the case studies of MPPT techniques, which includes stand-alone and hybrid PV systems; in Sect. 9.4, performance comparison of MPPTs are depicted and at last this part concluded with related discussion.

9.2 Maximum Power Point Tracker

Different MPPT algorithms are used for the determination of MPP. These algorithms are divided into two groups: direct and indirect. The direct methods are; sampling methods, methodology by modulation and other methods. The indirect methods are; curve-fitting, look-up table, open-circuit voltage, short-circuit current and open-circuit voltage of test modules.

9.2.1 Modeling of MPPT Algorithms

This part is presented as a summary of our published conference paper [13]. MPPT algorithms control the PV output to take the PV power to the maximum power point. This control is basically changing of duty-cycle of the dc-dc converter. Duty-cycle changing decision depends on the: PV current in only current photovoltaic (OC) algorithm, short circuit current in short-circuit current (SC) algorithm, PV current and voltage in P&O and IC algorithms. Basic grid-connected PV-battery hybrid system is depicted in Fig. 9.2.

Control part of the dashed diagram (MPPT) in Fig. 9.2 is a MPPT algorithm. Control and Duty part of the MPPT system is depicted as a Matlab/Simulink model in Fig. 9.3.

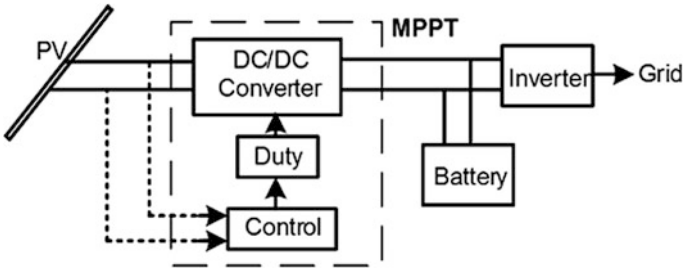

Fig. 9.2 Basic grid-connected PV/battery hybrid system diagram

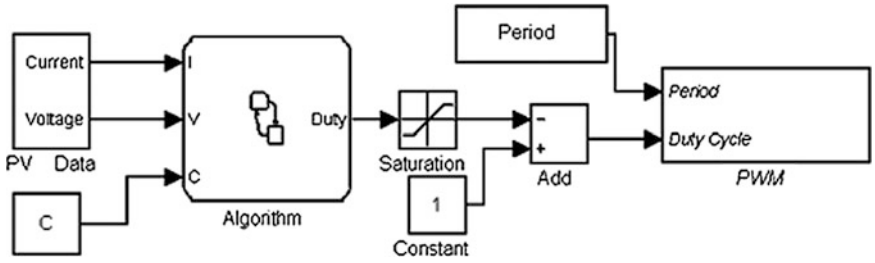

Fig. 9.3 Matlab/Simulink model of the MPPT algorithm

Algorithm blog of the Fig. 9.3 is an actual maximum power point control of the MPPT system. In Fig. 9.3, PV output current, PV output voltage and C (the step-size of the algorithm) input values of algorithm. Duty is an output of the algorithm which is converted to PWM signal.

In this part, Matlab/Stateflow based modeling methodology of four commonly used MPPT algorithms (SC, OC, P&O and IC) are presented. Stateflow is an environment for modeling and simulating combinatorial and sequential decision logic based on state machines and flow charts. Stateflow provides combine tabular and graphical representations, including flow charts, state transition diagrams, state transition tables and truth tables to model how your system reacts to events, time-based conditions, and external input signals. With Stateflow you can design logic for supervisory control, task scheduling, and fault management applications [14].

9.2.1.1 Perturbation and Observe Algorithm

Perturbation and Observe algorithm uses an iterative method to extract maximum power from PV. P&O algorithm measures the power values of PV array and then compares the measured power with prior power to perturb the operation point of PV. If the PV power error is positive, then it changes the duty in same direction. On the other hand, if the PV power error is negative, then it changes the duty in reverse

direction. This duty change continues until PV output power reaches the MPP power level. Figure 9.4 illustrate a basic flowchart and Matlab/Stateflow model of P&O algorithm.

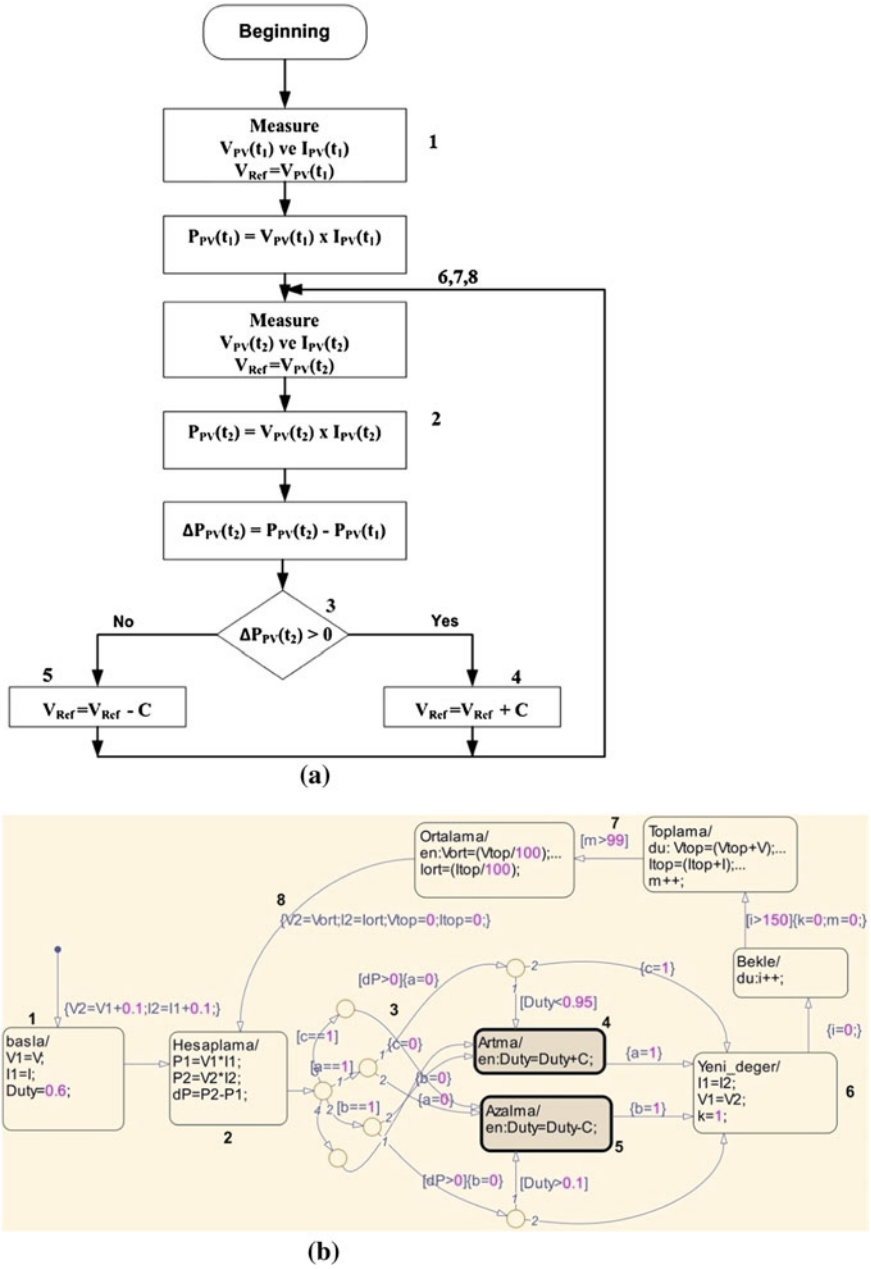

Fig. 9.4 **a** Basic flowchart, **b** Matlab/Stateflow model of P&O algorithm [13]

Table 9.1 Matlab/Stateflow model description of the P&O algorithm

No.	Comment	No.	Comment
1	Beginning	5	Decrease duty
2	Calculate $P_{PV}(t_1)$, $P_{PV}(t_1)$ and ΔP	6	Assign $V_{PV}(t_1)$, $I_{PV}(t_1)$
3	Evaluate ΔP	7	Measure $V_{PV}(t_2)$, $I_{PV}(t_2)$
4	Increase duty	8	Go to 2

Detailed description of the Matlab/Stateflow model in Fig. 9.4 is given in Table 9.1 according to the numbers in the model.

9.2.1.2 Incremental Conductance Algorithm

IC algorithm forced the PV to the MPP based on the observation of conductivity by taking the instantaneous output voltage and output current of PV. Conductivity observation is based on the differentiation of PV power with respect to the PV voltage and setting result to zero. Equations (9.1) and (9.2) give the conductivity observation of the IC method [2].

$$\frac{dP_{PV}}{dV_{PV}} = I_{PV}\frac{dV_{PV}}{dV_{PV}} + V_{PV}\frac{dI_{PV}}{dV_{PV}} = I_{PV} + V_{PV}\frac{dI_{PV}}{dV_{PV}} = 0 \tag{9.1}$$

$$-\frac{I_{PV}}{V_{PV}} = \frac{dI_{PV}}{dV_{PV}} \tag{9.2}$$

In (9.2), the right side of the equation is the incremental conductance and the left side of the equations is the negative conductivity. Figure 9.5 shows the basic flowchart and Matlab/Stateflow model of IC algorithm.

Detailed description of the Matlab/Stateflow model in Fig. 9.5 is given in Table 9.2 according to the numbers in the model.

9.2.1.3 Only Current Photovoltaic Algorithm

In the OC algorithm, the PV is forced to operate at the maximum power point by using only PV current. Equation (9.3) can be obtained from boost type dc-dc converter equation.

$$P_{PV} = V_{PV}I_{PV} = V_o(I_{PV}(1-D)) = P^*_{boost}V_o \tag{9.3}$$

In the OC algorithm, PV current and PV voltage are measured and then PV power is calculated. Then duty-cycle is changed. PV current and PV voltage are measured again and then PV power calculated. PV power compares with prior one.

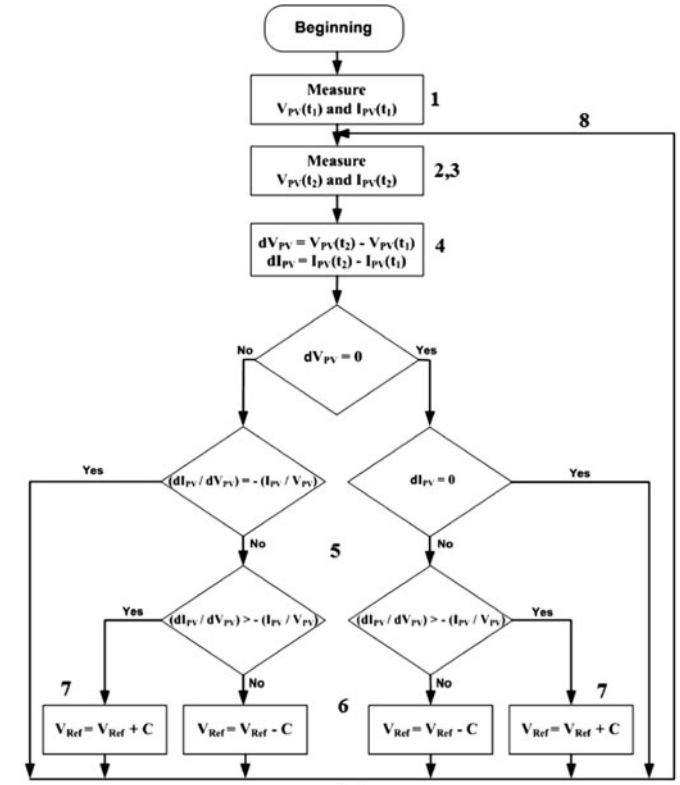

(a)

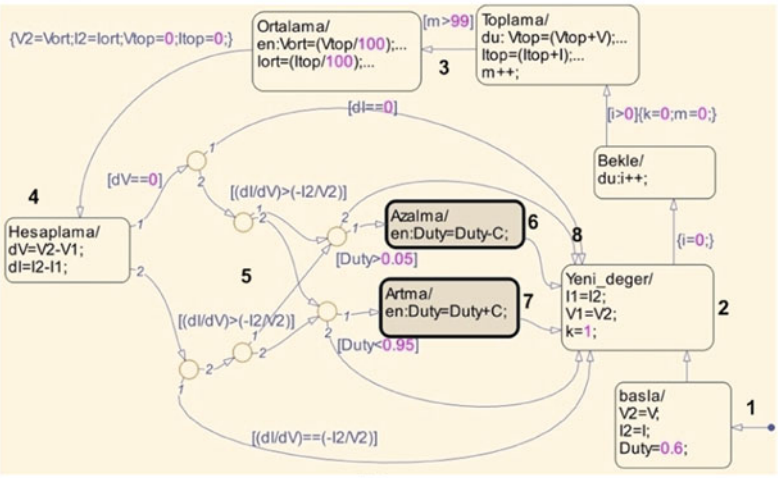

(b)

Fig. 9.5 **a** Basic flowchart, **b** Matlab/Stateflow model of IC algorithm [13]

Table 9.2 Matlab/Stateflow model description of the IC algorithm

No.	Comment	No.	Comment
1	Beginning	5	Evaluate conductance
2	Assign $V_{PV}(t_1)$, $I_{PV}(t_1)$	6	Increase duty
3	Measure $V_{PV}(t_2)$, $I_{PV}(t_2)$	7	Decrease duty
4	Calculate dV and dI	8	Go to 2

Table 9.3 Matlab/Stateflow model description of the OC algorithm

No.	Comment	No.	Comment
1	Beginning	5	Evaluate duty
2	Measure $I_{PV}(t_1)$, calculate $P_{PV}(t_1)$	6	Increase/decrease duty
3	Measure $I_{PV}(t_2)$, calculate $P_{PV}(t_2)$	7	Assign $P_{PV}(t_1)$
4	Evaluate $P_{PV}(t_1)$ and $P_{PV}(t_2)$	8	Go to 3

As a result of the comparison, algorithm decides to increase/decrease the duty-cycle. Figure 9.6 shows the basic flowchart and Matlab/Stateflow model of the OC algorithm.

Detailed description of the Matlab/Stateflow model in Fig. 9.6 is given in Table 9.3 according to the numbers in the model.

9.2.1.4 Short Circuit Current Algorithm

SC algorithm depends on the linear relation between maximum power point current and PV short circuit current. The relation is actually a proportional constant (k). The proportional constant mainly depends on the fill factor, solar cells fabrication technology and the environmental conditions [2].

$$k = \frac{I_{MPP}}{I_{SC}} \doteq \text{Constant} < 1 \tag{9.4}$$

SC algorithm flowchart and Matlab/Stateflow model are depicted in Fig. 9.7.

Detailed description of the Matlab/Stateflow model in Fig. 9.7 is given in Table 9.4 according to the numbers in the model.

9.3 Case Studies of the MPPT Algorithms

Many researches in the literature [7–13, 15–21] investigated different MPPT systems. Some of these studies are given below as stand-alone and hybrid application.

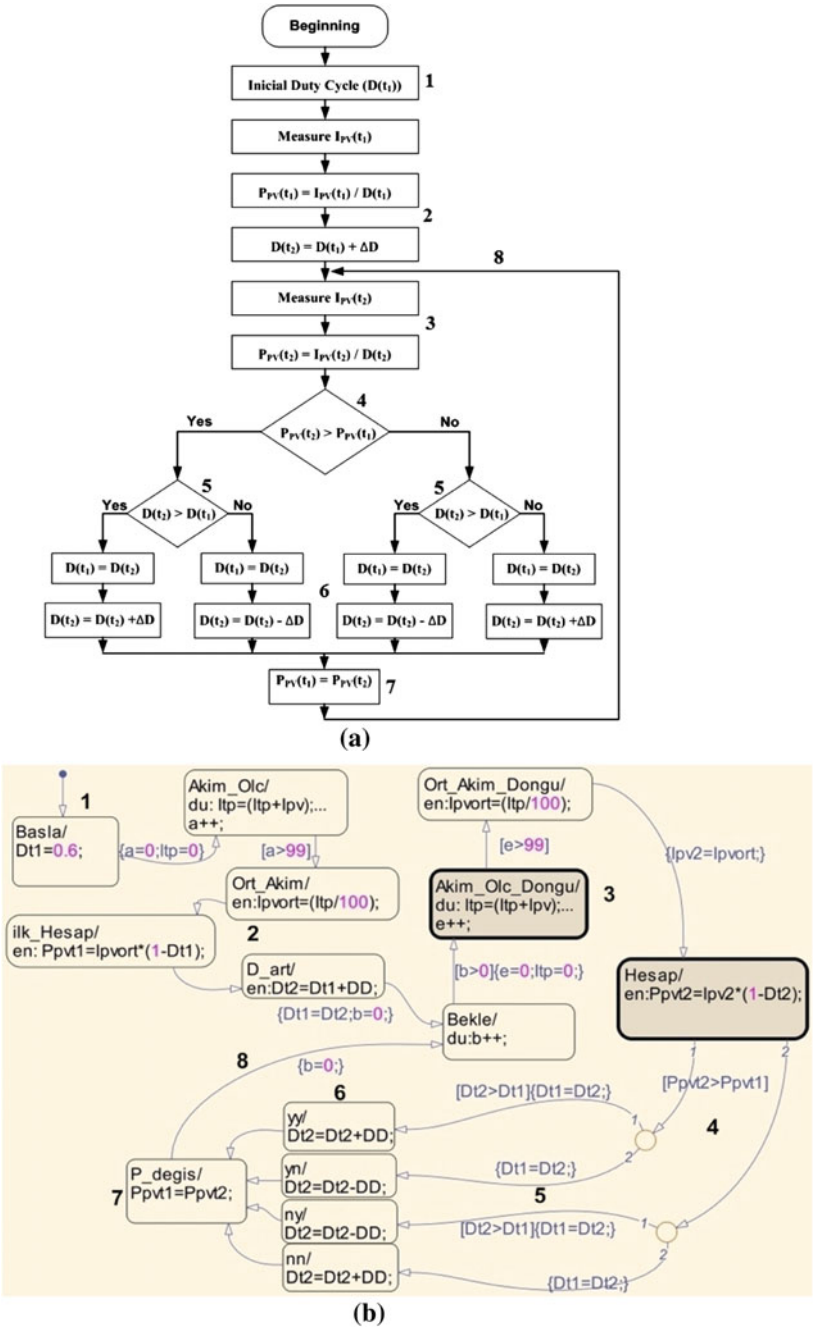

Fig. 9.6 **a** Basic flowchart, **b** Matlab/Stateflow model of OC algorithm [13]

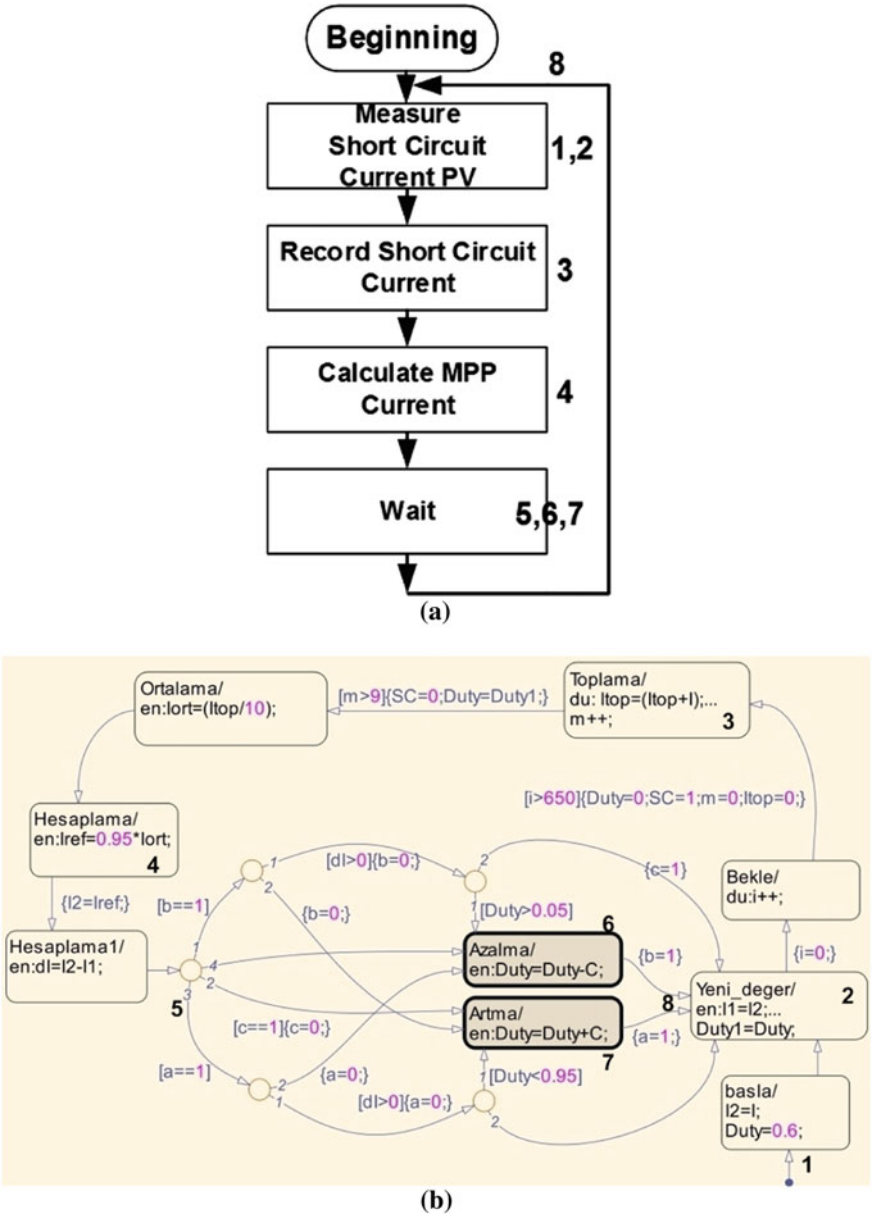

Fig. 9.7 **a** Basic flowchart, **b** Matlab/Stateflow model of SC algorithm [13]

Table 9.4 Matlab/Stateflow model description of the SC algorithm

No.	Comment	No.	Comment
1	Beginning	5	Evaluate I_{MPP}
2	Assign $I_{SC}(t_1)$	6	Decrease duty
3	Measure $I_{SC}(t_2)$	7	Increase duty
4	Calculate I_{MPP}	8	Go to 2

9.3.1 Stand-Alone Applications

Stand-alone applications are given in this part as a summary of our previous published paper [15, 16].

9.3.1.1 Widely-Used MPPT Algorithms Comparison

In this part, unlike the MPPT performance studies which are investigated before, four commonly used MPPT algorithms performances are compared under real ambient conditions. The MPP tracking systems are realized with an experimental setup, which is capable of running four commonly used MPPT algorithms (P&O, IC, OC and SC). As a result under real environmental condition, the performances of the MPPT algorithms are measured and compared [16].

The realized experimental setup is constituted of five main elements: control unit, the dc-dc converters, battery, two identical PV panels and a power analyzer for measuring PV module output values. Figure 9.8 shows the block diagram of the

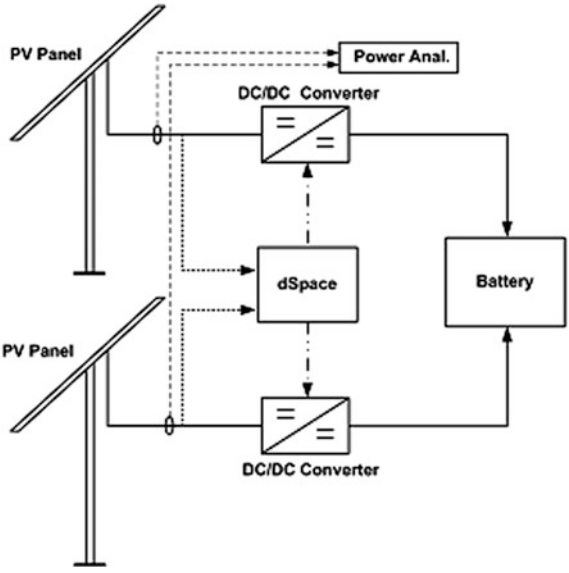

Fig. 9.8 Experimental test system diagram for performance evaluation of MPPT methods [15]

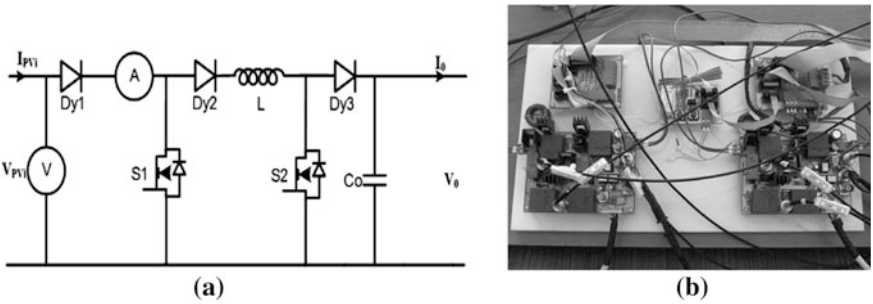

Fig. 9.9 **a** Dc-dc converter circuit, **b** converter power boards [15]

experimental setup. Identical boost type dc-dc converters are connected identical PV panels which are fixed at same position. Dc-dc converters are controlled by the same controller (dSpace). 24 V battery bank is connected to the dc-dc converters' outputs [15].

Step-up type dc-dc converters are employed for the comparison. All of four above mentioned MPPT algorithms can be easily obtained by changing the control algorithm in the control system. Detailed information about dc-dc converter is given in [1]. Converters are operated at 35 kHz frequency. Dc-dc converters control is based on the current and voltage measurements of PV panels which are obtained by hall-effect sensors. Designed power boards and dc-dc converter circuit are depicted in Fig. 9.9. Figure 9.9a also shows that, there is a S1 switch which is necessary for measuring the short circuit current of PV for the SC method.

MPPT algorithms are designed in Matlab/Stateflow Toolbar. Dc-dc converters are controlled by running the algorithms in the dSpace. Herein, algorithm codes are generated in Matlab-Simulink. Basic control scheme of the test bench is shown in Fig. 9.10.

Matlab/Simulink based dSpace control is used for performance comparison of SC, IC, OC and P&O MPPT algorithms. MPP control diagrams for each of algorithm modeled in Matlab/Simulink individually. The algorithm in Fig. 9.10 is a Matlab/Stateflow based designed subsystem of the control unit. The input C (step size of the algorithms) is selected as 0.01 to compare MPPT algorithms under the same conditions.

9.3.1.2 Performance Comparison of MPPT Algorithms for Vehicle Integrated PV Modules

This part presents performance comparison of IC, P&O and OC algorithms examined under real environmental conditions. Performance of algorithms are comparing as a double groups on a special test bench. Potential performance of MPPT algorithms regulating output of solar modules on a vehicle is assessed by controlled moving modules at the special test bench [16].

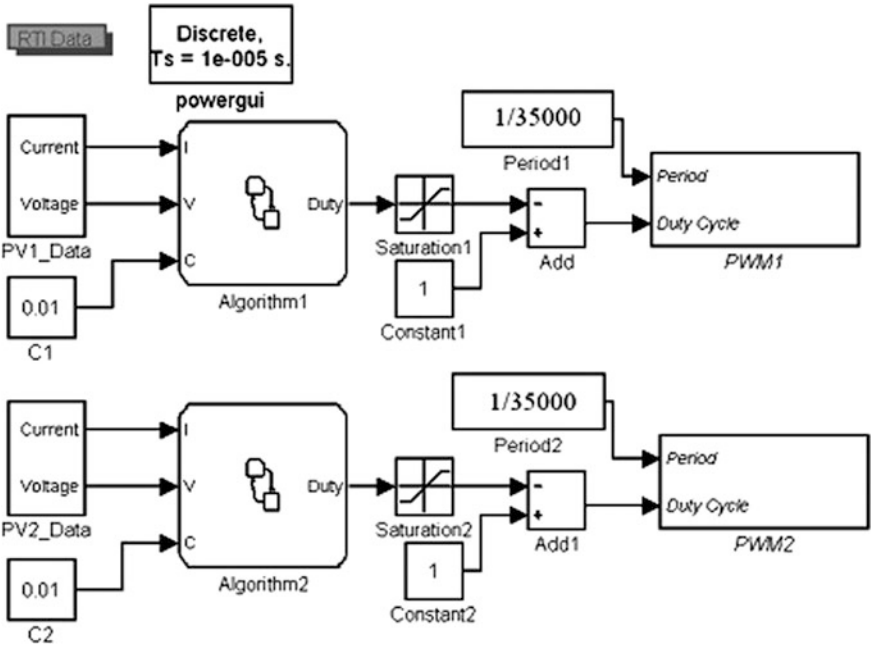

Fig. 9.10 Basic Matlab/Simulink based control scheme of MPPT system [15]

The test bench employed for performance evaluation of MPPT algorithms is constituted from a measurement system (power analyzer) for measuring output power of PV modules, two identical dc-dc converters, two identical PV modules and control unit for employing three MPPT algorithms. The basic block scheme of the test bench is illustrated in Fig. 9.11. PV modules are mounted on test platform to simulate fluctuating irradiance of solar panels on a vehicle in motion. This platform can change both azimuth angle and tilt angle of PV modules. In this study, the platform is moved regarding to a defined motion loop to test realizations of three MPPT algorithms with variation of solar irradiance.

Motion loop of the platform consist of four time intervals and motion ratio of platform is increased at each time interval to simulate fluctuation of solar irradiance with different ratios. This motion loop makes possible to verify responses of MPPT algorithms to the variation of solar irradiance. Consequently, the test platform can simulate instant solar irradiance changes that MPPTs will face for vehicle integrated solar panels. Figure 9.12 shows an example of change in solar radiation of motion loop.

Motion loop of the platform is composed of four time intervals to simulate changing of solar irradiance with higher ratios at each time interval. This effect is simulated by making solar panels move in four different ways with four different motion loops of the platform. Between 0 and 50 s time intervals, only tilt angle slightly changes by time. Between 50 and 100 s time intervals, tilt angle changes are considerably much bigger than first time interval. 100–160 s time intervals are

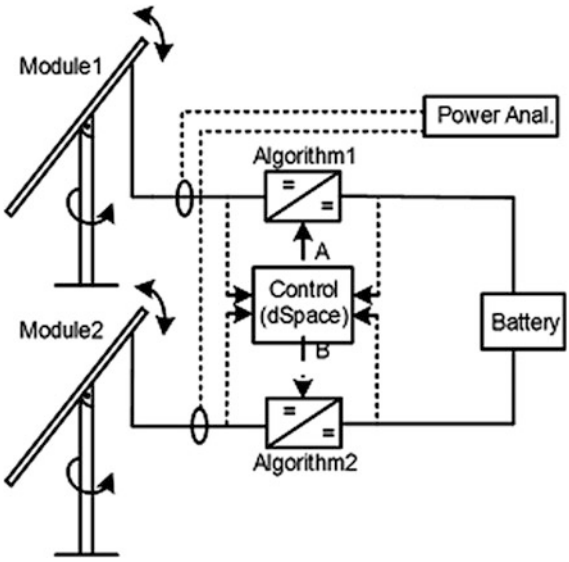

Fig. 9.11 Basic block scheme of the test bench [16]

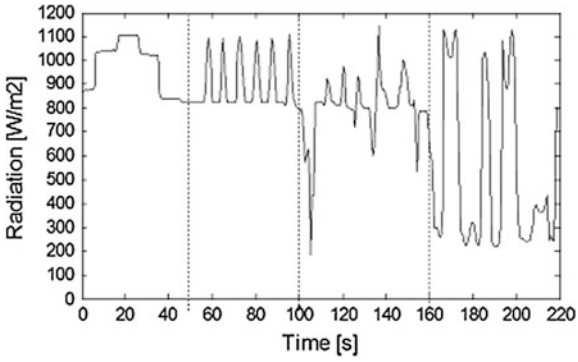

Fig. 9.12 An example of change in solar radiation in motion loop [16]

for changing of both azimuth angle and tilt angle at the same time. Between 160 and 220 s time intervals, while tilt angle of platform is constant, only direction of panels is altered rapidly. As it is understood from each interval, for getting maximum radiation variation, motion of platform is increased from first interval to last interval. Motion loop is designed this way, to measure success of each MPPT algorithms under high variation of solar irradiance which they should deal with for vehicle integrated solar panels.

In the designed test bench, dSPACE is employed as a control unit. This controller manages both control signals of dc-dc converters and defined motion loop simultaneously. Algorithm codes for defined motion loop and dc-dc converters are generated in Matlab/Simulink. Three different control algorithm codes for converters are generated for each MPPT algorithm and implemented as double combinations of three algorithms to compare each other. A sample control diagram, which is modeled in Matlab/Simulink, for one of the comparison is shown in Fig. 9.13.

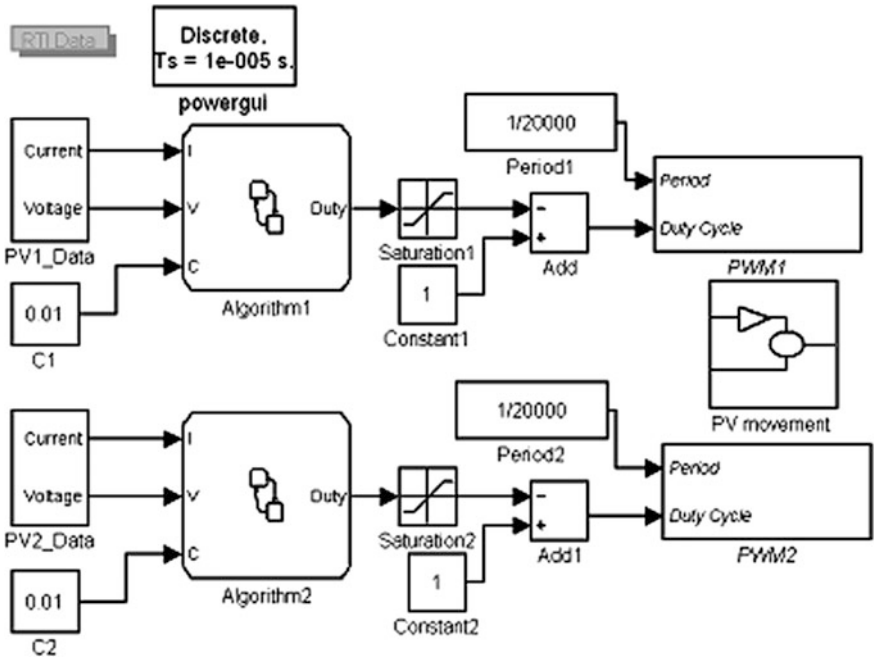

Fig. 9.13 Basic Matlab/Simulink control diagram of the test bench [16]

9.3.2 Hybrid System Application

Hybrid system applications are given in this part as a summary of our previous published paper [17]. In this part, wind-solar-battery hybrid system constructed on the roof of Electrical Engineering Department Building, Yildiz Technical University, Istanbul, Turkey is studied. A wind turbine which is equipped with permanent magnet synchronous generator (PMSG), two PV arrays and battery group are employed as hybrid system equipment in the system. In addition, an inverter, a MPPT controller and a hybrid charge controller are employed as power conditioner unit. A measurement and a data logging system are also exist in the hybrid system. It is planned to realize reliability analysis and wind/solar energy potential of investigated area with measurements.

Hybrid system has eight PV modules. PV modules are divided into two groups. One of the groups (PV1: four modules) is connected to hybrid charge controller with wind turbines. The other PV group (PV2: four modules) is connected to the MPPT charge controller. Hybrid charge controller and MPPT charge controller are connected to 24 V DC bus. Battery group has two series (for reaching the DC bus voltage level) and two parallel elements. Figure 9.14 illustrates the basic block scheme of the wind-solar-battery hybrid system.

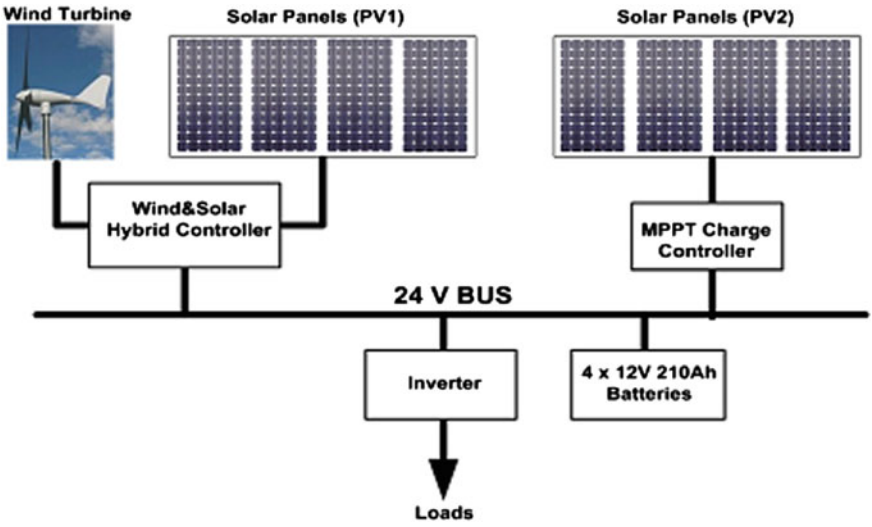

Fig. 9.14 Block diagram of the wind&PV hybrid system [17]

Hybrid charge controller has 1000 W nominal power which is designed for low power wind-solar applications which controls the wind turbine and PV1. Hybrid charge controller adjusts the sources depends on battery voltage level. Moreover, controller also employed for some protection features such as solar wind turbine automatic brake, battery over voltage, cells reverse charging, etc.

MPPT charge controller controls the PV2. MPPT charge controller adjust the PV2 depends on the battery voltage level. Moreover, controller also employed for some protection features such as battery over/deep voltage protection, PV reverse current protection, etc.

The inverter is employed for supplying loads power from DC bus. Inverter has 1000 W nominal power and 3% THD value. Input DC voltage range is various from 21 to 30 V to protect batteries from over charge and deep discharge.

As illustrated in Fig. 9.15, loads are halogen lamps (100 W). Load power is supplied by hybrid system. Three 100 W halogen lamps are connected to system as

Fig. 9.15 Loads of the system

loads. Loads can be switched individual switches to analyze dynamic response of the system.

Measurements, control and the monitoring elements of the hybrid system are depicted in Fig. 9.16.

Fig. 9.16 Measurements, control and monitoring elements of the hybrid system

9.4 Performance Comparison of the MPPTs

9.4.1 Widely-Used MPPT Algorithms Comparison

In this section, the experimental system performances of four algorithms are presented. In this study two identical dc-dc converters are connected to two identical PV panels. These dc-dc converters are controlled by two different MPPT algorithms for a period of 240 s. This comparison process is carried out until all algorithms' comparisons with each other are done. Because two algorithms are compared together on same platform and environmental conditions are same for each PV panel in all comparisons [15].

In order to analyze the performance of four MPP tracking algorithms, algorithms are experimentally compared under medium-high (540–640 W/m^2) radiation level. This comparison process is carried out between 13:35 pm and 14:35 pm time intervals on 26 Dec. 2012. Figure 9.17 shows the wind speed and ambient temperature variation between 13:35 pm and 14:35 pm (1 h) during the comparison process. As it can be seen in Fig. 9.17, while ambient temperature is almost stable, wind speed change between 1–5 m/s. Wind speed decreases the PV temperature which is one of the affecting factor of PV performance. Wind speed variation is neglected in this study due to the PV performance is mainly affected from temperature and radiation. The output power values of PV modules employed by each algorithm are depicted in Fig. 9.18.

Numerical result of these comparisons are given in Table 9.5. The test results show that real environmental conditions, IC algorithm is the most successful MPPT algorithm. However P&O algorithm performance is very close to the IC algorithm. When the P&O algorithm is optimized, the MPP tracking performance of IC and P&O algorithms will be the same. The IC algorithm success based on [15];

- IC algorithm oscillates around the MPP less then P&O algorithm,
- IC algorithm does not diverge from MPP under rapidly changing radiation,
- IC algorithm uses PV current and voltage to track the MPP,
- IC algorithm does not cut the power flow for measuring the PV current/voltage.

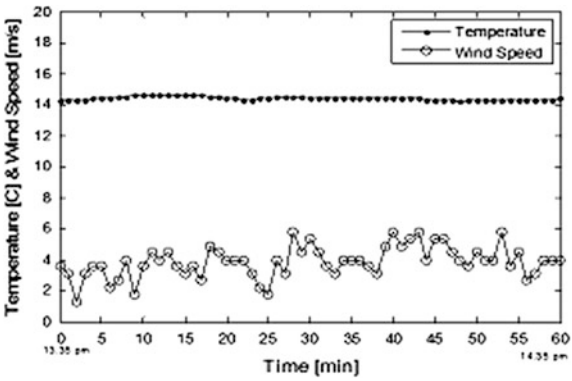

Fig. 9.17 Wind speed and temperature variation during the comparison process [15]

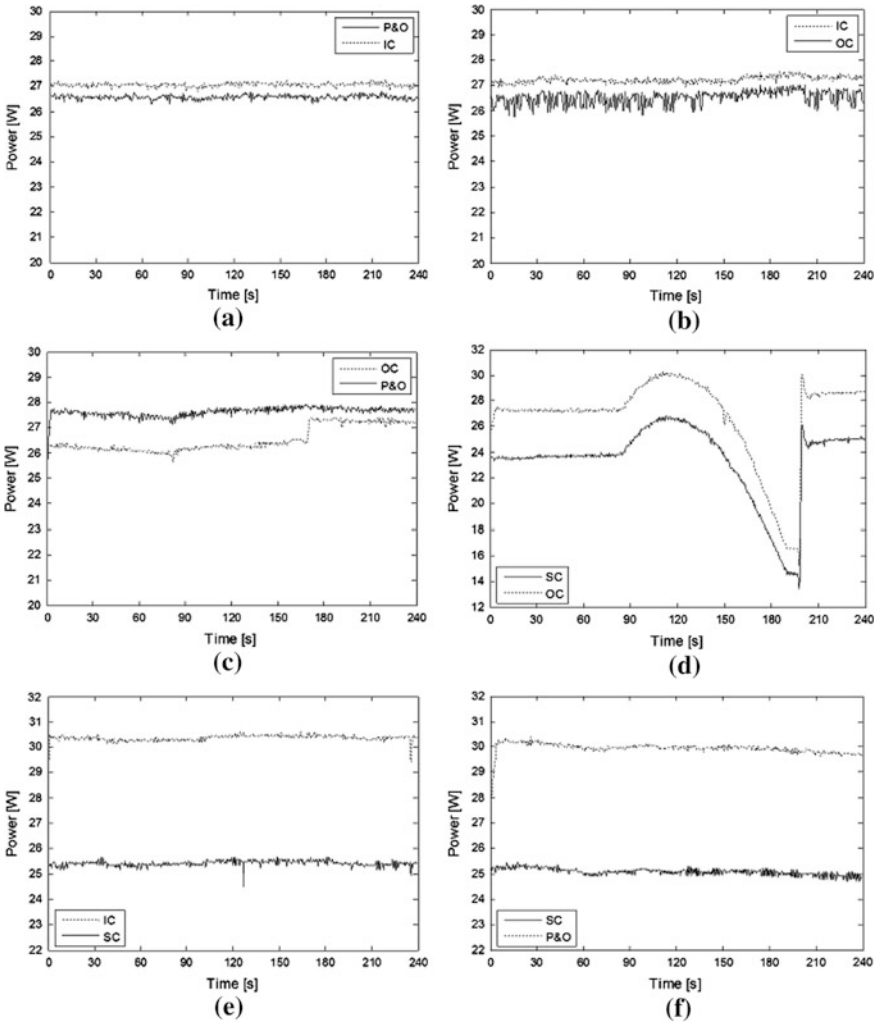

Fig. 9.18 Comparison results of **a** IC and P&O, **b** OC&IC, **c** OC and P&O, **d** SC and OC, **e** IC and SC, **f** SC and P&O algorithms [15]

9.4.2 Vehicle Integrated Solar System

This part presents performance comparison results related to the three MPPT algorithms. Three different algorithms compared as couples between each other and power values are measured. Power output values of each algorithm and the solar radiation variation on PV modules are illustrated in Fig. 9.19.

In Fig. 9.19b, power output result of OC and IC algorithms are depicted. Figure 9.19 confirms natural expectation, that power outputs of both algorithms are

Table 9.5 Numerical results of the comparisons [15]

Comparison	Algorithm	Energy	Delta energy (%)	
			Delta	%
P&O & IC	P&O	6376	IC	1.835
	IC	6493		
OC & IC	OC	6342	IC	2.806
	IC	6520		
OC & P&O	OC	6291	P&O	4.991
	P&O	6605		
SC& IC	SC	6097	IC	19.28
	IC	7273		
SC& P&O	SC	6035	P&O	19.27
	P&O	7198		
SC&OC	SC	5862	OC	14.35
	OC	6703		

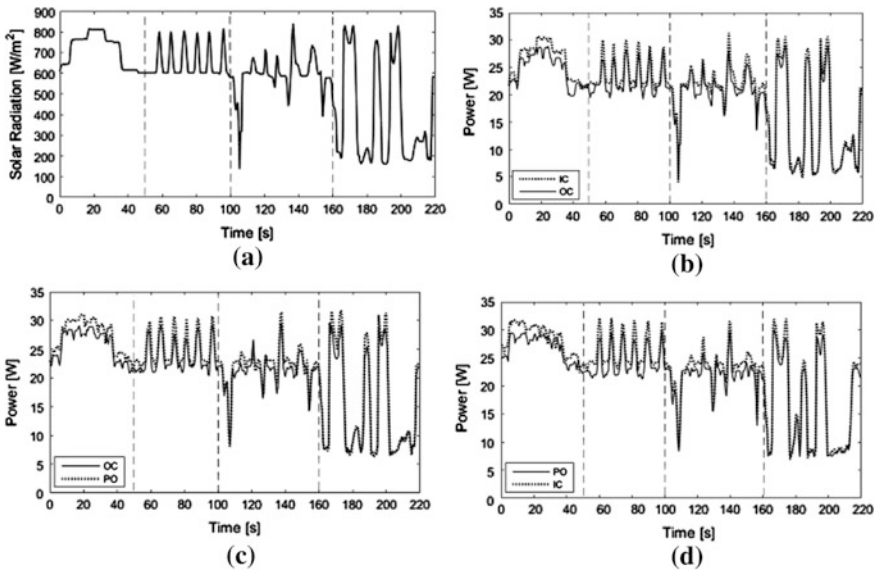

Fig. 9.19 **a** Solar radiation and comparison results of **b** OC and IC, **c** OC and P&O, **d** IC and P&O algorithms [16]

similar with solar radiation. On the other hand, power-time graph in Fig. 9.19b also shows that IC algorithm is more successful at tracking MPP. Total energy data acquired from the power analyzer that are given in Table 9.6 also proves it. Percentage of energy differences in Table 9.7 indicates that efficiency of IC algorithm is 5.536% higher than OC algorithm.

Table 9.6 Numerical results of the four section of motion loop [16]

Comparison	Algorithm	Energy (J)			
		Sect. 1	Sect. 2	Sect. 3	Sect. 4
OC & IC	OC	1234	1132	1233	826
	IC	1309	1190	1306	865
OC & P&O	OC	1290	1173	1273	881
	P&O	1365	1247	1324	925
P&O & IC	P&O	1348	1209	1305	969
	IC	1430	1300	1385	1026

Table 9.7 Energy differences results of the four section of motion loop [16]

Comparison	Delta	Energy differences (Delta energy) (%)				
		Sect. 1	Sect. 2	Sect. 3	Sect. 4	Total
OC & IC	IC	6.077	5.123	5.920	4.721	5.536
OC & P&O	P&O	5.813	6.308	4.006	4.994	5.284
P&O & IC	IC	6.083	7.526	6.130	5.882	6.416

In Fig. 9.19c, power output result of OC and P&O algorithms are depicted. This time P&O algorithm is more successful at tracking MPP. Total energy data in Table 9.6 which is acquired from the power analyzer also verifies this inference. Delta energy data in Table 9.7 reveals that P&O algorithm has 5.284% more total efficiency as compared to OC algorithm.

In Fig. 9.19d, power output result of winners of first and second comparisons are depicted. As depicted in Fig. 9.19d P&O algorithm is less successful than IC algorithm at finding MPP. It is also stated in Tables 9.6 and 9.7 with total energy data and energy differences data respectively. IC algorithm is more successful than P&O algorithm.

The test results show that IC algorithm is the most successful maximum power point tracker algorithm under fast altering solar irradiation. However this performance is not based on success of IC algorithm at radiation fluctuation. This situation is detected from energy differences data in Table 9.7. Although radiation variation values increased at every section, delta energy is not increasing regularly with each section. With presence of these results, it is not possible to show that IC algorithm is more adaptive to variation of irradiance than P&O and OC algorithms. Besides it can be claimed that IC algorithm is the most successful one between three algorithms at tracking MPP also in the case quick variations at irradiation.

9.4.3 Hybrid System

Hybrid system results are given in this part as a summary of our previous published paper [18]. In this study, the effects of two different charge controllers on PV panel performances are investigated as given in Fig. 9.20. The weather conditions and electrical values of the system are recorded simultaneously with a weather station

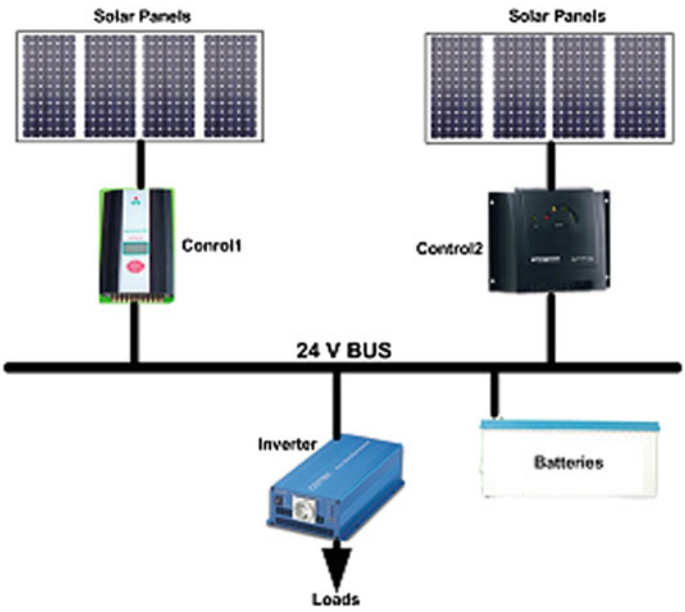

Fig. 9.20 Block diagram of the investigated system [18]

and a data logger. The analyzed data are recorded between 10 Oct. 2013 and 30 Oct. 2013 for 20 days. The variation of solar radiation on the location is shown in Fig. 9.21.

Current and voltage values of PV panels are recorded for duration of a minute. Output voltage and current values of two panels are shown in Fig. 9.22. Vmppt and Imppt define output voltage and current of PV2, V_{hybrid} and I_{hybrid} identify output voltage and current of PV1, and V_{bus} describes DC bus voltage.

DC bus voltage variation is kept in desired limit between 21 and 30 V as clearly seen in Fig. 9.22. The output voltages of both panels drop to 10 V when the solar

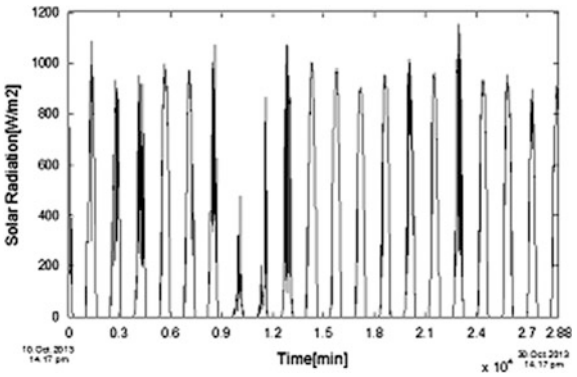

Fig. 9.21 Variation of the solar radiation during the comparison [18]

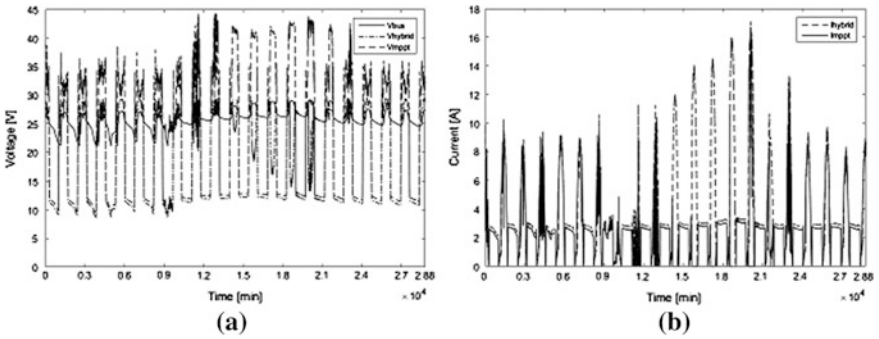

Fig. 9.22 **a** Output voltage, **b** output current of the PV system [18]

radiation is minimum. Output voltage of PV2 increases up to 45 V when the radiation is maximum whereas maximum output voltage of PV1 stays under 30 V.

If the current variations are examined, although PV1 gives higher current than PV2, similar characteristics can be seen in both systems. In the days between 9th and 15th that solar radiation is maximum in, output current of PV2 is minimum since Controller 2 monitors and controls the DC bus voltage to prevent the voltage exceed 27.8 V.

Output power variations of panels are shown in Fig. 9.23. The output power characteristic varies in proportion to solar radiation as seen in Fig. 9.23. Operation characteristic of PV2 panel group controlled by Controller 2 depending on DC bus voltage can be seen clearly in the Fig. 9.23.

Since DC bus voltage reaches to maximum value between 9th and 15th days, Controller 2 restricts the related panel output power. This feature contributes to system stability. In the same time interval, there is no limitation in other panel output power. Although Fig. 9.23 creates perception that the generated power by PV1 is higher than PV2, the total energy obtained from PV1 is 39,826 kWh whereas PV2 is 45,366 kWh in the measurement interval. The energy generated from PV2 is higher by 16.81% from PV1.

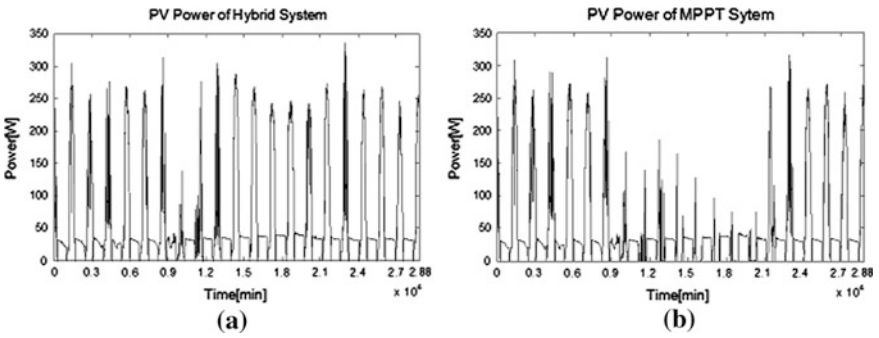

Fig. 9.23 **a** Output power of PVhybrid, **b** output power of the PVmppt [18]

The power difference between two panel groups is caused by Controller 2 that always provides maximum power point operating. While output power of PV1 oscillates in high range, there is stable output power in PV2. It clearly seen from Fig. 9.23a that DC bus voltage is higher than 27.8 V between the days 9th and 14th.

9.5 Conclusion

In this part, the case studies of MPPT system, which includes stand-alone and hybrid PV systems, are briefly reviewed, followed by discussion of the MPPT modeling, design, etc. Several stand-alone and hybrid MPPT application are presented then latest development in MPPT methods will be summarized and finally some of the present challenges facing the MPPT techniques are explored. Case studies and results are presented. Based on the chapter general results, main conclusions are as follows:

- MPPT system has a vital importance for PV applications.
- MPPT system improve the efficiency of PV systems.
- MPPT algorithms performance is affecting environmental conditions.
- The most successful MPPT algorithms among the four commonly used MPP methods is IC.
- The success of IC algorithm is coming from its success in comparison with P&O and OC algorithms at all ambient conditions.
- SC algorithm turned out to be the worst one.
- MPPT controllers have different algorithms and operating principle change the performance of PV modules.
- Controller selection has much importance as panel type, application area and battery size in photovoltaic system design.

References

1. Berrera M, Dolara A, Faranda R, Lova S (2009) Experimental test of seven widely-adopted MPPT algorithms. In: IEEE Bucharest Power Tech Conference, 2009, pp 1–8
2. Salas V, Olias E, Barrado A, Lazaro A (2006) Review of the maximum power point tracking algorithms for stand-alone photovoltaic systems. Sol Energy Mater Sol Cells 90:1555–1578
3. Kalogirou S (2009) Solar energy engineering: processes and systems. Academic Press, New York
4. Markvart T, Castaner L (2003) Practical handbook of photovoltaics fundamentals and applications. Elsevier, UK
5. Renewable Energy Policy Network for the 21st Century (2015) Renewables 2015 global status report. http://www.ren21.net/ren21activities/globalstatusreport.aspx
6. Mutoh N, Ohno M, Inoue T (2006) A method for MPPT control while searching for parameters corresponding to weather conditions for PV generation systems. IEEE Trans Ind Electron 53(4):1055–1065

7. Esram T, Chapman PL (2007) Comparison of photovoltaic array maximum power point techniques. IEEE Trans Energy Convers 22(2):439–449
8. Hohm DP, Ropp ME (2003) Comparative study of maximum power point tracking algorithms. Prog Photovolt Res Appl 11:47–62
9. Hua C, Shen C (1998) Comparative study of peak power tracking techniques for solar storage system. In: IEEE applied power electronics conference and exposition, pp 679–685
10. Reisi AR, Moradi MH, Jamas S (2013) Classification and comparison of maximum power point tracking techniques for photovoltaic system: a review. Renew Sustain Energy Rev 19:433–443
11. Subudhi B, Pradhan RA (2013) Comparative study on maximum power point tracking techniques for photovoltaic power systems. IEEE Trans Sustain Energy 4:89–98
12. Brito MAG, Galotto L, Sampaio LP, Melo GA, Canesin CA (2013) Evaluation of the main MPPT techniques for photovoltaic application. IEEE Trans Ind Electron 60:1157–1167
13. Durusu A, Nakir I, Tanrioven M (2014) Matlab/Stateflow based modeling of MPPT algorithms. Int J Adv Electron Electr Eng 3:117–120
14. MatWorks (2015) Stateflow support documents (Support). http://www.mathworks.com/help/stateflow/index.html
15. Durusu A, Nakir I, Ajder A, Ayaz R, Akca H, Tanrioven M (2014) Performance comparison of widely-used maximum power power point tracker algorithms under real environmental conditions. Adv Electr Comput Eng 14(3):89–94
16. Nakir I, Durusu A, Ugur E, Tanrioven M (2012) Performance assessment of MPPT algorithms for vehicle integrated solar system. In: 2nd IEEE energy conference and exhibition, pp 1034–1038
17. Arikan O, Isen E, Durusu A, Kekezoglu B, Bozkurt A, Erduman A (2013) Introduction to hybrid system-Yildiz Technical University. IEEE Eurocon 2013:1145–1149
18. Arikan O, Kekezoglu B, Durusu A, Isen E, Erduman A, Bozkurt A (2014) Comparison of charge controllers on PV performance: an experimental study. Int J Adv Electron Electr Eng 3:121–125
19. Nakir I, Durusu A, Akca H, Ajder A, Ayaz R, Ugur E, Tanrioven M (2016) A new MPPT algorithm for vehicle integrated solar energy system. J Energy Resour Tech 138 (2):021601-1-9
20. Hsieh GC, Hsieh HI, Tsai CY, Wang CH (2013) Photovoltaic power-increment-aided incremental-conductance MPPT with two-phased tracking. IEEE Trans Power Electron 28:2895–2911
21. Wang F, Wu X, Lee FC, Wang Z, Kong P, Zhuo F (2014) Analysis of unified output MPPT control in subpanel PV converter system. IEEE Trans Power Electron 29(3):1275–1284

Chapter 10
Maximum Power Point Tracking Algorithms for Partial Shaded PV Systems

Ibrahim Sefa, Necmi Altin and Saban Ozdemir

Abstract Photovoltaic modules have nonlinear current-voltage (*I-V*) characteristics. Thus, output power of the photovoltaic module varies with module specification and its operation point. It means that, the photovoltaic system generates maximum power at a single operation point for an environmental condition such as the irradiation level and angle, ambient temperature level etc. In addition, energy conversion efficiency varies with load level and operation point of the photovoltaic system. Since these parameters are variable, operation point of the photovoltaic system should be controlled to get maximum output power and maximum energy conversion efficiency. This action is called as maximum power point tracking. The maximum power point tracking action is usually performed with a power electronics converter. A number of maximum power point tracking methods have been introduced to obtain fast response, especially in rapidly-changing atmospheric conditions, low oscillation and higher energy conversion efficiency values. However, most of these methods are effective for uniform solar irradiation conditions. If the solar irradiation is non-uniform, the power-voltage (*P-V*) curve of the photovoltaic module or array has multiple peak points: Several local maximum power points and one global maximum point. In this case, traditional maximum power point tracking methods determine the nearest peak power point, which may be a local maximum point. Thus, some improved maximum power point tracking methods have been proposed to determine the global maximum power point of the photovoltaic system even under partial shading conditions. A discussion on different maximum power point tracking methods for the solution of these problems will be given and the most powerful techniques in the literature will be outlined.

I. Sefa · N. Altin (✉)
Department of Electrical and Electronics Engineering, Faculty of Technology, Gazi University, Ankara, Turkey
e-mail: naltin@gazi.edu.tr

I. Sefa
e-mail: isefa@gazi.edu.tr

S. Ozdemir
Vocational School of Technical Sciences, Gazi University, Ostim, Ankara, Turkey
e-mail: sabanozdemir@gazi.edu.tr

N. Bizon et al. (eds.), *Energy Harvesting and Energy Efficiency*,
Lecture Notes in Energy 37, DOI 10.1007/978-3-319-49875-1_10

Keywords Photovoltaic · MPPT · Partial shading condition · Global maximum power point

Abbreviation

ACA	Ant colony algorithm
ANN	Artificial Neural Network
CC	Constant current
CST	Current sweep technique
CV	Constant voltage
FLC	Fuzzy logic control
GP	Global peak
IC	Incremental conductance
LP	Local peak
MPP	Maximum power point
MPPT	Maximum power point tracking
PC	Pilot cell
P&O	Perturb and observe
RCC	Ripple correlation control
PSC	Partially shading condition
PSO	Particle swarm optimization
PV	Photovoltaic

10.1 Introduction

The increasing word power demand, limitation of the conventional energy sources and increasing environmental concerns increase the number of the studies on renewable energy sources. As a result of these studies, photovoltaic (PV) systems which are safe, modular, clean, inexhaustible, maintenance free and nearly reachable in all over the word have gained importance. Their modular structure, long lifetime, decreasing cost and recent advancements in static power conversion technologies allows implementing PV systems from a few Watts to MW power level. Because power level of the PV module is limited, numbers of modules are connected in series and parallel to obtain the high power levels [1–5].

The power generated by PV modules is depend on the module specifications, environmental issues such as pollution and temperature and solar irradiation level. So, the output power varies with operation conditions and this may reduce the module energy conversion efficiency. Therefore, maximum power point tracking (MPPT) methods are used to change the operation condition according to these effects to obtain maximum energy conversion efficiency. The perturb and observe (P&O) method, the incremental conductance (IC) method, the constant voltage (CV) method, the constant current (CC) method, the pilot cell (PC) method, the

ripple correlation control (RCC) method, the current sweep technique (CST), the parasitic capacitance method are the well-known MPPT methods. These methods have different specifications in complexity, convergence speed, module dependency, and track the maximum power point (MPP) of the PV system under uniform insolation condition where only one peak point exists in the *P-V* curve [2–5].

Unfortunately, there are many factors that affect the operation of each module and generate differences on the module characteristics. In this condition, multiple peaks may appear in *P-V* curve of PV system. The conventional circuit models of PV modules are changed because of passing clouds, manufacturing tolerances, dirt, aging, soldering errors or micro cracks which occur during production, transportation or installation periods, and this cause degradation of PV system performance [6]. This effect results an extra heat on PV module and may cause localized hot spot. A bypass diode is connected in parallel with each PV module to overcome these negative effects [7]. Especially non-uniform insolation of PV system because of passing clouds or another cause of shadow has great effect on system performance. The preventive methods can be grouped into three categories as (1) Modification of power converter topologies and their interconnections, (2) Modifying of the PV module connection (or generating dynamic connection patterns), (3) Modifying the MPPT algorithm in order to obtain maximum power even in multiple peak power points [6].

Characteristics of the shaded module will be different from the other ones under partially shading condition (PSC). So, using separate converter for each module seems as an effective way to prevent the negative effects of this condition. Thus, the power converter topologies are changed from centralized converters to string converters or to module integrated converters [6]. Also different connection patterns are investigated to mitigate the partial shading effects because performance degradation rate is not depending on shading area but depends on shading pattern, configuration of the array and location of the shaded module in the array []. In Fig. 10.1, *P-V* curve examples of a PV array for uniform and non-uniform insolation conditions are depicted [7]. As it is seen from the figure, the *P-V* curve can differ significantly. In addition, reconfiguration methods those dynamically change the array configuration with active switches have been proposed to adapt the PV

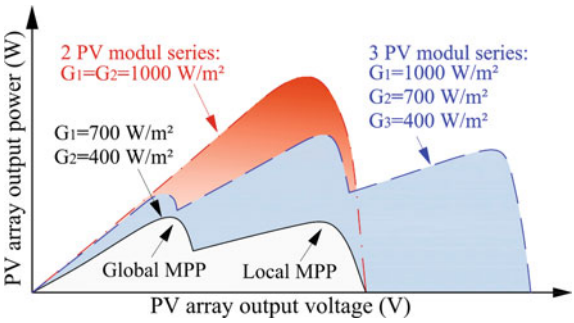

Fig. 10.1 *P-V* characteristics of a PV array with bypass diodes for different irradiations

system different PSCs. But these methods increase the system cost and complexity [8, 9].

Since the *P-V* curve of the PV system has multiple peaks with several local peaks (LPs) and a global peak (GP), the MPPT action is more complicated under PSCs. Conventional MPPT methods such as P&O and IC likely detect one of the LPs and oscillate around the vicinity of this LP. So, these methods cannot track the global MPP of partially shaded PV system. This may cause relevant energy loss. These issue has investigated lately, because the initial PV applications are usually rooftop and in rural areas [10]. Thus, enhanced MPPT methods have been investigated to improve the performance of the PV system under PSCs with the increasing usage and power levels of PV systems. Initial studies on MPPT methods under PSCs are usually based on modification of the conventional methods. But with advancements of the microcontroller and their computational capability new methods based on soft computing have also been investigated. Although main objective of these methods and the conventional MPPT methods are same, they have different specifications in terms of complexity, convergence speed, calculation effort, flexibility, steady state oscillation and etc.

10.2 Characteristics of Partially Shaded PV Module

Output electrical parameters of photovoltaic modules exhibit nonlinear behavior. Several PV cell equivalent circuit models are presented in the past literature. Generally, the model called as double-diode model and one-diode model (which is also called or five parameters model) are used [11, 12]. The one-diode model is obtained from a reduction of double-diode model. Also, simpler equivalent circuits are obtained by assuming that the equivalent series resistor of cell (R_s) is zero and parallel equivalent resistor of cell (R_p) is infinity. The equivalent circuit of one diode model is given in Figure "One-diode equivalent circuit of PV cell" (shown in other chapter of this book).

Two-diode model which is one of the common PV equivalent circuit models is obtained by adding second parallel diode to the model. The two-diode model provides more accurate *V-I* characteristics than one-diode model. In one diode model, the ideality factor *A* is assumed as constant. However, *A* is a function of voltage and its value is closer to one at high voltage levels approaches two at lower voltage. The junction recombination is modeled by adding a second diode in parallel with the first diode. This PV cell model is shown in Figure "Two-diode equivalent circuit of PV cell" (shown in other chapter of this book). Equations for the output current of the PV cell are also given in another chapter of this book for one-diode and two-diode equivalent circuits.

The output current of a PV cell has nonlinear characteristics. This results a nonlinear relation between the PV voltage and PV current and also between PV voltage and PV power. In addition, this relation is affected from operation conditions and environmental effects such as solar irradiation, ambient temperature,

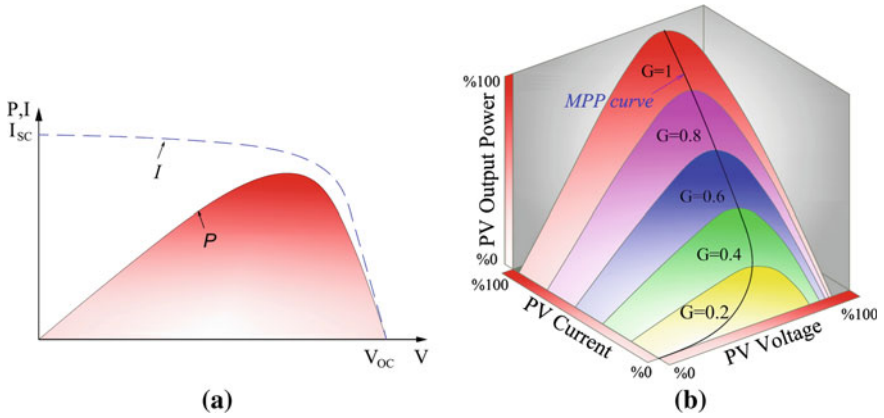

Fig. 10.2 **a** The *P-V* and *I-V* curves of the PV module. **b** *P-V* curves of the PV module for different solar irradiation conditions

pollution etc. The PV module current and power curve versus module voltage is given Fig. 10.2a. The module voltage, current and power variations for different solar radiation levels are given Fig. 10.2b. As it is seen from the figure, each solar irradiation value defines new *P-V* and *I-V* curves. Therefore, the operation point of the PV system has to be changed with the environmental effects to track the maximum power points of each curve and to obtain maximum efficiency. Otherwise, PV system may generate lower power than it can.

All curves in Fig. 10.2 are produced for ideal conditions. However, generally this is not valid all the time. Practically, it observed that dirtiness, shadow, unequal module specifications, aging of modules and usage of the by-pass diodes increase the nonlinearity and affect these curves [13, 14].

10.2.1 Hot Spot and Partial Shading Effect

Hot spot effect can be defined as occurring high temperature in any place of module. Shading, pollution, transportation damage, cracks during the installation and wrong soldering are the most important reasons of hot spot. The hot spot effect reduces the efficiency of the PV module and also if it goes on for a long time, it can shorten the life of the module. Moreover, PV modules can be out of order because of this effect [15].

Any size of PV installations from low power rooftop systems to high power PV power plant can meet partially or fully shading effect. PV modules and connections should be checked for maintenance purpose and some parameters should be monitored for early intervention. Thus, early aging and hot spot effects can be minimized and energy production can be maximized.

When the PV modules run into partially shading effects, they perform different output functions depending on module connections and shading formation. The shadowed cells in a serial, parallel or serial-parallel mixed connection stop the energy generating source operation and operate like an energy consuming load. This is the main reason of this variation on output function. The PV system contains series or parallel connected modules to reach high power levels. Thus above described process may be encountered any time in a day. The shadowed cell gets reverse bias and starts to draw current. Namely, shadowed cell does not produce energy but consume energy produced from the other cells. Then, total amount of generated energy is getting down and hot spot occurs around the reverse biased cells. This condition is depicted for serial connected PV modules in Fig. 10.3 [16].

Therefore, in a PV system which consists of several PV cell and modules connected in serial, parallel or serial-parallel to increase voltage and/or current levels, the *P-V* curve of entire PV system becomes different from ideal *P-V* curve which is given in Fig. 10.2a. The resultant *P-V* curve can be changed according to the module connection type and situation of the shaded module or modules. The partial shading effect on *P-V* curve is depicted in Figs. 10.4, 10.5 and 10.6 for serial, parallel and serial parallel mixed connection conditions, respectively [12]. Here, UR and PSC indicate the uniform insolation and the PSC, respectively.

The decrease in energy generation because of the partial shading is not only related with the size of shaded area (or number of shaded modules) but also it is related with the shaded pattern and situation of shaded PV modules and their connection. Therefore, configuration of the PV system such as numbers of serial and parallel connected modules has significant effect on performance of the PV system under PSCs. So, some connection strategies are investigated to reduce negative effects of the partial shading such as bridge link, total cross tied, honey-comb structures, etc. [17].

Commercially available PV modules contain one or more parallel connected by-pass diodes to protect the modules from the negative voltages caused by partial

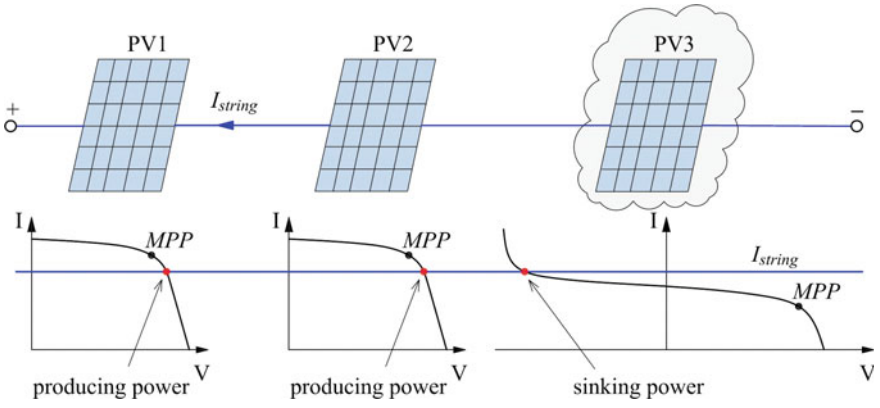

Fig. 10.3 Shading effect of the serial connected PV modules

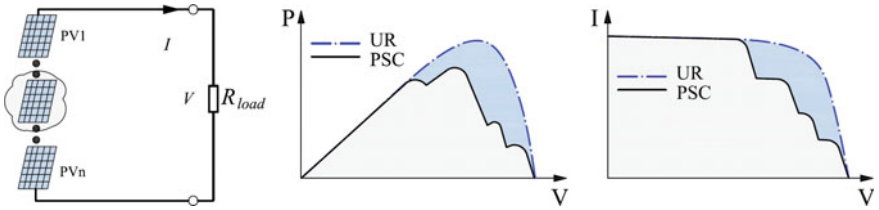

Fig. 10.4 The partial shading effect on *P-V* curve for serial connected PV modules

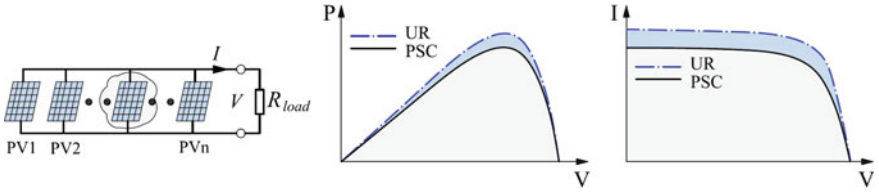

Fig. 10.5 The partial shading effect on *P-V* curve for parallel connected PV modules

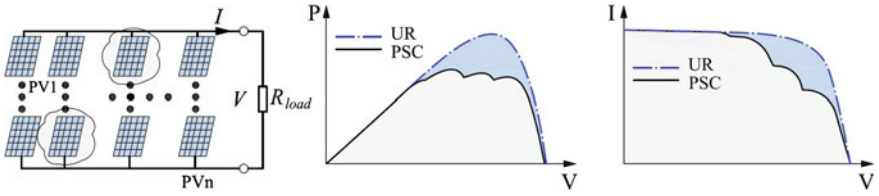

Fig. 10.6 The partial shading effect on *P-V* curve for serial-parallel mixed connected PV modules

shading and so prevent hot spot effects. The effect of the connected by-pass diode on PV module and serial connected cell string is depicted in Fig. 10.7 [18, 19].

As well as by-pass diodes, blocking diodes are also used between photovoltaic module strings. These diodes protect the modules from reverse power flow between strings. However, both bypass and blocking diodes cause power loses and increase the system cost and nonlinearity of the string behavior. Although, using by-pass diodes is a well-known protection method, some active structures like power converters are also studied in the recent years instead of these by-pass diodes [13, 14].

While objects with high volume such as building, tree, chimney and etc. cause partial shading, objects with low volume like pipe, wire, cable, rope can also cause partial shading of the PV. However, there is no direct relation between shadowed area of modules and degradation of efficiency. Therefore, degradation amount of efficiency can be more than the amount of shadowed area. Namely, a wire or a pipe based shadow can cause dramatic degradation on efficiency [20]. Cloudy or shaded operating conditions cause degradation of produced energy up to 70% even in the

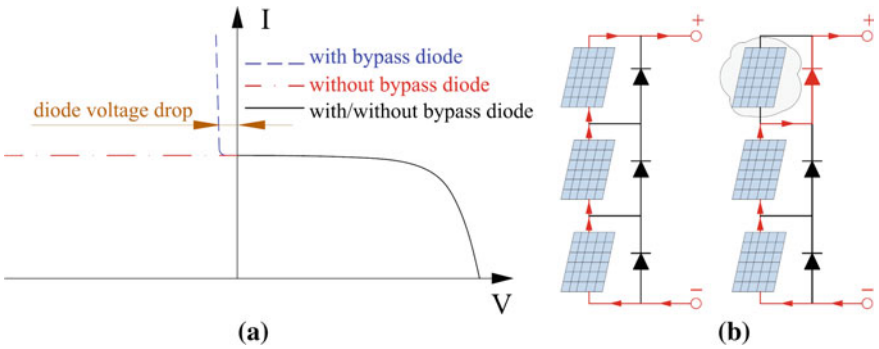

Fig. 10.7 The effect of the connected by-pass diode on **a** PV module, **b** serial connected string

power plants [21]. Moreover, if the reason of whole or partial shading is a moving object then, degradation of energy production can be dynamic [22].

The conventional equations given for the PV cell can be easily extended for a PV array. The PV modules are composed of serial, parallel and serial parallel mixed connected cells. Although several connection possibilities exist to form the arrays, serial, parallel and serial parallel mixed connected modules are usually used in arrays. The superposition can be applied them to obtain the equations for a module or an array [21]. If subscript M represents the module, N_{SM} and N_{PM} show the number of serial connected modules and parallel connected modules, respectively. The total number of modules can be written as $N_{SM}\ x\ N_{PM}$ for an array. While the PV array voltage is related with number of serial connected modules, the array current is related with number of parallel connected module strings. Thus, current of the array with $N_{SM}\ x\ N_{PM}$ serial-parallel connected modules can be written as [21]:

$$I_A = N_{PM} \cdot I_{scM} - \frac{N_{PM} \cdot I_{scM}}{e^{\frac{q \cdot V_{ocM}}{N_S \cdot k \cdot T}}} \left[e^{\frac{q \cdot (V_A + R_{SA} \cdot I_A)}{A \cdot k_B \cdot T \cdot N_S \cdot N_{SM}}} - 1 \right]. \tag{10.1}$$

where, I_A is array current, I_{scM} is short circuit current of module, A is the ideality factor of diode, q is the electronic charge, k_B is the Boltzmann's constant, T is the junction temperature, R_{SA} is the equivalent series resistance of the array, V_A is the array voltage, V_{ocA} is open circuit voltage of the array, N_s is number of the serial connected cells in modules. The Eq. 10.1 is valid for only uniform insolation conditions and it should be revised for non-uniform insolation conditions such as partial shading. The current equation can be written for array, which is composed of $N_{SM}\ x\ N_{PM}$ modules and has by-pass diodes, with some assumptions as given below:

$$I_A = \sum_{x=1}^{N_{PM}} I_{Ax} = \sum_{x=1}^{N_{PM}} I_{scAx} \left[1 - e^{\frac{q \cdot (V_A + R_{SAx} \cdot I_{Ax} - V_{ocAx})}{k_A \cdot k_B \cdot T \cdot N_S \cdot (N_{SM} - N_{Dx})}} \right] \tag{10.2}$$

Here, string represents the each parallel branch of the array which is composed of serial connected modules and x is number of the string ($x = 1, 2, \ldots, N_{PM}$), the voltage across on the by-pass diodes are assumed as zero, and N_{Dx} shows number of the shadowed module in xth string [21].

10.3 Maximum Power Point Tracking Under Partially Shading Conditions

Since the *P-V* curve of the PV array has multiple peak points, the conventional MPPT methods which usually use hill climbing method or are usually based on slope of the *P-V* curve may detect one of the local MPPs instead of the global MPP. This causes considerable energy losses, which is very important for today's energy markets and also for investors. So, a requirement of MPPT algorithms which can track the MPP of PV array even under PSCs is come out.

The PV inverters are used to export the energy generated by PV system to the grid and can be grouped into two categories such as single-stage PV inverter and two-stage PV inverter as shown in Fig. 10.8a, b, respectively. The main difference between these inverter topologies are the number of the power converter stages. Two-stage PV inverters exist a DC-DC converter and a DC-AC inverter. While the DC-DC converter regulates the DC voltage and performs the MPPT, the inverter converters DC to AC, regulates the AC voltage and/or current and exports the PV supplied energy to the loads or to the grid. In single-stage inverters, only an inverter exists and performs all required actions. The MPPT part is one of the key components of the PV inverter, because it determines the inverter reference current value and therefore inverter output power. Here, The MPPT method determines the global MPP of the PV system by using some variables such as actual PV voltage (V), actual PV current (I), short circuit current (I_{sc}), open circuit voltage (V_{oc}), solar irradiation level (I_r), temperature (T) and etc. according to the applied method. As explained in the previous sections, resultant *P-V* curve of the PV system is dependent on both solar irradiation levels of the each modules and shading pattern. Therefore, connection strategies of the PV modules have significant effect on the PV system performance and different connection strategies are investigated. Moreover, the MPPT methods examined in two categories as hardware based MPPT methods and firmware based MPPT methods. The hardware based methods include the module connection strategies, decentralization of the PV system. The decentralization method recommends connecting smaller strings with less number of modules to the grid through their own inverter or even connecting each module to the grid through its own module integrated inverter, instead of connecting all modules to the grid through the central inverter. The software based methods are the algorithms proposed to determine the global MPP under any operation condition. The most common software based methods are explained in the following sections.

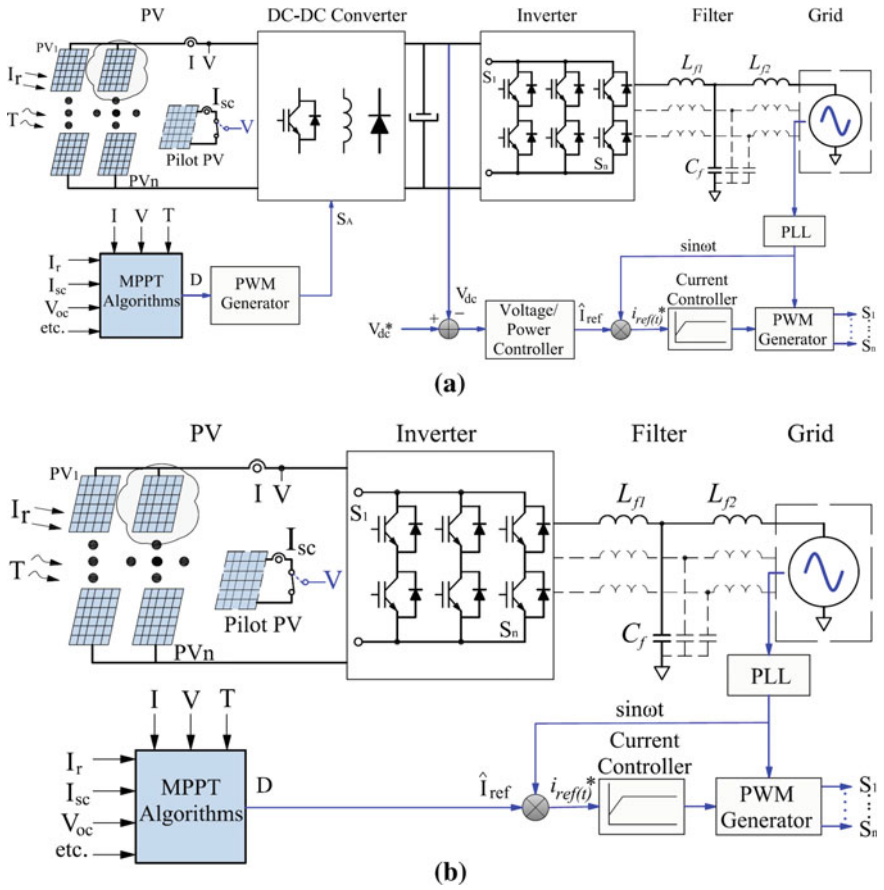

Fig. 10.8 Overall control diagram of the PV inverter. **a** Two-stage PV inverter. **b** Single-stage PV inverter

10.3.1 MPPT Methods for Partially Shaded PV Systems

In practical applications a number of PV modules are connected in series and parallel to obtain the required power level. Therefore, non-uniform insolation condition is very common. Because the energy conversion efficiency is very important value for PV systems and many MPPT methods which can track the global MPP even in PSCs are introduced [23–41].

10.3.1.1 Modified P&O Method

The P&O method is commonly used in MPPT systems because of its major advantages such as high tracking speed and simple implementation specifications.

However, this method is based on hill climbing rule and cannot track the global MPP when multiple peaks are occurring in *P-V* curve of PV system. Thus, some modifications have done to extend the advantages of this method to PSCs. After the experimental studies, some observations are reported about partially shaded PV systems characteristics. It is seen that, the peak points of the *P-V* curve are still about $0.8 \times V_{oc}$ [17, 24]. In addition, while magnitudes of the peak points are in tendency of increasing before the global MPP and they are in tendency of decreasing after the global MPP. Therefore, P&O method is commonly used to track the global MPP under PSCs.

Different modification schemes can be used for MPPT with P&O method under PSCs. The PV system is started to operate at $0.85 \times V_{oc}$ and the conventional P&O method is used to track the MPP until a disturbance such as the PSC is detected or an interrupt is generated. When the disturbance is detected or a timer interrupts which is generated every predetermined time interval (for example 20–25 s) occurs, the partial shading subroutine is activated. This situation is detected by monitoring the power variation (ΔP) value. If the power variation value is higher than the predefined critical power (ΔP_{crit}) value, this situation is labeled as PSC. The partially shading subroutine searches the other peak points on the *P-V* curve. It is also known that, voltage difference between the sequential peak points is almost equal to 80% of the open circuit voltage of the PV module (V_{oc_module}). Therefore, the operating voltage value is changed with a voltage variation step (ΔV_x) which is smaller than $0.8 \times V_{oc\_module}$. The lower voltage variation value provides higher possibility of tracking global MPP, but tracking time also increases. The large values of ΔV_x increase the risk of missing global MPP while reducing tracking time. After this variation is applied, *dP*/*dV* slope of *P-V* curve for this operation point is measured. If the slope is positive, the voltage variation action is repeated until minimum operation voltage value V_{min} is reached. If the slope is negative, this means that there is a peak point in vicinity of this operation point and the P&O method is activated to detect this peak point.

The PV power (P_{max_last}) and voltage (V_{max_last}) values are stored when the first peak point is reached and these values are compared with the values obtained at next peak point and higher power values is updated. This action is repeated towards to left side of the *P-V* curve until V_{min} or a peak point with lower power value is reached. If the power value of the peak point is lower than the previous one, operation point is slipped to last peak point with highest power value and voltage variation action is applied towards to other direction. The *dP*/*dV* slope of the *P-V* curve is measured for all voltage variation. The positive slope value represents that there is peak point in vicinity of this operation point. This peak value is tracked by activating the P&O method. The PV power and voltage values are read, and if these values are higher than the P_{max_last} and voltage $V_{max\_last,}$ this operation is repeated in same direction. If the obtained power value is lower than the P_{max_last} or V_{max} which is determined as $0.85 \times V_{oc\_module}$, operation point is transferred to previous peak point [24]. This modified method operates like double Perturb & Observe method. It generates relatively big perturbations to track the GMPP in case

of multiple peaks. However, the proposed modified P&O method may not track the GMPP under rapidly changing solar irradiation conditions [25].

In another study, an alternative P&O method which compares instantaneous measured power ($P_m(t)$) and instantaneous maximum power reference value is proposed [26]. The instantaneous measured power is calculated by multiplying instantaneous voltage and instantaneous current measurements. The *P-V* curve is divided into two regions. The instantaneous maximum power is related temperature and irradiance as Eq. 10.3:

$$P_{MPP}(t) = P_{MPP}(T(t), E(t)) = a[T(t)b(E(t)] \tag{10.3}$$

here, *T(t)* is temperature value, *E(t)* is irradiance value, *a(t)* is temperature factor and *E(t)* is irradiance factor which determines the maximum power current. The temperature factor is also called as voltage factor. In region I, maximum power point current is obtained by reducing the PV array current as given below:

$$I(t) = I_{meas}(t) - \Delta I \tag{10.4}$$

The performance of this method is depending on the ΔI. In region II, current reference is calculated by Eq. 10.5:

$$I(t) = \frac{P_{meas}(t)}{a(T)} \tag{10.5}$$

This algorithm is operated until the power error ratio becomes lower than the predetermined level:

$$\frac{P_m(t) - P_{ref}(t)}{P_m(t-1)} < \varepsilon \tag{10.6}$$

here, P_m(t) is the instantaneous measured power and P_{ref} (t) is the instantaneous maximum power reference. The P&O method is used to estimate $a(T)$. This method introduces various new coefficients which complicate the MPPT process to determine the global MPP in case of multiple local peak points.

Another P&O based MPPT method for DC-DC converter operating under PSCs is voltage sweep method. In this method, the PV array is changed voltage from its maximum value (near to V_{OC}) to a minimum value (near to I_{SC}) periodically [7]. At each sampling cycle, the voltage reference and by the way output power of the DC-DC converter is increased step by step and operating voltage and current are measured and stored. This action is sustained until PV system voltage reaches the predetermined minimum PV voltage. After determining the region of global MPP, the conventional P&O method is run to achieve operation at the global MPP [10].

In addition, measuring the voltage of all PV modules is another method. This method is based on the observation that the voltages of PV modules receiving different irradiances are different [27]. The operation of this method is always start

with reference voltage of $0.85 \times V_{oc}$ and calculates the number of PV modules. If all voltages of PV modules are equal, this means that solar irradiation is uniform and system operates with conventional P&O method. When the peak point is determined, the system stores the information (voltage and current values) of this point. Voltages of the PV modules are checked with a timer program. When voltage of a module is different from another, this is defined as PSC and a global MPP subroutine is called. This subroutine controls if any PV module voltage is less than zero or not. If there is a PV module with voltage less than zero, this means that, last peak point is left peak on the *P-V* curve. In this condition, reference voltage is set to $0.85 \times V_{oc}$ and then P&O method is used to determine the global MPP. If all PV modules' voltages is higher than zero, this means that, last peak point is right peak on the *P-V* curve. This means that some of PV modules are bypasses and do not provide power to the output. In this condition, subroutine classified the PV modules into two groups and determines the PV modules with low voltage. Then program set the reference voltage to $0.85 \times V_{oc}$ but, in this case number of modules with lower voltages is not used calculating the array open circuit voltage (V_{oc}). Again P&O method is used to track the global MPP [27].

10.3.1.2 Modified IC Method

Since there are multiple peak points are observed in the *P-V* curve of the PV array, conventional MPPT methods cannot track the global MPP of the PV system. However, some of the conventional methods have been modified to track the GMPP even in PSCs [25]. The conventional IC method is used with predetermined linear function to track the MPP even in PSCs without any additional circuits [21]. In this method, PV voltage and current values are evaluated to determine the PSCs by using Eqs. 10.7 and 10.8:

$$\Delta V_{PV} = V_{PV}[n] - V_{PV}[n-1] < \Delta V_{SET} \tag{10.7}$$

$$\frac{\Delta I_{PV}}{I_{PV}[n-1]} = \left| \frac{I_{PV}[n] - I_{PV}[n-1]}{I_{PV}[n-1]} \right| < \Delta I_{SET} \tag{10.8}$$

here ΔV_{SET} and ΔI_{SET} are predetermined voltage and current values and are defined according to manufacturer data. After this situation is determined, voltage reference of the system is set according to a linear function defined as given below:

$$V_{PV}^{*} = \left(\frac{V_{o,rms}}{I_{o,rms}} \right) \times I_{PV}[n]. \tag{10.9}$$

The *P-V* and *I-V* curves of a PV system for PSC and operation of the modified IC method are depicted in Fig. 10.9. As shown in the figure, the MPP of the PV system under uniform irradiation is depicted as point A and this point is tracked with conventional IC method. When a PSC occurs, operation point is changed to point

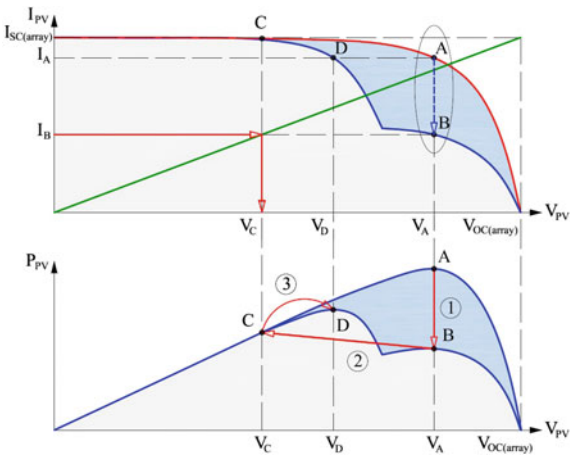

Fig. 10.9 Operation principle of modified IC method

B, while the real or global MPP is point D. In this condition, the IC method cannot track the GMPP and operates in vicinity of point B. The modified IC method check the Eqs. 10.7 and 10.8 and when both conditions are satisfied, the operation point is changed to point C which is located at lower voltage area via the linear function given in Eq. 10.9. When the operation point is reaches the point C, the conventional IC method is used again to track the global MPP and to reach the point D. In addition, using variable step size in conventional IC method improves the tracking performance and efficiency of the system and reduces the loss [21]. Moreover, this method is validated only two peaks condition and in case of multiple peak points at the left side is not considered.

Furthermore, conventional IC method is modified with some observations to track the MPPT even in PSCs. The critical observations which are also used in modified P&O method are:

- The maximum power points occur at the multiples of $0.8 \times V_{oc}$ which is also used in modified P&O method is combined.
- The magnitudes of the peak points increase before the global MPP and decrease after the global MPP.

According to these observations it is obtained that there are three possible options for position of global MPP as shown in Fig. 10.10: (a) The global MPP is located between the local peak points and local peaks are increasing until the global MPP and decreasing after the global MPP, (b) The global MPP is located at left end of the *P-V* curve and (c) The global MPP is located at right end of the *P-V* curve [25].

This method requires the V_{oc} voltage value of the PV module and maximum number of the serial connected modules (N_{max}), and determines the duty cycle value of the DC-DC converter. A reduced reference voltage value is determined and the operation starts with the conventional IC method. The conventional IC method tracks the first MPP that is depicted as peak point A in Fig. 10.10a. The duty cycle of the converter and maximum power value for this first MPP is stored. Then the

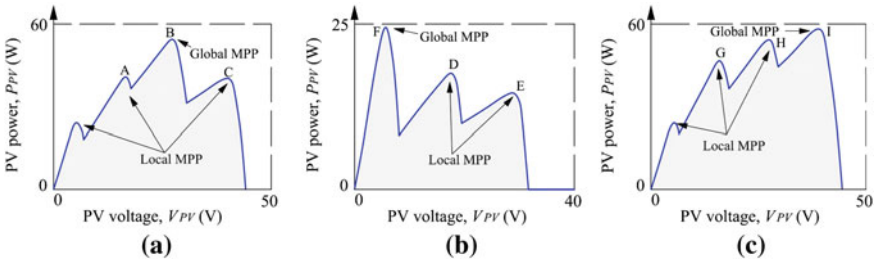

Fig. 10.10 Possible locations of GMMP and other peaks

reference value is changed by adding $0.8 \times V_{oc}$ to the voltage of the first MPP and operation point of the system is moved to right side of *P-V* curve (around B in Fig. 10.10a). The IC method is operated again and second MPP point is tracked. The power and duty cycle value at this point is stored. If power value of the second MPP is higher than the first MPP and V_{max} which is equal to multiply of V_{oc} and N_{max} is not reached, $0.8 \times V_{oc}$ is added to the previous reference voltage value and operation point is moved to right side of *P-V* curve according to observation 2. If the next power value is lower than the previous one (for example peak point C in Fig. 10.10a), the operation point is moved to the previous peak power point which is stored, and then the conventional IC method is operated. If the next power value is higher than the previous one (for example peak point H in Fig. 10.10c), $0.8 \times V_{oc}$ is added to the previous reference voltage value and operation point is moved to right side of *P-V* curve until the V_{max} is reached [25].

If the power value at the second MPP is lower than power at the first MPP as shown in Fig. 10.10b and minimum reference voltage is not attained yet, the first MPP voltage is reduced by $0.8 \times V_{oc}$ and operation point is moved to left side of first MPP. The conventional IC method is used again to track the peak point. This operation goes on until the minimum reference voltage is attained. A bias value for the slope in conventional IC method can be used to prevent the duty cycle variation in case of low power variations. Thus the total system efficiency is increased and oscillation in steady state is reduced [25].

10.3.1.3 Dividing Rectangles (DIRECT) Algorithm

The DIRECT algorithm uses Lipschitz function to describe the power/voltage relationship of PV cells and to track the global MPP of the partial shaded PV system [28]. Under PSC, connection of PV cells can be re-organized and new modules can be obtained with cells with similar irradiation condition. Then, these modules can be considered in series and/or parallel connection according to shading pattern to constitute a new PV array. Then, the output current (i_a) and voltage (v_a) of new configuration can be defined as given below:

$$i_a = \sum_{b=1}^{N_p} i_b \tag{10.10}$$

$$v_a = \sum_{j=1}^{N_s} v_j \tag{10.11}$$

where N_p is number of parallel branches, N_s is number of serial branches, i_b is the bth branch current and v_j is the voltage of jth module. The PV power can be calculated as:

$$p_a = v_a \cdot i_a. \tag{10.12}$$

The partial differentiation of power versus voltage is given below:

$$\frac{\partial p_a}{\partial v_a} = i_a + v_a \frac{\partial i_a}{\partial v_a} \quad \forall v_a \in |a, b|. \tag{10.13}$$

Equation 10.14 can be written for the jth module of the bth branch:

$$\frac{\partial v_j}{\partial i_b} = -\frac{1 + \frac{q}{kTA} I_{RS} e^{K\left(v_{bj} + i_{bj}\frac{n_s\_bj}{n_p\_bj}R_s\right)} + \frac{R_S}{R_{SH}}}{\frac{qn_p\_bj}{kTAn_s\_bj} I_{RS} e^{K\left(v_{bj} + i_{bj}\frac{n_s\_bj}{n_p\_bj}R_s\right)} + \frac{n_p\_bj}{n_s\_bjR_{SH}}}. \tag{10.14}$$

It is seen from Eqs. 10.10–10.14 that, there is a valid $\partial P_a/\partial V_a$ value and this value is bounded by a maximum value M. According to mean value theorem, there is $c \in |v_1, v_2|$ for every $v_1, v_2 \in |a, b|$ such that:

$$\frac{|p(v_1) - p(v_2)|}{|v_1 - v_2|} = \left.\frac{\partial p}{\partial v_a}\right|_c = p'(c), \quad c \in (v_1, v_2). \tag{10.15}$$

Since M bounds the $p'(c)$, Eq. 10.16 can be obtained from Eq. 10.15:

$$|p(v_1) - p(v_2)| \le M|v_1 - v_2| \quad \forall v_1, v_2 \in [a, b]. \tag{10.16}$$

Equation 10.16 is known a Lipschitz condition and the function $p(v)$ which satisfies this condition with constant M is known as Lipschitz function.

If v_1 is assumed as sampled point and v is a variable, Eq. 10.16 gives both lower and upper bounds and values of function $p(v)$ at other points can be obtained as:

$$p(v_1) - M|v - v_1| \le p(v) \le p(v_1) + M|v - v_1|. \tag{10.17}$$

If v_1 is assumed at center of $[a, b]$, Eq. 10.17 can be rewritten as:

$$p(v) \le \max_{v\in[a,b]} p(v) \le p(v_1) + M\frac{b-a}{2}. \tag{10.18}$$

Thus, bound of the distance from global maximum is observed from sample $p(v_1)$ with just one sample. Here, both M and $(b - a)$ might be big initially, but

$(b - a)$ can be replaced by smaller length of subintervals by using more samples. The DIRECT method is proposed to search the global extreme of this Lipschitz function in a finite number of iteration [28].

When a DC-DC converter is used, boundaries of the duty cycle is [0,1]. However, this bounded are can be narrowed by using PV parameters such as maximum and minimum values of the PV short circuit current, open circuit voltage and equivalent resistive load. Under PSC, while there are multiple peaks on *P-V* curve, *I-V* curve shows multiple steps characteristics. It is assumed that, the PV system is operating at its MPP depicted as D_{m1} in Fig. 10.11a. If a PSC occurs at this time, operation point of the PV system is move from 1 to 2 as shown in Fig. 10.11a.

This results decrease in output power and energy conversion efficiency of PV system. Now, the DIRECT method starts the sampling interval and takes three samples D_i (i = 1,2,3) to determine operation condition if it is uniform irradiation or PSC. Each step of the multistep *I-V* curve can be considered a part of the *I-V* curve of a PV module under uniform irradiation. Therefore, the *I-V* can be considered in three parts. If I_{di} and V_{Di} are well separated, means Eqs. 10.19 and 10.20 are satisfied, I_{D1} would be smaller than I_{MPP3} (MPP current of first step), and V_{D2} would also bigger than V_{OC} of the middle step [28]:

$$\frac{\Delta I_{D3,1}}{I_{D3}} = \frac{I_{D3} - I_{D1}}{I_{D3}} \geq 0.1 \tag{10.19}$$

$$\frac{\Delta V_{D1,2}}{I_{D2}} = \frac{V_{D2} - V_{D1}}{V_{D2}} \geq 0.2. \tag{10.20}$$

The 0.1 and 0.2 values are defined according the V_{MPP} and I_{MPP} and V_{OC} and I_{SC} relations:

$$I_{MPP} \approx 0.9 \times I_{SC} \tag{10.21}$$

$$V_{MPP} \approx 0.8 \times V_{OC}. \tag{10.22}$$

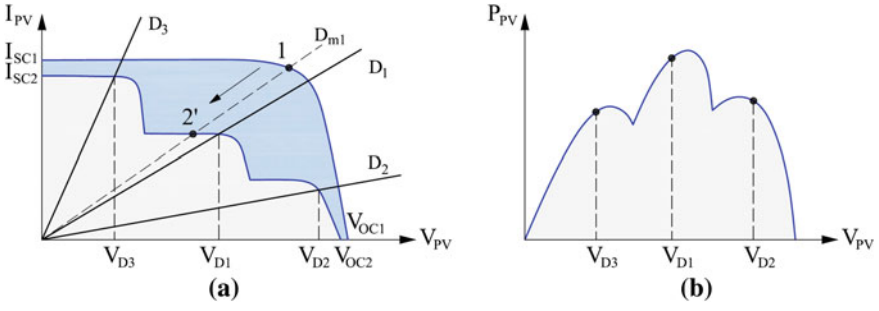

Fig. 10.11 **a** Variation of the operation point. **b** Illustration of first three samples

If the *I-V* curve has more than three steps, two sequential steps always considered as one step. In addition, if the Eq. 10.19 or Eq. 10.20 is not satisfied, one of the intervals should be divided into three subintervals and two new samples should be taken. DIRECT evaluate the values obtained from these three samples and determines the operation condition as uniform irradiation or partial shading.

If DIRECT determines the PSC, potentially optimal interval (for example *j*th interval) is divided into three subintervals by taking two new samples (D_{j2} and D_{j3}) as second iteration. In third and fourth iterations, DIRECT divides other two potentially optimal intervals into three subintervals by taking two new samples for each potentially optimal interval as depicted in Fig. 10.12. At the end, there are nine intervals and DIRECT evaluates the obtained data. In most application this operation is enough to determine some samples near the global MPP. If two samples that have the highest power values are sequential, the global MPP is in this interval

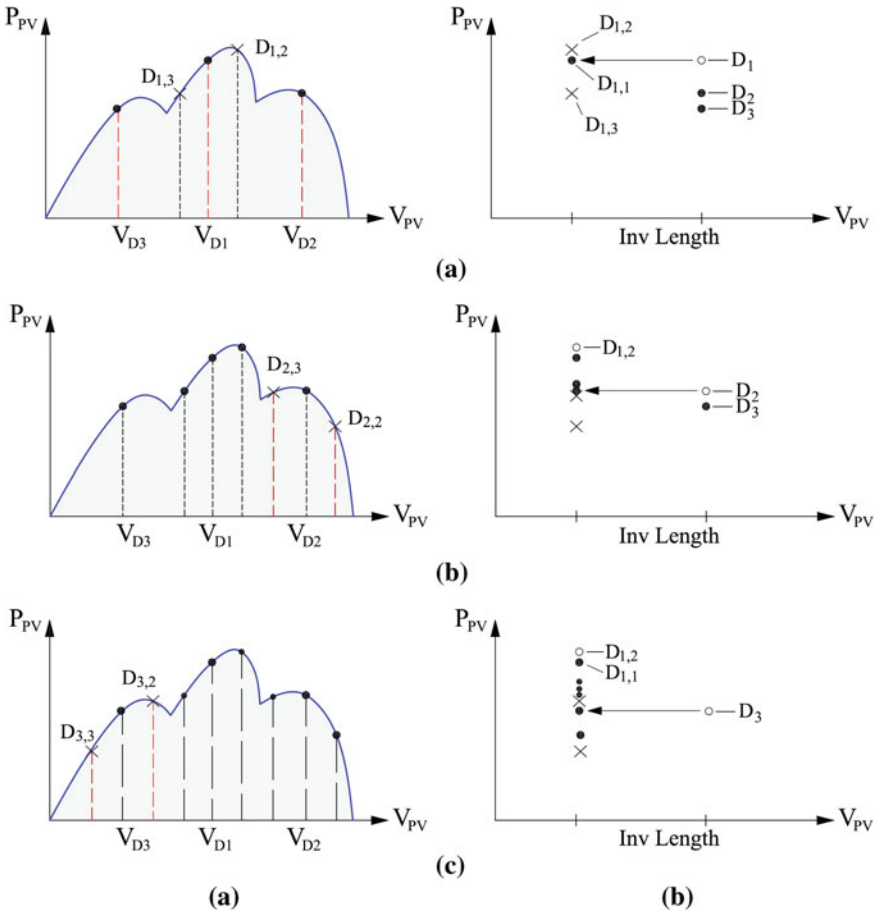

Fig. 10.12 Iterations of DIRECT method

and DIRECT moves the operation point to this interval and tracks the global MPP by using conventional P&O or IC methods. However, if these two samples are not sequential, this means that system has two global MPPs or one local MPP closed to global one. In this case DIRECT operates two more cycles and finally obtains 27 intervals [28].

10.3.1.4 Fuzzy Logic-Based MPPT Method

The fuzzy logic control (FLC) theory is vagueness and uncertainty based mathematical discipline and allows one to use non-precise or ill-defined concepts. The FLC removes the system's complete mathematical model requirement, but it requires prior knowledge about the system to provide proper design. The fuzzy logic control has robust performance even under some parameters of the system varies or and disturbances occur through its nonlinear and adaptive nature [3, 29, 30]. The FLC is applied to MPPT of PV system under uniform insolation conditions and fast tracking speed with reduced oscillation is obtained. The inputs of the FLC are usually defined as an error (E) and a change in error (ΔE), and these are calculated as:

$$E(k) = \frac{P(k) - P(k-1)}{V(k) - V(k-1)} \quad \text{or} \quad E(k) = \frac{P(k) - P(k-1)}{I(k) - I(k-1)} \tag{10.23}$$

$$\Delta E = E(k) - E(k-1) \tag{10.24}$$

Thus, the P&O method is evaluated with fuzzy logic controller with the advance of the variable size. Also the IC method can be evaluated by using change in PV power and change in PV voltage values as inputs and faster tracking speed and lower oscillation around the MPP are obtain with the help of variable step size [3]. Both two approaches combine the advantages of P&O or IC method such as fast response, easy to implement with the adaptive nature of the FLC.

However, these FLC based MPPT algorithms unable to track the MPP of PV system under PSCs because of the complex structure of *P-V* characteristics of the PV system. So some modifications have been done to prevent the MPPT system to trap the local MPP. The initial voltage tracking function is introduced for this aim. If the PSC is determined, the operation point of the PV system is changed to the computed initial voltage, and then the MPPT action is performed. The initial voltage tracking function is defined as given below [30]:

$$V_{initial} = \frac{V_{MPP}}{I_{MPP}} \times I \tag{10.25}$$

where V_{MPP} and I_{MPP} are MPP voltage and current values of PV array, respectively, and I is the instantaneous PV current. The V_{MPP} and I_{MPP} values can be obtained

from *I-V* and *P-V* characteristics of the PV array operating at standard test conditions [30].

In another method, the PV system is scanned and operating power of the PV system is stored. Then, these values are used together with the FLC based MPPT algorithm to track the global MPP even in PSCs. In this method, the operating area of PV system is scanned and obtained maximum power values are stored during the initial or changing weather conditions. A preset value representing admissible difference between the determined maximum power and operating power is used in control rules. If the actual power difference is greater than the pre-set power difference value, the duty cycle is increased; otherwise the FLC based MPPT algorithm is applied. The flowchart of this modified FLC based MPPT method is given in Fig. 10.13. This scanning and storing action and control rule prevent the system to trap the local MPP.

Three scanning and storing methods can be performed in this method: (*i*) Initializing system with maximum duty cycle, (*ii*) Increasing the duty cycle from a minimum value to a maximum value with a fixed step, (*iii*) Applying a large initial perturbation step to make a wide search. All three method guarantee to track the global MPP under PSCs but their detection speeds are different.

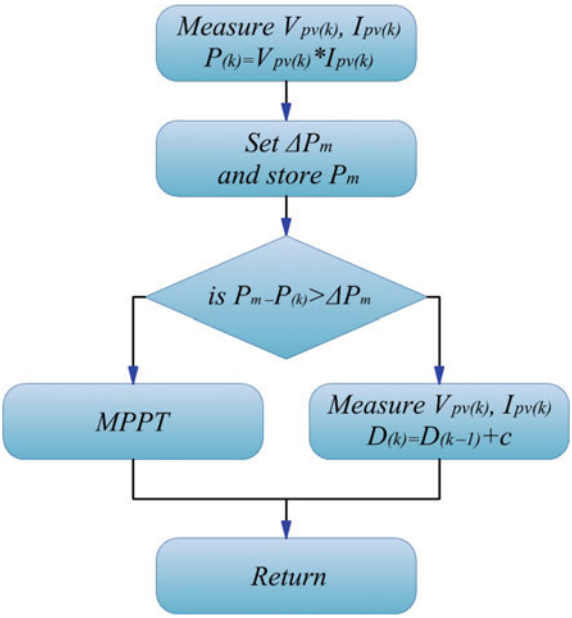

Fig. 10.13 Flowchart of the modified fuzzy logic based MPPT method

10.3.1.5 Artificial Neural Network Based MPPT Method

Artificial Neural Networks (ANNs) are computational computer systems which are designed to perform the characteristics of the human brain such as learning, producing new knowledge via learning and discovering new knowledge and skills automatically without any help. The ANN simulates the biological neural system by using artificial neurons instead of biological ones. These neurons are connected to each other with different weights to compose the artificial neural network which can learn, store in memory and discover the relations between the data.

The ANN is used to track the MPP of the uniformly insolated PV systems with its pattern recognition capability. The PV parameters such as PV voltage and PV current or environmental parameters such as temperature and insolation or combination of these two groups can be used as input parameters for the ANN. The V_{MPP}, the I_{MPP} and the converter duty ratio are usually used as outputs. The designers should decide parameters about the hidden layers. Design process of the ANN is completed after the weights are determined with intricate training stage by using the data obtained from simulation or experimental results. Although the ANN based MPPT method has some advantages, its performance is depended on the technical knowledge and skill of the designers, and PV module characteristics. The differences between the commercially available PV module characteristics bring out module dependency to performance of this method. In addition, retraining is required because of variation of PV characteristics with time, with solar insolation or with temperature. Therefore, number of studies on the ANN based MPPT method under non-uniform insolation and PSCs is very less because of these drawbacks. Instead, the ANN is used together with the other methods to provide learning and remembering features.

The conventional IC method that cannot track the global MPP can be combined with ANN to achieve improved performance in these conditions. The IC method is usually used together with the CV method to increase the tracking speed. The CV method uses the linear relation as given with Eq. 10.26 between the V_{MPP} and V_{OC}:

$$V_{MPP} = K \times V_{OC} \tag{10.26}$$

Here K is usually 0.7–0.8, and this value is related with the module characteristics. Thus, the operation point of the PV system transferred to the vicinity of MPP with one step, and then the IC method tracks the real MPP with improved tracking speed. However, these values are valid for only uniform insolation conditions. Under non-uniform insolation conditions, the parameter K can be determined with ANN to transfer the PV system to the vicinity of the global MPP and then IC method can track the global MPP with fast speed. A feedforward ANN with two inputs and one output can be used for this aim. Here, the PV voltage and PV current can be used as input signals and the parameter K or directly V_{MPP} can be used as the output value. After determining the numbers of the hidden layer and neurons at the hidden layer which have significant effect on ANN performance, the training process is executed with the training and test values obtained from experimental

studies. After the successful training stage, the ANN that can perform nonlinear input-output mapping for different operation conditions is obtained. Consequently, a method that can perform fast MPPT performance under both uniform and non-uniform insolation condition is obtained by combining the ANN and the IC method [31].

Similarly, the ANN and the FLC can be combined to achieve a fast and efficient MPPT method which can track the global MPPT even under PSCs. In this topology, while the ANN is determining the voltage reference (that is the required operation point), the FLC controls the power converter to transfer the actual operation point to the required operation point. Unlike the previous method, averaged solar insolation levels of modules and temperature value are used as inputs. The modules of the PV system are divided into four groups, and average insolation level value of each group is calculated by using Eqs. 10.27–10.30:

$$E_1 = 0.25 \times (E_{M1} + E_{M2} + E_{M4} + E_{M5}) \tag{10.27}$$

$$E_2 = 0.25 \times (E_{M2} + E_{M3} + E_{M5} + E_{M6}) \tag{10.28}$$

$$E_3 = 0.25 \times (E_{M4} + E_{M5} + E_{M7} + E_{M8}) \tag{10.29}$$

$$E_4 = 0.25 \times (E_{M5} + E_{M6} + E_{M8} + E_{M9}) \tag{10.30}$$

where E_{M1}-E_{M9} are the solar insolation level of the PV modules. Thus, the resultant *P-V* curve which is affected from the insolation level of each module and also the shading pattern is aimed to model. The output of the ANN is again voltage reference. The difference between the voltage reference and the actual PV voltage and the integral of this difference are used as input variables of the FLC. The output variable of the FLC is duty ratio value of the converter. Thus, different insolation levels of the PV modules, in other words shading pattern of the PV system, are taken into account by the ANN used in voltage reference determination and the operation point is transferred to the determined point via the FLC [32]. The ANN is sufficiently accurate in mapping between a partially shaded condition and optimum voltage and power of a PV array is obtained by this ANN-FLC combined method.

10.3.1.6 Particle Swarm Optimization Method

The particle swarm optimization (PSO) is population based and stochastic search technique which is developed by inspiring the behaviors of bird flocks [33–35]. This technique is presented for the multi-variable and multi-parameter optimization problems and successfully used in solution of nonlinear problems. This technique is evolutionary computing method and starts with random solutions which are called particles, and then optimum solution is obtained by updating the generations. Next directions of the each particle are determined according to its own success and

success of the best particle in a neighborhood (P_{best}) and success of the best particle in the population (G_{best}). The position of the particle x_i is adjusted by using:

$$x_i(k+1) = x_i(k) + v_i(k+1) \tag{10.31}$$

Here v_i is the velocity component representing the searching step size and can be calculated by

$$v_i(k+1) = wv_i(k) + c_1 r_1\{P_{best_i} - x_i(k)\} + c_2 r_2\{G_{best} - x_i(k)\} \tag{10.32}$$

where c_1 and c_2 are the acceleration coefficients, w is the weight of the inertia, r_1, $r_2 \in$ U(0, 1), P_{best_i} is the individual best position of particle i, and G_{best} is the best position of the population [33–35].

While the PSO based MPPT method can be used to track the global MPP, this method can also be used together with one of conventional method such as IC or P&O. In this situation, the conventional MPPT method tracks the MPP under uniform insolation conditions. When the PSC is detected, the PSO algorithm is activated and global MPP is detected even multiple peak points are occurring on *P-V* curve of the PV system.

Generally, solution vector with N_p particles is defined as given below:

$$x_i^k = d_g = [d_1, d_2, d_3, d_4, \ldots ..d_n] \quad \text{and} \quad n = 1, 2, \ldots ..N_p. \tag{10.33}$$

The objective function can be determined as:

$$f\left(x_i^k\right) > f(P_{best_i}). \tag{10.34}$$

If the condition given in Eq. 10.34 is satisfied the individual best position P_{best_i} is updated using Eq. 10.35:

$$P_{best_i} = x_i^k. \tag{10.35}$$

The algorithm generates three duty cycle values d_i ($i = 1, 2, 3$) and the optimization process is started and updates these three duty cycle values. After some iteration, all three duty cycles reach the MPP of PV system. Owing to the low velocity of the duty cycle variation, the MPPT action is obtained without any oscillation. In addition, since this MPPT method is not based on the slope or sign value of *P-V* curve of PV system, this method can successfully track the MPPT even in PSCs [34].

However, some problems may appear especially if the small but fast change in insolation occurs. In this case, small step sizes decrease the tracking speed of the system. In addition, bigger step sizes may cause skipping the global MPP and detecting local MPP instead of global MPP. Therefore, conventional PSO algorithm should be modified. The modification has two phases. In first one previous duty cycles are decreased and increased linearly according to the PV array power by

factor K_1. In second phase, after the three duty cycles reach the MPP, two of the three duty cycles are perturbed extremely in positive and negative directions with a constant K_2 [34].

The PSO algorithm can also be used together with conventional methods. In this case, if the solar insolation is uniform, the conventional MPPT method activated and tracks the MPP of the system. The operation condition of the system is checked by using Eqs. 10.19 and 10.20. If these equations are satisfied, this means that The PV system operates under PSCs and the PSO algorithm is activated to track the global MPP of system [33, 35].

In this study, the PSO based MPPT method is designed to track the global MPP for the PSCs. The number of the particles used in the PSO method is 11. The other parameters of the PSO method are $c_1 = 1.5$, $c_2 = 2.2$ and $w = 0.3$. The commercially available PV module, SunPower SPR305-WHT, is modeled with MATLAB/Simulink and a sample PV system which consists of three strings with five serial connected modules is built up. The solar insolation level of the modules is changed to test the performance of the designed PSO based MPPT method. The *P-V* curves of the PV system tested for the different insolation conditions and determined operation points by the proposed method are depicted in Fig. 10.14. As seen from the figure, the proposed scheme, determines the global MPP with great performance both in accuracy and speed, and improves the efficiency.

10.3.1.7 Modified Fibonacci Search Based MPPT Method

The Fibonacci search method is recursive method that uses the Fibonacci numbers. There is limitation about this method that the objective function is to be have only single extremum point (single maximum or single minimum point). Therefore, this method narrows down the search space and produces subintervals that includes single maximum or minimum by using Fibonacci numbers. The searching action can be performed in both directions. The values of the objective function at two check points (e.g. PV voltage values V_1 and V_2 in MPPT action) are used to determine the direction. The Fibonacci numbers that this method uses can be determined with the Eq. 10.36 [36–38]:

$$F_n = F_{n-1} + F_{n-2} \quad \text{for} \quad n = 2, 3, \ldots. \quad \text{and} \quad F_0 = 0, F_1 = 1 \tag{10.36}$$

As a result, Fibonacci numbers are 0, 1, 1, 2, 3, 5, 8 . . .

In this method a variable x and a function $f(x)$ are determined. The PV voltage, PV current or duty cycle of the converter may be used as variable x and PV output power is used as $f(x)$. Since the main aim is tracking the MPP, a search space should be determined as $[x_{min}, x_{max}]$ for the variable. At initializing stage two operation points (or voltage values), here variables x_1 and x_2 are determined as depicted in Fig. 10.15. If $f(x_1) < f(x_2)$, it means that the MPP should be in interval $[x_1, x_{max}]$ and range is shifted to the right as given in Fig. 10.15. In next iteration, x_2 becomes x_1

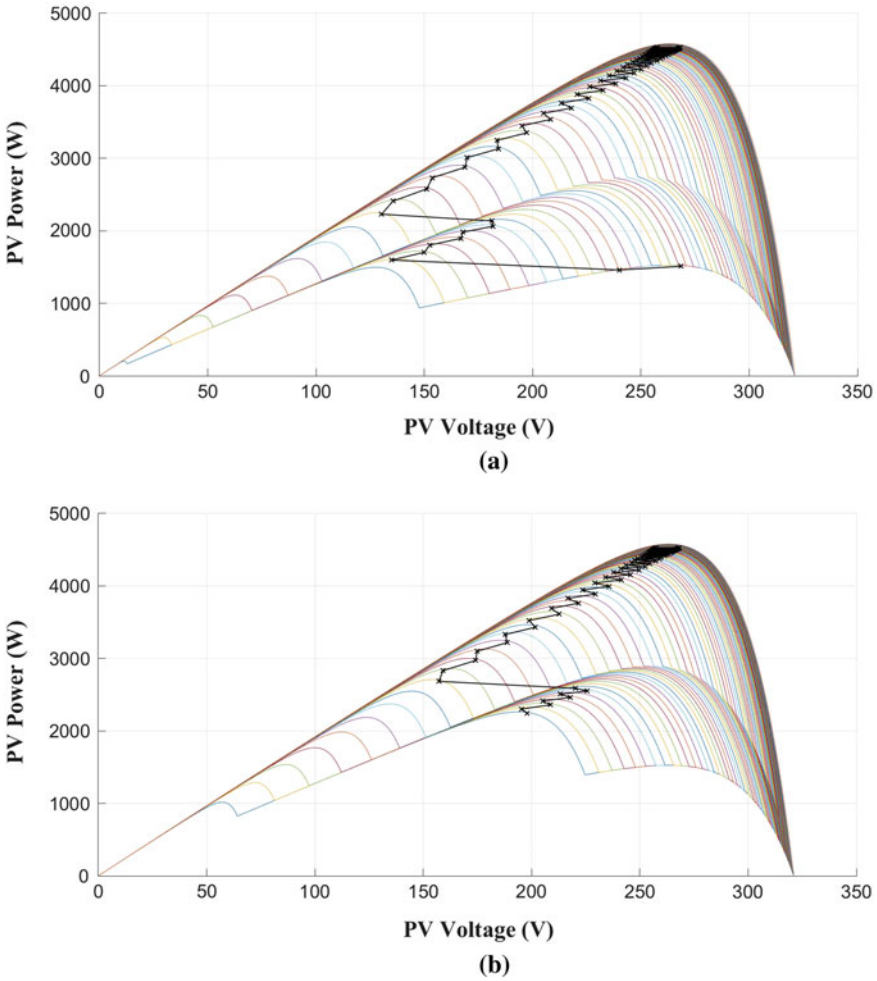

Fig. 10.14 Operation points determined by the PSO based MPPT method for two different shading patterns

and a new value for x_2 is calculated with Fibonacci search formula given in Eq. 10.37 [36]:

$$x_2 = x_{min} + \left[\frac{F(n-1)}{F(n)}\right] \times (x_{max} - x_{min}) \tag{10.37}$$

where, $F(n)$ is Fibonacci number. According to Eq. 10.37, the distance between the samples is given in Eq. 10.38 and it is seen that the distance becomes narrower in each iteration:

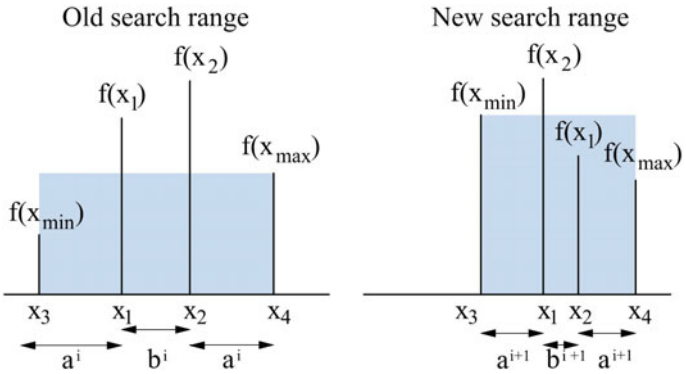

Fig. 10.15 Modified Fibonacci search algorithm based MPPT method

$$a^{i+1} + b^{i+1} + a^{i+1} = a^i + b^i \tag{10.38}$$

In the next iteration, if $f(x_1) < f(x_2)$, again the previous process is performed. If $f(x_2) < f(x_1)$, at that time the search space is limited with x_2, so x_{max} takes the value of x_2 and this means that the MPP should be in interval $[x_1, x_2]$ and range is shifted to the left. For the next iteration, x_1 becomes x_2 and a new value for x_1 is calculated with Eq. 10.39 [36]:

$$x_1 = x_{max} + \left[\frac{F(n-1)}{F(n)}\right] \times (x_{max} - x_{min}) \tag{10.39}$$

In next iteration again $f(x_1)$ and $f(x_2)$ values are compared. The shifting direction is determined according to their values, and new variable values are calculated by using Eq. 10.37 or Eq. 10.39 according to the direction. As declared above, the distances between the samples are narrowed after each iteration. This process is preceded until the MPP is reached [36–38].

10.3.1.8 Ant Colony Optimization Based MPPT

The ant colony algorithm (ACO) is a population based probabilistic algorithm for finding optimal paths. This method uses the behavior of ants searching for food and is used to solve difficult optimization problems [39]. In MPPT applications, the PV array output power can be selected as the fitness function. After the initializing step, the PV array power (here fitness value) is calculated for all the newly generated particles in the current generation. Then, all fitness values of the newly generated particles and the particles in the archive are ranked in ascending order. The archive is updated with K best results. The particles in this generation are updated and particles for the next generation are generated. This process is repeated until

reaching the maximum iteration number or termination condition. Here, the termination condition is reaching MPP of the PV system [39].

One of the major concerns of using ACO is algorithm speed. This is directly related with the tracking speed. The conventional MPPT methods such as P&O or IC method can be used to determine the first and the last local MPPs. Thus, these values are used as boundary of the searching space and the solution space is narrowed. Consequently, tracking speed is improved [39].

Other evolutionary algorithms such as the genetic algorithm, differential evolution algorithm are also used for MPPT of PV systems under PSCs. These systems can also be used together with the other methods to optimize the system parameters [39–41].

10.4 Comparison of Global MPPT Methods

As it is declared that, the PSC has great effect on PV system performance. After tests, it is obtained that power loss occurred at PV system as a results of partial shading can be high as 70% [24]. Therefore, the MPPT algorithm for partially shaded systems has gain importance and many algorithms have been investigated to improve the PV system performance. Initial studies are based on the modification of the commonly used MPPT methods like P&O and IC methods which are effective for uniform insolation conditions with their advantages such as ease implementation and fast tracking speed. So, a search algorithm is combined with conventional MPPT methods to overcome the disadvantage of getting trapped at local peak of *P-V* curve. This search algorithm may search the whole *P-V* curve periodically to detect the global MPP. This requires long time and cause reduction on generated power.

The DIRECT method is proposed to decrease the required search time and prevent the energy deduction. However, in some partially shading cases, this method cannot convergence to the global MPP in a few steps and therefore scanning time may be as long as ordinary search algorithm. The open circuit voltage or short circuit current of the PV module is also used to shorten the search time. Since this method is required the knowledge of PV module, the module dependency is come out. Besides, a declination on the PV module characteristics because of aging effect reduces the efficiency of this method. Although the line search algorithm with Fibonacci search has been used for tracking global MPP of partial shaded PV systems, this method does not guarantee converging to the global MPP for any PSCs. Similar to the conventional P&O or IC methods, the conventional extremum-seeking based MPPT method also is trapped at a local peak and therefore this cannot track the global MPP under PSCs. Thus, sequential extremum-seeking based MPPT method is investigated. This method can track the global MPP and eliminate the power ripple around MPP, but its convergence time is high because of the global scan requirement [42]. However, this method has some drawbacks such as high implementation difficulty, noise sensitivity [43]. In addition, global

perturbed-based extremum-seeking control method based on two band pass filters is also proposed to track the global MPP of partial shaded PV system. This topology reduces the noise sensitivities of band pass filter and improves the tracking performance and speed [44].

In addition, artificial intelligence based methods such as FLC, PSO and ANN are also used to track the global MPP of partially shaded PV system [45]. The FLC has advantages of eliminating the mathematical model requirement, handling nonlinearities and uncertainties and having adaptive nature. However, the conventional FLC method cannot guarantee to convergence to global MPP in PSCs. So modified FLC based MPPT methods have been implemented to increase the tracking speed and therefore efficiency of the PV system. The PSO is an optimization technique that models the behavior of bird flocks. The PSO uses a collection of particles to find the optimal solution for the problem. However, the PSO is used for time-invariant problems. Since the environmental conditions such as solar insolation and temperature vary with time, a detection and re-initialization procedures should be included in the PSO to re-initialize the system when a variation on environmental conditions is detected. The PSO with this specification has superior advantages such as tracking global MPP effectively in all insolation conditions, fast convergence speed and simple structure. However, initial particle positions affect the performance of PSO based MPPT method, and improper values may cause converging to a local MPP. The ANN methods are also used to track the global MPP [7, 45]. Although different neural network structures have different advantages and disadvantages, proper trained ANN based MPPT method can track the global MPP under any PSC. However, this method requires significant computational effort for training the ANN and also is model dependent. The main specifications of these methods are summarized in Table 10.1.

The ACO is another soft computing method based on the swarm intelligence. It has superior advantage as adapting its parameters according to changing environmental conditions. However, it is difficult to implement this topology with low cost microcontroller because of the great computational effort requirement. Therefore, the convergence speed of this method is relatively low and this drawback limits its applications. In addition, this method can be combined with another conventional method such as P&O or IC to narrow the search space and to improve the convergence speed especially for rapidly changing atmospheric conditions [39].

The chaos search method is stochastic search method which is based on chaos theory. This technique generates knowledge and variables by using past experiences. Therefore, it is superior to other techniques which use random variables. Although, this method has features to track the global MPP even under PSCs, number of studies are very limited and its performance has not been validated yet [43].

The Tabu search method is an iterative search algorithm and can be used to track the global MPPT of the partial shaded PV applications. This algorithm uses the previous data to prevent the staying at the local MPP. However, similar to the chaos search method, number of the studies on global MPPT application of the Tabu search method is also limited. The cuckoo search method is another search method which becomes popular recently. This method uses the brood parasitism of the

Table 10.1 Comparison of MPPT methods under PSCs

Method	Sensing variables	Implementation complexity	Tracking speed	Module dependency	Global MPP tracking capability
Modified P&O	*V*, *I*	Low	Fast	Yes	Medium
Modified IC	*V*, *I*	Low	Medium	Yes	Medium
DIRECT method	*V*, *I*	Medium	Fast	Yes	High
FLC based method	*V*, *I*	Medium	Medium	Yes	High
ANN based method [31]	*V*, *I*	Medium	Medium	Yes	High
ANN based method [32]	Solar insolation, temperature	Medium to high	Slow to medium	Yes	Guaranteed
PSO method	*V*, *I*	Medium	Slow to medium	No	Guaranteed
Modified Fibonacci search based method	*V*, *I*	Medium	Medium	No	Medium
ACO method	*V*, *I*	Medium to high	Slow	No	Guaranteed

cuckoo birds and presents superior performance on global optimization problems. This method is has only two parameters to tune, therefore it is simpler than the genetic algorithm and PSO method which have three parameters. The Levy flight is used in this method to determine the next step. Thus, short steps, long steps or short distance jumps can be determined as next step [43]. This method is used to track the global MPP with these features and provides fast and accurate performance. The differential evolution is another evolutionary algorithm and it can be used to track the global MPP of the partial shaded PV system. This method is an independent method but it has same disadvantages with the ACO based MPPT [39].

10.5 Conclusions

Obtaining maximum available power from PV system is very important. Therefore, high efficient power electronic converters, solar tracking systems and MPPT methods have been investigated to improve the efficiency of the PV system. Although various MPPT methods have been implemented and considerable results are obtained for uniform solar insolation conditions, these methods are not useful for PSCs. When the PV system does not receive uniform solar insolation, the resultant *P-V* characteristics of the entire PV system becomes more complex and have multiple peak points on it. Therefore, tracking the global maximum point of the *P-V* curve becomes more complicated and improved MPPT methods are

required. Following observations about the partial shaded PV system characteristics should be taken account while investigating maximum power point search algorithm to improve the partially shaded PV system efficiency [24, 27]:

- Under PSCs, the *P-V* curve of PV system has multiple peak points while *I-V* curve of the system has multiple steps.
- The maximum PV power value and the PV voltage value that it occurs are not only dependent on solar insolation and ambient temperature level but also on the shading pattern and array configuration.
- The global MPP of *P-V* curve of PV system may lie on the left side of the load line. Therefore, the two stage technique will not be able to track the global MPP of PV system.
- The peak points on the *P-V* curve of the array occur nearly at multiples of 80% of module open circuit voltage.
- Therefore, the minimum displacement (voltage difference) between any two consecutive peak power points is nearly 80% of module open circuit voltage.
- After extensive study of *P-V* curves, it is reported that when the *P-V* curve is traversed from either side, the magnitude of the peak points increases. After reaching the global peak point, the magnitude of the consecutive peaks (if they are present) decreases continuously.

References

1. Sefa I, Altin N (2009) Grid interactive photovoltaic inverters—a review. J Fac Eng Arch Gazi Univ 24(3):409–424
2. Sefa I, Ozdemir S (2010) Multifunctional interleaved boost converter for PV systems. In: IEEE international symposium on industrial electronics (ISIE 2010), pp 951–956
3. Altin N, Ozdemir S (2013) Three-phase three-level grid interactive inverter with fuzzy logic based maximum power point tracking controller. Energy Convers Manag 69:17–26
4. Esram T, Chapman PL (2007) Comparison of photovoltaic array maximum power point tracking techniques. IEEE Trans Energy Convers 22(2):439–449
5. Subudhi B, Pradhan R (2013) A comparative study on maximum power point tracking techniques for photovoltaic power systems. IEEE Trans Sustain Energy 4(1):89–98
6. Rodriguez JDB, Franco E, Petrone G, Paja CAR, Spagnuolo G (2014) Maximum power point tracking architectures for photovoltaic systems in mismatching conditions: a review. IET Power Electron 7(6):1396–1413
7. Koutroulis E, Blaabjerg F (2012) A new technique for tracking the global maximum power point of PV arrays operating under partial-shading conditions. IEEE J Photovoltaics 2(2):184–190
8. Rani BI, Ilango GS, Nagamani C (2013) Enhanced power generation from PV array under partial shading conditions by shade dispersion using Su Do Ku configuration. IEEE Trans Sustain Energy 4(3):594–601
9. El-Dein MZS, Kazerani M, Salama MMA (2013) Optimal photovoltaic array reconfiguration to reduce partial shading losses. IEEE Trans Sustain Energy 4(1):145–153

10. Ishaque K, Salam Z (2013) A review of maximum power point tracking techniques of PV system for uniform insolation and partial shading condition. Renew Sustain Energy Rev 19:475–488
11. Fathy A (2015) Reliable and efficient approach for mitigating the shading effect on photovoltaic module based on Modified Artificial Bee Colony algorithm. Renew Energy 81:78–88
12. Belhachat F, Larbes C (2015) Modeling, analysis and comparison of solar photovoltaic array configurations under partial shading conditions. Sol Energy 120:399–418
13. Daraban S, Petreus D, Morel C (2014) A novel MPPT (maximum power point tracking) algorithm based on a modified genetic algorithm specialized on tracking the global maximum power point in photovoltaic systems affected by partial shading. Energy 74:374–388
14. Olalla C, Clement D, Rodriguez M, Maksimovic D (2013) Architectures and control of submodule integrated DC–DC converters for photovoltaic applications. IEEE Trans Power Electron 28(6):2980–2997
15. Moretón R, Lorenzo E, Leloux J, Carrillo JM (2014) Dealing in practice with hot-spots. In: 29th European photovoltaic solar energy conference and exhibition, pp 1–6
16. Kim KA, Seo GS, Cho BH, Krein PT (2016) Photovoltaic hot-spot detection for solar panel substrings using AC parameter characterization. IEEE Trans Power Electron 31(2):1121–1130
17. Patel H, Agarwal V (2008) MATLAB-based modeling to study the effects of partial shading on pv array characteristics. IEEE Trans Energy Convers 23(1):302–310
18. Batzelis EI, Georgilakis PS, Papathanassiou SA (2015) Energy models for photovoltaic systems under partial shading conditions: a comprehensive review. IET Renew Power Gener 9(4):340–349
19. Ishaque K, Salam Z, Taheri H, Syafaruddin (2011) Modeling and simulation of photovoltaic (PV) system during partial shading based on a two-diode model. Simul Model Pract Theor 19:1613–1626
20. Hidalgo-Gonzalez PL, Brooks AE, Kopp ES, Lonij VP, Cronin AD (2012) String-level (kW-scale) IV curves from different module types under partial shade. In: 38th IEEE photovoltaic specialists conference (PVSC), pp 1442–1447
21. Ji Y-H, Jung D-Y, Kim J-G, Kim J-H, Lee T-W, Won C-Y (2011) A real maximum power point tracking method for mismatching compensation in PV array under partially shaded conditions. IEEE Trans Power Electron 26(4):1001–1009
22. Silvestre S, Kichou S, Chouder A, Nofuentes G, Karatepe E (2015) Analysis of current and voltage indicators in grid connected PV (photovoltaic) systems working in faulty and partial shading conditions. Energy 86:42–50
23. Bidram A, Davoudi A, Balog RS (2012) Control and circuit techniques to mitigate partial shading effects in photovoltaic arrays. IEEE J Photovoltaics 2(4):532–546
24. Patel H, Agarwal V (2008) Maximum power point tracking scheme for PV systems operating under partially shaded conditions. IEEE Trans Ind Electron 55(4):1689–1698
25. Tey KS, Mekhilef S (2014) Modified incremental conductance algorithm for photovoltaic system under partial shading conditions and load variation. IEEE Trans Ind Electron 61(10):5384–5392
26. Carannante G, Fraddanno C, Pagano M, Piegari L (2009) Experimental performance of MPPT algorithm for photovoltaic sources subject to inhomogeneous insolation. IEEE Trans Ind Electron 56(11):4374–4380
27. Chen K, Tian S, Cheng Y, Bai L (2014) An improved MPPT controller for photovoltaic system under partial shading condition. IEEE Trans Sustain Energy 5(3):978–985
28. Nguyen TL, Low K-S (2010) A global maximum power point tracking scheme employing direct search algorithm for photovoltaic systems. IEEE Trans Ind Electron 57(10):3456–3467
29. Alajmi BN, Ahmed KH, Finney SJ, Williams BW (2013) A maximum power point tracking technique for partially shaded photovoltaic systems in microgrids. IEEE Trans Ind Electron 60(4):1596–1606

30. Chin CS, Tan MK, Neelakantan P, Chua BL, Teo KTK (2011) Optimization of partially shaded PV array using fuzzy MPPT. In: IEEE colloquium on humanities, science and engineering (CHUSER), pp 481–486
31. Punitha K, Devaraj D, Sakthivel S (2013) Artificial neural network based modified incremental conductance algorithm for maximum power point tracking in photovoltaic system under partial shading conditions. Energy 62:330–340
32. Syafaruddin, Karatepe E, Hiyama T (2009) Artificial neural network-polar coordinated fuzzy controller based maximum power point tracking control under partially shaded conditions. IET Renew Power Gener 3(2):239–253
33. Ishaque K, Salam Z, Shamsudin A, Amjad M (2012) A direct control based maximum power point tracking method for photovoltaic system under partial shading conditions using particle swarm optimization algorithm. Appl Energy 99:414–422
34. Ishaque K, Salam Z, Amjad M, Mekhilef S (2012) An improved particle swarm optimization (PSO)–based MPPT for PV with reduced steady-state oscillation. IEEE Trans Power Electron 27(8):3627–3638
35. Ishaque K, Salam Z (2013) A deterministic particle swarm optimization maximum power point tracker for photovoltaic system under partial shading condition. IEEE Trans Ind Electron 60(8):3195–3206
36. Ramaprabha R, Mathur B, Ravi A, Aventhika S (2010) Modified Fibonacci search based MPPT scheme for SPVA under partial shaded conditions. In: IEEE third international conference on emerging trends in engineering and technology, pp 379–384
37. Tumbelaka HH, Miyatake M (2010) Simple integration of three-phase shunt active power filter and photovoltaic generation system with Fibonacci-search-based MPPT. In: IEEE symposium on industrial electronics and applications (ISIEA 2010), pp 94–99
38. Miyatake M, Inada T, Hiratsukai I, Zhao H, Otsuka H, Nakano M (2004) Control characteristics of a Fibonacci-search-based maximum power point tracker when a photovoltaic array is [1] partially shaded. In: IEEE the 4th international power electronics and motion control conference, (IPEMC 2004), pp 816–821
39. Jiang LL, Maskell DL (2014) A uniform implementation scheme for evolutionary optimization algorithms and the experimental implementation of an ACO based MPPT for PV systems under partial shading. In: IEEE symposium on computational intelligence applications in smart grid (CIASG), pp 1–8
40. Tajuddin MFN, Ayob SM, Salam Z (2012) Tracking of maximum power point in partial shading condition using differential evolution (DE). In: IEEE international conference on power and energy (PECON), pp 384–389
41. Ramli MAM, Ishaque K, Jawaid F, Al-Turki YA, Salam Z (2015) A modified differential evolution based maximum power point tracker for photovoltaic system under partial shading condition. Energy Build 103:175–184
42. Elnosh A, Khadkikar V, Xiao W, Kirtely Jr. JL (2014) An improved extremum seeking based MPPT for grid connected PV systems with partial shading. In: IEEE international symposium on industrial electronics, pp 2548–2553
43. Liu Z-H, Chen J-H, Huang J-W (2015) A review of maximum power point tracking techniques for use in partially shaded conditions. Renew Sustain Energy Rev 41:436–453
44. Bizon N (2015) Global maximum power point tracking based on new extremum seeking control scheme. Prog Photovoltaics Res Appl. doi:10.1002/pip.2700
45. Syafaruddin, Hiyama T, Karatepe E (2010) Investigation of ANN performance for tracking the optimum points of PV module under partially shaded conditions. In: Proceedings of international power energy conference, pp 1186–1191

Chapter 11
Solar Energy Harvesting in Electro Mobility

Aytaç Gören

Abstract Based on the experiences of five solar cars designed and manufactured in 11 years, participations in establishments of solar charging stations and local solar power plant projects, this chapter involves modeling energy harvesting and storing parts of solar cars, differences between maximum power point tracker topologies in implementations, the structures of *brushless direct current motors (BLDCMs)* and batteries as loads and the similarities of *brushless direct current motors*; briefly, solar energy harvesting for electro mobility. Light weight is one of the keys for efficiency in electro mobility. This enforces implementations of new technologies in manufacturing light weight electric vehicles. The end of the first section of this chapter is about using polymer composites in manufacturing process of solar cars. On the other hand, if energy harvesting should be separated from the vehicle, modular on or off-grid solar charging stations might be an efficient solution and an implementation of this type of energy harvesting is presented in the second section of this chapter. The last section in this chapter is about hybrid off-grid systems which also includes smart solutions. Implementations of this chapter are manufacturing process chassis and body of a solar car using polymer composites, a model of an off-grid PV charging station for *electric vehicles (EVs)* in a campus area, electrical units of a solar car for World Solar Challenge.

Keywords Solar car · Solar system modeling · Stand-Alone Photovoltaic (SAPV) · Brushless Direct Current Motors (BLDCMs) · Vacuum Assisted Resin Transfer Molding (VARTM)

Abbreviation and Acronyms

AM	Air Mass
BLDCM	Brushless Direct Current Motor
CAD	Computer Aided Design

A. Gören (✉)
Automatic Control and Robotics Laboratories, Department of Mechanical Engineering, Dokuz Eylul University, Izmir, Turkey
e-mail: aytac.goren@deu.edu.tr

N. Bizon et al. (eds.), *Energy Harvesting and Energy Efficiency*,
Lecture Notes in Energy 37, DOI 10.1007/978-3-319-49875-1_11

EMF	Electromotive Force
EV	Electric Vehicle
HAWT	Horizontal Axis Wind Turbines
ICE	Internal Combustion Engine
MPPT	Maximum Power Point Tracker
NOCT	Normal Operating Cell Temperature
PEM	Proton Exchange Membrane
P&O	Perturb & Observe
PV	Photovoltaic
SAPV	Stand-Alone Photovoltaic
SC	Solar Car
SCRIMP	Seemann Composites Resin Infusion Moulding Process
SOC	State of Charge
STC	Standard Test Conditions
VARTM/VARIM	Vacuum Assisted Resin Infusion Moulding
VAWT	Vertical Axis Wind Turbines
VBRTM	Vacuum Bag Resin Transfer Moulding
WT	Wind Turbine

11.1 Modeling of Solar Power Systems

11.1.1 Modeling of Semi Flex Silicon Solar Panel

Equivalent circuit of a PV cell can be simply modeled as a current source in parallel with a resistor and a diode those are connected in series with another resistor (Fig. 11.1). The output of the current source is directly proportional with the light on the cell. The open circuit voltage of the cell is quite different from the cell that is connected with the load which is shaped with R_s resistor in the same figure. Besides, the temperature effects the output of the cell as well. On the other hand, the mathematical model of the cell is defined using the Shockley Diode Equation in most of the researches about PVs (Eqs. 11.1 and 11.2) [1–3]. The parameters in

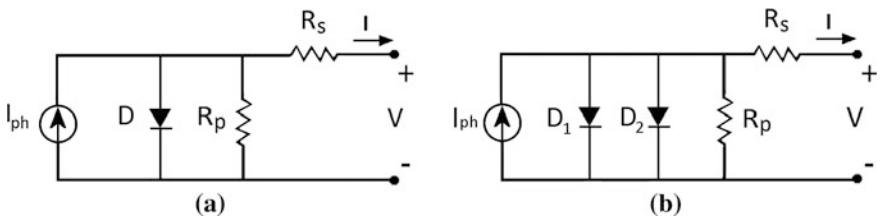

Fig. 11.1 PV cell models. **a** One diode model. **b** Two diode model

Table 11.1 Parameters of cell model

Parameters for cell current calculations			
I_{ph}	Light generated current (A)	V	Voltage (V)
I_S	Cell saturation of dark current (A)	k	Boltzmann cons. (1.38×10^{-23} (j/K))
T_C	Cell temperature (K)	A	Ideal factor ( )
q	Electron charge (1.6×10^{-19} (V))	I	Current (A)
I_{S1}	First diode saturation current (A)	I_{S2}	Second diode saturation current (A)
N_1	Quality factor of D_1 ( )	N_2	Quality factor of D_2 ( )
V_t	Thermal voltage (V), ($k*T_c$)/q	R_s	Internal series resistance (Ω)
R_p	Internal parallel resistance (Ω)		
Parameters given by manufacturers			
V_{OC}	Open circuit voltage @25 °C (V)	I_{SC}	Short circuit current @25 °C (A)
V_m	Voltage @MPP@25 °C (V)	I_m	Current @MPP@25 °C (A)
P_m	Maximum power @25 °C (W)		

Eqs. 11.1 and 11.2 and the parameters which are given by the manufacturers might be seen in Table 11.1.

$$I = I_{ph} - I_s\left[\exp\left(\frac{qV}{kT_cA}\right) - 1\right] \tag{11.1}$$

$$I = I_p - I_{s1}\left[\exp\left(\frac{V + I * R_s}{N_1 * V_t}\right) - 1\right] - I_{s2}\left[\exp\left(\frac{V + I * R_s}{N_2 * V_t}\right) - 1\right] - \frac{(V + I * R_s)}{R_p} \tag{11.2}$$

In Eqs. 11.1 and 11.2, the first one is the simple form of the solar cell which is represented by one diode or saturation current whereas the second equation is the cell representation with two diodes. Both models can be seen in Fig. 11.1a, b respectively.

Semi flex PV panels are the panels which are flexible in one direction. This advantage makes it possible to cover a surface of the solar car whose shape is formed using fluid dynamics analysis. On the other hand, the final shape of a solar car might be also similar with a tube for some designs. In that case, the solar irradiation received by the surface might differ from a flat surface that is perpendicular to the sun rays and for rough calculations, the average energy generation values might be used. Remembering that only one region receives the sun rays perpendicularly for this case, it is a big disadvantage for energy generation. So, for solar cars, there are some tube-like designs with transparent vehicle bodies and flat PV modules inside.

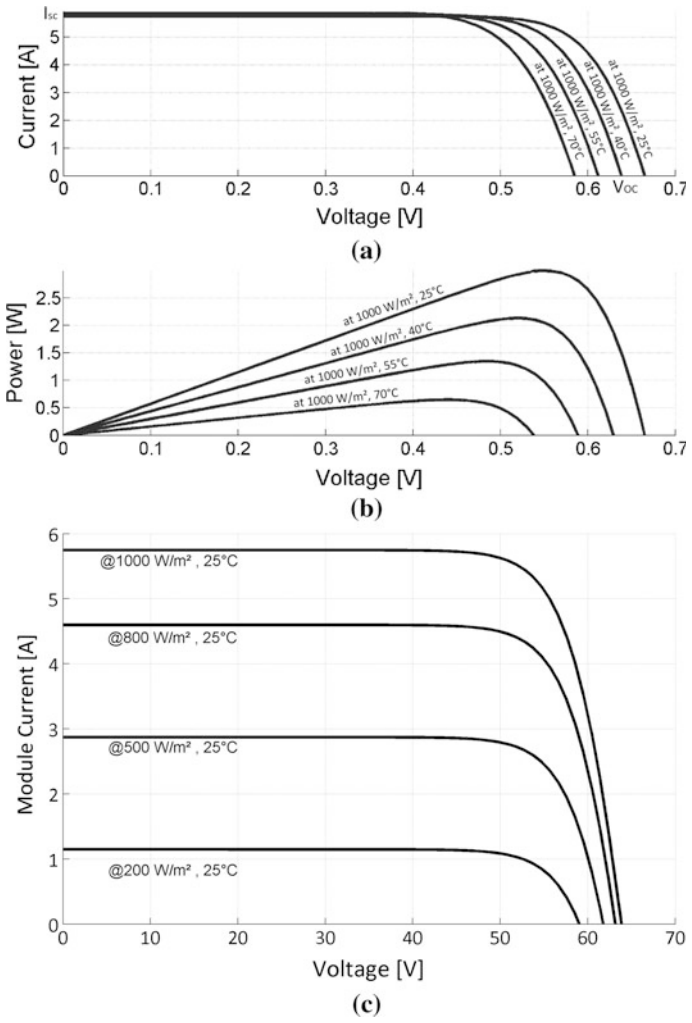

Fig. 11.2 PV curves. **a** Voltage-current. **b** Voltage-power @diff. temp. **c** Voltage-power @ diff. irradiance

In Fig. 11.2, current-voltage and power-voltage graphs of a PV cell at different cell temperatures might be seen. As it is known, the Silicon photovoltaic structure, in fact accidently discovered during photo diode experiments in 1950s. This was a discovery of a structure that does not control the current due to light, a structure that generates electrical energy due to light. So, the similarities in the graphics below come from the semi-conductor characteristics with electricity. It should be considered that the values in these graphs are taken under standard illumination 1000 W/m^2 at 1.5 AM that is generally called as *1 sun.* However, PVs can get more

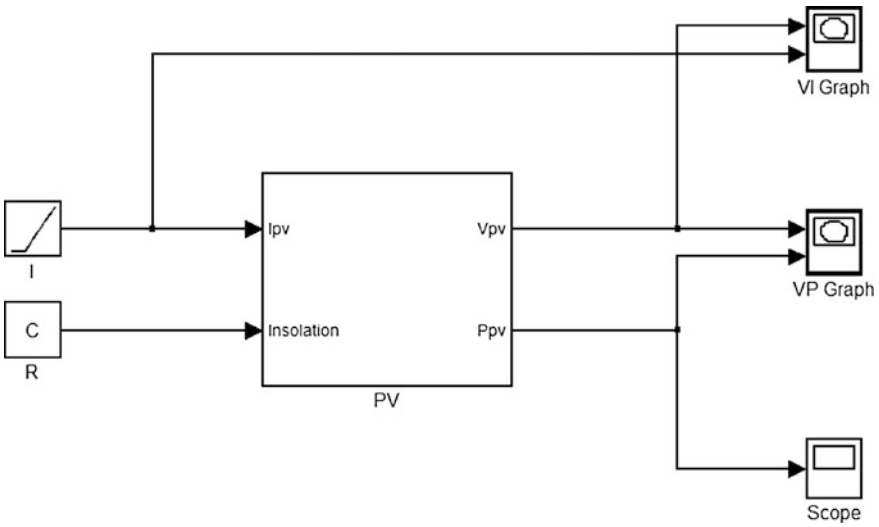

Fig. 11.3 A simple PV cell model in MATLAB Simulink

sun levels using optics. This systems are called as concentrators. Since the thickness of the body shell and mass are important parameters for solar cars, *Fresnel Lenses* are mostly used for this purpose.

For modeling the photovoltaic cell in MATLAB, it is common to form a model of a current source, that is effected by the parameters of light intensity (radiation) and temperature. Considering the one or two diode equations, using the parameters in Table 11.1, a more convenient model might be used. Chapter 2 in this book gives a detail photovoltaic cell model. Besides, a simple MATLAB model might be seen in Fig. 11.3.

Power generation optimization or finding the maximum point for the power generation is based on finding the maximum rectangular area in Fig. 11.2a or finding the peak point of the curve depending on the cell temperature and irradiance for Fig. 11.2c. The way of doing this is increasing or decreasing the output voltage level of a DC/DC converter (please see Fig. 11.7). One of the common techniques is to change the output voltage with a little difference and observe the output power with the previous output power value (perturb and observe). On the other hand, if the source is not just PV, but there are wind turbine(s), water turbine(s) or diesel generator in the system, total system output should be optimized due to energy efficiency or cost.

11.1.2 Types of Energy Loads for Stationary Solar Powered Systems and on Vehicles

11.1.2.1 Energy Loads for Stationary Solar Powered Systems

Stand alone photo voltaic (SAPV) systems are the system which have only PV to generate electricity and are more implemented systems than hybrid ones because of their simplicity in design and implementation. Energy consumption of a house differs with the area of the house, the location, the number of the people use the house, the characteristic of usage and some other parameters, the energy consumption of the house should not only be analyzed in details but the analysis should also cover the whole year usage. In some countries, like Turkey, the generated power can be also sold using the grid. So, it is the initial point to design the system if the system will be off-grid (not connected to the grid) or on-grid (connected to the grid). If the system is on-grid, it is more like that a huge capacitance is connected to the system; but, this time charging the capacitor is selling the energy generated to the grid and discharging the capacitor is buying energy from the grid. So, it is mostly not reasonable to connect a battery pack to the system. On the other hand, if it is an off-grid system, commonly a battery pack that its 80% can be charged by the PVs in 5 h mostly convenient in Aegean Region of Turkey. Table 11.2 shows energy consumption of some loads. Battery, as a load, modeled in next part of this section with different types of batteries.

If the system is an off-grid SAPV system, to be more efficient, loads are recommended to use direct current, since the inverter (the unit converts DC to AC) also draws energy. Loads connected to the system are mostly considered as resistive loads.

11.1.2.2 Energy Loads for Solar Powered Mobile Systems

Brushless Direct Current Motor (BLDCM) Model

The mathematical model of a linear BLDCM is generally related with the Lorentz force as in electric motors. Of course, there is a nominal force this time, but not a nominal torque.

$$\vec{F} = q \cdot \vec{v} \times \vec{B} \tag{11.3}$$

If the variations of the stator self inductance with rotor position and the mutual inductance between the stator windings considered as negligible; the electrical dynamics of a BLDCM may be modeled in an electrically balanced system [4–7]. In that case,

Table 11.2 Power of some loads in houses

Device	Power (W)	Device	Power (W)	Device	Power (W)
Coffee machine (Turkish cf.)	200	Washing m.	1200–1500	Tumble dryer	4000
Coffee machine (filter)	800	Hair dryer	1000–2000	Heater (res.)	1500–2500
Toaster	800–1500	Vac. cleaner		Air Condition	
		Big	200–700	Room	1000
		Compact	100	Central	2000–5000
Pop corn m.	250	Sewing m.	100	Fan	10–50
Blender	300	Iron	1000	Table fan	10–25
Microwave Oven	600–1500	Shaver	15	Electric blanket	200
Washing machine	500	Electric pan	1200	Computer	
				Laptop	20–50
				Desktop	80–150
TV		CD/VCR/DVD Player	35–50	Satellite receiver	30
(25″ LCD)	150				
(19″ LCD)	70				
9″ Angle grinding	1200	Wireless Phone sender	40–150	El. clock or radio cl.	1–3
		Receiver	5		
Cold saw	900–1400	Radio/CD/MP3 Player	10–30	Ham radio	5
12″ Saw	1100	Radio/MP3 player for car	8	Printer	100
1″ Drill	1000	Illumination 25 W Fluorsc.	28	Refrigerator/freezer	
		50 WDC inc. lamp	50	Old	475–540
		40 WDC hlg. lamp	40	New	60–112
		20 W Fluorsc.	22		

$$u_{si} - V_0 = L_s \frac{di_{si}}{d_t} + R_s i_{si} + e_i; \quad i = 1, 2, 3 \tag{11.4}$$

$$\sum i_{si} = 0 \tag{11.5}$$

In Eq. 11.4, R_s and L_s are the stator resistance and inductance, u_{si} is the motor terminal voltage, i_{si} is the phase current and e_i is the back-EMF associated with the ith phase. The potential of the motor neutral terminal in wye-connected windings is denoted as V_0. The back-EMF induced in each phase is;

$$\mathrm{e_i} = \frac{\mathrm{d}\psi_{\mathrm{ir}}}{\mathrm{d_t}} = \frac{\partial \psi_{\mathrm{ir}}}{\partial \theta}\frac{\mathrm{d}\theta}{\mathrm{dt}} = \omega \frac{\partial \psi_{\mathrm{ir}}}{\partial \theta} \tag{11.6}$$

If ψ_{ir} is the mutual magnetic flux between the permanent magnet and the stator windings in the ith phase, θ is the rotor position, and ω is the rotor speed. If the model is assumed as linear;

$$d\psi_{ir} = L_{ir} i_r \tag{11.7}$$

The mutual inductance L_{ir} is expressed, using the terms of the trigonometric Fourier series, as:

$$L_{ir} = \sum_{k=1}^{K} (L_{irak} \cos k(p\theta - \frac{2\pi}{3}(i-1)) \; + \; L_{irbk} \sin(p\theta - \frac{2\pi}{3}(i-1))) \tag{11.8}$$

The back EMF can be derived from (11.6) and (11.7) as;

$$e_i = i_r \omega \frac{\partial L_{ir}}{\partial \theta} \tag{11.9}$$

The electromagnetic motor torque can be derived as;

$$T = \sum_{i=1}^{3} T_i + T_{icogg} = i_r (\sum_{i=1}^{3} i_{si} \frac{\partial L_{ir}}{\partial \theta}) + \frac{1}{2} i_r^2 \frac{\partial L_{rr}}{\partial \theta} \tag{11.10}$$

The first three terms in Eq. 11.10 are mutual torques caused by interaction between the permanent magnet field and the phase currents. T_{icogg} is the cogging-torque, due to the attraction of the permanent to the salient portions of the stator iron. So, even in the absence of the phase currents, the cogging-torque is present.

If T_l is the load torque, J is the rotor inertia, B is the viscous friction coefficient C is the Coloumb friction coefficient, mechanical dynamics model of the motor is defined as;

$$\dot{\theta} = \omega; \quad \dot{\omega} = \frac{1}{\mathrm{J}}(\mathrm{T} - \mathrm{T_l} - \mathrm{B}\omega - \mathrm{C}\,\mathrm{sign}(\omega)) \tag{11.11}$$

Since efficiency of each part has importance for a solar car, *hub motor* use is very common for solar cars. Hub motor is the motor which the rim itself is also the rotor of the motor. Hence, there is no transmission system and the efficiency of the motor can reach 99% [4].

Model of the Batteries

Next step of generation energy comes with a harder engineering problem that is to store it. If it is a system that can be connected to grid, it is not needed to consider chemical reactions or heat up a mass to store energy; but if it is an off-grid one, the energy that is generated needs to be transformed in different forms or capacities. Capacity might be a water tank for a PV system that is for irrigation to reduce the costs and to increase the system life (see Fig. 11.17a). But, mostly it is the chemical reactions help us. Lead acid, NiCd, NiMH, LiIon, LiIonPo (or LiPo shortly) are mostly known rechargeable types of batteries for that purpose [8]. It is very common to use LiPo and LiIon batteries in electric vehicles (EVs) because of their advantage of high energy density (kWh/kg) values. Lead Acid types of batteries are used in off-grid SAPV or hybrid systems mostly because of their costs [9, 10].

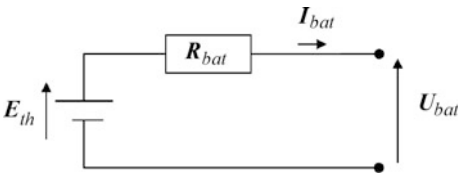

Fig. 11.4 Quasi-static model of equivalent electrical circuit of a battery

The quasi-static model of equivalent electrical circuit of the LiPo batteries which is based on Thevenin model (Fig. 11.4) is commonly used, but to understand the limits of the LiPo batteries, dynamic behavior should be also take into account especially for solar vehicles [11].

In Fig. 11.4, *E*th is the open circuit voltage, R_{bat} is the resistance of the battery, U_{bat} is the voltage of the battery and I_{bat} is the current of the battery.

The lead-acid battery voltage during charging can be expressed with Eq. 11.12 using the internal resistance of the battery (r_{bat}), the electrode potential (E_o), the number of cells in the battery (N), the charging current of the battery (I_{bat}), state of charge (SOC), η is the overpotential and a_1 is a parametric constant depends on the phase of charge [9, 12]:

$$\dot{\theta} = \omega; \quad \dot{\omega} = \frac{1}{\mathrm{J}}(\mathrm{T} - \mathrm{T_l} - \mathrm{B}\omega - \mathrm{Csign}(\omega)) \tag{11.12}$$

For discharging process, on the other hand, it can be defined with the following Eqs. 11.13 and 11.14.

$$U_{bat} = U_0 - \eta_{10} \tag{11.13}$$

$$\mathrm{U_{bat}} = [2.85 - 0.12(1 - \mathrm{SOC})] - \frac{1}{\mathrm{C_{10}}}\left(\frac{4}{1 + \mathrm{I}^{1.3}} + \frac{0.27}{\mathrm{SOC}^{1.5}} + 0.02\right) + (1 - 0.007\Delta\mathrm{T}) \tag{11.14}$$

11.1.3 Energy Needs of Solar Cars

Efficiencies of PVs for the known researches are between 6 and 46% for NREL [13] in year 2015. As for the same laboratory report, the most efficient ones are four junction or more GaAs ones whereas the maximum efficiency for Si panels is 27.6% which are the concentrated ones. As known, the efficiency of solar panel is calculated using Eq. 11.15. In this equation, η_{PV} is the efficiency of the panel, P_m is the output power in $\mathrm{W_p}$ at standard test conditions (STC) for one square meter of area under 1000 (W) of global irradiation at 25 °C and air mass (AM) of 1.5.

$$\eta_{PV} = \frac{P_m}{E \cdot A_c} \tag{11.15}$$

On the other hand, in real conditions the cell temperature is not at laboratory conditions first of all. And for a vehicle that is travelling with different velocities at different weather conditions to different directions, the energy taken from the solar array varies. For the first step of being realistic, power can be taken from the solar array at a known temperature and global irradiation can be calculated using the temperature difference Eq. 11.16. *NOCT* is the normal operating cell temperature whereas the ϕ is the solar irradiance. The difference between the temperature of the ambient air temperature (T_a) and the cell (T_c) is [14]:

$$T_C - T_A = \frac{NOCT - 20}{800} \times \phi \tag{11.16}$$

Energy need of a vehicle is calculated with the assumptions of all mechanisms run in ideal tolerances and in design phase it is mostly a prediction using these calculations. Unlike internal combustion engine cars, the electric car (EV) has highest torque at start and nearly a constant torque through running region. Considering the efficiencies of PVs which have the maximum efficiency of 46% even for the GaAs panels, for a vehicle which generates its energy from sun, the efficiencies and the robustness of the units have great importance. This also means nearly zero losses and very efficient systems. Electric motors of solar cars, for instance, have the efficiency of over 93% (most efficient 99.7%), the motor drivers mostly 99% and there is generally no transmission system.

Considering the weights and technologies of steel body with internal combustion engine vehicles, travelling from place to another place feels like asking a traveler if he travels to the place you travel and planning to go to your target city without forgetting the cities he will visit. Minimizing energy needs and optimizing energy usage starts with minimizing travelling mass and analyzing way of doing. Unlike classical concept of mass production cars, fibers whether they are carbon, aramid or glass make the polymer composite structure more and more strength, light and durable. Mass of a car we use in daily life is approximately 1200 kg whereas a solar car with the dimensions of 4.7 m × 1.8 m × 1.1 m 200 kg. This case not only reduces the energy needed to travel, but also gives a chance to manufacture the vehicle form more aerodynamics [15–18].

In designing phase of a solar car, the basic equation to calculate the energy needs is the Eqs. 11.18 and 11.17 might be used for the energy predicted for a solar car race [18, 19]. The parameters are defined in Table 11.3. In Fig. 11.5, the resistances affect the energy need of a solar car can be seen.

Table 11.3 Challenge strategy calculations for a solar car

Parameters for energy need calculations			
W_T	Total resistive forces (N)	x	Distance (m)
W_{R1}	Rolling resistance force (1) (N)	W	Weight of the vehicle (N)
W_{R2}	Rolling resistance force (2) (N)	C_{rr1}	Rolling resistance const. (1) ( )
W_B	Acceleration resistance force (N)	C_{rr2}	Rolling resistance const. (2) (Ns/m)
W_{ST}	Gradient resistance force (N)	N	Number of wheels ( )
m	Total mass of the vehicle (kg)	h	Total height vehicle climbs (m)
η	Motor, controller and drive train efficiency ( )	N_a	Number of times the vehicle will accelerate in a race day ( )
η_b	Watt-battery eff. ( )	g	Acc. due to gravity constant (m/s^2)
η_{PV}	Eff. of PV ( )	v	Av. velocity through the route (m/s)
E_b	Energy available in the batteries (joule)	v_a	Average velocity of the wind towards the vehicle (m/s)
P_m	Average power estimated from solar arrays (W)	λ	Factor for rolling mass' ( )

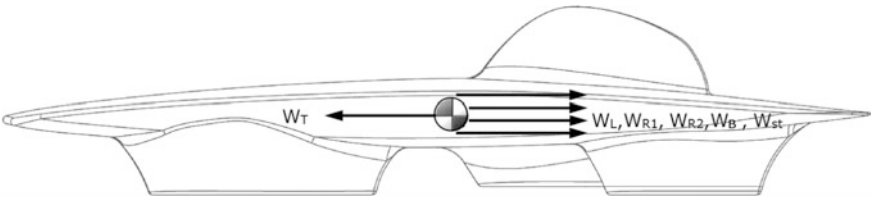

Fig. 11.5 Energy need of a car

$$\eta\left\{\eta_b E + \frac{P_x}{v}\right\} = \left\{WC_{rr1} + NC_{rr2}v + \frac{1}{2}\rho C_d A v^2\right\}x \; + \; Wh + \frac{N_a W v^2}{2g} \tag{11.17}$$

$$W_T = W_L + W_{R1} + W_{R2} + W_B \; + \; W_{ST} \tag{11.18}$$

$$\eta\left\{\eta_b E_b \; + \; \frac{P_m.x}{v}\right\} = W_T \tag{11.19}$$

11.1.4 MPPT's on Solar Cars

The electric vehicles (EVs) were built earlier than internal combustion engine (ICE) vehicles. Between late 1827 and 1839, different electric vehicles are built in Hungary, Netherlands, Scotland and US [20–23]; however, lack of usable rechargeable, high energy density batteries and the high popularity of ICE with easy

reloading of fuel. Since 1840s, EVs got popular for some time intervals like in 1910s with mass production concepts, late 1940s with invention of semiconductor structures, in 1970s with energy and petrol crisis. Besides, solar cars are not novel research areas, since it is known that the first was announced in 1955. The first solar car (SC) invented has 12 Selenium PV cells and a small electric motor rotating a the rear wheel shaft (Sunmobile, W.G. Cobb, 31.08.1955). Although the first solar car race was in 1985 (Tour Del Sol), it became popular with the Australian World Solar Challenge (WSC) in year 1987. The concept of WSC was devised by *Hans Tholstrup*, who is a Danish-born adventurer and traveled from Perth to Sydney (4130 km) in 20 days with a solar car called *Quiet Achiever*. Different concept solar car races are being organized in different continents nowadays. WSC (Australia, road challenge), European Solar Challenge (ESC, Europe, circuit race), American Solar Challenge (NASC, North America, combination of road and circuit races), Moroccan Solar Car Race (MSCR, road challenge), Alternative Energies Cup (Japan, circuit race), TUBİTAK Formula G (Turkey, circuit race), South African Solar Challenge (SASC, South Africa, road challenge) and Atacama Solar Challenge (CSA, Chile, road challenge) are some popular solar car races. In addition to these, some races are organized for one or two times in different countries. Today, SCs in races are classified with international motorsport federations and International Solar Car Federation which was formed in 1991 to give support to organizers.

A solar car is powered by PVs (mostly semi flex) which cover the surface of the car. The vehicle is designed with the concept of *'least energy need to travel'* (see Figs. 11.6 and 11.7). After achieving the DC formed electrical energy from the

Fig. 11.6 Solaris S7 solar car in world solar challenge

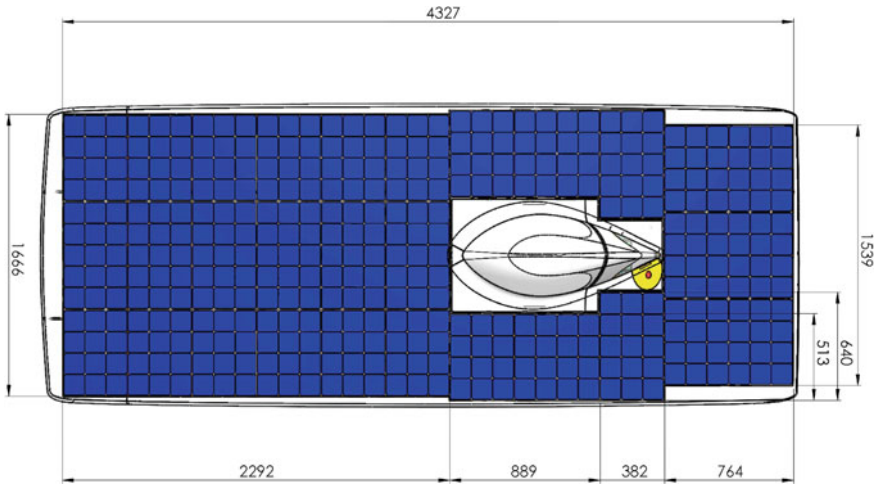

Fig. 11.7 DesTech Solaris (2015) solar car PV cell layout

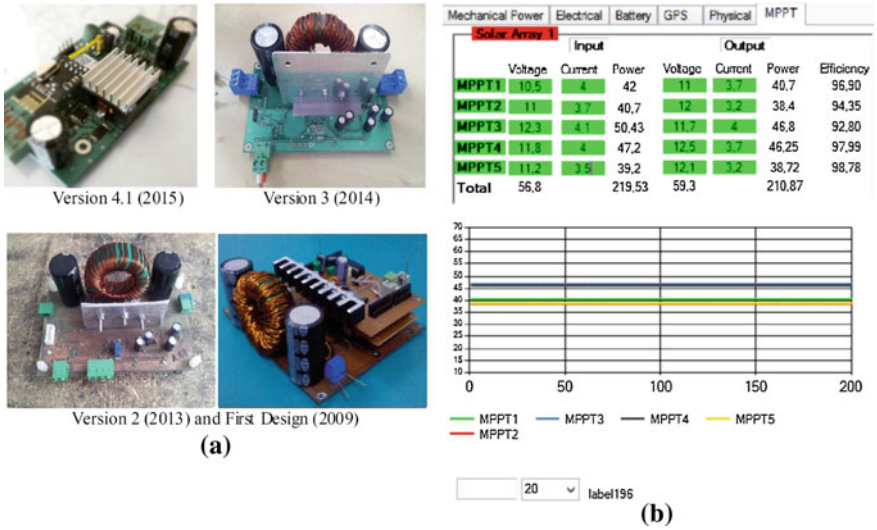

Fig. 11.8 **a** Solar team design MPPT's in Solaris solar car projects. **b** Developed telemetry interface of MPPTs

mono/poly Si or GaAs PVs, MPPTs provide high efficiencies of charging the high energy density batteries, mostly LiPo or LiIon (Fig. 11.8). With their polymer composite bodies and chassis, it is possible to achieve to manufacture a car that is 150 kg with the dimensions of 5.00 m × 1.8 m × 1.0 m (l/w/h) as will be told in following sections of this chapter. Some cars use solar concentrators, mostly

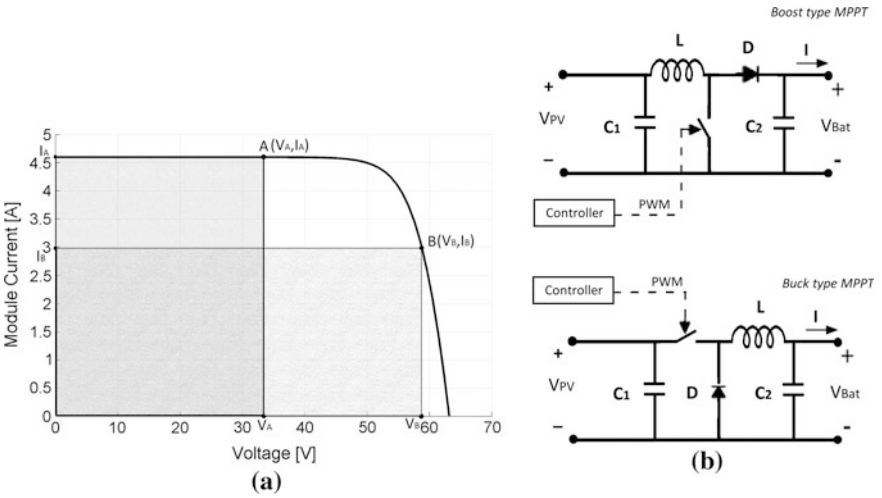

Fig. 11.9 **a** Maximum power point tracking. **b** Common MPPT topologies for SCs

Fresnel Lenses to concentrate the light intensity on the PV cell. This case, however means an additional weight to the car which makes the optimal energy usage problem a little bit more complex.

Power for a resistor in direct current (DC) is the product of applied voltage and the current. So, the most efficient implementation of a solar cell is maximizing the area in Fig. 11.7. PV cells are assumed as DC formed constant current generators which might be differ in real implementations, but for engineering calculations which have tolerances inside, said to be true. With this assumption, the VI curve of a cell is a horizontal line starting from I_{SC} then a line like curve falls down to V_{OC} with a slope which is connected to the first line with a radius simply (Fig. 11.9a). However, the output current is affected by the radiance directly and the temperature affects the point that the line like curve intersection point with the horizontal line, so the open circuit voltage. On the other hand, solar radiation and temperature change instantaneously in daytime as might be seen in Fig. 11.10. Maximum power point trackers are devices those find the point where the system gets maximum power from the photovoltaic.

In Fig. 11.10, irradiation levels taken by the pyranometer which is mounted on the roof of the main solar charging station in Tinaztepe Campus Location of Dokuz Eylul University can be seen. These data are used to make the results of calculations more real for solar car energy harvesting. This station is one of the stations generates the energy need of electric vehicles which are used in Dokuz Eylul University Tinaztepe Campus Location (please see Fig. 11.24b).

Consider two points on V-I curve of a PV cell. Output power is the product of output voltage and current. The greatest output power can be achieved with the maximum area of the rectangle. Knowing that the MPPTs are devices those are connected between PVs and loads, MPPT is a DC/DC converter which increase or

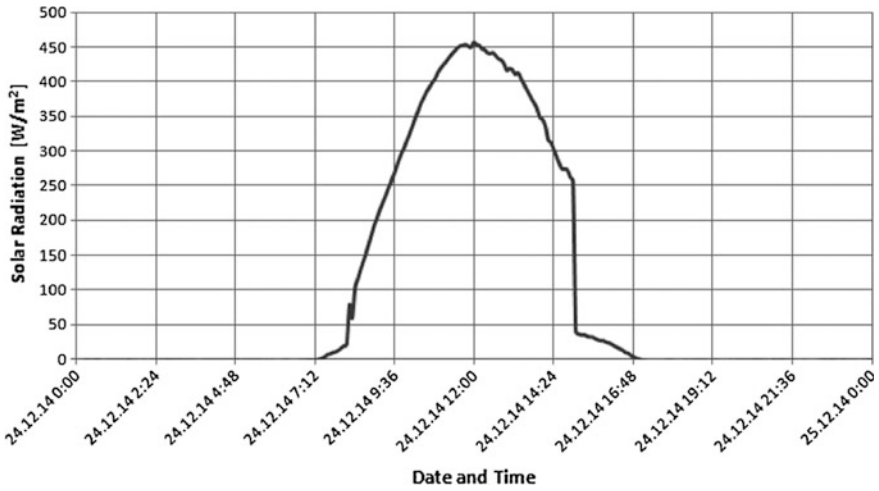

Fig. 11.10 Irradiation levels @ DEU Tinaztepe Campus Location on 24.12.2014

decrease the output voltage, to have the maximum area for the PV used (please see Fig. 11.9a). If the output voltage level of the MPPT is higher than input voltage level, it is *boost type*. If the output voltage level is lower than the input voltage level, it is *buck* type (please see Fig. 11.9b). Energy efficiency improvements using different MPPTs and different MPPT algorithms might be found in relevant chapters of this book.

Team Solaris of Dokuz Eylül University (Izmir) is a community of academicians, young investors and researchers from undergraduate to Ph.D. level, who gathered around the idea of designing/creating a car powered by solar energy in December 2003. As per date, over two hundred and fifty researchers took part, five solar cars and four EVs were designed and manufactured in Solaris Projects. Solaris Cars took part in WSC (Australia), ESC (Belgium), MSC (Morocco), Formula G (Turkey) and European Electric Vehicle Event (Austria). Just between May 2013 and November 2016, Team Solaris participated in eight international and five national solar car/EV races. Most of the implementations and information told about solar cars in this chapter are the technical experiences gained during Solaris projects design, manufacturing and challenging race phases.

Although some cars are still using stationary system type MPPTs for some solar car teams, it is common to use special designed boost type DC/DC converters with adaptive algorithms and wireless telemetry embedded circuits for this purpose.

Designing the PV array and battery capacity of a stationary solar power plant is mainly a cost optimization problem in engineering with more constant parameters. However, designing a solar array and energy storage system for a solar car is more complex which includes flow analysis, battery and PV combination calculations, energy need and optimization, strength analysis, efficiency analysis and more. The

voltage level itself for example changes the speed of the vehicle whereas torque generated by the motor is a result of battery type, parallel branches of the battery pack, C rating, racing conditions and regulations of the challenges. Every details have to be considered. For instance, if the *by-pass diode* that is needed for bypassing the module that has a shaded cell even has to be a fast, low voltage drop type diode in order not to cause a big loss. Or sometimes teams spray water to surface of cells in order to decrease the cell temperature. If we consider an area of 6 m^2 is used to be covered with PVs for solar cars, for use of Si cells which have approximately 22% efficient, the solar array can generate more than 1300 W @1000 W/m^2 global radiation @25 °C. However, the cell temperature almost never 25 °C, the global radiation level is limited just with laboratory conditions, the solar cells are just for a little time interval in daytime perpendicular to sun rays and 1000 W/m^2 is a rare value with limited time interval and affected with weather conditions. For an optimist prediction of average 1000 W output for a time interval from the solar array, the car itself should be very efficient in means of air flow, rolling resistances, the motor, driving unit and the batteries.

Photovoltaics are sources which the current generated by them changes due to incident light intensity. As mentioned before, every unit or every system model block on the solar car should be used in maximum efficient regions. On the other hand, the load connected to the system changes instantaneous, so the unit which simulate the load as maximum for PVs is called as maximum power point tracker [24–26]. This is explained in Fig. 11.9 in previous sections. Commercial product MPPTs which are used on stationary systems are also used on some solar cars. This case causes inefficiency, because of not only the commercial products are designed in run as boost, buck and voltage regulation regions, but also are heavy products with unneeded cases. A more common and effective way is to design the MPPT just as *buck* (input voltage is greater than output voltage) or *boost type* (output voltage is greater than input voltage). With the assumption of using the optimal number of series and parallel groups of PVs on a solar car, the most efficient type of MPPT topology for a solar car mainly the *boost type* and a common algorithm is hill-climbing/P&O (perturbation and observe) [1, 24–27]. The main disadvantage of this technique is the local maximum points that can cause not tracking the real maximum point. In Fig. 11.11, simplified electrical diagram of a solar car which designed by Team Solaris, might be seen. In this implementation, the cells are grouped in three groups. Each group has five MPPTs those are connected in series to charge a series of 32 LiPo cells connected also in series. The combination of the battery pack, however can be changed to different capacity of LiIon or LiPo cells and also the number of series-connected cells. If the values changes, developed bi-directional telemetry system and its software is used to change the charging voltage. The output voltage level is limited with the efficient test regions for MPPT. MPPTs in series can increase the efficiency, especially when some cells are shaded.

A method of using solar energy more efficient is to rotate the PVs of the solar car towards the sun to be sure that the arrival of the sun's rays are as close to perpendicular as possible (see Fig. 11.12). This is very common when the solar car is not travelling, but even they are rare, there are also some implementations of using

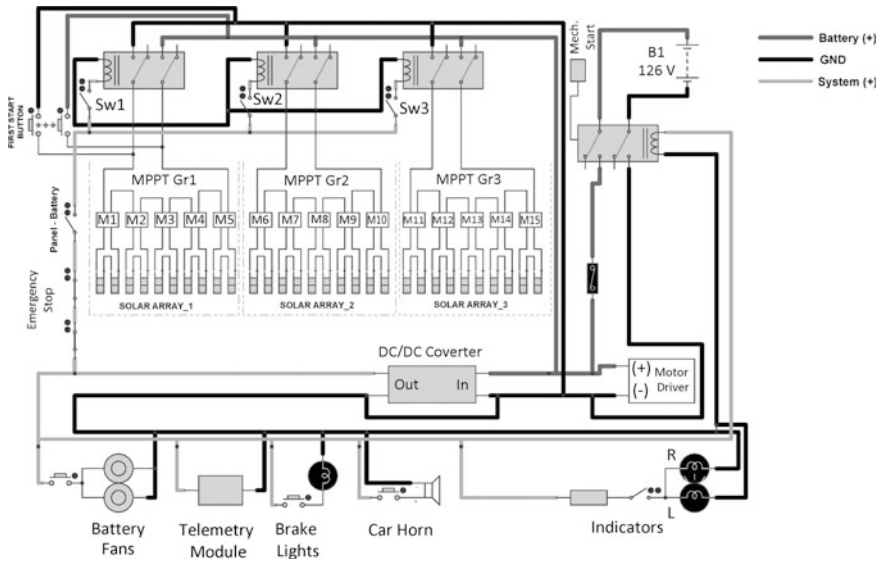

Fig. 11.11 DesTech Solaris solar car electrical connections

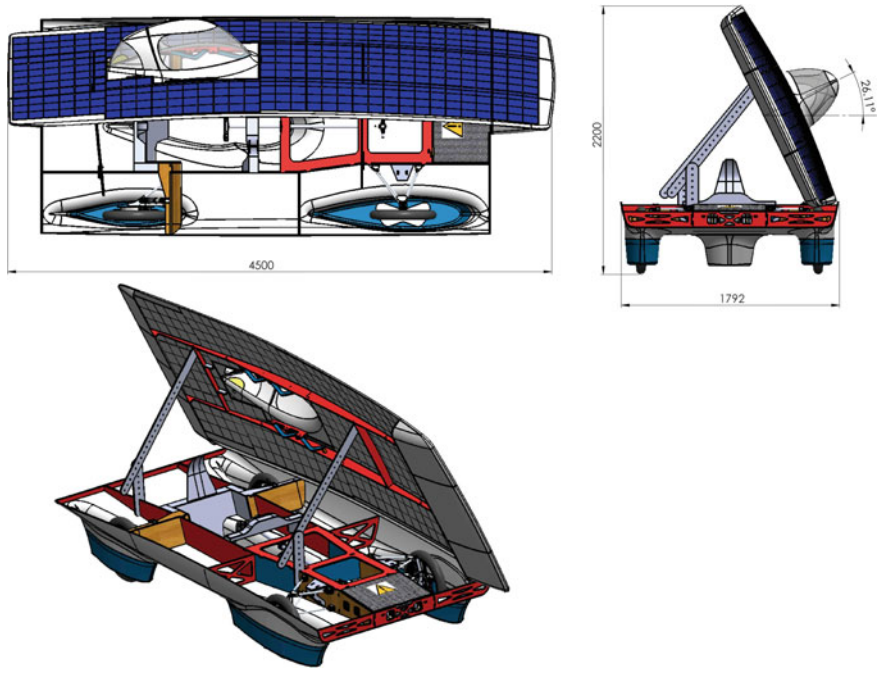

Fig. 11.12 DesTech Solaris upper car body orientation towards the sun

during the race like a group of *sun trackers*. In that case, not only the route direction and car direction should be good analyzed, but also the energy used to control the angle of the panels and the energy generated by the panels and the change in center of gravity should be well analyzed.

Before DesTech Solaris Solar Car, two common combinations of MPPTs are tested. First one was to divide the PV surface into two groups and to use two MPPTs. This selection, naturally was generally related with the voltages of battery and PV combination. As might be expected, this caused important power losses during the races because of damaged cells or connections of PV modules. Revised solution was to change the battery voltage level and PV groups. The groups increased to three with three boost type MPPTs whose algorithm also improved. This revision increased the efficiency level significantly. DesTech Solaris, on the other hand, uses fifteen MPPTs (five series, three parallels) which are optimized for shades and connection damages (please see Fig. 11.11).

11.1.5 Using Polymer Composites for Increasing Efficiency of Energy Harvesting

Wind turbine (WT) electric generation systems have less subsystems than in thermal, hydroelectric or nuclear power plants. And one of the great advantages of a wind turbine is, like PVs, it is easier to scale the structure. WT has three main parts, the electric generator, blades and the wind turbine tower. It has control systems to control the angles of the blades or the tail and for energy transfer. The electric is generally a three phase form which has 120° between each other. Based on the orientation of the axis of rotation, wind turbines have two main types: Horizontal axis wind turbines (HAWT) and vertical axis wind turbines (VAWT). Figure 11.13 shows (a) VAWT and (b) HAWT. HAWTs can be scalable from 500 W to MWs, but VAWTs are generally chosen for their motion of less vibration and esthetics, however they are less efficient and less scalable (mostly 10 kW). The output form of both types is alternate current form, as seen in previous section that is on Hybrid System. Blades, mechanical connection of blades and if the dimensions of the turbine has a small value in scale, sometimes the WT tower can be also polymer composites and they are manufactured using vacuum assisted resin transfer method which will be told with solar car body production in this section.

There has been a growing interest to use composite materials in structural applications ranging from aircraft and space structures to automotive and marine applications instead of conventional materials. This is because advanced composites exhibit desirable physical and chemical properties that include high specific stiffness and strength, dimensional stability, temperature and chemical resistance, and relatively easy processing. A variety of manufacturing methods can be used according to the end-item design requirements. Most commercially produced composites use a polymer matrix with textile reinforcements such as glass, aramid

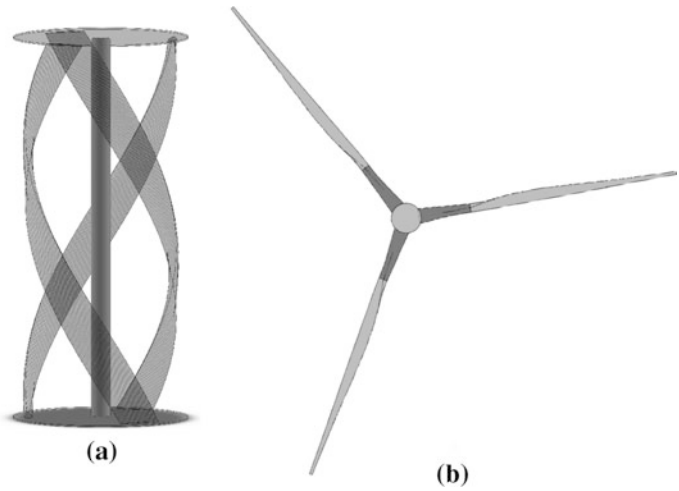

Fig. 11.13 Blades of wind turbines. **a** Vertical axis type. **b** Horizontal axis type

and carbon. Besides, the structures and parts which need light weight but also greater strength values need to be optimized in more cycles. Analyzing, reconstruction using CAD model, redesigning and remanufacturing phases include more details and loops. Solar Cars, ballistic parts, fifty meter long wind turbine wings are some examples of these light weight technological parts. This section is based on solar car manufacturing steps and techniques which is very similar with wind turbine blade manufacturing.

Vacuum assisted resin infusion techniques have become popular in manufacturing of these composites. In the literature, vacuum infusion is known under different acronyms. The most popular terms to describe vacuum infusion processes are: VARTM-Vacuum Assisted Resin Transfer Moulding, VARIM-Vacuum Assisted Resin Infusion Moulding, SCRIMP™-Seemann Composites Resin Infusion Moulding Process, VBRTM-Vacuum Bag Resin Transfer Moulding, VARI-Vacuum Assisted Resin Infusion process and so on. All involve basically the same technology, and describe methods based on the impregnation of a dry reinforcement by liquid thermoset resin driven under vacuum [28]. Stages can be simplified as:

1. Identifying the important parameters for design,
2. Preliminary design with constraints,
3. Identifying the types of fibers and analysis,
4. Improving design with the conclusions of analysis,
5. Model production (1:1),
6. Mould production,
7. Moulding.

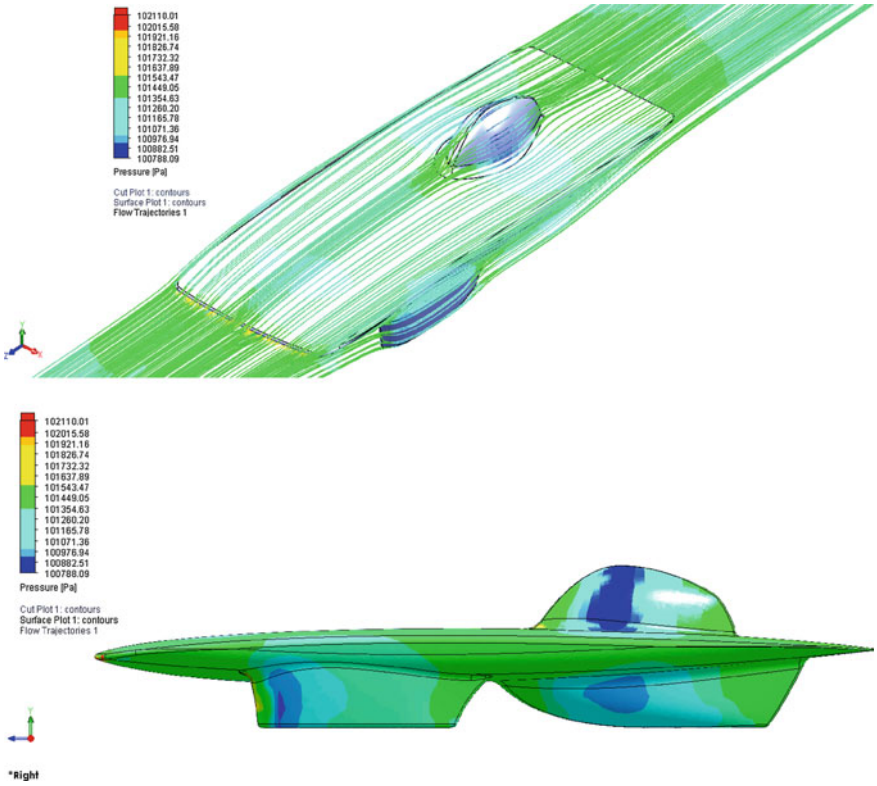

Fig. 11.14 Fluent analysis of Solaris S7 (2013)

In manufacturing stages of polymer composite products, the analysis' of a solar car are based on strength, vibration, fluent and efficiency [18, 29]. Figure 11.14 shows the fluent analysis of Solar Car Solaris S7 (2013) whereas Fig. 11.15 shows the fluid mechanics analysis of Solar Car DesTech Solaris (2015). DesTech Solaris is 4500 mm in length and 1800 mm in width. Foam mold is formed from modular small foam parts. You may find the static structural analysis of Solar Car DesTech Solaris in Fig. 11.16.

In flow analysis of the body, the regions which has turbulences or the regions against the flow are found. If vacuum is formed during flow, this causes the vehicle pulled backwards by the flow which is called as parachute effect. And if the analysis shows high regional forces against flow, this shows the need of smoothing the edges or angles of the form. Considering these two main cases, car body is optimized once more to be efficient. On the other hand, static and dynamic mechanical analysis determines the textile fiber angles and density per area (Fig. 11.16). These analysis determine the types (carbon, aramid or different fiber glass types) and layers of textiles. Analyzing person should not consider just material characteristics, but also some special characteristics of the selected types. For example, carbon,

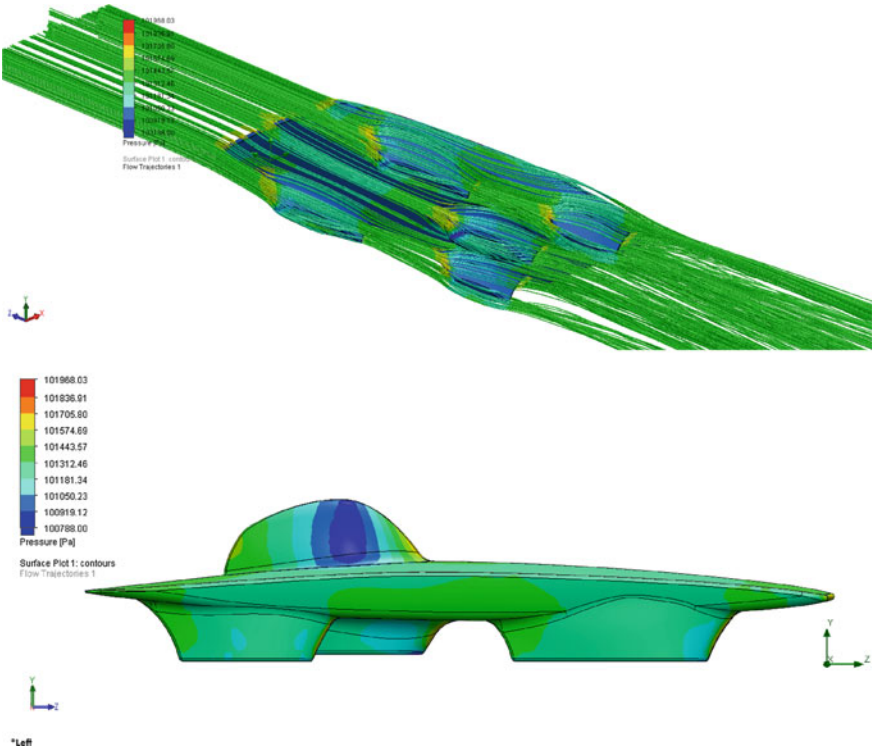

Fig. 11.15 Fluent analysis of DesTech Solaris S8 (2015)

even it is in fiber formed textile, a good conductor which is not so needed when transmitting wireless signals or if there are non-isolated poles in a box of carbon polymer composites.

Vacuum Assisted Resin Infusion Moulding (VARIM or VARTM) is a polymer composite manufacturing process to produce high-quality large-scale components. In this process, dry preform fabrics are placed in an open mold and a plastic vacuum bag is placed on the top of the mold. The one-sided mold is connected with a resin source and a vacuum pump. The liquid resin infuses into the reinforcing fibers thanks to the vacuum drawn through the mold. Curing and de-molding steps follow the impregnation process to finish the product. Curing process is very important to produce composite parts with optimum mechanical properties [30]. All regions in a composite part are supposed to be produced almost at the same curing conditions. So, a uniform temperature distribution through the mould surface is of high importance.

The main steps of the process are:

a. A dry fabric or preform and accompanying materials such as release films, peel plies are laid on tool surface.

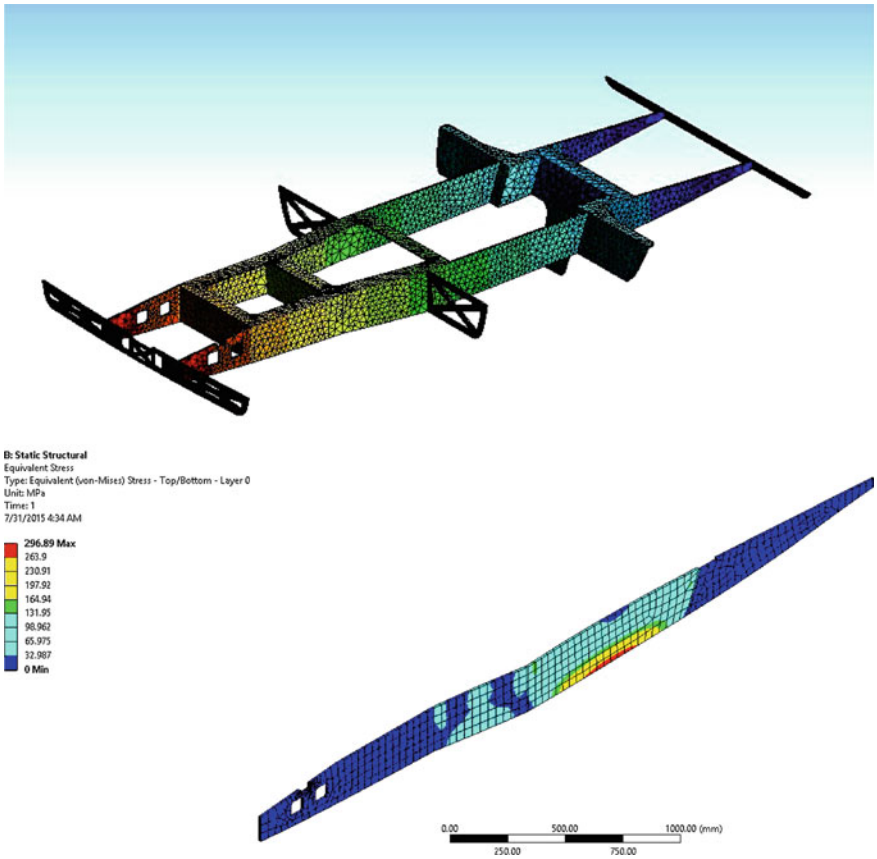

Fig. 11.16 Static structural analysis of DesTech Solaris (2015)

b. The preform is sealed with a vacuum bag and the air is evacuated by a vacuum pump.
c. Liquid resin with hardener from an external reservoir is drawn into the component by vacuum.
d. The liquid resin with hardener is infused into the preform until complete impregnation.
e. Curing and de-molding steps follow the impregnation to finish the product.

The components of the infusion process utilized in this work are illustrated in Fig. 11.17. The function of the each component, given in Fig. 11.17, during manufacturing can be summarized as:

Vacuum bagging films are sealed to the edge of the mould with vacuum bag sealant tape to create a closed system.

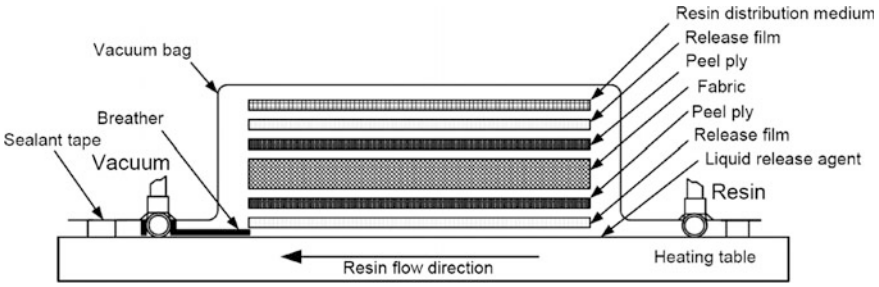

Fig. 11.17 Vacuum assisted resin transfer molding (VARTM) process control diagram

Fig. 11.18 Model production of Solaris Erke solar car for moulding

Double side bag *sealant tapes* are used to provide a vacuum-tight seal between the bag and the tool surface.

Release films are typically placed directly in contact with the laminate. They separate the laminate from the distribution medium. Release films are often perforated to ensure that any trapped air or volatiles, which may compromise the quality of the laminate, are removed.

Release fabrics and *peel plies* are placed against the surface of the laminate. They are woven products which are strong and have good heat resistance. Release films

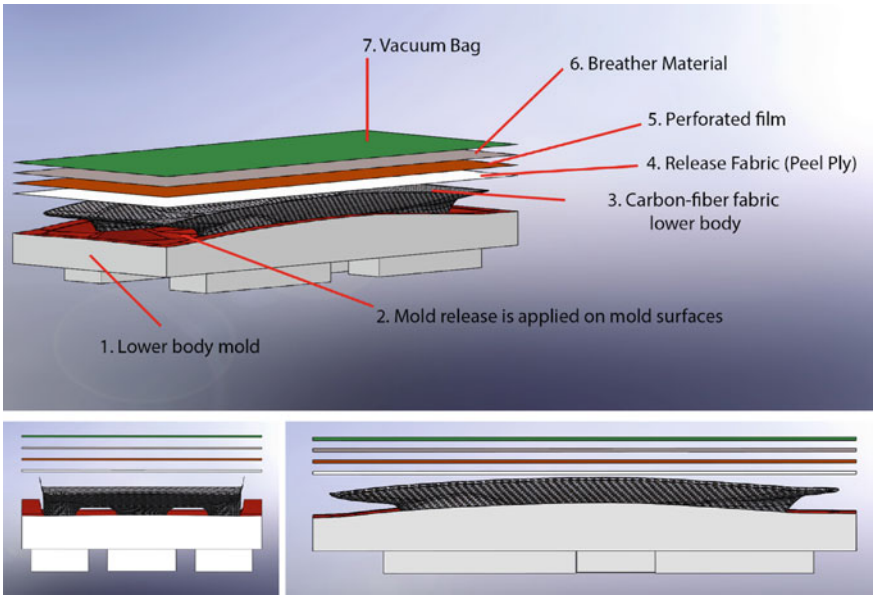

Fig. 11.19 VARTM process for solar car Molding

impart a gloss finish on the cured laminate, whereas peel plies and release fabrics leave an impression of the weave pattern. Peel plies provide a clean, uncontaminated surface for subsequent bonding or painting (Fig. 11.18).

Tool release materials are used to release the product from tools easily and obtain a smooth surface finish. For this purpose, either self adhesive Teflon films or liquid release agents are utilized. In certain situations Teflon films can also temporarily solve tool porosity problems.

A highly permeable layer called "*resin distribution medium*" placed on the top of the preform spreads the resin quickly over the lateral extent of the part.

Bleeder/breather fabrics are non-woven fabrics allow air and volatiles to be removed from within the vacuum bag throughout the cure cycle. They also absorb excess resin present in some composite lay ups.

For moulding (*VARTM* or *VARTM*) process, model of the product which has the scale of one is manufactured mostly (Fig. 11.18). However, for some cases which the time is very limited for manufacturing the product or if the product is a prototype that will be improved or the products will be manufactured in small numbers; the mold itself might be also manufactured without manufacturing the model (Fig. 11.19).

The next step for manufacturing polymer composites is to tool the real model of the CAD model. This is needed for manufacturing the mould. However, having the exothermic reaction precautions of the curing process of polymer composite

moulding, it is reasonable to tool the mould itself without manufacturing the real model if the product is a solar car body.

Manufacturing the chassis of the solar car, is another challenging process which includes mechanical stress analysis and structural optimization. After optimization, one of the most efficient way of forming the chassis is to manufacture flat polymer composite sandwich parts and cut them using water jet and then form the chassis from cut modular parts. In Fig. 11.20, this process and fixing the chassis with the shell of the vehicle can be seen. Fixing the chassis with body needs reference points in order to have the exact solid model designed. This makes a even 150 kg total weight achievable as a solar car (pilot weight excluded).

Figure 11.21 shows the latest solar car of Solaris Projects (Solaris 8 Project/2013–2015). This solar car is designed and manufactured for WSC 2015, so most of the technical specifications are the results of regulations of this event. It is a four wheel vehicle with one motor on the left rear side. The total weight of the

Fig. 11.20 Combining chassis and body of the DesTech Solaris Solar Car (2015)

Fig. 11.21 DesTech Solaris Solar Car (2015)

vehicle is 182 kg for the first version, but increased to 199 kg because of the extra weights to improve the stabilization of rear suspensions, electrical isolation and upper body orientation apparatus. Carbon polymer composite monocoque body has different textiles in different locations of the car. The car has also a telemetry system to analyze the energy used, generated and also to sense the operating conditions. Telemetry system send the data of voltage and temperature of each thirty series battery group, battery current, MPPTs (so, the current and voltage of PV groups), motor and vehicle speed and motor driver current. Voltage and temperature of each

Table 11.4 Technical specifications of DesTech Solaris

Name	DesTech Solaris (S8)
Production year	2015
Dimensions	4.5 (m) × 1.80 (m) × 1.05 (m)
Weight	182 (kg) (without driver)
Body and chassis	Carbon fiber sandwich—monocoque body and chassis
Wheels	2 front, 2 rear
Power of PV array	1341 (W_p)
Number of PV cells	392
Efficiency of PV cells	22.8%
Nominal voltage of the system	111 (V)
Max. voltage of the system	126 (V)
Battery capacity	4.7 (kWh) 30 series and 8 parallel groups—5.3 (Ah) battery cells
Battery type	Lithium polymer
Motor	3 (kW) BLDC hub motor, max eff. 95%
MPPTs	Boost type, 98% max eff., connected as 5S3P

eight parallel—thirty series LiPo battery cell and the current from battery pack are sensed and also the cells are protected by battery management system (please see Table 11.4).

11.2 Modular Off-Grid Solar Energy Charging Stations for EVs

Project EYLEM is a project supported by Izmir Development Agency (IZKA) and Dokuz Eylul University which is aimed to be a model for e-mobility in campus areas [22, 31]. Not only three EVs are designed and manufactured by Solaris Team,

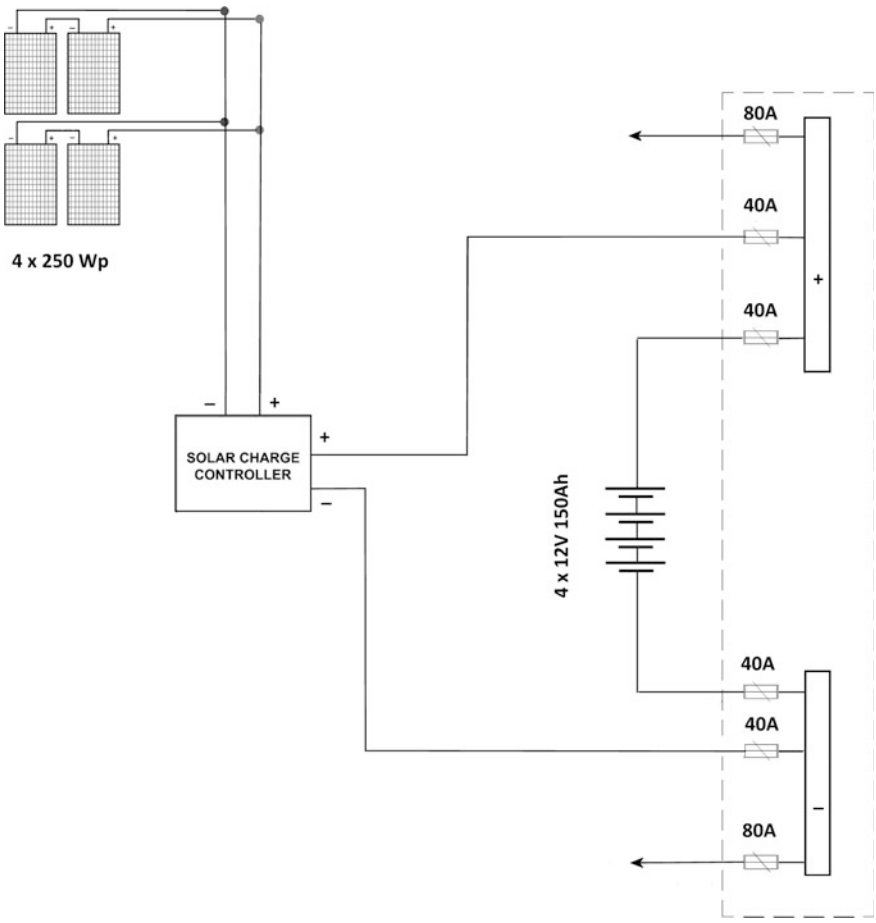

Fig. 11.22 A 1 kWp off grid charging station connection

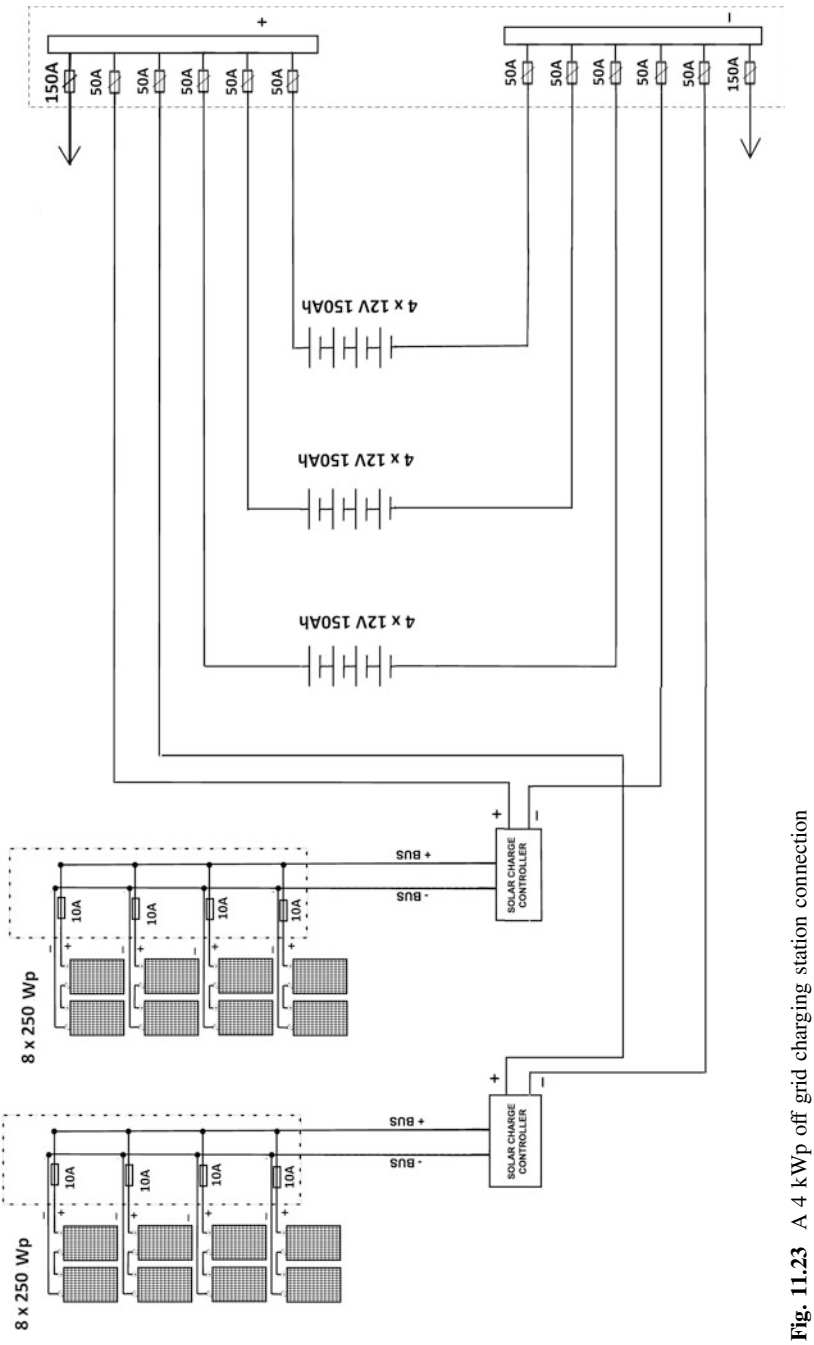

Fig. 11.23 A 4 kWp off grid charging station connection

Fig. 11.24 A Charging stations (DECharge 1, 2 and 3) in campus area and charging EVs (DEMobils) at the station

but also three solar powered charging stations are established in campus area (see Fig. 11.15). Project is proposed with the analysis of daily usage of ICE vehicles by campus security which is resulted as approximately 50 km. This limited the capacity of the batteries on EVs, since the batteries are gel lead acid type of batteries for the EVs in this project. A main solar charging station of 54 m^2 that has a PV group of 5 kW_p (4 kW_p + 1 kW_p) and a battery group of 28.8 kWh (21.6 kWh + 7.2 kWh) is located at the center of the campus area. The main station is also aimed to be used as a workstation for EVs. The second and third solar charging stations are located on 21 m^2 and have 1 kW_p PVs and 7.2 kWh battery groups (see Figs. 11.22 and 11.23). All stations are off-grid designed. So, the reasons of having battery packs at charging stations are to schedule the charging at night, to use batteries for illumination and hand-held electric motor operated tool purposes.

An enhanced version of these EVs is also designed for EV car races in Turkey which is more light and efficient than other three (see Fig. 11.24).

The electrical connection diagram of the main solar charging station (DECharge 1) and two other stations might be seen in Fig. 11.25a, b. System output is 48 VDC for all. An additional DC/DC converter of 48/72 is used when the nominal voltage of the EV which is connected for charging is 72 V.

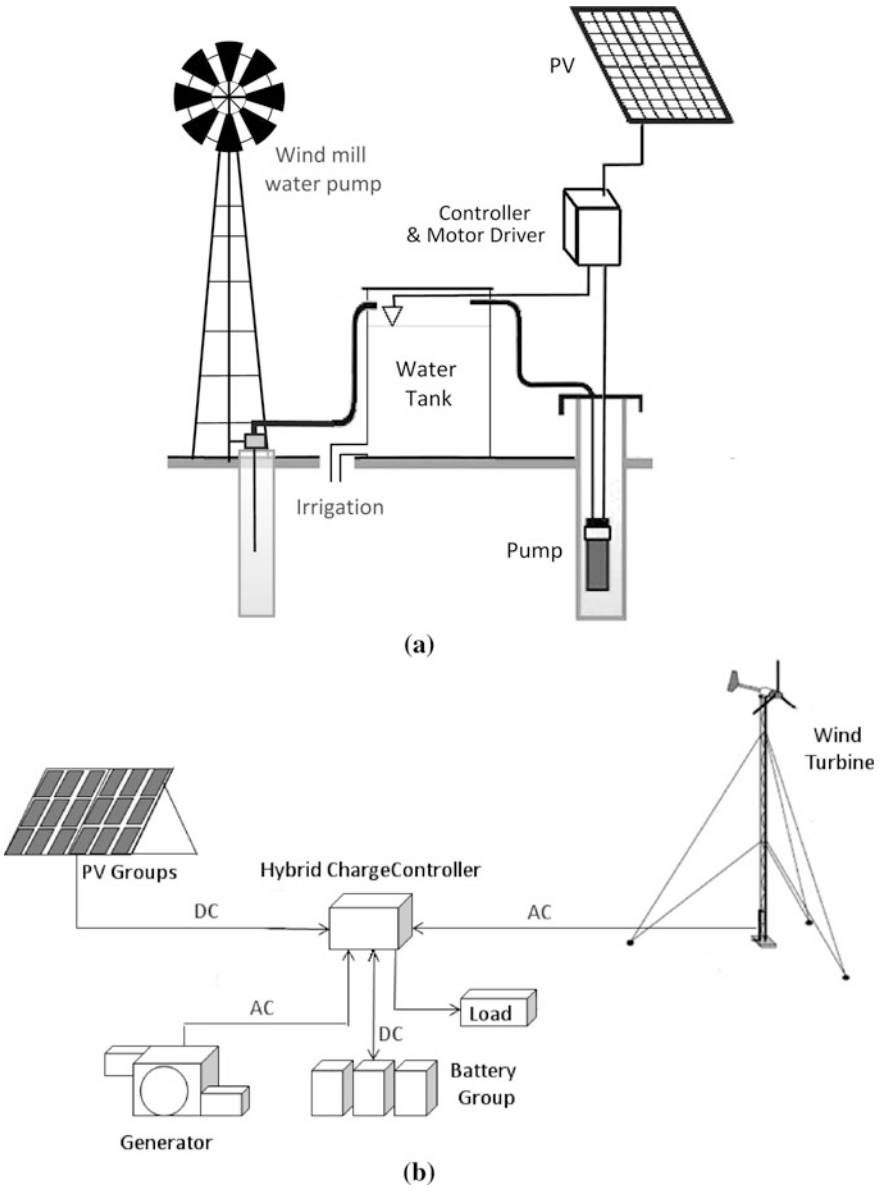

Fig. 11.25 **a** Hybrid PV and wind mill system without batteries for irrigation. **b** Hybrid electric generation system

11.3 Hybrid Combination of Power Generation Systems

A system is called *off-grid,* if it is not connected the interconnected electrical grid whereas *on-grid* if it is connected. Storing energy is a more challenging engineering problem than generating mainly. If the energy generation system has its own simple natural solutions inside, it is more efficient and cost effective. A simple example of this is a solar energy generation system for irrigation. It is more efficient and cost effective to replace batteries with a water tank which is also a capacity for the system model (please see Fig. 11.25a). In this system, electricity generated by PVs runs the pump motor and water tank is a capacity that is charging for a potential energy level and discharging it through the system which is similar with the battery pack replaced. It is sure that if the system is on-grid, the grid itself behaves like an infinite capacity that can be used with the unit currency/kWh.

Figure 11.25b shows another way of forming a hybrid system which is more common than Fig. 11.25a. A hybrid system which generates electricity from solar, wind and kinematic energy from water flow might be seen in Fig. 11.7b. Hybrid charge controller is the point where different sources are combined. Mobile phone base stations in outback are good implementations of hybrid systems since hybrid systems fills the lack of each other.

It is well known that the source of a system should be well analyzed and designed due to the energy generation efficiencies, cost and dimensions. An important point is that the only DC generation is the PV cell part. Mostly, three or mono phase AC forms are the outputs of a turbine even it is a wind or another type of energy conversion implementation. If it is in mono phase form which is the voltage is generally represented with the Eq. 11.20 whereas if it is in three phase form that the voltages are represented with the Eqs. (11.21)–(11.23) (remember that $\omega = 2\pi f$). In that case, the balanced system calculations are used which is based on the assumption that all three phases are following each other with 120° angles and all loads are compensated.

$$v_m = V_{\max} \sin(2\pi ft) \tag{11.20}$$

$$v_A = \sqrt{2}V \sin\omega t \tag{11.21}$$

$$v_B = \sqrt{2}V \sin(\omega t - 120^\circ) \tag{11.22}$$

$$v_C = \sqrt{2}V \sin(\omega t - 240^\circ) \tag{11.23}$$

Figure 11.17b shows a generalized schematic of a hybrid system which is composed of a PV group, a wind turbine, a generator (it can be either a water turbine generator, diesel generator, etc.), a battery system (generally for backup in case of no electricity generation), system load(s) and a hybrid charge controller that optimizes the source usages due to power generation of each source. Eliminating the peaks of switching on or off, calculation of power of a direct current system is

just multiplying voltage and current in steady state, the power of mono-phase and three-phase systems can be calculated using the Eqs. 11.24–11.26. V_{LL} is the line-to-line voltage, I_L is the line current, θ is the angle between the phase voltage and the phase current—the impedance angle. P_{tp} is the real, Q_{tp} is the reactive and S_{tp} is the apparent powers for an uncompensated three-phase system.

$$P_{tp} = \sqrt{3} V_{LL} I_L \cos\theta \tag{11.24}$$

$$Q_{tp} = \sqrt{3} V_{LL} I_L \sin\theta \tag{11.25}$$

$$S_{tp} = \sqrt{3} V_{LL} I_L \tag{11.26}$$

Stand alone photo voltaic (SAPV) systems are more implemented systems than hybrid ones because of their simplicity in design and implementation. Besides, installation and maintenance are simpler for SAPV systems. Hybrid systems might be efficient and cost effective if there is a great potential of flow in means of wind or water. Diesel engine generator or as a very rare implementation, the PEM fuel cell can be added to the system, if the system is a continuous generation system like a research laboratory which is far away from grid.

11.4 Conclusion

In this chapter, it is aimed to convey the experiences gained through several solar projects which are stationary or mobile to researchers who are studying on solar cars, system modeling and searching for more efficient algorithms or designing solar systems. Most of the loads and units of an EV or a SC are modeled and tried to be explained how to design with implementations. Solar system can be on a mountain that for a research center or on wheels to be challenged. The purpose and the output of the system aimed to be analyzed well in order to construct a system that is both cost effective and efficient. Last but not least, simplicity should be the main target, like as in every design, for being sustainable and stable.

Acknowledgements The author would like to thank Osman Korkut, Eren Gül for their technical support and valuable discussions; Yusuf Can Arslan, Umut Bozok, Hasan Çekem for their help in analyzing the energy need of a solar car in challenge and each member of Team Solaris project generations for their great effort of working days and nights to manufacture five solar cars and four electric vehicles. The support of sponsors into Solaris Projects during 2004–2016 years are gratefully acknowledged.

References

1. Walker G (2001) Evaluating MPPT converter topologies using a MATLAB PV model. Aust J Electr Electron Eng 21(1):49–55
2. Gow JA, Manning CD (1999) Development of a photovoltaic array model for use in power-electronics simulation studies. IEEE Proc Electric Power Appl 146(2):193–200
3. Krismadinata, Nasrudin AR, Hew WP, Jeyraj S (2013) Photovoltaic module modeling using Simulink/Matlab. Procedia Environ Sci 17:537–546
4. Goren A (2011) Gunes arabaları icin yuksek verimli fircasiz dogru akim motoru tasarimi ve uretimi. Endustri ve Otomasyon 173:34–39
5. Tsai CC, Lin SC, Huang HC, Cheng YM (2009) Design and control of a brushless DC limited-angle torque motor with its application to fuel control of small-scale gas turbine engines. Mechatronics 19:29–41
6. Kapun A, Curkovic M, Hace A, Jezernik K (2008) Identifying dynamic model parameters of a BLDC motor. Simul Model Pract Theor 16:1254–1265
7. Ku CL, Tan YK, Panda SK (2006) High-precision position control of linear permanent magnet BLDC servo motor for pick and place application. In: ICIT 2006, pp 2919–2924
8. Kennedy B, Patterson D, Camilleri S (2000) Use of Lithium-ion batteries in electric vehicles. J Power Sour 90:156–162
9. Armenta-Deu C (2003) Prediction of battery behaviour in SAPV applications. Renew Energy 28:1671–1684
10. Manzetti S, Mariasiu F (2015) Electric vehicle battery technologies: from present state to future systems. Renew Sustain Energy Rev 51:1004–1012
11. Devillers N, Péra M-C, Jemei S, Gustin F, Bienaimé D (2015) Complementary characterization methods for Lithium-ion Polymer secondary battery modeling. Int J Electr Power Energy Syst 67:168–178
12. Achaibou N, Haddadi M, Malek A (2012) Modeling of lead acid batteries in PV systems. Energy Procedia 18:538–544
13. NREL (2015) http://www.nrel.gov/ncpv/images/efficiency_chart.jpg. Accessed 27 Aug 2015
14. Mattei M, Notton G, Cristofari C, Muselli M, Poggi P (2006) Calculation of the polycrystalline PV module temperature using a simple method of energy balance. Ren Energy 31(4):553–567
15. Baser O, Goren A (2007) Gunes enerjisi ile calisan araclarda govde tasarimi ve guc ihtiyaci. MakinaTek 11:124–129
16. Goren A, Baser O, Polat C (2007) Gunes enerjisi ile calisan arac icin monokok govde tasarimi ve imalati. Muhendis ve Makina 48–569:62–68
17. Ozawa H, Nishikawa S, Higashida D (1998) Development of aerodynamics for a solar race car. JSAE Rev 19:343–349
18. Shimizu Y, Komatsu Y, Torii M, Takamuro M (1998) Solar car cruising strategy and its supporting system. JSAE Rev 19:143–149
19. Patterson DJ (1995) An efficiency optimized controller for a brushless DC machine, and loss measurement using a simple calorimetric technique. In: Power electronics specialists conference, vol 1, pp 22–27
20. Vancouver Electric Vehicle Association (2011) A brief history of electric vehicles
21. Harding GG (1999) Electric vehicles in the next millennium. J Power Sourc 78–1(2):193–198
22. Kley F, Lerch C, Dallinger D (2011) New business models for electric cars-a holistic approach. Energy Policy 39:3392–3403
23. Domingo BG (2015) A differential evolution proposal for estimating the maximum power delivered by CPV modules under real outdoor conditions. Expert Syst Appl 42(13):5452–5462
24. Mohanty P, Bhuvaneswari G, Balasubramanian R, Dhaliwal NK (2014) Matlab based modeling to study the performance of different MPPT techniques used for solar PV system under various operating conditions. Renew Sustain Energy Rev 38:581–593

25. Rezk H, Eltamaly AM (2015) A comprehensive comparison of different MPPT techniques for photovoltaic systems. Sol Energy 112:1–11
26. Esram T, Chapman PL (2007) Comparison of photovoltaic array maximum power point tracking techniques. IEEE Trans Energy Convers 22(2):439–449
27. Carroll DR (2003) The winning solar car: a design guide for solar race car teams, 1. Solar cars -design and construction. SAE International, Warrendale, pp 71–118
28. Goren A, Atas C (2008) Manufacturing of polymer matrix composites using vacuum assisted resin infusion molding. Arch Mater Sci Eng 34(2):117–120
29. Arkesteijin GCM, Jong ECW, Polinder H (2007) Loss modeling and analysis of the nuna solar car drive system. In: International conference on ecologic vehicles and renewable energies
30. Arslan YC, Goren A (2015) Using mold materials in polymer composite car body manufacturing. PuTech Compos 6(23):10–20
31. Torreglosa JP, García-Triviño P, Fernández-Ramirez LM, Jurado F (2016) Decentralized energy management strategy based on predictive controllers for a medium voltage direct current photovoltaic electric vehicle charging station. Energy Convers Manag 108:1–13

Part III
Energy Efficiency of the Hybrid Power System

Chapter 12
Energy Harvesting from the Fuel Cell Hybrid Power Source Based on Extremum Seeking Control Schemes

Nicu Bizon

Abstract Energy harvesting is known as the conversion process of ambient energy into usable electrical energy, including the available and free energy of the renewable and green energy sources. This chapter analyzes the possibility to use the Extremum Seeking Control schemes for harvesting the hydrogen energy via a Fuel Cell Hybrid Power Source. The new Extremum Seeking Control schemes proposed here are based on a band-pass filter with the frequencies' band larger than that of the series combination of high-pass and low-pass filters used in the classical Extremum Seeking Control scheme. The mathematical modeling of the Extremum Seeking Control scheme that is applied to nonlinear dynamic plant shows the close relations between the search speed, the derivatives of the unknown input-to-output map, and the cut-off frequencies of the band-pass filter. The simulation results are compared with the results of classical Extremum Seeking Control schemes. The ratio of these search speeds is used as the performance indicator, besides the tracking accuracy evaluated for each control scheme. A Maximum Power Point tracking technique is proposed for the Fuel Cell stack based on a modified Extremum Seeking Control that slightly improves the performance. A higher value of the searching speed is obtained for the same tracking accuracy. The search speed will increase proportionally with the product of both control parameters (the closed loop gain and the dither gain), so it is practically limited for safe reasons. An advanced Extremum Seeking Control scheme is proposed here to further reduce the power ripple and obtain the imposed performance related to the search speed and tracking accuracy. Finally, the dynamical operation of the Fuel Cell stack under constant and variable load is shown.

N. Bizon (✉)
Department of Electronics, Computers and Electrical Engineering,
University of Pitesti, Pitesti, Romania
e-mail: nicu.bizon@upit.ro

N. Bizon
University Politehnica of Bucharest, Bucharest, Romania
e-mail: nicubizon@yahoo.com

N. Bizon et al. (eds.), *Energy Harvesting and Energy Efficiency*,
Lecture Notes in Energy 37, DOI 10.1007/978-3-319-49875-1_12

Keywords Fuel cell hybrid power source (FCHPS) · Extremum seeking control (ESC) · Maximum power point (MPP) · Search speed · Tracking accuracy · FC system · Energy harvesting

Abbreviation and Acronyms

aESC	advanced Extremum Seeking Control
ANN	Artificial Neural Network
BPF	Band Pass Filter
bpfESC	Band Pass Filter ESC
EA	Evolutionary Algorithms
ES	Energy Sources
ESS	Energy Storage System
EQ	Equivalent
ESC	Extremum Seeking Control
FC	Fuel Cell
FCHPS	Fuel Cell Hybrid Power Source
FLC	Fuzzy Logic Controller
GMPP	Global Maximum Power Point
GMPPT	GMPP Tracking
HF	High Frequency
hoESC	high-order Extremum Seeking Control
HPF	High-Pass Filter
HC	Hill Climbing
HPS	Hybrid Power Source
H_1	First Harmonic
IC	Incremental Conductance
LF	Low Frequency
LPF	Low-Pass Filter
MEP	Maximum Efficiency Point
MPP	Maximum Power Point
MPPT	MPP Tracking
mESC	modified Extremum Seeking Control
P&O	Perturb & Observe
PEM	Proton Exchange Membrane
PV	Photovoltaic
RCC	Ripple Correlation Control
RES	Renewable Energy Sources
WT	Wind Turbines

12.1 Introduction

In general, the conversion process of ambient energy into usable electrical energy using Renewable Energy Sources (RESs), such as Photovoltaic (PV) panels, and Wind Turbines (WT), or on hydrogen energy via a Fuel Cell (FC) stack can be modeled by a nonlinear dynamic plant having an unknown input-to-output map, $y = f(x)$ with one or more maximums. Usually, one Maximum Power Point (MPP) appears in the stationary regime and more local extremes appear on the power profile during transitory regimes. The control variable used for searching the MPP or global MPP (GMPP) is the current or the voltage, or the power generated by the RESs [1, 2] (see Fig. 12.1). Note, that the GMPP must be accurately tracked in dynamic regime, too [3, 4].

The Fuel Cell Hybrid Power Source (FCHPS) architecture which will be analyzed in this chapter (see Sect. 12.6) is based on the generic Hybrid Power Source (HPS) architecture shown in Fig. 12.1. Note that the FC stack will be connected to the ESS bus by a unidirectional DC-DC converter that is controlled using a Maximum Power Point (MPP) tracking or a Maximum Efficiency Point (MEP) algorithm. The MPP tracking (MPPT) controller will control the FC power flow acquiring the samples of FC current and FC voltage (which are noted with iFC and vFC in Fig. 12.1). The MPP of the FC stack under different fuelling modes will be tracked using the Extremum Seeking Control (ESC) based on adaptive dithering action of the reference current (iref) (see Fig. 12.2). The reference current is compared to the FC current to generate the switching pulses based on an appropriate current-mode control strategy.

The MPP tracking (MPPT) algorithms and GMPP tracking (GMPPT) algorithms were extensively analyzed in last decade, starting with the required applications developed for an array of PV panels [5]. In general, some 1-D models were used to

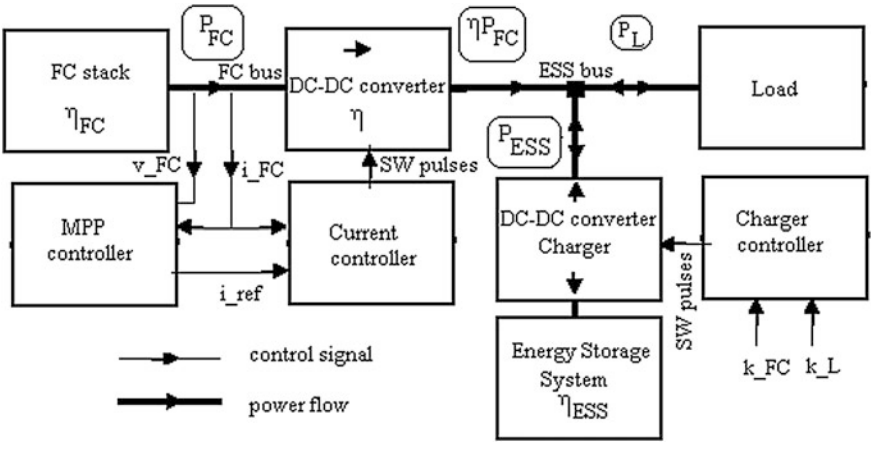

Fig. 12.1 Architecture of the fuel cell hybrid power source

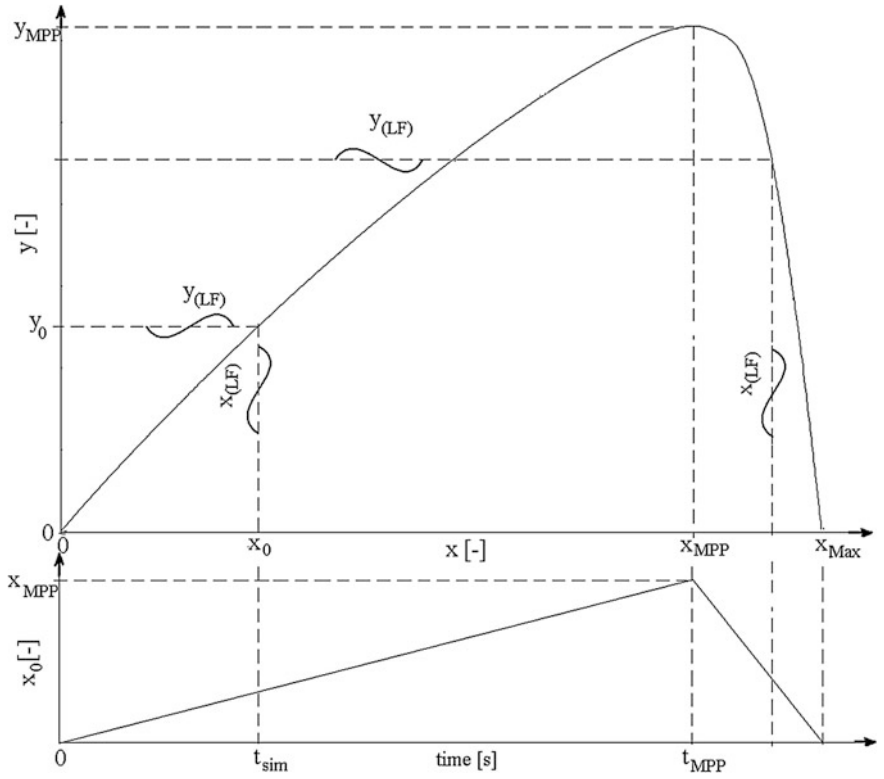

Fig. 12.2 Searching of the MPP based on dither signal ESC scheme [25]

model the nonlinear behavior of the PV system related to solar irradiance level. The PV power profile has multiple extremes due to the partially shading conditions. The temperature is also a very important parameter that affects the PV power, so a 2-D model may be used for the PV system using the irradiance and temperature as input variables. Also, the 2-D model for Proton Exchange Membrane (PEM) FC system (which is also known as Polymer Electrolyte Membrane FC system) will use the oxygen and hydrogen fueling flow rates. The GMPPT algorithm must track the GMPP between the multiple local extremes based on an ESC 2D-scheme, but this case will not be approached here.

A huge number of MPPT and GMPP algorithms have been developed in the last decades [6, 7], which are classified as offline, online and hybrid algorithms [6] or as conventional, computational, and soft computing techniques [7]. It is obvious that these MPPT and GMPP algorithms may be easily applied to harvest energy from all types of energy sources such as WT [8] and Fuel Cell (FC) stacks [9]. In this chapter the analysis of the MPPT and GMPP algorithms applied to FCHPS is shown.

The most know MPPT algorithms are the Perturb and Observe (P&O) [10], the Incremental Conductance (IC) [11] and the Hill Climbing (HC) [12] based on fixed or variable small searching steps to accurately track the MPP, but with limited searching speed because these performance indicators require opposite design values for the searching steps. Thus, if the step-size is increased to obtain a higher searching speed, then the tracking accuracy will be lower and vice versa.

Therefore, the advanced ESC schemes for the MPPT algorithms are usually proposed here to solve this problem and make less dependent the tracking accuracy to model used [5].

The group of soft computing techniques includes Artificial Intelligence (AI) algorithms such as the Fuzzy Logic Controller (FLC) [13], Artificial Neural Network (ANN) [14] and Evolutionary Algorithms (EA) [15]. As it was mentioned before, these AI-based MPP tracking algorithms are used to optimize the GMPP localization [15] in the first stage of searching, level of tracking oscillations [16] in second stage of searching or during the tracking phase, and control robustness [17].

Real-time optimization techniques such as the Ripple Correlation Control (RCC) [18] and ESC [19] schemes may increase the performance of searching of the GMPP. These GMPPT algorithms are based on perturbed signal injected in the control loop, which is usually named dither, or on ripple that normally exists on the HPS over the power generated by the energy source, being concentrated in harmonics at multiples of the grid (the low frequencies (LF) ripple) and switching frequency (the high frequency (HF) ripple).

Because it is impossible to simultaneously obtain a high searching speed and a good tracking accuracy using classical ESC schemes (such the high order ESC scheme (hoESC) [20]), advanced ESC schemes were reported in literature [21, 22]. Two classes of ESC approaches are reported in the literature: perturbation-based [23] and model-based methods [24].

The performance of the 1-D ESC schemes will be analyzed here based on the Band Pass Filter ESC (bpfESC) scheme proposed in [25–27] to increase both searching speed and tracking accuracy indicators.

Hydrogen is recognized as a viable energy source because it is widely spread in the Universe, being the most abundant elements in the Universe. The hydrogen energy is converted to electrical energy via the PEMFC systems that supply the FCHPS. This FCHPS is potentially a green energy resource that has no territorial restrictions, a competitive price, and a life cycle which continues to increase each year. Because it still requires expensive investments for hydrogen production, it is important to extract as much energy as possible from the PEMFC stack in order to reduce the hydrogen consumption [28]. Consequently, the PEMFC systems must operate close to MPP or MEP. The FC efficiency is with about 5% lower than the highest efficiency obtained at the MEP [28]. The MPPT algorithms for FC stack are retrieved from the PV system experience, but, in comparison with the PV systems, the operating point of a FC stack depends by more parameters of each subsystems of the FC system [29, 30]. Hybridization of the FC system with a Storage Devices, such as batteries and ultracapacitors which can be mixed in an Energy Storage System (ESS), and/or use of some RESs may be an effective technology to

overcome the disadvantages of the FC-alone-powered source [31–33]. The energy harvesting techniques need a MPPT control of adaptive type to harvest all the energy available from the microbial FC stacks used to treat the wastewater [34].

The FC power characteristic can be modeled using analytical equations [29] or numerical approximations [35] based on the loading and fueling conditions, stoichiometric air-fuel ratio, temperature and other parameters, such as transfer coefficients, internal humidity level, and catalyst layer thickness. Note that the last parameters are not simple simply available if these are not specified in the data sheet. The temperature is considered constant for the simulations performed here because its variation is slower than that on loading and fueling conditions.

As it was mentioned before, the P&O algorithms are the most used MPPT algorithms used for FC system, too [10, 36]. The design of the MPPT algorithms must carefully consider the tradeoffs between performance indicators (the searching speed and tracking accuracy) and safety operation. The FC power ripple must be as small as possible to increase the harvested power and to reduce the mechanical and electrical stress of the PEMFC membrane [37]. The control robustness to load dynamic could be assured by the load following control combined with the MPPT algorithms based on the ESC schemes [38, 39]. Although the ESC-based MPPT control is a well-established algorithm [20, 40, 41], certain instability may appear when the control parameters vary more quickly than action elements (for example, the air compressor) in order to increase the overall FC system efficiency [42, 43]. So, an MPPT-based energy management to load dynamic is required for the fueling flow rates [44–47]. The MPPT control would be beneficial to operate the FC stack because the MEP is difficult to be tracked [48] and in some cases the power density is more required than the fuel efficiency [49, 50].

In this chapter, three real-time optimization algorithms based on ESC schemes are compared as performance under different operating conditions of the PEMFC system. The ESC has been successfully applied in different engineering applications [51], which include the FCHPSs [52, 53]. The tracking accuracy reported for the PV inverters is higher than 99.98% [54], but lower accuracy (<99%) is reported for the FC inverter [55, 56]. Note that the tracking accuracy is defined as, where PMPP is the FC power at the MPP and PFC is the average power effectively generated by the FC system operating under MPPT control.

The chapter is organized as follows. Section 12.2 presents the classical High-Order ESC (hoESC) and bpfESC schemes used in simulation. If the transfer function of the Band Pass Filter (BPF) from the bpfESC scheme is equivalent to the series combination of the High-Pass Filter (HPF) and Low-Pass Filter (LPF) filters from the hoESC scheme, then the hoESC and bpfESC schemes are functionally equivalent, too. This aspect is briefly shown in this section. Section 12.3 deals with signal processing in the loop of the bpfESC scheme. An analytical analysis in the frequency and time domain of the bpfESC scheme is presented in order to compare the searching speed for both ESC schemes. The simulation results based on generic input-output maps validate the analytical results obtained. Section 12.4 briefly presents briefly the issue of modeling and control of the PEMFC system. Section 12.5 reviews the classical ESC, mESC and aESC schemes applied for the

PEMFC system, highlighting the main topological differences. The performance obtained is shown in Sect. 12.6 using the mESC and aESC schemes for PEMFC system under constant fueling rate and dynamic load profile. Last Section concludes the paper.

12.2 The Equivalence of the hoESC and bpfESC Schemes

The ESC schemes scans the plant's input, x, based on the plant's output, y, so that $y = f(x)$ is maximized (see Fig. 12.2). The searching of the MPP ($y \rightarrow y_{MPP}$) is assured if the staring value, x_0, will be set in the region of the MPP attraction. The noise level (n) does not affect the searching process in the closing loop [25, 26].

The performance's analysis of the hoESC (Fig. 12.3) and bpfESC (Fig. 12.4) schemes is performed in this section. It can be observed that both ESC schemes have the same operating relationships, excepting the signal filtering and demodulation [20, 24–26].

For brevity, only relationships of the bpfESC scheme are shown below, considering $G_{BPF}(s) = G_{HPF}(s) \cdot G_{LPF}(s) = [Y_{BPF}(s)/Y_F(s)] \cdot [Y_F(s)/Y_N(s)] = [s/(s + \omega_h)] \cdot [\omega_l/(s + \omega_l)]$:

$$y = f(x), y_{out} = y + n, y_N = k_N \cdot y_{out} \tag{12.1}$$

$$\begin{aligned} \dot{y_F} &= -\omega_h y_F + \omega_h y_N, y_{BPF} = y_N - y_F, \\ \dot{y_{BPF}} &= -\omega_l y_{BPF} + \omega_l y_F, y_{DM} = y_{BPF} \cdot \sin(\omega_d t) \end{aligned} \tag{12.2}$$

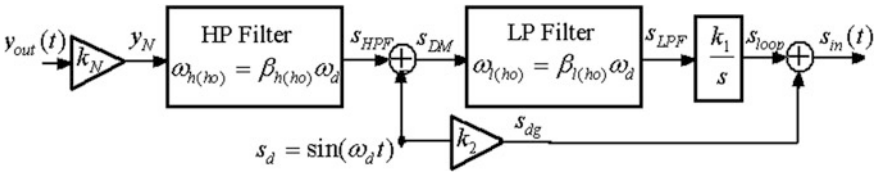

Fig. 12.3 The hoESC scheme [25]

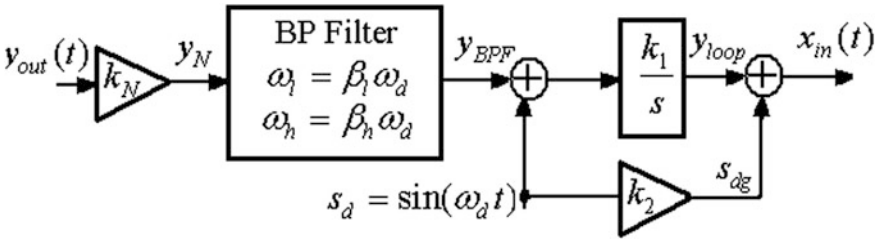

Fig. 12.4 The bpfESC scheme [25]

$$\dot{y_{loop}} = k_1 y_{DM} \tag{12.3}$$

$$x \cong x_{in} + x_0, x_{in} = y_{loop} + s_{dg}, s_{dg} = k_2 \cdot \sin(\omega_d t) \tag{12.4}$$

where Eqs. (12.1), (12.3), and (12.4) represent the input-to-output map, the integrator, the MPP current controller based on x_{in} reference, and Eq. (12.2) represent the signal processing based on BPF and demodulation.

The following notations are used (see Fig. 12.4):

- k_1 is the loop gain;
- k_2 is the gain of the dither amplitude;
- ω_d is the frequency of the dither signal;
- $\omega_l = \beta_l \omega_d$, $0 < \beta_l < 6$, is the cut-off frequency of the LPF;
- $\omega_h = \beta_h \omega_d$, $0 < \beta_h < 1$, is the cut-off frequency of the HPF;
- y_N is the signal after normalization (to the maximum value of y, y_{MPP});
- y_F is an intermediate variable related to HPF operating;
- y_{BPF} is the output signal from the BPF;
- y_{DM} is the signal after demodulation;
- y_{loop} is the output signal from the ESC loop;
- x_{in} is the estimation signal of the unknown parameter;

Relationships of the hoESC scheme related to signal processing based on LPF and HPF and demodulation are:

$$\begin{aligned} \dot{s_F} &= -\omega_h s_F + \omega_h s_N, s_{HPF} = s_N - s_F, \\ \dot{s_{LPF}} &= -\omega_l s_{LPF} + \omega_l s_{HPF} \sin(\omega t) \end{aligned} \tag{12.2'}$$

where s_N, s_{HPF}, and s_{LPF} are the signals after normalization, HPF, and LPF.

If $G_{BPF}(s) = G_{HPF(ho)}(s) \cdot G_{LPF(ho)}(s)$, then:

$$\begin{aligned} |G_{BPF}(\omega)| &= \left|G_{HPF(ho)}(\omega)\right| \left|G_{LPF(ho)}(\omega)\right|, \\ \phi_{BPF(ho)}(\omega) &= \arg(G_{BPF(ho)}) = \phi_{HPF(ho)}(\omega) + \phi_{LPF(ho)}(\omega) \end{aligned} \tag{12.5}$$

where:

$$\begin{aligned} \left|G_{HPF(ho)}(\omega)\right| &= 1/\sqrt{1 + \left(\omega_{h(ho)}/\omega\right)^2}, \\ \phi_{HPF(ho)}(\omega) &= \arg(G_{HPF(ho)}) = \arctan\left((\beta_{h(ho)}\omega_d)/\omega\right) \end{aligned} \tag{12.6}$$

$$\begin{aligned} \left|G_{LPF(ho)}(\omega)\right| &= 1/\sqrt{\left(\omega/\omega_{l(ho)}\right)^2 + 1}\,, \\ \phi_{LPF(ho)}(\omega) &= \arg(G_{LPF(ho)}) = -\arctan\left(\omega/(\beta_{l(ho)}\omega_d)\right) \end{aligned} \tag{12.7}$$

In this case, it was shown in [25] that the ratio of the searching speeds ($K_{SS(bpf)}$ and $K_{SS(ho)}$, respectively) is:

$$R_{SS} = \left|K_{SS(bpf)}/K_{SS(ho)}\right| = \left|\cos(\phi_{HPF(ho)} + \phi_{LPF(ho)})\right| / \cos(\phi_{HPF(ho)}) \tag{12.8}$$

If

$$0 < \beta_{h(ho)} < 1 < 3 < \beta_{l(ho)} \tag{12.9}$$

then

$$1 < R_{SS} \leq 1/\cos(\phi_{HPF(ho)}) \leq 1.0541 \tag{12.10}$$

the equality being obtained when:

$$\phi_{HPF(ho)} = \left|\phi_{LPF(ho)}\right| \Leftrightarrow \beta_{l(ho)} \cdot \beta_{h(ho)} = 1 \tag{12.11}$$

Thus, if $G_{BPF}(s) = G_{HPF(ho)}(s) \cdot G_{LPF(ho)}(s)$, then the hoESC (Fig. 12.3) and the bpfESC (Fig. 12.4) schemes will have almost the same search speed. So, from this point of view, the hoESC and the bpfESC schemes are functionally equivalent. It was shown in [25, 26] that almost the same tracking accuracy is obtained.

Relationship (12.11) also defines the condition to have the highest value of the search speed, $K_{SS(bpf)}$. It is important to know how much the search speed is improved for the bpfESC schemes, $K_{SS(bpf)}$, in comparison with hoESC scheme, $K_{SS(ho)}$.

If identical HPFs will be considered in both bpfESC and hoESC schemes, which means identical cut-off frequencies:

$$0 < \beta_{h(ho)} = \beta_{h(bpf)} < 1 \tag{12.12}$$

then the ratio of the searching speeds ($K_{SS(bpf)}$ and $K_{SS(ho)}$, respectively) is:

$$R_{SS} = \left|K_{SS(bpf)}/K_{SS(ho)}\right| \cong \left|G_{LPF(bpf)}\right| / \left|G_{LPF(ho)}\right| \tag{12.13}$$

If

$$0 < \beta_{l(ho)} < 1 < 3 < \beta_{l(bpf)} \tag{12.14}$$

then

$$\left(\beta_{l(bpf)}/\sqrt{\beta_{l(bpf)}^2 + 1}\right) \geq 0.95 \tag{12.15}$$

Thus, the following average approximation can be used [24]:

$$R_{SS} \cong \sqrt{1 + 1/\beta_{I(ho)}^2} \tag{12.16}$$

In the next section a better approximation will be developed based on the signal processing in the bpfESC loop.

12.3 The Signal Processing in the ESC Loop

The probing signal related to the input-output map, y = f(x), can be approximated by the Taylor series:

$$y(x) = \sum_{i=0}^{\infty} \frac{(x - x_0)^i}{i!} \cdot \frac{d^i f}{dx^i}(x_0) \tag{12.17}$$

where (x_0, $y_0 = f(x_0)$) is a point on the static power map, which slowly varies in time as it is shown in Fig. 12.1. If the starting point is considered the origin, (0, 0), then the ramp for $t < t_{MPP}$ is given by relationship:

$$x_0(t) = \frac{x_{MPP}}{t_{MPP}} \cdot t = G \cdot t \tag{12.18}$$

Note that t_{MPP} is the time of simulation and G is the slope of the ramp used to test the nonlinear plant in open loop or it is the gradient that is estimated in closed loop, K_{SS}.

In both cases, the derivatives can be computed during the simulation based on relationship:

$$\frac{df}{dx}(x_0) = \frac{df}{dt} \Big/ \frac{dx}{dt} \cong G^{-1} \cdot f^{(1)}(t) \tag{12.19}$$

In general:

$$\frac{d^i f}{dx^i}(x_0) \cong G^{-i} \frac{d^i f}{dt^i}(t) = G^{-i} f^{(i)}(t) \tag{12.20}$$

The main LF components in the ESC loop are set by the frequencies band of the BPF or equivalent series connection of the HPF and LPF:

$$x_{LF}(t) = \sum_{j=1}^{[\beta_I]} a_j \sin(j\omega_d t) \tag{12.21}$$

where the integer $[\beta_l]$ can be set higher than 3 to increase the ration of searching speeds.

The magnitudes of the LF components, a_j, are lower than the x_0 value, so:

$$x = x_0 + x_{LF} \cong x_0 \tag{12.22}$$

and

$$\frac{dx}{dt} \cong \frac{dx_0}{dt} \tag{12.23}$$

Consequently:

$$y_{BPF}(t) \cong k_N \sum_{i=1}^{\infty} \left\{ \left[\sum_{j=1}^{[\beta_l]} a_j \sin(j\omega_d t) \right]^i \frac{G^{-i} f^{(i)}(t)}{i!} \right\} \tag{12.24}$$

12.3.1 Estimation of the Searching Speed in the bpfESC Loop

The estimation of the searching speed in the bpfESC closed loop will be performed considering the following assumptions:

- only three components of the Taylor series will be considered;
- the BPF is ideal, having $\beta_{h(bpf)} = 0.5$ and $\beta_{l(bpf)} = 3.5$;
- $G = 1$ and $k_N = 1$.

Under these conditions the relationship (12.24) will become:

$$y_{BPF}(t) \cong \sum_{i=1}^{3} \left\{ \left[\sum_{j=1}^{3} a_j \sin(j\omega_d t) \right]^i \frac{f^{(i)}(t)}{i!} \right\} \tag{12.25}$$

If the superposition technique will be considered, then the relation (12.25) will be written as:

$$y_{BPF}(t) \cong \sum_{i=1}^{3} \left\{ \left[\sum_{j=1}^{3} a_j^i \sin^i(j\omega_d t) \right] \frac{f^{(i)}(t)}{i!} \right\} \tag{12.26}$$

The signal after the demodulation

$$y_{DM}(t) = y_{BPF}(t) \cdot \sin(\omega_d t) \tag{12.27}$$

can be written as:

$$y_{DM}(t) \cong K_{sg} + \sum_{j=1}^{3} \left[b_j \sin(j\omega_d t) + c_j \cos(j\omega_d t) \right] \tag{12.28}$$

where:

$$K_{sg} = \frac{f^{(1)}(t) \cdot a_1}{2} + \frac{f^{(3)}(t) \cdot a_1^3}{16} \tag{12.29}$$

and

$$\begin{aligned}
b_1 &= \frac{f^{(2)}(t) \cdot a_1^2}{8}, \\
c_1 &= \frac{f^{(1)}(t) \cdot a_2}{2} + \frac{f^{(3)}(t) \cdot a_2^3}{16}, \\
b_2 &= 0, \\
c_2 &= \frac{f^{(1)}(t) \cdot (a_1 - a_3)}{2} + \frac{f^{(3)}(t) \cdot \left(4 \cdot a_1^3 - 3 \cdot a_3^3\right)}{48}, \\
b_3 &= \frac{f^{(2)}(t) \cdot \left(a_2^2 - a_1^2\right)}{8}, \\
c_3 &= -\frac{f^{(1)}(t) \cdot a_2}{2} - \frac{f^{(3)}(t) \cdot a_2^3}{16}
\end{aligned} \tag{12.30}$$

The K_{sg} parameter will be computed in simulation based on the next relationship:

$$K_{sg} = \frac{a_1}{2} \cdot \frac{df}{dx}(x_0) + \frac{a_1^3}{16} \cdot \frac{d^3 f}{dx^3}(x_0) \tag{12.29'}$$

Relationships (12.30) can be used to estimate the harmonics magnitudes in the bpfESC open loop, but to accurately compute these magnitudes in the closed loop these relationships must be rewritten considering the derivatives as above.

The signal injected in the loop will be:

$$y_{loop}(t) = k_1 \int y_{DM}(t)dt \cong k_1 K_{sg} \cdot t + \sum_{j=1}^{3} \left[\frac{k_1 c_j}{j\omega_d} \sin(j\omega_d t) - \frac{k_1 b_j}{j\omega_d} \cos(j\omega_d t) \right] \tag{12.31}$$

The loop gain, k_1, is set proportional to the dither frequency in order to assure the dither persistence in the ESC loop [25, 26]. So, if

$$k_1 = \gamma_{sd} \cdot \omega_d \tag{12.32}$$

then

$$y_{loop}(t) \cong K_{SS(bpf)} \cdot t + \sum_{j=1}^{3} \left[H_j \sin(j\omega_d t + \varphi_j) \right] \tag{12.33}$$

where $K_{SS(bpf)}$ and H_j are the values estimated in the closed loop for the searching speed and the magnitude of the j-harmonic:

$$\begin{aligned} K_{SS(bpf)} &= K_{sg} \cdot \gamma_{sd} \cdot \omega_d \\ H_j &= \frac{\gamma_{sd}}{j} \cdot \sqrt{b_j^2 + c_j^2} \end{aligned} \tag{12.34}$$

Note that these parameters are time variables based on relationships (12.29) and (12.30).

12.3.2 Estimation of the Searching Speed in the hoESC Loop

The estimation of the searching speed in the hoESC closed loop will be performed considering the same assumptions as in the section above, excepting that $\beta_{h(ho)} = 1.5$.

The LF components in the hoESC loop are filtered by the LPF, thus only the first harmonic will be considered:

$$x_{LF}(t) = a_1 \sin(\omega_d t) \tag{12.35}$$

The signal after the HPF is:

$$s_{HPF}(t) \cong a_1 \frac{df}{dx}(x_0) \cdot \sin(\omega_d t) \tag{12.36}$$

Thus, the signal after demodulation can be written as:

$$\begin{aligned} s_{DM}(t) &= s_{HPF}(t) \cdot \sin(\omega_d t) \cong a_1 f^{(1)} \cdot \sin^2(\omega_d t) \\ &= a_1 f^{(1)}/2 - a_1 f^{(1)} \cdot \cos(2\omega_d t)/2 \end{aligned} \tag{12.37}$$

Consequently, the signal after the LPF will be:

$$s_{LPF}(t) \cong a_1 f^{(1)}/2 \tag{12.38}$$

so:

$$s_{loop}(t) = k_1 \int s_{LPF}(t)dt \cong \left(k_1 a_1 f^{(1)}/2\right) \cdot t = K_{SS(ho)} \cdot t \tag{12.39}$$

where:

$$K_{SS(ho)} = k_1 a_1 f^{(1)}/2 = \gamma_{sd}\omega_d \frac{a_1}{2} \cdot \frac{df}{dx}(x_0) \tag{12.40}$$

12.3.3 Estimation of the Speeds' Ratio During the Searching Phase

The ratio of the searching speeds can be estimated based on relationship (12.35) and (12.40) as below:

$$R_{SS}(t) = \frac{K_{SS(bpf)}}{K_{SS(ho)}} = 1 + \left|\frac{df^3}{dx^3}(x_0)/\frac{df}{dx}(x_0)\right| \cdot \frac{H_1^2(t)}{8} \tag{12.41}$$

where the magnitude of the first harmonic, H_1, for the y_{BPF} signals will be estimated using the Fast Fourier Transform (FFT). The diagram shown in Fig. 12.5 is implemented in Matlab-Simulink® and used for comparative tests for the hoESC and bpfESC schemes operating in closed loop, considering different input-output maps such as:

$$y_p = f_p(x) = 1 - (1 - x)^{2p}, p = 1, 2, 3 \tag{12.42}$$

The computing block (see Fig. 12.5) estimates the ratio of the searching speeds based on (12.41).

12.3.4 Simulation Results

The following parameters are used for the bpfESC schemes in all simulations: $\gamma_{sd} = 0.2$ ($k_1 = 2\pi\gamma_{sd}f_d$), $\beta_{h(bpf)} = 0.18$ and $\beta_{l(bpf)} = 5.5$. Besides these, two values are used for the dither frequency (f_d) and for the gain of the dither magnitude (k_2) to highlight some analytical results using the simulation performed. The used values for the dither are mentioned in each case.

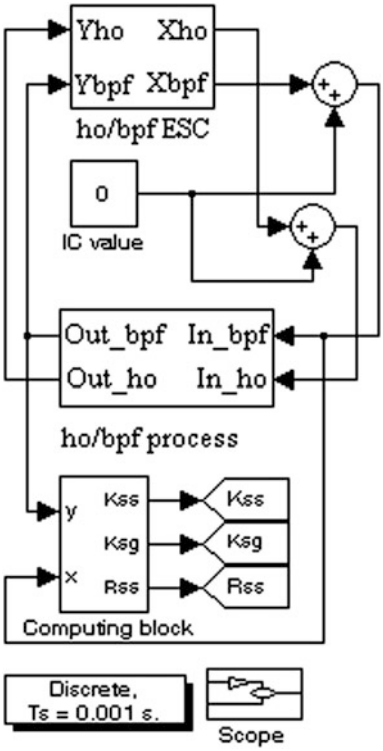

Fig. 12.5 The diagram for performance's comparison of the hoESC and bpfESC schemes [25]

The derivatives for the input-output maps considered, $y_p = f_p(x) = 1 - (1 - x)^{2p}$, p = 1, 2, 3, are:

$$\begin{aligned} y_p^{(1)}(x_0) &= \frac{df}{dx}(x_0) = 2p(1-x_0)^{2p-1}, p = 1,2,3 \\ y_p^{(3)}(x_0) &= \frac{d^3f}{dx^3}(x_0) = 2p(2p-1)(2p-2)(1-x_0)^{2p-3}, p = 2,3 \\ y_1^{(3)}(x_0) &= 0, p = 1 \end{aligned} \tag{12.43}$$

These relationships (12.43), above mentioned, were implemented in the computing block for both ESC schemes.

The simulations presented in Fig. 12.6 related to the searching phase for the hoESC (●) and bpfESC (■) schemes, using f_d = 50 Hz (case a), and f_d = 5 Hz

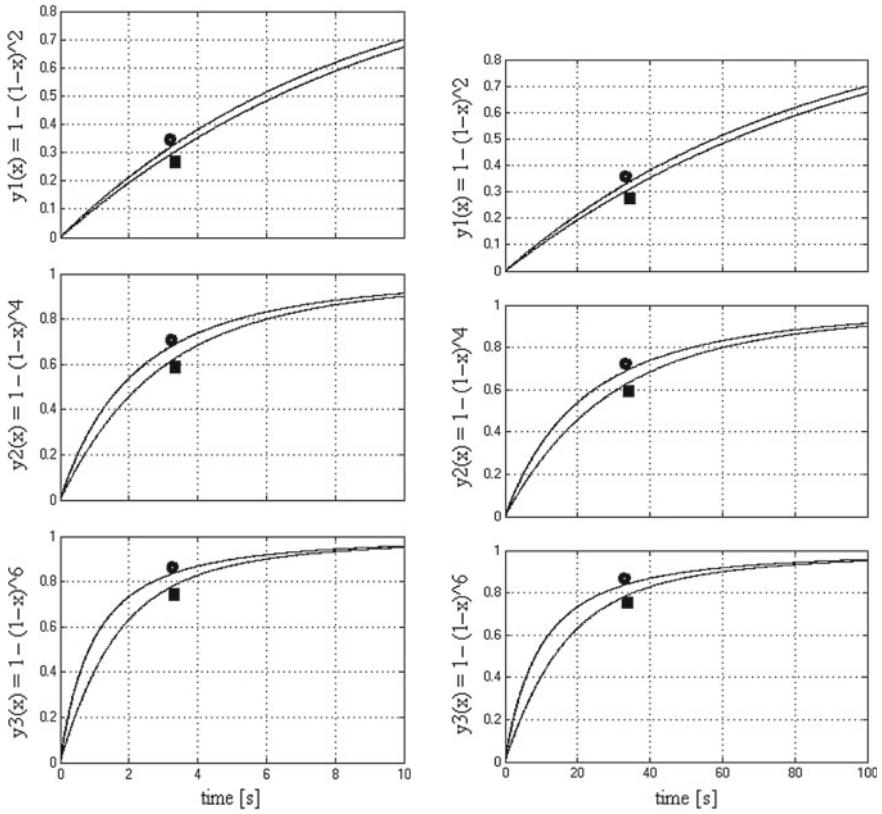

(a) f_d=50 Hz **(b)** f_d=5 Hz

Fig. 12.6 The search phase for the hoESC (●) and bpfESC (■) schemes with γsd = 0.2 ($k_1 = 2\pi fd$), k_2 = 0.001, βl(ho) = 1.5, βh(bpf) = 0.18 and βl(bpf) = 5.5 [25]

(case b), shown that the number of iterations (or dither's periods) is almost the same for each ESC scheme.

Based on the zooms shown in Fig. 12.7 at t = 0.2 s (case a), and t = 2 s (case b), the ratio of the searching speeds can be estimated for each input-output maps, $y_p = f_p(x)$, as being about 1, 1.3, and 1.8 for p = 1, 2, and 3, respectively. The average value computed based on (12.16) is 1.2 and 2.2, for the $\beta_{l(ho)}$ value of 1.5 and 0.5, respectively.

The searching speeds are computed based on (12.34) and (12.29') and the simulation results are shown in Fig. 12.8 for the same cases and parameters

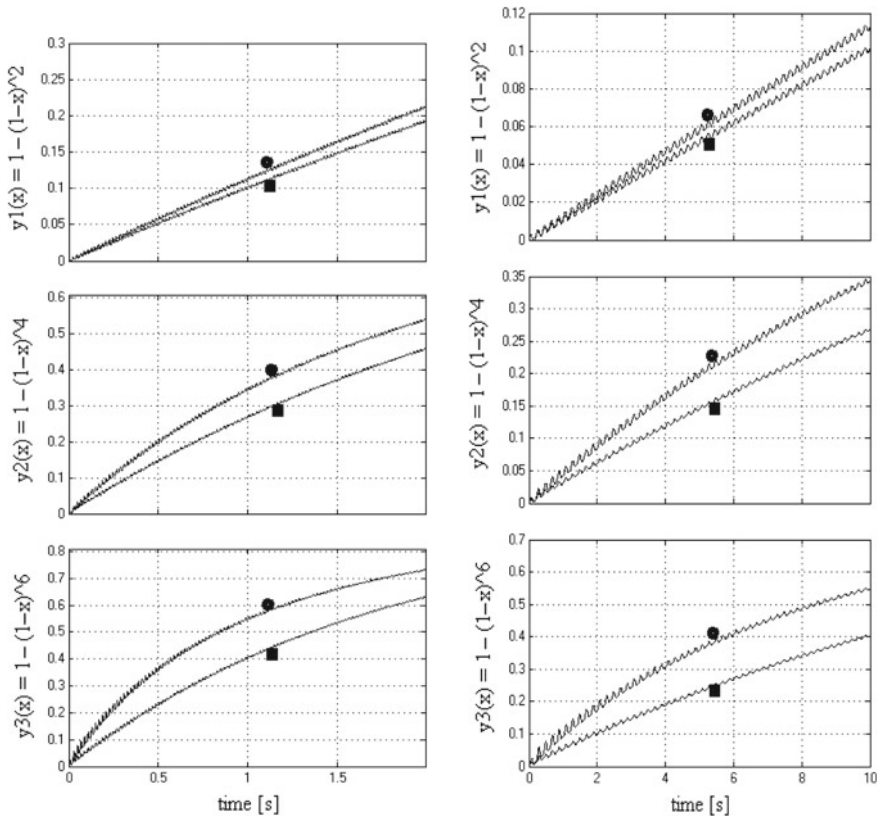

(a) f_d=50 Hz **(b)** f_d=5 Hz

Fig. 12.7 Zooms of the search phase for the hoESC (●) and bpfESC (■) schemes with γsd = 0.2 ($k_1 = 2\pi\gamma sdfd$), k_2 = 0.001, βl(ho) = 1.5, βh(bpf) = 0.18 and βl(bpf) = 5.5 [25]

mentioned above. The simulation results shown in Fig. 12.8 validate the analytical results presented above for the bpfESC scheme:

- The shape of the $K_{SS(bpf)}$ (top), $K_{sg(bpf)}$ (middle) and H_1 (bottom) during the search phase is the same (see Fig. 12.8).
- The average value of the $K_{sg(bpf)}$ (middle) and H_1 (bottom) is almost the same for both frequencies.
- The initial value for the $K_{sg(bpf)}$ parameter is about 0.07 (for p = 3) and 0.018 (for p = 2) in both cases. Also, the initial value for the H_1 magnitude is about 0.024 (for p = 3) and 0.09 (for p = 2) in both cases. On the other hand, considering the above comments and the value of $a_1 = H_1$, the initial value for the $K_{sg(bpf)}$ parameter can be estimated based on (12.29') as:

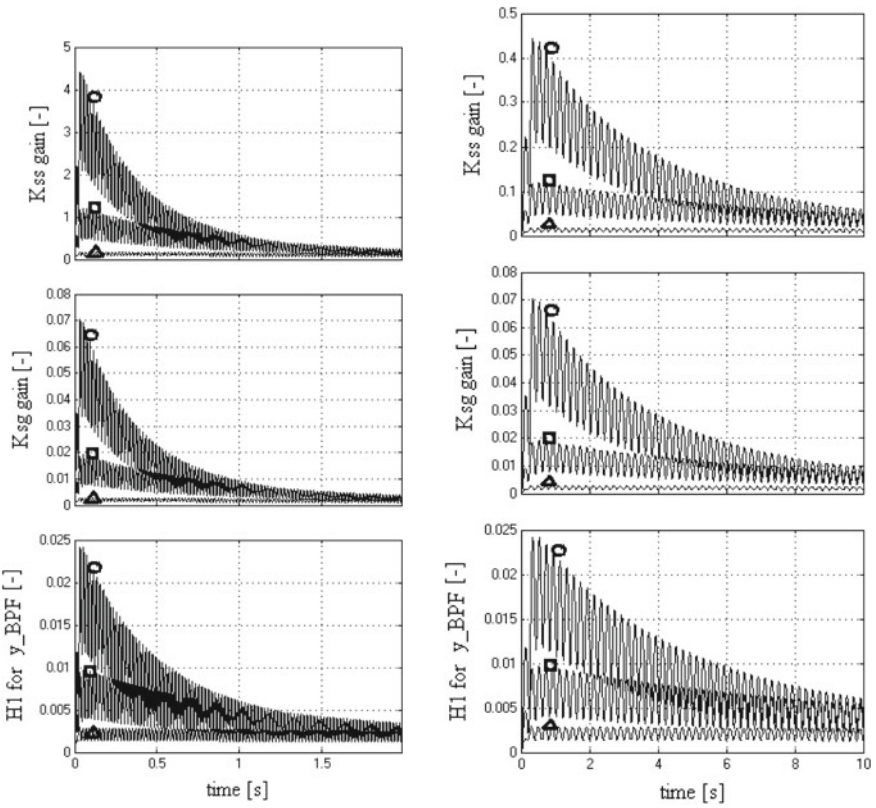

Fig. 12.8 KSS(bpf) (*top*), Ksg(bpf) (*middle*) and H_1 (*bottom*) during the searching phase for the bpfESC scheme with γsd = 0.2 ($k_1 = 2\pi\gamma sdfd$), k_2 = 0.001, βh(bpf) = 0.18 and βl(bpf) = 5.5, and different input-output map: yp = 1 – (1 – x)2p, p = 1 (●), 2 (□), and 3 (△) [25]

$$K_{sg}(0) \cong \frac{a_1}{2} \cdot \frac{df}{dx}(0) = p \cdot H_1,\ p = 1, 2, 3 \tag{12.44}$$

It is easy to notice that the above simulation results validate the relationship (12.44). For example, considering γ_{sd} = 0.2 and f_d = 50 Hz (case a), the initial value for the $K_{SS(bpf)}$ indicator is about 0.7 (for p = 3) and 0.18 (for p = 2). Thus, considering the initial value for the simulated $K_{sg(bpf)}$ parameter mentioned above, the γ_{sd} parameter can be estimated based on (12.34) as 4.4/(314 · 0.07) ≅ 0.2 (for p = 3) and 1.2/(314 · 0.018) ≅ 0.21 (for p = 2).

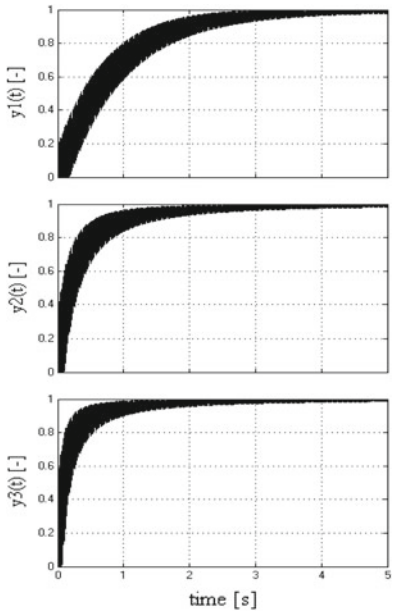

(a) The output during the searching phase for different input-output map, $y_p=1-(1-x)^{2p}$, p=1 (top), 2 (middle), 3 (bottom)

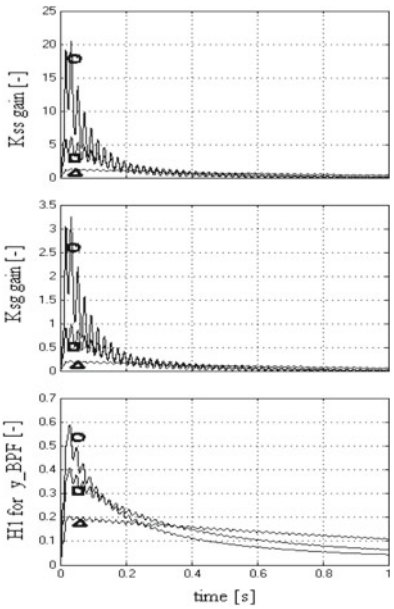

(b) $K_{SS(bpf)}$ (top), $K_{sg(bpf)}$ (middle) and H_1 (bottom) for different input-output map: $y_p=1-(1-x)^{2p}$, p=1 (●), 2 (□), 3 (△)

Fig. 12.9 The bpfESC scheme with $\gamma sd = 0.02$ ($k_1 = 2\pi\gamma sdfd$), $k_2 = 0.1$, fd = 50 Hz, $\beta h(bpf) = 0.18$ and $\beta l(bpf) = 5.5$ [25]

Also, it is easy to notice that the values for the $K_{SS(bpf)}$ indicator are 10-times lower in case b, when the dither frequency is set to be 10-times lower than in case a. Thus, the analytical result given by (12.34), related to the $K_{SS(bpf)}$ indicator, is validated through simulation.

In order to highlight the second term of the relationship (12.29'), some simulations related to the searching phase for the bpfESC schemes using $k_2 = 0.1$, which is 100-times higher than the above value, are presented in Fig. 12.9. To assure the loop stability the k_1 gain is set 10-times lower than the above value considering in simulation $\gamma_{sd} = 0.02$ and $f_d = 50$ Hz.

The simulation results validate the analytical results presented above for the bpfESC scheme:

- The convergence time is proportional to the product of the frequency and magnitude of the dither. The convergence time is 10-times lower in Fig. 12.10 than in Fig. 12.7a.
- Considering the initial value for the $K_{SS(bpf)}$ indicator and $K_{sg(bpf)}$ parameter, the γ_{sd} parameter can be estimated based on (12.34) as $20/(314 \cdot 3) \cong 0.021$ (for p = 3) and $6/(314 \cdot 0.9) \cong 0.021$ (for p = 2). Thus, the analytical result given by (12.34) is further validated through simulation.

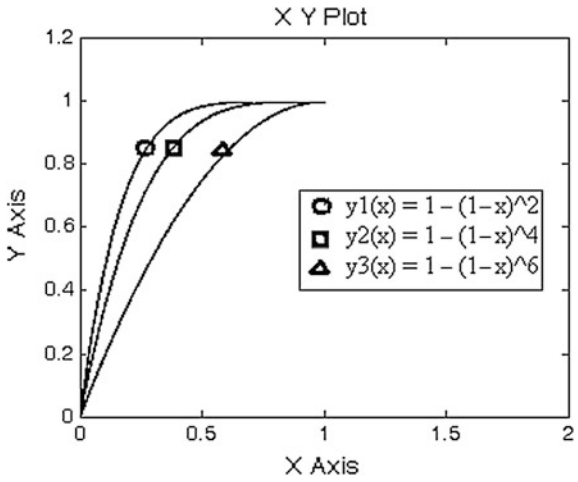

Fig. 12.10 The search phase is shown in the Y-X phase plane for yp = 1 – (1 – x)2p: p = 1(○), 2(□), 3(△) [25]

The searching phase is shown in the Y-X phase plane for different $y_p = 1-(1-x)^{2p}$ is shown in Fig. 12.10.

The ratios of the searching speeds can be estimated based on (12.41) for the mESC and bpfESC scheme using $y_p = 1 - (1 - x)^{2p}$, and these value are validated by the simulations shown in Fig. 12.11.

The simulation results validate the analytical results obtained based on (12.43):

- Case p = 3: the initial ratio of the searching speed is $1 + (120/6) \cdot (0.6)^3/8 = 1.9$; the initial ratio computed from the simulation results is about 2.
- Case p = 2: the initial ratio of the searching speed is $1 + (24/4) \cdot (0.4)^3/8 = 1.12$; the initial ratio computed from the simulation results is about 1.14.

Note that the dither has a higher magnitude during the search phase (see bottom plot in Fig. 12.8b). The ripple during the stationary phase is shown in Fig. 12.12.

The ripple measured during the stationary phase (around t = 4 s) is about 3.5% (for p = 1), 2.5% (for p = 2), 2% (for p = 3). For example, if a FC stack has 10 kW power, then the power ripple is higher than 200 W, which means a lot from energy efficiency point of view of energy efficiency. Furthermore, the ripple affects the life cycle of the PEMFC stack. As it was mentioned, a solution to improve the tracking accuracy was proposed in [26].

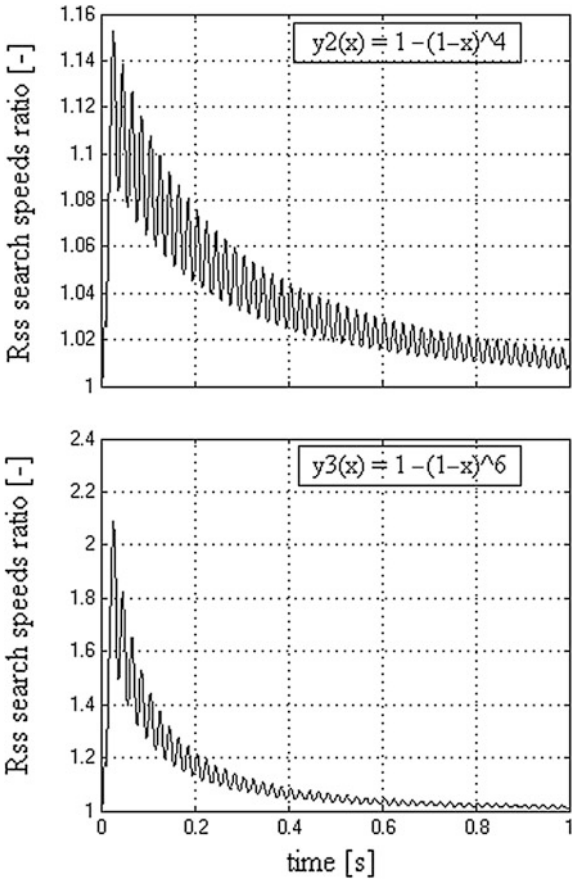

Fig. 12.11 The ratio of the searching speeds for the mESC and bpfESC scheme (with γsd = 0.02, k_2 = 0.1, fd = 50 Hz, βh(bpf) = 0.18 and βl(bpf) = 5.5) using $y_p = f(x) = 1 - (1 - x)2p$: p = 2 (*top*), 3(*bottom*) [25]

12.4 FC System Modeling and Control

12.4.1 FC System Modeling

The PEMFC system converts the hydrogen energy into electrical energy. Besides other FC types, the PEMFC system has some advantages in operating such as low operating temperature, compactness, and more simplified procedures to start-up and shut-down.

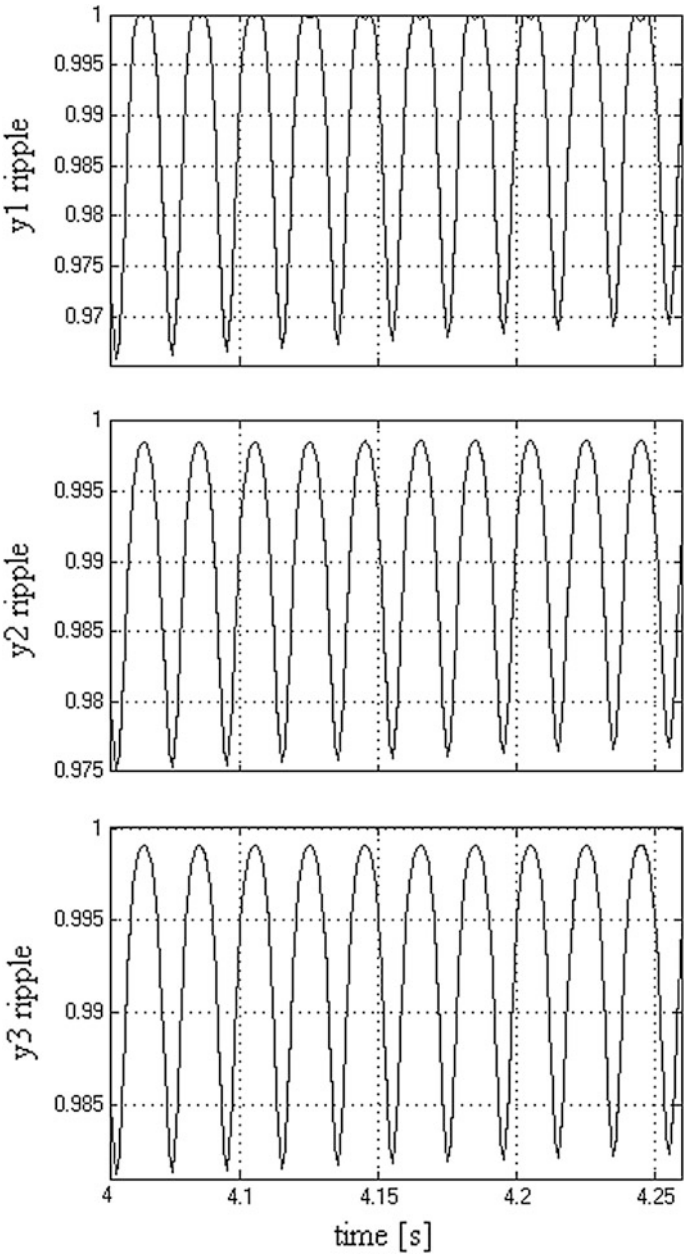

Fig. 12.12 Ripple during the stationary phase for the bpfESC scheme with $\gamma sd = 0.02$ ($k_1 = 2\pi\gamma sdfd$), $k_2 = 0.1$, fd = 50 Hz, $\beta l(bpf) = 0.18$, $\beta h(bpf) = 5.5$, and $y_p = 1 - (1 - x)2p$: p = 1(*top*), 2(*middle*), 3(*bottom*) [25]

The model used for the FC system should be able to accurately reflect the PEMFC fueling and loading, the mass transfer and electrochemical phenomena, which have time constants that must be included into the PEMFC dynamic. The analytical models are focused on different processes encountered on the FC system such as heat, mass transfer, electrochemical phenomena and other [57], or on entire system [58, 59]. The empirical models are based on experimental data and focused to predict the effect of different input parameters on the FC power, without in-depth analysis of the physical and electrochemical phenomena involved [35, 60].

The PEMFC model implemented in Matlab/Simulink® will be used here because this model has good accuracy in reflecting the PEMFC operation. The model accuracy is not a critical issue: the ESC-based MPPT algorithm will track the MPP of the FC power characteristic that is simulated at 3380 K (because the effects of temperature are negligible on MPP position during the tracking process).

The hydrogen consumption is proportional to the FC current. The MPP controller will regulate the FC current to maximize the FC power by controlling the fueling rate [42, 47]. The humidified air flow is regulated by the air controller, which commands the compressor's speed for the required FC power [42]. The classical control of the air flow rate is based on maintaining the oxygen excess ratio close to 2 [57]. Both fuel flow rates can be used to control the FC power [47], but for high FCHPS the air control is usually used [42, 60], without maximization of the FC system efficiency [61].

It is obvious that the FC power could be controlled by both fueling rates or only by air flow rate [62, 63], this choose being in general an experimental challenge for the FCHPS designers [64–67]. Anyway, a model for the FCHPS is necessary to design the fueling controller. In general, a nine or five states variables are used to model the PEMFC system (named full-order model [63, 65] or reduced model [66, 67], respectively).

12.4.2 FC System Control

12.4.2.1 Air Flow Control

The air flow rate must be efficiently controlled based on the load following controller. If the air flow rate is higher that the needed rate then the efficiency of the PEMFC system decreases, but also if this decreases under the needed rate, close to critical rate, then the air is insufficient and the oxygen starvation may appear. The controlled compressor can regulate the cathode excess oxygen ratio, avoiding this phenomenon. The air rate may be controlled using a dynamic feed-forward control,

linear quadratic regulator, robust control, predictive control, sliding control, MPPT control and so on [18, 43, 63, 67, 68]. Here, the ESC-based MPPT control will be analyzed.

12.4.2.2 Hydrogen Flow Control

The hydrogen flow rate can directly regulate the FC power, respecting the stoichiometric ratio of hydrogen and oxygen flow rates and dynamic range of the mass flow controllers. The hydrogen flow rate is a very good manageable variable, instead of the oxygen flow rates that is a poor manipulated variable to control the FC power [62–64]. The optimal hydrogen flow rate is estimated in real-time based on the PEMFC efficiency map [69]. This control is benefic for small PEMFC systems, where it is impractical to recycle the unreacted hydrogen [50].

The FC power will fall after few FC time constants after the shutdown of the fuel valve and the FC power returns to the previous value if the fuel valve is reopened during this delay in powering (when the reactants in the manifolds are not consumed) [62]. So, the control of the on-off fuel valve must be made at a switching frequency lower than 0.5 Hz. Thus, this control of the FC power is impractical due to the slow response of the control loop. Consequently, a linear controlled valve is used to regulate the pressure of hydrogen [50] or oxygen [45]. The control loop is more complex, containing a valve, flowmeter, and an appropriate controller. A simple and cheap control loop may be obtained using a digital valve, which is a set of carefully sized sonic chokes installed in parallel (supplied by one common inlet line and all discharged into a common exit manifold). The chokes calibrated and sized in a binary pattern flowing may be digitally controlled using the on-off fuel valves in series with each choke. A digital approximation is obtained for the hydrogen flow rate that may be designed to be close to those given by the linear controlled valve.

12.4.2.3 Control of Both Fueling Flow Rates

The control objective is to maximize the net FC power based on the both fueling rates that are controlled in the admissible 2-D domain specified by the constraints. In this case, a 2D-scheme for controlling both fueling flows can be used [21, 47, 70]. In general, a large tracking accuracy error is obtained due to the weak controllability of the fueling flow rates under pulsed load [71]. The modeling and the control of the air stream and hydrogen flow with recirculation in a PEMFC system with constraints is shown in [66, 72]. The ESC 2D-scheme to control both fueling

flows is analyzed in [47]. Here, the proposed mESC scheme of single input single output type will be analyzed to highlight its advantages in comparison with the classical control schemes.

12.5 The ESC-Based MPPT Control for FC System

The objective of the ESC scheme is to generate the control reference (Iref) that generates the FC output power close to PMPP without knowing the FC power characteristic, PFC = f(IFC). Consequently, the current control mode based on the ESC-based MPPT control will be implemented to regulate the fuel flow rate (FuelFr) using the following load technique [26, 39].

12.5.1 The Classical ESC Schemes

The first order ESC scheme is based on a scalar scheme, which is as that represented in Fig. 12.3, but without use of the filters' blocks [73].

The hoESC scheme is augmented with filters of LPF and HPF type, as in Fig. 12.3 [25] or adapted for the FC system in Fig. 12.13 [26], where the dither gain is $k_A = A \cdot k_2$. Note that the LPF is not always necessary in searching and tracking of the MPP, excepting the noise environment [52].

12.5.2 The mESC Scheme

The mESC scheme was shown in Fig. 12.3 [25] and adapted to the FC system in Fig. 12.14 [26], where the dither gain is $k_A = A \cdot k_2$. The initial value of the FC current, I_{FC0}, must be set in the attraction region that assures $i_5 \rightarrow I_{MPP}$.

The analysis performed in next sections for the ESC schemes is based on a sinusoidal dither, but the dithers' shape does not influence the performance [74].

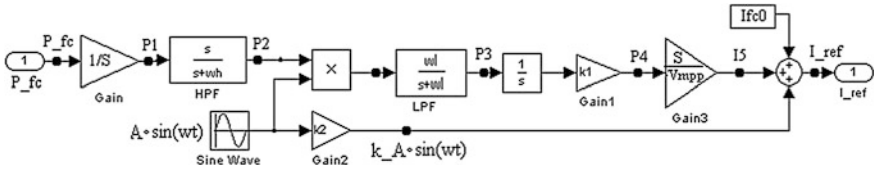

Fig. 12.13 The hoESC scheme for FC system [26]

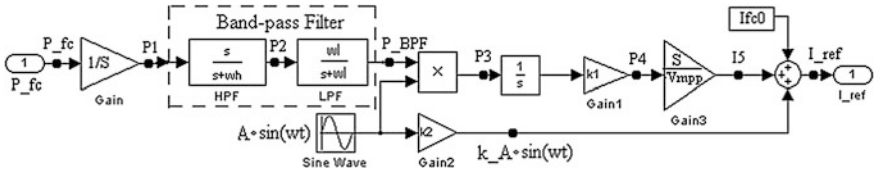

Fig. 12.14 The mESC scheme for FC system [26]

12.5.3 The aESC Scheme

The aESC scheme is shown in Fig. 12.15 [27]. Note that the dither amplitude is set to be proportional with the first harmonic's magnitude (H_1) of the FC power: Thus, the dither gain is $k_A = A \cdot k_2 \cdot H_1$. The first harmonic's magnitude (H_1) decreases during the searching process to almost zero at MPP. Consequently, an insignificant ripple of FC power will be on FC bus during the stationary phase. The proposed aESC scheme outperforms the classical ESC schemes and the mESC scheme in global power efficiency if the search speed is limited to be the same for all ESC schemes.

Note that aESC scheme will have the same operating relationships as mESC scheme (1–4), excepting that dither gain is $k_A = A \cdot k_2 \cdot H_1$.

The equivalent aESC (EQaESC) scheme that uses a series connection of HPF and LPF, instead of a BPF, is also shown in Fig. 12.15. The aESC and EQaESC schemes are functionally equivalent if the filters have the same cut-off frequencies. So, the performance of both aESC and EQaESC schemes are almost the same. The demonstration can be made in the same manner as in Sect. 12.2 for hoESC and bpfESC schemes.

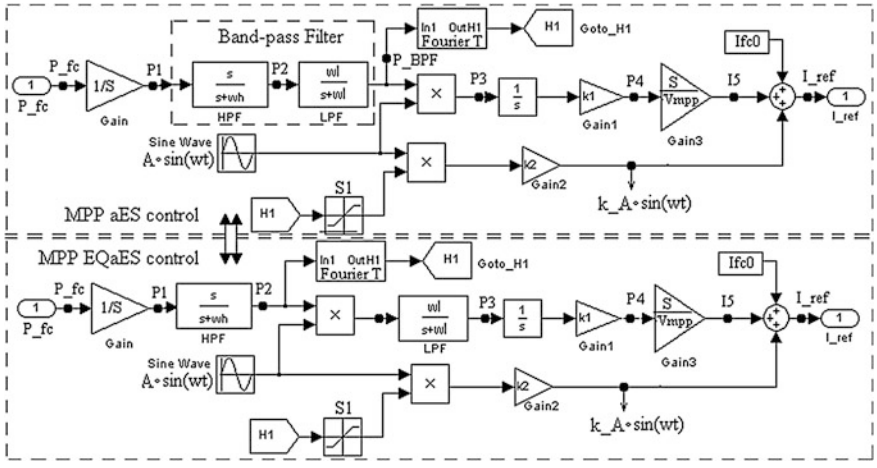

Fig. 12.15 The aESC scheme and its equivalent scheme (EQaESC) [27]

12.6 Testing of the ESC Schemes on PEMFC System

12.6.1 Testing at Constant Fueling Rate

The Matlab-Simulink® diagram shown in Fig. 12.16 contains the 6 kW–45 V PEMFC stack system that has the fueling rate set by the FuelFr constant and the FC current controlled by the ESC-based MPP controller.

The preset PEMFC model has the nominal flow rates for hydrogen and air of 50 and 300 lpm, membrane aria (S) of about 65 cm^2, 65 cells in series (resulting the voltage at light load, $V_{FC(0)}$, of about 60 V), and the MPP will be around 129 A (I_{MPP}) and 6175 W (P_{MPP}). The PEMFC characteristic shown in Fig. 12.17 is obtained for the nominal fueling conditions mentioned in this figure, too. The PEMFC time constant was set in range 0.2–2 s and the dither frequency in the range 1–100 Hz in order to analyze the dynamic effects.

The MPPT process is represented in the P-I phases plane (see Figs. 12.17 and 12.18). The dither's gain (k_2) and dither's frequency modifies the magnitude and position of the limit cycle (see Fig. 12.17). This means that the power ripple remains constant during the stationary phase (see the zoom on Fig. 12.18). The power ripple decreases to zero during the stationary phase if the aESC scheme is used. This aESC scheme will be analyzed in Sect. 12.6.4, highlighting its performance in comparison with mESC scheme.

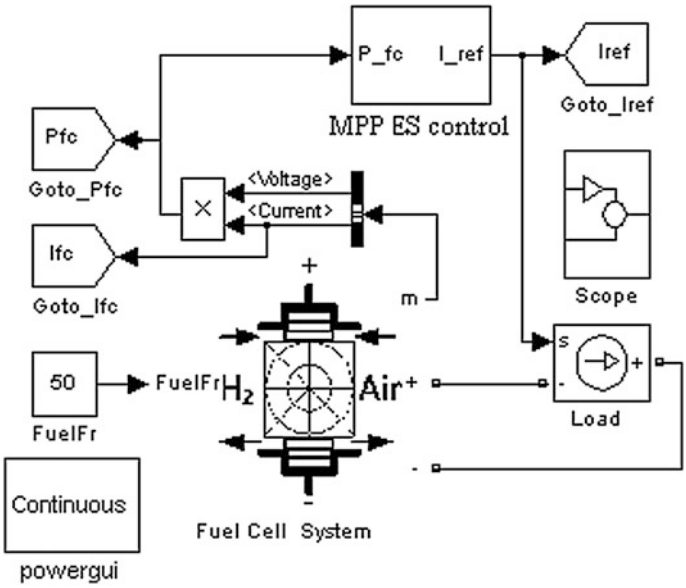

Fig. 12.16 Diagram for testing the ESC schemes [26]

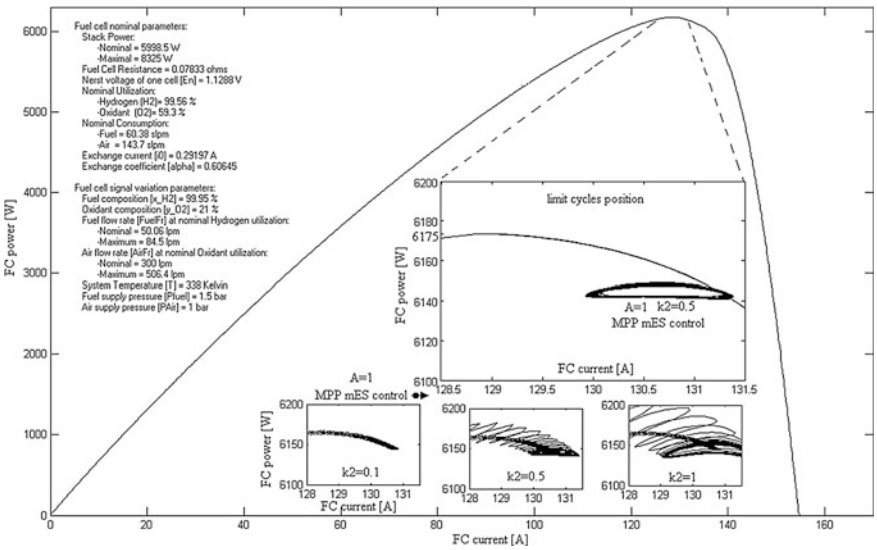

Fig. 12.17 The FC power characteristics versus the FC current, and the MPP position close to limit cycle obtained for the mESC scheme [26]

The harmonics' magnitudes for three level of the FC power are also shown in Fig. 12.17. The magnitude (H_1) of the first harmonic decreases during the searching phase, being almost zero close to the MPP. In this section the performance of the mESC scheme in comparison with the EQmESC and the hoESC scheme will be shown using the diagram from Fig. 12.19. The FC system without MPP control is used as reference

The fuel flow rate, FuelFr (lpm), is computed based on the load current, i_L (see Fig. 12.20):

$$FuelFr = \frac{60000 \cdot R \cdot (273 + \theta) \cdot N_C \cdot (i_L \cdot G_i)}{2F \cdot (101325 \cdot P_f) \cdot (U_{f(H2)}/100) \cdot (x_{H2}/100)} \tag{12.45}$$

where:

R = 8.3145 J/(mol K);
F = 96485 A s/mol;
N_C represents the number of cells in series (65);
$U_{f(H2)}$—nominal hydrogen utilization (99.56%);
θ—operating temperature (65 °C);
P_f—fuel pressure (1.5 bar);
x_{H2}—H_2 composition (99.95%);
$G_i = I_{FC}/I_L$.

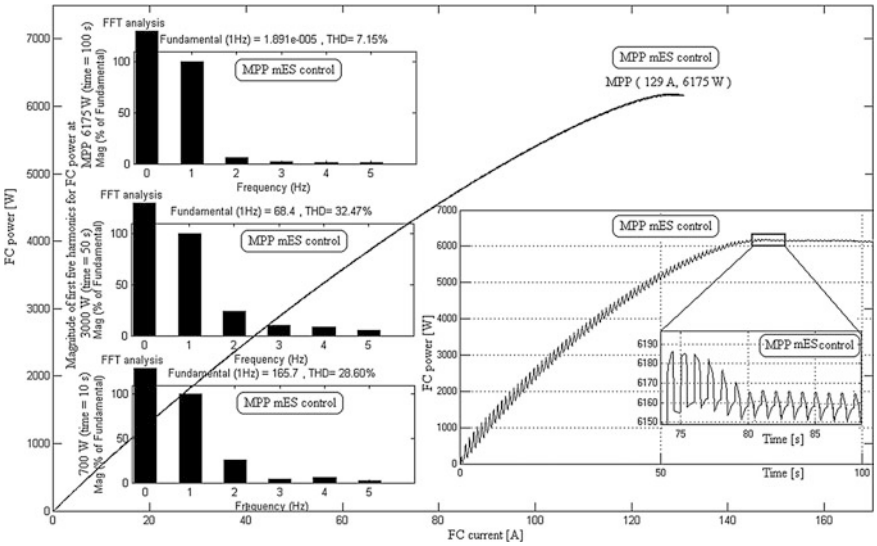

Fig. 12.18 The MPP tracking on the P-I phases plane for the mESC scheme (a zoom of the tracking accuracy is included) [26]

The G_i gain will be used to set the charge-sustained regime for the ESS [39]. Here, $G_i = 1$ in all simulations, so it was omitted in Fig. 12.20. The rate limiter with saturation of the FuelFr value assures safe operation for the PEMFC system.

12.6.2 The Equivalence of the mESC and EQmESC Schemes for FC System

The LF equivalence (EQ) of the hoESC and bpfESC schemes was theoretically approached in Sect. 12.2 of this chapter. Some simulations to validate this theoretical result were shown in Sect. 12.3.4 and will be shown here for the mESC and EQmESC schemes adapted from the hoESC and bpfESC schemes (see Figs. 12.2, 12.3, 12.13 and 12.14, respectively) for a FC system. The simulation results are shown in Fig. 12.21. The FC system behavior under the mESC and EQmESC schemes is almost the same (see the profile of the FC power and the LF harmonics of the i_{ref}). The simulation parameters for the both mESC and EQmESC schemes are the following: $k_1 = 400$, $k_A = A \cdot k_2 = 0.1$ ($k_2 = 1$, and $A = 0.1$), $f_d = \omega_d/(2\pi) = 100$ Hz, $\beta_l = 5.5$, and $\beta_h = 0.5$ (thus $\beta_l \cdot \beta_h = 2.75$). The fuel flow rate is nominal (50 lpm). A saw-tooth load is used for the FC system without MPP control in order to estimate the tracking accuracy (see the top zoom on right part of Fig. 12.21). Also, the zooms on the left part of Fig. 12.21 are obtained for $\beta_l = 5.5$

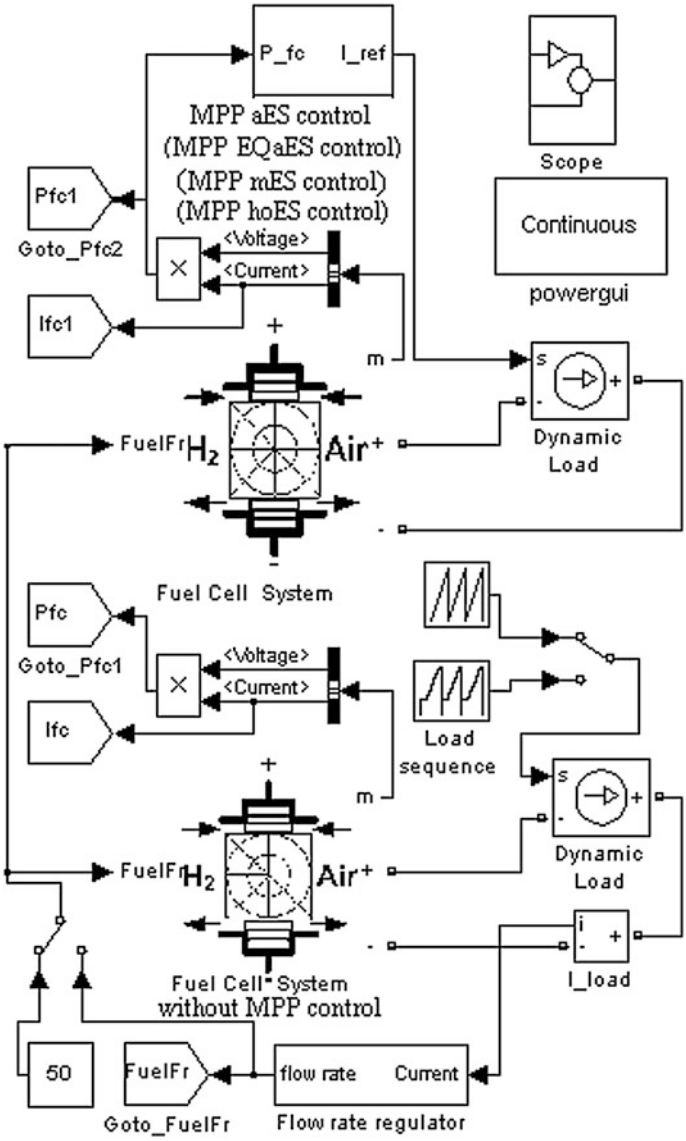

Fig. 12.19 The diagram for comparative tests for different ESCschemes analyzed [25]

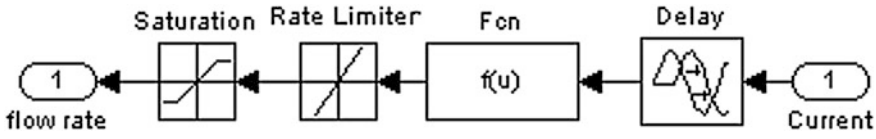

Fig. 12.20 The diagram of the flow rate regulator [26]

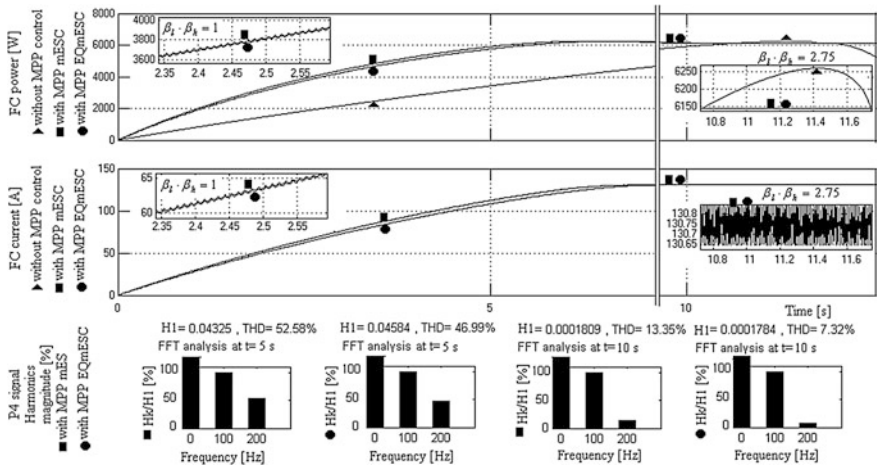

Fig. 12.21 Simulation results for the mESC and EQmESC schemes [26]

and $\beta_h = 1/\beta_l \cong 0.18$ (because $\beta_h \cdot \beta_l = 1$) and highlights the validity of the relationship (12.11) during the search time phase: $\beta_l \cdot \beta_h = 1$.

Thus, the simulation results have again validated the analytical results reported in Sect. 12.2. The main performances of the mESC scheme based on the results shown in Fig. 12.21 are the following:

- The oscillations of the FC current is about 0.2 A peak-to-peak, being obtained if the dither period (10 ms) is chosen lower than the FC time constant (2 s).
- The power ripple is about 9 W (0.2 A · 45 V) for $k_A = 0.1$, and the normalized power ripple is about 9/6000 = 1.5%, being on admissible range mentioned in [55].
- The tracking accuracy is 6150/6250 ≅ 0.984 = 98.4% (see Fig. 12.21), being lower than 99% of the value reported in [56];
- The both mESC and EQmESC schemes have almost the same searching speed. For example, the initial search rate of the FC current is about 30 A/s, so the power increases with a rate of 1800 W/s, which is verified on the FC power shown on the top of Fig. 12.21.

12.6.3 The Performance of the mESC and hoESC Schemes for FC System

The ratio of the searching speeds for mESC and hoESC schemes is given by (12.46):

$$R_{SS} \cong \sqrt{1 + 1/\beta_{l(ho)}^2} \tag{12.46}$$

where the approximation was made because

$$\left(\beta_{l(bpf)}/\sqrt{\beta_{l(bpf)}^2 + 1}\right) \geq 0.95 \quad \text{for} \quad 0 < \beta_{l(ho)} < 1 < 3 < \beta_{l(bpf)}.$$

The simulations shown in Fig. 12.22 validate again the relationship (12.16). All parameters used in simulation were set the same for both mESC and hoESC schemes ($k_1 = 400$, $k_2 = 1$, $A = 0.1$, $f_d = \omega_d/(2\pi) = 100$ Hz, and $\beta_h = 0.5$), with the exception of the cut-off frequency of the filters ($\beta_{l(m)} = 5.5$ and $\beta_{l(ho)} = 0.5$).

The comparison of the performance obtained for both ESC schemes is as following:

- The searching speeds for both mESC and hoESC schemes are time dependent variable. For example, the speeds' rates evaluated at 2 s are about 1500 Ws^{-1} and 1000 Ws^{-1} for the mESC and hoESC schemes, respectively. The speeds' ratio is 2.2 based on (12.16), being higher than the ratio evaluated based on the simulation results (which is 1500/1000 = 1.5) due to the harmonics effects explained in Sect. 12.3.
- The searching speed is proportional to the dither magnitude based on relationship (12.35) and (12.40). This results are validated by the results shown in Fig. 12.22 (see zoom on left of Fig. 12.22) for $k_2 = 1$ and $A = 1$. The searching speed is about ten time higher for both ESC schemes if the dither amplitude is 10 times higher than the value $A = 0.1$, which was mentioned above.

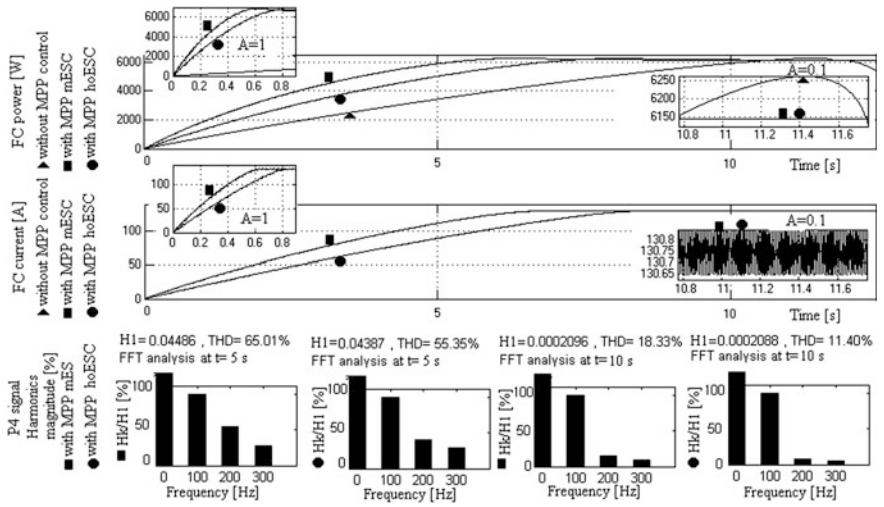

Fig. 12.22 Simulation results for the mESC and hoESC schemes [26]

- The LF harmonics content of the i_5 control signal is different for the ESC schemes (see the spectrums shown on bottom of the Fig. 12.22) due to different values used for the cut-off frequencies: $0 < \beta_{l(ho)} < 1 < 3 < \beta_{l(bpf)}$. For example, the magnitude of second harmonic is with about 30% higher, so the dither's persistence on the mESC loop is better than that resulting on the hoESC loop.
- The design of the k_1 gain to be proportional to the dither frequency will assure certain dither's persistence on the mESC loop, which will guarantee the convergence of the ESC algorithm.

12.6.4 The Comparative Analysis of the aESC and mESC Schemes

As it was mentioned above, the main difference between the mESC scheme and the aESC scheme is related to the dither gain, which is constant, $k_{A(m)} = A \cdot k_2$, and time variable, $k_{A(a)} = A \cdot k_2 \cdot H_1$, respectively, where H_1 is the magnitude of first harmonic of the FC power.

Consequently, the searching speed for the aESC and the mESC schemes are given by (12.46) and (12.47) [25, 26]:

$$\begin{aligned} K_{SS(i)(aES)} &= K_{SS(p)(aES)}/V_{MPP} \\ &= \dot{p_{FC}}\, k_{1(a)} k_{2(a)} A \left| G_{BPF(a)} \right| \cos(\phi_{BPF(a)})/(2V_{MPP}) \end{aligned} \tag{12.46}$$

$$\begin{aligned} K_{SS(i)(mES)} &= K_{SS(p)(mES)}/V_{MPP} \\ &= \dot{p_{FC}}\, k_{1(m)} k_{2(m)} H_1 A \left| G_{BPF(m)} \right| \cos(\phi_{BPF(m)})/(2V_{MPP}) \end{aligned} \tag{12.47}$$

If the same design parameters will be used for the aESC and mESC schemes ($k_{1(a)} = k_{1(m)}$ and $k_{2(a)} = k_{2(m)}$ and so on), then the ratio of searching speeds will be:

$$R_{SS} = \left| K_{SS(aESC)}/K_{SS(mESC)} \right| \cong H_1 \tag{12.48}$$

If the same filters are used, $BPF_{(a)} \equiv BPF_{(m)}$, and the S1 saturation block has the limits 0 and 1, then $k_{A(a)} = k_{A(m)}$ during the searching phase (when $H_1 > 1$) and $k_{A(a)} = H_1 k_{A(m)}$ if the MPP was located and $H_1 < 1$. The H_1 magnitude is very small close to the MPP, so the FC power ripple is negligible during the stationary phase and the MPP is found accurately (see Fig. 12.23, where the magnitudes of the first three harmonics (H_1, H_2, and H_3) of the FC power are shown).

Note that the searching speed will be H_1—times higher for the aESC scheme in comparison with the mESC scheme if the S1 saturation block has the upper limit set to infinit. The rate limiter with saturation of the FuelFr value will assure the safe operation for the PEMFC system (see the flow rate regulator diagram in Fig. 12.23).

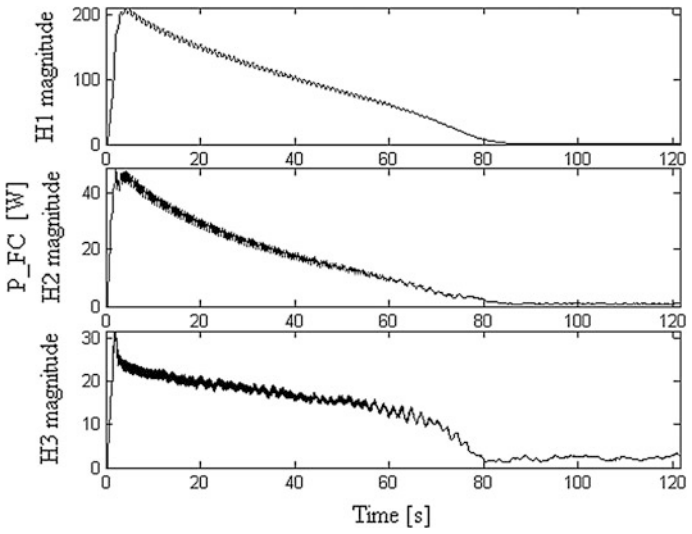

Fig. 12.23 The harmonics of the FC power [27]

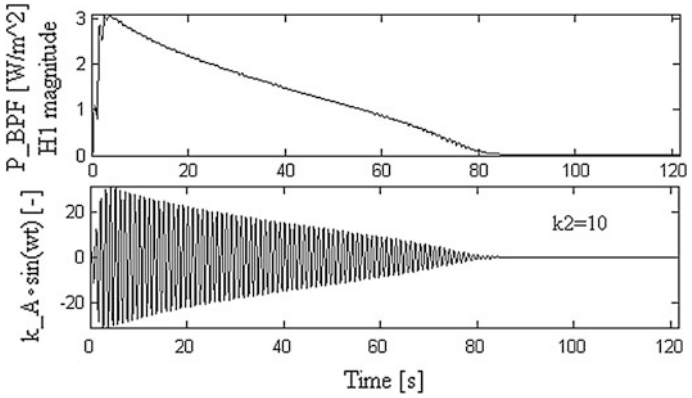

Fig. 12.24 The shape of the 100 Hz dither signal [27]

The FC power density (the ratio of the FC power to membrane aria), which is the p_1 signal in Fig. 12.15, is filtered by the BPF, resulting the p_{BPF} signal. This signal modulates the dither signal (with A = 1 and the dither gain $k_2 = 10$; see Fig. 12.24).

If the same k_1 gain ($k_{1(a)} = k_{1(m)}$) and filters ($BPF_{(a)} \equiv BPF_{(m)}$) are used, A = 1 and the S1 saturation block has the upper limit 0.5, then $k_{A(a)} = 0.5$ (because $H_1 > 1$) and $k_{A(m)} = k_2$ during the searching phase. See the searching speeds in the first column of zooms on Fig. 12.25, where the load sequence is stair step type and

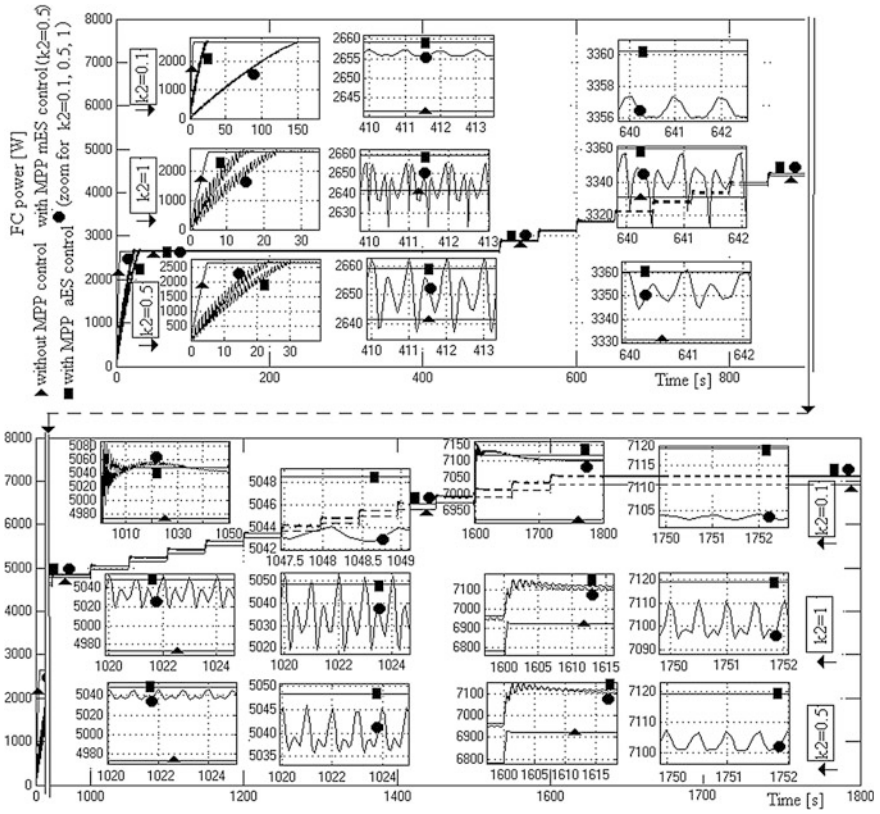

Fig. 12.25 The FC power using the aESC (■) and mESC (●) schemes, and without MPP control (▲); the zooms shown the details of MPP searching and tracking process [27]

three values are considered for the k_2 parameter: $k_2 = 0.5$, $k_2 = 1$, and $k_2 = 0.1$ for zooms shown on bottom, middle and top of Fig. 12.25.

The next columns of zooms show the MPP tracking process for the aESC (when $k_{A(a)} = H_1 k_{A(m)}$ because $H_1 < 1$ if the MPP was located) and mESC schemes. The tracking accuracy for aESC scheme is higher than that of the mESC scheme, which is 6160/6175 = 0.9976 = 99.76% at full load (see Fig. 12.18).

The comparative results highlight the advantages of the aESC scheme in comparison with the mESC scheme:

- the ratio of search speeds is $R_{SS} = \left| K_{SS(aESC)} / K_{SS(mESC)} \right| \cong H_1$;
- the MPP tracking accuracy is higher than 99.76% for the aESC scheme;
- the FC power ripple using the aESC scheme is negligible, but the FC power ripple using the mESC scheme is about 1 W, 10 W, and 20 W for k_2 parameter set to 0.1, 0.5, and 1, respectively.

12.6.5 Testing the aESC Scheme on FCHPS

The FCHPS is shown in Fig. 12.26, where an equivalent load is used to test the FCHPS. The design of the FCHPS is detailed in [27]. Here, only the results are shown to validate the performance of the aESC scheme. Two control loops can be identified in Fig. 12.26: the load following loop (with $G_i = 4$ set in relation (12.45)) and the aESC-based MPPT loop.

The results of the FCHPS behavior under aESC-based MPPT control are shown in Fig. 12.26 as following:

- Plot 1: the load power profile, including a zoom of load ripple and its power spectrum;
- Plot 2: the FC power (●) and the H_1 magnitude of the p_{BPF} signal (■);
- Plot 3: the FC current, including a zoom of the load ripple and its power spectrum.

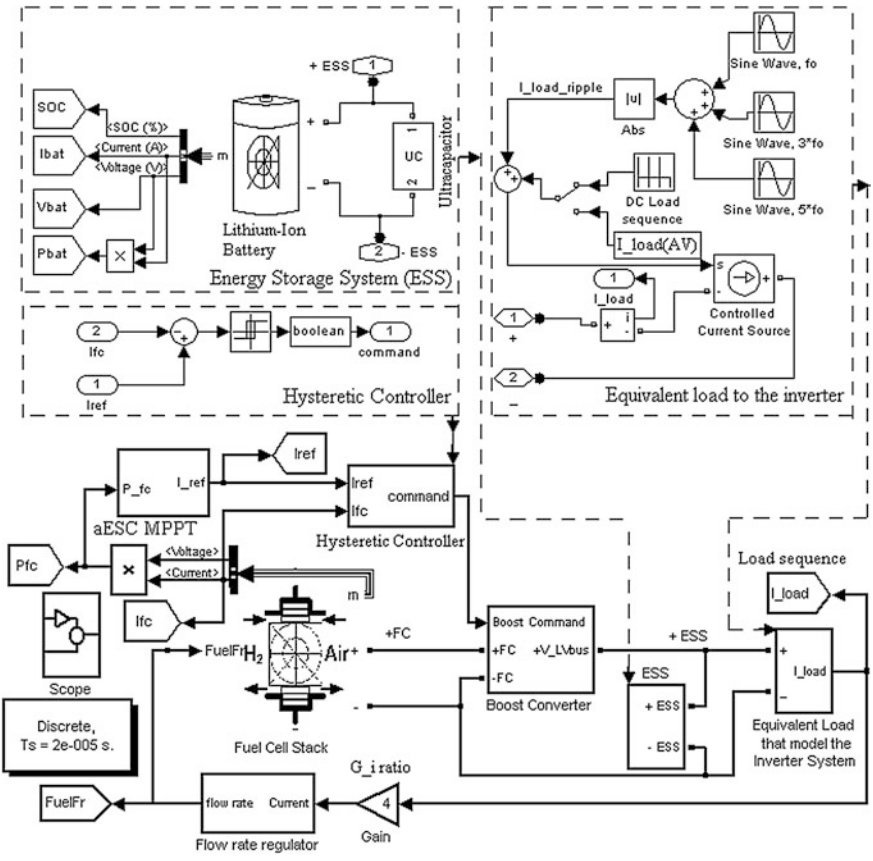

Fig. 12.26 The FCHPS diagram under aESC-based MPPT control [27]

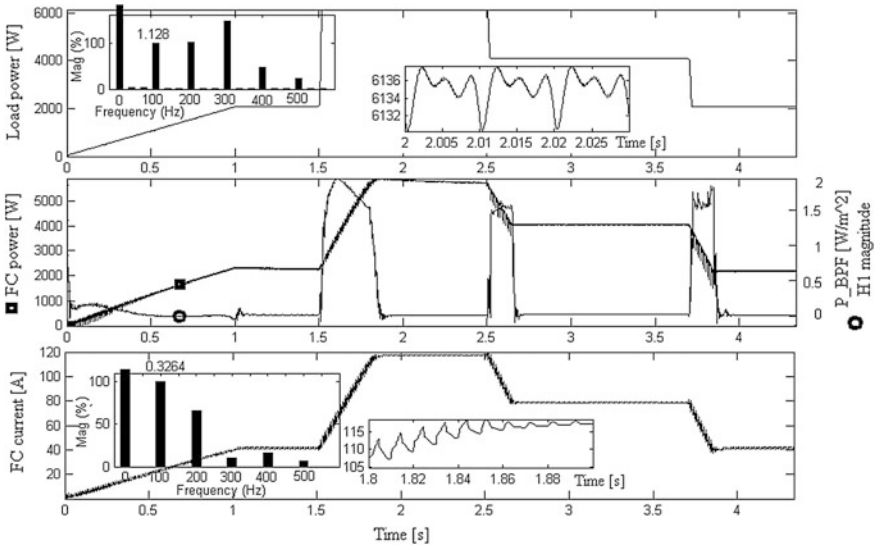

Fig. 12.27 The FCHPS behavior under aESC-based MPPT control [27]

The MPPT process can be understood based on the results shown in Fig. 12.27: the H_1 magnitude increases quickly at any load variation, which actually means a FC power that follows the load profile based on the load following control implemented.

The search speed is about a few kW/s (see plot 2 on Fig. 12.27).

The power flow balance on DC bus is assured by the ESS, which will operate in charge depletion mode load ($P_{load} > \eta_{boost} P_{FC} \Rightarrow P_{ESS} > 0$) or in the charge increasing mode ($P_{load} < \eta_{boost} P_{FC} \Rightarrow P_{ESS} < 0$).

12.7 Conclusion

In this chapter, besides the well-known results for the hoESC scheme, which are obviously available for the all ESC schemes, new analytical results related to the bpfESC scheme are shown. The main results are: (1) the searching speed may be estimated based on the derivatives of the unknown input-output map; (2) the harmonics magnitudes during the searching phase could be evaluated based on (12.34); (3) the ratio of the searching speeds can be estimated during the searching phase based on (12.41).

Note that these results related to ratio estimation must be interpreted in the context of the modeling approach considered, which was kept at a simple level for the signal processing in the ESC loop. All the analytical results obtained were validated by simulation using generic input-output maps. The FC power

characteristic was used as input-output map to validate the above results on this nonlinear map (see Sect. 12.6). The mean value of the searching speeds ratio was computed to shown that this is close to the average approximation of this ratio based on a frequency approach given by (12.13). Also, it can be noted that the dither persistence is dependent to the BPF cut-off frequencies.

The mESC scheme based on the bpfESC was proposed to improve the performance related to searching speed process. The main results of the comparison of the mESC scheme with the hoESC scheme are the following: (1) the rate of searching speeds is higher than 1.5 in all cases; (2) the dither's persistence is improved if the frequencies band of the BPF is enlarged; (3) the search speed could be set up to safe value by increasing the dither gain until the admissible value that is designed for an imposed performance for the tracking accuracy and the FC power ripple.

Note that the FC power ripple and tracking accuracy are almost the same for both ESC schemes analyzed. These performance indicators were improved by the aESC scheme that was analyzed in comparison with mESC scheme (see Sect. 12.6.4): (1) the tracking accuracy is higher than 99.76%, (2) the FC power ripple is negligible during the stationary phase after the MPP is found; (3) the search speed could be set up to safe value, but maintaining the performance related to the tracking accuracy and the FC power ripple; (4) the aESC-based MPPT control is robust to load profiles that include high dynamic variations; (5) the aESC-based MPPT control is simple to be implemented.

It was shown that the aESC scheme slightly outperforms the mESC scheme in total power efficiency and performance obtained for any load profile. The aESC searching speed is H_1 times higher than the mESC searching speed, which finally means a very short time to find and track the current MPP.

Thus, the aESC-based MPPT control combined with the load following control has good performance for nonlinear loads with unmodeled dynamics.

The performance of the FCHPS with two control loops that was highlighted in this chapter could influence the designers to experiment this control architecture.

Acknowledgements The research that led to the results shown here has received funding from the project "Cost-Efficient Data Collection for Smart Grid and Revenue Assurance (CERA-SG)", ID: 77594, 2016-19, ERA-Net Smart Grids Plus. Some figures, tables and text are reproduced from [25–27] here with kind permission from Elsevier Limited, UK, and IJTPE—IOCTPE, [February 13, 2016].

References

1. Dargahi M, Rouhi J, Rezanejad M, Shakeri M (2009) Maximum power point tracking for fuel cell in fuel cell/battery hybrid power systems. Eur J Sci Res 25(4):538–548
2. Esram T, Chapman PL (2007) Comparison of photovoltaic array maximum power point tracking techniques. IEEE Trans Energy Convers 22(2):439–449
3. Salas V, Olías E, Barrado A, Lázaro A (2006) Review of the maximum power point tracking algorithms for stand-alone photovoltaic systems. Sol Energy Mat Sol Cells 90(11):1555–1578

4. Caux S, Hankache W, Fadel M, Hissel D (2010) On-line fuzzy energy management for hybrid fuel cell systems. Int J Hydrogen Energy 35(5):2134–2143
5. Wang J-C, Su Y-L, Shieh J-C, Jiang J-A (2011) High-accuracy maximum power point estimation for photovoltaic arrays. Sol Energy Mat Sol Cells 95:843–851
6. Reisi AR, Moradi MH, Jamasb S (2013) Classification and comparison of maximum power point tracking techniques for photovoltaic system: a review. Renew Sust Energy Rev 19:433–443
7. Ishaque K, Salam Z (2013) A review of maximum power point tracking techniques of PV system for uniform insolation and partial shading condition. Renew Sust Energy Rev 19:475–488
8. Dali M, Belhadj J, Roboam X (2010) Hybrid solar-wind system with battery storage operating in grid–connected and standalone mode: control and energy management—experimental investigation. Energy 35(6):2587–2595
9. Khanh LN, Seo JJ, Kim YS, Won DJ (2010) Power-management strategies for a grid-connected PV-FC hybrid system. IEEE Trans Energy Convers 25(3):1874–1882
10. Giustiniani A et al (2010) Enhancing polymeric electrolyte membrane fuel cell control by means of the perturb and observe technique. Fuel Cell Sci Technol 7(1):11021–11031
11. Liu F, Duan S, Liu F, Liu B, Kang Y (2008) A variable step size INC MPPT method for PV systems. IEEE Trans Ind Electron 55(7):2622–2628
12. Xiao W, Elnosh A, Khadkikar V, Zeineldin H (2011) Overview of maximum power point tracking technologies for photovoltaic power systems. In: 37th annual conference of IEEE IES 2011. IECON 2011, pp 3900–3905
13. Bouchafaa F, Hamzaoui I, Hadjammar A (2011) Fuzzy logic control for the tracking of maximum power point of a PV system. Energy Procedia 6:633–642
14. Karlis AD, Kottas TL, Boutalis YS (2007) A novel maximum power point tracking method for PV systems using fuzzy cognitive networks (FCN). Electr Power Syst Res 77(3–4):315–327
15. Liao C-C (2010) Genetic k-means algorithm based RBF network for photovoltaic MPP prediction. Energy 35(2):529–536
16. Chen LR, Tsai CH, Lin YL, Lai YS (2010) A biological swarm chasing algorithm for tracking the PV maximum power point. IEEE Trans Energy Convers 25(2):484–493
17. Kadri R, Andrei H, Gaubert J-P, Ivanovici T, Champenois G, Andrei P (2012) Modeling of the photovoltaic cell circuit parameters for optimum connection model and real-time emulator with partial shadow conditions. Energy 42(1):57–67
18. Becherif M, Hissel D (2010) MPPT of a PEMFC based on air supply control of the motocompressor group. Int J Hydrogen Energy 35(22):12521–12530
19. Esram T, Kimball JW, Krein PT, Chapman PL, Midya P (2006) Dynamic maximum power point tracking of photovoltaic arrays using ripple correlation control. IEEE Trans Power Electron 21(5):1282–1291
20. Ariyur KB, Krstić M (2003) Real-time optimization by extremum-seeking control. Wiley, New York
21. Gelbert G, Moeck JP, Paschereit CO, King R (2012) Advanced algorithms for gradient estimation in one- and two-parameter extremum seeking controllers. J Process Control 22:700–709
22. Azar FE, Perrier M, Srinivasan B (2011) A global optimization method based on multi-unit extremum-seeking for scalar nonlinear systems. Comput Chem Eng 35:456–463
23. Manzie C, Krstić M (2009) Extremum seeking with stochastic perturbations. IEEE Trans Autom Control 54:580–585
24. Guay M, Dochain D, Perrier M (2004) Adaptive extremum seeking control of continuous stirred tank bioreactors with unknown growth kinetics. Automatica 40:881–888
25. Bizon N, Oproescu M, Raducu M, Constantinescu LM (2013) The extremum seeking control based on band pass filter for the dither signal processed in the control loop. Int J Tech Phys Probl Eng (IJTPE) 16(5/3):133–143

26. Bizon N (2013) Energy harvesting from the FC stack that operates using the MPP tracking based on modified extremum seeking control. Appl Energy 104:326–336
27. Bizon N (2013) FC energy harvesting using the MPP tracking based on advanced extremum seeking control. Int J Hydrogen Energy 38(4):1952–1966
28. Bizon N (2012) Distributed generation systems integrating renewable energy resources. Nova Science Publishers Inc., New York
29. Musio F et al (2011) PEMFC system simulation in MATLAB–Simulink® environment. Int J Hydrogen Energy 36(13):8045–8052
30. Linares JI, Herranz LE, Moratilla BY (2011) Maximum efficiency of direct energy conversion systems. Application to fuel cells. Int J Hydrogen Energy 36(18):11871–11885
31. Ahluwalia RK, Wang X (2005) Direct hydrogen fuel cell systems for hybrid vehicles. J Power Sources 139:152–164
32. Ahmed NA, Al-Othman AK, Al-Rashidi MR (2011) Development of an efficient utility interactive combined wind/photovoltaic/fuel cell power system with MPPT and DC bus voltage regulation. Electr Power Syst Res 81(5):1096–1106
33. Mehrdad E, Yimin G, Ali E (2010) Modern electric, hybrid electric, and fuel cell vehicles, vol 15. CRC Press, Boca Raton
34. Degrenne N, Buret F, Allard B, Bevilacqua P (2012) Electrical energy generation from a large number of microbial fuel cells operating at maximum power point electrical load. J Power Sources 205:188–193
35. Soltani M, Bathaee SMT (2010) Development of an empirical dynamic model for a Nexa PEM fuel cell power module. Energy Convers Manag 51(12):2492–2500
36. Ramos-Paja CA, Spagnuolo G, Petrone G, Giral R, Romero A (2010) Fuel cell MPPT for fuel consumption optimization. In: IEEE international symposium on circuits and systems, pp 2199–202
37. Giustiniani A, Petrone G, Spagnuolo G, Vitelli M (2010) Low-frequency current oscillations and maximum power point tracking in grid-connected fuel-cell-based systems. IEEE Trans Ind Electron 57(6):2042–2053
38. Bizon N, Radut M, Oproescu M (2015) Energy control strategies for the fuel cell hybrid power source under unknown load profile. Energy 86:31–41
39. Bizon N (2014) Load-following mode control of a standalone renewable/fuel cell hybrid power source. Energy Convers Manag 77:763–772
40. Krstić M (2000) Performance improvement and limitations in extremum seeking. Syst Control Lett 39(5):313–326
41. Krstić M, Wang H-H (2000) Design and stability analysis of extremum seeking feedback for general nonlinear systems. Automatica 36(2):595–601
42. Bizon N (2014) Tracking the maximum efficiency point for the FC system based on extremum seeking scheme to control the air flow. Appl Energy 129:147–157
43. Tirnovan R, Giurgea S (2012) Efficiency improvement of a PEMFC power source by optimization of the air management. Int J Hydrogen Energy 37(9):7745–7756
44. Segura F, Andújar JM (2012) Power management based on sliding control applied to fuel cell systems: a further step towards the hybrid control concept. Appl Energy 99:213–225
45. Wong KH et al (2011) A theoretical study of inlet relative humidity control in PEM fuel cell. Int J Hydrogen Energy 36(18):11871–11885
46. Bizon N, Oproescu M, Raceanu M (2015) Efficient energy control strategies for a standalone renewable/fuel cell hybrid power source. Energy Convers Manag 77:768–772
47. Bizon N (2014) Improving the PEMFC energy efficiency by optimizing the fuelling rates based on extremum seeking algorithm. Int J Hydrogen Energy 39(20):10641–10654
48. Loo KH, Zhu GR, Lai YM, Tse CK (2011) Development of a maximum-power-point tracking algorithm for direct methanol fuel cell and its realization in a fuel cell/supercapacitor hybrid energy system. In: 8th international conference on power electronics and ECCE Asia, pp 1753–1760

49. Woodward L, Perrier M, Srinivasan B, Pinto RP, Tartakovsky B (2010) Comparison of real-time methods for maximizing power output in microbial fuel cells. AIChE J 56(10):2742–2750
50. Woo CH, Benziger JB (2007) PEM fuel cell current regulation by fuel feed control. Chem Eng Sci 62:957–968
51. Zhang C, Ordóñez R (2012) Extremum-seeking control and applications: a numerical optimization-based approach. Springer, London
52. Bizon N (2010) On tracking robustness in adaptive extremum seeking control of the fuel cell power plants. Appl Energy 87(10):3115–3130
53. Chang YA, Moura SJ (2009) Air flow control in fuel cell systems: an extremum seeking approach. In: American Control Conference, pp 1052–1059
54. Bower W, Whitaker C (2002) Certification of photovoltaic inverters: the initial step toward PV system certification. In: IEEE conference photovoltaic specialists, pp 1406–1409
55. Zhong Z-D, Huo H-B, Zhu X-J, Cao G-Y, Ren Y (2008) Adaptive maximum power point tracking control of fuel cell power plants. J Power Sources 176:259–269
56. Tang Y, Yuan W, Pan M, Li Z, Chen G, Li Y (2010) Experimental investigation of dynamic performance and transient responses of a kW-class PEM fuel cell stack under various load changes. Appl Energy 87:1410–1417
57. Ramos-Paja CA, Giral R, Martinez-Salamero L, Romano J, Romero A, Spagnuolo G (2010) A PEM fuel-cell model featuring oxygen-excess-ratio estimation and power-electronics interaction. IEEE Trans Ind Electron 57(6):1914–1924
58. Springer TE, Zawodzinski TA, Gottesfeld S (1991) Polymer electrolyte fuel cell model. J Electrochem Soc 138(8):2334–2342
59. Wang Y, Chen KS, Mishler J, Cho SC, Adroher XC (2011) A review of polymer electrolyte membrane fuel cells: technology, applications, and needs on fundamental research. Appl Energy 88(4):981–1007
60. Gou B, Na WK, Diong B (2010) Fuel cells: modeling, control, and applications, vol 6. CRC Press, New York
61. Larminie J, Dicks A (2000) Fuel cell systems explained, 1st edn. Wiley, Chichester
62. Zenith F, Skogestad S (2007) Control of fuel cell power output. J Process Control 17:333–347
63. Pukrushpan JT, Stefanopoulou AG, Peng H (2004) Control of fuel cell power systems: principles, modeling and analysis and feedback design. Springer, London
64. Wahdame B, Candusso D, Kauffmann J-M (2006) Study of gas pressure and flow rate influences on a 500 W PEM fuel cell, thanks to the experimental design methodology. J Power Sources 156:92–99
65. Kolavennu PK, Palanki S, Cartes DA, Telotte JC (2008) Adaptive controller for tracking power profile in a fuel cell powered automobile. J Process Control 18:558–567
66. Bao C, Ouyang M, Yi B (2006) Modeling and control of air stream and hydrogen flow with recirculation in a PEM fuel cell system—II. Linear and adaptive nonlinear control. Int J Hydrogen Energy 31:1897–1913
67. Choe S-Y (2008) Dynamic simulator and controls for a PEM fuel cell power system. World Electr Veh J 2(3):46–62
68. Kunusch C, Puleston PF, Mayosky MA, Riera J (2009) Sliding mode strategy for PEM fuel cells stacks breathing control using a super-twisting algorithm. IEEE Trans Control Syst Technol 17(1):167–173
69. Feroldi D, Serra M, Riera J (2009) Energy management strategies based on efficiency map for fuel cell hybrid vehicles. J Power Sources 190:387–401
70. Dochain D, Perrier M, Guay M (2011) Extremum seeking control and its application to process and reaction systems: a survey. Math Comput Simul 82:369–380
71. Chen P-C (2011) The dynamics analysis and controller design for the PEM fuel cell under gas flow rate constraints. Int J Hydrogen Energy 36(4):3110–3122

72. Chen P-C (2011) Output-feedback voltage tracking control for input-constrained PEM fuel cell systems. Int J Hydrogen Energy 36(22):14608–14621
73. Tan Y, Nesic D, Mareels I (2006) On non-local stability properties of extremum seeking control. Automatica 42(6):889–903
74. Tan Y, Nesic D, Mareels I (2008) On the choice of dither in extremum seeking systems: a case study. Automatica 44:1446–1450

Chapter 13
Energy Efficiency of PEM Fuel Cell Hybrid Power Source

Nicu Bizon and Mircea Raceanu

Abstract The chapter deals with a single DC bus hybrid configuration of a power source required for an automotive application. Such system architecture is the best choice for interconnecting multiple energy sources in order to meet the load profile in the most efficient way. This work analyzes a new PEM Fuel Cell stack-Hybrid Power Source (PEMFCs-HPS) topology consisting of a 5 kW PEMFC stack (primary source of power) and a bank of ultracapacitors (130 F, 56 V, 57 Wh) (auxiliary power source) to fulfill the high energy and high power requirements of the vehicle applications, wherein the power demand is impulsive rather than constant. This topology uses three programmable unidirectional DC/DC converters which connects the PEMFCs, the UC and the programmable electronic load. The energy management strategy (EMS) for different power sources has great effect in decreasing the fuel consumption, increasing the performance and the lifetime of the fuel cells. The proposed EMS is based on the FC efficiency map and on the state of charge of the UC. The EMS is used to split the power between the PEMFCs and the UC in the hybrid arrangement to fulfil the power requirement, which depends on the operating conditions considering the optimum power of PEMFCs and UC. An algorithm the EMS is able to achieve the steady-state PEMFCs operating with minimum hydrogen consumption and the UC state of charge (SoC) maintaining at values higher than 20%. The system ability to efficiently follow the load variations under that EMS is also presented. The consumption of hydrogen was reduced by

N. Bizon (✉)
University of Pitesti, Targu din Vale Street no. 1, 110040 Pitesti, Romania
e-mail: nicu.bizon@upit.ro

M. Raceanu
National Research and Development Institute for Cryogenics and Isotopic Technologies - ICSI Rm.Valcea, Uzinei Street no. 4, P.O. Box Râureni 7, 240050 Râmnicu Vâlcea, Romania
e-mail: mircea.raceanu@icsi.ro

N. Bizon · M. Raceanu
University Politehnica of Bucharest, Splaiul Independentei Street no. 313, 060042 Bucharest, Romania
e-mail: nicubizon@yahoo.com

N. Bizon et al. (eds.), *Energy Harvesting and Energy Efficiency*,
Lecture Notes in Energy 37, DOI 10.1007/978-3-319-49875-1_13

11.8% in comparison with the system without UC. The experimental data acquisition system is monitored and controlled using the NI Labview® software with the NI Compact-RIO hardware.

Keywords Hybrid power source · PEM fuel cell · Ultracapacitor · Energy management

Abbreviation and Acronyms

PEMFCs	Proton Exchange Membrane Fuel Cell stack
UC	Ultracapacitor
SoC	State of Charge
EMS	Energy Management Strategy
HPS	Hybrid Power Sources
BoP	Balance of Plant
DC	Direct Current

13.1 Introduction

Due to their operating principle through which hydrogen and oxygen are electrochemically converted into electricity, with high conversion efficiency, low temperature operation and practically no pollutant emissions, Proton Exchange Membrane Fuel Cell stack (PEMFCs) became very attractive for both mobile and stationary power applications [1–3].

Unfortunately, PEMFCs are characterized by relatively poor dynamics, being unable to follow fast transients in power demand. Besides that, it was observed that operating a fuel cell on pulsed load causes its relatively fast degradation [4, 5]. One of the main weak points of the PEMFCs is its slow dynamics mainly due to the hydrogen and air supply subsystems [6, 7]. The fuel starvation phenomenon will occur during fast load demand, which will cause a high voltage drop in a short time [8]. To solve this problem, the PEMFCs must to be efficiently operated in conjunction with other energy sources or energy storage systems [9, 10].

Taking into account these aspects we can conclude that adding on an energy storage system (ESS) to the PEMFCs power source is a necessary step [11, 12]. These are some reasons of adding an energy storage system (ESS) to the PEMFCs power system. The PEMFCs/ESS hybrid could be operated so that PEMFCs should meet the load power demand at steady-state and ESS (Energy Storage System) is buffering power transients [13].

Rechargeable batteries are the most common devices used for electric energy storage, but recent advances in manufacturing and materials technology made that ultracapacitors (UC) into be considered strong competitors. Unlike battery storage, based on chemical reactions, which gives a slower energy transfer process in both

directions, UCs store energy electrostatically and have very low internal resistance, resulting in very fast charge/discharge rates with very little power loss and great overall efficiencies [3, 14]. It seems that the energy density remains the last advantage that batteries have over ultracapacitors, but only transitory, new better materials resulting in narrowing the gap between them.

Hybrid Power Sources (HPS) in general and PEMFCs/UC sources in particular are currently being intensively investigated because of their use in stationary and vehicular applications [4, 15, 16]. PEMFCs are designed for continuous energy supply and are best operated at constant operating conditions [17]. They work poorly in the presence of power fluctuations and cannot handle high power demands. UCs, on the other hand, have relatively very low energy densities and very high power densities. UCs are used for energy storage and to protect the FC from power transients. The purpose of any hybrid power sources that involves more than one device is to put together the advantage of the various devices in one single system and increase the fuel cell operating life and improve the device efficiency [18].

In specialized literature, passive and active hybrid configurations are usually presented separately. The passive hybrid configuration is based on parallel connection between main and auxiliary sources. In a passive configuration the choice of energy management algorithms are greatly limited [19]. Active hybrid configuration needs the introduction of energy conversion steps between main and auxiliary sources. This provides great flexibility during design and different configurations can be realized. Through the power converters, power-sharing between the main and auxiliary source can be successfully implemented.

Various control strategies to manage energy in a hybrid system [20–22] have been proposed in various applications. In some papers [23, 24], EMS are applied to high-power electric vehicles based on FC, battery and UC. Other papers [25–28] use control strategies based on fuzzy logic control, which determine the operating point of the power converter FC depending on the load power and the battery state of charge (SoC).

In the paper [29] three energy management strategies for fuel cell hybrid vehicles were presented. The strategies are based on the knowledge of the fuel cell efficiency map: two of them are heuristic type strategies and the third strategy is based on constrained nonlinear programming.

Due to the different characteristics of the various sources of energy, efficiency and fuel economy the HPS mainly depend on an adequate strategy for the energy management. In this chapter, the Energy Management Strategy between PEMFCs and UC is based on setting a number of power sub-regions of 1000 W in the range of 1–5 kW, in which we know the point of maximum efficiency, respectively the gas consumption in those sub-regions. Each sub-region has a maximum efficiency point while PEMFCs works in stationary conditions, at the lowest consumption of the hydrogen. Depending on the load and on the UC state of charge (SoC > 20%) the power that is generated by the PEMFCs is established, according to the fuel cell power and efficiency map the hydrogen and air supply flows are established. The EMS algorithm identifies the sub-region in which the PEMFCs works with the maximum efficiency. If the power supplied by the fuel cell is greater than the power

loads, the EMS will manage the UC surplus power through the DC/DC charge UC and this charging is controlled. The EMS algorithm is developed in NI LabVIEW using a state machine architecture, implemented in FPGA to run at a speed of execution of 100 μs. The novelty of this article is to use a DC/DC converter which is connected between PEMFCs and UC, and is designed to load the power excess in UC, thus making the PEMFCs to operate in regime static. The decreasing of hydrogen consumption depends on the operation of PEMFCs in the maximum efficiency point in that sub-region. The EMS algorithm proposed is tested experimentally and the results show favourable performances.

The chapter is organized as follows: Sect. 13.2 introduces the configuration of the HPS and describes the experimental setup including the NI Compact-RIO hardware; Sect. 13.3 proposes the EMS based on the fuel cell efficiency map and on the state of charge of the UC including the NI Labview software; In Sect. 13.4, the experimental results are presented and discussed; and finally the conclusions are summarized in Sect. 13.5.

13.2 Hybrid Power Sources Design

13.2.1 General Architecture of the Hybrid Power Source

In order to increase the power of the fuel cells from 10 to 90% is about 2 s are required [30]. On the other hand, the sudden variations of the load power could lead to a dramatic decrease of the life of cell. Hybridized fuel cell power sources for automotive applications can tolerate in this way much more transitory than a single cell. The hybrid system has a much better dynamic response, thus contributing to increasing the lifetime of the fuel cells.

Figure 13.1 shows a generic HPS with two power flows (FC and UC), the required power load of the fuel cell being provided by a unidirectional converter.

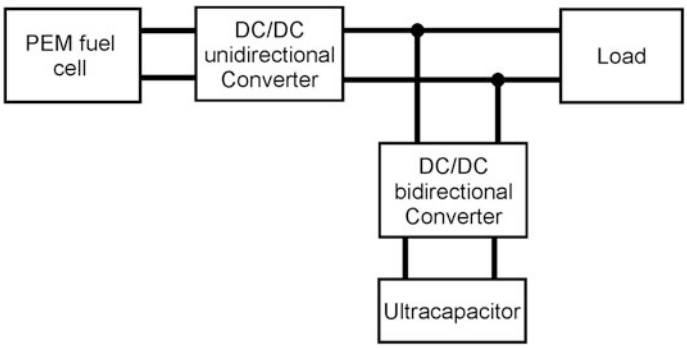

Fig. 13.1 Generic architecture of the FC/UC power source

UC is directly connected to the load through a bidirectional converter. It provides a good suppression of transition and peak power. The energy stored in the UC is not limited to the fuel cell or the load. The power of each source can be controlled. UC shows its usefulness when braking regenerative.

The disadvantage of this architecture is that the fuel cell connection always aims the load profile. The power management strategy is more difficult for small variations in the load. To remove these disadvantages, between fuel cell and UC, an unidirectional converter DC/DC was inserted. The role of this converter is to guide the surplus power from the fuel cell to the UC.

13.2.2 Proposed Architecture of the Hybrid Power Source

A hybrid fuel cell/ultracapacitor architecture (photos in Fig. 13.2) is proposed for a FC power system intended to be used in an automotive application. A single DC BUS topology was chosen because it seems to be the best choice for interconnecting multiple energy sources in order to meet the load profile in the most efficient way [31].

The power system, schematically presented in Fig. 13.3, is based on a 40 cells, 5 kW, 40 V NEDSTACK PEM Fuel cell stack and a 23 cells, 130 F, 56 V MAXWELL Ultracapacitor bank.

The PEMFC stack is fed with humidified hydrogen and air, at a stoichiometry of 1.25 and 2, respectively. The load of the system is represented by a 60 V, 240 A, 5 kW IT8518C electronic load.

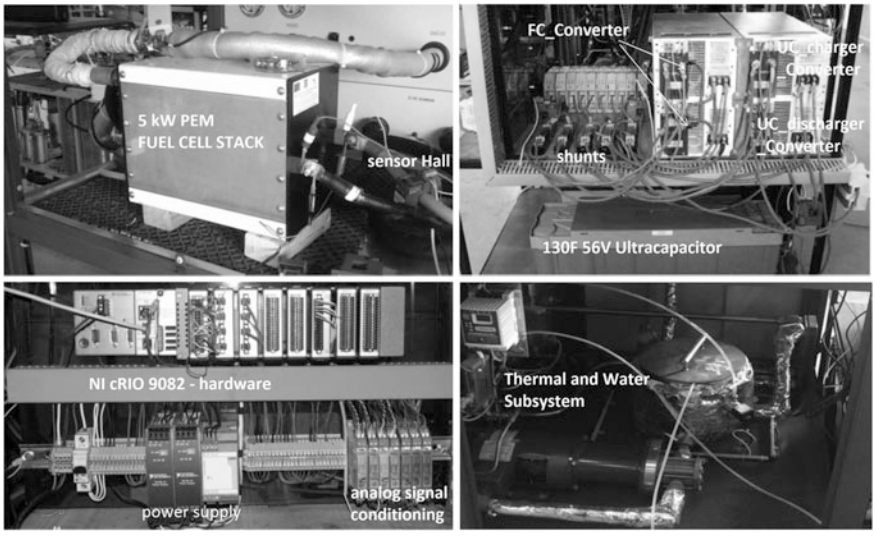

Fig. 13.2 Test bench PEMFCs/UC—Hybrid Power Sources for real-time control

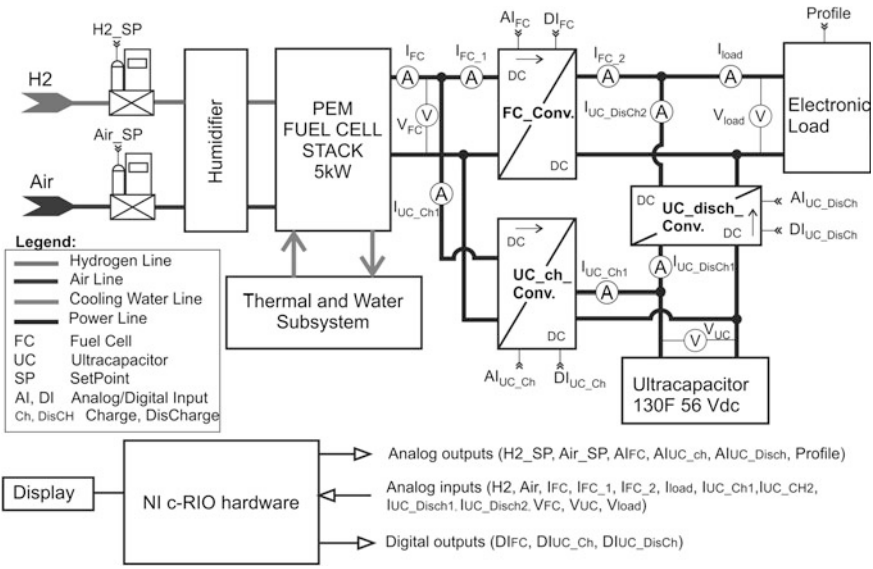

Fig. 13.3 Proposed block diagram of the FCS/UC power source

Since the power system has two sources, it takes at least two converters to control the bus voltage and the power split between the two sources. The independent control through the DC/DC converters of both FC and UC allows combining the energy sources on a BUS, each operating at a different voltage. As it is shown in Fig. 13.2, a unidirectional DC/DC boost converter is used to connect the fuel cell stack to the bus (DC/DC boost FC_Conv), and two unidirectional DC/DC boost converters are used to connect the ultracapacitor bank to the FCs for charging (DC/DC boost UC_ch_Conv) and to the DC BUS for discharging (DC/DC boost UC_disch_Conv), respectively. The latter ones could be replaced by a single bi-directional converter.

The power system objective is to meet the load power demand at the lowest fuel consumption and to reduce the transitional demands for the PEMFCs, simultaneously with keeping the UC State of Charge (SoC) above 20%. SoC is defined as the UC voltage multiplied by 100 over its maximum rated voltage and ranges from 0% at no charge to 100% at full charge.

13.2.3 PEM Fuel Cell Stack

The main part of the Hybrid Power Sources is the fuel cell stack, where the electrochemical reaction between the fuel (hydrogen) and the oxidant (usually oxygen from air) occurs, producing electricity and heat. The behaviour of the PEM fuel cell stack depends of particularly variables. A Nedstack P5.0-40 PEMFCs,

Table 13.1 Product specifications and operating conditions

Specification	Value
Active area	250 cm^2
Stack output rated parameters	5000 W @ 36 VDC
Stack maximum voltage	40 VDC
Cell voltage	0.95–0.5 V per cell
Minimum allowable cell voltage	0.3 V for the lowest performing cell
Current range	0–230 A
Maximum allowable current	230 A
Nominal operating temperature	65 °C
MEA pressure difference	<0.3 bar

composed from 40 cells for a nominal maximum power of 5 kW, operated at atmospheric pressure to about 3 bar, was used for experimental investigation [32]. The operating voltage of the stack is a function of current and decreased with increasing power (Table 13.1).

The test bench is represented by a hydrogen supply subsystem to the anode, air supply subsystem to the cathode, de-ionized water serving as coolant in the cooling channel, de-ionized water to humidify the hydrogen and the air flow, a programmable electronic load, DC/DC converters, a control process and an interface.

High purity hydrogen (99.995%) and compressed air are used as a fuel and as an oxidant. The hydrogen is supplied as fuel and air is supplied as oxidant reactant. Both reactants are controlled at the entrance of the fuel cell stack with two mass flow controllers, located before the bubble humidifiers. Pressures of the anode and cathode sides are controlled by back pressure regulators (Alicat Instruments). The voltage set point for the flow rates and pressures are connected to the NI 9263 analog output module. Humidity levels are verified time to time with downstream humidity sensors. The maximum mass flow rates are calculated at the maximum power demand, maximum stoichiometric ratios, and the minimum cell voltage, taking into account the specification of the 5000 W PEM fuel cell. The minimum cell voltage is 0.5 V because any voltage below this value may result in deterioration of the PEM fuel cell stack.

An important parameter namely the temperature is measured by T-type thermocouples inserted in a NI 9213 thermocouple input module system and regulated by a cooling water circuit which includes a water pump, a needle valve for flow water control, a cold exchanger and a heater. Another water circuit is used to condense the water in the gaseous phase.

The tests were carried out by initialling the PEMFCs in flow-through anode fuelling mode. This operation was necessary to estimate the current/voltage reference characteristics. The next step was focused on the comparison between the PEMFCs as single equipment and the PEMFCs & BoP Balance of Plant (BoP) assembly.

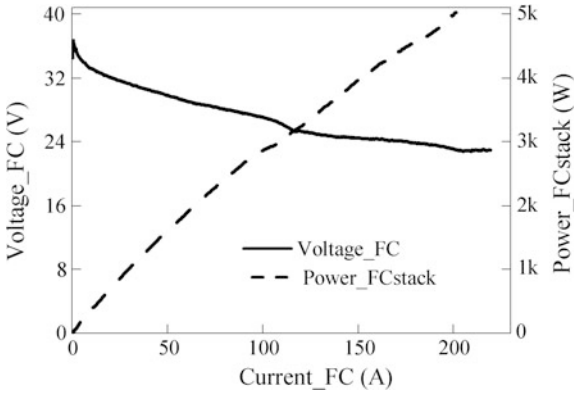

Fig. 13.4 Polarization curve for 5 kW PEM Fuel Cell power stack [33]

The reference characteristics of the NEDSTACK FCS were determined by supplying pure hydrogen at anode and air at cathode, in the following conditions:

- Anode supply stoichiometry of 1.25 and cathode stoichiometry of 2.0;
- Relative humidity: 80–100% for gaseous phase;
- Stack temperature: 65 °C.

The obtained polarization curve (Fig. 13.4), illustrates the power versus current characteristic. We have to mention that the hydrogen and air flow rates are proportional to the current produced by the stack. Moreover, the consumptions of reactants according to the power fuel cells, is presented in Fig. 13.5.

The polarization curve obtained herein provides the ideal electrochemical results from the fuel cell stack. It could be considered as reference point for adjusting of the stoichiometric ratios, during sudden load. During this test the PEM fuel cell stack voltage decreases proportionally with the current and reaches the minimum corresponding to the maximum current. The PEM fuel cell stack power increases proportionally with the current and the maximum is obtained at the maximum current (230 A) [6, 33].

13.2.4 Ultracapacitor

Ultracapacitors are devices for storing energy much more attractive than batteries, which have a much higher yield, higher power density and the number of charge/discharge up to a million times. The energy density of UC-s is much higher than traditional electrolytic capacitors, therefore, they can act as a bridge between the high power capacitors and high energy batteries.

The ultracapacitor used in this application is produced by Maxwell. The ultracapacitor electrolyte uses as an organic substance that is called acetonitrile. This

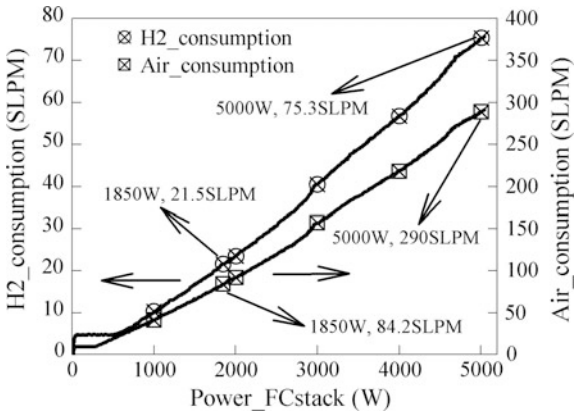

Fig. 13.5 The hydrogen and air consumption depending on the PEMFCs power

Table 13.2 Specification of the ultracapacitor

Manufacturer	Maxwell
Type	BMODO130-P056
Rated voltage	56 V
Rated capacitance C_{UC}	130 F
Maxim ESR DC initial	8.1 mΩ la 100 A
Specific energy	3.1 Wh/kg
Specific power	2,600 W/kg
Number of cells	23
Stored energy	57 Wh
Mass	18 kg

allows a higher operating voltage than an aqueous electrolyte. Organic electrolyte has a lower freezing point allowing use in a wider range of temperatures (−40 to +40 °C). Carbon electrodes are activated and use as a cellulose separator. Its specifications are shown in Table 13.2. The reason for the high nominal voltage VUC, max = 56 V means that several cells are connected in series in order to form a module or a bank of ultracapcitoars. Next it will be labelled "UC—ultracapacitor".

The ultracapacitor must not be exploited over the specified maximum voltage. If it accidentally exceeds the upper limit of the mentioned voltage, it will result in shortened life and, in extreme cases, flue gas accumulated in the cell, due to overvoltage condition. To ensure maximum performance and longer life, the operating voltage should be between nominal voltage (56 V) and half the voltage (28 V). Usually in this operating range, the energy available is about 75%. Figure 13.6 shows the ultracapacitor characteristics of discharge at different current constant values.

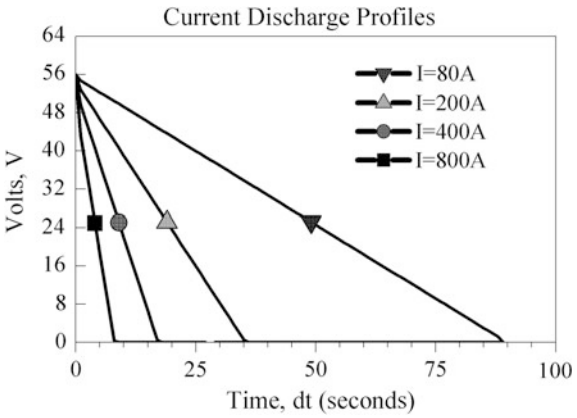

Fig. 13.6 Current discharge profiles for different values

13.2.5 DC/DC Boost Converters

Our application is built with three DC/DC unidirectional converters: the first converter is disposed between the PEMFCs and load, it has an output power of 5000 W (DC/DC boost FC_Conv.); the second converter is placed between PEMFCs and UC, it has a power of 1,250 W, and it is designed to load the excess power from the PEMFCs in the UC (DC/DC boost UC_ch. Conv.); the third converter is connected between UC and load, and it is designed to supplement the power flow, when the PEMFCs power is smaller than the load power, the power output being 1,250 W (DC/DC boost UC_Disch. Conv.). The DCC5500 type converters are built by the company Ripenergy.

The characteristics of the converter are: variable input voltage: 20–40 V; output voltage: 40–60 V; adjustable output voltage via 0–10 V input signal; remote shut down with digital output from PLC (Programmable Logic Controller) and efficiency: 75–94% depending on input/output combination.

13.2.6 NI Compact-RIO Hardware

The test station is fully automated using a supervisory control and data acquisition system that utilizes the NI CompactRIO 9082 platform. The system consists of an embedded controller for communication and processing, a reconfigurable chassis housing the user-programmable FPGA and graphical LabVIEW software for rapid real-time, windows and FPGA programming.

The system has two NI 9205 analog input modules to read the analog parameters of the fuel cell stack, one NI 9263 analog output module for control mass-flow/pressure controllers and DC/DC converters, one NI 9213 thermocouple input module, one NI 9481 relay module for solenoid valve control and one NI 9401 digital I/O module to

output the PWM (pulse-with modulation) for the heating SSR (solid state relay) and coupling/decoupling of the DC/DC converters.

The aim of the hardware system was to control the power between the PEMFCs and the UC, which depends on the operating conditions by taking into account the optimum power of the PEMFCs and the UC state of charge, by adjusting of their control loops of the DC/DC converters. The reconfigurable input and output functionality of the cRIO-9082 allowing a rapid implementation of real time (RT) and field programmable gate array (FPGA) capabilities, with a closed loop proportional integral derivative (PID) control scheme for the hydrogen and air/oxygen mass flows using a high-level LabView programming interface.

13.3 Energy Management Strategy

13.3.1 Efficiency Analysis for the Hybrid PEMFCs/UC Power Source

The load power at all times, $P_{load}(t)$, has to be supplied by the FC power, $P_{FC}(t)$, and by the UC power, $P_{UC}(t)$, so that the power balance on the DC bus must be fulfilled permanently.

At every moment,

$$P_{FC}(t) \cdot \eta_{FC} \cdot \eta_{FC/B} + P_{UC}(t) \cdot \eta_{UC} \cdot \eta_{FC/UC} \cdot \eta_{UC/B} = P_{load}(t), \forall t \qquad (13.1)$$

where: $\eta_{FC}, \eta_{FC/B}, \eta_{UC}, \eta_{FC/UC}, \eta_{UC/B}$ are respectively the efficiency of the FC, the efficiency of the power converter connecting the FC to the BUS, the efficiency of the UC, the efficiency of the UC charging power converter and the efficiency of the power converter connecting the UC to the BUS.

In order to set up an Energy Management Strategy (EMS) for the hybrid PEMFCs/UC power source that meets the above mentioned objective, the 5 kW PEMFCs efficiency versus load power characteristic was determined.

As presented in the Fig. 13.7, there is an operational zone where the PEMFCs efficiency is the highest, and another zone, where the PEMFCs efficiency is unacceptably low. This efficiency map shape at low power is due to the need of using almost all the generated power to compensate the parasitic power losses.

The implemented EMS is intended to solve the problem of the power split between the PEMFCs and the UC, in compliance to Eq. (13.1) and in accordance with the following constraints:

- restricted PEMFCs power dynamics to avoid damage the stack;
- using UC state of charge as a parameter to be maintained in the fixed limits: 20–100%.

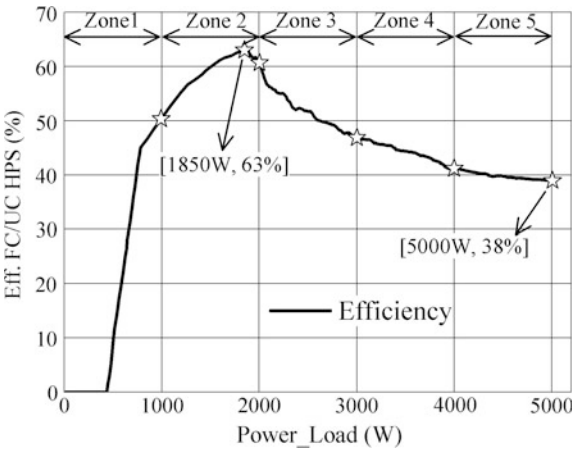

Fig. 13.7 Fuel cell efficiency versus load demand

In addition to these constraints, the hydrogen consumption has to be monitored.

As we already mentioned, a PEMFCs could not operate alone and some sub-systems to provide and control the operating conditions and parameters are necessary, but not limited to, pumps, blowers, heat-exchangers, sensors and controllers, all being named BoP. The power conditioning system, including the DC/DC converter, is consuming power too [33].

The PEMFCs efficiency is defined as the ratio between the maximum generated power and the heating power of the hydrogen consumed at anode to generate that power [34].

$$\varepsilon_{st} = \frac{P_{st}}{P_{H_2}} = I_{st} \cdot \frac{V_{st}}{M_{H_2}} \cdot m_{H_2} \cdot \Delta h \tag{13.2}$$

where subscript *st* refers to the stack and H_2 refers to hydrogen, ε means efficiency, *P*—power, *I*—current, *V*—voltage, *m*—mass flow, *M*—molar mass, and *Δh*—enthalpy.

The consumed hydrogen mass flow is measured, and the generated power results from the measured generated voltage multiplied by the measured generated current.

The fuel cells based energy system efficiency is defined as the ratio between the load power and the heating power of the hydrogen consumed at anode to generate that power.

$$\varepsilon_{system} = \frac{P_{load}}{P_{H_2}} = I_{load} * \frac{V_{load}}{M_{H_2}} * m_{H_2} * \Delta h \tag{13.3}$$

where subscript *system* refers to the PEMFCs & BoP assembly and *load* refers to the energy user.

As concerning the (PEMFCs & BoP) system the efficiency is zero for the stack generated power lower than 0.45 kW, because all the generated power is used for

BoP supply, and it begins to rise, reaching up to 63% for a generated power of 1850 W. Over that limit, a slight decrease in system efficiency is noticed, because of the greater increase in BoP supply when the generated power is increasing.

13.3.2 EMS Algorithm

The EMS algorithm is based on the above mentioned PEMFCs efficiency map and was implemented in one main routine and five subroutines.

In Fig. 13.8 the main routine schematic is presented. This routine is programmed into a technical "state machine" and it is called the software interface (Fig. 13.10). The first block decision of the routine, *Run Control*, if it is true (controlled from the software interface) then the EMS algorithm is ran. The last block of decision, *Stop Control*, if it is true then the controller switches the safety system (gas flow stops and lock converters). As a method to reduce the PEMFCs transients, its power range was divided in 5 equal sub-domains (1000 W), depending on the load power, P_L, the algorithm execute one of the sequences from 1 to 5. The PEMFCs power on each of them was being set to the value corresponding to the local maximum efficiency and allowing in this way a smooth transition. In order to avoid operating

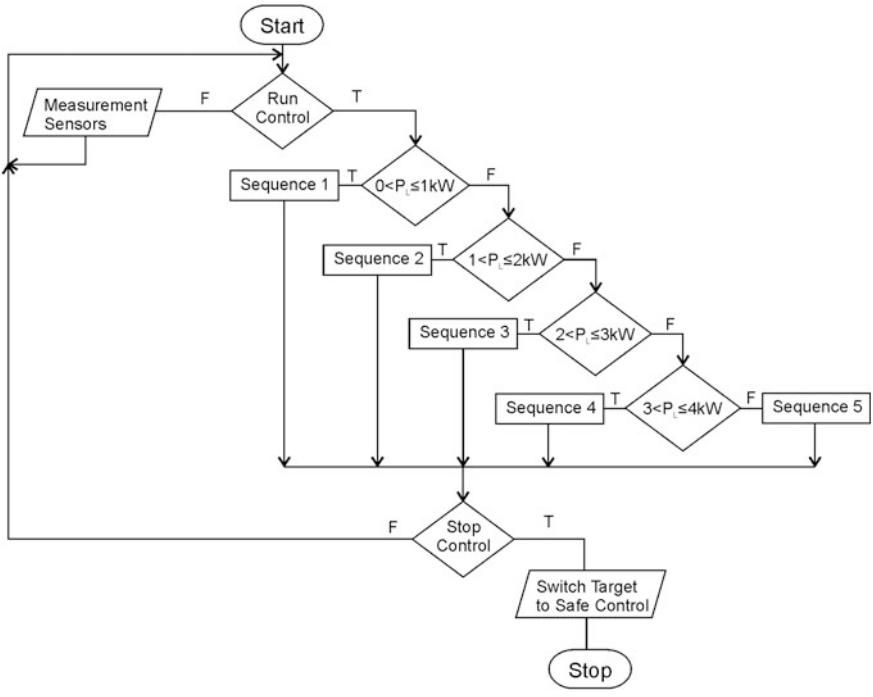

Fig. 13.8 EMS main routine

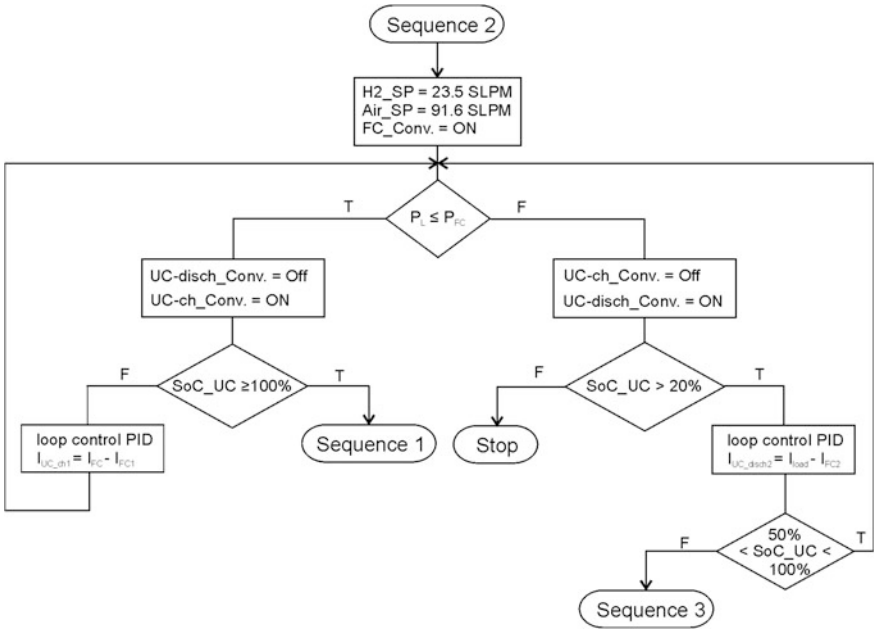

Fig. 13.9 Schematic of the sub-routine 2

the PEMFCs in the low efficiency zone, at the power system switch-on the PEMFCs operational point will be always set to the highest efficiency point by feeding it with the corresponding hydrogen and air flows.

In the Fig. 13.9 one of the sequences is presented (Sequence 2) was chosen as an example, but it should be noted that all sequences are logically identical. The input signals of the EMS algorithm are SoC of the ultracapacitor (*SoC_UC*), fuel cell power (P_{FC}), load power (P_L), fuel cell total current (I_{FC}), load current (I_L), charge current in UC (I_{UC_ch1}), discharge current from UC (I_{UC_disch2}), fuel cell current before FC converter (I_{FC1}), fuel cell current after FC converter (I_{FC2}) and output signals are hydrogen and air flow values (*H2_SP, Air_SP*) and the reference of the DC/DC converter for switching (*FC_Conv, UC-ch_Conv, UC-disch_Conv*).

For each PEMFCs power sub-domain, if the load power required exceeds the available PEMFCs power, the difference will be supplied by discharging the UC, as long as it meets the SoC imposed restriction, namely to maintain it above 20%. The energy level stored in UC is considered sufficient to start the UC discharging as soon as SoC level reaches 50%. For $50\% \geq \text{SoC} \geq 20\%$, the EMS commands the PEMFCs power to go to the upper level and to continue the UC charging.

If the set FC power level exceeds the load power needed, then the UC will be charged until it will become fully charged.

13.3.3 NI Labview Software Development for Control and Monitoring of PEMFCs/UC-HPS

Dedicated software has been developed in the NI Labview 2015 environment to control the test station operation and acquire experimental data. All DC/DC unidirectional converters (analog output and digital output) and mass flow controllers (hydrogen and air) are controlled by the software. The current, voltage and gas flow rates are measured. The software allows the visualization data in real time through a Graphical User Interface. All data is saved in a database at a frequency of 0.2 Hz. Figure 13.10 includes a screen shot of the test station software front panel along the location of the controls and indicators for each subsystem. The block diagram (Fig. 13.11) is a graphical representation of the monitoring and control software.

13.4 Experimental Results

Experimental tests were performed on a known load profile. This profile was implemented by programming an electronic load IT8518C (5 kW air cooled) profile consisting of 8 segments, which have been chosen so that, to have all cases the algorithm implemented EMS (Fig. 13.12). Thus, the segment 1 is the scroll for 15 s with a rated load of 1,200 W (zone 2 from the map efficiency FC); thereafter, accelerating the dP/dt 80 W/s variation power is passed in segment 2 (zone 2 + zone 3), segment 3 there for 45 s at a constant power of 2,400 W (zone 3), then is passed in segment 4 with ascension in ramp to 3,100 W for 35 s (zone 3 and 4), the segment 5 is 50 s at a power of 3,100 W (Zone 4), the segment 6 is a ramp 70 W/s. (Zone 4 and 5) for 10 s. At a power of 4,500 W until to the segment 7 (Zone 5), then is passed in segment 8, which consists of a brake of 20 s. until to the power load equals zero (here through all the zones). The ultracapacitor's initial charge status is 76%, which was calculated by measuring the voltage UC in real time and dividing it by 56 V, the maximum voltage of the UC.

The EMS algorithm was implemented in FPGA using method called "state machine". For the segment 1, the EMS algorithm determined PEMFCs to operate in Zone 2, fueling PEMFCs with H2 = 23.5 SLPM and Air = 91.6 SLPM providing power 2000 W. Excess power is directed by controlling the DC/DC converter charging in UC. When is passed in segment 2, PEMFCs remains to Zone 2 until the power load exceeds the threshold of 2000 W, then it passes into zone 3. In Segment 3 is observed as at a time, the ultracapacitor state of charge reaches 100%, at which point the routine is triggered, it passes in previous zone (Zone 2), the power difference to cover the load is made by controlling the discharge of DC/DC converter. The EMS algorithm passes through all segments correct profile, in the last segment when the load power goes under 1000 W to observe as PEMFCs remains in Zone 1 of operation so that the surplus power is charged in the ultracapacitor.

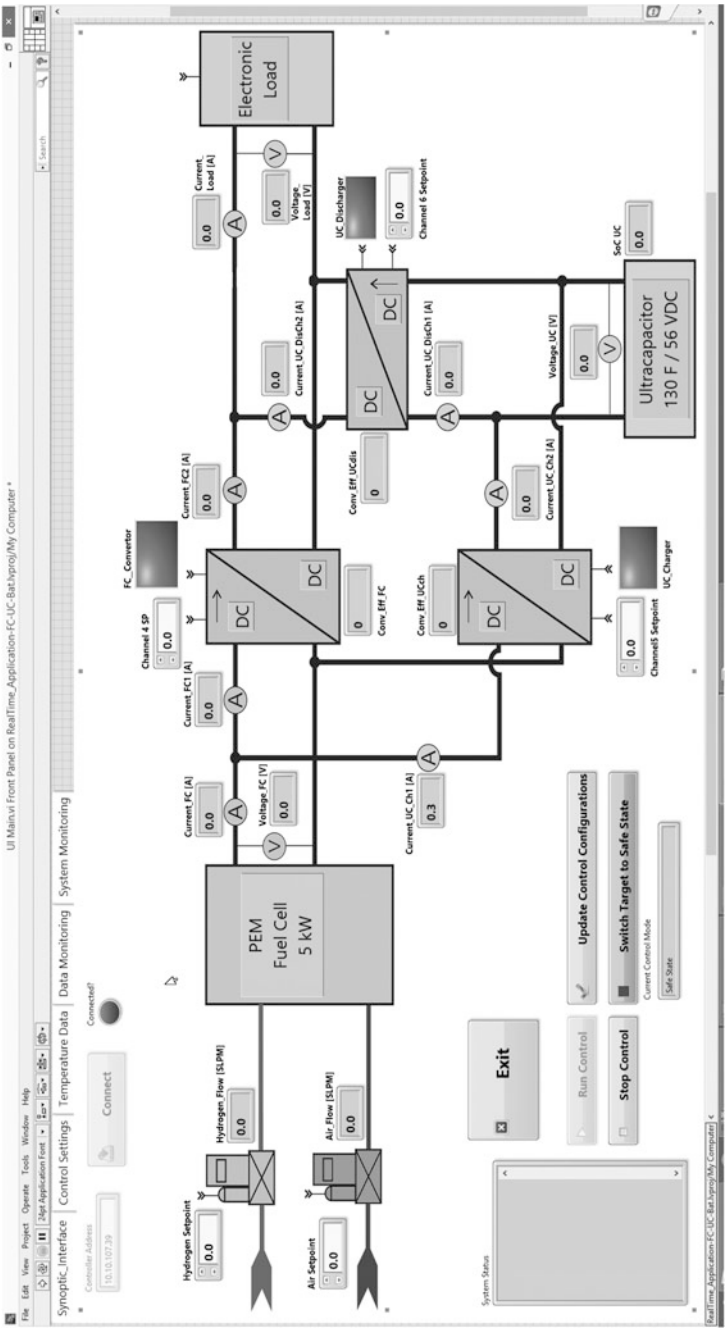

Fig. 13.10 GUI of the software to control the test station and acquire experimental data

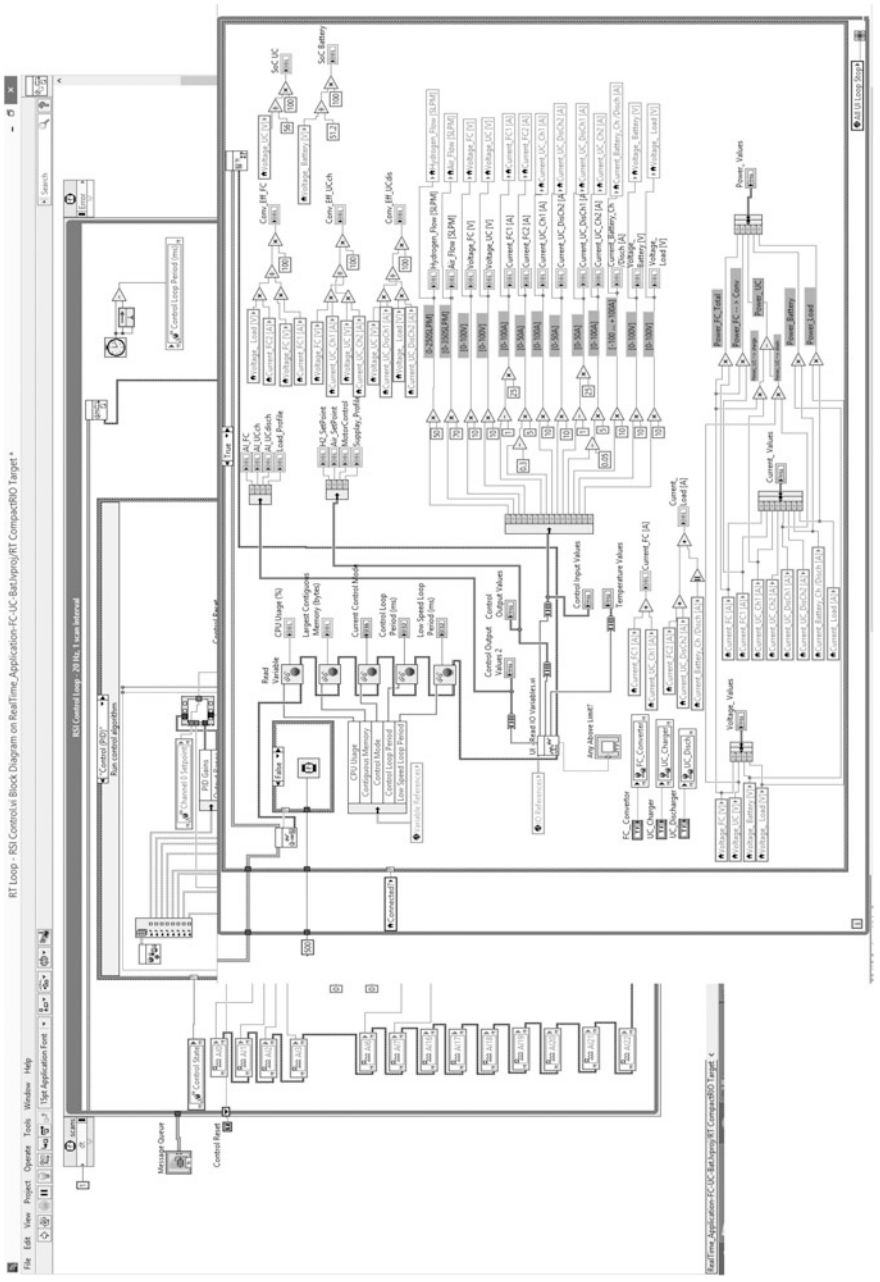

Fig. 13.11 Block diagram for control and monitoring

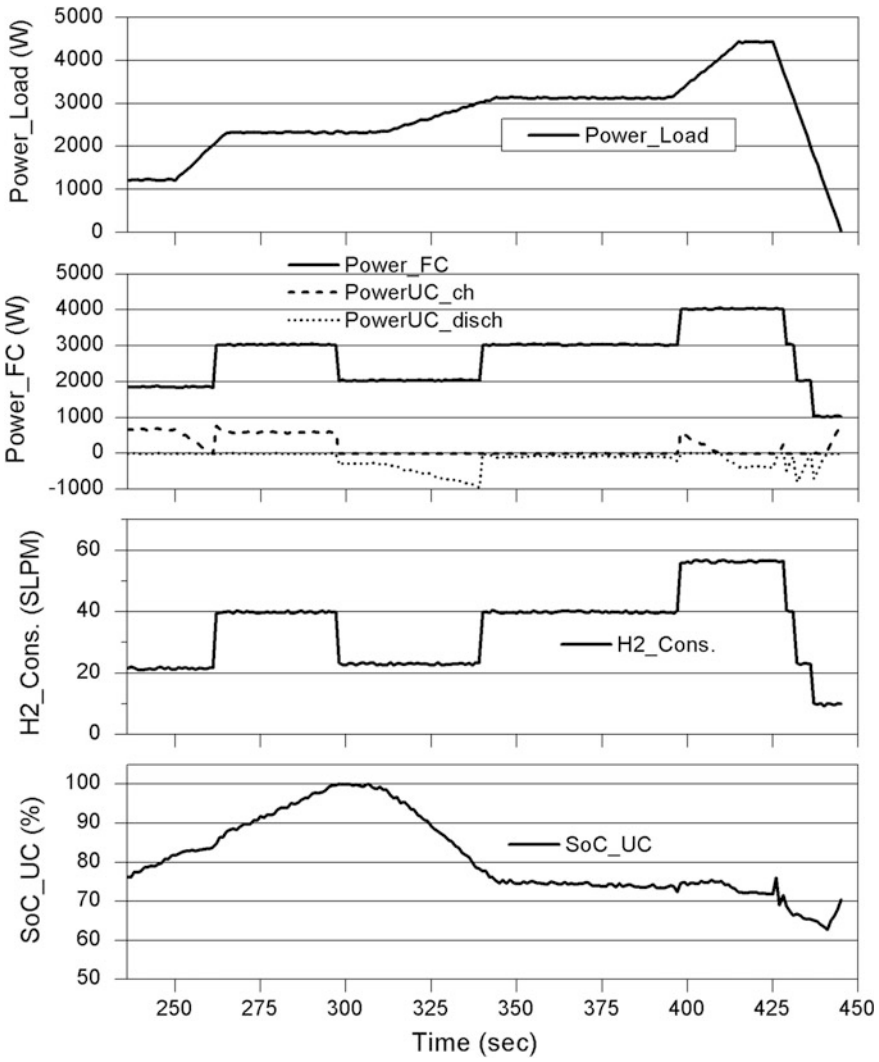

Fig. 13.12 Power split and the evolution of the SoC using EMS based on efficiency map

By using this algorithm EMS it has been observed that PEMFCs works on different levels in stationary conditions prolonging the life of FC. The ultracapacitor is protected for SoC less than 20%. Through the operation of PEMFCs at maximum efficiency on the level of operation has achieved a reduction in fuel consumption of 11.8%. Note that during load profile of 200 s the quantity of hydrogen consumed in FC/UC hybridized mode (with UC driven by EMS algorithm) and the pure mode (without UC) is of 1.05 and 1.18 g, respectively.

13.5 Conclusions

A new topology of HPS that consists in a PEM Fuel Cell stack (5 kW power) and a bank of ultracapacitors (130 F, 56 V, 57 Wh) was investigated in this chapter. It is used to meet the high power demand of the automotive applications, where the power demand fluctuates a lot. The PEMFCs operate in the flow-through mode fuelling and it is cooled with deionized water (65 °C). The stack is fed with humidified hydrogen and air, at a stoichiometry of 1.25 and 2 respectively and the gases are controlled by two mass flow controllers.

To protect the fuel cell against the power load fluctuations an EMS algorithm has been designed. This algorithm aims to direct the flow of power toward UC, when we have an excess of power from the PEMFCs, and vice versa, when the power produced by the PEMFC is not enough to take the power requirement from UC. The power flow is controlled using three DC/DC converters.

The EMS algorithm was based on an FC efficiency map and on the UC state of charge. This algorithm was implemented in a main routine and five subroutines. The main routine split the load power in five equal zones (1000 W per one zone). It is aimed that in each area the fuel cell to operate at the point of maximum efficiency. This algorithm was implemented in a Supervisory Control and Data Acquisition system that utilizes the NI CompactRIO That 9082 platform, software developed in the NI Labview 2015.

PEMFCs/UC HPS have been tested experimentally on a known load profile. The advantages of this new HPS topology are: extended lifetime of the PEMFCs by its operation in a stationary regime, protecting the state of UC Charge below 20% and reducing the consumption of hydrogen by 11.8% compared to a system without UC. This reduction in fuel consumption was due to PEMFCs operation in the areas with maximum efficiency.

Acknowledgements This work is supported by the Sectoral Operational Programme Human Resources Development (SOP HRD), financed from the European Social Fund and the Romanian Government under the contract number POSDRU/159/1.5/S/137390.

References

1. Bubna P, Brunner D, Advani SG, Prasad AK (2010) Prediction-based optimal power management in a fuel cell/battery plug-in hybrid vehicle. J Power Sources 185:6699–6708
2. Toufik A, Olivier B, Ghislain R, Claude M (2011) Saturation management of a controlled fuel-cell/ultracapacitor hybrid vehicle. IEEE Trans Veh Technol 60(9):4127–4138
3. Bizon N, Dascalescu L, Tabatabaei NM (2014) Autonomous vehicles: intelligent transport systems and smart technologies. Engineering tools, techniques and tables. Nova Science Publishers Inc., USA
4. Pei P, Chen H (2014) Main factors affecting the lifetime of Proton Exchange Membrane fuel cells in vehicle applications: a review. Appl Energy 125:60–75

5. Bizon N (2012) Fuel cell hybrid power source that operates efficiently under dynamic loads. In: 2012 international conference on applied electronics (AE), pp 21–24
6. Bucci G, Ciancetta F, Fiorucci E, Veglio F (2007) An experimental approach to the modeling of PEM fuel cells in dynamic conditions. In: 2007 IEEE Lausanne power tech, pp 1094–1099
7. Bizon N, Stork M, Oproescu M (2012) Fuel cell hybrid power source for pulsed current loads. In: 2012 international conference on applied electronics (AE), pp 25–28
8. Thounthong P, Chunkag V, Sethakul P, Davat B (2009) Comparative study of fuel-cell vehicle hybridization with battery or supercapacitor storage device. IEEE Trans Veh Technol 58(8):3892–3904
9. Bizon N (2013) FC energy harvesting using the MPP tracking based on advanced extremum seeking control. Int J Hydrogen Energy 38(4):1952–1966
10. Bizon N (2013) Energy efficiency for the multiport power converters architectures of series and parallel hybrid power source type used in plug-in/V2G fuel cell vehicles. Appl Energy 102:726–734
11. Latha K, Umamaheswari B, Chaitanya K, Rajalakshmi N, Dhathathreyan KS (2015) A novel reconfigurable hybrid system for fuel cell system. Int J Hydrogen Energy 40(43): 14963–14977
12. Boscaino V, Miceli R, Capponi G, Galluzzo GR (2014) A review of fuel cell based hybrid power supply architectures and algorithms for household appliances. Int J Hydrogen Energy 39(3):1195–1209
13. Bizon N (2014) Load-following mode control of a standalone renewable/fuel cell hybrid power source. Energy Convers Manage 77:763–772
14. Greenwell W, Vahidi A (2010) Predictive control of voltage and current in a fuel cell-ultracapacitor hybrid. IEEE Trans Ind Electron 57(6):1954–1963
15. Aouzellag H, Ghedamsi K, Aouzellag D (2015) Energy management and fault tolerant control strategies for fuel cell/ultra-capacitor hybrid electric vehicles to enhance autonomy, efficiency and life time of the fuel cell system. Int J Hydrogen Energy 40(22):7204–7213
16. Corbo P, Migliardini F, Veneri O (2008) Experimental analysis of a 20 kWe PEM fuel cell system in dynamic conditions representative of automotive applications. Energy Convers Manage 49(10):2688–2697
17. Zhan Y, Guo Y, Zhu J, Li L (2015) Power and energy management of grid/PEMFC/battery/supercapacitor hybrid power sources for UPS applications. Int J Electr Power Energy Syst 67:598–612
18. Chao Ch, Shieh J (2012) A new control strategy for hybrid fuel cell-battery power systems with improved efficiency. Int J Hydrogen Energy 37(17):13141–13146
19. Chen Y, Lin S, Hong BS (2013) Experimental study on a passive fuel cell/battery hybrid power system. Energies 6:6413–6422
20. Bizon N, Oproescu M, Raceanu M (2015) Efficient energy control strategies for a standalone renewable/fuel cell hybrid power source. Energy Convers Manage 90(15):93–110
21. Zhan Y, Guo Y, Zhu J, Li L (2015) Power and energy management of grid/PEMFC/battery/supercapacitor hybrid power sources for UPS applications. Int J Electr Power Energy Syst 67:598–612
22. Bizon N (2014) Load-following mode control of a standalone renewable/fuel cell hybrid power source. Energy Convers Manage 77:763–772
23. Li Q, Chen W, Liu Z, Li M, Ma, L (2015) Development of energy management system based on a power sharing strategy for a fuel cell-battery-supercapacitor hybrid tramway. J. Power Sources 279:267–280
24. García P, Torreglosa JP, Fernández LM, Jurado F (2012) Viability study of a FC-battery-SC tramway controlled by equivalent consumption minimization strategy. Int J Hydrogen Energy 37(11):9368–9382
25. Hemi H, Ghouili J, Cheriti A (2014) A real time fuzzy logic power management strategy for a fuel cell vehicle. Energy Convers Manage 80:63–70

26. Eren Y, Erdinc O, Gorgun H, Uzunoglu M, Vural B (2009) A fuzzy logic based supervisory controller for an FC/UC hybrid vehicular power system. Int J Hydrogen Energy 34(20): 8681–8694
27. Thounthong P, Tricoli P, Davat B (2014) Performance investigation of linear and nonlinear controls for a fuel cell/supercapacitor hybrid power plant. Int J Electr Power Energy Syst 54:454–464
28. García P, Torreglosa JP, Fernández LM, Jurado F (2013) Control strategies for high-power electric vehicles powered by hydrogen fuel cell, battery and supercapacitor. Expert Syst Appl 40(12):4791–4804
29. Feroldi D, Serra M, Riera J (2009) Energy Management Strategies based on efficiency map for Fuel Cell Hybrid Vehicles. J Power Sources 190(2):387–401
30. Bernard J, Delprat S, Büchi FN, Guerra TM (2009) Fuel-cell hybrid powertrain: toward minimization of hydrogen consumption. IEEE Trans Veh Technol 58(7):3168–3176
31. Siang FT, Chee WT (2013) A review of energy sources and energy management system in electric vehicles. Renew Sustain Energy Rev 20:82–102
32. Nedstack PEM fuel cell product specifications. http://www.nedstack.com/images/stories/products/nedstack_product-specifications-of-hp-stacks.pdf
33. Raceanu M, Marinoiu A, Culcer M, Varlam M, Bizon N (2014) Preventing reactant starvation of a 5 kW PEM fuel cell stack during sudden load change. In: Electronics, computers and artificial intelligence (ECAI), pp 55–60
34. Raceanu M, Iliescu M, Culcer M, Marinoiu A, Varlam M, Bizon N (2015) Fuelling mode effect on a PEM fuel cell stack efficiency. Prog Cryogenics Isot Sep 18(1):15–24

Chapter 14
Integration and Management Technique of Renewable Energy Resources in Microgrid

Hossein Shayeghi and Elnaz Shahryari

Abstract Ever increasing demand for electricity supply along with higher power quality and reliability, available fossil fuels restrictions and environmental pollutions led to aggregation of clean energy resources (distributed generations) and developing microgrids. Integration of distributed generations such as wind power and solar energy are challenging with various problems such as non-deterministic nature of available wind power and solar energy. On the other hand, power systems are subject to other uncertainties such as load and energy prices in day-ahead (DA) and balancing markets. Hence, intermittence could be highlighted as the main obstacle of distributed generations' aggregation which cause to imbalance charges set by uncertain market prices and accordingly economic losses. To this end, a comprehensive study should be performed to elaborate aforementioned issues. In this chapter, a stochastic model with the goal of profit maximization and imbalance cost minimization is presented. Unlike previous works, in the proposed model all existent uncertainties related to wind power, solar energy, load, day ahead and imbalance market prices altogether are considered by the means of scenario based investigations. In order to generate probable scenarios, uncertain parameters should be predicted. In this framework, a new method based on neural network theory is proposed for predicting wind speed and solar radiation. Afterwards, pumped-storage plant and demand response program are utilized as two complementary resources to compensate power imbalances. Storage devices are used as flexible resources to exchange power between low consumption—cheap hours and peak hours. Finally, to investigate efficiency of the proposed method two operating modes, namely coordinated and uncoordinated operation of clean energy resources, are assumed and testified on a test microgrid.

H. Shayeghi (✉) · E. Shahryari
Department of Technical Engineering, University of Mohaghegh Ardabili, Ardabil, Iran
e-mail: hshayeghi@gmail.com

E. Shahryari
e-mail: elnaz.shahryari@yahoo.com

N. Bizon et al. (eds.), *Energy Harvesting and Energy Efficiency*,
Lecture Notes in Energy 37, DOI 10.1007/978-3-319-49875-1_14

Keywords Clean energy resources · Uncertainty · Demand response · Microgrid · Pumped-storage power plant · Mathematical modeling · Wind power producer · Photovoltaic · Scenario generation

List of Symbols

Indices and numbers

S Set of scenarios
T Settlement time period

Parameters and constants

ρ_s	Probability of scenario s
$P^{W\,max}$	Maximum energy of wind turbine, kW
$P^{PV\,max}$	Maximum energy of PV system, kW
V^{UU}	Maximum charging capacity of storage, kW
V^{DU}	Minimum charging capacity of storage, kW
V^{UL}	Maximum discharging capacity of storage, kW
V^{DL}	Minimum discharging capacity of storage, kW
η_1	Percentage of demanded load reduction
η_2	Percentage of demanded load increase
Vf^U	Primary and ultimate energy value of upper reservoir, kW
Vf^L	Primary and ultimate energy value of bottom reservoir, kW
η	Operation efficiency of pumped-storage unit in pumping and generating mode
N	Number of the pumped-storage units
α	Factor of load recovery
β	Elasticity factor

Variables and parameters

$\pi_{DA,t,s}$	Day-ahead electricity price at time period t and output scenario s, $/MWh
$\alpha^+_{t,s}$	Overproduction imbalance price ratio at time period t and output scenario s
$\alpha^-_{t,s}$	Underproduction imbalance price ratio at time period t and output scenario s
P^{WPP}_t	Offered power by wind power producer in *t*th hour, kW
P^{PV}_t	Offered power by PV system in *t*th hour, kW
P^{PUMP}_t	Offered power by storage in *t*th hour, kW
D_t	Offered power by demand response in *t*th hour, kW
$P^{WPP}_{t,s}$	Real scheduled power of wind power in *S*th scenario and *t*th hour, kW
$P^{PV}_{t,s}$	Real scheduled power of PV system in *S*th scenario and *t*th hour, kW
$D_{t,s}$	Real scheduled demanded load in *S*th scenario and *t*th hour, kW

$g_{t,S}^{Pump}$ Discharge power output of storage in Sth scenario and tth hour s, kW
$d_{t,S}^{Pump}$ Pumping power of storage in Sth scenario and tth hour, kW

Integer variables

$t_{t,S}$ Binary variable to specify if the storage unit is capable to operate as a turbine or not in Sth scenario and tth hour
$u_{t,S}$ Number of units running in pumping mode in Sth scenario and tth hour
$y_{t,S}, z_{t,s}$ Number of start-ups and shut-downs in Sth scenario and tth hour

Abbreviation and Acronyms

DA Day-ahead
DG Distributed generation
DO Disjoint operation
MCP Marginal clearing price
MG Microgrid
MLP Multi-layer perceptron
MSE Mean square error
MT Micro turbine
NN Neural network
PV Photovoltaic
WT Wind turbine

14.1 Introduction

Recently, there is a strong attitude toward utilizing distributed generations (DGs) as the alternative to traditional ones. Distributed generations are small scale generation units such as small wind turbines (WTs), Photovoltaic (PV), fuel cells, and Micro turbines (MTs) which are installed close to the consumers [1]. Electricity cheapness, higher reliability and quality in providing power services and satisfying environmental concerns are the most important benefits of using DGs [2].

By aggregation of distributed generations, loads and energy storage devices a microgrid (MG) is formed [3] which can be operated in a grid-connected or islanding mode. Since, the output voltage and frequency of DGs are not regulated and on the other hand, these power sources have stochastic nature, their output is in DC or unregulated Ac form. This makes it necessary to connect and control output power of distributed generation units via power electronic converters [4, 5].

In the grid-connected mode, the main grid is responsible for regulating voltage and frequency of microgrid [6]. To reach this goal, the difference between generated and demanded power in the microgrid is calculated and then the main grid is responsible to hold balance in the microgrid. So, lack of main grid in islanding operating mode makes difficulties in microgrid control. The control method of microgrid in islanding mode should be able to regulate its voltage and frequency in order to maintain its dynamic stability at any time which can be performed by fast-response storage devices such as batteries. The second aim of microgrid controlling is to provide power balance between generation and consumption [7]. Therefore, an efficient power management method is required to make the most appropriate decision for various conditions of power sources, demanded load, electricity price and many other circumstances.

On the other hand, deregulation is new template of power industry which tries to reach a high level of competition between market participants, maximizing economic benefits, and also creating new options for consumers [8]. In deregulation template, electricity market price for each hour of future is determined by offers of consumers and power generators. By the way, because of non-deterministic nature of DGs, the amount of future generation for these units should be estimated by short term forecasting tools [9]. Various prediction methods have been presented in the literature such as artificial neural network [10], ANFIS [11] wavelet transform [12], Kalman filtering [13]. Also, researchers in [14] proposed a method to forecast two dependent parameters, load and market clearing price, simultaneously as a multi-input multi-output model.

Taking into account deregulation rules, wind and solar power producers submit their offers to the market while they are unaware of their exact production level. This leads to generation of unbalances between scheduled and delivered energy which should be compensated in balancing markets [15]. Prior to introduction of MG, various studies have been performed about DGs. For instance, in [16] wind and photovoltaic generations for supplying an office building are designed in such a way that annual costs of the overall system are minimized and economical and environmental profits are maximized. The effects of distributed generations on expansion of sub-transmission system is studied in [17] and all of fixed and variable costs of DGs are considered in mathematical formulation. A mixed-integer mathematical formulation is presented in [18] in order to determine the optimal offers of wind farm and storage unit in day-ahead market. In this formulation, market prices related to power imbalances are assumed to be known. Authors of [19] employed stochastic programming techniques to simulate participation of wind power and storage unit owners in day-ahead and ancillary service markets as an integrated self-schedule. Reference [20] proposed a new method to model wind power and storage unit while utilizing Value at Risk (VaR) of units to measure their operation. In [21] profit maximization and optimal bids for participation of wind farm and demand response are calculated. In the presented method marginal and imbalance prices are considered known and wind producer offering is improved by using demand response as a storing device.

Research studies prove that independent utilization of DG units in power system can lead to lots of difficulties. So, in order to solve these problems, microgrid concept has been presented [22]. According to above claims, many researches have been carried out to identify different aspects of microgrids. Considering uncertainties related to wind speed, solar irradiance and load, reference [23], focuses on integration of DG units in a microgrid to reach maximum profit. In [24], microgrid planning is done in such a way to achieve the least amount of cost and emission. In [25] a novel coordinated bidding strategy is addressed to aggregate multiple DGs and storage units and demand response as an independent power producer in the microgrid in order to increase their revenue in intra-day market. Stochastic coordination of distributed resources considering related uncertainties in an islanding microgrid is studied in [26]. This paper takes into account intermittencies related to load, wind and solar generation by a set of probable scenarios. Authors of [27] have performed the optimal energy management for microgrid as a multi-objective problem while considering uncertain nature of wind and solar power. In this paper an incentive based demand response program is proposed to cover power uncertainties which makes it possible for various kinds of residential, commercial and industrial consumers to participate in demand response program. An energy management system is suggested by [28] to determine the optimal operating point of wind turbines along with storage devices in a microgrid and minimize its cost and emissions while considering wind uncertainty. Reference [26] models operation of distributed energy sources in a microgrid as a stochastic mathematical model which utilizes various possible scenarios in order to cover load, wind and solar uncertainties. In [29], a matrix real coded genetic algorithm method is applied to optimize the operation of microgrid. In this study, energy storage system is used to manage uncertainties of PV.

In this chapter, bidding strategy of microgrid components are discussed in detail and a scenario generation process based on prediction errors is utilized to cover existing uncertainties. Also demand response and pumped-storage are utilized as both storage device and power generator to adjust power imbalances. Comprehensive description of the issue is provided in the following sections.

14.2 Problem Description

In this section background knowledge related to the power markets and role of pumped-storage and demand response participation in power markets are discussed.

14.2.1 Day-Ahead and Balancing Market

The market considered in this chapter is composed of two sub-markets with distinct planning horizons which are named day-ahead (DA) and balancing market. Most of

power is exchanged in day-ahead markets. The basis of this market is auctions in which power producers and consumers propose their hourly offers based on final predictions before termination time which happens at 10:00 am and lasts for 15 until 38 h. Finally by computing junction point of summated hourly demand and supply functions, the marginal clearing price (MCP) for each hour is calculated. This price is the minimum price which satisfies all purchase bids with enough accepted sell offers. The payment process in day-ahead market is to pay multiplication of real generation and marginal price for each hour.

The wind and solar power producers must predict their future generation for next day in order to participate in day-ahead power market, however due to uncertain nature of wind and solar, always there are differences between predicted value and the real one. So in order to reduce imbalances between demand and generation power, balancing markets are employed in real time horizon. Power imbalances which can be calculated by subtraction of cleared generated power from real value, are settled and fined in balancing market. If there is overproduction, it will be settled cheaper than marginal price. Controversy, if there is underproduction, it will be compensated more expensive than marginal price. If $\pi_{up,t}$ and $\pi_{down,t}$ represent the imbalance prices for excess and lack of produced power, respectively, it can be said that $\pi_{up,t} \leq \pi_{DA,t} \leq \pi_{down,t}$ and the revenue earned from this market at time t is calculated as below:

$$R(\Delta P) = \begin{cases} \pi_{up,t}\left(P_{Gen,t} - P_{Bid,t}\right) & if \quad P_{Gen,t} \geq P_{Bid,t} \\ \pi_{down,t}\left(P_{Bid,t} - P_{Gen,t}\right) & if \quad P_{Gen,t} < P_{Bid,t} \end{cases} \tag{14.1}$$

Here $P_{Gen,t}$ and $P_{Bid,t}$ represent the actual and submitted generation offer in day-ahead market, respectively. By supposing $\alpha_t^+ \leq 1$ and $\alpha_t^- \geq 1$ as the ratio between sell and buy imbalance prices to marginal prices, imbalance prices can be computed as below:

$$\pi_{up,t} = \alpha_t^+ \pi_{DA,t}, \quad \pi_{down,t} = \alpha_t^- \pi_{DA,t} \tag{14.2}$$

By replacing Eq. (14.2) with Eq. (14.1), imbalance revenue is rewritten as below:

$$R(\Delta P) = \begin{cases} \alpha_t^+ \pi_{DA,t}\left(P_{Gen,t} - P_{Bid,t}\right) & if \quad P_{Gen,t} \geq P_{Bid,t} \\ \alpha_t^- \pi_{DA,t}\left(P_{Bid,t} - P_{Gen,t}\right) & If \quad P_{Gen,t} < P_{Bid,t} \end{cases} \tag{14.3}$$

14.2.2 Role of Pumped-Storage Unit

The aim of power producers in construction of pumped-storage plant is to support uncertainty of wind and solar power generations and provide flexibility to power generators by this complementation. For example, suppose that wind or solar power producers face with an overproduction in real time operation, it means that the

generated power in real time is more than the power which they should provide. In this situation, the surplus power is saved by pumping water from bottom tank to the upper. Vice versa, if there is lack of generation, this shortage could be compensated by hydro turbine. In this condition, delivered power is accurate and equals to the cleared amount in market. However, it should be considered that this flexibility depends on the characteristics of pumped-storage unit, too.

14.2.3 Role of Demand Response

Demand response (DR) is a program which enables end-users to participate in electricity markets. In this procedure, consumers submit their demanded loads to the market. After clearing the day-ahead market, consumers are charged for their submitted bids and also the value of MCP and production of each generating unit is specified. This program enables end-users to propose their load reduction bids to the market and to be paid by MCP in the case of admission. Response of consumers to the market price is called elasticity. Higher amount of elasticity makes consumers to react well in response to power price changes. So when the electricity price is high, consumers can adjust themselves by reducing consumption.

Coordinated operation of DR and clean energy sources like wind and solar power, could cover uncertainties of wind and solar. For example, in peak hours consumers can decrease their consumption and compensate uncertainty of wind power and photovoltaic. On the other hand, applying flexible load helps in improving welfare of power producers and minimizing the penalties that they should pay to imbalance market resultant from their uncertain nature.

The overall process of this chapter to aggregate clean energy sources in a microgrid is depicted in Fig. 14.1 which shows the total stages step by step.

14.3 Modelling Uncertainties

A situation in which there is lack of accurate and detailed information about present or future conditions is called uncertainty. Power systems confront with two main types of uncertainties which caused by failure of generation units or by prediction errors. Failure of generation units leads to lack of production which can be compensated via spinning or non-spinning reserves; but uncertainties related to prediction accuracy is consisted of load, produced power and market price uncertainties for each hour of next day. In this chapter second type of uncertainties is studied which can be controlled with stochastic programming techniques. In this method, aforementioned uncertain parameters must be predicted at first, then a scenario generation process based on prediction error is utilized to generate probable values of stochastic parameters. Finally, in order to speed up computation a scenario reduction technique is employed. Each of these steps are explained in detail as follows.

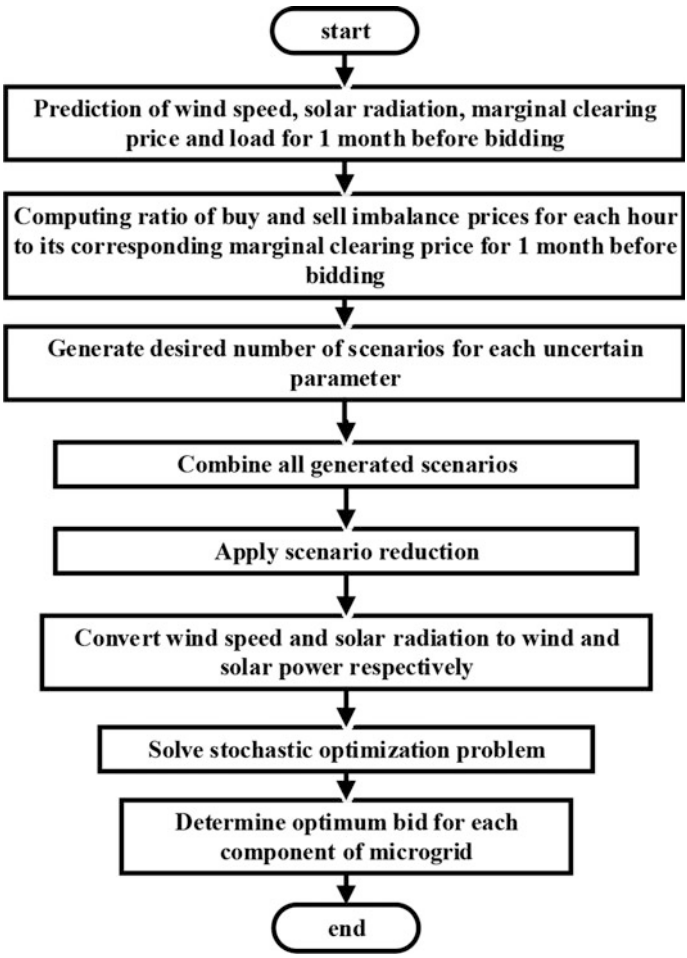

Fig. 14.1 Flowchart of aggregation of clean energy sources

14.3.1 Prediction Method

This chapter proposes a new technique for short term prediction of uncertain parameters based on neural network (NN). NN is a nonlinear modeling technique which is trained by historical data to specify the relation between input and output data. In this chapter, Multi-layer Perceptron (MLP) neural network with one hidden layer is utilized to do forecasting. MLP networks are composed of three layers named as input, hidden and output layer that are connected to each other linearly through connection weights. Consider $W^1 = \left\{ w_{ij}^1(n) \right\}$ and $W^2 = \left\{ w_{jk}^2(n) \right\}$ are the

weight matrixes which are used to link neurons of input layer to hidden ones and relate hidden layer neurons to the output one, respectively.

In order to convert output values of neurons to nonlinear ones, sigmoid function is utilized as activation function which is defined below:

$$F(x) = \frac{1}{1 + exp(x)} \tag{14.4}$$

Using the aforementioned NN, The kth output is given by:

$$y_k(n) = F\left(\sum_{j=0}^{M} w_{jk}^2(n) F\left(\sum_{i=0}^{N} w_{ij}^1(n) x_i(n)\right)\right) \tag{14.5}$$

where M and N denote the neuron number in hidden and input layer, respectively and $x_i(n)$ represents the ith input signal of nth training data.

In this chapter back propagation method is utilized to train neural network in which, MLP's estimated output value, $y_k(n)$, is compared to the desired one, $t_k(n)$, and the mean square error (MSE) value is calculated as below:

$$\begin{aligned} MSE &= \sum_{n=1}^{N} Error(n) \\ Error(n) &= \frac{1}{K} \sum_{k=1}^{K} (y_k(n) - t_k(n))^2 \end{aligned} \tag{14.6}$$

Here, n and k denote the number of training pattern and output neurons, respectively. Finally, moving in a backward direction, from output layer to input one, connection weights are modified in such a way to minimize MSE value.

In the presented method a new combination of last three years' wind speed data of Sotavento wind farm in Spain [30] is used for training MLP neural network. The important property of learning data is that other historical parameters such as pressure or temperature are not considered but the earning results were accurate enough. In the presented combination, data for each season is used as training data of that season. Totally there would be 75 inputs and 24 outputs. The input signals are 24-h wind speed of a day before prediction day, wind speed data for 24 h of the prediction day in the previous week, wind speed for all hours of prediction day in two weeks ago and the mean, maximum and minimum value of wind speed for prediction day that these last three input values are collected from weather prediction station. The output values are the 24-h wind speed of the desired prediction day.

To choose the best number for hidden layer neurons which has the least training error, neuron number in hidden layer are changed from 1 to 10 and proportional training error value is calculated for each one. Figure 14.2 depicts the proportionate training error for each number. As can be seen, 9 neurons have the least error value and it is chosen as the best neuron number of hidden layer. Neural network parameters are expressed in Table 14.1.

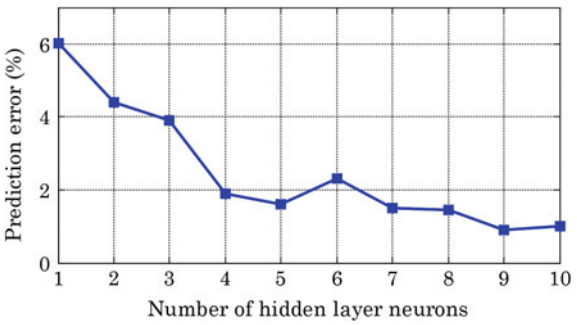

Fig. 14.2 Variation of neuron number in hidden layer and training error

Table 14.1 Neural network parameters

Neuron number in input layer	75
Neuron number in hidden layer	9
Neuron number in output layer	24
Learning factor	0.1
Learning time	2000
Transfer function	Sigmoid

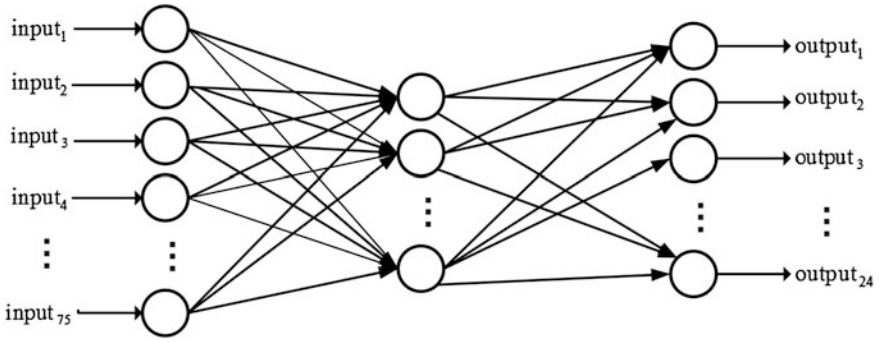

Fig. 14.3 Structure of multi-input multi-output neural network

Figure 14.3 shows the structure of a multi-input multi-output MLP neural network which is used in this work. In addition to wind speed, other uncertain parameters named above are predicted by this method too.

14.3.2 Scenario Generation Technique

Step 1. First of all, all uncertain parameters are forecasted for each hour of a 1 month period before bidding time.

Step 2. By comparing the prediction values and actual ones for the respective month, hourly error values of prediction is calculated as below:

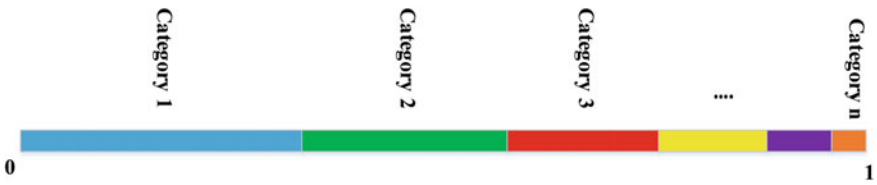

Fig. 14.4 Cumulative normalized probabilities of the prediction error categories

$$Error_t = \frac{Actual_t - Forecast_t}{Actual_t} \times 100 \tag{14.7}$$

where here $Actual_t$ and $Forecast_t$ symbolize the real and forecasted values of uncertain parameter at hour t in the respective month.

Step 3. The resulting error values proportional to each hour are classified in 1% distances while each class symbolizes a probable scenario. By dividing the frequency of each class to total month hours, occurrence probability of each error value is computed.

Step 4. In this step, the probability of categories are normalized in such a way that their total sum equals to unity. Afterward, a cumulative normalized probability is assigned to each category as shown in Fig. 14.4.

Step 5. Existence of multiple categories with various probabilities led to employ Roulette Wheel mechanism in order to generate favorite number of scenarios (here 10) for each hour. In this mechanism, a number is generated between 0 and 1, randomly and then it is compared with sorted categories. First category with cumulative probability equal or greater than random value, is selected.

Step 6. Now all of uncertain parameters are predicted for next 24 h, bidding interval, and the proportion value of each scenario is calculated as below:

$$UP_{S,t} = P_t + Error_S \times P_t \tag{14.8}$$

where $UP_{S,t}$, P_t and $Error_S$ symbolize the uncertain parameter in Sth scenario and rth hour, predicted value in hour t and prediction error in Sth scenario respectively.

Step 7. Finally, after generating desired number of scenarios, occurrence probability of each scenario is calculated as below:

$$\pi_S = \frac{\prod_{t=1}^{24} \left(\rho_{t,S}^{WT}, \rho_{t,S}^{PV}, \rho_{t,S}^{MCP}, \rho_{t,S}^{ImP}, \rho_{t,S}^{L}\right)}{\sum_{S=1}^{N_S} \prod_{t=1}^{24} \left(\rho_{t,S}^{WT}, \rho_{t,S}^{PV}, \rho_{t,S}^{MCP}, \rho_{t,S}^{ImP}, \rho_{t,S}^{L}\right)} \tag{14.9}$$

Here N_S represents total number of scenarios and $\rho_{t,S}^{WT}, \rho_{t,S}^{PV}, \rho_{t,S}^{MCP}, \rho_{t,S}^{ImP}, \rho_{t,S}^{L}$ are occurrence probability of Sth scenario of wind turbine, photovoltaic, marginal clearing price in DA market, imbalance balancing market prices and load, respectively. Flowchart of explained scenario generation process is depicted in Fig. 14.5.

In this chapter to cover all uncertainties, 10 scenario is generated for each uncertain parameter. So totally 10^5 scenarios will be existed and scenario tree for overall uncertainties is depicted in Fig. 14.6 which explains the concept of generated scenarios clearly.

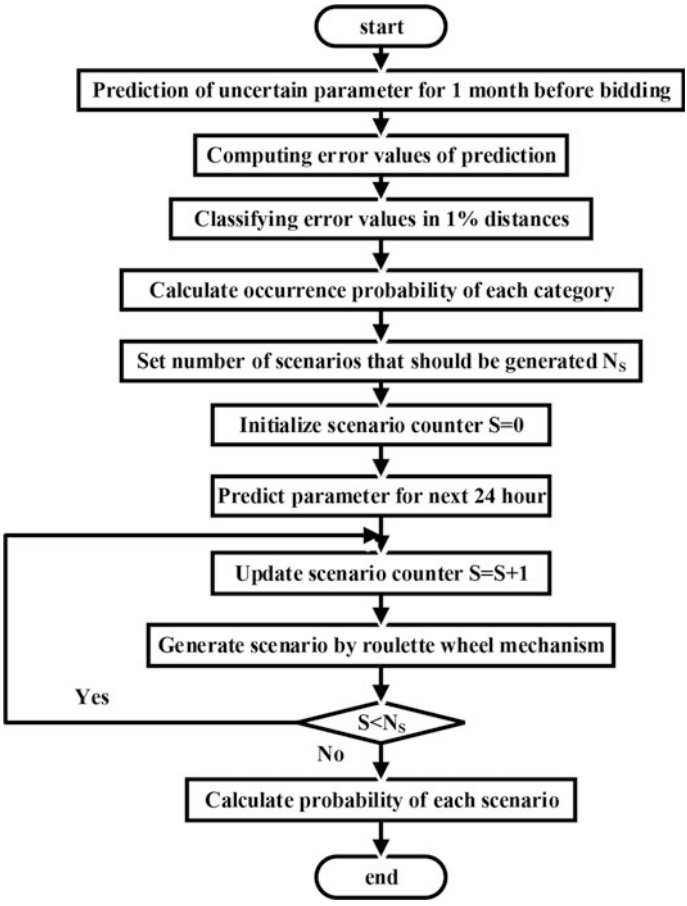

Fig. 14.5 Flowchart of scenario generation process

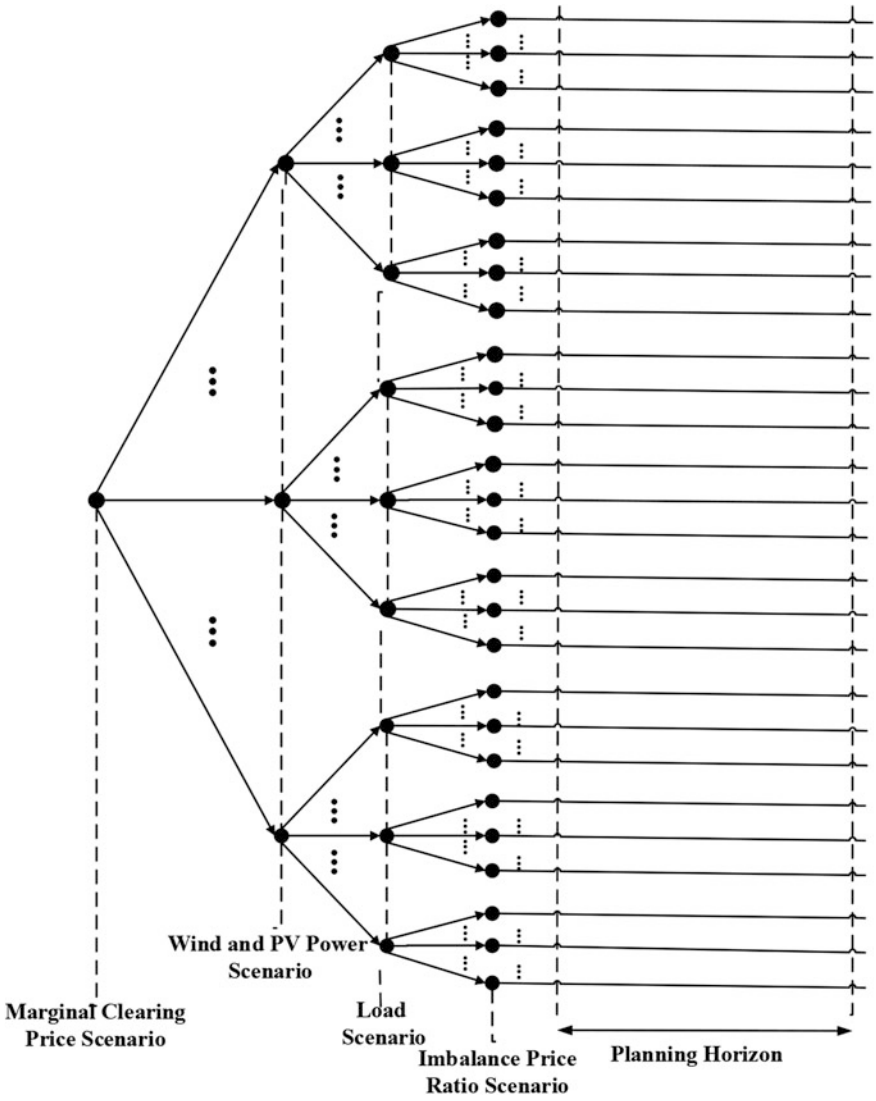

Fig. 14.6 Scenario tree of the proposed strategy

14.3.3 Scenario Reduction Technique

The aim of scenario reduction technique is to speed up optimization process. That is why in this technique some of scenarios similar to each other or the ones with very small probability of occurrence, have been omitted. Although a higher number of scenarios along with a higher computational burden can result in an accurate

modeling of the uncertainty, but a proper scenario reduction method can also approximate system's uncertain behavior efficiently. Consider S as the total set of scenarios, here 10^5, which are generated in the scenario generation process. DS symbolize the scenarios that should be omitted and is initially null. Also initialize N_D as the desired number of scenarios after reduction process. This steps of aforementioned scenario reduction process is as below:

Step 1. First of all, calculate the distance of all scenarios, two by two as below:

$$DT_{S,S'} = \sqrt{\sum_{i=1}^{d} (V_i^S - V_i^{S'})^2} \quad S, S' = 1, 2, \ldots, N_S \tag{14.10}$$

Step 2. For each scenario k, find the scenario r with least distance from scenario k as formulated below:

$$DT_{k,r} = min(DT_{k,S'}) \tag{14.11}$$

Step 3 Calculate amount of $\pi_S \times DT_{k,r}$ and elect scenario d which has the minimum production value. The election process results in selection of a scenario which has the least probability of occurrence and the most similarity to other scenarios simultaneously.

Step 4. Omit the selected scenario, $S = S - \{d\}$ and add it to omissions category, $DS = DS + \{d\}$ and also occurrence probability of d is added to its similar scenario r, $\pi_r = \pi_r + \pi_d$.

Step 5. If the favorable number of scenarios are not omitted reached, go to Step 2.

Flow chart of the explained scenario reduction process is depicted in Fig. 14.7.

14.4 Mathematical Modelling of Clean Energy Sources

The next subsections present detailed optimization formulation of abovementioned configurations. Each of these models makes effort to maximize its welfare and minimize unbalanced costs. It is worth mentioning that all equations are expressed in hourly intervals.

14.4.1 Disjoint Operation (DO)

In this operating mode, each of energy sources participate independently in power markets while aim to maximize their own income. In this mode, utilities sell their produced power to spot markets and compensate their unbalances in imbalance market. So the total income function is composed of earnings from selling power to

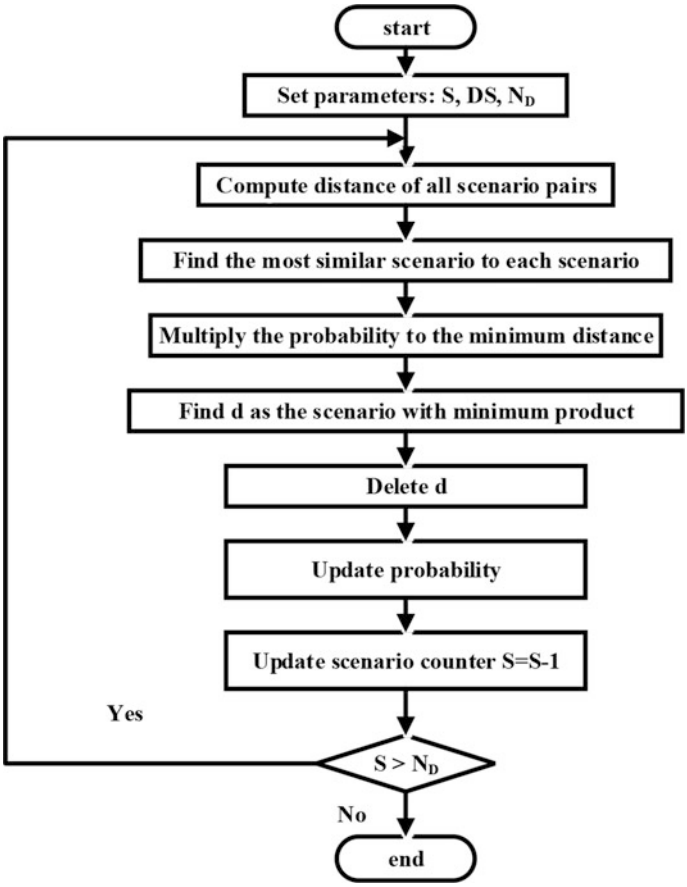

Fig. 14.7 Flowchart of scenario reduction process

day-ahead markets plus revenues from imbalance market when facing with surplus production minus penalties costs to compensate lack of committed power in imbalanced market. Welfare function related to each clean energy source along with considering its own technical constraints are formulated as below.

14.4.1.1 Wind Power Producer

Considering probable nature of available wind power, wind power producer (WPP) participate in power markets based on predicted values in scenarios but as mentioned above, scenarios are generated by forecasted wind speed values. So in order to make it possible to participate in power markets, these speed amounts must be converted to power. The relation between wind speed and power is as follow [23]:

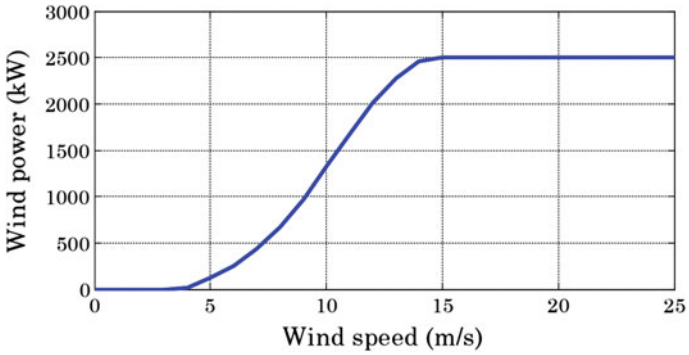

Fig. 14.8 Wind turbine power curve

$$P_{Wind} = \begin{cases} 0 & v \le v_{ci} \\ k_1 v + k_2 & v_{ci} \le v \le v_r \\ P_r & v_r \le v \le v_{co} \\ 0 & v \ge v_{co} \end{cases} \tag{14.12}$$

$$k_1 = \frac{P_r}{v_r - v_{ci}}; \quad k_2 = -k_1 \times v_{ci} \tag{14.13}$$

where v, v_{ci}, v_r and v_{co} represent the predicted wind speed, the cut-in speed of wind, the cut-out speed of wind and the wind speed at knee point of power curve, respectively. In this chapter, Nordex N80/2500 [31] which is shown in Fig. 14.8 is utilized as wind turbine power curve to transform wind speed into power.

Based on the forecasted wind power, marginal and imbalance market prices, the expected profit of wind power producer in the settlement period is described below:

$$F_{WPP} = F_{DA} + F_{Pos\_Imb} - F_{Neg\_Imb} \tag{14.14}$$

where F_{DA}, F_{Pos_Imb} and F_{Neg_Imb} are profits of day-ahead and imbalance markets and economic losses of balancing market, respectively, which are defined as follows:

$$F_{DA} = \sum_{t=1}^{24} \sum_{s=1}^{S} \rho_s \pi_{DA,t,s} P_t^{WPP} \tag{14.15}$$

$$F_{Pos\_Imb} = \sum_{t=1}^{T=24} \sum_{s=1}^{S} \rho_s \pi_{DA,t,s} \alpha_{t,s}^{+} \Delta_{t,s}^{+WPP} \tag{14.16}$$

$$F_{Neg\_Imb} = \sum_{t=1}^{T=24} \sum_{s=1}^{S} \rho_s \pi_{DA,t,s} \alpha_{t,s}^{-} \Delta_{t,s}^{-WPP} \tag{14.17}$$

The output power limits of WPP is given by:

$$0 \leq P_t^{WPP} \leq P^{W\,max} \tag{14.18}$$

$$\Delta_{t,s}^{-WPP} = P_t^{WPP} - P_{t,s}^{WPP} \tag{14.19}$$

$$\Delta_{t,s}^{+WPP} = P_{t,s}^{WPP} - P_t^{WPP} \tag{14.20}$$

$$\Delta_{t,s}^{+WPP}, \Delta_{t,s}^{-WPP} \geq 0 \tag{14.21}$$

14.4.1.2 Photovoltaic

Similar to wind power, hourly available solar energy confront with uncertainties. To manage this stochastic nature, probable solar radiation for each hour was forecasted in previous section. Now in order to calculate available solar energy, radiation must be converted to energy via underneath equation [22]:

$$P_{PV} = A_{pv}x^2 + B_{pv}x \tag{14.22}$$

While, x symbolizes the solar radiation (W/m^2), P_{PV} signifies the available solar power and A_{pv} and B_{pv} are constants which are equal to 2 and 3.6, respectively and are derived from radiation curve which is illustrated in Fig. 14.9.

Formulating profit function of photovoltaic arrays are similar to wind power producer and their both production is cost free. So, considering uncertainties of solar radiation and market prices, the profit function is contained of three terms as below:

$$F_{PV} = F_{DA} + F_{Pos\_Imb} - F_{Neg\_Imb} \tag{14.23}$$

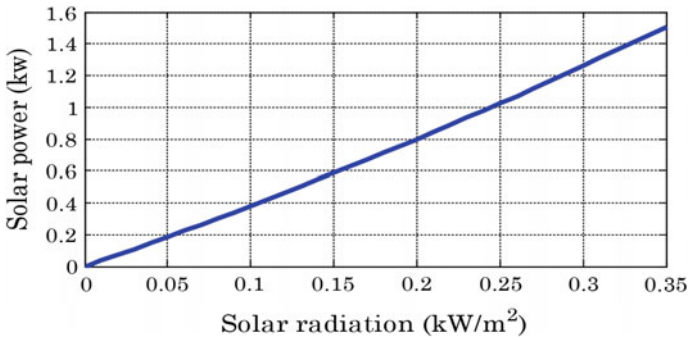

Fig. 14.9 Power-radiation curve of PV

The only difference between WPP and PV profit function is substituting solar energy instead of wind power as follow:

$$F_{DA} = \sum_{t=1}^{T} \sum_{s=1}^{S} \rho_s \pi_{DA,t,s} P_t^{PV} \tag{14.24}$$

$$F_{Pos\_Imb} = \sum_{t=1}^{T} \sum_{s=1}^{S} \rho_s \pi_{DA,t,s} \alpha_{t,s}^{+} \Delta_{t,s}^{+PV} \tag{14.25}$$

$$F_{Neg\_Imb} = \sum_{t=1}^{T} \sum_{s=1}^{S} \rho_s \pi_{DA,t,s} \alpha_{t,s}^{-} \Delta_{t,s}^{-PV} \tag{14.26}$$

Finally, the only constraint which is given here, is power limitation.

$$0 \le P_t^{PV} \le P^{PV\,max} \tag{14.27}$$

$$\Delta_{t,s}^{-PV} = P_t^{PV} - P_{t,s}^{PV} \tag{14.28}$$

$$\Delta_{t,s}^{+PV} = P_{t,s}^{PV} - P_t^{PV} \tag{14.29}$$

$$\Delta_{t,s}^{+PV}, \Delta_{t,s}^{-PV} \ge 0 \tag{14.30}$$

14.4.1.3 Demand Response

In this section mathematical formulation of demand response profit is presented. As explained before, the elasticity between MCP and demanded load has an exponential relation [21] as below:

$$Demand = ke^{\gamma \pi_{DA}} \tag{14.31}$$

where γ is a parameter to depict the relation between elasticity and market price. Participating in market, the profit of consumers equals to:

$$F_{DR} = I(D_t) - \pi_{DA} \cdot D_t \tag{14.32}$$

Equation 14.32 can be developed by Taylor series and profit function of demand side can be rewritten as:

$$F_{DR} = I\left(D_{t,s}\right) + \frac{\partial R(D_t)}{\partial D_t} \cdot \Delta D_t + \frac{1}{2} \frac{\partial^2 R(D_t)}{\partial D_t^2} \cdot (\Delta D_t)^2 - \pi_{DA} \cdot D_t \tag{14.33}$$

Substituting Eq. (14.31) with Eq. (14.33), the profit of demand side participation can be computed as:

$$F_{DR} = \sum_{t\in T}\sum_{s\in S}\rho_s((D_{t,s} - D_t) \times \pi_{DA} + \frac{1}{2} \times \frac{1}{\gamma \times D_{t,s}} \times (D_t - D_{t,s})^2) \quad (14.34)$$

Constraints of DR are as following:

$$D_t > \eta_1 \times D_{t,S} \quad \forall s \in S, \forall t \in T \quad (14.35)$$

$$D_t < (1 + \eta_2) \times D_{t,S} \quad \forall s \in S, \forall t \in T \quad (14.36)$$

Inequalities (14.35) and (14.36) define variation limits of load considering parameters η_1 and as the allowable percent of load decrease and increase. Based on (14.35) normal load level cannot decrease too much and according to (14.36) it cannot increase consumedly.

14.4.1.4 Pumped-Storage Unit

As a storage unit, pumped-storage plant conserves electricity power within low consumption and cheap hours by pumping water into top tank and releases this energy when it is needed by turbine. This process matches network delivered power to the cleared value with high accuracy.

The expected income of participating pumped-storage unit in power markets is a function of selling power $g_{t,S}^{Pump}$ to, and buying energy $d_{t,S}^{Pump}$ from, the market while considering C^{Su} and C^{Sd} as the pumping start-up and close down expenses and also two terms to cover shortage or surplus of power in balancing market. All of these functions are expressed in Eq. (14.37). Here F_{DA}, F_{Su}, F_{Sd}, F_{Pos_Imb} and F_{Neg_Imb} represent the income function in DA market, start-up and close down expenses and income and penalty in imbalance markets, respectively. Each of them are expressed in detail in Eqs. (14.38)–(14.42).

$$F_{PUMP} = F_{DA} - F_{Su} - F_{Sd} + F_{Pos\_Imb} - F_{Neg\_Imb} \quad (14.37)$$

$$F_{DA} = \sum_{t\in T}\sum_{s\in S}\rho_s \pi_{DA,t,s} P_t^{PUMP} \quad (14.38)$$

$$F_{Su} = \sum_{t\in T}\sum_{s\in S}\rho_s C^{Su} y_{t,S} \quad (14.39)$$

$$F_{Sd} = \sum_{t\in T}\sum_{s\in S}\rho_s C^{Sd} z_{t,S} \quad (14.40)$$

$$F_{Pos\_Imb} = \sum_{t\in T}\sum_{s\in S} \rho_s \pi_{DA,t,s} \alpha^{+}_{t,s} \Delta^{+PUMP}_{t,s} \tag{14.41}$$

$$F_{Neg\_Imb} = \sum_{t\in T}\sum_{s\in S} \rho_s \pi_{DA,t,s} \alpha^{-}_{t,s} \Delta^{-PUMP}_{t,s} \tag{14.42}$$

Constraints:

$$V^{U}_{t,S} = V^{U}_{t-1,S} + \eta d^{Pump}_{t,s} - g^{Pump}_{t,s} \quad \forall s \in S, \forall t \in T \tag{14.43}$$

$$V^{L}_{t,S} = V^{L}_{t-1,S} - \eta d^{Pump}_{t,s} + g^{Pump}_{t,s} \quad \forall s \in S, \forall t \in T \tag{14.44}$$

$$V^{DU} \le V^{U}_{t,S} \le V^{UU} \quad \forall s \in S, \forall t \in T \tag{14.45}$$

$$V^{DL} \le V^{L}_{t,S} \le V^{UL} \quad \forall s \in S, \forall t \in T \tag{14.46}$$

$$V^{U}_{t,S} = Vf^{U} \quad \forall s \in S, t = 1, 24 \tag{14.47}$$

$$V^{L}_{t,S} = Vf^{L} \quad \forall s \in S, t = 1, 24 \tag{14.48}$$

$$u_{t+1,S} = u_{t,S} + y_{t,S} - z_{t,S} \quad \forall s \in S, t = 1, 24 \tag{14.49}$$

$$d^{D} \cdot u_{t,S} \le d^{Pump}_{t,S} \le d^{U} \cdot u_{t,S} \quad \forall s \in S, \forall t \in T \tag{14.50}$$

$$0 \le g^{Pump}_{t,S} \le t_{t,S} \cdot g^{U} \cdot N \quad \forall s \in S, \forall t \in T \tag{14.51}$$

$$t_{t,S} \le 1 - \tfrac{1}{N} \cdot u_{t,S} \quad \forall s \in S, \forall t \in T \tag{14.52}$$

$$-d^{U} \cdot N \le P^{PUMP}_{t} \le g^{U} \cdot N \quad \forall t \in T \tag{14.53}$$

$$\Delta^{+PUMP}_{t,S} = g^{Pump}_{t,S} - d^{Pump}_{t,S} - P^{PUMP}_{t} \quad \forall s \in S, \forall t \in T \tag{14.54}$$

$$\Delta^{-PUMP}_{t,S} = P^{PUMP}_{t} - g^{Pump}_{t} + d^{Pump}_{t,S} \quad \forall s \in S, \forall t \in T \tag{14.55}$$

$$t_{t,S} \in \{0, 1\} \quad \forall s \in S, \forall t \in T \tag{14.56}$$

$$u_{t,S}, y_{t,S}, z_{t,S} \in \{0, 1, \ldots, N\} \quad \forall s \in S, \forall t \in T \tag{14.57}$$

Water balance equation in terms of energy for upper and lower reservoir is expressed in (14.43) and (14.44), in which the efficiency has an effect on the amount of energy which is pumped from bottom tank to the upper one. Equations (14.45) and (14.46) frames both reservoirs capacity limitations. Conserved energy at the end of the considered time scope is given by (14.47) and (14.48). N depicts number of identical units which form the storage unit. Also

start-up and close down expenses are taken into account in objective function by integer variables $y_{t,S}$ and $z_{t,S}$. The variable $u_{t,S}$ is allocated to the unit numbers which are functioning as turbine or pump at hour *t*. Equation (14.49) expresses the mathematical relationship between these three integer values. According to (14.50) and (14.51) pumping and turbine capacities are limited, which causes limitation on market offers (14.53). Equation (14.51) In order to prevent storage plant from operating simultaneously as a pump and turbine, binary variable t_{Sh} is defined which equals to zero in pumping mode by (14.52). Existed imbalances in each scenario and hour resulted from surplus or lack of power production are calculated by (14.54) and (14.55).

14.4.2 Joint Operation

By integration of wind power, photovoltaic, pumped storage power plant and demand response total benefit is increased in comparison to summation of individual units' profit since demand response and pumped-storage add flexibility to wind and solar power and though can complement their uncertainty. Considering above statements, microgrid profit function is formulated as below:

$$F_{PUMP} = F_{DA} - F_{Su} - F_{Sd} + F_{Pos\_Imb} - F_{Neg\_Imb} \tag{14.58}$$

$$F_{DA} = \sum_{t=1}^{T}\sum_{s=1}^{S} \rho_s \pi_{DA,t,s} P_t^{JOINT} \tag{14.59}$$

$$F_{Su} = \sum_{t=1}^{T}\sum_{s=1}^{S} \rho_s C^{Su} y_{t,S} \tag{14.60}$$

$$F_{Sd} = \sum_{t=1}^{T}\sum_{s=1}^{S} \rho_s C^{Sd} z_{t,S} \tag{14.61}$$

$$F_{Pos\_Imb} = \sum_{t=1}^{T}\sum_{s=1}^{S} \rho_s \pi_{DA,t,s} \alpha_{t,s}^{+} \Delta_{t,s}^{+JOINT} \tag{14.62}$$

$$F_{Neg\_Imb} = \sum_{t=1}^{T}\sum_{s=1}^{S} \rho_s \pi_{DA,t,s} \alpha_{t,s}^{-} \Delta_{t,s}^{-JOINT} \tag{14.63}$$

Constraints:

$$-d^U \cdot N \le P_t^{JOINT} \le P^{W\,max} + P^{PV\,max} + g^U \cdot N \quad \forall t \in T \tag{14.64}$$

$$\Delta_{t,S}^{+PUMP} = g_{t,S}^{Pump} - d_{t,S}^{Pump} - P_t^{PUMP} + D_{t,s} - D_t \quad \forall s \in S, \forall t \in T \tag{14.65}$$

$$\Delta_{t,S}^{-PUMP} = P_t^{PUMP} - g_t^{Pump} + d_{t,S}^{Pump} + D_t - D_{t,s} \quad \forall s \in S, \forall t \in T \tag{14.66}$$

In this configuration total profit is composed of 5 terms as Eqs. (14.59)–(14.63). Constraints related to joint operation is as the same as clean energy's uncoordinated operation and its difference is just in bidding limitations and imbalances calculation which are rewritten in Eqs. (14.64)–(14.66).

14.5 Simulation Results

In this part of chapter, numerical studies have been done in order to analyze joint and disjoint operation of clean energy sources and to determine bids and benefits of each configuration. To do so a test system which is composed of all these clean energy sources is considered. The proposed method has a MILP nature which is solved by CPLEX solver of GAMS software. The numerical results has been performed on a 2.3-GHz based processor with 4 GB of RAM.

14.5.1 Studied System

The schematic diagram of studied system is shown in Fig. 14.10. The case study system is composed of a 2500 kW wind turbine, solar resource with nominal power of 300 kW and two pumped-storage units with 300 and 100 kW storage and generation capacity, respectively. The wind speed data of Sotavento wind farm in Spain [30] is employed. In this chapter, annual solar radiation of Madrid, Spain which is freely available for public in SAM website [32] is utilized. The MCP is extracted from Spanish electricity market [33]. The case study is simulated for 10 February 2014. Table 14.2 shows the parameters of storage units. The start-up cost for each unit is equal to $C^{su} = 100\$$ while the close down expense is assumed to be 10$. The basic values of demand response program parameters are given in Table 14.3. Also, overall scenarios are reduced to 1000 by the aforementioned scenario reduction process.

14.5.2 Numerical Results

In this section the abovementioned method for integration of DGs is applied on a typical microgrid and numerical results are extracted. First of all it is necessary to model uncertainties and generate required scenarios. In order to analyze behavior of

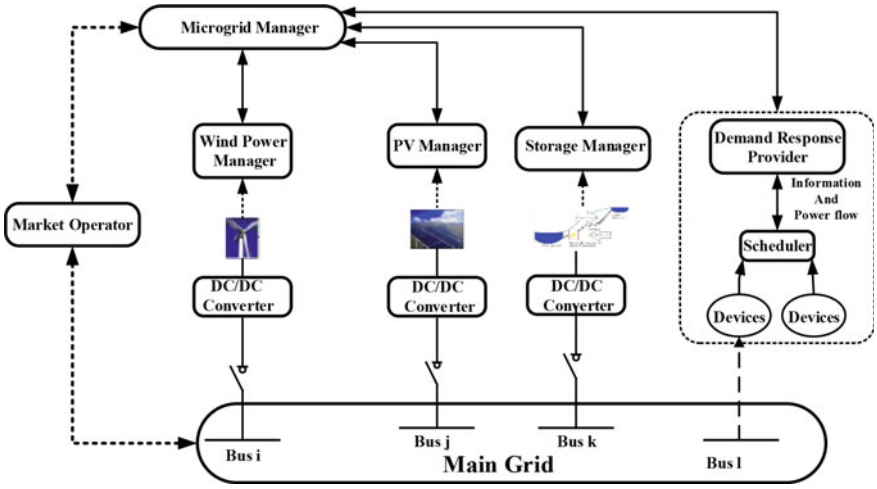

Fig. 14.10 Schematic diagram of virtual microgrid

Table 14.2 Pumped-storage characteristics

d^U (kW)	g^U (kW)	C^{su} ($)	C^{sd} ($)	η (%)	N
300	100	100	10	67	2
Upper reservoir	V^{UU} (kW)	V^{DU} (kW)		Vf^U (kW)	
	1500	0		900	
Lower reservoir	V^{UL} (kW)	V^{DL} (kW)		Vf^L (kW)	
	1500	0		900	

Table 14.3 Parameters of demand response program

Parameter	η_1	η_2	β	α
value	0.8	0.2	−0.3	0.95

imbalance market prices, hourly buy and sell imbalance prices and also hourly MCP values throughout January is extracted from [33]. Then by dividing extracted imbalance prices to their proportional MCP value, their hurly ratios are computed. In this chapter in order to demonstrate the occurrence number of ratios, box plot for ratios of buy and sell imbalance prices is depicted in Fig. 14.11. Selling power in imbalance market occurs when there is a surplus generated power with respect to the commitment. Excess of generated power will be sold cheaper than MCP and sell imbalance price ratio will be lower than unity as shown in Fig. 14.11a. On the other hand, buying imbalance power results from shortage of produced power with respect to the promised value. So it clear that this deficiency will be traded in a higher price than MCP and as can be seen in Fig. 14.11b buy imbalance price ratios will be greater than unity. Each of these buy and sell ratios are a probable scenario which can be happened.

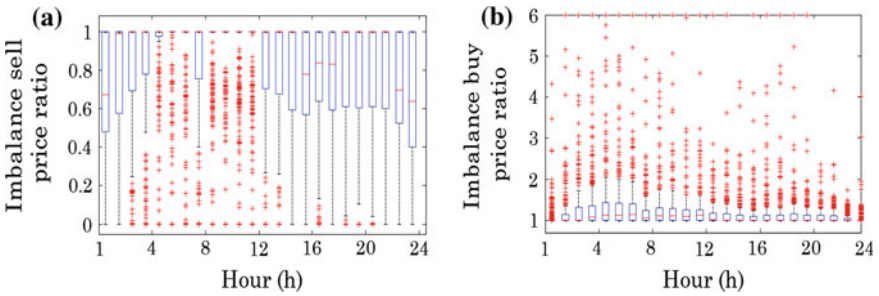

Fig. 14.11 Box plot of ratio between imbalance and marginal clearing prices

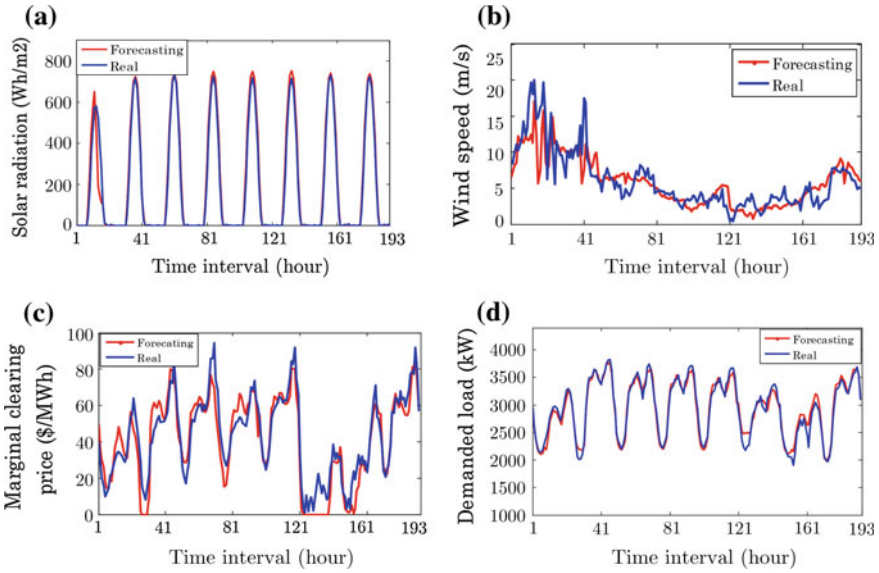

Fig. 14.12 Real and forecasted values of: **a** solar radiation, **b** wind speed, **c** marginal clearing price, and **d** demanded load

Happening probability of each these scenarios is calculated by dividing its number of occurrences to the total hours of month which equals to 720. At this point, required number of buy and sell imbalance price ratio scenarios (here 10 for each one) are generated by roulette wheel mechanism. Figure 14.12 shows the real and forecasted values of wind speed, solar radiation, MCP and load. As can be seen the prediction results are not accurate completely and there is a prediction error for most of the hours between real and forecasted values.

These error values are categorized in 1% distances for each uncertain parameter while each of these categories is considered as a probable scenario. Same as above, occurrence probability of each error value is computed by dividing its abundance to

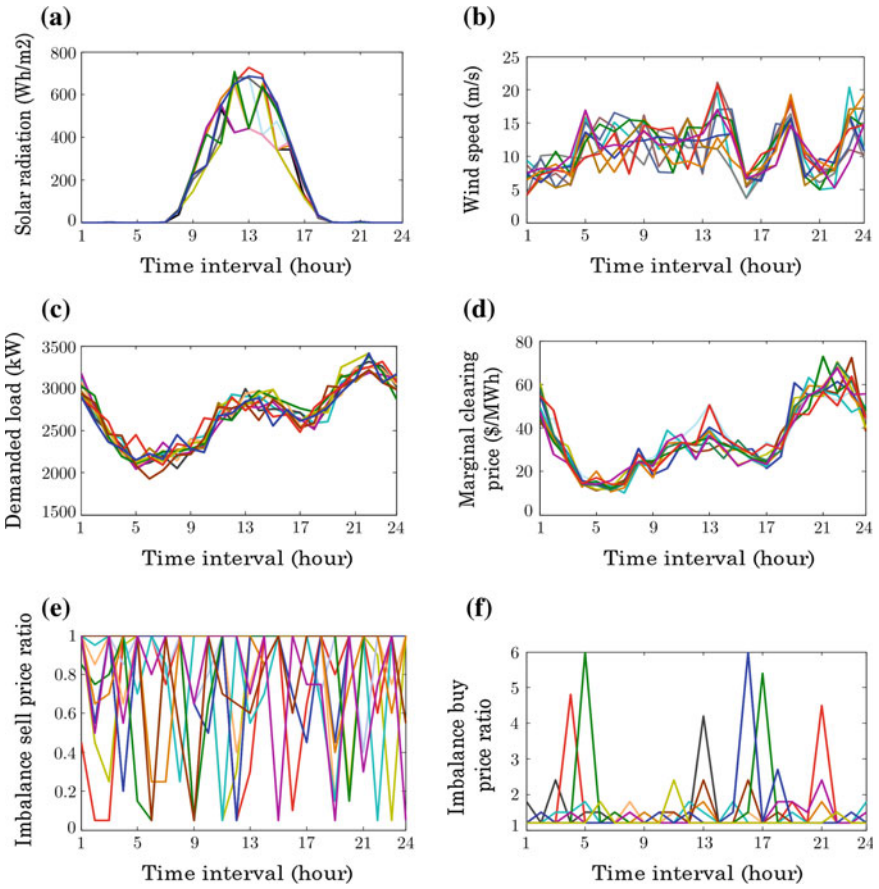

Fig. 14.13 Generated scenarios for: **a** solar radiation, **b** wind speed, **c** demanded load, **d** marginal clearing price, **e** sell imbalance price ratio and **f** buy imbalance price ratio

total number of error values. Roulette wheel mechanism is applied to generate desired number of scenarios (here 10) for each uncertain parameter. Ten generated scenarios for each of six uncertain parameters are depicted in Fig. 14.13.

The aim of optimization models is to find optimal bidding values for next day in such a way that the social welfare is maximized. In this chapter in order to explain effects of uncertainties on earned profit, optimization is done on two configurations named as disjoint and joint operation. In disjoint configuration, each of microgrid elements bid independently to maximize their own profit but in the joint operation, all of microgrid elements suggest their offers to the market by considering effects of other participants to reach the maximum profit of microgrid. Figure 14.14 depicts the optimal bidding values for each hour in these two configurations. In disjoint configuration WPP and PV offer based on their available power. As Fig. 14.14 shows PV offers only for hours between 10 till 17 while solar radiation is nonzero.

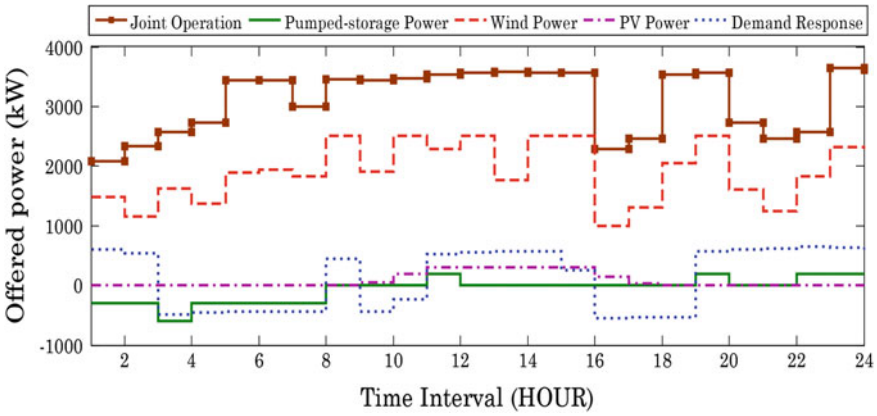

Fig. 14.14 Hourly offering quantities on 10/02/2014

Also demand response and pumped storage unit bid based on load and MCP. For example during 11 till 16 when MCP and load are high, demand response program submit its bid to reduce load but between 16 till 19 when MCP is low, it will compensate the reduced loads. On the other hand, pumped-storage unit pumps water between 1 and 8 while demanded load and MCP are low and release this energy at 11 when load is high.

By comparing the joint and disjoint operation results, it can be seen that offered power in joint mode during expensive hours is more than summation of units' individual offers because of flexibility which arises from pumped-storage plant and demand response. On the other words, during off peak and cheap hours when WPP and PV's output power is high, pumped-storage unit acts in pumping mode to store energy. To do so, it buys inexpensive power and pumps water to the upper tank in order to save energy. The stored energy is sold to earn much profit during expensive hours or to reduce penalties when WPP and PV producers face with lack of generated power because of their uncertain nature. Also, end users help this flexibility by reducing their demand during expensive hours and compensate them in cheap hours.

Numerical results related to the expected profit for each configuration is expressed in Table 14.4. WPP, PV producer, pumped-storage units and DR program earn 1663.332$, 195.957$, 367.526$ and 120$ profit when they try independently to maximize just their own profit whose summation equals to 2346.812$. But in the joint mode, integration of all units together increases overall flexibility against existence uncertainties which lead to an overall profit which equals to 2556.492$. Simulation results approve that aggregating all sources together was successful in increasing the profit by 8.9% in the case study.

This profit increase in joint mode results from hedging against solar and wind production uncertainty which is provided by pumped-storage unit and demand response via pumping water to upper reservoir and saving energy during cheap hours and releasing water and generating energy during expensive hours or by reducing consumption in costly hours and buying it in inexpensive hours.

Table 14.4 Expected profit for each configuration

Configuration		Profit ($)
DO	Wind power producer	1663.332
	PV	195.957
	Pumped-storage unit	367.526
	DR	120
	Sum	2346.815
JO		2556.492

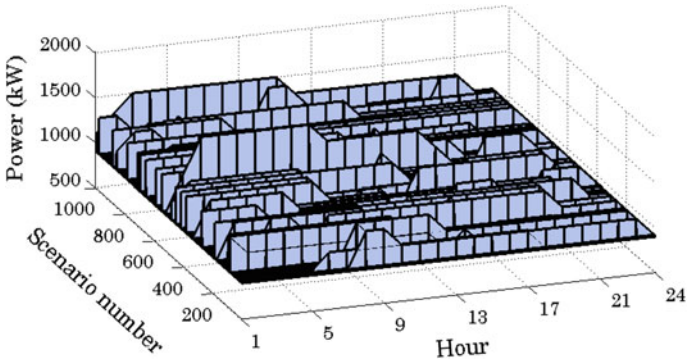

Fig. 14.15 Stored power in upper reservoir for each hour and scenario of joint operation

Figure 14.15 depicts the operation of upper reservoir of pumped-storage unit for each hour and scenario in the joint configuration. As can be seen during inexpensive hours, off-peak hours, the reservoir pumps water to its upper tank until it reaches to its upper reservoir limitation which equals to 1500 kW. Then in expensive hours it releases this energy to avoid economic losses. On the other hand, this figure proves that the initial and final value of stored energy in this reservoir equals to 900 kW which was constrained in the mathematical modeling of pumped storage unit.

14.6 Conclusion

Through this chapter, a scenario based stochastic method is proposed for planning the aggregated operation of wind turbine, photovoltaic arrays, pumped-storage unit and demand response with the goal of profit maximization. The proposed strategy considers uncertainties related to wind power, solar radiation, load, marginal and imbalance market prices over the 24 h study horizon. Using neural networks, uncertain variables are forecasted and then according to prediction errors, possible scenarios are generated and the proportional occurrence probability of each scenario is calculated. In order to save computation time, a backward scenario reduction process is applied.

The proposed four-stage-scenario-based method is tested on a typical microgrid for various operating circumstances. Numerical results approve that aggregation of all units in a microgrid can significantly increase profit value in comparison to units disjoint operation. The results also approve that, demand response and pumped-storage plant as storage devices can efficiently cover production power uncertainties of microgrid units and make wind and solar producers more competitive in day-ahead power markets. On the other hand, by considering uncertainties of negative/positive imbalance market prices and marginal prices of day-ahead market, more probable prices are considered.

References

1. Shi L, Luo Y, Tu GY (2014) Bidding strategy of microgrid with consideration of uncertainty for participating in power market. Int J Electr Power Energy Syst 59:1–13
2. Niknam T, Azizipanah-Abarghooee R, Narimani R (2012) An efficient scenario-based stochastic programming framework for multi-objective optimal micro-grid operation. Appl Energy 99:455–470
3. Lidula NWA, Rajapakse AD (2011) Microgrids research: a review of experimental microgrids and test systems. Renew Sustain Energy Rev 15:186–202
4. Blaabjerg F, Chen Z, Kajaer SB (2004) Power electronics as efficient interface in dispersed power generation systems. IEEE Trans Power Electr 19(5):1184–1194
5. Rocabert J, Luna A, Blaabjerg F et al (2012) Control of power converters in AC microgrids. IEEE Trans Power Electr 27(11):4734–4749
6. Katiraei F, Iravani R, Hatziargyrious N et al (2008) Microgrids management. IEEE Power Energy Mag 6(3):54–65
7. Eghtedarpour N, Farjah E (2014) Power control and management in a hybrid AC/DC microgrid. IEEE Trans Smart Grid 5(3):1494–1505
8. Anbazhagan S, Kumarappan N (2014) Day-ahead deregulated electricity market price forecasting using neural network input featured by DCTO. Energy Convers Manage 78:711–719
9. Sharma KC, Bhakar R, Tiwari HP (2014) Strategic bidding for wind power producers in electricity markets. Energy Convers Manage 86:259–267
10. Koo J, Han GD, Choi HJ et al (2015) Wind-speed prediction and analysis based on geological and distance variables using an artificial neural network: a case study in South Korea. Energy 93:1296–1302
11. Pousinho HMI, Mendes VMF, Catalao JPS (2011) A hybrid PSO-ANFIS approach for short term wind power prediction in Portugal. Energy Convers Manage 52:397–402
12. Shayeghi H, Ghasemi A (2013) Day-ahead electricity prices forecasting by a modified CGSA technique and hybrid WT in LSSVM based scheme. Energy Convers Manage 74:482–491
13. Zuluaga CD, Alvarez MA, Giraldo E (2015) Short-term wind speed prediction based on robust Kalman filtering: an experimental comparison. Appl Energy 156:321–330
14. Shayeghi H, Ghasemi A, Moradzadeh M et al (2015) Simultanous day-ahead forecasting of electricity price and load in smart grids. Energy Convers Manage 95:371–384
15. Pousinhoa HMI, Mendesc VMF, Catalo JPS (2012) A stochastic programming approach for the development of offering strategies for a wind power producer. Electr Power Syst Res 89:45–53
16. Shayeghi H, Hashemi Y (2015) Application of fuzzy decision-making based on INSGA-II to designing PV-wind hybrid system. Eng Appl Artif Intell 45:1–17

17. Shayeghi H, Bagheri A (2013) Dynamic sub-transmission system expansion planning incorporating distributed generation using hybrid DCGA and LP technique. Int J Electr Power Energy Syst 48:111–122
18. García-González J, de la Muela RMR, Santos LM et al (2008) Stochastic joint optimization of wind generation and pumped-storage units in an electricity market. IEEE Trans Power Syst 23 (2):460–468
19. Karimi Varkani A, Daraeepor A, Monsef H (2011) A new self-sceduling strategy for integrated operation of wind and pumped-storage power plants in power markets. Appl Energy 88:5002–5012
20. Parastegari M, Hooshmand RA, Khodabakhshian A et al (2013) Joint operation of wind farms and pump-storage units in the electricity markets: Modeling, simulation and evaluation. Simul Model Pract Theor 37:56–69
21. Mohammadi J, Rahimi-Kian A, Ghazizadeh MS (2011) Aggregated wind power and flexible load offering strategy. IET Renew Gener 5:439–447
22. Mohammadi M, Hosseinian SH, Gharehpetian GB (2012) Optimization of hybrid solar energy sources/wind turbine systems integrated to utility grids as microgrid (MG) under pool/bilateral/hybrid electricity market using PSO. Sol Energy 86:112–125
23. Mohammadi S, Soleymani S, Mozafari B (2014) Scenario-based stochastic operation management of MicroGrid including wind, photovoltaic, micro-turbine, fuel cell and energy storage devices. Int J Electr Power Energy Syst 54:525–535
24. Sortomme E, El-Sharkawi MA (2009) Optimal power flow for a system of microgrids with controllable loads and battery storage. In: IEEE/PES Power System Conference, pp 1–5
25. Shayeghi H, Sobhani B (2014) Integrated offering strategy for profit enhancement of distributed resources and demand response in microgrids considering system uncertainties. Energy Convers Manage 87:765–777
26. Alharbi W, Raahemifar K (2015) Probabilistic coordination of microgrid energy resources operation considering uncertainties. Electr Power Syst Res 128:1–10
27. Aghajani GR, Shayanfar HA, Shayeghi H (2015) Presenting a multi-objective generation scheduling model for pricing demand response rate in micro-grids energy management. Energy Convers Manage 106:308–321
28. Motevasel M, Seifi AR (2014) Expert energy management of a microgrid considering wind energy uncertainty. Energy Convers Manage 83:58–72
29. Chen C, Duan S, Cai T et al (2011) Smart energy management system for optimal microgrid economic operation. IET Renew Power Gen 5:258–267
30. http://www.sotaventogalicia.com/index.php
31. Nordex N80/2500 wind turbine catalogue. http://www.nordex-online.com/en/produkte-service/wind-turbines/n80-25-mw.html
32. http://www.solargis.info
33. http://www.esios.ree.es/web-publica/

Chapter 15
Optimal Planning of a Micro-combined Cooling, Heating and Power System Using Air-Source Heat Pumps for Residential Buildings

Farkhondeh Jabari, Behnam Mohammadi-Ivatloo and Mohammad Rasouli

Abstract This chapter explains a methodology for optimal planning of a micro-combined cooling, heating and power system driven by a solar dish Stirling heat engine. The solar dish concentrator collects the sun radiations and transforms them into thermal energy. The absorber and thermal storage systems are employed to absorb and store the thermal energy collected by a solar dish for continuous energy supplying when the sunlight is insufficient. The solar energy is absorbed and transferred to the working fluid in the hot point of the Stirling engine. The air source heat pump has been proposed to cool and heat the residential buildings in hot and cold weather conditions, respectively. During a hot weather, the air to air heat pump receives heat from the inside air and transfers it into the outside air, and vice versa in a cold climate. The heating energy obtained from air source heat pumps is not generated by a combustion process, rather it is transferred from the inside air to the outside air. Hence, the most promising aspect of the proposed micro-combined cooling, heating and power system is that it can be solar driven and transfer heat from the inside air during summer. Note that the process is reversed in winter times. Due to the increasing rate of carbon dioxide and more attention paid to the greenhouse gas emissions, use of solar energy and air source heat pumps in a micro-trigeneration system, which does not use any fossil fuel such as gasoline or natural gas, not only gives more chances to significant reduction of carbon dioxide, greenhouse gas emissions, and environmental pollution, but also increases the economic saving in fuel consumption. In an air to air heat pump, the electricity

F. Jabari · B. Mohammadi-Ivatloo (✉)
Faculty of Electrical and Computer Engineering, University of Tabriz, Tabriz, Iran
e-mail: bmohammadi@tabrizu.ac.ir

F. Jabari
e-mail: f.jabari@tabrizu.ac.ir

M. Rasouli
Department of Electrical and Computer Engineering, School of Engineering,
Penn State University, Erie, PA, USA
e-mail: mur37@psu.edu

N. Bizon et al. (eds.), *Energy Harvesting and Energy Efficiency*,
Lecture Notes in Energy 37, DOI 10.1007/978-3-319-49875-1_15

energy is only used by indoor/outdoor fans, and a compressor. Hence, the small-scale tri-generation system consumes less electrical energy than the traditional ones. In order to conduct an optimization, the mathematical model and thermodynamic analysis of proposed microsystem have been provided. Several key parameters related to solar dish Stirling heat engine and air to air heat pumps have been selected as the decision variables to minimize the cost of the electricity energy purchased from the main grid.

Abbreviation and Acronyms

AAHP	Air to Air Heat Pump
ASHP	Air Source Heat Pump
CCHP	Combined Cooling Heating and Power
CCP	Combined Cool and Power
CHP	Combined Heat and Power
CVaR	Conditional Value at Risk
DNLP	Discontinuous Nonlinear Program
GAMS	General Algebraic Modeling System
MILP	Mixed-Integer Linear Programming
ORC	Organic Rankine Cycle
SDSHE	Solar Dish Stirling Heat Engine
SOFC	Solid Oxide Fuel Cell
TVAC-PSO	Time Varying Acceleration Coefficients Particle Swarm Optimization
WAST	Warm Air Storage Tank

15.1 Introduction

In recent years, the urgent need to meet the increased power demand and to address the concerns over the environmental pollution as well as the greenhouse gas emissions reduction have led to employment of the tri-generation technology powered by renewable energy sources. The combined cooling, heating and power (CCHP) systems not only provide the cooling, heating and electricity demands of different customers such as residential, commercial and industrial loads, but also can provide reserve, peak saving and demand response services. As shown in Fig. 15.1, a typical tri-generation system consists of the following main components:

- Renewable energy sources such as solar, wind, hydroelectric energy, biomass, hydrogen and fuel cells, and geothermal power.
- Prime mover such as reciprocating internal combustion engine, combustion turbine, steam turbine, micro turbine, gas turbine, fuel cell, and Stirling engine as an external combustion engine.

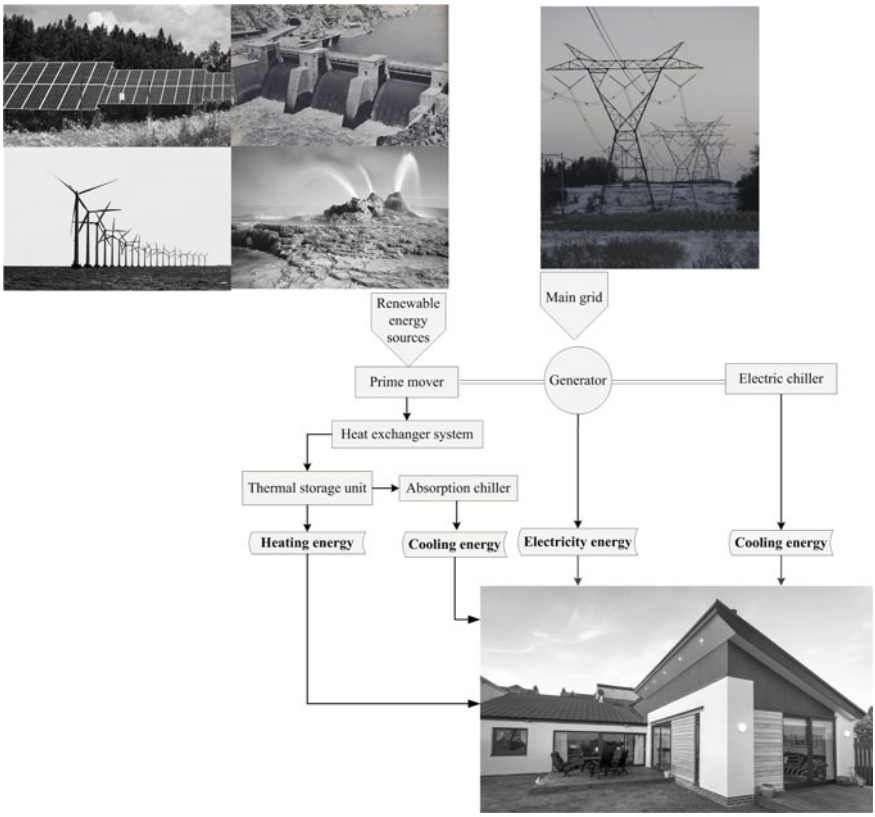

Fig. 15.1 Structure of a CCHP system

- Power generation unit.
- Electric chiller.
- Absorption chiller.
- Energy storage and thermal storage units.
- Electricity, cooling and heating loads.

Recently, several remarkable researches have been carried out to plan and evaluate a tri-generation system. In [1], a novel energy management strategy based on the variational electric cooling with combined electric and absorption chillers under unlimited and limited power generation unit capacity has been proposed. The variational electric cooling to cool load ratio has been optimized according to electric and thermal demands in every hour. In [2], a multi-objective optimization of a CCHP microgrid driven by solar energy has been investigated. The flat-plate solar collectors have been employed to collect the sun beam radiations and transform them into thermal energy. The heat storage system has been installed to store the collected thermal energy. Turbine inlet temperature, turbine inlet pressure, condensation temperature and pinch temperature difference in vapor generator have

been selected as the optimization decision variables to assess the performance of the entire solar CCHP microsystem. A two-stage optimal planning of tri-generation microgrid has been investigated in [3]. Total net present cost and carbon dioxide emission in life circle have simultaneously been minimized using non-dominated sorting genetic algorithm-II and mixed-integer linear programming (MILP) algorithm. In [4], exergoeconomic optimization of a CCHP system has been applied to maximize the total revenue requirement and the cost of the total system product using a genetic algorithm. Air compressor pressure ratio, gas turbine inlet temperature, pinch point temperatures in dual pressure heat recovery steam generator, pressure of the steam that enters the generator of the absorption chiller, process steam pressure and evaporator of the absorption chiller chilled water outlet temperature have been chosen as decision variables.

Reference [5] considers exergy modeling of a solar powered CCHP system consists of a single-effect absorption chiller, a heat exchanger, thermal storage tank, evaporator, absorber, solution expansion valve, solution pump, desorber, condenser, and organic Rankine cycle (ORC) components. Three operating conditions have been considered in this study: low solar radiation, high solar radiation, and storage mode in night. A real-time model of hydrogen tri-generation system and onsite hydrogen dispensing systems in the presence of price and market uncertainties has been developed in [6]. Application of two multi criteria decision-making algorithms denoted as fuzzy logic and the grey incidence methods are discussed in [7] to select the best prime mover for a residential tri-generation microgrid under five different climates. Technological, economic, environmental and social have been considered in the optimization process. Reference [8] introduces a novel CCHP system including a low temperature polymer electrolyte fuel cell and a desiccant wheel-based air handling unit. An integrated solid oxide fuel cell (SOFC) cogeneration micro-grid, fueled by coke oven gas that needs large amount of hydrogen is developed in [9]. Exhaust gas deep-recovery and thermoelectric generator based tri-generation system is presented in [10]. Thermoelectric generator and condenser are used to efficiently recover the exhaust gas waste heat of internal combustion engine. In [11], a small-scale solar tri-generation cycle combined with ORC has been proposed for hot and cold weather conditions. Turbine inlet temperature and pressure, turbine back pressure, evaporator temperature and heater outlet temperature are selected as the decision variables to improve thermal efficiency, exergy efficiency and total product cost rate. The proposed system could continuously and stably operate with installed thermal storage tank.

A novel CCHP microgrid with significant economic and environmental benefits, which consists of a power generation unit, an absorption chiller, two ground source heat pumps, a storage tank and two electric chillers has been introduced in [12]. The hourly programming with different cooling and heating demands has been carried out according to the outdoor climatic condition to improve system efficiency. In [13], a biomass tri-generation microgrid including a biomass gasifier, a heat pipe heat exchanger, an internal combustion engine, an absorption chiller and a heater for cooling and heating, and a heat exchanger to produce domestic hot water has been proposed. Operational planning has been provided in three modes: summer,

winter, and the transient seasons. In [14], a novel micro-CCHP equipped with 20 kW Lombardini diesel engine and a double effect water-LiBr absorption chiller has been introduced to generate hot water, by recovering heat from the engine cooling system, and chilled water, by recovering heat from the engine exhaust gasses. The engine and the absorption chiller have been modeled by means of 0–1D dimensional and thermochemical models, respectively. A Honda gas engine based micro-CCHP, which utilizes a heat recovery system, has been proposed to satisfy the required heating, cooling and electrical energy of a residential building according to the air conditions [15]. The formulation of a CCHP system including an air-conditioning system and a heat storage tank in residential and office buildings in Dalian, China is presented in [16]. The energy saving, total cost, and environmental pollution reduction have been considered as main objectives in the genetic based optimization process. In [17], a small scale CCHP system has been introduced. The waste heat of internal combustion engine is collected and managed using a thermal management controller. The waste heat can be used for heating or cooling cycle. The part load ratio of the internal combustion engine, buffer tank set point temperature, hot water tank set point temperature, chilled water temperature and cooling water temperature of adsorption chiller are treated as decision variables. Thermal management controller is used to manage the waste heat. The heating output of the thermal management controller is regulated via buffer tank and hot water tank set point temperatures. A CCHP microgrid with a gas turbine, a heat recovery steam generator unit and an absorption heat pump driven by a steam turbine has been designed in [18]. Genetic algorithm is used to minimize the total annual cost and maximize the exergy efficiency. In [19], a reliable grassroots biomass based cogeneration system has been designed according to the equipment redundancy. Chance constrained programming and k-out-of-m system modeling have been applied to solve a multi period optimization process.

A tri-generation system including a solid oxide fuel cell, an air pre-heater, an ethanol reformer, a steam generator and a double-effect $LiBr/H_2O$ absorption chiller, which uses the heat recovery of the solid oxide fuel cell exhaust gas, has been proposed in [20]. In order to evaluate the performance of the presented microgrid, a parametric assessment of the effects of the current density, solid oxide fuel cell temperature, fuel consumption ratio and solid oxide fuel cell anode recirculation ratio variations on total net electrical, heating and cooling energies have been provided. An energy management strategy has been proposed to increase the biomass-CCHP yearly efficiency by managing the output heating energy [21], where double piping district heating and cooling demands of a residential building have been considered. In the maximization process of the net present value, hourly heating and cooling load have been forecasted using the degree-hour method. Energy and exergy based management of a three-reactor chemical looping hydrogen generation process of a zero emission tri-generation plant has been presented in [22]. The proposed tri-generation microsystem involves an air separation unit, gasification unit, a chemical looping hydrogen generation system, an extended heat recovery steam generation unit, an ORC and space heating, a two-stage steam Rankine cycle with reheat and regenerator and an ORC. The optimal energy

management in energy hubs has recently attracted a great deal of attention around the world. The energy hub consists of several inputs (energy resources) and outputs (energy consumptions) and also some energy conversion/storage devices. The energy hub can be a home, large consumer, power plant, etc. The objective is to minimize the energy procurement costs (fuel/electricity/environmental aspects) subject to a set of technical constraints. In [23], a comprehensive multi-objective model is proposed to minimize both the energy procurement cost and risk level in energy hub. For controlling the pernicious effects of the uncertainties, conditional value at risk (CVaR) is used as risk management tool. A novel time varying acceleration coefficients particle swarm optimization (TVAC-PSO) algorithm is implemented to solve combined heat and power economic dispatch problem in [24].

To achieve a practical planning of CCHP microgrids with no combustion process and no emission of potentially dangerous gases, high economic and technological efficiency are difficult challenges to be addressed. In the literature, remarkable efforts have been made to manage on the energy and exergy of tri-generation systems. However, some problems have not been resolved yet. Among those are the significant reduction of the greenhouse gas emissions and the risk of the environmental pollutants, reducing the fossil fuel consumption using renewable energy sources, and economic savings due to energy exchanges with the main grid. This chapter develops an hourly scheduling of a novel micro tri-generation system to satisfy the electrical, heating and cooling demands of a residential building. A solar dish Stirling heat engine (SDSHE) is used as the prime mover to provide the required input mechanical power for the power generation unit. Thus, there is no need for a combustion process, fossil fuel consumption or equipment in the combustion process such as a combustion chamber, an air compressor and a gas turbine. Therefore, there will be no greenhouse gas emissions involved. The proposed small-scale CCHP system is designed to operate in two different modes:

- Combined heat and power (CHP) mode based on the heating cycle of the air to air heat pump (AAHP) in the cold weather.
- Combined cool and power (CCP) mode based on the refrigeration cycle of the air to air heat pump on hot days.

The electric chiller is also used to supply a part of the required cold energy in the cooling mode. Furthermore, the proposed air to air heat pump based small-scale CCHP microgrid has the following advantages:

- Air to air heat pumps can provide cooling energy in hot climate condition, and vice versa.
- Air to air heat pumps requires less maintenance than the combustion process based heating systems.
- Similar to the SDSHE, air to air heat pumps are safe. No combustion or emission is involved.

- Air to air heat pumps save carbon emissions. Unlike the burning oil, gas, and biomass, an air to air heat pump produces no carbon emissions on site (no greenhouse gas emissions at all, if a renewable source of electricity such as solar or wind is used to power them).
- Air to air heat pumps are cheaper to run than the oil boilers and can be cheaper than the running gas boilers.

The remainder of this chapter is organized as follows: Sect. 15.2 expresses the basic concepts related to the solar powered Stirling heat engine and the refrigeration cycle of the air source heat pumps. The energy and the exergy of the proposed micro-combined cooling, heating and power system are analyzed in Sect. 15.3. Simulation results and discussions are presented in Sect. 15.4. Finally, Sect. 15.5 concludes the chapter.

15.2 Proposed Small-Scale Tri-generation System for Residential Buildings

15.2.1 Solar Dish Stirling Heat Engine (SDSHE)

In this chapter, the solar energy is used as a renewable energy source to drive a Stirling engine, which is used to supply the primary mechanical power required for a power generation unit [25]. The location of an absorber and a thermal storage unit on a solar-dish concentrator are illustrated in Fig. 15.2.

As shown in Fig. 15.3, the Stirling cycle comprises of four processes. Process 1–2 is an isothermal process, in which the working fluid after compressing at constant temperature T_c and rejected heat to the heat sink at low temperature T_{L_1}, the temperature of heat sink is increased to T_{L_2}. Then, the working fluid crosses over the regenerator and warms up to T_h in an isochoric process 2–3. In process 3–4, the working fluid is expanded in a constant temperature T_h process and receives heat from the heat source in which its temperature is reduced from T_{H_1} to T_{H_2}. Last process (4–1), is an isochoric cooling process, where the regenerator absorbs heat from the working fluid.

The actual useful heat gain of the dish collector, q_u, considering the conduction, convection and radiation losses can be obtained as [25]:

$$q_u = IA_{app}\eta_0 - A_{rec}[h(T_{H_{ave}} - T_0) + \varepsilon\delta(T_{H_{ave}}^4 - T_0^4)] \tag{15.1}$$

where:

I Direct solar flux intensity in $\mathrm{W} \cdot \mathrm{m}^{-2}$
A_{app} Collector aperture area in m^2
η_0 Collector optical efficiency
A_{rec} Absorber area in m^2

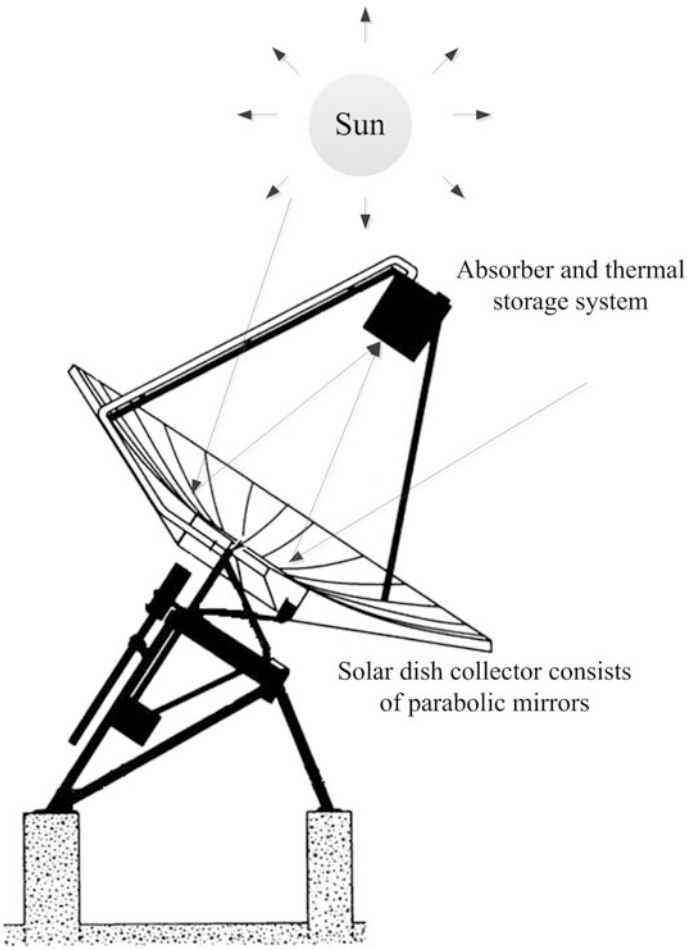

Fig. 15.2 The location of an absorber and a thermal storage unit on a solar-dish concentrator

h Conduction-convection heat transfer coefficient in $W \cdot m^{-2} \cdot K^{-1}$
$T_{H_{ave}}$ Average absorber temperature in K
T_0 Ambient temperature in K
ε Effectiveness factor of collector
δ Stefan's constant in $W \cdot m^{-2} \cdot K^{-4}$

Thermal efficiency of the dish collector, η_s is calculated from:

$$\eta_s = \frac{q_u}{IA_{app}} = \eta_0 - \frac{h(T_{H_{ave}} - T_0) + \varepsilon\delta(T_{H_{ave}}^4 - T_0^4)}{IC} \tag{15.2}$$

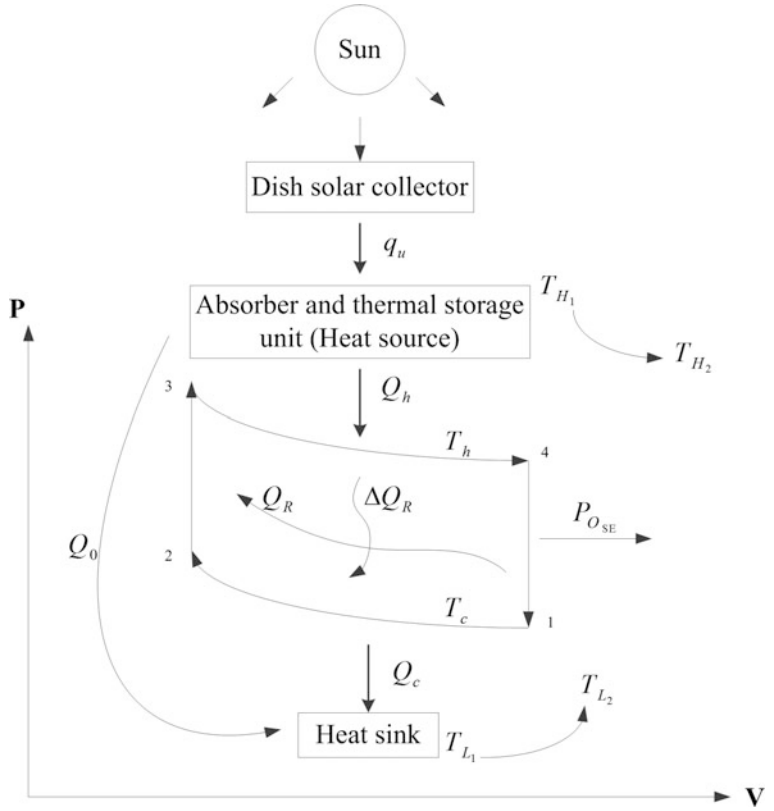

Fig. 15.3 Stirling cycle of a solar dish Stirling heat engine [23]

where, C is heat capacitance rate in $\mathrm{W} \cdot \mathrm{K}^{-1}$. The regenerative heat transfer and the heat loss during two regenerative processes are given by following equations:

$$Q_R = nC_v\varepsilon_R(T_h - T_c) \tag{15.3}$$

$$\Delta Q_R = nC_v(1 - \varepsilon_R)(T_h - T_c) \tag{15.4}$$

where:

Q_R Regenerative heat transfer in J
n Number of moles
C_v Specific heat capacity in $\mathrm{J} \cdot \mathrm{mol}^{-1} \cdot \mathrm{K}^{-1}$
ε_R Effectiveness of regenerator
T_h Working fluid temperature in the hot space in K
T_c Working fluid temperature in the cold space in K
ΔQ_R Heat loss during two regenerative processes in the cycle in J

The temperature of the working fluid in the regenerative processes can be calculated as follows:

$$\frac{dT}{dt} = \pm M_i \tag{15.5}$$

where, M is the regenerative time constant in $\mathrm{K} \cdot \mathrm{s}^{-1}$. The positive and negative signs are considered for the heating and cooling processes, respectively. The times of the two isochoric heating ($i = 1$) and cooling ($i = 2$) processes are calculated according to (15.6) and (15.7), respectively.

$$t_3 = \frac{T_1 - T_2}{M_1} \tag{15.6}$$

$$t_4 = \frac{T_1 - T_2}{M_2} \tag{15.7}$$

The heat released between the heat source and the working fluid and the heat absorbed between the working fluid and the heat sink are given by (15.8) and (15.9), respectively [25].

$$\begin{aligned} Q_h &= nRT_h \ln \lambda + nC_v(1 - \varepsilon_R)(T_h - T_c) \\ &= t_h\left[C_H \varepsilon_H (T_{H_1} - T_h) + \xi C_H \varepsilon_H (T_{H_1}^4 - T_h^4)\right] \end{aligned} \tag{15.8}$$

$$Q_c = nRT_c \ln \lambda + nC_v(1 - \varepsilon_R)(T_h - T_c) = t_l C_L \varepsilon_L (T_c - T_{L_1}) \tag{15.9}$$

where:

Q_h Heat released between the heat source and the working fluid in J
R Gas constant in $\mathrm{J} \cdot \mathrm{mol}^{-1} \cdot \mathrm{K}^{-1}$
λ Ratio of volume during the regenerative processes
t_h Heat exchanging time at heat source in s
C_H Heat capacitance rate of the heat source in $\mathrm{W} \cdot \mathrm{K}^{-1}$
ε_H Effectiveness of the high temperature heat exchanger
T_{H_1} Primary heat source temperature in K
Q_c Heat absorbed between the working fluid and the heat sink in J
t_l Heat exchanging time of the heat sink in s
C_L Heat capacitance rate of the heat sink in $\mathrm{W} \cdot \mathrm{K}^{-1}$
ε_L Effectiveness of the low temperature heat exchanger
T_{L_1} Primary heat sink temperature in K

The cyclic period of the SDSHE can be calculated from [25]:

$$t = \frac{nRT_h \ln \lambda + nC_v(1-\varepsilon_R)(T_h - T_c)}{C_H \varepsilon_H (T_{H_1} - T_h) + \xi C_H \varepsilon_H (T_{H_1}^4 - T_h^4)} + \frac{nRT_h \ln \lambda + nC_v(1-\varepsilon_R)(T_h - T_c)}{C_L \varepsilon_L (T_c - T_{L_1})} + \left(\frac{1}{M_1} + \frac{1}{M_2}\right)(T_h - T_c) \tag{15.10}$$

where, t is the cyclic period in s. The conductive thermal losses from the heat source to the heat sink can be obtained from the following equations:

$$Q_0 = tK_0(T_{H_{ave}} - T_{L_{ave}}) \tag{15.11}$$

$$T_{H_{ave}} = \frac{T_{H_1} + T_{H_2}}{2} \tag{15.12}$$

$$T_{L_{ave}} = \frac{T_{L_1} + T_{L_2}}{2} \tag{15.13}$$

in which:

Q_0 Conductive thermal losses in J
K_0 Heat leak coefficient in $\mathrm{W} \cdot \mathrm{K}^{-1}$
$T_{H_{ave}}$ Heat source average temperature in K
T_{H_2} Secondary heat source temperature in K
$T_{L_{ave}}$ Heat sink average temperature in K
T_{L_2} Secondary heat sink temperature in K

Note that:

$$T_{H_2} = (1-\varepsilon_H)T_{H_1} + \varepsilon_H T_h \tag{15.14}$$

$$T_{L_2} = (1-\varepsilon_L)T_{L_1} + \varepsilon_L T_c \tag{15.15}$$

Hence,

$$Q_0 = \frac{K_0}{2} t[T_{H_1}(2-\varepsilon_H) - T_{L_1}(2-\varepsilon_L) + \varepsilon_H T_h - \varepsilon_L T_c] \tag{15.16}$$

The net heat released from the heat source and the net heat absorbed by the heat sink can be obtained from (15.17) and (15.18), respectively.

$$Q_H = Q_h + Q_0 \tag{15.17}$$

$$Q_L = Q_c + Q_0 \tag{15.18}$$

where:

Q_H Net heat released from the heat source in J
Q_L Net heat absorbed by the heat sink in J

The output power of the SDSHE is given by (15.19) [25]:

$$\begin{aligned} P_{O_{\mathrm{SE}}} &= \frac{nR\ \ln\lambda(T_h - T_c)}{F_1 + F_2 + F_3} \\ F_1 &= \frac{nRT_h \ln\lambda + nC_v(1-\varepsilon_R)(T_h - T_c)}{C_H\varepsilon_H(T_{H_1} - T_h) + \xi C_H\varepsilon_H(T_{H_1}^4 - T_h^4)} \\ F_2 &= \frac{nRT_h \ln\lambda + nC_v(1-\varepsilon_R)(T_h - T_c)}{C_L\varepsilon_L(T_c - T_{L_1})} \\ F_3 &= (\frac{1}{M_1} + \frac{1}{M_2})(T_h - T_c) \end{aligned} \tag{15.19}$$

In (15.19), $P_{O_{\mathrm{SE}}}$ is the output power in kW.

15.2.2 Air Source Heat Pumps (ASHPs)

An air source heat pump is an electrical device that extracts heat from the inside air and transfers it to the outside air in hot climate and vice versa in cold weather [26]. In other words, the air source heat pump's cycle is reversible. Based on the heating and the cooling energy exchange sources, the air source heat pumps can be classified in two general categories:

- Air to water heat pump
  The first type is the air to water heat pump. In cold weather, it absorbs heat from the outside air and transfers it to the water in the hydronic distribution unit. In hot weather conditions, it extracts heat from the water in the hydronic distribution unit and pumps it to the outside air.
- Air to air heat pump (AAHP)
  The most common type of the air source heat pumps is the air to air heat pump. An AAHP extracts heat from the air and transfers it to the inside or the outside air of the building depending on the season. There are two cycles for an air source heat pump: The cooling cycle and the heating cycle.

15.2.2.1 The Cooling Cycle of the Air to Air Heat Pump

The cooling cycle of the building using the air to air heat pump is shown in Fig. 15.4. In the cooling process of the building inside space, the heating energy is taken from the indoor air and then pumped to the outdoor air. An AAHP contains the following component: compressor, evaporator, condenser, and an expansion valve. The liquid refrigerant enters the indoor evaporator coils. In the inside evaporator, the low pressure liquid refrigerant absorbs heat from the warm inside air, vaporizes, and changes into a low temperature or cold vapor. The compressor coil then pumps the vapor, increases its pressure, and changes it into a hot high pressure vapor. The generated high-temperature high-pressure vapor passes over the condenser coil and then heating energy is given off to the outside air, and the vapor condenses to change to a high-temperature high-pressure liquid. The generated liquid then passes over the expansion valve and changes into the low-temperature low-pressure liquid refrigerant. The cooling cycle is then repeated again. The energy required to operate the cooling cycle is the electrical energy, which powers the compressor inside and outside fans.

15.2.2.2 The Heating Cycle of the Air to Air Heat Pump

In the heating process, the heating flow is taken from the outdoor cold air and then pumped to the inside cold air. The outside air always contains some heat, a heat pump can supply heat to a building even on cold days [26]. The heating process of the residential buildings using the AAHPs is shown in Fig. 15.5.

During the heating process, the liquid refrigerant enters the outdoor evaporator coil and absorbs heat from the outdoor air to evaporate, and changes into the low temperature liquid and vapor mixture. The vapor then enters the compressor, compressed, changes into the high temperature high pressure vapor. The heating

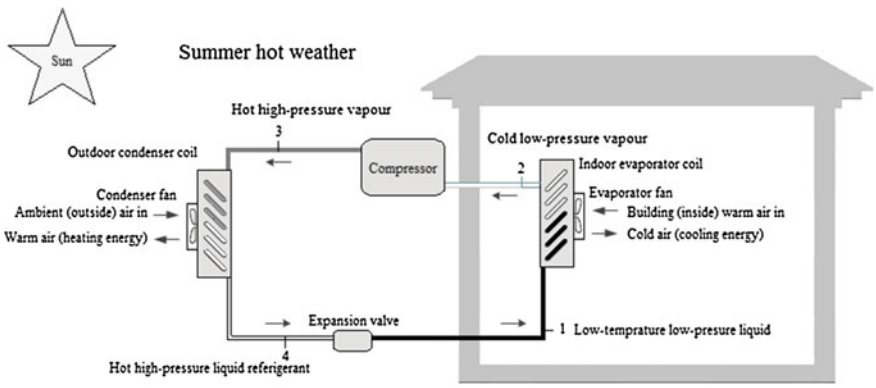

Fig. 15.4 The cooling cycle of the building using the air to air heat pump

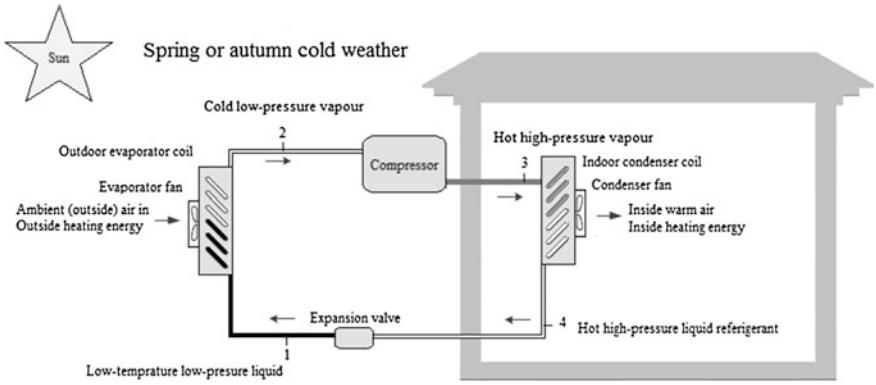

Fig. 15.5 The heating cycle of the building using the air to air heat pump

energy from the high temperature high pressure vapor is transferred to the inside cold air, causing the refrigerant to condense into the high temperature high pressure liquid. The hot high pressure liquid passes though the expansion valve and changes into the low temperature low pressure liquid refrigerant. Similar to the cooling cycle, the electrical energy powers the compressor, the inside and the outside fans.

15.3 Energy and Exergy Analysis of the Proposed Micro Tri-generation System

15.3.1 Combined Cooling and Power (CCP) Mode for Hot Weather Conditions

The CCP mode of the proposed micro-CCHP system, which can be used for residential buildings, is shown in Fig. 15.6. According to Fig. 15.6, the SDSHE is used to drive the power generation unit. The output electric power generated by the power generating unit can be obtained from (15.20):

$$P_{PGU} = \eta_{elec} P_{O_{SE}} \tag{15.20}$$

where, P_{PGU} is the output electric power in kW and η_{elec} is the electrical efficiency of the power generating unit. The cooling energy generated by an AAHP, Q_{evap}, can be calculated from the following equation:

$$Q_{evap} = \dot{m}_4 (h_1 - h_4) \tag{15.21}$$

where, Q_{evap} and $\dot{m}_4$ are the cooling energy generated by the AAHP in kW, and the mass flow rate of the refrigerant through each component such as evaporator, compressor, condenser and expansion valve in kg $\cdot$ s^{-1}, respectively. Variables h_1 and h_4

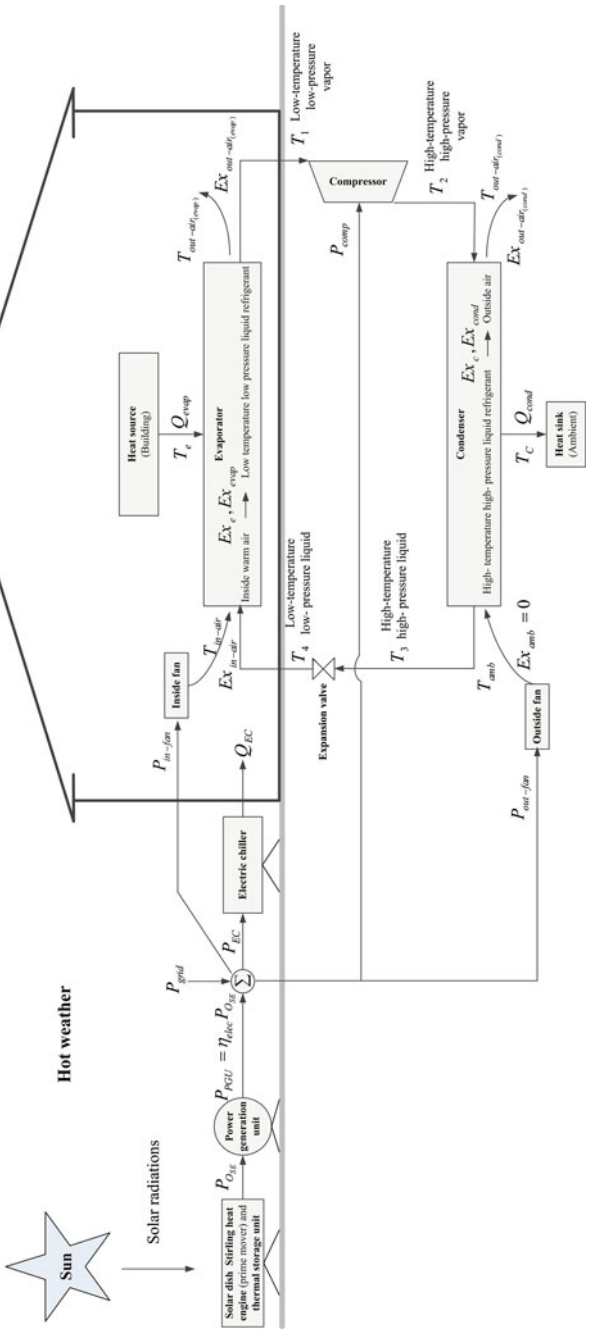

Fig. 15.6 The schematic of the proposed micro tri-generation system in CCP mode

are the rate of heat transfer per unit mass in $kJ \cdot kg^{-1}$ in the states 1 and 4, respectively. As (15.22), the electric energy consumed by the electric chiller can be calculated according to the coefficient of performance and its output cooling energy, that is:

$$P_{EC} = \frac{Q_{EC}}{COP} \tag{15.22}$$

where, Q_{EC} is the output cooling energy generated by the electric chiller, which can be obtained from (15.23):

$$Q_{EC} = Q_{Cool} - Q_{evap} \tag{15.23}$$

The Q_{Cool} is the cooling demand in a residential building in kW. The electric energy consumed by the indoor fan is given by:

$$P_{in-fan} = C_a m_{in-air}(T_{out-air_{evap}} - T_{in-air}) + Q_{evap} \tag{15.24}$$

where:

P_{in-fan}	Electric energy consumed by indoor fan in kW
C_a	Specific heat capacity of air in $kJ \cdot kg^{-1} \cdot K^{-1}$
m_{in-air}	Airflow rate of the inside fan in $kg \cdot s^{-1}$
$T_{out-air_{evap}}$	Chilled inside air temperature in K
T_{in-air}	Indoor air temperature in K

The consumed and the transferred exergy at the evaporator can be computed from (15.25)–(15.29):

$$Ex_{in-air} = C_a m_{in-air}\left[(T_{in-air} - T_{amb}) - T_{amb}\ln\left(\frac{T_{in-air}}{T_{amb}}\right)\right] \tag{15.25}$$

$$Ex_{out-air_{evap}} = C_a m_{in-air}\left[(T_{out-air_{evap}} - T_{amb}) - T_{amb}\ln\left(\frac{T_{out-air_{evap}}}{T_{amb}}\right)\right] \tag{15.26}$$

$$S_{evap} = C_a m_{in-air}\ln\left(\frac{T_{out-air_{evap}}}{T_{in-air}}\right) + \frac{Q_{evap}}{T_e} \tag{15.27}$$

$$Ex_{evap} = S_{evap} T_{amb} \tag{15.28}$$

$$P_{in-fan} + Ex_e - Ex_{evap} = Ex_{out-air_{evap}} - Ex_{in-air} \tag{15.29}$$

where:

Ex_{in-air}	Indoor air exergy in kW
T_{amb}	Ambient temperature in K
$Ex_{out-air_{evap}}$	Supplied inside air exergy in kW

S_{evap} Entropy generated in the heat exchanging process between indoor air and the refrigerant in $kW \cdot K^{-1}$

Ex_{evap} Exergy consumed in the heat exchanging process between the indoor air and the refrigerant at the evaporator in kW

Ex_e Exergy transferred from the indoor air to the refrigerant at the evaporator in kW

The electric energy consumed by the outdoor fan can be determined from Eqs. (15.30)–(15.34):

$$Q_{cond} = \dot{m}_2(h_2 - h_3) \tag{15.30}$$

$$Ex_c = Q_{cond}\left(\frac{T_C - T_{amb}}{T_C}\right) \tag{15.31}$$

$$S_{cond} = C_a m_{out-air} \ln\left(\frac{T_{out-air_{cond}}}{T_{amb}}\right) - \frac{Q_{cond}}{T_C} \tag{15.32}$$

$$Ex_{cond} = S_{cond} T_{amb} \tag{15.33}$$

$$P_{out-fan} + Ex_c - Ex_{cond} = Ex_{out-air_{cond}} - Ex_{amb} \tag{15.34}$$

where:

Q_{cond} Energy flux between refrigerant and outdoor air in kW

$\dot{m}_2$ Mass flow rate of refrigerant through each component such as evaporator, compressor, condenser and expansion valve in $kg \cdot s^{-1}$

h_2, h_3 Rate of heat transfer per unit mass in $kJ\,kg^{-1}$ in states 2 and 3, respectively

Ex_c Exergy transferred from the refrigerant to the outdoor air in kW

T_C Refrigerant condensation temperature in K

S_{cond} Entropy generated in the heat exchanging process between the outdoor air and the refrigerant in $kW \cdot K^{-1}$

Ex_{cond} Exergy consumed between the outdoor air and refrigerant in kW

$P_{out-fan}$ Electric energy consumed by the outdoor fan in kW

Ex_{amb} Ambient air exergy (=0) in kW

$Ex_{out-air_{cond}}$ Outlet air exergy of the outdoor fan in kW, which can be calculated from (15.35):

$$Ex_{out-air_{cond}} = C_a m_{out-air}\left[(T_{out-air_{cond}} - T_{amb}) - T_{amb} \ln\left(\frac{T_{out-air_{cond}}}{T_{amb}}\right)\right] \tag{15.35}$$

where:

$m_{out-air}$ Airflow rate of outside fan in $kg \cdot s^{-1}$

$T_{out-air_{cond}}$ Supplied outside air temperature in K

The electric energy consumed by the compressor can be obtained using (15.36) and (15.38):

$$S_{cycle} = \frac{Q_{cond}}{T_3} - \frac{Q_{evap}}{T_1} \tag{15.36}$$

$$Ex_{cycle} = S_{cycle} T_{amb} \tag{15.37}$$

$$P_{comp} = Ex_c + Ex_e + Ex_{cycle} \tag{15.38}$$

where:

S_{cycle} Entropy generated in the refrigerant cycle in $kW \cdot K^{-1}$
Ex_{cycle} Exergy consumed in the refrigerant cycle in kW
P_{comp} Electric energy consumed by the compressor in kW

The electricity energy need to be purchased from the main grid, and can be computed from the following energy balance equation:

$$P_{grid} = (P_{comp} + P_{in-fan} + P_{out-fan}) + P_{EC} + P_{demand} - P_{PGU} \tag{15.39}$$

where, P_{grid} and P_{demand} are the electricity energy purchased from the local network and the electrical demand in the residential building, respectively in kW.

15.3.2 Combined Heating and Power (CHP) Mode for Cold Weather Condition

The combined heating and power mode of the proposed micro CCHP system for residential applications is depicted in Fig. 15.7. The heating energy generated by the AAHP, Q_{cond}, can be calculated from (15.30). The electric energy consumed by the outdoor fan is given by Eq. (15.40).

$$P_{out-fan} = C_a m_{out-air} (T_{out-air_{evap}} - T_{amb}) + Q_{evap} \tag{15.40}$$

where, $T_{out-air_{evap}}$ is the chilled outside air temperature in K. The consumed and the transferred exergy at the evaporator can be calculated attained from Eqs. (15.28) and (15.41)–(15.43):

$$S_{evap} = C_a m_{out-air} \ln\left(\frac{T_{out-air_{evap}}}{T_{amb}}\right) + \frac{Q_{evap}}{T_e} \tag{15.41}$$

$$Ex_{out-air_{evap}} = C_a m_{out-air} \left[(T_{out-air_{evap}} - T_{amb}) - T_{amb} \ln\left(\frac{T_{out-air_{evap}}}{T_{amb}}\right)\right] \tag{15.42}$$

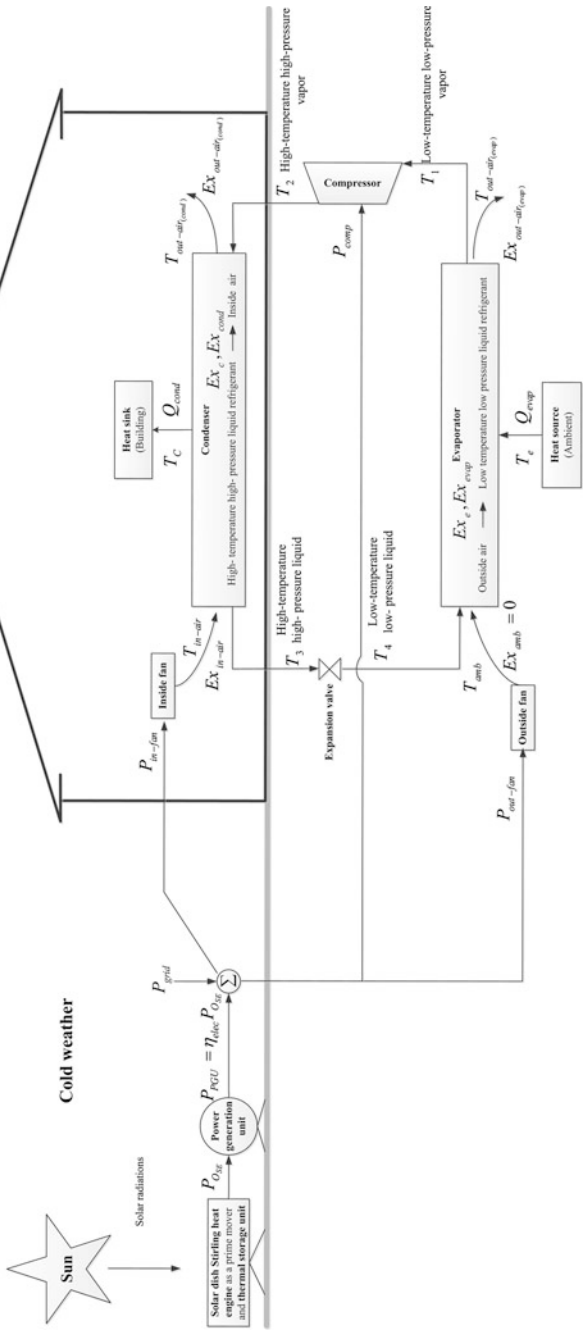

Fig. 15.7 The schematic of the proposed micro-CCHP system in CHP mode

$$P_{out-fan} + Ex_e - Ex_{evap} = Ex_{out-air_{evap}} - Ex_{amb} \tag{15.43}$$

where:

S_{evap} Entropy generated in the heat exchanging process between outdoor air and the refrigerant in $\text{kW} \cdot \text{K}^{-1}$

$Ex_{out-air_{evap}}$ Supplied outside air exergy in kW

Ex_{evap} Exergy consumed in the heat exchanging process between the outdoor air and the refrigerant at the evaporator in kW

Ex_e Exergy transferred from the outdoor air to the refrigerant at the evaporator in kW

The consumed and the transferred exergy at the condenser can be calculated from Eqs. (15.25), (15.33) and (15.44)–(15.46):

$$S_{cond} = C_a m_{in-air} \ln\left(\frac{T_{out-air_{cond}}}{T_{in-air}}\right) - \frac{Q_{cond}}{T_C} \tag{15.44}$$

$$Ex_{out-air_{cond}} = C_a m_{in-air}\left[(T_{out-air_{cond}} - T_{amb}) - T_{amb} \ln\left(\frac{T_{out-air_{cond}}}{T_{amb}}\right)\right] \tag{15.45}$$

$$P_{in-fan} + Ex_c - Ex_{cond} = Ex_{out-air_{cond}} - Ex_{in-air} \tag{15.46}$$

where:

$Ex_{out-air_{cond}}$ Outlet air exergy of indoor fan in kW

$T_{out-air_{cond}}$ Supplied inside air temperature in K

Similar to the cooling process, the electric energy consumed by the compressor can be obtained from (15.36)–(15.38).

15.3.3 Optimization Problem Formulation

The following objective function is considered to minimize the total hourly energy cost purchased from the main network:

$$\text{Objective} = Min\{\lambda_t P^t_{grid}\} \tag{15.47}$$

where, λ_t is the energy price at time t in $\$ \cdot \text{kW}^{-1}\text{h}^{-1}$. In the optimization process, C_H, C_L, T_h, T_c, $T_{out-air_{cond}}$, $T_{out-air_{evap}}$ (For CHP mode) are the decision variables. The optimization constraints for finding optimal operating scenario can be summarized as follows:

$$300 < C_H < 2000 \tag{15.48}$$

$$300 < C_L < 2000 \tag{15.49}$$

$$800 < T_h < 1200\,\mathrm{K} \tag{15.50}$$

$$400 < T_c < 710\,\mathrm{K} \tag{15.51}$$

$$P_{comp} > 0 \tag{15.52}$$

$$P_{in-fan} > 0 \tag{15.53}$$

$$P_{out-fan} > 0 \tag{15.54}$$

$$Ex_{out-air_{evap}} > 0 \tag{15.55}$$

$$Ex_e > 0 \tag{15.56}$$

$$Ex_{out-air_{cond}} > 0 \tag{15.57}$$

$$T_{in-air} < T_{amb} \quad \text{for CCP mode} \tag{15.58}$$

$$T_{out-air_{cond}} > T_{amb} \exp\left(\frac{Q_{cond}}{C_a m_{out-air} T_c}\right) \quad \text{for CCP mode} \tag{15.59}$$

$$T_{in-air} > T_{amb} \quad \text{for CHP mode} \tag{15.60}$$

$$T_{out-air_{evap}} > Max\left\{T_{amb} \exp\left(\frac{-Q_{evap}}{C_a m_{out-air} T_e}\right), \left(\frac{-Q_{evap}}{C_a m_{out-air}} + T_{amb}\right)\right\} \quad \text{for CHP mode} \tag{15.61}$$

$$T_{out-air_{evap}} = 292\,\mathrm{K}\ (19\,^{\circ}\mathrm{C}) \quad \text{for CCP mode} \tag{15.62}$$

$$T_{out-air_{cond}} > 180\,^{\circ}\mathrm{F}\,(355.22\,\mathrm{K}) \quad \text{for CHP mode} \tag{15.63}$$

$$P_{grid} < P_{grid}^{\max} \tag{15.64}$$

15.4 Simulation Results and Discussion

In order to achieve the optimal performance of the proposed micro tri-generation system, the optimization process is conducted in two typical conditions: hot weather (CCP mode), and cold weather (CHP mode). A discontinuous nonlinear program (DNLP) is solved using CONOPT solver under general algebraic modeling system (GAMS) optimization software. The required parameters for the simulation of the solar micro-CCHP system are listed at appendix. In this chapter,

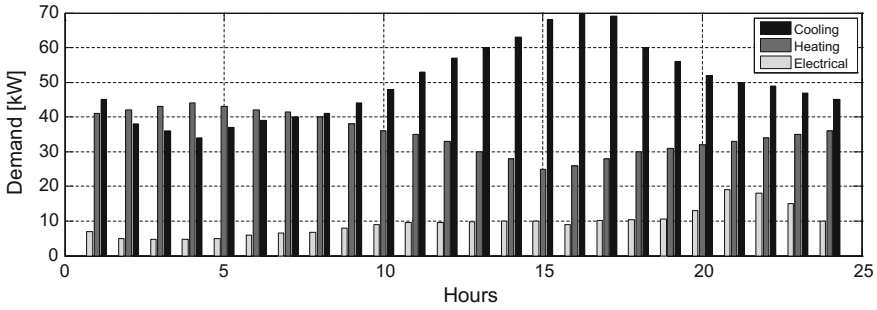

Fig. 15.8 Cooling, heating and electrical demands of test building located in Tabriz, Iran [27]

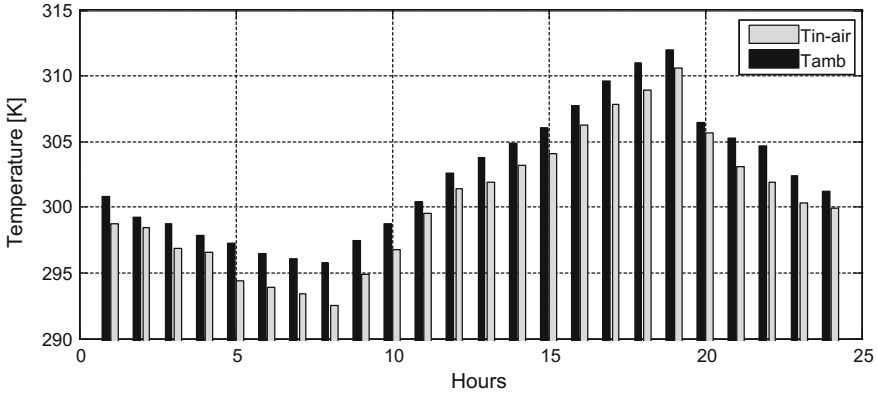

Fig. 15.9 The ambient and the indoor air temperatures during a sample hot day in Tabriz, Iran

the mass flow rate of the refrigerant, and the specific heat capacity of air are assumed to be constant due to the negligible changes during a hot or cold day. A benchmark residential building is considered in Tabriz, Iran to demonstrate the robustness and the effectiveness of the proposed CCHP system. The cooling, heating and electrical demands are shown in Fig. 15.8.

15.4.1 CCP Mode

The variations of the ambient and the indoor air temperatures during a sample summer day is depicted in Fig. 15.9.

The obtained optimal operating points of the proposed micro-CCHP system during the typical summer day are reported in Figs. 15.10, 15.11 and Table 15.1.

As shown in Fig. 15.11, the output mechanical power of the SDSHE increases monotonically as the sum of the electric energy consumed by compressor, inside

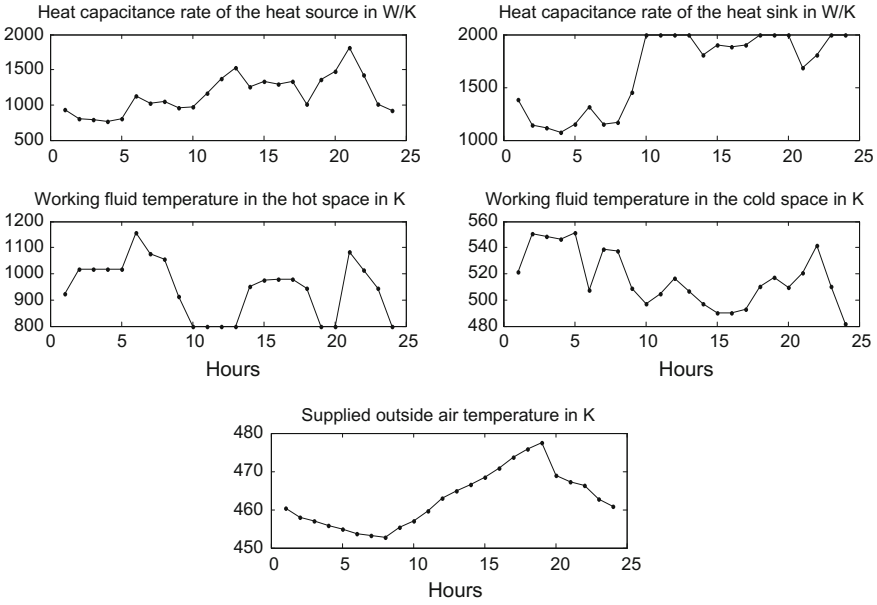

Fig. 15.10 Obtained decision variables in the optimization process of CCP mode

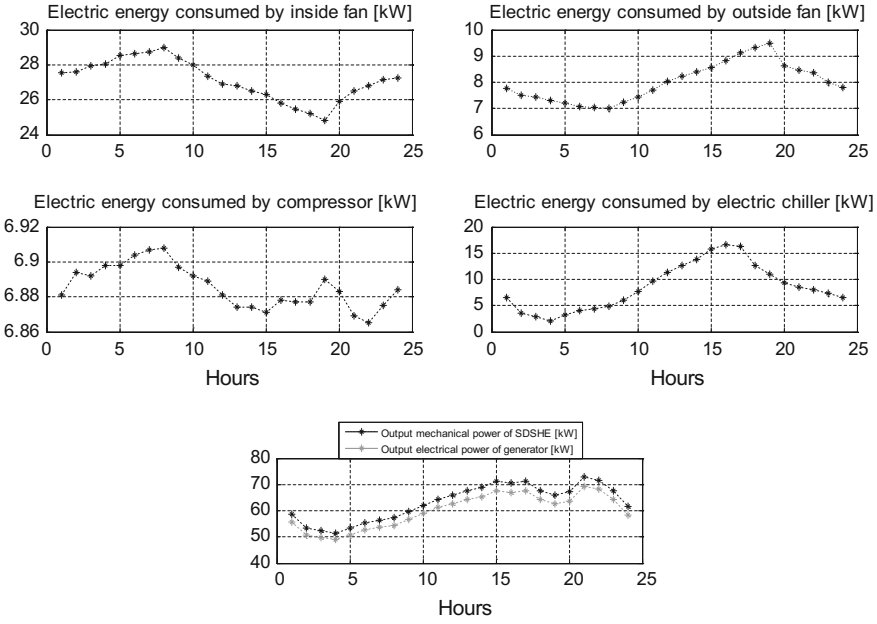

Fig. 15.11 Electric energy consumed by AAHP and electric chiller and generated power during sample summer day in Tabriz, Iran

Table 15.1 Entropy, energy flux between refrigerant and outdoor air, cooling energy generated by AAHP and electric chiller, chilled inside air temperature and exergy flow during sample summer day in Tabriz, Iran

S_{cycle} (kW K^{-1})	S_{evap} (kW K^{-1})		S_{cond} (kW K^{-1})		Q_{cond} (kW)		Q_{evap} (kW)		$T_{out-air_{evap}}$ (K)
0.013	0.095		7.0391E-6		38.660		29.080		292
t (h)	Ex_c (kW)	Ex_{evap} (kW)	$Ex_{out-air_{evap}}$ (kW)	Ex_{in-air} (kW)	Ex_e (kW)	Ex_{cond} (kW)	$Ex_{out-air_{cond}}$ (kW)	Ex_{cycle} (kW)	Q_{EC} (kW)
24–1	1.976	28.611	0.030	0.002	1.100	0.002	9.727	3.805	15.920
1–2	2.171	28.527	0.020	2.464287E−4	0.938	0.002	9.675	3.785	8.920
2–3	2.232	28.819	0.017	0.001	0.882	0.002	9.659	3.779	6.920
3–4	2.329	28.810	0.013	6.543044E−4	0.800	0.002	9.633	3.768	4.920
4–5	2.403	29.255	0.011	0.003	0.734	0.002	9.614	3.761	7.920
5–6	2.500	29.291	0.008	0.003	0.653	0.002	9.588	3.751	9.920
6–7	2.549	29.367	0.007	0.003	0.612	0.002	9.575	3.746	10.920
7–8	2.573	29.555	0.006	0.005	0.592	0.002	9.568	3.743	11.920
8–9	2.378	29.159	0.012	0.003	0.755	0.002	9.620	3.763	14.920
9–10	2.232	28.841	0.017	0.001	0.881	0.002	9.659	3.779	18.920
10–11	2.024	28.393	0.027	3.107073E−4	1.064	0.002	9.714	3.800	23.920
11–12	1.756	28.173	0.043	5.487082E−4	1.297	0.002	9.785	3.828	27.920
12–13	1.610	28.172	0.053	0.001	1.421	0.002	9.824	3.843	30.920
13–14	1.476	27.984	0.063	0.001	1.541	0.002	9.860	3.857	33.920
14–15	1.329	27.893	0.075	0.002	1.669	0.002	9.898	3.872	38.920
15–16	1.134	27.551	0.092	7.347613E−4	1.851	0.002	9.950	3.892	40.920
16–17	0.902	27.390	0.115	0.001	2.058	0.002	10.011	3.916	39.920
17–18	0.732	27.272	0.133	0.002	2.211	0.002	10.057	3.934	30.920
18–19	0.610	26.989	0.147	7.246043E−4	2.333	0.002	10.089	3.947	26.920
19–20	1.281	27.575	0.079	2.405492E−4	1.725	0.002	9.911	3.877	22.920
20–21	1.427	28.043	0.067	0.002	1.580	0.002	9.872	3.862	20.920
21–22	1.500	28.256	0.061	0.003	1.511	0.002	9.853	3.854	19.920
22–23	1.781	28.401	0.041	0.002	1.270	0.002	9.779	3.825	17.920
23–24	1.927	28.378	0.032	6.471150E−4	1.147	0.002	9.740	3.810	15.920

and outside fans, electric chiller and building's electric demand increases. On the other hand, the hourly electrical energy purchased from the local grid during the sample hot day is equal to zero. According to the above results, the AAHP generates 29.080 kW of total cooling energy required for the test residential building. The electric power consumed by the electric chiller and the cooling demand change in a similar manner during the hot day. In the meantime, the minimum and maximum cooling demands are equal to 34 and 70 kW, respectively. Hence, supposing $\dot{m} = 0.2\,\mathrm{kg\,s^{-1}}$ in CCP mode, the AAHP provides almost 41.5% of the total cooling demand during the hottest hour ($t = 16$). If the mass flow rate of the refrigerant increases, the AAHP's thermal capacity and the electric power consumed by the electric chiller will increase and decrease, respectively. Based on Figs. 15.9, 15.10 and 15.11, the electric power consumed by the outside fan, ambient temperature and the supplied outside air temperature change in a similar fashion. According to Eq. (15.24) and assuming that $T_{out-air_{evap}} = 292\,\mathrm{K}$, if the inside air temperature increases, $T_{out-air_{evap}} - T_{in-air}$ becomes more negative. Hence, the electric power consumed by the inside fan will decrease. The electric power consumed by the inside fan maximized and minimized at $t = 8$ and $t = 11$, respectively. These two points coincide with the maximum and minimum points of the inside air temperature. As a result, an air to air heat pump can provide efficient cooling energy for a large-scale residential building using air as a renewable energy source, especially in a warm area. Finally, the cooling distribution systems such as forced air units can distribute the generated cooling energy and the cold weather between different flats and floors.

15.4.2 CHP Mode

The variations of ambient and indoor air temperatures during a sample autumn day are plotted in Fig. 15.12.

The obtained optimum operating points of the proposed tri-generation system in CHP mode can be summarized in Table 15.2 and shown in Figs. 15.13 and 15.14.

According to Figs. 15.8 and 15.14, the mass flow rate of the refrigerant increases monotonically as the value of heating demand increases. Hence, the values of $\dot{m}$ and the maximum and minimum of the heating load occur at $t = 4$ and $t = 15$, respectively. The energy flux between the refrigerant and the outside air will be increased as the values of $\dot{m}$ and heating demand increase. Also, if the heating load increases, the electric energy consumed by the inside fan, required to supply the inside cold weather, will increase. As shown in Fig. 15.14, the sum of the electrical energy consumed by the inside and outside fans, compressor and building's electric demand can be met by generator output power driven by a SDSHE (Thermal storage unit has been used for continuous energy supplying when sunlight is

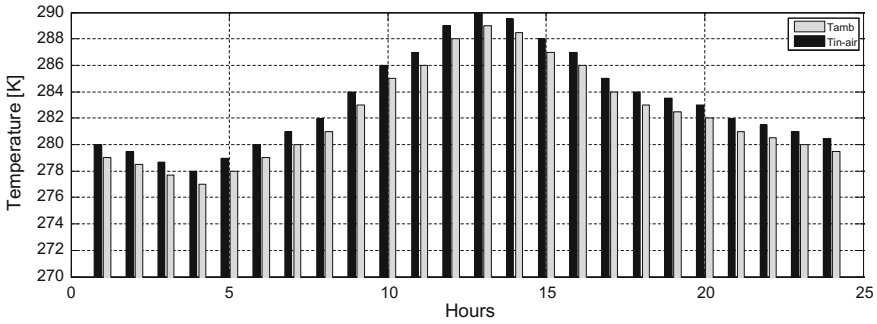

Fig. 15.12 The ambient and indoor air temperatures during an autumn cold day in Tabriz, Iran

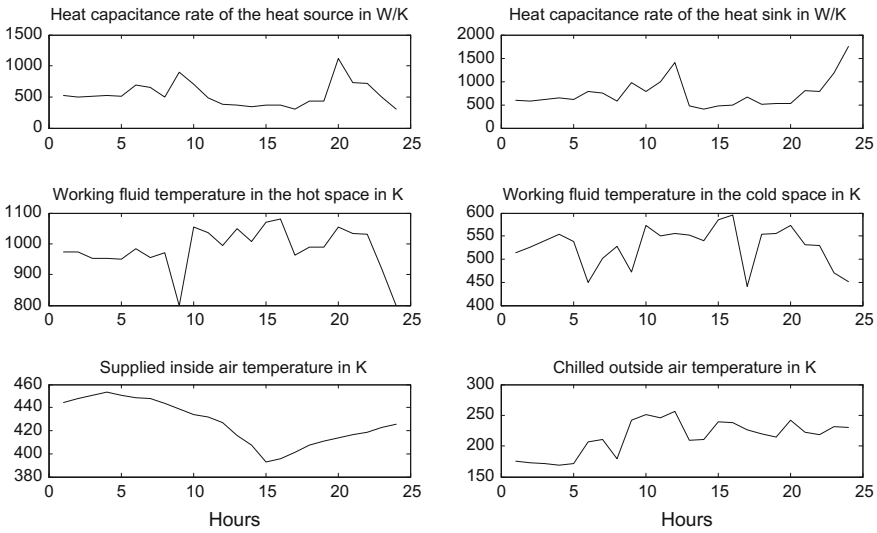

Fig. 15.13 Obtained decision variables in optimization process of CHP mode

insufficient or nighttime). Note that the hourly objective cost obtained from optimizing of CHP mode is zero. From Fig. 15.13, the minimum value of the supplied inside air temperature is equal to 393.12 K. Assuming 10% heat losses in warm air storage tank (WAST), this value is reduced to 353.8080 K. In central heating system, minimum inlet water temperature to radiators is equal to 180 °F or 355.22 K. Hence, the supplied inside air stored in WAST can satisfy the inlet water temperature to radiant floor systems. As an important result, an AAHP can supply

Table 15.2 Exergy flow, entropy, energy flux between refrigerant and outdoor air during sample cold day in Tabriz, Iran

t (h)	Ex_c (kW)	Ex_{evap} (kW)	$Ex_{out-air_{evap}}$ (kW)	Ex_{in-air} (kW)	Ex_e (kW)	Ex_{cond} (kW)	$Ex_{out-air_{cond}}$ (kW)
24–1	4.798	5.914	4.397	0.00033315	3.228	1.676	11.305
1–2	4.972	6.173	4.559	0.00038762	3.306	1.662	11.823
2–3	5.209	6.43	4.715	0.00033471	3.344	1.696	12.338
3–4	5.427	6.692	4.874	0.00033555	3.39	1.706	12.867
4–5	5.168	6.437	4.72	0.00033435	3.382	1.698	12.351
5–6	4.915	13.748	2.159	0.00033315	0.961	1.691	11.844
6–7	4.726	14.049	2.01	0.00033197	0.934	1.691	11.614
7–8	4.429	5.689	4.26	0.00033079	3.326	1.676	10.856
8–9	3.968	18.416	0.069	0.00032846	0	1.66	9.903
9–10	3.532	18.753	0.471	0.00032616	0.004	1.644	8.987
10–11	3.312	16.741	0.647	0.00040116	0.283	1.601	8.543
11–12	2.915	17.463	0.39	0.00039838	0.219	1.585	7.684
12–13	2.555	4.207	2.514	0.00039701	2.436	1.546	6.425
13–14	2.429	2.986	2.432	0.00039769	2.324	1.513	5.624
14–15	2.287	7.784	0.888	0.00039977	0.693	1.459	4.512
15–16	2.461	8.258	0.925	0.00040116	0.655	1.468	4.843
16–17	2.835	7.442	1.33	0.0003273	0.895	1.517	5.536
17–18	3.132	7.503	1.619	0.00032846	1.074	1.54	6.292
18–19	3.276	7.208	1.85	0.00040612	1.247	1.519	6.687
19–20	3.442	14.094	0.668	0.00032962	0.004	1.564	7.093
20–21	3.654	10.427	1.436	0.00033079	0.666	1.572	7.497
21–22	3.808	10.553	1.552	0.00092082	0.67	1.375	7.911
22–23	3.975	14.217	0.974	0.00040974	0.066	1.56	8.364
23–24	4.145	14.72	1.007	0.00041047	0.027	1.571	8.813

(continued)

Table 15.2 (continued)

t (h)	Ex_c (kW)	Ex_{evap} (kW)	$Ex_{out-air_{evap}}$ (kW)	Ex_{in-air} (kW)	Ex_e (kW)	Ex_{cond} (kW)	$Ex_{out-air_{cond}}$ (kW)
t (h)	Ex_{cycle} (kW)	S_{cycle} (kW K^{-1})	S_{evap} (kW K^{-1})	S_{cond} (kW K^{-1})	Q_{evap} (kW)		
24–1	3.743	0.013	0.021	0.006	30.84		
1–2	3.827	0.014	0.022	0.006	31.592		
2–3	3.907	0.014	0.023	0.006	32.345		
3–4	3.988	0.014	0.024	0.006	33.097		
4–5	3.912	0.014	0.023	0.006	32.345		
5–6	3.834	0.014	0.049	0.006	31.592		
6–7	3.802	0.014	0.05	0.006	31.216		
7–8	3.678	0.013	0.02	0.006	30.088		
8–9	3.519	0.012	0.065	0.006	28.584		
9–10	3.357	0.012	0.066	0.006	27.079		
10–11	3.275	0.011	0.059	0.006	26.327		
11–12	3.11	0.011	0.061	0.006	24.823		
12–13	2.837	0.01	0.015	0.005	22.566		
13–14	2.643	0.009	0.01	0.005	21.062		
14–15	2.348	0.008	0.027	0.005	18.805		
15–16	2.433	0.009	0.029	0.005	19.557		
16–17	2.602	0.009	0.026	0.005	21.062		
17–18	2.778	0.01	0.027	0.005	22.566		
18–19	2.866	0.01	0.026	0.005	23.318		
19–20	2.953	0.01	0.05	0.006	24.07		
20–21	3.034	0.011	0.037	0.006	24.823		
21–22	3.115	0.011	0.038	0.005	25.575		
22–23	3.207	0.011	0.051	0.006	26.327		
23–24	3.292	0.012	0.053	0.006	27.079		

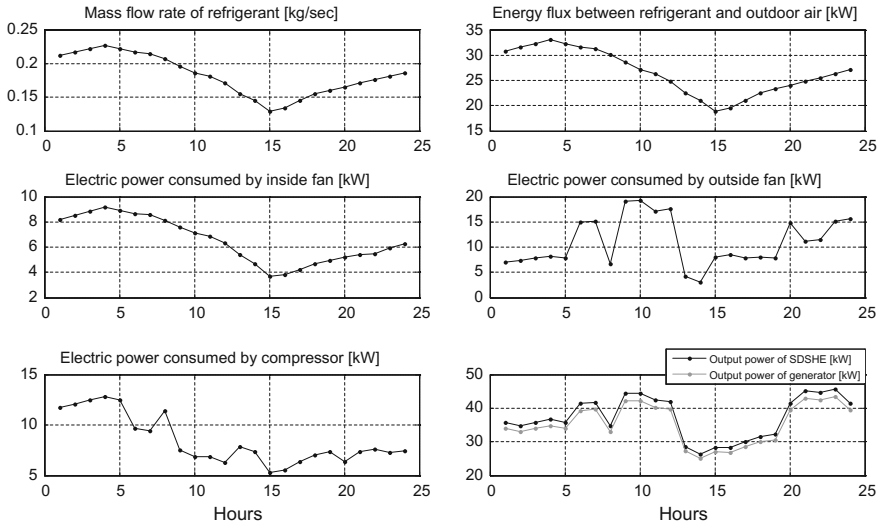

Fig. 15.14 Mass flow rate of refrigerant, energy flux between refrigerant and outdoor air, consumed and generated power during sample cold day in Tabriz, Iran

the total heating demand (Q_{cond}) of large residential towers with different flats and floors during a simple refrigeration cycle using evaporator, compressor, condenser and expansion valve at no cost and without environmental pollutants and greenhouse gas emissions.

15.5 Conclusion

In this chapter, a novel methodology was introduced for short-term scheduling of small-scale tri-generation system, which can be used to provide cooling, heating and power for residential applications. The solar energy may be used as a renewable energy to drive a Stirling engine, which is used to deliver the primary mechanical power required for driving a generator. The heat absorber and thermal storage unit are employed to absorb and store sun radiations collected by the solar dish. The air to air heat pumps were proposed to cool and heat the residential buildings during summer and spring/autumn days, respectively. The proposed micro-CCHP system does not use any fossil fuel such as gasoline and natural gas. Thus, use of solar energy and ASHPs in a CCHP system not only reduces the carbon dioxide, greenhouse gas emissions and environmental pollution, but also reduces the fuel consumption. Meanwhile, the proposed CCHP microgrid consumes less electricity energy than the traditional tri-generation systems. The contributions of the current chapter can be summarized as follows:

- Environmental friendliness: In this chapter, solar energy and air are used as renewable energy sources to drive a prime mover and an air to air heat pump, which is required in order to provide mechanical and cooling/heating energies for a modern residential tower.
- Cost-cutting: The air to air heat pump was proposed to cool and heat the residential buildings in CCP and CHP modes. The energy required to operate the refrigeration cycle is the electrical energy, which powers the compressor, inside and outside fans. Hence, AAHPs based CCHP consumes less electrical energy than the traditional fossil fuels-based tri-generation systems.
- On-site fulfillment: The heating energy obtained from ASHPs is not generated by a combustion process, but is transferred from one place to another.

It is clear that building's insulation reduces heat losses and can decrease the heating and the cooling demands. Hence, the electrical energy consumed by AAHP and electric chiller will be reduced. In a nutshell, a novel zero energy system was proposed to make residential tower technology smarter.

Appendix

The specifications of the solar powered Stirling engine are considered as follows [25, 28]:

$I = 1000\,\mathrm{Wm^{-2}}$, $C = 1300$, $\varepsilon = 0.9$, $\eta_0 = 0.9$, $K_0 = 2.5\,\mathrm{WK^{-1}}$, $n = 1$, $C_v = 15\,\mathrm{J\,mol^{-1}\,K^{-1}}$, $R = 4.3\,\mathrm{J\,mol^{-1}\,K^{-1}}$, $T_{H_1} = 1300\,\mathrm{K}$, $T_{L_1} = 290\,\mathrm{K}$, $\xi = 2 \times 10^{-10}$, $h = 20\,\mathrm{Wm^{-2}K^{-1}}$, $\lambda = 2$, $1/M_1 + 1/M_2 = 2 \times 10^{-5}\,\mathrm{sK^{-1}}$, $\delta = 5.67 \times 10^{-8}\,\mathrm{Wm^{-2}K^{-4}}$, $\varepsilon_H = \varepsilon_L = \varepsilon_R = 0.9$,$\eta_{elec} = 0.95$

The electricity energy price at each hour has been reported in Table 15.3 [28].

The specification of the AAHP's refrigeration cycle and the electric chiller's COP are given as follows [29]:

$P_1 = 100\,\mathrm{kPa}$, $P_2 = 800\,\mathrm{kPa}$, $T_1 = -20\,^{\circ}\mathrm{C}$, $T_2 = 50\,^{\circ}\mathrm{C}$, $T_3 = 30\,^{\circ}\mathrm{C}$, $T_4 = -25\,^{\circ}\mathrm{C}$, $h_1 = 387.2\,\mathrm{kJ\,kg^{-1}}$, $h_2 = 435.1\,\mathrm{kJ\,kg^{-1}}$ $h_3 = h_4 = 241.8\,\mathrm{kJ\,kg^{-1}}$, Energy requirement of electric chiller $= 0.7\,\mathrm{kWton^{-1}}$, $COP = 2.46$, $C_a = 1.15\,\mathrm{kJ\ kg^{-1}K^{-1}}$, $m_{in-air} = 0.2\,\mathrm{kg\,s^{-1}}$, $m_{out-air} = 0.2\,\mathrm{kg\,s^{-1}}$, $\dot{m} = 0.2\,\mathrm{kg\,s^{-1}}$ for CCP mode, $T_C = 317\,\mathrm{K}$, $T_e = 290\,\mathrm{K}$

Table 15.3 Hourly electricity price

t (h)	24–1	1–2	2–3	3–4	4–5	5–6	6–7	7–8
λ_t ($/kWh)	0.068	0.090	0.093	0.095	0.097	0.099	0.098	0.096
t (h)	8–9	9–10	10–11	11–12	12–13	13–14	14–15	15–16
λ_t ($/kWh)	0.095	0.092	0.094	0.097	0.100	0.120	0.103	0.099
t [hour]	16–17	17–18	18–19	19–20	20–21	21–22	22–23	23–24
λ_t ($/kWh)	0.085	0.078	0.075	0.084	0.096	0.081	0.067	0.063

Table 15.4 The specifications of the test building [28]

Building type	Residential
Number of floors	6
Number of flats	12
Total effective floor area in m^2	1080
Average ceiling height in m	3

Table 15.5 Equipment cost of proposed tri-generation system's components

Equipment	Cost ($)	Equipment	Cost ($)
Solar dish Stirling heat engine	12680	Condenser	6280
Thermal storage tank	4400	Evaporator	9600
Power generation unit	3015	Compressor	7700
Electric chiller	585	Expansion device	600
Inside fan	450	Warm air storage tank	7600
Outside fan	725		

In this chapter, a benchmark residential building with 1080 m^2 area is assumed in Tabriz, Iran to be delivered cool, heat and power by the proposed micro-trigeneration system. The specifications of the benchmark building are reported in Table 15.4.

Equipment cost of proposed micro-CCHP system's components has been reported in Table 15.5.

References

1. Liu M, Shi Y, Fang F (2012) A new operation strategy for CCHP systems with hybrid chillers. Appl Energy 95:164–173. doi:10.1016/j.apenergy.2012.02.035
2. Wang M, Wang J, Zhao P, Dai Y (2015) Multi-objective optimization of a combined cooling, heating and power system driven by solar energy. Energy Convers Manag 89:289–297. doi:10.1016/j.enconman.2014.10.009
3. Guo L, Liu W, Cai J, Hong B, Wang C (2013) A two-stage optimal planning and design method for combined cooling, heat and power microgrid system. Energy Convers Manag 74:433–445. doi:10.1016/j.enconman.2013.06.051
4. Ghaebi H, Saidi MH, Ahmadi P (2012) Exergoeconomic optimization of a trigeneration system for heating, cooling and power production purpose based on TRR method and using evolutionary algorithm. Appl Therm Eng 36:113–125. doi:10.1016/j.applthermaleng.2011.11.069
5. Al-Sulaiman FA, Dincer I, Hamdullahpur F (2011) Exergy modeling of a new solar driven trigeneration system. Sol Energy 85(9):2228–2243. doi:10.1016/j.solener.2011.06.009
6. Gharieh K, Jafari MA, Guo Q (2015) Investment in hydrogen tri-generation for wastewater treatment plants under uncertainties. J Power Sourc 297:302–314. doi:10.1016/j.jpowsour.2015.07.093
7. Ebrahimi M, Keshavarz A (2012) Prime mover selection for a residential micro-CCHP by using two multi-criteria decision-making methods. Energy Build 55:322–331

8. Intini M, De Antonellis S, Joppolo CM, Casalegno A (2015) A trigeneration system based on polymer electrolyte fuel cell and desiccant wheel—Part B: overall system design and energy performance analysis. Energy Convers Manag 106:1460–1470. doi:10.1016/j.enconman.2015.10.005
9. Zhao H, Jiang T, Hou H (2015) Performance analysis of the SOFC–CCHP system based on H2O/Li–Br absorption refrigeration cycle fueled by coke oven gas. Energy 91:983–993. doi:10.1016/j.energy.2015.08.087
10. Wang JL, Wu JY, Zheng CY (2014) Simulation and evaluation of a CCHP system with exhaust gas deep-recovery and thermoelectric generator. Energy Convers Manag 86:992–1000. doi:10.1016/j.enconman.2014.06.036
11. Boyaghchi FA, Heidarnejad P (2015) Thermoeconomic assessment and multi objective optimization of a solar micro CCHP based on Organic Rankine Cycle for domestic application. Energy Convers Manag 97:224–234. doi:10.1016/j.enconman.2015.03.036
12. Liu W, Chen G, Yan B, Zhou Z, Du H, Zuo J (2015) Hourly operation strategy of a CCHP system with GSHP and thermal energy storage (TES) under variable loads: a case study. Energy Build 93:143–153. doi:10.1016/j.enbuild.2015.02.030
13. Wang J-J, Yang K, Xu Z-L, Fu C (2015) Energy and exergy analyses of an integrated CCHP system with biomass air gasification. Appl Energy 142:317–327. doi:10.1016/j.apenergy.2014.12.085
14. Jannelli E, Minutillo M, Cozzolino R, Falcucci G (2014) Thermodynamic performance assessment of a small size CCHP (combined cooling heating and power) system with numerical models. Energy 65:240–249. doi:10.1016/j.energy.2013.11.074
15. Rey G, Ulloa C, Cacabelos A, Barragáns B (2015) Performance analysis, model development and validation with experimental data of an ICE-based micro-CCHP system. Appl Therm Eng 76:233–244. doi:10.1016/j.applthermaleng.2014.10.087
16. Li L, Mu H, Gao W, Li M (2014) Optimization and analysis of CCHP system based on energy loads coupling of residential and office buildings. Appl Energy 136:206–216. doi:10.1016/j.apenergy.2014.09.020
17. Wu JY, Wang JL, Li S, Wang RZ (2014) Experimental and simulative investigation of a micro-CCHP (micro combined cooling, heating and power) system with thermal management controller. Energy 68:444–453. doi:10.1016/j.energy.2014.02.057
18. Jabbari B, Tahouni N, Ataei A, Panjeshahi MH (2013) Design and optimization of CCHP system incorporated into kraft process, using Pinch Analysis with pressure drop consideration. Appl Therm Eng 61(1):88–97. doi:10.1016/j.applthermaleng.2013.01.050
19. Andiappan V, Tan RR, Aviso KB, Ng DKS (2015) Synthesis and optimisation of biomass-based tri-generation systems with reliability aspects. Energy 89:803–818. doi:10.1016/j.energy.2015.05.138
20. Tippawan P, Arpornwichanop A, Dincer I (2015) Energy and exergy analyses of an ethanol-fueled solid oxide fuel cell for a trigeneration system. Energy 87:228–239. doi:10.1016/j.energy.2015.04.072
21. Dominković DF, Ćosić B, Bačelić Medić Z, Duić N (2015) A hybrid optimization model of biomass trigeneration system combined with pit thermal energy storage. Energy Convers Manag 104:90–99. doi:10.1016/j.enconman.2015.03.056
22. Ozcan H, Dincer I (2014) Thermodynamic analysis of a combined chemical looping-based trigeneration system. Energy Convers Manag 85:477–487
23. Soroudi A, Mohammadi-Ivatloo B, Rabiee A (2014) Energy hub management with intermittent wind power. In: Large scale renewable power generation. Springer, pp 413–438
24. Mohammadi-Ivatloo B, Moradi-Dalvand M, Rabiee A (2013) Combined heat and power economic dispatch problem solution using particle swarm optimization with time varying acceleration coefficients. Electr Power Syst Res 95:9–18
25. Yaqi L, Yaling H, Weiwei W (2011) Optimization of solar-powered Stirling heat engine with finite-time thermodynamics. Renew Energy 36(1):421–427
26. Turner LW (1979) Heat pumps for residential heating and cooling: some questions and answers. Michigan State University Energy for Agriculture Series ENR, USA, No 80–35

27. Karami R, Sayyaadi H (2015) Optimal sizing of Stirling-CCHP systems for residential buildings at diverse climatic conditions. Appl Therm Eng 89:377–393. doi:10.1016/j.applthermaleng.2015.06.022
28. Kaushik SC, Kumar S (2001) Finite time thermodynamic evaluation of irreversible Ericsson and Stirling heat engines. Energy Convers Manag 42(3):295–312. doi:10.1016/S0196-8904(00)00063-7
29. Sonntag RE, Borgnakke C, Van Wylen GJ, Van Wyk S (1998) Fundamentals of thermodynamics, vol 6. Wiley, New York

Part IV
Technical Strategies, Efficient Methods and Applications

Chapter 16
Communication Methods for Smart Buildings and Nearly Zero-Energy Buildings

Yasin Kabalci

Abstract This chapter presents wired and wireless communication systems in smart homes and smart buildings by considering the recent developments seen in applications. In order to provide further knowledge for readers, the basic principles of the smart homes and energy efficient buildings are firstly introduced. Then, the nearly zero-energy buildings and renewable energy integration in buildings issues are comprehensively explained by taking into account existing applications. In addition, advanced metering infrastructure that is a vital component of the smart home systems is expressed in detail. Afterwards, the potential candidates of communication systems for smart buildings that have an important role to realize nearly zero-energy buildings are discussed by comparing each method and application types thoroughly. These communication systems are classified as wired and wireless communication systems to examine more detailed and the communication systems are compared according to several considerable parameters such as used spectrum, modulation types, bit rates, supported network topologies, media access control (MAC) schemes, carrier types, and application areas. Moreover, several applications of examined communication systems are presented both for outdoor and indoor scenarios.

Keywords Smart homes · Smart building energy management systems (SBEMS) · Advanced metering infrastructure (AMI) · Power line communication (PLC) systems · Wireless communication systems

Abbreviation and Acronyms

AES	Advanced Encryption Standard
AMI	Advanced Metering Infrastructure
AMM	Automatic Meter Management

Y. Kabalci (✉)
Department of Electrical and Electronics Engineering, Faculty of Engineering, Omer Halisdemir University, 51240 Nigde, Turkey
e-mail: yasinkabalci@ohu.edu.tr

N. Bizon et al. (eds.), *Energy Harvesting and Energy Efficiency*, Lecture Notes in Energy 37, DOI 10.1007/978-3-319-49875-1_16

AMR	Automatic Meter Reading
AP	Access Point
ARIB	Association of Radio Industries and Businesses
BAN	Body Area Network
BB	Broadband
BP	Belief Propagation
BPSK	Binary Phase Shift Keying
CC	Convolutional Codes
CCK	Complementary Code Keying
COFDM	Coded OFDM
CP	Cyclic Prefix
CSMA	Carrier Sense Multiple Access
CSMA/CA	Carrier Sense Multiple Access/Collision Avoidance
CSMA/CD	Carrier Sense Multiple Access/Collision Detection
D8PSK	Differential 8-Phase Shift Keying
DBPSK	Differential Binary Phase Shift Keying
DCSK	Differential Chaos Shift Keying
DG	Distributed Generation
DMS	Data Management System
DQPSK	Differential Quadrature Phase Shift Keying
DSL	Digital Subscriber Line
EU	European Union
FCC	Federal Communications Commission
FEC	Forward Error-Correction
FFT	Fast Fourier Transform
FSK	Frequency Shift Keying
GFSK	Gaussian Frequency Shift Keying
HAN	Home Area Network
IRRWBF	Implementation-Efficient Reliability Ratio Based Weighted Bit Flipping
ITU	International Telecommunication Union
IWBF	Improved Weighted Bit Flipping
LAN	Local Area Network
LDPC	Low-Density Parity-Check
LLR	Log-Likelihood Ratio
MAC	Media Access Control
MPPT	Maximum Power Point Tracking
NB	Narrowband
OFDM	Orthogonal Frequency Division Multiplexing
OOK	On-Off Keying
OPGW	Optical Power Ground Wire
O-QPSK	Offset Quadrature Phase-Shift Keying
P&Q	Perturb and Observe

PAM	Pulse Amplitude Modulation
PAN	Personal Area Network
PLC	Power Line Communication
PPM	Pulse Position Modulation
PV	Photovoltaic
QAM	Quadrature Amplitude Modulation
QPSK	Quadrature Phase Shift Keying
RS	Reed Solomon
SBEMS	Smart Building Energy Management Systems
S-FSK	Spread Frequency Shift Keying
SM	Smart Meter
SS	Spread Spectrum
TDD	Time Division Duplexing
TDMA	Time Division Multiple Access
THD	Total Harmonic Distortion
WAN	Wide Area Network
WBF	Weighted Bit Flipping
WLAN	Wide Local Area Network
WM-Bus	Wireless M-Bus
WPAN	Wireless Personal Area Network
WSN	Wireless Sensor Network

16.1 Introduction

The smart grid is defined as the integration of information, telecommunication, and network technologies in order to provide the conventional grid more reliable and more controllable. The mentioned integration provides several advantages such as more automation in daily life and industry, security of electric services, increased life-time of home appliances, and increasing the comfort of consumers. Owing to the improvement of smart grids, various developing methods and technologies have been reported in past decade by researchers across the globe. The most widely known technologies among them are smart meters (SMs), advanced metering infrastructure (AMI), home automation, bidirectional communication, and home area networks (HANs). The conventional electric power grid has been serving more than one century. The increasing and varying consumer profile depending to the increased population requires the conventional grid to supply electrical devices more than ever that causes instability of the electric power grid. The applications of the smart grid include generation, transmission, distribution, and consumption of electrical energy. The most important advance provided by the smart grid during the generation is to enable the distributed power generation, where power can be generated locally; to use the required energy and sale excess power back to utility.

In transmission and distribution applications, the smart grid enables electric providers to increase control capabilities by improving the reliability, stability, and sustainability of the system. Therefore, it is also demonstrated that economic and social benefits can be provided by consuming electrical energy efficiently. The smart building energy management systems (SBEMS) increase the efficient consuming, and any consumer can reduce the energy bill and decrease peak demand.

In recent years, the home environment has been rapidly converted to network enabled digital technologies. This improvement enabled the home appliances to increase the connectivity within the buildings for the purpose of home automation in novel and exciting opportunities. Power line communication (PLC) systems and mobile devices increase their communication speeds due to their portability and their wide range of capabilities. Hence, this chapter intends to comprehensively describe the communication methods for smart buildings that have an important role to realize nearly zero-energy buildings. The distributed generation (DG) that is one of the basic features of smart grids can be enabled to integrate to the management system to allow consumers to manage renewable energy sources such as solar panels and wind turbine, electric vehicles and energy storage system comprised of batteries that may be included in the energy infrastructure of the buildings. Thus, the SBEMS permits consumers to decrease the energy consumption and bill costs owing to the renewable energy sources that are controlled by the SBEMS besides security, illumination, heating, and multimedia system controls. The main features of the SBEMS are online control capability, renewable energy integration and consumption control, the charge amount of energy storage system, listing of monthly energy consumption rates saved bill costs, wireless monitoring and management system, and user interface to control home appliances. The communication methods utilized for the smart buildings and nearly zero-energy buildings can be classified into two categories as wired and wireless communication systems. The PLC system provides an efficient communication scheme for transmitting and receiving any type of data by employing existing power lines. In addition, the PLC system presents an inexpensive and suitable communication channel for data transmission and is a potential candidate in many application areas such as smart homes, vehicles, home automation systems, smart grids and so on. On the other hand, the wireless technologies such as Bluetooth, ZigBee, Wi-Fi can be utilized in the smart buildings alternatively. In this chapter, emerging communication technologies, advanced design and modeling studies on nearly zero-energy buildings are comprehensively discussed.

16.2 Smart Homes and Energy Efficient Buildings

Smart home term can be defined as the integration of technology and services in order to present for a better quality of living, where the transmission of information is provided by means of home networking. This technology offers several features to users such as connecting, controlling and monitoring home appliances and

Fig. 16.1 The concept of smart home systems

performing the functions with respect to predefined conditions. These features can be accomplished with communication systems of the smart homes based on the internet, mobile phones and PLC systems. In addition, developments on sensor technologies, embedded systems and communication systems have enabled the control of the smart homes in an easy and manageable way [1]. A smart home concept is shown in Fig. 16.1.

The smart homes that offer flexibility and functionality advantages require an energy management system called the SBEMS to provide economic and social benefits to users. In addition to conventional home management systems, the SBEMS controls the DG that is one of the basic features of smart grids, renewable energy sources and the interaction of electric vehicles with homes. The technical background of the SBEMS can be classified into two categories as home management system and energy management system. The home management system contains the control of electrical appliances used by the user's daily life and is concerned with user's comfort and other necessities. For instance, it comprises control of illumination, heating, cooling, multimedia systems and electrical household appliances. The second part of the SBEMS, which is the energy management system, includes details that are more technical. The DG systems of the renewable energy sources such as wind turbine and solar panels, support units of

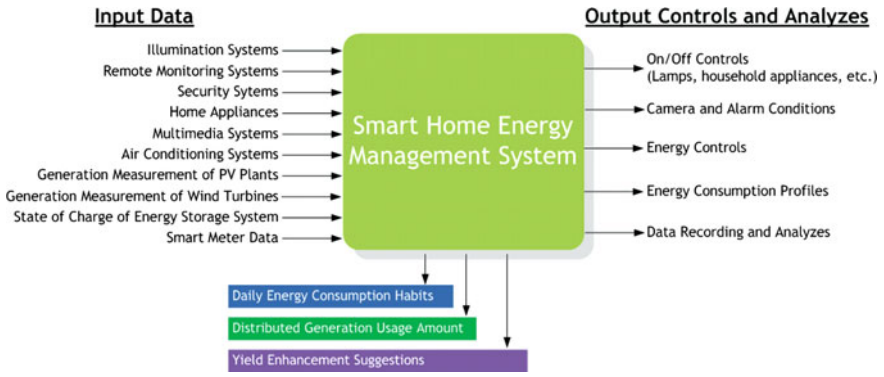

Fig. 16.2 Control and interface infrastructure of the SBEMS

these systems such as energy conversion and storage systems and the integration of electric vehicles can be utilized more efficiently owing to the energy management features of the SBEMS. A control and interface infrastructure diagram of the SBEMS is illustrated in Fig. 16.2.

The main features of SBEMS given in the Fig. 16.2 can be summarized as renewable energy integration, energy consumption control, the charge amount of energy storage system, online control capability, listing of daily, weekly or monthly energy consumption rates to save bill costs, communication capability for monitoring and management system, and user interface to control home appliances. Input data of the SBEMS that are shown on the left side of the Fig. 16.2 are transferred to the energy management system to inform users about actual status of the building. On the other hand, the right side of the figure indicates output controls and analyzes that can be carried out by the users. For instance, on/off control system contains basic level controls for starting or stopping commonly used electrical appliances and devices such as lamps, television, washing machine, refrigerator, air conditioning and so on.

In recent years, the development of internet technology has led to social and economic developments. Depending on the rapid spreading of wireless internet, people can take advantage of internet technology even if they are outdoors and are able to follow their all activities. Furthermore, the interaction between internet and daily family life has enabled the creation of the infrastructure for smart home technologies. Internet based management systems can be provided remote control for electrical household appliances to form intended comforts before the users reach home. In addition to this, the conducted investigations shown that hard-working people did not take the time to track these systems and they considered the tracking process as a waste of time. Therefore, some of the users also expect that the system is able to track the situation automatically and able to predict or remember user's habits according to the user's requests [2–5]. Although these demands are noted among the features of the home management system, the smart home management

systems used in the Far East and the United States carry out the management of the home, by recognizing the user's behavior, according to the user's habits rather than simply fulfill the user's commands.

16.3 Nearly Zero-Energy Buildings and Renewable Energy Integration in Buildings

Energy efficiency has become an important issue since energy consumption has been increased throughout the world in recent years. The decreasing fossil fuels directed governments to encourage use of the renewable energy sources and to draw attention to the energy efficiency. Recently, researchers have made many studies on the energy efficiency. Tascikaraoglu et al. [6] has presented a study on the concept of smart home and energy efficiency by examining the structure and requirements of the smart grids. According to this study, the smart homes that use the production and transmission characteristics of smart grids can provide energy savings between 10 and 30%. It is also emphasized in the study that user habits on this ratio are highly effective [6–8]. In addition, it is important to note that the SMs, energy management system and user habits should be considered to obtain energy savings in the specified ratio [8]. In [9], Missaoui et al. has reported that intensive researches, which are mostly carried out considering the consumption side have been done on the smart grid technology and load control issues in the last 2 years. The total energy consumed at homes corresponds to 32% of the total amount consumed in the world according to results of this study. At the same time, 36% of the carbon emissions occurred in the European Union (EU) countries is caused by the homes. Within the scope of the EU's climate and energy policy, not only the energy performance but also load management in the homes has been identified as an important issue and was included in the 2020 plans [9, 10]. Moreover, a building energy management system is designed to control an electric kettle, heating, cooling, ventilation system and thermodynamic system in [9]. Research results shown that home appliances such as the heater, washing machine, dishwasher and refrigerator caused by 80% of energy consumption resulting from home. Mahmood et al. [11] realized a study based on demand response and consumption side of energy management similar to previously mentioned work. For this purpose, they focused on linear programming and developed an optimization algorithm to reduce the power consumption at homes. They built an infrastructure enabling the use of smart devices for smart home energy management and called this system as "home appliances coordination scheme". Capitanelli et al. [12] also proposed another simulation model for smart home management system, where authors utilized this simulation model to manage household appliances in terms of performance and energy consumption. Accordingly, the proposed method is carried out in six stages. In the first two stages, users' requirements are determined and these requirements are defined as the smart home functions. The third stage covers classification and

identification operations of the household appliance characteristics. In the following stage, a general information management model is created. After defining the rules and tasks for intelligent system, service functions are performed and are stored in the last stage.

In another study, the most widely used devices in the homes and their usage rates are investigated as a special case study for the Canada [13]. According to this work, the most widely used home devices are heating systems, refrigerators, electric cars, washing machines, dishwashers and lighting systems in terms of electricity consumption. In addition, the 45.6% of homes do not have the stereo system whereas there is at least one at 43.2% of them. The obtained results shown that annual energy consumption results are 19.3 MWh for heating devices, 5.5 MWh for water heaters, 3.6 MWh for electric cars, 1.364 MWh for washing machines and dryers and 1.277 MWh for lighting systems. The communication systems used in home management systems are indicated as Wi-Fi, WiMax, 3G, DSL, Ethernet, ZigBee and fiber optics. The ZigBee that is one of the mentioned communication methods is employed on an energy management system reported by Batista et al. [14]. Although many communication technologies are appropriate, the ZigBee is preferred in this study due to low power consumption in wireless communication protocols and suitability to the control and monitoring applications. In studies about the SMs conducted from 2009 to 2015, the ZigBee has become rapidly widespread and showed an increase of 35%. Therefore, authors establish a ZigBee communication platform to monitor renewable energy grid consisting of wind and solar energy. In [15], Al-Ali et al. have proposed a GSM based energy management system for smart homes integrated with renewable energy sources.

It is understood from these studies that a large number of the existing homes over the world and energy-consuming devices in these buildings increase the energy demands excessive. However, decreasing of fossil fuels requires efficient use of available energy sources and ensuring energy efficiency as soon as possible. The main legislations of the EU are the 2010 Energy Performance of Buildings Directive (2010/31/EU) and the 2012 Energy Efficiency Directive (2012/27/EU) and these legislations are aimed to reduce energy consumption in the buildings. These legislations are also intended to ensure all new buildings to be nearly zero-energy buildings by 2020. At this point, the commission defines nearly zero-energy buildings as follow: Nearly zero-energy building is a building that is capable of a very high-energy performance. The required low amount energy should be provided from renewable energy sources which are constructed on-site or nearby of these buildings.

16.4 Advanced Metering Infrastructure (AMI)

The smart metering systems that are composed of measurement and monitoring process are intended to provide information to users about energy consumption of the smart homes. The acquired data are mapped with respect to utilized

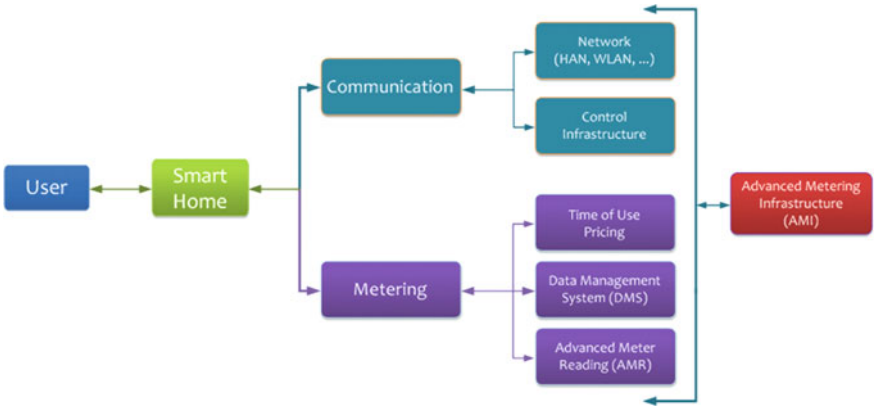

Fig. 16.3 The components of the AMI system in the smart homes [18]

communication protocol standards and are conveyed to management system over wired or wireless communication networks. The AMI system could be considered as an improved type of the conventional automatic meter reading (AMR) and automatic meter management (AMM) systems since it includes various developed technologies such as the SMs, HANs, wide area networks (WANs) or neighbored networks [16, 17]. The smart measurement process can be carried out by employing a SM that computes the energy consumption of any smart home. Hence, the SMs should have the ability to determine energy consumption rates of the smart homes in real-time by measuring parameters such as voltage, current, phase angle and frequency. A smart metering system involved in the metering and communication infrastructures is depicted in Fig. 16.3.

As can be seen from the figure, the metering section of the SM contains time-of-use pricing control system, data management system (DMS), and AMR framework. Wired or wireless communication techniques can be used in the communication part of the smart metering system. The communication substructure should permit a two-way data flow between smart homes and users. Therefore, network connection and control substructure are also required in the communication part of the SM. In addition to these two main sections, the SM modules may contain power supply module, timing module, indicating module, and encoding module. Besides, the SMs control the energy demand of the user by restricting consumption. It is noteworthy that the SMs will cover important roles in the future of the smart home applications due to their real time management, scalability, and security features. It is important to note at this point that the use of the access point architecture is also required to communicate with several hundreds of the SMs in an area. Therefore, the security issue should be taken into account for preserving measurement information in the SMs.

16.5 Wired Communication Systems for Smart Buildings

The most significant advantages provided by wired communication systems are reliability and insensitivity to interference. While the PLC systems utilize conventional power lines, fiber optic and digital subscriber line (DSL) systems use telephone lines as a communication medium. The capability of transmitting Gbps data packets to several kilometers and ability of strength against electromagnetic interference are the most important advantages of optical communication systems [19, 20]. The optical communication systems can be used over high voltage power lines due to these advantages. Moreover, optical power ground wire (OPGW) cables that are a special type of optical cables are able to transmit high capacity data over long distances. The DSL systems, which permit to transmit digital data by telephone lines can be utilized as a wired communication technology in smart homes. High-speed data transmission can be accomplished by using digital communication methods. For instance, while the DSL systems provide up to 10 Gbps data rates, coaxial and fiber optic cables reach between 155 Mbps and 160 Gbps data rates [19, 21, 22].

Recently, the PLC systems have gained a great deal of attention in the field of communication, smart grid and home automation systems. These systems provide an efficient communication scheme for transmitting and receiving any type of data, voice, and internet by using existing power lines [23–29]. When the PLC systems are compared with the other communication systems, the most important advantage offered by the PLC systems is obvious that there is no need to construct a new communication medium because of the fact that they utilize the current power lines to convey any type of data. Generally, the PLC applications can be classified into two categories as indoor and outdoor in terms of their application types. The most remarkable outdoor applications of the PLC systems are the smart grids that intent to accomplish several processes of conventional and renewable grids such as remote sensing, measurement, monitoring, and control in a maintainable and trustworthy way [20, 27, 28]. In addition, attention paid to this system is growing owing to numerous reasons such as the DGs, energy planning, remote monitoring and demand prediction issues. On the other hand, indoor applications of these systems aim to ensure high-data rate communication benefits for homes and offices.

The PLC systems can utilize different frequency bands called as narrowband (NB) and broadband (BB) according to types of applications. In addition, many national and international organizations are started to define standards for countries. These standards aim to identify substantial criteria such as types of modulation, bandwidth, channel and source coding schemes, operating frequency and limits of electromagnetic compatibility for indoor and outdoor applications of the PLC systems. In general, it can be noted that while the BB PLC systems ensure high data rates thanks to wide bandwidth, the NB PLC systems are preferable in low-data rate applications such as remote data acquisition, AMR systems, remote fault localization and fault type recognition. The NB PLC standard utilized in Europe exploits between 3 and 148.5 kHz frequency band with respect to European CENELEC

Standard EN50065. Furthermore, the NB PLC standards of the U.S. and Japan are 9–490 kHz in accordance with Federal Communications Commission (FCC) and 10–450 kHz with respect to Association of Radio Industries and Businesses (ARIB), respectively [30]. On the other hand, while the operating frequency of the BB PLC is proposed between 2 and 50 MHz according to the IEEE 1901-2010 standard, the International Telecommunication Union (ITU) recommends between 2 and 100 MHz frequency band. The standards, technical specifications and application areas for the BB and NB PLC systems are given in Tables 16.1 and 16.2, respectively.

16.5.1 Outdoor Application Examples for the PLC Systems

Several SG examples for outdoor application of the PLC systems are given in this subsection. First example deals with the feasibility of the PLC systems in renewable energy generation system modeled in Matlab/Simulink [32]. The aim of this system is to demonstrate that the electrical power lines are not only utilized to carry line voltages but also to transmit several measurement data of the renewable energy grids. Thus, monitoring costs can be reduced by using the reported technique rather than the SCADA, Ethernet or GSM based systems. The main parts of the designed system in the Matlab/Simulink are the photovoltaic (PV) panels, boost converter with perturb and observe (P&O) control algorithm, full bridge inverter, coupling circuits and the binary phase shift keying (BPSK) modem that is exploited to transmit measured data over the power lines. The block diagram of the system is depicted in Fig. 16.4.

As can be seen from the block diagram, the BPSK modulator structure is connected to the output of the full bridge inverter to employ power lines as a communication channel. The modulator aims to convey output power information of the PV panels over the 10 km transmission line which is also modeled in Matlab/Simulink depend on the PI section line model. A coupling device usage is also required in order to combine the BPSK modems with transmission lines. The BPSK demodulator structure is established at the end of the transmission line to acquire the output power information of the PV panels at the monitoring center.

Figure 16.5 shows obtained results for modeled remote monitoring system where two different scenarios are considered in terms of filtering circuit utilized in the BPSK demodulator structure. The cut-off values of the filter are set to 250 Hz and 4 kHz in the performed simulations. The fine filtering term is used for the 250 Hz filter that provides better performance as can be shown from the Fig. 16.5b. While the first curves given in Fig. 16.5 show the measured output data of the PV panels, the second curves depict the quantized data signals of the BPSK modulator. The demodulated data acquired from the output of the BPSK demodulator are given in the third curves and the filtered and calibrated data are shown in the fourth and

Table 16.1 Standards, technical specifications and applications of the BB PLC systems [31]

Technology/standard	Spectrum	Modulation/coding	Bit-rate	MAC	Carrier
HomePlug AV	2–28 MHz	OFDM (1536 tones)	200 Mbit/s	TDMA-CSMA/CA	Multiple
		Bit-loading up to 1024-QAM/convolutional, Turbo codes			
HomePlug Green PHY	2–28 MHz	OFDM (1536 tones) QPSK	3.8–9.8 Mbit/s	CSMA/CA	Multiple
HD-PLC	2/4–28 MHz	Wavelet OFDM (512 tones)	190 Mbit/s	TDMA-CSMA/CA	Multiple
		Bit-loading up to 16-PAM/RS, convolutional, LDPC			
IEEE P1901	2–28 MHz	OFDM (HPAV) (3072 tones)	540 Mbit/s	TDMA-CSMA/CA	Multiple
		Bit-loading up to 4096-QAM			
	2–60 MHz	W-OFDM (HD-PLC) (1024 tones)			
		Bit-loading up to 32-PAM			
ITU-T G.hn ITU-T G.9960	PLC, Coax, phone line: up to 100 MHz (BB) PLC: 100–200 MHz (PB) Coax: up to 100 MHz (PB, Fc = 0.35–2.45 GHz)	OFDM (up to 4096 tones)	>200 Mbps up to 1 Gbps	TDMA-CSMA/CA	Multiple
		Bit-loading up to 4096-QAM/ LDPC			

Table 16.2 Standards, technical specifications and applications of the NB PLC systems [31]

Technology/standard	Spectrum	Modulation	Bit-rate	MAC	Carrier	Application
Insteon/proprietary	CENELEC C	BPSK	2.4 kbps	–	Single	Home automation
Konnex/EN50090 EN13321-1 ISO/IEC14543	CENELEC B	S-FSK	1.2 kbps	CSMA	Single	Home automation
X10/proprietary	CENELEC B	PPM	50 or 60 bps	CSMA/CD	Single	Home automation
CEBus/EIA-600	CENELEC C, FCC, ARIB	SS	8.5 kbps	CSMA/CD	Single	Home automation
UPB/proprietary	CENELEC A	PPM	240 bps	–	Single	Home automation
HomePlug C&C/HomePlug consortium	CENELEC A, C, FCC, ARIB	DCSK	0.6–7.5 kbps	CSMA/CA	Single	Command and control
Meters and more/proprietary	CENELEC	BPSK	Up to 4800 bps	–	Single	Advanced metering infrastructure
G3-PLC/ERDF	CENELEC A, FCC	OFDM DQPSK DBPSK	34–240 kbps	CSMA/CA	Multiple	Advanced metering infrastructure
PRIME/prime alliance	CENELEC A	OFDM D8PSK DQPSK DBPSK	128 kbps	CSMA/CA TDMA	Multiple	Advanced metering infrastructure
G.Hnem ITU-T 9955	CENELEC A, B, C, D, FCC	OFDM QPSK 16-QAM	up to 1 Mbps	CSMA/CA	Multiple	Advanced metering infrastructure
IEEE P1901.2	CENELEC A, B, C, D, FCC	–	–	–	Multiple	Advanced metering infrastructure

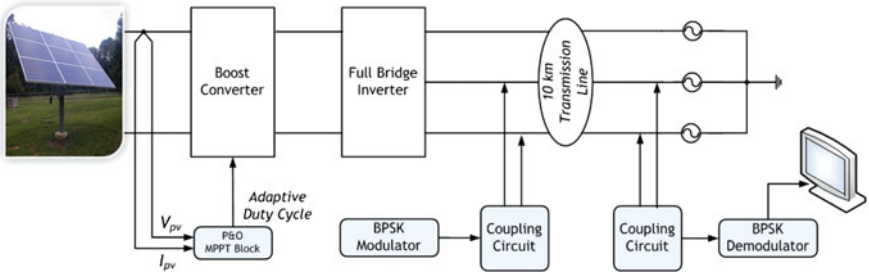

Fig. 16.4 Block diagram of the PLC system with BPSK modem for the PV panels [32]

fifth curves, respectively. When the reported results in the Fig. 16.5a, b are compared, it is clearly shown that the filtering process has an important effect on the performance of the system. It is important to note that even though the modulated data of the output power information are embedded into the grid, there is no distortional effect in the power line and the total harmonic distortion (THD) values of the system are in the suitable ranges according to IEEE-519-1992 and IEC-61000 standards.

An improved PLC system model is presented as the second application where the Quadrature Phase Shift Keying (QPSK Quadrature) modems are designed to create the PLC infrastructure. The modeled energy monitoring system in Matlab/Simulink is shown in Fig. 16.6. First part of the model is the solar plant which is constituted by regarding 170 W commercial solar panels.

In addition, the solar plant contains parallel-connected PV panels with the capability of maximum power point tracking (MPPT) algorithm. While the converter output of the modeled system is fed to a three-phase IGBT inverter, generated AC output voltages are delivered to the grid over 10 km transmission line that are created in accordance with practical parameters. The QPSK modems which are located at the plant side and grid side are utilized to monitor generated power by the solar plant. In addition, coupling devices are employed to prevent information losses due to any mismatch.

Different measurement results of the energy monitoring system are depicted in Fig. 16.7a, b. While cutoff frequency of used low pass filter in the QPSK modem is adjusted as 500 Hz in the Fig. 16.7a, the cutoff frequency is set to 250 Hz in another condition given in the Fig. 16.7b. As can be seen from the measurement results, the 250 Hz filtering provides better performance according to the 500 Hz filtering. As a final remark, the introduced results shown that use of the QPSK modems in the PLC applications to monitor energy plants can provide more accurate results according to use of the BPSK modem.

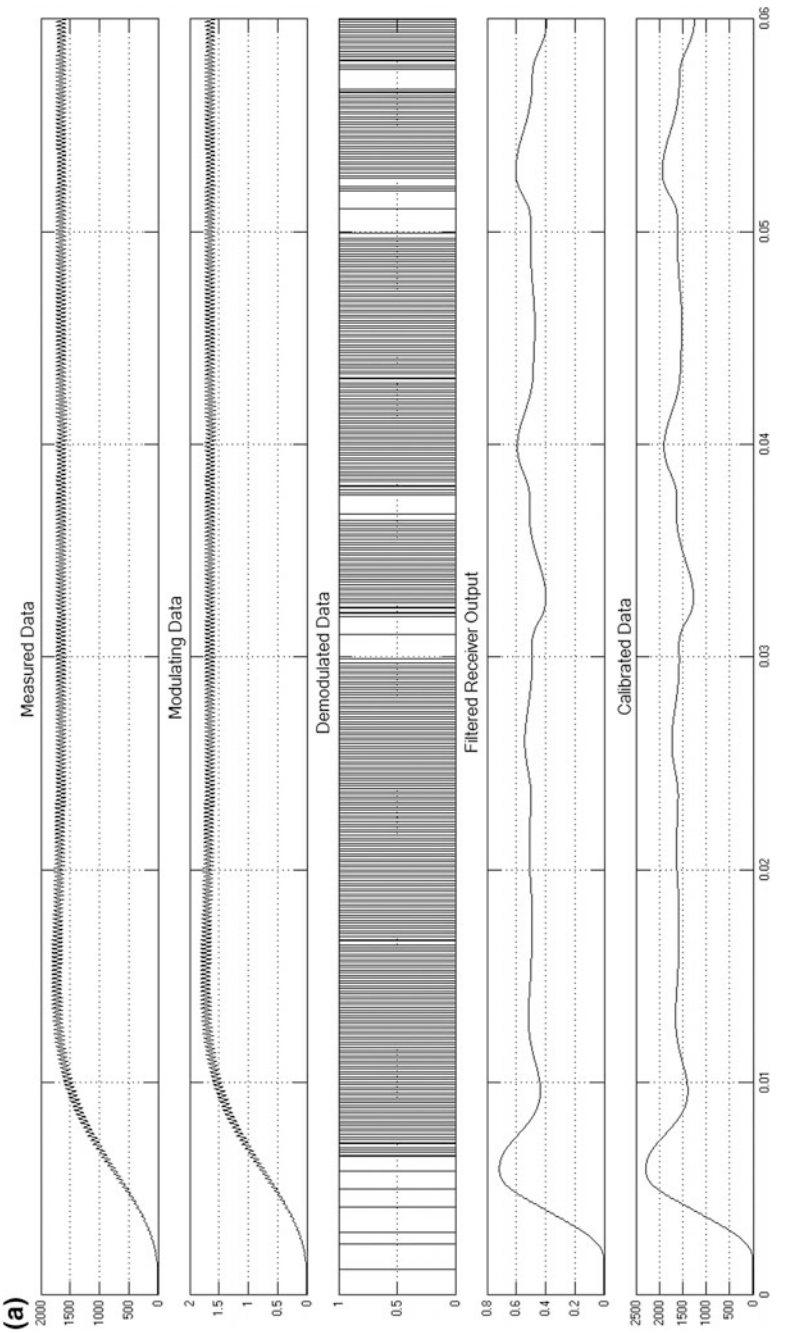

Fig. 16.5 Simulation results of the reported system with the BPSK modem: **a** Coarse filtering. **b** fine filtering [32]

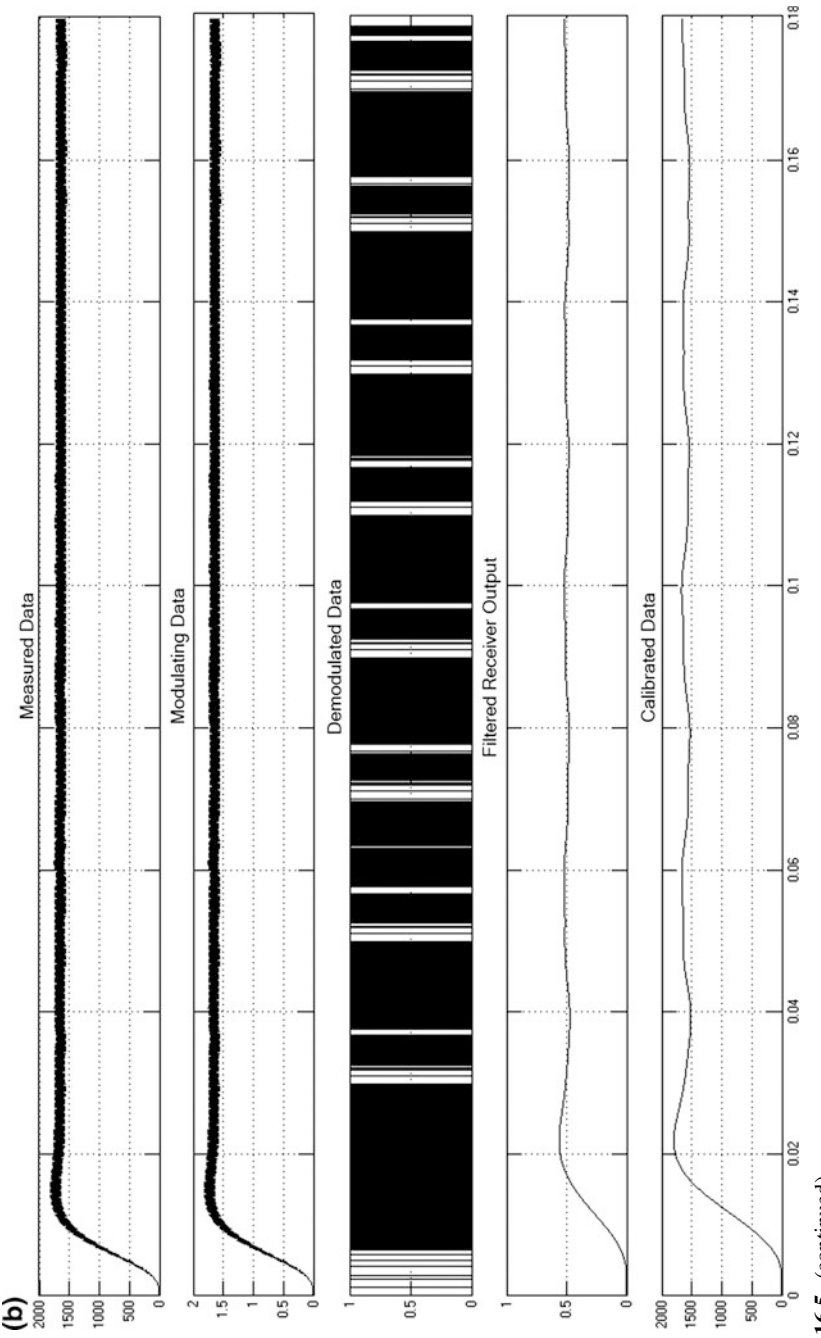

Fig. 16.5 (continued)

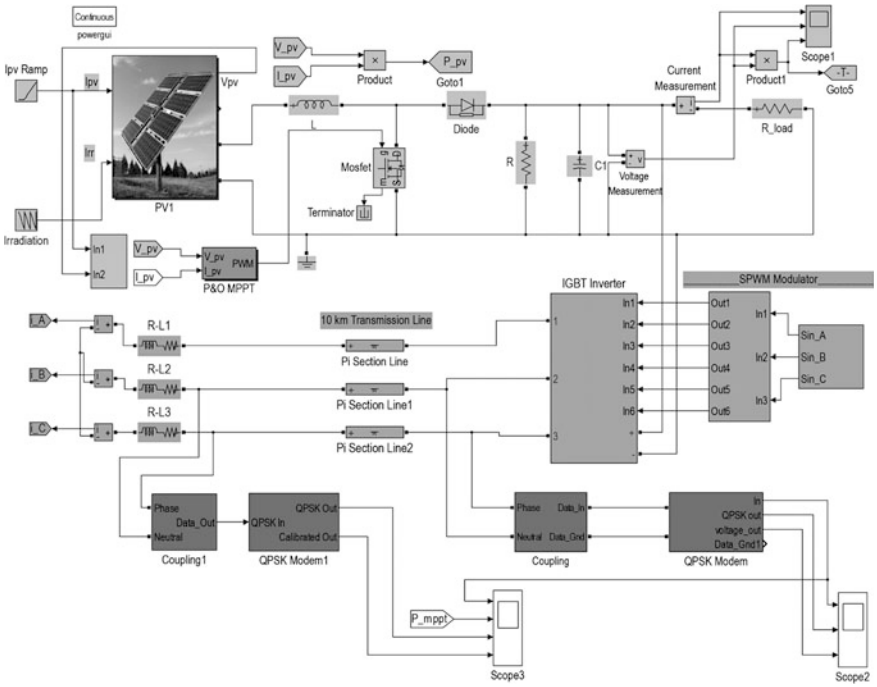

Fig. 16.6 Matlab/Simulink design of the energy monitoring system with QPSK modem [27]

16.5.2 Indoor Applications for the PLC Systems

In this subsection, different applications of the PLC systems for indoor environments are presented. The PLC system can be utilized to transmit data, which may be acquired information from any sensor located in the smart buildings, over indoor PLC channels. On the other hand, since the power lines have been fundamentally designed to deliver electricity over the world, they exhibit a destructive channel effect for communication signals. Hence, transmitting high frequency communication signals over actual power lines is a difficult problem and the PLC channel need to be accurately characterized to solve this problem. A BB indoor PLC channel model was reported by taking into account of a realistic network infrastructure for homes and small offices in [33].

In this PLC channel model, structural features of building electricity network are considered to characterize the indoor PLC channel in terms of network scheme, employed cable types, and loads connected to the grid. Furthermore, this model offers more appropriate channel conditions in point of the attenuation, delay spread and average channel gain. Thus, this PLC channel model is exploited to create indoor PLC channel conditions in the application examples presented in this subsection.

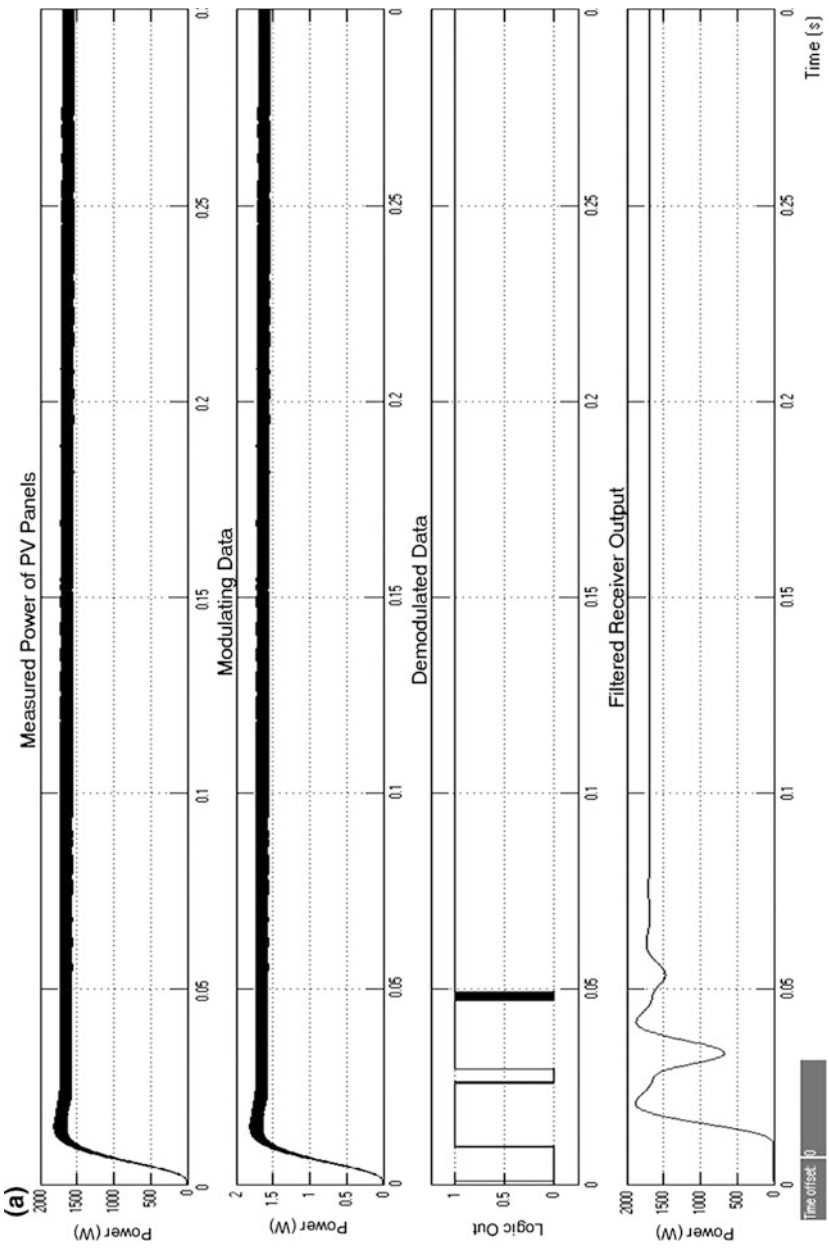

Fig. 16.7 Results of energy monitoring system: **a** QPSK modem with 500 Hz cutoff frequency filter, **b** QPSK modem with 250 Hz cutoff frequency filter [27]

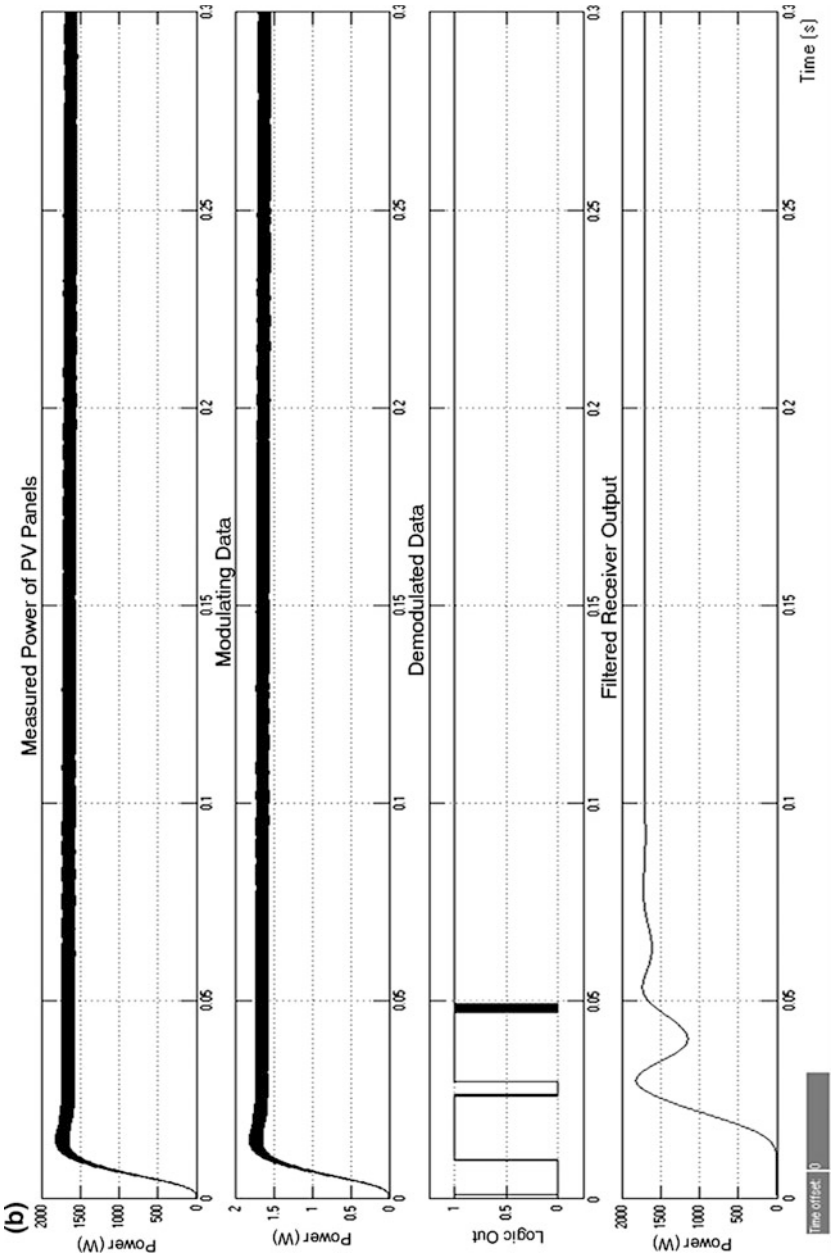

Fig. 16.7 (continued)

Table 16.3 Parameters of computer simulation exploited to evaluate BER performances [34]

Parameter	Value
Block numbers	1000
Size of parity-check matrices	(273,191), (495,433)
LDPC code rates	0.3, 0.125
LDPC decoder schemes	BP, WBF, IWBF, IRRWBF
Convolutional code rate	1/3
Convolutional code decoder	Hard decision Viterbi decoder
Maximum iteration number	30
Modulation type	BPSK
Channel model	Canete's PLC channel model
Noise types	Background and impulsive

In order to evaluate the bit error rate (BER) performances of different channel coding schemes, several computer simulations over the BB PLC channels are performed in [34]. Since low-density parity-check (LDPC) codes and convolutional codes (CC) are widely exploited channel coding codes in the communication systems, their performance comparison is presented when they are utilized as channel coding schemes in the indoor PLC channels. Two different-rate LDPC codes are tested to determine effect of the code rate on the performance of the communication systems. In addition, different soft and hard decision LDPC decoder schemes such as belief propagation (BP), implementation-efficient reliability ratio based weighted bit flipping (IRRWBF), improved weighted bit flipping (IWBF) and weighted bit flipping (WBF) decoders are considered in realized simulations. Simulation parameters of the designed communication system are given in Table 16.3.

The performance results of the LDPC and CC coded communication systems in terms of BER versus E_b/N_0 value are shown in Fig. 16.8. While (273,191) LDPC codes are selected in the Fig. 16.8a, (495,433) LDPC codes are used in the Fig. 16.8b. As expected from the disruptive effects of the indoor PLC channels, communication systems cannot supply an acceptable performance up to 15 dB E_b/N_0 value for both results. When this E_b/N_0 point is exceeded, performances of the LDPC decoders are increased rapidly. As can be seen from the Fig. 16.8a, b, the best performance result is provided by the BP decoder scheme for both results. The supplied coding gains by this decoder scheme are as much as 18 dB for a BER of 10^{-2} and 17 dB for a BER of 10^{-1} as seen in Fig. 16.8a and b, respectively. Though the worst BER performance among the other LDPC decoders is presented by the IWBF decoder scheme, it provides up to 9 dB better performance than that of the CC at a BER level of 10^{-2}. The simulation results shown in the Fig. 16.8a, b clearly indicate that the BP decoder scheme presents best performance results because of using log likelihood ratio (LLR) for decision procedure. On the other hand, decoding complexity of the BP decoders is too high. However, WBF and IWBF decoders, which are hard decision decodes as mentioned before, offer

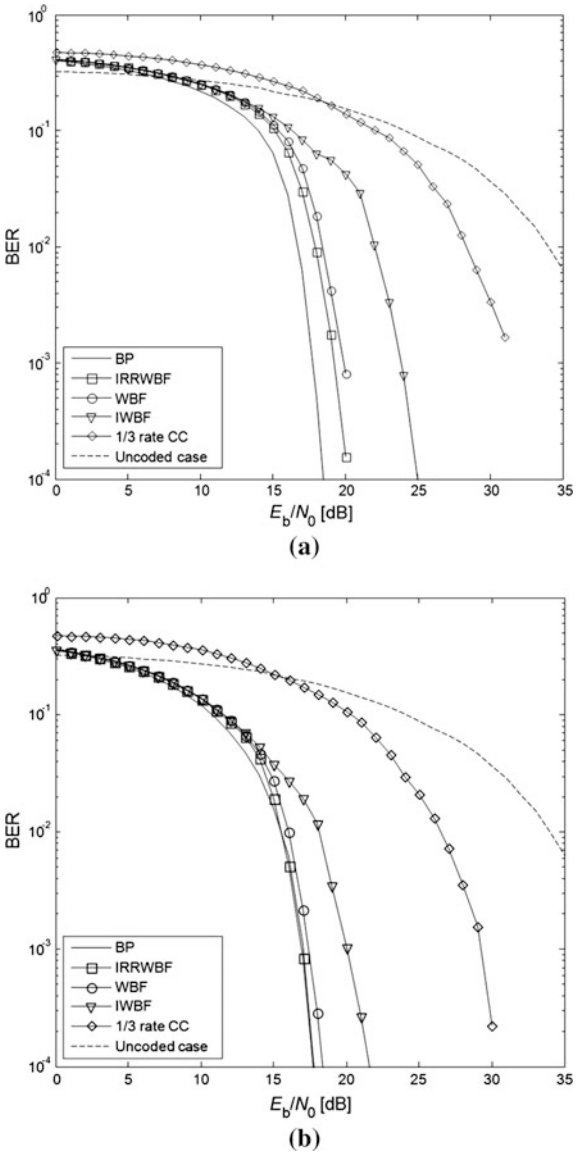

Fig. 16.8 The BER performance comparison of coded and uncoded systems in the BB PLC channel conditions: **a** Performance results for (273,191) LDPC codes, CC and uncoded case, **b** performance results for (495,433) LDPC codes, CC and uncoded case [34]

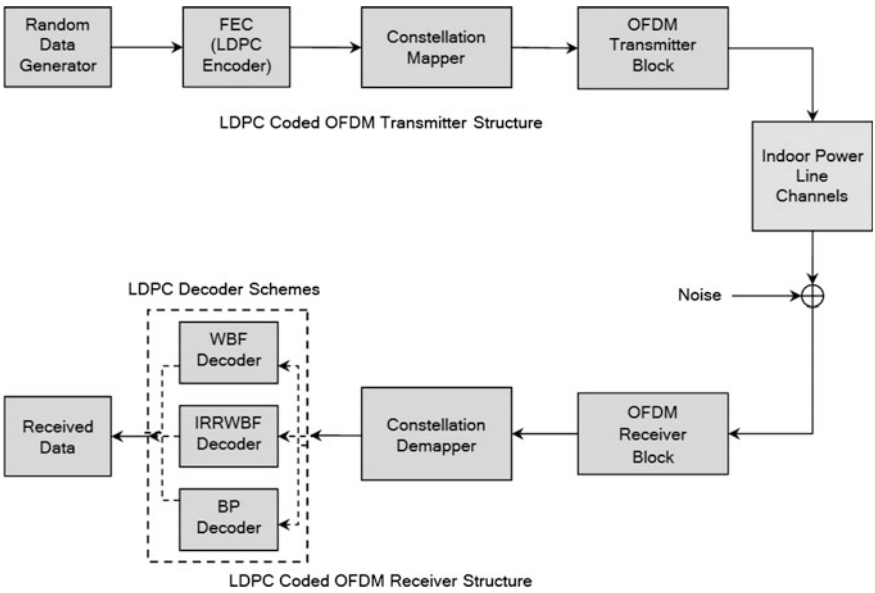

Fig. 16.9 The LDPC coded OFDM system with different decoder structures in indoor PLC channels [35]

tradeoff advantage between error correction and decoding complexity. In addition to reduce decoding complexity, IRRWBF decoders ensure very valuable performance on the error correction.

The BER performances of LDPC coded orthogonal frequency-division multiplexing (OFDM) systems are investigated in another indoor PLC application. This example aims to examine effects of the LDPC decoder schemes on the system performance which is evaluated over the BB PLC channels provided by Canete [33]. The block diagram of the LDPC coded OFDM system with different soft and hard decision decoder schemes is illustrated in Fig. 16.9.

The upper part of the block diagram shows transmitter of the LDPC coded OFDM system. Even though input message of the communication system is generated by random data generator block, the input message can be also supplied from any sensor located in homes or buildings. Later, input message is fed to forward error-correction (FEC) block where the LDPC encoder block fulfills channel-coding process. The constellation mapper block applies the mapping process, in other words modulation process, to the LDPC coded input data. In OFDM transmitter block, several important processes such as pilot symbol insertion, cyclic prefix (CP) adding and parallel to serial conversion are conducted and then coded data are sent to the indoor PLC channels. Several disruptive effects such as noise and attenuation that are originated by the characteristics of the power lines impress the data sent to the indoor PLC channels. The noise shown in these channels is composed of the background noise, impulsive noise and narrowband interferences. The underside of

the block diagram denotes the receiver part of the communication system. In the first block of the receiver part, the input serial data are firstly transformed to parallel data type and then the CPs of the data are cancelled in order to perform fast Fourier transform (FFT) process. After the FFT process, pilot symbol removal and demodulation process are respectively applied to the data. The last step of the receiver unit is decoding process, which can be implemented by employing soft or hard decision decoders.

In simulation carried out by using Matlab software, the LDPC codes with (96,48) and (1080,540) code lengths are exploited to obtain the BER performances of the modeled communication system. While the BP, WBF and IRRWBF decoders are utilized in the simulation, the maximum iteration number is adjusted as 50 for entire decoder schemes. In addition, the subcarrier space and CP of the modeled OFDM system are established as 468.75 kHz and 0.53 μs, respectively. The BER performance results of coded and uncoded OFDM systems in indoor PLC channels are illustrated in Fig. 16.10.

It is clearly seen from the figure that the LDPC coded OFDM systems outperform with regard to the BER performance than that of the uncoded OFDM system. The BER of (96,48) LDPC coded OFDM system shows virtually 9.5 dB better performance according to the uncoded system at a BER level of 10^{-3}. Furthermore, the (1080,540) LDPC coded system demonstrates 0.7 dB better performance results with respect to (96,48) LDPC coded system with BP decoder. When the performances of the WBF and IRRWBF decoders are considered, it is obvious that the IRRWBF decoder scheme ever provides approximately 0.5 dB better performances. In addition, it is detected that the hard decision decoder schemes present as well as 7.5 dB performance improvement at a BER level of 10^{-3} with respect to the uncoded OFDM communication system.

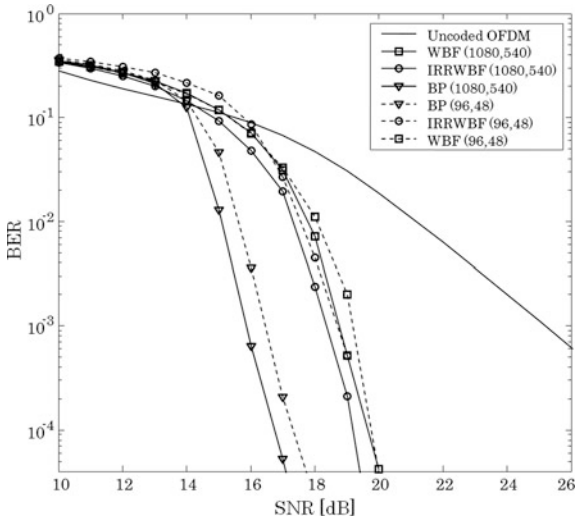

Fig. 16.10 The LDPC coded OFDM system with different decoder structures in indoor PLC channels [35]

16.6 Wireless Communication Systems for Smart Buildings

The wireless communication systems are one of the most powerful candidates in smart homes. Despite offering several advantages in terms of installation and coverage, the main problems of the wireless systems are reflection, diffraction, scattering and multipath propagation. Since the local area network (LAN), body area network (BAN) and personal area network (PAN) are generally utilized to create small area networks, they can be also employed to define HAN in the smart homes and nearly zero-energy buildings. Low-cost local network applications are generally exploited these network schemes. The HAN, which is formed to realize energy management and demand planning has a small coverage area with low latency advantage. In addition, the wireless networks contain hierarchical mesh networks thanks to wireless LANs to interact with electrical home appliances. On the other hand, wireless sensor networks (WSN) can be also used as an alternative cost effective solution in the smart homes owing to their low energy requirements.

The wireless PAN (WPAN or IEEE 802.15.4 standard) intends to define the PHY layer for low data rate, low power consumption, and low-cost network. The basic PHY layer of the WPAN ensures 256 kbps data rate in the coverage area, which covers between 10 and 1600 m in the star topology for single-hop, cluster-tree, and mesh topology for multi-hops. In order to control the entire network, a PAN coordinator is placed in each type of the topology. Moreover, mesh and tree topologies are required additional router nodes to establish multi-hop connections between coordinator and devices. The IEEE 802.15.4 standard is utilized in various industrial standards to accomplish monitoring and control applications. The ISA 100.11a, Wireless-HART, and the ZigBee are the most popular standards in this classification. The ZigBee is the most distinguished one rather than the other standards since it is widely approved in both industrial and commercial applications due to its capabilities on the network management. ZigBee systems employ digital radios with low power consumption depending on the IEEE 802.15.4 standard. The IEEE 802.11 standards utilize 2.4 or 5.8 GHz frequency band to standard the PHY and MAC layers of wide LANs (WLAN). The WLANs promote two different modes called ad hoc and infrastructure. The ad hoc permits stations to form a wireless LAN automatically where entire stations can communicate in peer-to-peer architectures with each other. In the second operation mode, the network contains at least one access point (AP) in its structure and each terminal is accessed through one or more than one access point to another.

There are various protocols such as Insteon, Z-Wave, SimpliciTI, EnOcean, Wavenis and Wireless M-BUS in applications apart from the above-mentioned standards [36]. The Insteon is an automation technology, which can be control electrical home appliances by using the PLC or wireless communication techniques. This protocol uses a dual mesh network topology at the 915 MHz frequency band [37]. The Z-Wave system has widely employed to control home appliances thanks to mesh network topology [38]. A protocol called SimpliciTI is developed by Texas

Table 16.4 Technical specifications and application areas of the wireless systems depend on the IEEE standards [36]

Protocols → / Specifications ↓	ZigBee over IEEE 802.15.4	WirelessHART over IEEE 802.15.4	MiWi over IEEE 802.15.4	Isa100.11 over IEEE 802.15.4	Bluetooth (IEEE 802.15.1)	Wi-Fi IEEE 802.11 a/b/g/n/ac/i
Frequency	2.4 GHz/915 MHz (USA) 868 MHz(EU)				2.4 GHz	2.4 GHz 5 GHz
RF channel numbers	16 (2.4 GHz)/10 (915 MHz) 1 (868 MHz)				79 40 (v4.0)	14 (2.4 GHz) 8 (5 GHz)
Network types	Peer-to-peer, mesh and star	Star, peer-to-peer and mesh	Star, peer-to-peer	Star, peer-to-peer and mesh	Star, peer-to-peer	Star, peer-to-peer
MAC scheme	CSMA/CA TDMA + CSMA/CA (star topology)	TDMA + CSMA/CA (beacon mode)	CSMA/CA (beaconless mode)	TDMA + CSMA/CA (beacon mode)	TDD	CSMA/CA + PCF
Mapping	BPSK (868-915 MHz) Q-QPSK (2.4 GHz)	O-QPSK (2.4 GHz)	FSK/OOK	O-QPSK (2.4 GHz)	GFSK/ DQPSK 8DPSK (optional)	BPSK, QPSK, COFDM, CCK, M-QAM
Nominal data rate	250 kbps (2.4 GHz) 40 kbps (915 MHz) 20 kbps (868 MHz)				1 Mbps (v1.2/v4.0) 3 Mbps (v2.0) 24 Mbps (v3.0)	11-65-450 (IEEE 802.11 n) Mbps
Encryption	AES128				AES64 and AES128	CCMP 128
Data authentication	MIC-32; MIC-64; MIC-128 (shared key) ENC-MIC-32; ENC-MIC-64; ENC-MIC-128 (encrypted key)				Challenge response scheme	4-Way handshake
Data integrity	CRC16	CRC16	CRC32	CRC16	CRC32	CRC32

(continued)

Table 16.4 (continued)

Protocols → / Specifications ↓	ZigBee over IEEE 802.15.4	WirelessHART over IEEE 802.15.4	MiWi over IEEE 802.15.4	Isa100.11 over IEEE 802.15.4	Bluetooth (IEEE 802.15.1)	Wi-Fi IEEE 802.11 a/b/g/n/ac/i
Autonomy (days)	100 to 1000+	Varies according to the battery features			1–10	0.5–5
Coverage area (meters)	10–300	100	20–50	100–200	10	10–100
Application areas	Remote control and automation in buildings	Industrial and building control	Automatic metering, home and industrial applications	Industrial and control market	Wireless connectivity between devices	Wireless LAN, broadband internet access
Advantages	Low power consumption, different application profiles and topology flexibility	Security, reliability and compatibility with wired systems	Flexible, cost-effective	Low energy consumption, flexible and security	Speed and flexibility	

Table 16.5 Technical specifications and application areas of the wireless systems depend on the IEEE standards [36]

Protocols → / Specifications ↓	SimpliciTI	Z-Wave	Insteon	EnOcean	Wavenis	WM-Bus
Frequency	2.4 GHz and Sub 1 GHz	2.4 GHz 908.4 MHz (USA) 868.4 MHz(EU)	915 MHz (USA)	315 MHz 902.875 MHz (USA) 868 MHz (EU)	433 MHz 868 MHz(EU) 915 MHz (USA) 2.4 GHz	169 MHz 433 MHz 868 MHz
RF channel numbers	Set by the application	2	34	1	1	12
Network types	Star and peer-to-peer	Mesh	Dual-mesh, peer to peer and mesh	Star, peer-to-peer and mesh	Star, peer-to-peer and mesh	Star, Peer-to-Peer
MAC scheme	LBT (listen-before-talk)	CSMA/CA	CSMA/CA	CSMA/CA	CSMA/TDMA and CSMA/CA	CSMA/CA
Mapping	MSK	FSK, GSK, narrowband	BPSK, FSK (in ISM Band)	ASK	GFSK	FSK, GFSK, MSK, OOK, ASK
Nominal data rate	Up to 250 kbps	9.6 kbps (868 MHz) 40 kbps (915 MHz)	38.4 kbps	120 kbps (868.3 MHz)	From 4.8 kbps to 100 kbps. Usually 19.2 kbps	2.4 kbps to 100 kbps
Encryption	Varies according to the MAC	AES128	No	No	3DES AES128	DES AES128
Data authentication	Varies according to the MAC	8-bit node I.D 32-bit home I.D	24 bit pre-assigned module I.D	8/32-bit	48-bit MAC addresses	–
Data integrity	Varies according to the MAC	Assigned by primary controller	CRC16	CRC8	BCH (32,21)	CRC16

(continued)

Table 16.5 (continued)

Protocols → / Specifications ↓	SimpliciTI	Z-Wave	Insteon	EnOcean	Wavenis	WM-Bus
Autonomy (days)	Depends on battery specifications			No batteries (solar cells)	Varies according to the battery features	
Coverage area (meters)	10	30	45 (outdoors)	30	200 (indoors) 1000 (outdoor)	Up to 1000
Application areas	Distributed alarm and security devices, energy meters and home automation	Remote control lighting and automation, in residential and commercial buildings	Energy measurement, Energy savings, irrigation control, occupancy sensing, remote control heating, air conditioning	Building automation, smart homes, logistics, industry and transportation	Industrial automation, AMI, AMR, smart homes, lighting and access control, RFID applications	Smart meters (electricity, gas, water, and heat)
Advantages	Small code size and low software complexity	Controllers and slaves network, flexible network configuration	Reliability, low cost, scalability and flexibility	Ultra-low power, no batteries, easy to install and time is saved	Ultra-low-power energy consumption, multiple years battery life	Very cost effective

Instruments to provide simple and low-power RF network protocol. This protocol supports star and peer-to-peer network topology [39]. The EnOcean standard is firstly utilized automation systems in buildings, and then it is used in different areas such as industry, logistics and smart homes. The peer-to-peer, mesh and star network topologies can be established in this standard [40]. The Wavenis technology is introduced by Coronis systems as a wireless protocol to control and monitor several applications of home and building automation. The Wavenis technology supports the peer-to-peer, mesh and star network topologies. Although data rates of the Wavenis can be programmable up to 100 kbps, most applications exploits at 19.2 kbps [36]. The Wireless M-Bus (WM-Bus) standard has recently proposed for metering applications such as the SMs. The energy requirement of the WM-Bus is very low owing to used protocol and frequency bands. In addition, the WM-Bus can allow transmission over longer distances than that of the IEEE 802.15.4 standard [41]. Technical specifications and application areas of the wireless network protocols utilized in the smart homes are listed in Tables 16.4 and 16.5. All of these network protocols support power saving feature.

16.7 Conclusions

Smart home systems aim to integrate technology and services to provide a better living quality. These systems can provide several benefits to users such as connecting, controlling and monitoring home appliances. In addition, they can realize various functions according to predefined circumstances. The entire of these features can be achieved by the communication systems that are one of the most important components of the smart homes, smart buildings and nearly zero-energy buildings. Hence, the wired and wireless communication systems of the smart buildings and nearly zero-energy buildings are introduced in this chapter. When the wired communication systems are considered, the wired communication systems provide two crucial advantages such as reliability and insensitivity to interference. Recently, the PLC systems which are based on the idea of conveying any type of data by exploiting the power lines originally designed for electrical energy delivery have gained a great deal of attention in the field of communication, smart grid and home automation systems. The most important advantage provided by the PLC systems against the optic fiber and the DSL systems is clearly that they do not require a new communication medium owing to being power lines in living areas. Therefore, the strongest candidate among the wired communication systems in the smart homes is the PLC systems. On the other hand, the wireless technologies can be also considered to build wireless HAN in the smart homes. Hence, several wireless technologies that are IEEE or not IEEE based standards are discussed for the smart homes. The IEEE standards such as ISA 100.11a, Wireless-HART, ZigBee and the Wi-Fi are the most popular standards in this classification. The ZigBee technology is the most distinguished one rather than the other standards since it is widely approved in both industrial and commercial applications due to its capabilities on the network

management. Although the low-power and low data protocols provided by the MiWi, ZigBee or Wavenis are sufficient for energy management purposes in smart homes, the EnOcean and Insteon cannot ensure a satisfactory security feature. As a final remark, it is important to note that the wired and wireless communication technologies may be cooperated to establish an efficient, reliable and stable communication environment in the smart homes and smart buildings.

References

1. Suryadevara NK, Mukhopadhyay SC (2015) Smart homes design, implementation and issues, vol 14. Springer, Switzerland, pp 15–16
2. Shen VRL, Yang CY, Chen CH (2015) A smart home management system with hierarchical behavior suggestion and recovery mechanism. Comput Stand Interface 41:98–111
3. Wu CL, Fu LC (2012) Design and realization of a framework for human-system interaction in smart homes. IEEE Trans Syst Man Cybern Part A 42:15–31
4. Wu C-L, Liao C-F, Fu L-C (2007) Service-oriented smart-home architecture based on OSGi and mobile-agent technology. IEEE Trans Syst Man Cybern Part C 37:193–205
5. Bench-Capon TJM, Dunne PE (2007) Augmentation in artificial intelligence. Artif Intell 171:619–641
6. Tascikaraoglu A, Boynuegri AR, Uzunoglu M (2014) A demand side management strategy based on forecasting of residential renewable sources: a smart home system in Turkey. Energy Build 80:309–320
7. Chen X, Wei T, Hu S (2013) Uncertainty-aware household appliance scheduling considering dynamic electricity pricing in smart home. IEEE Trans Smart Grid 4:932–941
8. Yohanis Y, Mondol J, Wright A, Norton B (2008) Real-life energy use in the UK: how occupancy and dwelling characteristics affect domestic electricity use. Energy Build 40:1053–1059
9. Missaoui R, Joumaa H, Ploix S, Bacha S (2014) Managing energy smart homes according to energy prices: analysis of a building energy management system. Energy Build 71:155–167
10. OECD/IEA (2013) International energy agency. http://goo.gl/HFwk1J. Accessed 27 Sept 2015
11. Mahmood A, Khan I, Razzaq S, Najam Z, Khan NA, Rehman MA, Javaid N (2014) Home appliances coordination scheme for energy management (HACS4EM) using wireless sensor networks in smart grids. Procedia Comput Sci 32:469–476
12. Capitanelli A, Papetti A, Peruzzini M, Germani M (2014) A smart home information management model for device interoperability simulation. Procedia CIRP 21:64–69
13. Beaudin M, Zareipour H (2015) Home energy management systems: a review of modelling and complexity. Renew Sust Energy Rev 45:318–335
14. Batista NC, Melício R, Matias JCO, Catalao JPS (2013) Photovoltaic and wind energy systems monitoring and building/home energy management using ZigBee devices within a smart grid. Energy 49:306–315
15. Al-Ali AR, El-Hag A, Bahadiri M, Harbaji M, El Haj YA (2011) Smart home renewable energy management system. Energy Procedia 12:120–126
16. Siano P (2014) Demand response and smart grids-a survey. Renew Sust Energy Rev 30:461–478
17. Fangxing L, Wei Q, Hongbin S, Hui W, Wang J et al (2010) Smart transmission grid: vision and framework. IEEE Trans Smart Grid 1:168–177
18. Kabalci Y (2016) A survey on smart metering and smart grid communication. Renew Sust Energy Rev 57:302–318

19. Ancillotti E, Bruno R, Conti M (2013) The role of communication systems in smart grids: architectures, technical solutions and research challenges. Comput Commun 36:1665–1697
20. Galli S, Scaglione A, Wang Z (2011) For the grid and through the grid: the role of power line communications in the smart grid. Proc IEEE 99:998–1027
21. Wang W, Xu Y, Khanna M (2011) A survey on the communication architectures in smart grid. Comput Netw 55:3604–3629
22. Liu S, Liu XP, El Saddik A (2014) Modeling and distributed gain scheduling strategy for load frequency control in smart grids with communication topology changes. ISA Trans 53:454–461
23. Lin YJ, Latchman HA, Lee M et al (2002) A power line communication network infrastructure for the smart home. IEEE Wirel Commun 9:104–111
24. Gao J, Xiao Y, Liu J et al (2012) A survey of communication/networking in smart grids. Future Gener Comput Syst 28:391–404
25. Gungor VC, Sahin D, Kocak T et al (2011) Smart grid technologies: communication technologies and standards. IEEE Trans Ind Inf 7:529–539
26. Gotz M, Rapp M, Dostert K (2004) Power line channel characteristics and their effect on communication system design. IEEE Commun Mag 42:78–86
27. Kabalci E, Kabalci Y, Develi I (2012) Modelling and analysis of a power line communication system with QPSK modem for renewable smart grids. Int J Electr Power 34:19–28
28. Kabalci Y, Develi I, Kabalci E (2013) LDPC coded OFDM systems over broadband indoor power line channels: a performance analysis. In: 4th IEEE international conference on power engineering, energy and electrical drives, Istanbul, pp 1581–1585
29. Bilim M, Develi I, Kabalci Y (2013) Multiuser communications for broadband indoor power line channels using IDMA technology. In: 4th IEEE international conference on power engineering, energy and electrical drives, Istanbul, pp 1586–1590
30. Develi I, Kabalci Y, Basturk A (2015) Artificial bee colony optimization for modelling of indoor PLC channels: a case study from Turkey. Electr Power Syst Res 127:73–79
31. Tonello AM (2012) Advances in power line communications and application to the smart grid. In: Tutorial at EUSIPCO, Bucharest
32. Kabalci E, Kabalci Y (2013) A measurement and power line communication system design for renewable smart grids. Meas Sci Rev 13:248–252
33. Canete FJ, Cortes JA, Diez L, Entrambasaguas JT (2011) A channel model proposal for indoor power line communications. IEEE Commun Mag 49:166–174
34. Develi I, Kabalci Y (2014) Highly reliable LDPC coded data transfer in home networks by using Canete's PLC channel model. Int J Electr Power 62:912–918
35. Develi I, Kabalci Y (2014) Analysis of the use of different decoding schemes in LDPC coded OFDM systems over indoor PLC channels. Elektronika Ir Elektrotechnika 20:76–79
36. Mendes TDP, Godina R, Rodrigues EMG, Matias JCO, Catalao JPS (2015) Smart home communication technologies and applications: wireless protocol assessment for home area network resources. Energies 8:7279–7311
37. Gomez C, Paradells J (2010) Wireless home automation networks: a survey of architectures and technologies. IEEE Commun Mag 48:92–101
38. Zensys (2006) INS10244, Instruction, Z-Wave node type overview and network installation guide. http://goo.gl/y7naF8. Accessed 27 Sept 2015
39. Friedman L (2007–2009) SimpliciTI: Simple modular RF network developers notes, Texas Instruments, Inc., San Diego
40. Li X, Chen G, Zhao B, Liang X (2014) A kind of intelligent lighting control system using the EnOcean network. In: International conference on computer, information and telecommunication systems, Jeju, pp 1–5
41. Squartini S, Gabrielli L, Mencarelli M, Pizzichini M, Spinsante S, Piazza F (2013) Wireless M-Bus sensor nodes in smart water grids: the energy issue. In: Fourth international conference on intelligent control and information processing, Beijing, pp 614–619

Chapter 17
Power Architectures and Power Conditioning Unit for Very Small Satellites

Sergiu Oprea, Constantin Radoi, Adriana Florescu, Andrei-Stefan Savu and Adrian-Ioan Lita

Abstract Space agencies all over the world are interested today in very small satellites because of their advantages compared to heavier satellites. This chapter starts with the general characteristics, Earth orbits, eclipses and current missions of very small satellites. It continues with a brief summary of the component parts of the electrical power system: the array of solar cells, batteries for space applications, 3 power architectures and 19 maximum power point tracker's algorithms. Authors' attention is mainly focused on designing, simulation and practical demonstration of a prototype with a flexible hybrid proposed architecture of the power conditioning unit for very small satellites, whose component blocks are the battery charge unit (BCU) including the dc–dc converter, the digital controller, the BCU sensors circuitry and the BCU prototype) and the battery charge/discharge monitor unit (BCDMU) including the microcontroller, the BCDMU sensors circuitry, the battery switch, the battery heater and the telemetry system.

Keywords Very small satellites · Earth orbits and eclipses · Electrical power system · Flexible power architectures · Battery charger unit · Battery charge/discharge monitor unit

S. Oprea · C. Radoi · A. Florescu (✉) · A.-S. Savu · A.-I. Lita
University POLITEHNICA of Bucharest, Bucharest, Romania
e-mail: adriana.florescu@yahoo.com; adriana.florescu@upb.ro

S. Oprea
e-mail: oprea_serg@yahoo.com

C. Radoi
e-mail: conrad_1944@yahoo.com

A.-S. Savu
e-mail: savucfa@yahoo.com

A.-I. Lita
e-mail: adrian.lita@ieee.org

N. Bizon et al. (eds.), *Energy Harvesting and Energy Efficiency*,
Lecture Notes in Energy 37, DOI 10.1007/978-3-319-49875-1_17

Abbreviations and Acronyms

BCDMU	Battery Charge/Discharge Monitor Unit
BCU	Battery Charger Unit
BDR	Battery Discharge Regulator
BFV	Best Fixed Voltage
BOL	(Battery's) Beginning of Life
BU	Battery Unit
CCM	Continuous Current Mode
CMMR	Common Mode Rejection Ratio
COTS	Commercial-Off-The-Shelf
CU	Chargers Unit
DET	Direct Energy Transfer
DOD	Depth of Discharge
e.i.r.p.	equivalent isotropic radiated power
EOL	(Battery's) End of Life
ESA	European Space Agency
GEO	Geosynchronous Earth Orbit
GSTP	General Support Technology Programme
GUI	Graphical User Interface
HEO	Highly Elliptical Orbit
IC	Integrated Circuit
IOD	In-Orbit Demonstration
IU	Isolation Unit
LEO	Low Earth Orbit
LRCM	Linear Reoriented Coordinates Method
MEO	Mid Earth Orbit
MPPT	Maximum Power Point Tracker
NGSO	Non-Geostationary Orbit
NTC	Negative Temperature Coefficient
OCC	One-Cycle Control MPPT
P&O	Perturb and Observe
PEC	Packet Error Check
PI	Proportional-Integral
POL/D	Point-Of-Load/Distribution
PV	Photovoltaic
PWM	Pulse Width Modulation
RCC	Ripple Correlation Control
S3R	Sequential Switching Shunt Regulator
SEPIC	Single-Ended Primary Inductor Converter
STAR	Space Technology and Advanced Research
TT&C	Telemetry, Tracking and Telecommand

17.1 Introduction in Very Small Satellites

The spaceflight literature defines today the artificial satellite (usually, simply called satellite) as an object placed on purpose into a space orbit to fulfill a specific mission [1]. Small satellites, also known as miniaturized satellites, are defined as low mass satellites (up to 500 kg) and small size [2]. The definition of very small satellites varies today, sometimes gathering together micro-, nano-, pico- and femto-satellites [3], sometimes defining only nanosatellites and picosatellites (such as CubeSats) [4], sometimes including all small satellites having under a kilogram mass [5] etc.

Many reasons justified small and very small satellites to appear and develop:

- big amount of energy saving
- to lower the cost of the existing heavier satellites, that impose massive rockets to make possible the launch operation in space and possibility of multiple launch;
- to allow with few finance in formation flight of a small satellites cluster;
- to allow low cost design;
- to make easier the mass production;
- to facilitate not solvable missions by larger satellites, such as:
  - formations missions dedicated to low data rate communications;
  - data collection missions from multiple points that need formation flights;
  - in-space inspection and service for larger satellites placed in orbit;
  - research and design missions for universities.

Today the very small satellites become a usual presence in space. A significant increase of the number of space experiments is also observed. As a direct consequence of these, are the increased demands and technical challenges for the power system. The miniaturized satellites standards like the “nanosat” or “picosat” push the limits even harder: the engineers face the problem of designing in a restricted space, with a limited amount of the available energy and financial resources while satisfying in the same time the criteria of maximum capabilities and performances.

17.1.1 Characteristics of Small Satellites

The block diagram in Fig. 17.1 points out the mandatory systems present in any satellite in order to accomplish the proposed mission (marked with solid lines) and its essential supporting systems (marked with intermittent lines).

In terms of spacecrafts, these systems are usually known and clustered as: the payload and the bus. The payload refers to the main communications equipment/science instruments for the commercial/research satellites. The bus gathers all the other essential systems that assist the payload such as: the electrical power system, the communications and data coordinating systems, all on-board telemetry sensors, the main satellite’s computer etc.

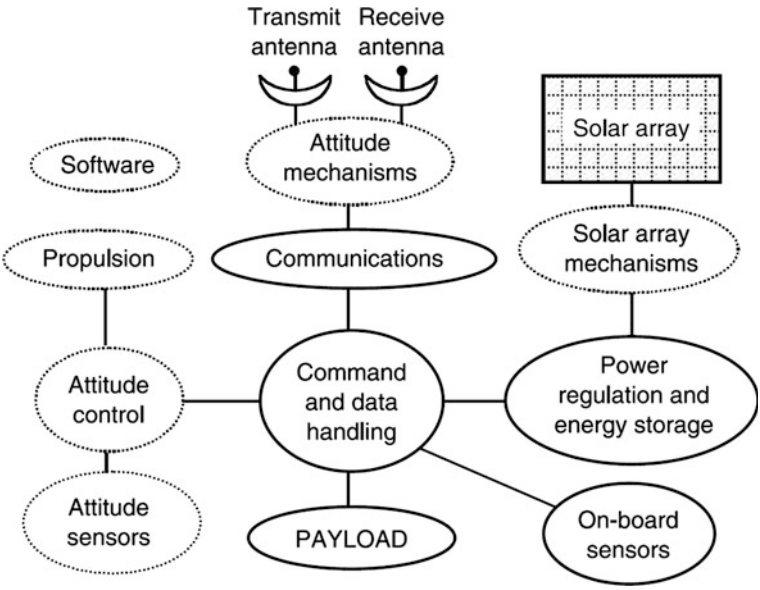

Fig. 17.1 Satellite systems

The electrical power system contains: the solar array as satellite's primary electric source of energy, the batteries to store and regulate this energy and all their associated power electronics to convert, control and distribute the electric energy to the payload [6]. A part of the electrical power system for very small satellites, namely the power conditioning unit, represents the subject of this chapter. Usually, the most popular theoretical approach to sort small satellites is by their mass, as shown in Table 17.1, where the presented values are just for reference and were taken according to the year 2014. In space field, a satellite may have different characteristics and still be in one of the presented categories.

Aside from size and/or mass and the other typical classification criteria presented in Table 17.1, there are also some rather important factors such as orbital uncertainty, low satellite equivalent isotropic radiated power (e.i.r.p.) and speed of development [7].

17.1.2 The Earth Orbits

The Earth is almost a sphere with the mean radius of 6371.0 km, equatorial radius of 6378.1 km and the polar radius of 6356.8 km, that has a reduced flattening (as a measure of compression from sphere to spheroid) only of 0.0033528. Starting from the surface and up to 160 km in the air, Earth's atmosphere is present and then it gradually vanishes into the vast space [6].

Table 17.1 Typical classification criteria of small satellites

Satellite's category	Mass (kg)	Maximum bus power (W)	Typical costs (USD)	Maximum dimensions (m)	Development time (years)	Orbit types	Mission endurance (years)
Minisatellite	100–500	1000	30–200 M	3–10	3–10	GEO MEO LEO HEO	5–10
Microsatellite	10–100	150	10–150 M	1–5	2–5	LEO (HEO)	2–6
Nanosatellite	1–10	20	100 k–10 M	0.1–1	1–3		1–3
Picosatellite	0.1–1	5	50 k–2 M	0.05–0.1			
Femtosatellite	< 0.1	1	<50 k	0.01–0.1	1		<1

Table 17.2 The Earth orbits and their major characteristics

Orbit	Apogee[a] (km)	Perigee[b] (km)	Eccentricity[c]	Inclination[d] (°)	Perioad[e]
GEO	35,786	35,786	0	0	1 sidereal day
GSO	35,786	35,786	0	0–90°	1 sidereal day
LEO	Variable	Variable	0–High	0–90°	>90 min
HEO	39,400	1000	High	62.9°	1/2 sidereal day

[a] Closest distance from the Earth surface
[b] Farthest distance from the Earth surface
[c] Ratio of difference to sum of apogee and perigee radii
[d] Angle between orbit plane and equatorial plane
[e] One sidereal day is 23 h, 56 min, 4.09 s

The Earth orbits of the artificial satellites are mentioned in Table 17.2 with their major characteristics. The standard abbreviations of these orbits are:

- GEO Stationary (abbreviated GEO): the Earth Orbit with an orbital period the same as the Earth's rotation period, placed above the Earth's equator
- GEO Synchronous (abbreviated GSO): the Earth orbit which enables to be synchronized with the rotation of the Earth
- MEO: mid Earth orbit, circular at 2000–20,000-km altitude
- LEO: low Earth orbit, generally circular at 200–2000-km altitude
- HEO: highly elliptical orbit, such as Molniya.

Van Allen radiation belts, depicted in Fig. 17.2, represent layers of energetic charged particles coming from the solar wind and cosmic rays, which are held in place by Earth's magnetic field [8]. The inner belt is formed by o combination of many protons and less electrons and the outer belt only of electrons, both being very dangerous for satellites. In order to avoid Van Allen belts, the orbit parameters of LEO and MEO satellites are chosen to surround the Earth at altitudes of 1.3–1.7 and 3.1–4.1 Earth radii. So, a typical LEO satellite has an altitude of 500–1500 km, an orbit period of 1.5–2 h, and is visible to a given Earth station for only a few

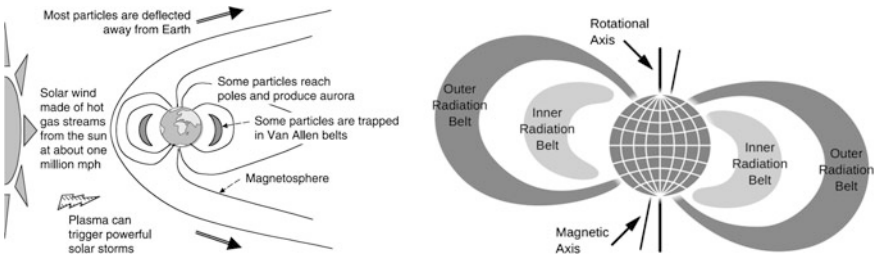

Fig. 17.2 The Van Allen Belts

minutes in every orbit period, while a typical MEO satellite is between 5000 and 12,000 km altitude with orbit period of several hours.

Today, most of the very small satellites operate in low Earth orbits (LEO), but there are no restricted orbits because of two reasons:

- mainly, their missions are usually technological demonstrations/verifications/tests/maneuvers etc. and they last as long as the communication with the Earth is maintained;
- their orbital parameters are defined at the end of the design process because of the multitude of launch possibilities, altitude and inclination flexibilities as secondary payloads.

17.1.3 Eclipses on Earth Orbits

When a satellite is on an Earth orbit (Fig. 17.3)—mostly during the equinox days when the longest eclipse appears and consists in the Earth totally blocking the solar light to illuminate the satellite—, the solar array ceases to generate the primary electrical power for the satellite and its temperature quickly falls. Therefore, for a

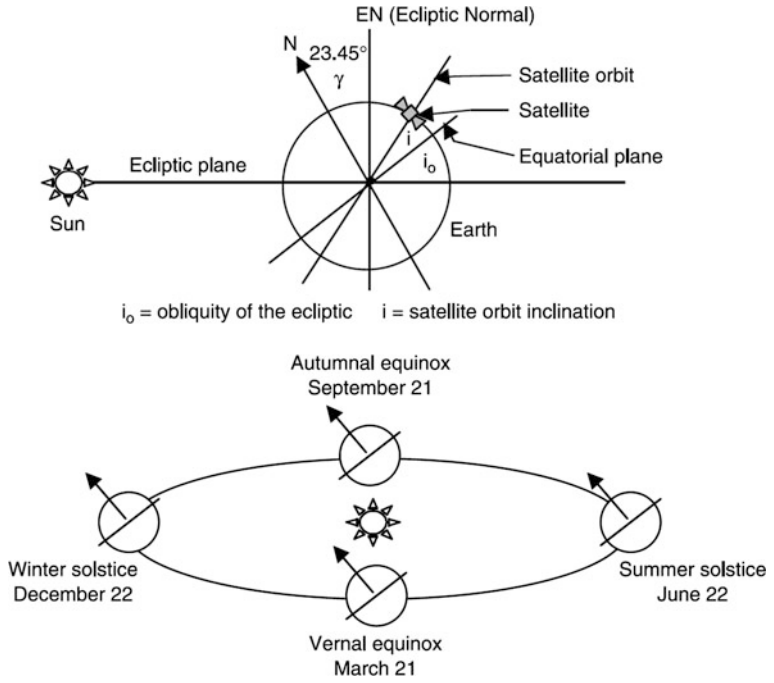

Fig. 17.3 Satellite in Earth's orbit with seasonal variations

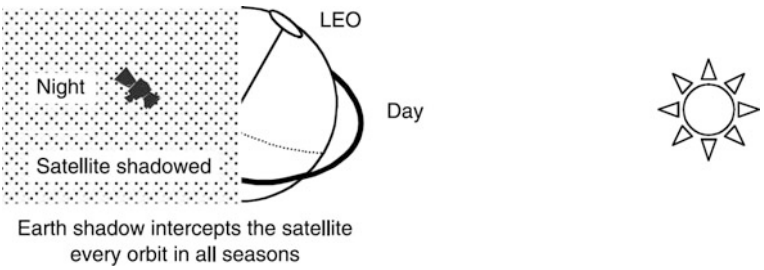

Fig. 17.4 Eclipse in near-equatorial LEO, once per orbit in all seasons

circular Earth orbit of a satellite, the eclipse duration in hours is calculated using the equation [6]:

$$T_e = \frac{1}{2} + \frac{1}{\pi} \cdot \sin^{-1} \frac{\sqrt{1 - (R_{Earth}/R_{orbit})^2}}{\cos \beta}, \tag{17.1}$$

where β is the angle of the sunlight incidence on the orbit plane that varies seasonally between ±(i + γ), i is the orbit inclination with respect to the equator and γ is the angle between the sun line and the ecliptic plane (23.45°).

Equation (17.1) above shows how the eclipse duration T_e depends on β angle: when β grows, T_e is diminished, which improves the load capability of the electrical power system. There is a specific high value of β angle when no eclipse occurs: there are polar and near-polar low Earth orbits (LEO) that never have an eclipse of the sun and $T_e = 0$. The opposite situation is when $\beta = 0$ and creates the case of the longest eclipse: in near-equatorial, circular, low Earth orbits (LEO), eclipses of approximately equal duration occur once every orbit period. As a consequence, the power system engineer starts with the orbit parameters indicated by the customer in order to obtain the orbit period, calculates the eclipse duration Te (that determines battery requirements onboard the satellite on a certain day) according to β angle.

In addition, other parameters may appear if a Moon eclipse occurs simultaneously with the Earth eclipse, when the battery must support an additional depth of discharge while temperature falls. Also, the solar flux depends of equinox and solstice and varies the power in the solar arrays with 11%. Figure 17.4 shows how the eclipse duration T_e varies with the orbit altitude, inclination, and the sunlight incidence angle on the orbit plane-in LEO, it can vary by one of two factors. All these parameters greatly affect the power system design.

17.1.4 Example of Very Small Satellites: CubeSats

A typical example of very small satellites is strongly represented today by CubeSats [9], that has been widely adopted both by universities and industry as well [10, 11]

due to many reasons distinctive from big satellites: a cheaper and faster design and launch, a larger modularization capacity by packaging many devices and sensors, project management's cost reduction, availability of the satellite's subsystems as Commercial-Off-The-Shelf (COTS) components, the control from Earth through amateur stations, simple architecture and aims etc. CubeSats are in many situations called nanosatellites, but they represent only a class of them.

The elementary cube unit of 10 cm (10 × 10 × 10 cm) and the mass smaller than 1.33 kg is known as 1U CubeSat, though even 0.5U modules are manufactured nowadays. Still, only starting from 3U CubeSat dimensions (10 × 10 × 30 cm) with a mass of 3–4 kg, small payloads can be carried in space, without mentioning the additional mandatory equipment that expands these dimensions.

CubeSats' missions are generally classified in: experimental and research missions, educational and radio amateur missions and commercial missions. As an example of the first mentioned mission, the European Space Agency (ESA) started in 2013 and will launch in 2016 (a development of 3 years) a number of four 3U CubeSats projects (GomX-3, SIMBA, QARMAN and Picasso) that are part of the QB50 flight of the In-Orbit Demonstration (IOD), which is part of the General Support Technology Programme (GSTP). Other ESA nanosatellite missions that begun in year 2014: cooperative nanosatellites (four parallel 'Sysnova' studies within the General Studies Programme), commercial telecom services nanosatellites (within ARTES 1 programme) etc. [9].

Still, there are a number of world organizations from academic and industry who design, manufacture and send in space nanosatellites whose buses comply with the requirements of a specific mission. In this case, CubeSat design specifications may be not followed.

17.2 The Electrical Power System

The electrical power system (Fig. 17.5) generates, stores, conditions, controls, and distributes power within the specified voltage band to all bus and payload equipment.

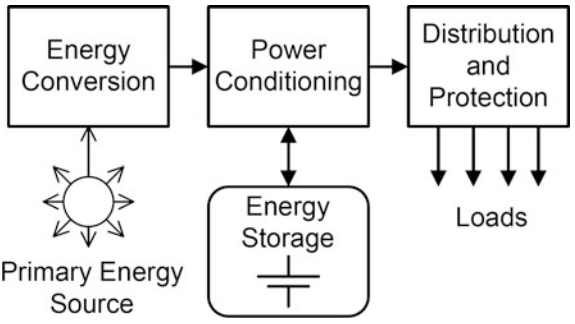

Fig. 17.5 Typical block diagram of the electrical power system

This system includes also the protection circuitry for all credible faults. For satellites that orbit Earth the primary energy source is the sun. For deep space missions, the primary energy may be supplied by other sources like the radioactive generators. The electrical energy provided by the energy conversion unit is further processed by the power conditioning unit. Power conditioning unit includes the maximum power point tracker, bus voltage regulator, battery charge and discharge regulators and additional DC–DC converters. Some energy may be stored into batteries in order to be delivered to the system during eclipses or high power demand periods. The distribution and protection unit includes the load switches, fuses, additional protection circuitry and the distribution harness. The harness consists of conducting wires and connectors that connect various components together.

17.2.1 The Array of Solar Cells

With few minor exceptions (low-cost, limited life missions that use non-rechargeable batteries as primary source) all satellites that orbit Earth use the solar energy. The solar energy is converted into electrical energy by meaning of the solar cells. The technology of solar arrays evolves continuously during years and the conversion efficiency increase significantly. Table 17.3 presents the typical solar cells and their characteristics ilicon solar cells have been used for electrical power on almost all space satellites since 1958. Their scalability, reliability, and predictability have made solar cell/arrays the prime choice for spacecraft designers. Early silicon solar cells were typically ~11% efficient, and the conversion efficiency of silicon cells currently flown varies between 12.7 and 14.8%.

Table 17.3 Solar cells for space applications and their characteristics

Parameter	Silicon	High efficiency silicon	Single-junction GaAs	Dual junction GaAs + Ge	Triple junction
STC[a] efficiency (%)	12.7–14.8	16.6	19	22	26–30
STC[a] operating Voltage (V)	0.5	0.53	0.9	2.06	2.26
Cell weight (mg/cm^2)	13–50	–	80–100	80–100	80–100
Temp coefficient (%/C) at 28C	−0.0055	–	−0.0021	–	−0.0019
Cell thickness (μ)	50–200	76	140–175	140–175	140–175
Status	Obsolete	In Use	Obsolete	Nearly Obsolete	State-of-Art

[a]Standard test conditions

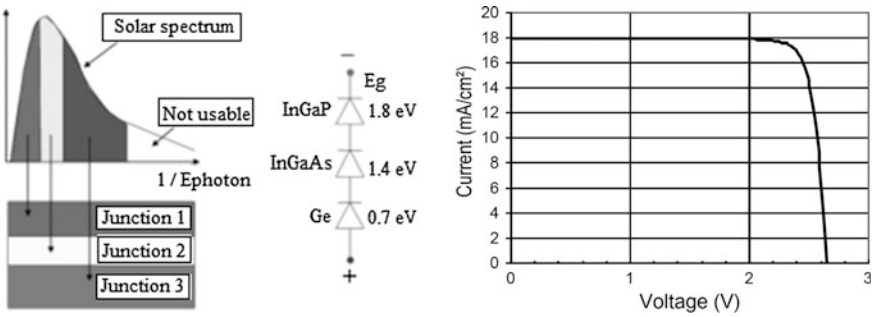

Fig. 17.6 The triple junction solar cell and the typical IV characteristic (Spectrolab)

Advanced solar cells with improved efficiency developed over the past fifteen years include: (1) single junction GaAs solar cells, (2) dual junction III-V compound semiconductor solar cells utilizing atoms from the 3rd and 5th columns of the periodic table, and (3) triple-junction III-V compound semiconductor solar cells. GaAs/Ge cells currently available on the market have an average conversion efficiency of 19% at AMO. The GaAs-type solar cells have higher radiation resistance than silicon solar cells. Dual-junction and triple-junction solar cells are presently available from several vendors. Commercially available dual-junction solar cells are 21–22% efficient.

Currently, triple-junction cells consisting of GalnP, GaAs, and Ge layers, are grown in series connected layers, and are 27% efficient in production lots [12–14]. A typical triple junction solar cell is depicted in Fig. 17.6.

17.2.2 Batteries for Space Applications

The energy storage is required to meet the spacecraft load demand not only during eclipse, but also when the demand exceeds the power generation at any time. The most widely used energy storage technology is the battery, which stores energy in an electrochemical form. There are two basic types: primary batteries (for very short duration missions) and secondary (rechargeable) batteries.

Major batteries used in the spacecraft industry at present are nickel cadmium (NiCd), nickel hydrogen (NiH2), and lithium-ion (Li-ion):

- NiCd batteries were the first type used in space applications. They have a medium energy density of about 30 Wh/l, the depth of discharge (DOD) is of 0.5%/day, and their operating temperature is from 0 up to 40 °C, offer relatively lower specific energy, is temperature sensitive, each elementary cell develops 1.2 V and has shorter cycle life. Even if SuperNiCd has better parameters, under environmental regulatory scrutiny, the cadmium has been placed, and today NiH2 has replaced the NiCd batteries for most space applications;

- NiH2 batteries were the last 20 years the main option for LEO and GEO applications because of their higher medium energy density of 60 Wh/l, having a the depth of discharge (DOD) is of 0.5%/day. Each elementary cell develops 1.2 V and the operating temperature starts at −20 °C support up to 30 °C;
- Li-ion batteries offer significantly higher specific energy density over that of NiH2 (from 150 up to 400 Wh/l) and perform better at low temperatures. Modern Li-Ion batteries can operate with good performance in a range between −40 and 65 °C. The production cost is relatively high but can be competitive with NiH_2 in the same volume production. It is vulnerable to damage under over-charging or other shortcomings in the battery management. Therefore, it requires more elaborate charging circuitry with adequate protection against over-charging [15].

17.2.3 Topologies of the Power Conditioning Unit (PCU) for Small Satellites

The three most common power system implementation approaches found on today's small satellites that are presented below are: Direct Energy Transfer (DET) with Battery Bus, DET with Regulated Bus and the Maximum Power Point Tracker with Battery Bus The following sections describe the operation of each of the above systems.

17.2.3.1 Direct Energy Transfer with Battery Bus (DET-BB)

This topology is depicted in Fig. 17.7. The DET topology offers simplicity being often selected for space missions where the mass is critical. There are no switch-mode DC–DC converters involved in this topology, a major advantage for mass (no magnetic components), reliability (no high speed power components) and EMI. There are few disadvantages associated with this topology. The battery is directly connected to the PV voltage and a larger solar panel is required in this case to ensure the proper energy transfer. A larger panel means a higher price for the mission. Also in order to avoid excessive losses due to the presence of the Shunt Regulator the voltage and operating point of panel should be well known before launching.

17.2.3.2 Direct Energy Transfer with Regulated Bus (DET-RB)

This second topology is favored by the European Space Agency (ESA) and can be found in many European spacecrafts [16]. Typical architecture of this topology is depicted in Fig. 17.8. A Sequential Switching Shunt Regulator (**S3R**) regulates the

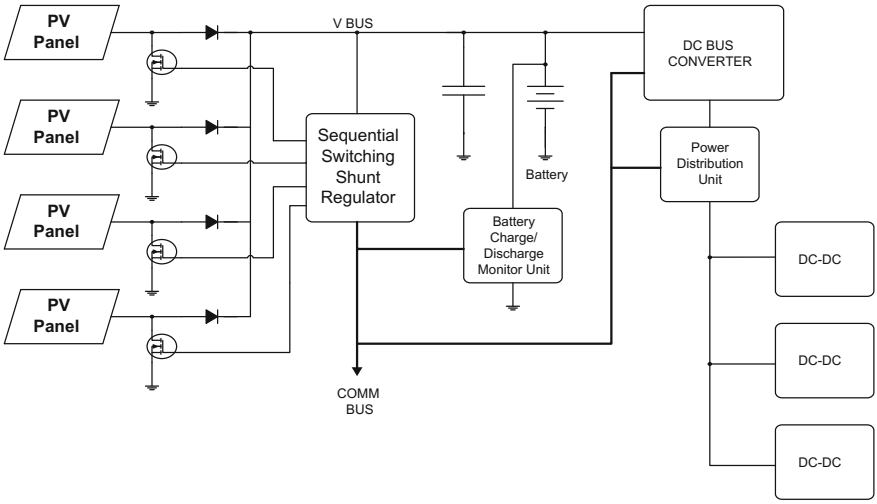

Fig. 17.7 Direct energy transfer with battery bus topology

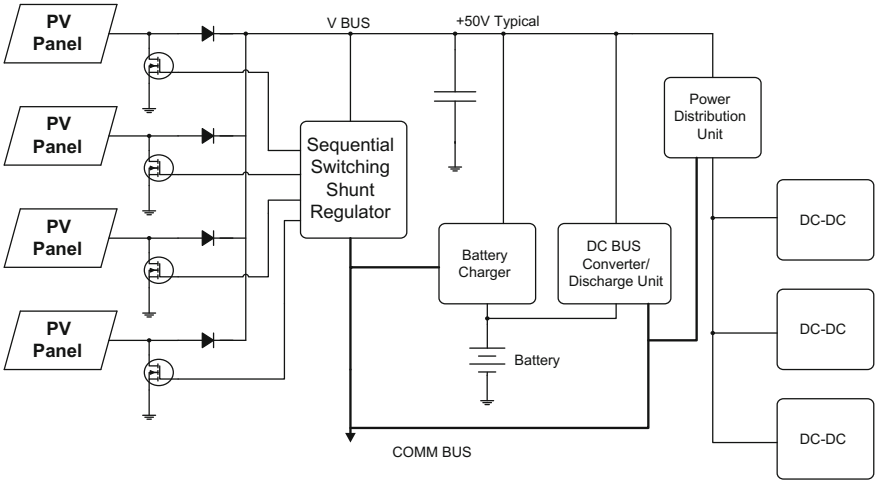

Fig. 17.8 Direct energy transfer with regulated bus

bus voltage (V BUS) to a typical value, usually between 24 and 50 V. This topology is well suited for missions where the spacecraft experiences extended periods of sunlight plus occasional long eclipse period like in case of GEO satellites.

Power flows directly from panels to the bus via the blocking diodes and is regulated by S3R regulator during sunlight period. The Battery Discharge Regulator (BDR) will keep the bus voltage within regulation limits during eclipses or periods

with high power demand. The DET-RB topology offers high efficiency for spacecrafts with medium to high power demands orbiting GEO or GTO. The solar arrays must operate at maximum power point for optimum performance of this topology. When used in LEO, this power system will require the use of solar arrays much larger than that required by an MPPT bus, but for GTO or GEO, the solar arrays can be sized for the equilibrium array temperature so that a smaller proportion of the potential array power is left in the panels.

The battery must be discharged during eclipses by BDR to a value that ensures optimum regulation of the bus voltage by S3R regulator. The BDR is usually implemented using a switch-mode DC–DC converter and this may impact the final efficiency of the system especially in case of prolonged eclipses.

This topology can be implemented using simple components like operational amplifiers and comparators already qualified for space operation, which is considered a major advantage for larger satellites at higher orbits.

17.2.3.3 Maximum Power Point Tracker with Battery Bus (MPPT-BB)

This power system architecture uses a different approach. Instead of connect directly the output of the solar array to the battery a Maximum Power Point Tracker (MPPT) is used now to process the available energy from array. During sunlight the MPPT charge the battery, supply the bus voltage and ensure that the array operates at maximum power point. The MPPT also regulates the bus voltage after the battery reaches the end of charge state, the shunt regulator being now eliminated.

A block diagram of this topology is depicted in Fig. 17.9. The MPPT is usually implemented using a switch-mode DC–DC converter and a special control loop

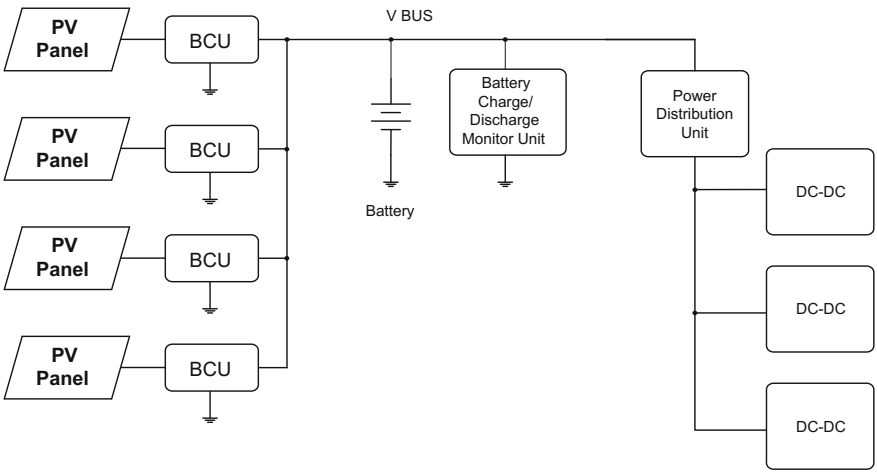

Fig. 17.9 Maximum power point tracker with battery bus

capable to track the maximum power point (MPP) of the array. The efficiency of this DC–DC converter should be as high as possible in order to minimize energy losses. A small amount of the available energy (5–10%) will be lost due to this converter. However, this architecture may achieve a better overall efficiency compared with previous topologies in case of satellites orbiting LEO where the array temperature, and hence MPP, changes considerably over the sunlight period of the orbit. This topology can be used also for small satellites without pointing gimbals where the solar array is not always oriented towards the sun. For GEO satellites where there are extended periods of sunlight and solar arrays at equilibrium temperature, the inefficiency of the MPPT would make the use of this topology impractical [11].

This topology is preferred for very small satellites like Cube Sat orbiting on LEO. The presence of the MPPT regulator increases the complexity of this topology. While the MPPT controller can be implemented in the analog domain using simple, space qualified components (operational amplifiers and comparators), the best performance of the MPPT algorithms requires digital implementation. The presence of a microcontroller or a digital signal processor (DSP) for implementing the MPPT algorithms reduces the radiation hardness of the system. This is not usually a problem for low cost LEO missions with limited life span.

17.2.4 Maximum Power Point Tracker (MPPT)

The MPPT is a common technique for terrestrial applications due to the typical output characteristic of a PV panel. The MPP of the panel depends on many factors like the irradiation and operating temperature. MPPT will ensure that the maximum available energy is processed and delivered to the load. However, for space applications this technique is in many cases avoided. For satellites orbiting high orbits the complexity associated with the implementation of MPPT is not justified. The orbit parameters are well defined before launching and the power system can be designed for optimum performance without the presence of MPPT. Here, architectures based on Direct Energy Transfer (DET) are more appropriate as the eclipse period is shorter.

In LEO, where the battery must be charged in a short period, the power point tracker (PPT) allows maximum power to be captured for several minutes after each eclipse when the array is cold. Architecture without the PPT feature, such as a direct energy transfer (DET) bus (as presented in Sects. 17.2.3.1 and 17.2.3.2), would waste a significant amount of power, as shown in Fig. 17.10. If DET systems were designed to deliver the required power at one-half the illumination at battery's end of life (EOL), the power waste would be C-D watts at EOL full sun, B-C-D watts at battery's beginning of life (BOL) full sun, and A-B-C-D watts at EOL full sun on a cold array. The PPT design eliminates this waste by utilizing all the power that can be generated.

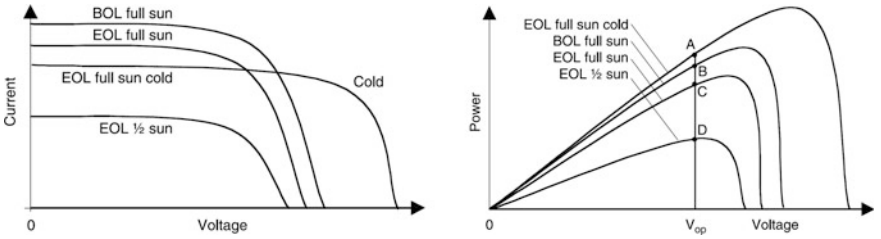

Fig. 17.10 Power wasted in direct energy transfer architecture in certain conditions

The main advantages of the peak power tracking are that it maximizes the solar array output power all the time, and it does not require the shunt regulator and the battery charge regulator. On the other hand, the MPPT requires a DC–DC converter and there are losses associated with this converter that may affect the efficiency of the power system. Moreover, since this loss is dissipated inside the spacecraft body, it negatively impacts the thermal system. For very small satellites orbiting LEO the power system based on MPPT brings real advantages. This system will maximize the utilization of PV panels and due to low energy requirement of these satellites, the additional DC–DC converter losses will not significantly affect the thermal system.

17.2.4.1 The Model of the Solar Cell

A photovoltaic (PV) cell is basically a large photodiode that will convert the incident solar energy to electricity based on the well-known photovoltaic effect. The electrical equivalent model of a PV cell is depicted in Fig. 17.11.

A PV panel is made from n identical cells connected in series, like in Fig. 17.12. The current source in Fig. 17.11, i_{sun}, is proportional to the amount of irradiation, and linear with respect to the PV cell temperature. The current is given by:

$$i_{sun} = \left(i_{sun,STC} + k_{temp} * (T_{cell} - T_{cell,STC})\right) * \frac{P_{sun}}{P_{sun,STC}} \tag{17.2}$$

where i_{sun} and $i_{sun,STC}$ is the short circuit current at the given working point and standard test conditions (STC), respectively. The constant k_{temp} is the temperature

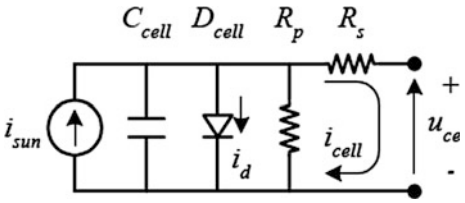

Fig. 17.11 PV cell equivalent model

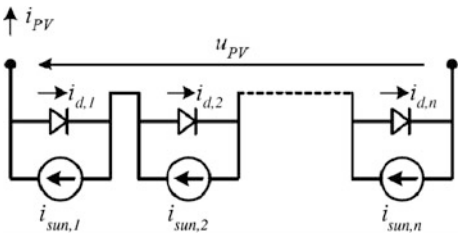

Fig. 17.12 PV panel schematic

coefficient of i_{sun}. T_{cell} and $T_{cell,\ STC}$ are the actual and STC cell temperatures, respectively. Finally, P_{sun} and $P_{sun,STC}$ are the irradiations at the present operating point and at STC, respectively [17]. The current through the diode is expressed by:

$$i_d = i_S * \left(e^{\frac{q*u_d}{k*A*T_{cell}}} - 1\right) \tag{17.3}$$

where i_S is the reverse saturation current, A is the diode idealization factor (usually defined between 1 and 5), and u_d is the voltage across the diode. The PV cell equivalent model contains some additional elements, R_p and R_s. These circuit elements are associated with parasitic like the connection wires between cells. A more detailed description of these parasitic elements is found in [12, 13]. The C_{cell} is the capacity associated with the pn junction of the diode. Finally, the current, voltage and power generated by a single PV cell are expressed by:

$$i_{cell} = i_{sun} - i_d \tag{17.4}$$

$$u_d = u_{cell} + R_s * i_{cell} \tag{17.5}$$

$$P_{cell} = u_{cell} * i_{cell} \tag{17.6}$$

A family of curves that plot the i_{cell} and u_{cell} versus the irradiation is depicted in Fig. 17.13. The power delivered by the PV cell under different irradiation conditions is depicted in Fig. 17.14 [18].

The power delivered by the PV cell has a maximum at certain voltage and this maximum depends on the irradiation. In order to extract the maximum available power delivered by the PV panel in certain illumination conditions, a certain techniques must be implemented in the system that process the photovoltaic energy.

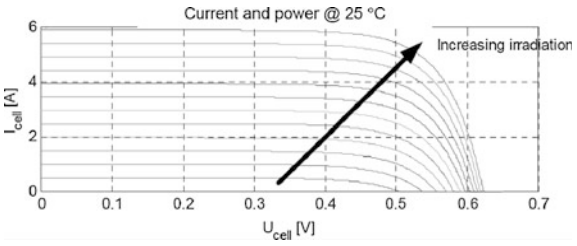

Fig. 17.13 I_{cell} and U_{cell} versus irradiation

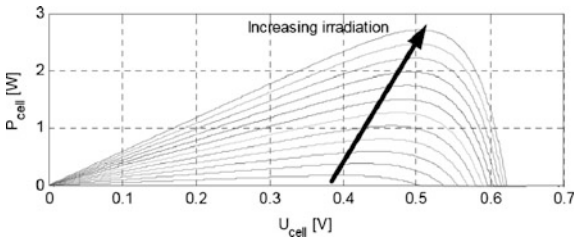

Fig. 17.14 P_{cell} and U_{cell} versus irradiation

17.2.4.2 Algorithms for the MPPT

There are many MPPT algorithms developed during years. Table 17.4 summarize the available algorithms and presents their important features and characteristics [19, 20]. Simple algorithms like Hill-climbing/Perturb&Observe gain popularity over years due to simplicity but suffer from certain drawbacks like inability to distinguish between a local and absolute power maximum. The scientific community concentrates the efforts to solve various drawbacks associated with simple algorithms and finally the complexity of the MPPT grows exponentially. The MPPT algorithms become more robust but the complexity and cost of the implementation increases substantially. However, for space applications main criteria are reliability and simplicity. The MPPT should be able to continuously track the true MPP in minimum amount of time and should not require periodic tuning. In this case, hill climbing/P&O, fractional V_{OC} or I_{SC} with their low implementation complexity are appropriate.

The Fractional Open-Circuit Voltage Algorithm

This algorithm is based on the observation that the MPP voltage is a fraction of the open voltage of the solar panel.

$$U_{MPP} = K * U_{OC} \tag{17.7}$$

where: U_{MPP}—MPP voltage, U_{OC}—open circuit voltage, K—a constant (usual between 0.7 and 0.85 for silicon cells).

The implementation of this algorithm is depicted in Fig. 17.15. A switch disconnects momentarily the panes from the load and the MPPT bloc measure the open circuit voltage of the PV panel. The MPP voltage is estimated using (17.7). This simple algorithm requires only one sensor for implementation (voltage sensor). The associated are:

- relative low efficiency of MPPT due to the fact that the K constant cannot be very precise determined.
- when the panel is disconnect from the load, no power flows for a short period of time. This may decrease the efficiency of the system.

Table 17.4 Major MPPT techniques and their salient characteristics

MPPT technique	PV array dependent?	True MPPT?	Analog or digital?	Periodic tuning?	Convergence speed	Implementation complexity	Sensed parameters
Hill-climbing/P&O	No	Yes	Both	No	Varies	Low	Voltage, current
IncCond	No	Yes	Digital	No	Varies	Medium	Voltage, current
Fractional V_{OC}	Yes	No	Both	Yes	Medium	Low	Voltage
Fractional I_{SC}	Yes	No	Both	Yes	Medium	Medium	Current
Fuzzy logic control	Yes	Yes	Digital	Yes	Fast	High	Varies
Neural network	Yes	Yes	Digital	Yes	Fast	High	Varies
RCC	No	Yes	Analog	No	Fast	Low	Voltage, current
Current sweep	Yes	Yes	Digital	Yes	Slow	High	Voltage, current
DC link capacitor droop control	No	No	Both	No	Medium	Low	Voltage
Load *I* or *V* Maximization	No	No	Analog	No	Fast	Low	Voltage, current
dP/*dV* or *dP*/*dI* feedback control	No	Yes	Digital	No	Fast	Medium	Voltage, current
Array reconfiguration	Yes	No	Digital	Yes	Slow	High	Voltage, current
Linear current control	Yes	No	Digital	Yes	Fast	Medium	Irradiance
I_{MPP} & V_{MPP} computation	Yes	Yes	Digital	Yes	N/A	Medium	Irradiance. Temperature
State-based MPPT	Yes	Yes	Both	Yes	Fast	High	Voltage. Current
OCC MPPT	Yes	No	Both	Yes	Fast	Medium	Current
BFV	Yes	No	Both	Yes	N/A	Low	None
LRCM	Yes	No	Digital	No	N/A	High	Voltage. Current
Slide control	No	Yes	Digital	No	Fast	Medium	Voltage, Current

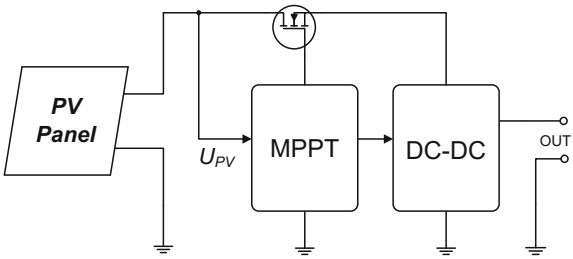

Fig. 17.15 Implementation of the "Fractional open-circuit voltage algorithm"

The inherent low complexity makes this algorithm a potential candidate for space applications. The algorithm can be implemented using only analog components, a significant advantage for space applications. However, the presence of a microcontroller will increase the flexibility of the MPPT system.

A simplified version of this algorithm is usually implemented in commercial integrated circuits. In this simplified implementation, the MPP voltage is set to a fix value by the circuitry and the panel is not disconnected from the load. The MPP voltage can be determined from the datasheet of the PV panel or by measurements.

For very small satellites where the orbit parameters are known this algorithm may be a good option. However, the orbit parameters are usually not well defined before launching for most very small satellites.

The Fractional Short-Circuit Current Algorithm

This algorithm is similar with the previous one and is based on the observation that the maximum delivered current for a panel is a fraction of the short-circuit current.

$$I_{MPP} = K*I_{SC} \tag{17.8}$$

where: I_{MPP}—current at MPP, I_{SC}—short-circuit current, K—a constant (usual between 0.7 and 0.85 for silicon). The implementation of this algorithm is depicted in Fig. 17.16.

A switch short circuit momentarily the output of the PV panel and the short-circuit current is measured by the MPPT block. The optimum output current of panel is determined with Eq. (17.8).

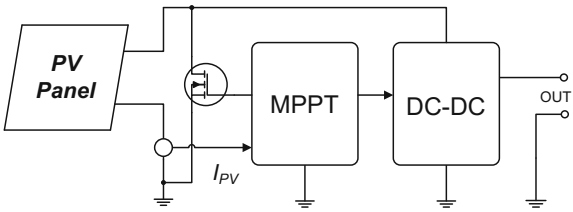

Fig. 17.16 Implementation of the "Fractional short-circuit current algorithm"

The advantages and disadvantages of this algorithm are similar with the fractional open circuit voltage algorithm. Some topologies of power converters, where the main switch is referred to ground like boost and SEPIC, can be used for implementation of this algorithm. In this case, the main switch of the converter is also used as short-circuit switch for the PV panel.

The Perturb and Observe Algorithm

This algorithm is probably the most used for MPPT systems (Fig. 17.17). The main advantage of this algorithm is his inherent insensitivity to PV panel parameters and operating conditions. The P&O is a high performance algorithm capable to find and track the MPP with greater accuracy. This algorithm perturbs the operating point of the PV panel and monitors the effects of this perturbation on the output power. If the power increases, the perturbation should be kept in the same direction; otherwise, it should be reversed [21].

In order to implement this algorithm, two parameters of the PV panel must be measured: the output voltage and the output current. The presence of two sensors increases the complexity of the MPPT system (Fig. 17.18).

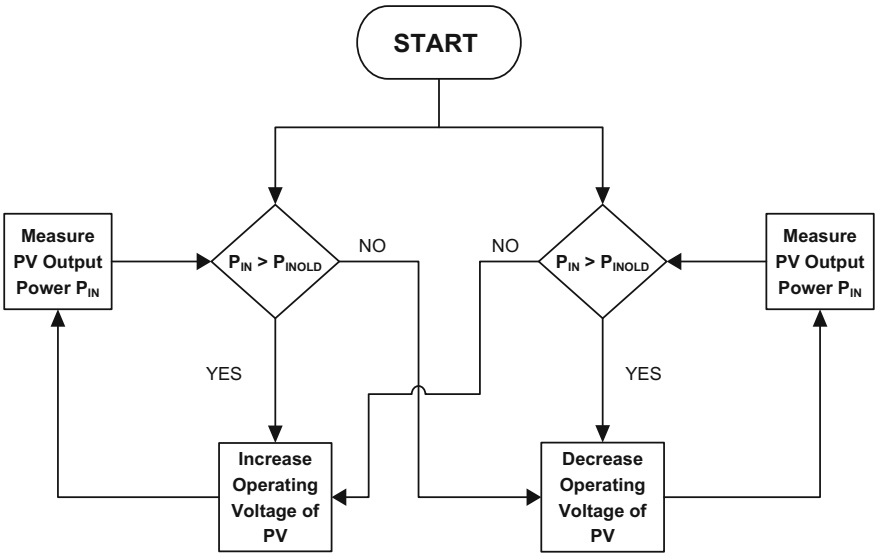

Fig. 17.17 Logic diagram of P&O algorithm

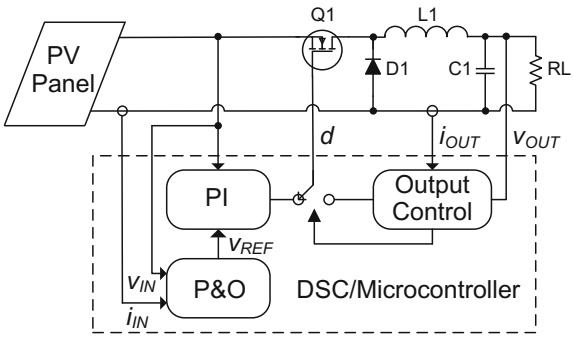

Fig. 17.18 Implementation of P&O algorithm using a DSC or microcontroller

17.3 A Flexible Architecture of Power Conditioning Unit (PCU) for Very Small Satellites

A flexible, scalable architecture for Power Conditioning Unit (PDU) of very small satellites is presented in Fig. 17.19. This architecture can be used for nanosatellites and picosatellites on LEO with maximum power requirement up to 50 W. The architecture contains the following functional blocks:

- the Chargers Unit (CU)—this unit is responsible for processing the power available from the PV panels.
- the Battery Unit (BU)—this unit contains the main battery of the PCU and the associated monitoring electronics (The Battery Charge/Discharge Monitor Unit (BCDMU)).
- the Isolation Unit (IU)—this unit provides galvanic isolation between the main battery unit and the rest of the PCU, a requirement for some missions. This unit is optional and can be removed if the mission does not require a galvanic isolation.
- the Point-of-Load/Distribution Unit (POL/D). This unit contains the Point-of-Load converters and the distribution switches. This unit includes a variable number of converters that produces the required voltages.

This architecture is well suited for satellites that orbits LEO, where the number of eclipses is high and the solar panels experience large temperature variations. The system provides the required redundancy for certain satellites as well as some advanced features that can be usually found in larger satellites like galvanic isolation. Each functional subsystem is independent and can be used as a standalone building block for simple or more complex applications. For example, the BCU unit can be used as a standalone battery charging block for low cost missions, where the space and weight is a premium.

The BCU unit implements a high performance MPPT algorithm and this is an important advantage especially for very low cost missions where the orbit can be changed just before or during launching and reprogramming of the energy

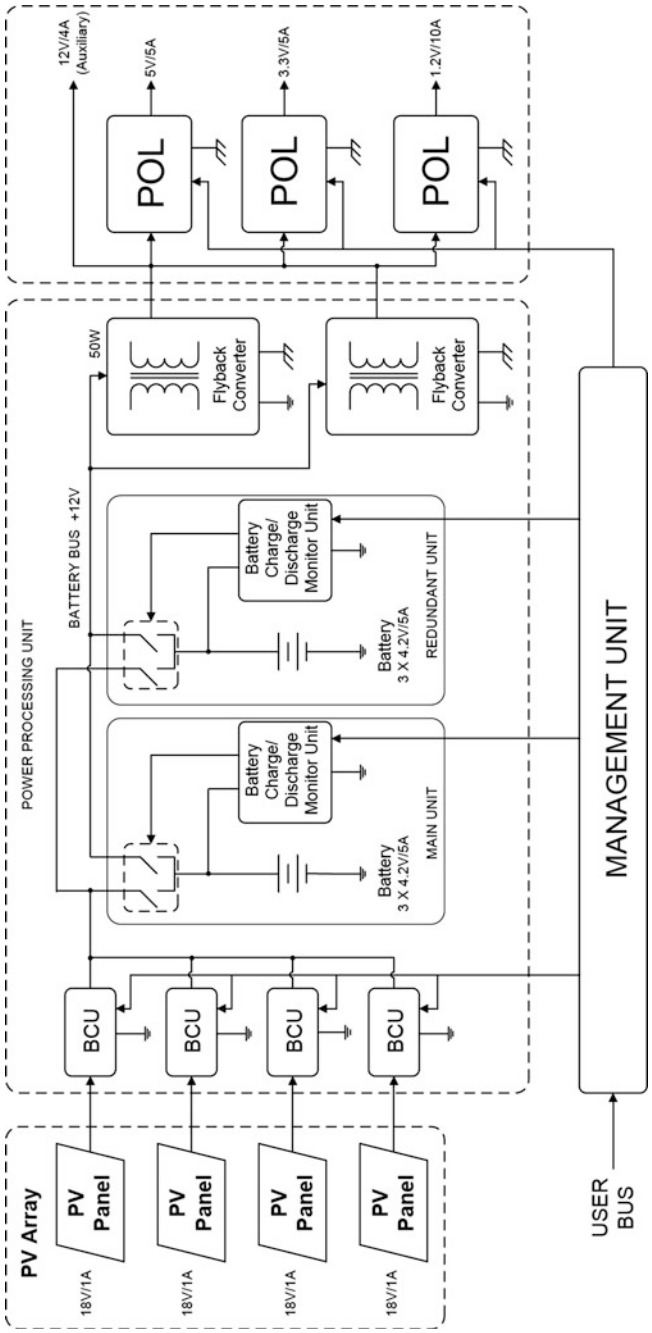

Fig. 17.19 Flexible architecture for power conditioning unit

processing unit is basically impossible or very difficult. The isolation unit and the POL units are implemented using planar magnetics in order to achieve best performance and high power density.

17.3.1 The Battery Charger Unit (BCU)

The Battery Charger Unit (BCU) is the frontend of the proposed architecture. The MPPT and battery charger algorithms are implemented by this unit (Fig. 17.20).

Due to the physical dimensions constraints, this board uses fully digital control. Digital control offers increased flexibility as most of the control parameters can be now adjusted by firmware. The BCU has two functional subunits:

- the DC–DC Power Converter, responsible with the energy conversion.
- the Digital Controller, responsible with the implementation of the MPPT algorithm, battery charging algorithm and power converter control.

The measured parameters are: the input voltage (panel voltage), the input current (panel current) and the output voltage (battery voltage). The input voltage and current are used for the MPPT algorithm implementation, while the output voltage is regulated as part of the battery charging algorithm.

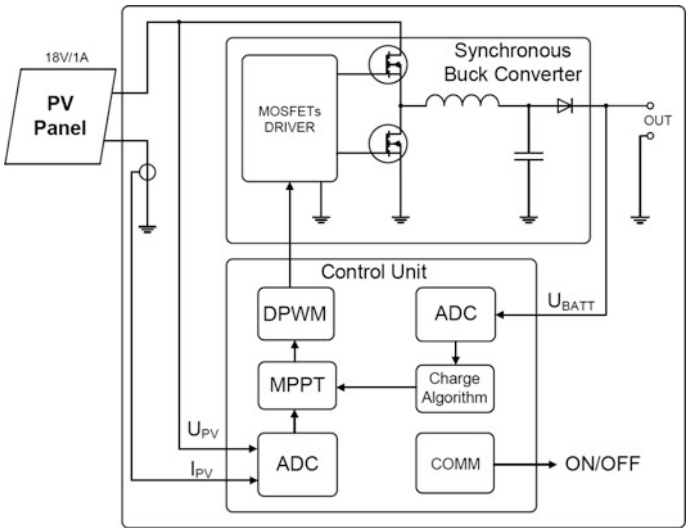

Fig. 17.20 Bloc diagram of the BCU unit

17.3.1.1 The DC–DC Power Converter

The DC–DC power converter uses the synchronous buck converter topology [22]. This topology offers high conversion efficiency and a good controllability. The output voltage is always lower than the input voltage, this topology being recommended for satellites with larger solar panels like the 2U and 3U CubeSats. For satellite with small solar panels like 1U CubeSat, the topology must offer boost or buck-boost capability. Such topologies are boost and Single-Ended Primary Inductor Converter (SEPIC) [23].

The power train of the synchronous buck converter is represented in Fig. 17.21. The freewheeling diode D is replaced by a synchronously-controlled switch Q2. In this case the losses associated with voltage drop on D are greatly reduced, a significant advantage for high output current converters.

The design entry parameters are summarized in Table 17.5. The BCU accepts 7 to 24 V at input. The output voltage is adjustable between 4.2 V (floating voltage for a single cell Li-Ion battery) to 16.8 V (floating voltage of four cells Li-Ion battery). The maximum output current is 1.75 A and is adjustable from firmware. The switching frequency is fixed, 62.5 kHz but the microcontroller has the option to internally adjust this frequency if dithering is required.

The typical design equations for synchronous buck converter are summarized in Table 17.6.

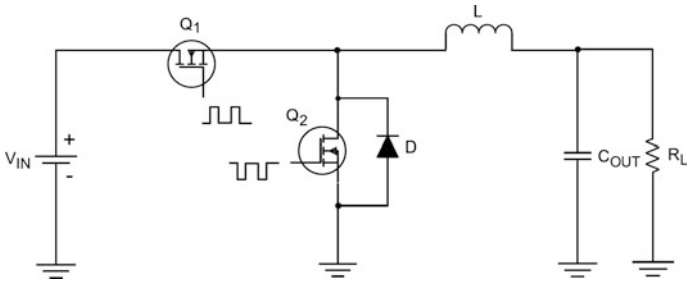

Fig. 17.21 The synchronous buck converter

Table 17.5 Design entry parameters for synchronous buck converter

Input voltage range	7–24	V
Output voltage range	4–18	V
Maximum input current	1.5	A
Maximum output current	1.75	A
Maximum output power	15	W
Input voltage ripple	≤ 500	mVpp
Output voltage ripple	≤ 150	mVpp
Switching frequency	62.5	kHz
Target efficiency	≥ 90	%

Table 17.6 Design equations for synchronous buck converter

Inductor value (H)	$L = (V_{IN_{MAX}} - V_{OUT}) * \frac{V_{OUT}}{V_{IN_{MAX}}} * \frac{1}{f_{SW}} * \frac{1}{0.5 \times I_{OUT_{MAX}}}$
Inductor peak current (A)	$I_{L_{PEAK}} = I_{OUT_{MAX}} + \frac{0.5 * I_{OUT_{MAX}}}{2}$
Inductor RMS current (A)	$I_{L_{RMS}} = \sqrt{I_{OUT}^2 + \frac{I_{Ripple}^2}{3}}$
Minimum capacitance for input capacitor (F)	$C_{IN_{MIN}} = \frac{I_{OUT} * D * (1-D)}{f_{SW} * (V_{Ripple} - D * I_{OUT} * ESR)}$
RMS current in the input capacitor (A)	$I_{RMS(C_{IN})} = \left(I_{OUT} + \frac{I_{Ripple}}{12}\right)\sqrt{D} - \frac{V_{OUT} * I_{OUT}}{V_{IN}}$
Output voltage ripple (V)	$V_{Ripple} = I_{Ripple} * \left(ESR + \frac{1}{8 * C_{Out} * f_{SW}}\right)$
RMS value for high-side current (A)	$I_{RMSHigh-Side} = \sqrt{D * \left(I_{OUT}^2 + \frac{I_{Ripple}^2}{12}\right)}$
Conduction losses for high-side MOSFET (W)	$P_{CONDHigh-Side} = I_{RMSHigh-Side}^2 * R_{DS(on)HS(max)}$
Switching losses for high-side MOSFET (W)	$P_{SWHigh-Side} = \left(\frac{V_{IN} * I_{OUT}}{2}\right) * \left(t_{s(HL)} + t_{s(LH)}\right) * f_{SW}$
Total power losses for high-side MOSFET (W)	$P_{LossHigh-Side} = P_{CONDHigh-Side} + P_{SWHigh-Side}$
RMS current for low-side MOSFET (W)	$I_{RMSLow-Side} = \sqrt{(1-D) * \left(I_{OUT}^2 + \frac{I_{Ripple}^2}{12}\right)}$
Conduction losses for low-side MOSFET (W)	$P_{CONDLow-Side} = I_{RMSLow-Side}^2 * R_{DS(on)LS(max)}$
Body diode conduction losses (W)	$P_{LossBD} = I_{OUT} * V_F * t_{BD} * f_{SW}$
Body diode reverse recovery losses (W)	$P_{RR} = \frac{Q_{RR} * V_{IN} * f_{SW}}{2}$
Total power losses for low-side MOSFET (W)	$P_{Loss} = P_{CONDLow-Side} + P_{LossBD} + P_{RR}$
Controller losses (W)	$P_{loss} = V_{in}(0.005 + F_s(Q_{gate,low} + Q_{gate,high})$
Inductor losses (W)	$P_{loss} = DCR_L * I_{L,RMS}$
Output capacitor losses (W)	$P_{loss} = ESR_{Cout} * \sqrt{\frac{(0.3 * I_{out})^2}{3}}^2$
Input capacitor losses (W)	$P_{loss} = ESR_{Cin} * \left(I_{rms.high} - \frac{V_{out} * I_{out}}{V_{in}}\right)^2$
Bootstrap capacitor (F)	$C_{BOOT} = \frac{Q_{G(Total)}}{\Delta V_{DROOP}}$

A SIMPLIS model is developed and presented in Fig. 17.22, where: f_{SW}—switching frequency [Hz], I_{OUTMAX}—maximum output current [A], D—duty cycle, I_{RIPPLE}—inductor's current ripple [A]. The SIMPLIS™ small signal model of the synchronous buck converter and the associated Bode plots are presented in Fig. 17.23.

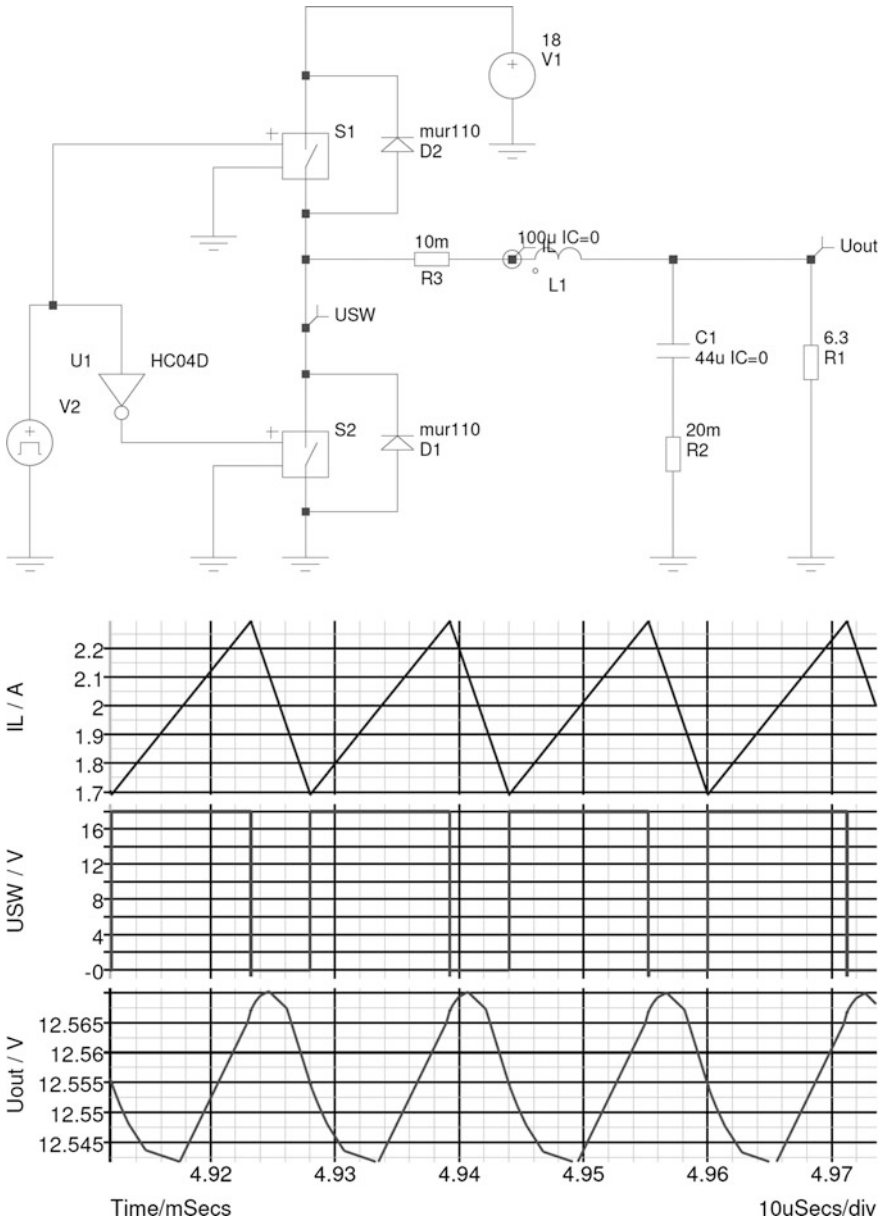

Fig. 17.22 The SIMPLISTM model of the proposed synchronous buck converter and associated waveforms of synchronous buck converter

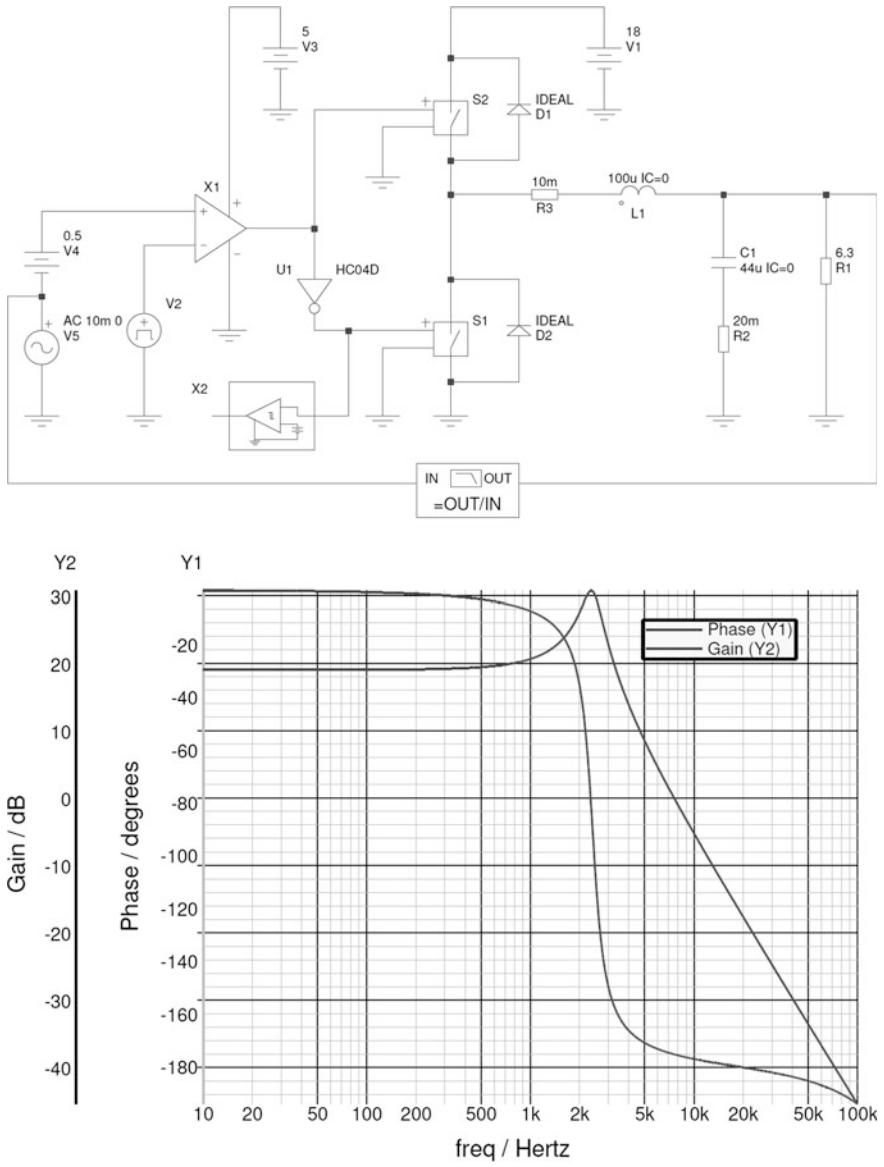

Fig. 17.23 SIMPLISTM small signal model of synchronous buck converter and the associated Bode plots

A double pole is introduced at the resonant frequency by the output LC filter. Phase sharply decrease to −180° after the resonant frequency point. There is a gain associated with the analog PWM modulator which can be calculated with:

$$G_{PWM} = \frac{V_{IN}}{V_{RAMP}} \tag{17.9}$$

where V_{IN} is the input voltage and V_{RAMP} is the amplitude of the ramp signal used to generate the PWM signal. For digital control systems the PWM modulator gain is set to 0 dB.

The synchronous buck converter requires a specialized driver circuit for MOSFETs. In case of the proposed prototype, the MOSFETs drivers are integrated into a specialized circuit, the MCP14628. This circuit is specifically designed for driving the power MOSFETs of a synchronous buck converter.

Figure 17.24 presents the internal simplified diagram of this part. This circuit is packaged in an 8-pin SOIC package and operates up to 125 °C ambient temperature. The MCP14628 driver offers also the diode emulation feature. A specific internal circuitry automatically adjust the "dead time" in order to prevent the cross-conduction phenomenon that can occurs if the "dead time" is missing or is too small.

Notable advantages of the buck converter are:

- the output voltage has a low ripple/noise, a consequence of the continuous output current of the buck converter. This is a significant advantage if the switching frequency is relatively low like in case of converters controlled by low cost digital systems.
- the buck converter running in continuous current mode (CCM) has a linear DC conversion ratio (M) equal with D (the duty cycle). This is a significant advantage if the converter is controlled by low cost digital microcontrollers with limited PWM resolution.

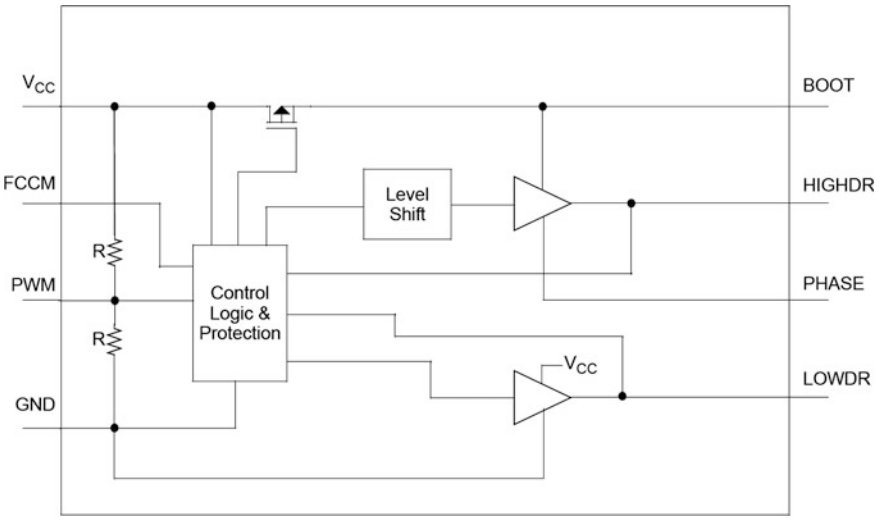

Fig. 17.24 The internal simplified diagram of MCP14628 and the package

- the buck converter has simple small signal model and is very well suited for digital control. The non-linear control techniques can be also easily implemented for this topology. The dynamic response of buck converter is excellent being the most used topology for high performance DC–DC converters.

The disadvantages of the buck converter are:

- the input current is discontinuous, creating high ripple/noise on the input voltage. The electrical stress on the input filter capacitor is high.
- the output voltage is always lower than the input voltage. This may limit the usability of this topology for certain applications.
- the buck converter requires a high-side switch driver. This increases the complexity and the cost of the schematic. Additionally, the implementation of the programmed current mode control (like the peak current mode control) is difficult due to the presence of a high-side current sensor. All these problems are solved by using monolithic integrated circuits already available from many IC producers. However, in this case the flexibility of the system may decrease and some advance control (like the implementation of the MPPT) becomes difficult to be implemented.

The buck converter is well suited for space applications either with analog or digital control. The only mandatory requirement is that the input voltage (the PV panel voltage in this case) should be always higher that the output voltage (the battery voltage in case of the proposed prototype).

17.3.1.2 The Digital Controller

The digital control of BCU is implemented using a commercial, low pin count microcontroller PIC12F1822 developed by Microchip Inc (Fig. 17.25). This microcontroller is packaged in an 8-pin package and includes all necessary blocks/features to develop a power converter:

- 10-bit Analog-to-Digital converter with up to four inputs selectable by an analog multiplexer
- digital PWM generator with up to 10-bit resolution
- low power consumption and advanced power management modes
- 8 MIPS core computational power
- internal reference voltage generator
- extended temperature operating range −40–125 °C

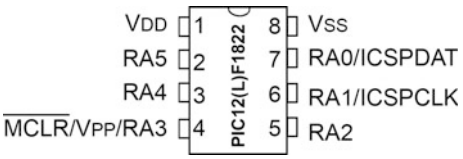

Fig. 17.25 PIC12F1822 microcontroller and the firmware flowchart

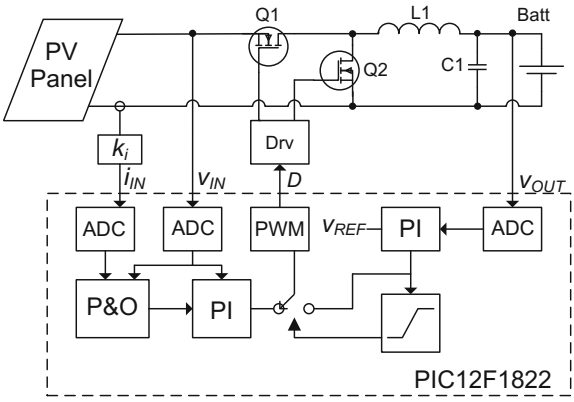

Fig. 17.26 Implementation of the BCU using PIC12F1822

The MPPT algorithm implemented in BCU is P&O and the typical block diagram of the system is depicted in Fig. 17.26. There are two PI controllers, one for the P&O algorithm and one that controls the output voltage. This architecture prevents the negative effects introduced by the transitions between operating modes of the converter (continuous conduction mode CCM and discontinuous conduction mode DCM) over the functionality of the P&O algorithm.

The firmware flowchart is presented in Fig. 17.27. Timer T1 interrupt is used for measure the required parameters. The P&O state machine runs inside the main loop and is triggered by the Measurements_Done flag set inside T1 interrupt after the completion of the measurements. The PI controllers are run inside the T1 interrupt and the update of the PWM duty cycle is done also here. The specific charging algorithm and protection state machine runs in the main loop.

The measured parameters are: the input current, the input voltage and the output voltage. The output current, necessary for chemistry-specific charging algorithm is estimated from the input power. The decision between the two operating modes, tracking and regulating, were taking based on the output of the voltage PI anti-windup comparator. If the output voltage PI controller is saturated, the system is in tracking mode and the P&O loop is executed every 15 ms. The PI controllers run simultaneous at 8 kHz.

The difference equation for each PI controller is (17.10). This equation is tailored to be implemented using only shifting operations, a significant advantage for low computational power microcontrollers:

$$y(T) = 2^m\,(y(T-1) + 2^n\ e(T) + 2^k\ e(T-1)) \tag{17.10}$$

where: e(T) = Vout(T) − Vref, m, n, k—real integers, y(n)—output of PI controller.

This simplified implementation of the PI controller may introduce additional constraints for the controlled system. The corresponding s-domain equation is:

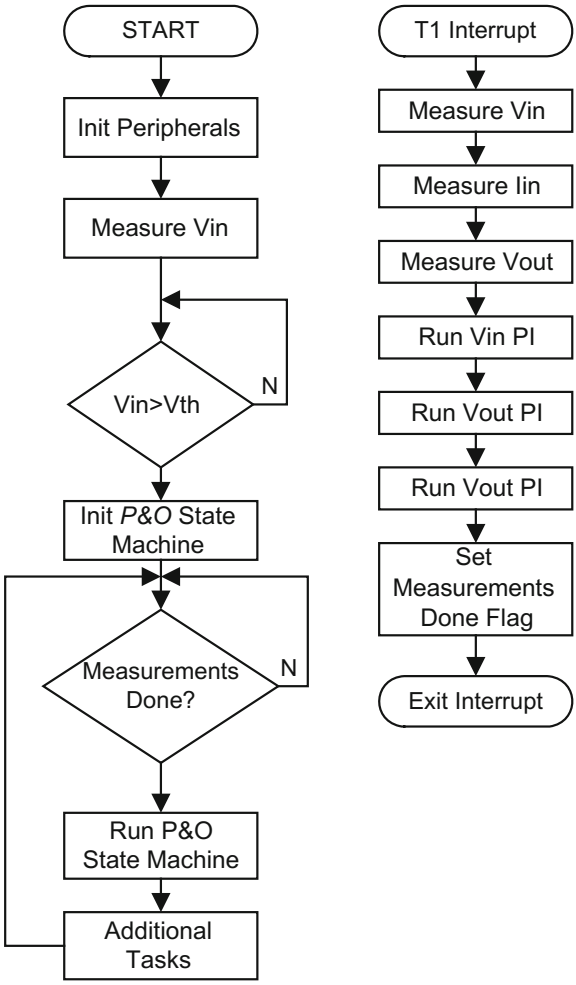

Fig. 17.27 The firmware flowchart

$$Y(s) = \frac{0.5s - 6.485E - 13}{s} \tag{17.11}$$

In this case m = 0.5, n = 0 and k = 0.

The Bode plots of the compensated system are represented in Fig. 17.28. The system using this simplified control has a slow response but the phase and gain margins are good. The slow response of the system is not a problem as the load is a battery and the input voltage has also a slow variation. Some adjustments of the system phase and gain margins can be done by slightly adjusting the value of the inductor and/or the value of the output capacitor.

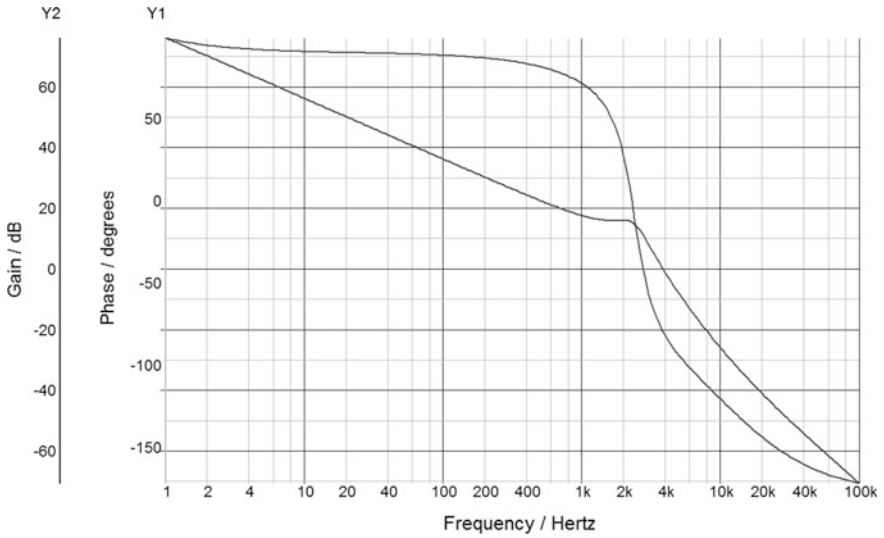

Fig. 17.28 Bode plots of the compensated system

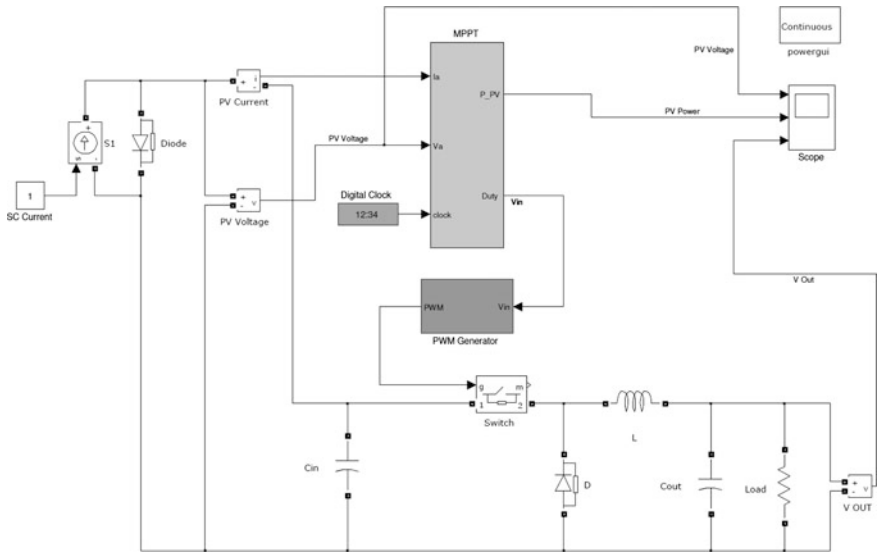

Fig. 17.29 The SimulinkTM model of the system

A Simulink™ model of the P&O algorithm implemented using a buck converter is presented in Fig. 17.29. The perturbation step is set to 1%. In this case the MPP voltage and current of the panel are of 10 V and 1 A, so that the MPP power is 10 W (Fig. 17.30).

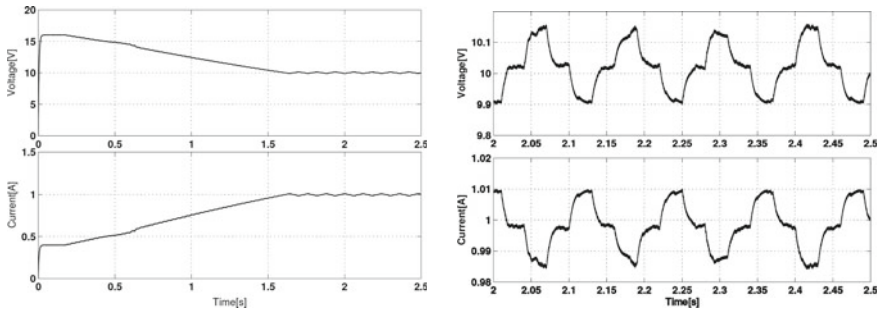

(a) PV vol voltage and current during locking phase

(b) PV voltage and current during steady state

Fig. 17.30 PV voltage and current during locking phase and during steady state

17.3.1.3 The BCU Sensors Circuitry

The BCU unit monitors three parameters: input voltage (panel voltage), input current (panel current) and the output voltage (battery voltage). The input voltage and the input current are used for the implementation of the MPPT algorithm and the output voltage is used for the implementation of the battery-specific charging algorithm.

The input voltage is measured using a voltage divider. The ratio of this divider should be adjusted according with the input voltage range in order to maximize the dynamic range of the input voltage measurement circuitry. For the input voltage range between 9 and 24 V the divider ration is set to 4.7 (100 K with 27 K). A small capacitor is placed in parallel with the low-side resistor in order to form a low-pass filter that cleans the output of the voltage divider.

The input current is measured using a 0.1 Ω low-side shunt placed in series with the "Negative" terminal. An inverting amplifier is used to amplify the voltage drop across the shunt and to restore the correct polarity of the current sense signal. The gain of this amplifier should be adjusted according with the hardware requirements in order to maximize the dynamic range of the current sense circuitry. For the proposed prototype, the gain of this amplifier is set to −20X resulting in a conversion gain of the current sense circuitry of 2 V/A. A snapshot of the input current sense amplifier and the output voltage sense buffer circuits are presented in Fig. 17.31. The response of the sense amplifier is set to be of a low-pass filter (with pole introduced by C9) in order to provide a clean output signal and reject the noise introduced by the switch-mode power converter. The circuit is built around MCP6022 dual operational amplifier. The bandwidth of this operational amplifier is 10 MHz and the maximum operating ambient temperature is 125 °C.

The output voltage is measured using a voltage divider. Because this divider is always connected across the battery voltage and because up to four charger units can be connected in parallel in the same time, the values of the resistors are very

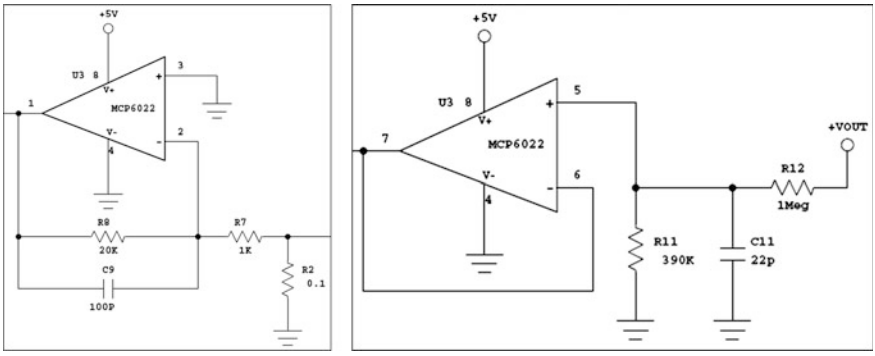

Fig. 17.31 The input current sense amplifier and the output voltage sense buffer

high. This avoids any significant current that can be drawn from the battery during eclipses via the measurement divider. The divider ratio can be again adjusted according with hardware requirements in order to maximize the dynamic range of the output voltage sensing circuitry. A buffer amplifier implemented with the second amplifier of MCP6022 is used to avoid any potential errors that may be introduced by the leakage currents of the analog input of the microcontroller. A small capacitor C11 placed in parallel with R12 forms a low-pass filter that rejects the output voltage ripple occurring at the switching frequency of the power converter.

The internal temperature sensor of the microcontroller can be used for measuring the temperature of the microcontroller's die which depends on the ambient temperature and perform a correction of the internal loop parameters (ex. the reference voltages for output voltage regulation).

17.3.1.4 The BCU Prototype

The prototype of the BCU unit is implemented in a 50 × 35 mm dual layer PCB. All components were selected with extended temperature range (−40–125 °C). The 3D representation of the prototype and associated top PCB layer are represented in Fig. 17.32.

All components are COTS and the radiations hardness tests/reports are unavailable for these components. The initial functional tests were conducted in laboratory conditions at the ambient temperature (25 °C). The PV can be simulated by placing a variable resistor (rheostat) in series with a voltage source. According with the maximum power transfer theorem, the maximum power point occurs at the half of the voltage of the voltage source.

The main switching node (source of the high-side MOSFET transistor) and the input voltage ripple waveforms are presented in Fig. 17.33.

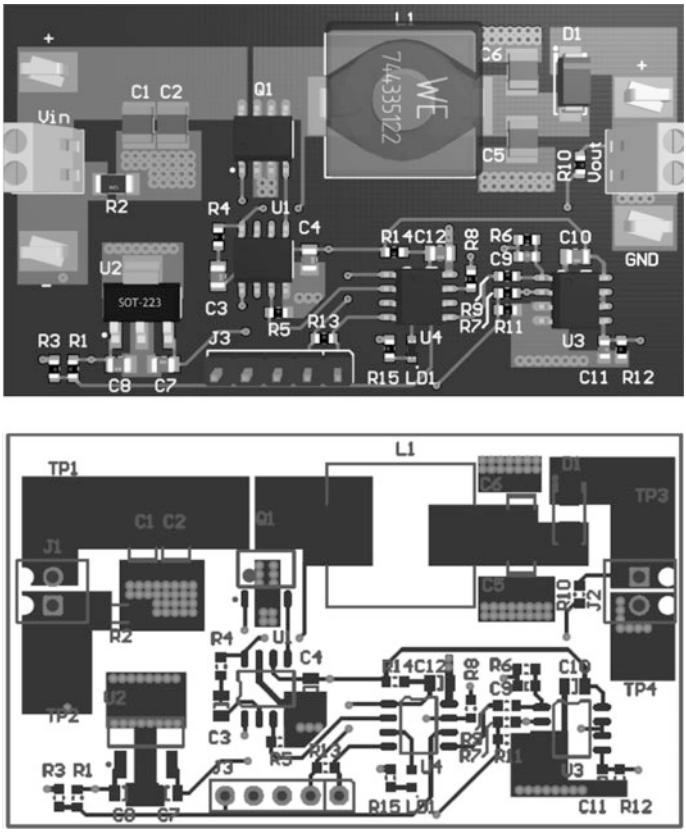

Fig. 17.32 The 3D representation of BCU board and top layer of PCB

The waveforms for output voltage ripple and input voltage perturbed by the P&O algorithm are presented in Fig. 17.34. The perturbation step is set to approximate 1% of the input voltage. The perturbation frequency is 20 Hz. The measured efficiency is 93% at maximum load.

17.3.2 The Battery Charge/Discharge Monitor Unit (BCDMU)

This unit monitors the state of the battery. Various protections like deep discharge protection and low temperature protection are implemented by this unit. The telemetry system—which reports various parameters like the battery voltage, current, stored capacity and temperature—is also implemented by this unit. The typical characteristics are listed in Table 17.7 and the block diagram is presented in Fig. 17.35.

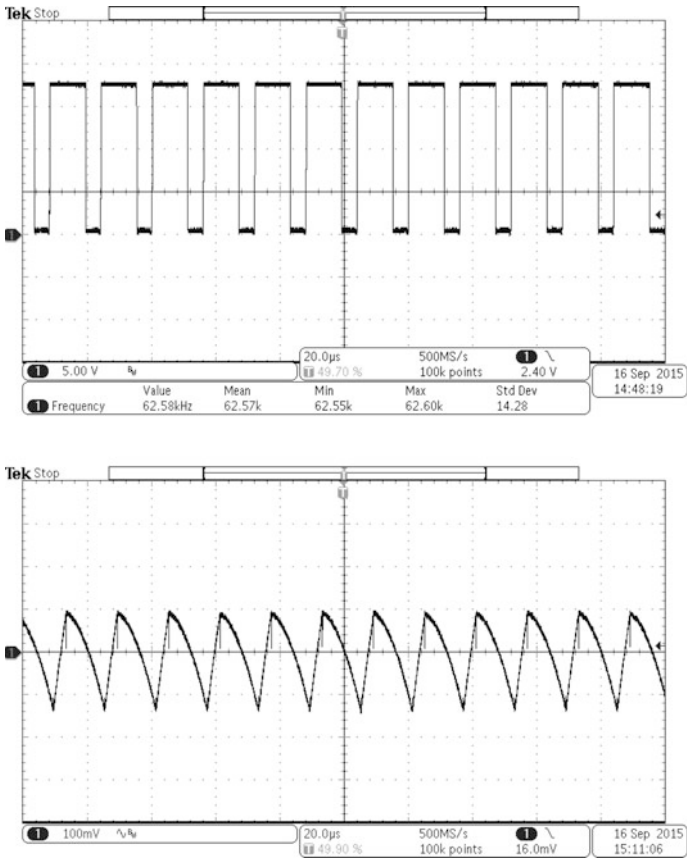

Fig. 17.33 The switch node and the input voltage ripple (BW = 20 MHz)

17.3.2.1 The Microcontroller

The BCDMU unit is controlled by a 16-bit low power microcontroller PIC24FV32KA301. This microcontroller is packaged in a 20-lead package (Fig. 17.36) and can be powered from 3.3 V (PIC24F) or 5 V (PIC24FV) sources. Notable features of this microcontroller are:

- 16-bit Modified Hardware Architecture
- 32 KB flash memory, 2 KB SRAM
- up to 16 MIPS computational power
- 8 MHz Internal Oscillator with 4x PLL Option and Multiple Divide Options
- 17-Bit by 17-Bit Single-Cycle Hardware Multiplier
- 32-Bit by 16-Bit Hardware Divider, 16-Bit × 16-Bit Working Register Array

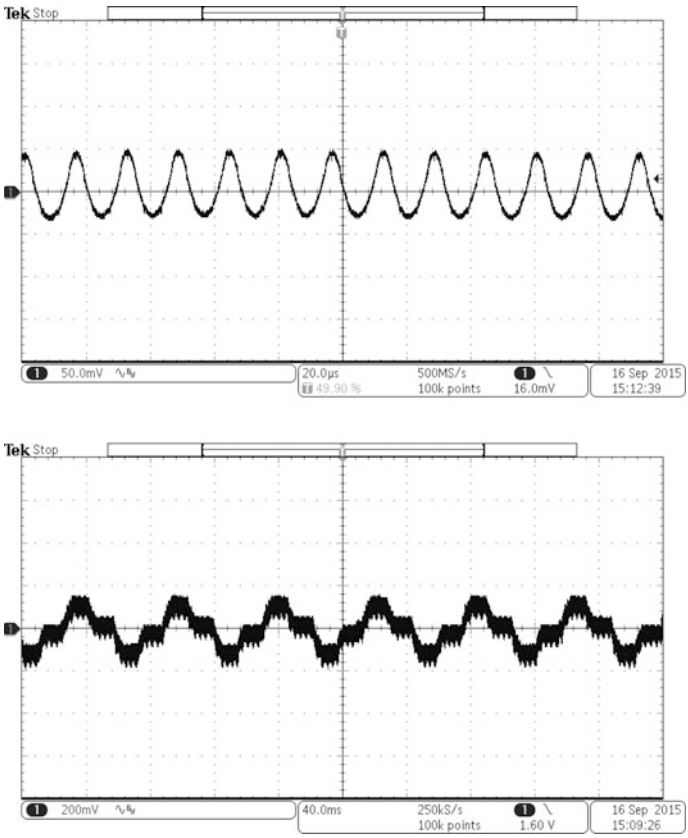

Fig. 17.34 The output voltage ripple and the input voltage perturbation during tracking phase (BW = 20 MHz)

Table 17.7 Typical electrical characteristics of BCDMU

Battery voltage range	3.6–16	V
Battery type	Li–Ion	
Maximum battery capacity	10	Ah
Maximum battery delivered current	4	A
Maximum output power	48	W
Fuse current	8	A
Maximum delivered current by the heater circuit	100	Ma

- very low power consumption (down to 8 μA, running)
- 12-Bit, Up to 16-Channel Analog-to-Digital Converter
- real-time Clock/Calendar
- operating temperature range: −40–125 °C

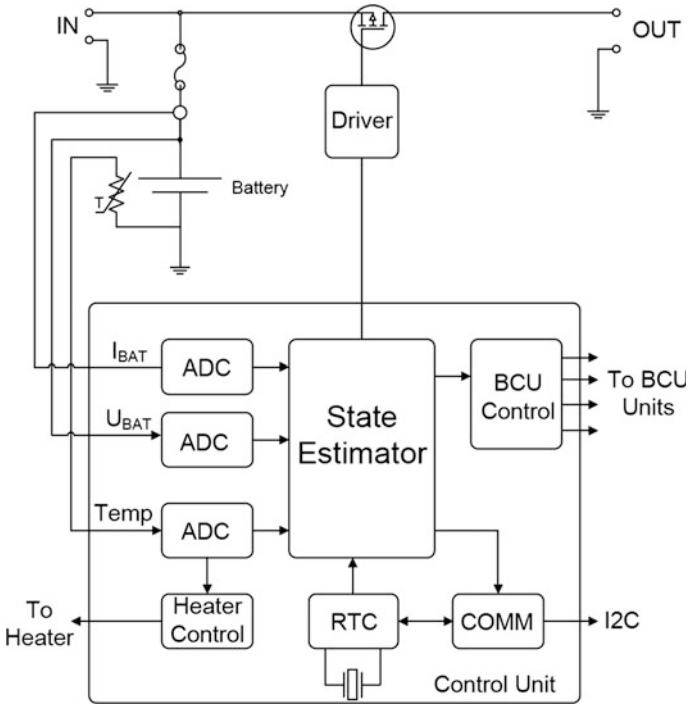

Fig. 17.35 Bloc diagram of the battery charge/discharge monitor unit

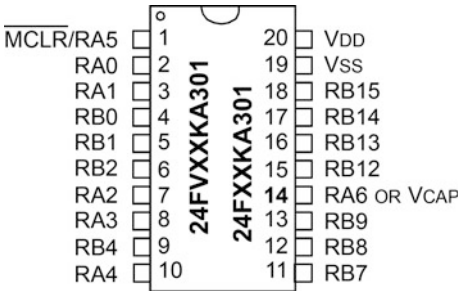

Fig. 17.36 PIC24FV16KA301 microcontroller

Measuring and reporting the battery parameters is a computational-intensive process. The presence of the hardware multiplier and divider greatly reduces the time necessary to perform various calculations. The integrated I2C controller allows the users to develop a simple and effective interface between BCDMU and central processing unit of satellite [24]. The real-time unit can be used for implementing the coulomb counting algorithm necessary for measure the battery capacity. The power consumption of this microcontroller is very low, a useful feature when the satellite enters into eclipse and the only available energy source is the battery.

17.3.2.2 The BCDMU Sensors Circuitry

BCDMU monitors three parameters of the battery: voltage, current and temperature. The parameters are used for various protections and to be reported by the telemetry system.

The battery voltage is measure the internal 12-bit Analog-to-Digital Converter (ADC) via a 4.09:1 voltage divider. The values of the resistors used to implement the voltage divide are high in order to minimize the current drawn from the battery (680 and 220 kΩ). A buffer amplifier is implemented with the OPA2170 dual rail-to-rail input/output amplifier. This buffer creates the low impedance source necessary for the microcontroller's ADC input. A snapshot of the voltage sense circuitry is presented in Fig. 17.37. Capacitors C4 and C5 are used to construct low-pass filters for avoiding the noise-induced problems.

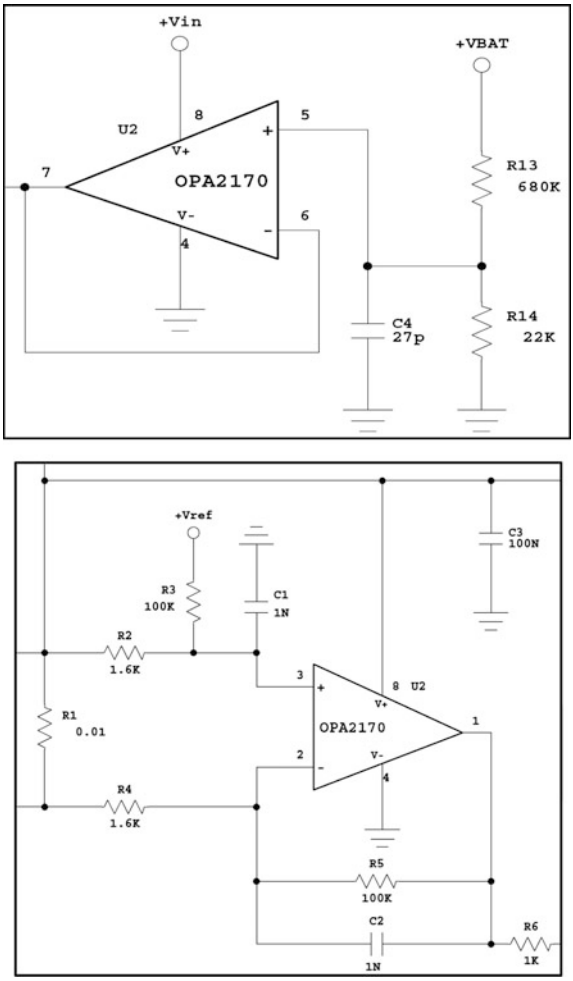

Fig. 17.37 The battery voltage measurement circuit and the current sense amplifier

The battery current is measured using a bidirectional differential amplifier. This amplifier allows the measurement of the battery current in both directions: when the battery delivers the current to the load or when the battery is charged by the BMU units. A shunt of 10 mΩ is used for the current measurement. The low value of this shunt minimizes the associated losses. The gain of differential amplifier is set to 62.5 (36 dB). By the resistors R2, R3, R4 and R5 and the output of the amplifier is centered to about 2.5 V by adding a DC offset. In order to prevent errors introduced by low Common Mode Rejection Ratio (CMMR) the gain set resistors R2, R3, R4 and R5 should be matched within 0.1%. Gain of this amplifier can be adjusted for different batteries currents for maximizing the dynamic range of the measurement circuit. A low-pass filter that rejects the high frequency noise is constructed with the aid of C1 and C2. The output of this amplifier is clamped in order to avoid damage of the microcontroller analog input using the circuit constructed with R6 and D2. For proposed prototype, the gain of the current sense amplifier is set to 0.625 V/A.

The battery temperature is measured by using a thermistor usually attached to the battery's body. The thermistor provides a very wide measurement range (usually exceeding 150 °C) and is very well suited for space applications. The output characteristic is non-linear (Fig. 17.38) and the microcontroller should perform a linearization operation for accurate temperature measurement. The thermistor used in the proposed prototype is of NTC (Negative Temperature Coefficient) type. The nominal value of this thermistor is 10 kΩ.

The equation that describes the thermistor's resistance with temperature is:

$$\frac{1}{\mathrm{T}} = \frac{1}{\mathrm{T}_0} + \frac{1}{\beta}\left(\frac{R}{R_0}\right) \tag{17.12}$$

where: T and T_0 are the ambient respective the reference temperatures (in °C), R and R_0 are the resistance and the reference resistance (specified at 25 °C), and β is a parameter specified by the thermistor manufacturer.

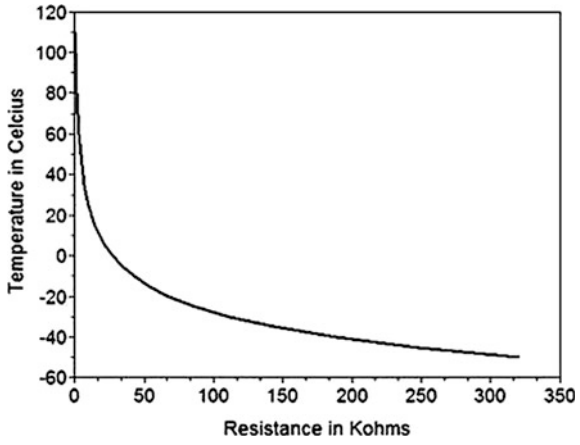

Fig. 17.38 Typical NTC thermistor characteristics

The BCDMU microcontroller will perform the linearization step by solving Eq. (17.12).

17.3.2.3 The Battery Switch

A power switch is placed between the BCDMU and the rest of the system. The role of this switch is to protect the battery against severe overload, deep discharge or accidental discharge during launch process. The power switch is implemented using a P-channel MOSFET and is activated by pulling his gate to the ground potential. The schematic of this switch is depicted in Fig. 17.39.

A resettable PTC fuse is placed in series with the battery positive terminal in order to protect against severe overcurrent that can potentially occurs if the other protections become inoperative.

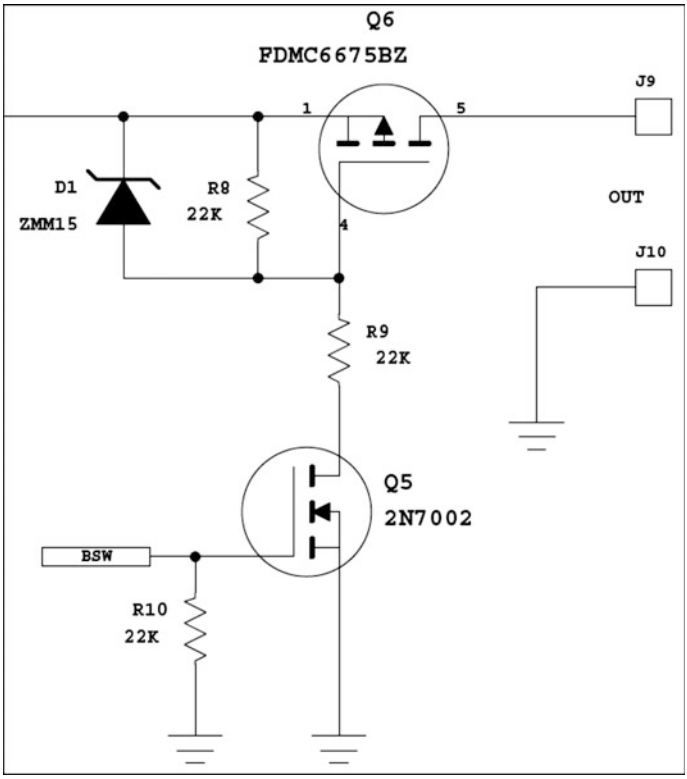

Fig. 17.39 The battery switch

17.3.2.4 The Battery Heater

If the battery's temperature drops below a certain level usually specified by manufacturer, the capacity can be severely affected. In order to prevent this phenomenon that can occurs during eclipses, the BCDMU can activate a heater circuit if the measured temperature is below a specified threshold. The heater circuit can provides up to 200 mA current and the thresholds can be programmed inside the BCDMU firmware.

17.3.2.5 Telemetry System

The Telemetry, tracking and telecommand (TT&C) system measures and reports various parameters of the battery. The parameters are available via the I2C interface provided by the BCDMU.

The I2C interface provides support for 100 or 400 kHz data rates. The number format uses the mantissa/exponent format in order to achieve good resolution without using floating point format numbers. The exponent is fixed, equal with ten [25].

Table 17.8 presents the BCDMU telemetry system set of commands.

The general packet structure is represented in Fig. 17.40. The slave address is fixed for each unit and can be set in firmware. The BCDMU firmware provides a mechanism for error detection in the form of a CRC-8 generally known as "Packet Error Check" (PEC). This PEC byte is optionally and the firmware will automatically check for the presence of this byte.

"**COM_BAT_VOLTAGE**" (0x01) command is used to read the battery voltage. The battery voltage is reported directly in volts.

"**COM_BAT_CURRENT**" (0x02) command is used to read the battery current. The battery current is reported as a signed value as the battery can deliver current during eclipses and absorb current during charging phase.

Table 17.8 Telemetry system commend list

Command	HEX code	Transmitted # bytes	Received # bytes
COM_BAT_VOLTAGE	0x01	1	2
COM_BAT_CURRENT	0x02	1	2
COM_BAT_TEMPERATURE	0x03	1	2
COM_BAT_CAPACITY	0x04	1	2
COM_BAT_STATUS	0x05	1	2

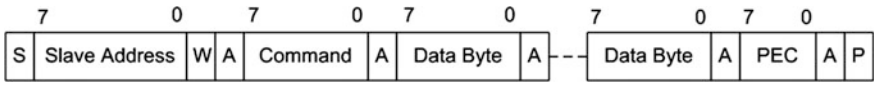

Fig. 17.40 General structure of an I2C packet of telemetry system

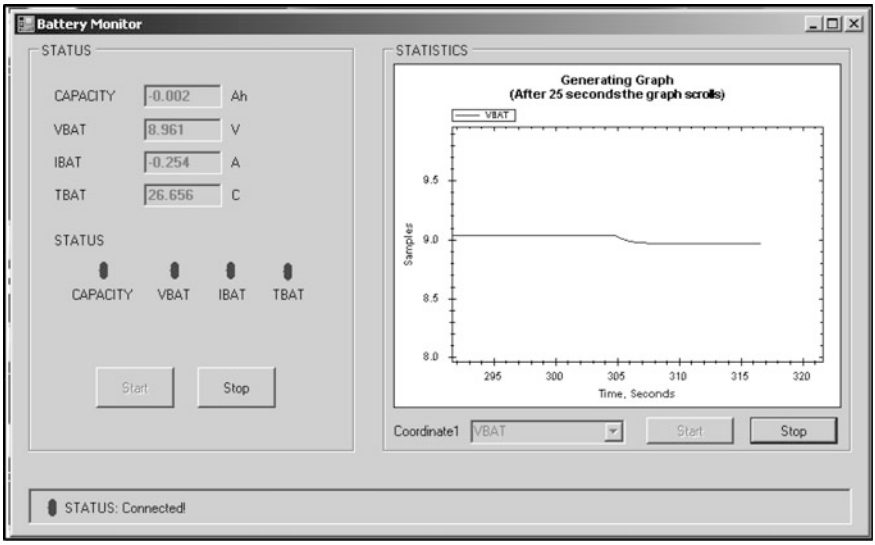

Fig. 17.41 The BCDMU PC GUI

"**COM_BAT_TEMPERATURE**" (0x03) command reads the battery's temperature. The temperature is reported directly in Celsius degrees and covers a range between −50 and 125 °C.

"**COM_BAT_CAPACITY**" (0x04) command reports the battery's current capacity. The read value is a signed number that represents the capacity directly in Ah. Before using this command, it must perform a complete charge-discharge cycle in order to calibrate the coulomb counting block of BCDMU.

"**COM_BAT_STATUS**" (0x05) command is used for fast estimation of the battery status. The number of bits on functionality of these bits can be set in the BCDMU firmware as a function of the system requirements.

A PC Graphical User Interface (GUI) was developed in order to retrieve main battery parameters from BCDMU unit. Figure 17.41 presents the GUI screen. The parameters can be plotted versus time for convenient representation.

17.3.3 The Effects of Space Radiation on Electronic Components

The space is a harsh environment. All electronic components, semiconductor materials and assemblies are affected by this environment. The main factor that causes this is the space radiation. There are four major components that form the space radiation:

- Trapped electrons found in the Van Allen Outer Belt. These are negatively charged particles with low mass but high energy (up to 7 meV). Trapped electrons can be found on orbits with high altitude like GEO (mostly telecom satellites and GPS).
- Trapped protons found in the Van Allen Inner Belt. These are positively charged particles held captive by the Earth magnetosphere. Can have energies up to 400 meV and dominates the low orbits (LEO).
- Solar particles. These are protons and heavy ions ejected from the Sun during solar flares. The energy of these particles is high enough to produce damages to electronics and the occurrence is essentially unpredictable.
- Cosmic rays. They are produced by some galactic phenomena like supernovae and contain particles with very high energy (sometimes up to 10^{20} eV). The flux is relatively low, 4 particles/cm^2/s.

There are two major categories of effects generated by space radiation on materials used for electronic devices:

- **Cumulative effects**. Long term exposure to space radiation produces a progressive degradation of semiconductor materials. There are two major effects related to long term exposure: the Total Ionization Doze (**TID**) and Displacement Damages [**DD**]. The TID is measured in grey [SI] or rad [CGI] and indicates the accumulated doze where the electrical parameters of a semiconductor device start to degrade. For radiation-hardened devices TID is between 100 krad (Si) and 1 Mrad (Si) while for COTS are between 1 krad (Si) and 100 krad (Si) (mostly below 30 krad (Si)). The displacement damages are produced by high energy particles that affect the lattice structure of the semiconductor.
- **Single event effects**. These effects are produced by a single high-energy particle that passes the semiconductor structure and disturb the normal functionality of the device. There are few categories of single event effects:
- **Single Event Upset** (**SEU**). This disturbance affects mostly the digital circuitry especially memories and is essentially non-destructive. The particle may change the state of a memory cell producing a temporary malfunction of the circuit or data loss.
- **Single Event Latch-Up** (**SEL**). This disturbance affects the circuitry that presents the latch-up phenomenon like CMOS. Essentially the particle trigger the latch-up into the semiconductor structure and the current drawn by the device may become very large and uncontrollable. The SEL can produce destructive effects unless the current drawn by device is limited.
- **Single Event Transient** (**SET**). Here the particle produces a temporary disturbance of a parameter like a voltage or current. Mostly affects the analog circuitry like the voltage regulators but may also affect indirectly the digital circuits.
- **Single Event Burnout** (**SEB**). This is the most dangerous single-event effect because produces permanent failure of the semiconductor structure. Is often

triggered by a SEL and if the current into device is not limited the temperature of the semiconductor structure will exceeds the safety limit.

For low cost, limited time space missions the cumulative effects are not a problem. However, the single event effects may severely affect the mission and some countermeasures against these effects are always necessary.

17.3.4 Countermeasures Against the Effects of Space Radiation

The cost of a space mission is very high and in this context the reliability of the electronic systems became of critical importance. A short list of specific techniques used for preventing catastrophic failure due to space radiation:

- **Use of radiation-hardened components**. These are specially developed components capable to sustain large doses of radiation without significant degradation of electrical parameters. The cost of these components is very high and the availability is limited. The typical development cycle is between five and seven years and the testing and validation effort is significant. Space agencies regularly publish documents with radiation tests done for various components.
- **Redundancy**. Redundancy is the primary option for increase the reliability of critical mission blocks or assemblies. Redundancy is obtained when more components than a specific operation needs are placed in a specific configuration so that in case that one component fails another takes instantaneously its place and the functionality is preserved. This method involves high cost and cannot be implemented for all components and assemblies for example the solar array and batteries. For very small LEO satellites this option is somehow limited by the cost and the mass/dimensions.
- **Shielding**. Shielding is an effective way to protect the electronic components against the effects produced by low-mass particles (electrons). The electronic assemblies can be covered by metal shields aluminum being the primary option due to its low mass. Shielding is not effective against large mass, high energy particles like those from the cosmic rays.

17.3.5 Reliability of Low-Cost Designs Based on COTS

The proposed PCU is entirely built with COTS. While the radiation tolerance of COTS is in most of the cases unknown there are few techniques that can improve the reliability of electronic blocks built using these components.

The redundancy is primary option also in case of low-cost designs. In case of the proposed PCU there are three functional blocks that involves redundancy:

- The Battery Charger Unit (BCU). There are four independent BCU units in this design. Each BCU is designed with a typical 30% power reserve.
- The Battery Charge/Discharge Monitor Unit (BCDMU). There are two BCDMU units that can run in parallel each one with his own battery. The telemetry system is independent for each BCDMU.
- The Isolation Unit (IU). There are two independent IU with outputs connected in parallel.

The effects induced by SEU can be minimized by using a special technique in firmware. This technique involves the use of redundant code: critical code is executed multiple times and the results are checked by a voter. The same variable is stored in three different locations and the voting system decides if this variable was affected by SEU. All constants are stored in the non-volatile memory of microcontroller and fetched before being used in code.

The most dangerous phenomenon for low-cost, COTS-based designs is SEL. SEL can produce severe malfunctions to the systems and is the primary cause for failure of these systems. The SEL can be prevented by using latch-up proof components and designs. Unfortunately most of the COTS components based on CMOS technology are not latch-up proof. In this category enters microcontrollers, volatile and non-volatile memories often used by low-cost designs. The countermeasures against SEL include:

- Use of the "Watch Dog" circuits. This circuit can reset the microcontroller in case of a malfunction produced by SEL. In order to be effective the "Watch Dog" is usually combined with other circuits like voltage supervisors.
- Use of the input current monitors. These circuits are able to detect an overcurrent that typically occurs in case of a latch-up and can be used to cycle the input power of the protected device. This kind of protection is effective against SEL and their circuitry can be implemented using radiation-hardened components.

17.4 Conclusions

In this chapter a brief overview about the characteristics and specific demands of very small satellites together with their electrical power system topologies are firstly presented. The proposed flexible hybrid power is then introduced and only the power conditioning unit that includes the battery charger unit (BCU) and the battery charge/discharge monitor unit (BCDMU) are further detailed for a specific application of a very small satellite similar to a CubeSat.

The battery charger unit (BCU) includes the DC–DC synchronous Buck converter, the digital controller implemented using a commercial, low pin count microcontroller and the BCU sensors' circuitry that monitors three parameters: input voltage (panel voltage), input current (panel current) and the output battery's

voltage. The input voltage and the input current are used for the MPPT implementation of the P&O algorithm and the output voltage is used for the implementation of the battery-specific charging algorithm. At the end of this subchapter, the BCU prototype is explained from the practical perspective of the built prototype.

The battery charge/discharge monitor unit (BCDMU) contains at its turn a 16-bit low power microcontroller, the BCDMU's sensors circuitry that monitors other three battery parameters: voltage, current and temperature, the battery switch power whose role is to protect the battery against severe overload, deep discharge or accidental discharge during the launch process, the battery heater activated during eclipses in order to prevent battery's temperature drops below a certain level and finally the telemetry, tracking and telecommand (TT&C) system that measures and reports various parameters of the battery available via the I2C interface provided by the BCDMU. The blocks described above are completely functional, being the subject of a national program, according to acknowledgements below.

Acknowledgements This work was supported by a grant of the Romanian National Authority for Scientific Research, Program for research Space Technology and Advanced Research - STAR, project number 80/29.11.2013.

References

1. https://en.wikipedia.org/wiki/Satellite
2. https://en.wikipedia.org/wiki/Miniaturized_satellite
3. http://space.stackexchange.com/questions/5676/aocs-for-very-small-satellites-micro-nano-pico-femto
4. http://www.nasa.gov/mission_pages/smallsats/
5. http://arc.aiaa.org/doi/abs/10.2514/1.28678?journalCode=jsr
6. Patel MR (2005) Spacecraft power systems. CRC Press, Boca Raton
7. https://www.itu.int/dms_pub/itu-r/opb/rep/R-REP-SA.2312-2014-MSW-E.docx
8. Martin L, Jones WH, Shiroma WA (2014) Small-satellite projects offer big rewards. IEEE Potentials 33(4):24–30
9. http://www.esa.int/Our_Activities/Space_Engineering_Technology/Technology_CubeSats
10. Strain A (2010) User manual: CubeSat 1U electronic power system and batteries: CS-1UEPS2-NB/-10/-2. Clyde Space Ltd
11. http://www.clyde-space.com/
12. Surampudi R, Hamilton T, Rapp D (2002) Solar cell and array technology for future space science missions, June 2002, NASA, pp 1–100
13. De Luca A (2011) Architectural design criteria for spacecraft solar arrays (Chap 8) in solar cells—thin-film technologies. InTech Publishing House, Vienna. ISBN 978-953-307-570-9
14. Colasanti S, Nesswetter H, Zimmermann CG, Lugli P (2014) Modeling and parametric simulation of triple junction solar cell for space applications. In: IEEE 40th photovoltaic specialist conference (PVSC 2014), pp 1784–1789
15. Pearson C, Thwaite C, Russel N (2005) Small cell lithium-ion batteries: the responsive solution for space energy storage. In: American institute of aeronautics and astronautic (AIAA) 3rd responsive space conference, 25–28 April 2005, Los Angeles, USA

16. Olsson D (1993) A power system design for a microsatellite. In: ESA/ESTeC, European space power conference, 23–27 August 1993, Graz, Austria
17. Oprea S, Tanase MC, Florescu A (2012) PV charger system using a synchronous buck converter. In: Proceedings of SNET2012, 14 December 2012, Bucharest, Romania, vol 3(1), pp 328–333. ISSN 2067-4147
18. Castaner L, Silvestre S (2002) Modelling photovoltaic systems using PSpice. Wiley, New York. ISBN 978-0-470-84527-1
19. Esram T, Chapman JR (2007) Comparison of photovoltaic array maximum power point tracking techniques. IEEE Trans Energy Convers 22(2):439–449 ISSN 0885–8969
20. Femia N, Petrone G, Spagnuolo G, Vitelli M (2012) Power electronics and control techniques for maximum energy harvesting in photovoltaic systems. CRC Press, Boca Raton. ISBN 9781466506909
21. Sera D, Mathe L, Kerekes T, Spataru SV, Teodorescu R (2013) On the perturb-and-observe and incremental conductance MPPT methods for PV systems. IEEE J Photovoltaics 3 (3):1070–1078
22. Demirel S, Sanli E, Gokten M, Yagli AF (2012) Properties and performance comparison of electrical power sub-system on TUSAT communication satellite. In: 2012 IEEE first AESS European conference on satellite communications (ESTEL 2012), 2–5 October 2012, Italy, Rome. Print ISBN:978-1-4673-4687-0
23. Erickson RW, Maksimovic D (2001) Fundamentals of power electronics, 2nd edn. Springer, New York. ISBN 13: 978-1475705591
24. Oprea S, Rosu-Hamzescu M, Radoi C (2014) Implementation of simple MPPT algorithms using low-cost 8-bit microcontrollers. In: IEEE conference on electronics, computers and artificial intelligence (ECAI 2014), 23–25 October 2014, pp 31–34
25. Rosu-Hamzescu M, Oprea S (2012) High-power CC/CV battery charger using an inverse SEPIC (Zeta) topology. Microchip Technology Inc., AN1467, pp 1–16

Chapter 18
Power Conversion and Energy Management for Mission-Critical Systems

Andrei-Stefan Savu, Adrian-Ioan Lita, Constantin Radoi, Adriana Florescu, Sergiu Oprea and Ioan Lita

Abstract The need for high power density has been the trend of the power conversion industry for many years. The key to obtain a high power density is to increase system's efficiency. In the case of space applications, there is the same need for high power density but with the very important note that the reliability of the system must not be compromised. In order to increase system's efficiency while maintaining reliability, the latest soft switching converter topologies, high power density packaging, improved heat extraction and planar magnetics are used. Other key parameters are: the digital loop control and the digital energy management through microcontrollers, and digital signal controllers.

Keywords Mission-critical systems · Planar transformer technology · Variable width winding method · Adiabatic point of load · Quasi resonant flyback · Two transistor forward and LLC converters · Intermediate bus converter · Very small satellites

A.-S. Savu · A.-I. Lita · C. Radoi · A. Florescu (✉) · S. Oprea
University Politehnica of Bucharest, Bucharest, Romania
e-mail: adriana.florescu@yahoo.com; adriana.florescu@upb.ro

A.-S. Savu
e-mail: savucfa@yahoo.com

A.-I. Lita
e-mail: adrian.lita@ieee.org

C. Radoi
e-mail: conrad_1944@yahoo.com

S. Oprea
e-mail: oprea_serg@yahoo.com

I. Lita
University of Pitesti, Pitesti, Romania
e-mail: ioan.lita@upit.ro

N. Bizon et al. (eds.), *Energy Harvesting and Energy Efficiency*,
Lecture Notes in Energy 37, DOI 10.1007/978-3-319-49875-1_18

List of Abbreviations and Acronyms used:

ASM	Assembly
BGA	Ball Grid Array
CT	Copper Thickness
DCM	Discontinuous Conduction Mode
DRIBA	Double Regulated Intermediate Bus Architecture
EMP	Electromagnetic Pulse
ESA	European Space Agency
ESR	Equivalent Series Resistance
FEA (FEM)	Finite Element Analysis (Finite Element Method)
GaN	Gallium Nitride
ICs	Integrated Circuits
LET	Linear Energy Transfer
MPPT	Maximum Power Point Tracking
MTBF	Mean Time Between Failures
ORING	OR-ing Output Logic Function
PCB	Printed Circuit Board
PI	Proportional Integral
PID	Proportional Integral Derivative
POL	Point Of Load
POU	Point Of Use
PWM	Pulse Width Modulation
RF	Radio Frequency
RMS	Root Mean Square
SEB	Single Event Burnout
SEBP	Single Event Burnout Phenomenon
SEE	Single Event Phenomenon
SEGR	Single Event Gate Rupture
SEL	Single Event Latch-up
SEU	Single Event Upset
SGEMP	System Generated EMP
SMPS	Switched Mode Power Supply
TID	Total Ionizing Doze
VRM	Voltage Regulated Module
ZCS	Zero Current Switching
ZVS	Zero Voltage Switching

A mission-critical system represents a system whose failure due to any part of it (a procedure, process, software, hardware such as an equipment, etc.) would compromise the whole mission and the organization as well. On Earth, examples of mission-critical systems are: the online banking system, railway and aircraft operating and control system, electric power systems, computer systems whose collapse would seriously affect the organization or, worse, the whole society.

In space, examples of a mission-critical system are: the navigation system for a space mission, or the electric power system (conversion and management).

Electrical energy is one of the vital elements in keeping a satellite operational in orbit. Solar panels convert solar energy into electrical energy. From there, the electrical energy is processed, stored, regulated and distributed to electronic loads which consist mainly of analog and digital semiconductors, RF, optical, sensors, lasers and electromechanical devices. To underline the importance of the electrical power system in space applications as a mission-critical system whose failure would compromise the whole mission of any satellite, European Space Agency (ESA) briefly states that "a satellite without electricity is nothing but space junk" [1].

In Chap. "Power Architectures and Power Conditioning Unit for Very Small Satellites", an introduction in very small satellites (characteristics, Earth orbits and eclipses, Cube Sats brief presentation and missions) was made and some blocks of the electrical power system were discussed (the solar array, batteries for space applications, space power architectures, maximum power point tracker) and developed (the flexible architecture of the power conditioning unit). In this chapter focused on space power conversion units and energy management strategies, a brief presentation of space requirements for power conversion is introduced and the advanced technology of planar transformers—as part of the power conversion units—is detailed. Then, all the other remaining blocks of the satellite's electrical power system from the above mentioned chapter (the intermediate bus converter and the adiabatic point of load power converter) are developed, together with the power management block that links all the component blocks in both chapters. In the end, the original prototype of the whole energy management system for a very small satellite application is exposed, as the best obtained variant of practical demonstrator for the architectures, technologies, algorithms, methods, devices etc. presented in both chapters.

18.1 Overview of Space Requirements for Power Conversion Units

The technology of power electronics for space applications has special peculiarities. The most remarkable difference between power electronics for space and the terrestrial environment one consists of space radiation. Power semiconductor devices such as MOSFET can fail after exposure to heavy ions due to SEGR (single event gate rupture) or SEBP (single event burnout phenomenon). Also controlling semiconductor integrated circuits (Ics) such as microcontrollers, microprocessors, analog to digital converters and sensors can suffer from heavy ions exposure, causing faulty data which may lead to catastrophic failure. To stress this even further, just considering one single bit alteration in the microcontroller's memory can lead to abnormal behavior of the control system, which can distort the control loop, which in the end may lead to damaging the electronic loads.

Converters are generally required to operate continuously in the radiation environment without damage and performance degradation with accumulative total ionizing doze (TID) in the range of 2–3 kiloradiatios (Krads) to 100 Krads or more. TID level is mission dependent. Also required is the converter's ability to survive and recover from singe event phenomena (SEE), e.g. single event upset (SEU), single event latch up (SEL) and single event burnout (SEB). The typical SEE level is linear energy transfer (LET) or 37–83 meV-cm^2/mg. SEE level is mission dependent, too. Other radiation requirements may include performance under neutron, proton, and high doze rate radiation. However, these requirements are unique to strategic weapon applications. Table 18.1 lists the typical requirements of a space DC-DC converter [2].

Unlike terrestrial applications, where mass and volume may not always be a big concern, space applications require the most compact and light design possible,

Table 18.1 Typical requirements of a space DC-DC converter

Parameter	Typical requirement
Electrical	
Input voltage	28 V unregulated; 50, 70 and 100 V regulated
Input inrush current	Required at the system level, but frequently flowed down
Output	Single, dual or triple
Output 1 (main)	+1.0 to +15 V
Output 2	+5 to +15 V, 5 to 15% of total output power
Output 3	−5 to −15 V, 5 to 15% of total output power
Output power	A few watts to 40 watts
Input-output isolation	Required
Output ripple	20 to 50 mVp-p typical, 1–5 mVp-p for some RF applications
Efficiency	50−70% for 5−15 W, and 70−90% for 15−40 W
EMI	Conducted emission (CE) and conducted susceptibility (CS) requirements modified versions of MIL-STD-461C/D/E
Overvoltage protection	Yes, shut down, limit 10−20% above Vnom (generally required for redundant applications)
Turn-on overshoot	<5% Vnom, output rises monotonically
Turn-on delay time	0.5 to 10 mS
Bus current telemetry	At the system level
Step load response	<2–5%, < 200–500 μS, half-load/full-load
Output telemetry	Yes
Temp telemetry	Required on some programs
Remote sense	Required for main output
Synchronization	Yes
Undervoltage lockout (UVLO)	Yes
Soft start	Yes

(continued)

Table 18.1 (continued)

Parameter	Typical requirement
On/Off command	Yes, bi-level or pulse command
On/Off status telemetry	Yes
Output voltage adjustment	Yes
Derating	NASA PPL-21/MIL-STD-1547/MIL-STD-975/ESA PSS-01-301
Mechanical/Environment	
Operating temp	−34 to +71 C qualification, program dependent, often has a wider temperature range for qualification level than acceptance requirement of flight hardware
Storage temp	−40 to +85 C, typical, program dependent
Random vibration	Dependent of launch platform
Pyrotechnic shock	Dependent of launch platform
Acceleration	Dependent of launch platform
Humidity	60–95% RH
Explosive atmosphere	Shall not cause ignition
Size	Key design requirement
Mass	Key design requirement
Qualification	MIL-PRF-38534, Class K
Package construction	Hermetically sealed thick film hybrid
Radiation	
Total ionizing dose (TID)	25 to 100 Krads, may be with shielding
Single event effect (SEE)	37–83 meV-cm^2/mg, shall not sustain permanent damage from cosmic ray or performance degradation from SEE: no SEU, no SEB, no SEGR, no SEL, no SET
Neutron	If required, shall be designed to withstand, without permanent performance degradation after exposure to neutron equivalent influence of $\leq 5 \times 10^{12}$ n/cm^2
Dose rate upset/recovery	Classified, x to y rad(si)/s, recover autonomously
Dose rate survival	If required, shall not sustain permanent damage or permanent performance degradation after exposure to dose rate of X $\leq$ rad(si)/s. The pulse has FWHM (full-width half-maximum) of 18–100 nS
Dose rate operate thru	If required, must operate thru after exposure to X $\leq$ rad(si)/s
Electromagnetic pulse (EMP)	If required, is designed to prevent EMP, hardening techniques are required
System-generated EMP (SGEMP) burnout	If required, is designed to prevent SGEMP burnout, hardening techniques are required
Enhanced low dose rate effects (ELDRS)	5 to 10 mrads/s, becoming a standard

which is also true for military and aerospace applications. Some aerospace power system designs are also suitable for satellite use. Specific power/energy per unit mass is defined as power-to-weight ratio.

Power system's thermal dissipation is a limiting parameter for power electronics design. Unlike the design for terrestrial applications, there is no atmosphere which leads to no convection process in outer space. Only conduction and radiation cooling can be used, which makes a lot of cooling methods unavailable in space applications.

Space power systems must be very reliable, must maintain their functionality and have failure isolation capability. Power system failures can be temporary or permanent. Temporary failures include overheating and non-damaging memory corruption due to radiation. Overheating can be addressed by the controller through power derating or temporary latch. Memory corruption can be addressed by a governing watchdog which reboots the process when corruption is detected. In order to prevent permanent failures, key system parameters are closely monitored by the controller. Such parameters include temperatures in key component areas, memory coherence, voltage and current levels and power levels. The controller makes judgments to implement predictive maintenance. The mean time between failures (MTBF) calculation of such a power systems should exceed the mission lifetime. To successfully implement this, the individual components' electrical and thermal derating levels must be kept lower than the terrestrial 80%.

Some electronic components are restricted for space usage due to their inherent small lifetime. Such components, especially electrolytic and film capacitors, must be replaced by ceramic, tantalum or mica capacitors. Optoelectronic devices are also restricted for space usage due to electroluminescent effects caused by radiation. For mechanical restrictions, vibrations and thermal cycles impose larger footprints and components that are not soldered underneath. For example, chip film resistors and ceramic capacitors have a minimum footprint of 0805. For controller ICs, the footprint should be SOIC, TQFP or larger. Accepted transistor footprints are TO-252 or larger.

18.2 Technological Trends of High Power Density Converters for Space Applications

For the last few decades the focus of power subsystems development and advancement has revolved around the needs and requirements of large high power missions, mainly for telecommunication applications. The challenges to increase efficiency and simultaneously to reduce mass and volume in this application are valid, but for small satellite missions these challenges have been overlooked. From the power system's perspective, it is safe to say that the power challenges and requirements are common across the full spectrum of small satellite missions. Small satellites can have a range of power requirements from as little as 1 or 2 W to a few kW. As a result, there is a need for the power systems' electronics to be compatible with a multitude of mission profiles and to be scalable in power handling capability.

The trends presented in this chapter are focused on planar magnetics and their variable width winding structures, which are very good candidates for various power supply applications, including space power converters.

18.2.1 Variable Width Winding Concept Summary

Power density (or volume power density, or volume specific power) is the amount of power (time rate of energy transfer) per unit volume. The trend toward high power density, high operating frequency, and low profile in power converters determined the appearance of limitations regarding the use of conventional wire-wound transformers. An alternative to conventional wire-wound transformers are planar transformers, which exhibit a unique set of advantages: good thermal characteristic, higher power density and low leakage inductance. The increase of power density is obtained by increasing the switching frequency which decreases the size of the passive components. However, this increase of the switching frequency creates a different set of problems regarding the skin and proximity effects of the transformer windings, especially with frequencies over 100 kHz [3]. The finite element analysis simplifies the computation of the DC and AC losses in the windings. Also analytical approach is presented in [4]. In [5] a comparison between simulation and analytical results for magnetic components is made. Windings with variable width turns are considered in [6], but they are not experimentally confirmed. The limitations of planar transformer designs are the subject of [7, 8].

In this chapter the DC and AC resistance of the windings have been analyzed via a finite element analysis, and a novel variable width winding concept is compared to the fixed with winding approach. The variable winding widths are chosen so the winding exhibits the same DC resistance per turn and so balancing the magnetic flux. This optimized variable width winding brings an improvement at DC and AC frequencies. Combined with a 10 W LLC application, the classical constant width and variable width windings are compared and the detailed experimental results are shown.

18.2.2 Design with Constant Width Planar Winding

The design process for a constant width planar winding is very straight forward. According to the desired application, the core size and type are chosen in the beginning. For a 10 W LLC converter, a Ferroxcube E32/6/20 3F3 core meets the requirements. The turn ratio of the transformer according to the input and output voltage needs are $N_p = 6$ turns for the primary and $N_s = 2$ turns for the secondary. The design has a 2 layer structure with the primary and secondary windings on separate layers.

For the E32/6/20 core, the winding window is 9.19 mm. The effective winding window is obtained by introducing 0.5 mm of tolerance in each side resulted from the ferrite core and PCB manufacturing tolerances. The resulted effective winding window is wind = 8.19 mm.

Building the transformer on a 2 layer structure assumes that the copper thickness (CT) should be set to a typical printed circuit board (PCB) manufacturer capability of 3 oz. This thickness dictates the distance between turns (x), which will be x = 0.3 mm. The primary winding width will be:

$$W_{prim} = \frac{wind - (N_p - 1) \cdot x}{N_p}, \tag{18.1}$$

which computes to W_{prim} = 1.115 mm.

Starting from (18.1), a similar equation for the secondary winding constant width can be found:

$$W_{sec} = \frac{wind - (N_s - 1) \cdot x}{N_s}, \tag{18.2}$$

resulting in W_{sec} = 3.945 mm.

Once the winding widths have been determined, in order to calculate the DC resistance, the windings length has to be determined. Due to the shape of the ferrite core, the winding has a rectangular shape. Additional parameters need to be defined the winding length calculation (Fig. 18.1) are: t—turn number, L—center core leg length, l—center core leg width, L_t—partial winding length, l_t—partial winding width.

The partial long length for a turn t is:

$$L_t = L + 2t \cdot w + (2t - 1) \cdot x \tag{18.3}$$

and for the short length t is:

$$l_t = l + 2t \cdot w + (2t - 1) \cdot x \tag{18.4}$$

Equations (18.3) and (18.4) apply for primary and secondary constant width windings and combining them the total length for t = 6 turns primary winding can be determined:

$$L_{totalprim} = 2 \cdot \left(\sum_{t=1}^{N_p} L_t + \sum_{t=1}^{N_p} l_t \right) \tag{18.5}$$

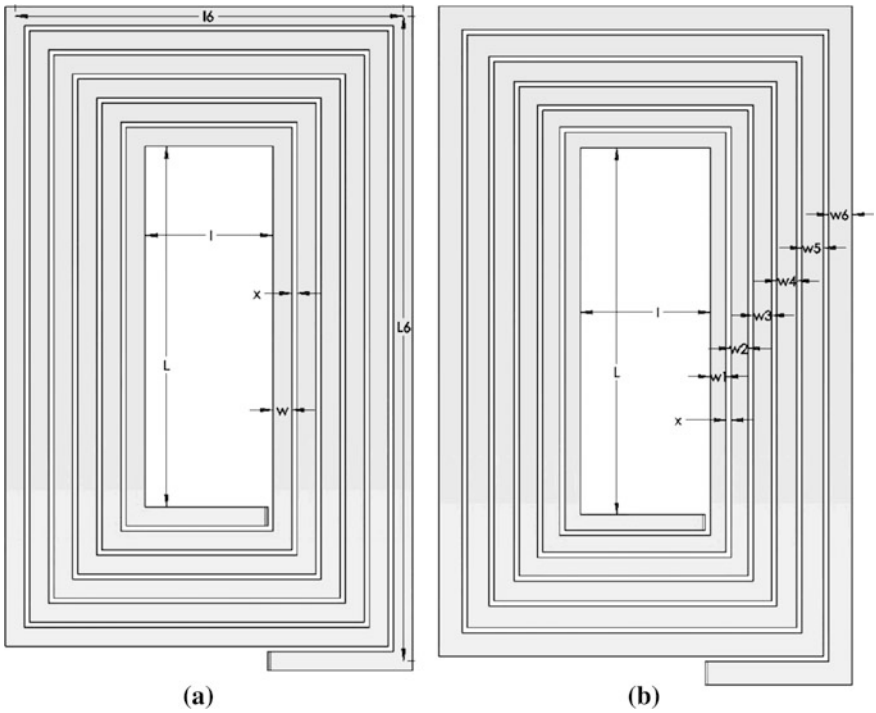

Fig. 18.1 Constant width primary winding (**a**), variable width primary winding (**b**)

The total length for t = 2 turns secondary winding is:

$$L_{totalsec} = 2 \cdot \left(\sum_{t=1}^{N_s} L_t + \sum_{t=1}^{N_s} l_t \right) \tag{18.6}$$

From (18.5) and (18.6) the following lengths are obtained: $L_{totalprim}$ = 549.45 mm and $L_{totalsec}$ = 188.81 mm.

Following the results from (18.1), (18.2), (18.5) and (18.6) the DC resistance of the windings is calculated considering the copper thickness CT:

$$R_{primcons} = \rho \cdot \frac{L_{totalprim}}{CT \cdot W_{prim}}, \tag{18.7}$$

where $\rho = 1.724 \cdot 10^{-8}$ Ωm is the copper resistivity. A similar equation is defined for the secondary winding:

$$R_{sec\ cons} = \rho \cdot \frac{L_{total\ sec}}{CT \cdot W_{sec}} \tag{18.8}$$

The DC resistances for the constant width design will be: $R_{primcons} = 59.727\ \text{m}\Omega$ and $R_{sec\,cons} = 5.801\ \text{m}\Omega$.

18.2.3 Proposed Design with Variable Width Winding Method

The variable with winding design begins with the assumption that the resistance of each turn is equal to each other. By maintaining this assumption, the flux is balanced between the windings having the same current flowing through each turn. For simplicity only the primary winding will be a variable width. In Fig. 18.2 the complete transformer assembly is shown.

Step 1: Design starts by choosing the width of the first inner turn $w_1 = 0.9$ mm, according to [6]. This will be a temporary value and will be adjusted. In order to comply with the maximum winding space the following in equation must be fulfilled:

$$\left(N_p - 1\right) \cdot x + \sum_{t=1}^{6} w_t \leq wind, \tag{18.9}$$

meaning that the sum of all widths and winding distances must not exceed the maximum winding window. The relation between widths will be dictated by a multiplier coefficient y, as it follows:

$$\begin{cases} w_1 = 0.9\ \text{mm} \\ w_2 = w_1 y \\ \cdots \\ w_n = w_{n-1} y \end{cases}, \tag{18.10}$$

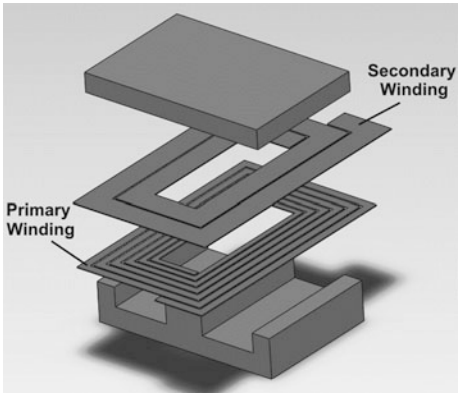

Fig. 18.2 Two layer transformer assembly

where $y = 1.085$ is chosen for N_p = 6 turns and winding window of wind = 8.19 mm to satisfy (18.9). Based on the calculations above the temporary winding widths can be determined.

Step 2: Is to calculate the winding lengths, using the same (18.3) and (18.4) as for the constant with design. Since the resistance of each turn needs to be calculated, the average length of each turn, which is a similar calculation to the (18.3)–(18.5) but with a variable with introduced, is calculated:

$$Lavg_t = 2 \cdot [L + 2t \cdot w_t + 2 \cdot (2t - 1) \cdot x + l_t + l + 2t \cdot w_t] \tag{18.11}$$

Having the widths and average lengths of each turn calculated the resistance per turn is:

$$R_t = \rho \cdot \frac{Lavg_t}{CT \cdot w_t} \tag{18.12}$$

Step 3: Is to equalize the resistances. The simplest way of doing this is by using a mathematical calculation program like Mathcad and use (18.9), (18.10), (18.11) and (18.12). Two parameters can be adjusted: the inner winding with w_1 and the multiplier coefficient y. When the two conditions are fulfilled (the resistance is the same per turn and the maximum winding window is not exceeded), the calculation is over. For a six turn variable winding, the winding resistances per turn results are as follows:

$$R_1 = 8.781\ \text{m}\Omega, \quad R_2 = 8.707\ \text{m}\Omega, \quad R_3 = 8.628\ \text{m}\Omega$$
$$R_4 = 8.545\ \text{m}\Omega, \quad R_5 = 8.458\ \text{m}\Omega, \quad R_6 = 8.368\ \text{m}\Omega$$

The total DC resistance for the variable with is be: $R_{primvar} = 57.487\ \text{m}\Omega$.

18.2.4 Comparisons Between Designs via FEA Simulations

As a result from subchapter above, the DC resistance of the proposed variable width design has a 3.5% lower resistance that the constant width design. A finite element analysis is performed on the constant width and variable width designs. An AC magnetostatic solver is used. The excitation is a sinusoidal current of 1A peak amplitude which applies to both primary and secondary windings.

At a first instance to obtain the DC resistance of the windings, the solver frequency is set to 0 Hz. To solve for skin and proximity effects the solver frequency has to be the operating design frequency of the converter, in our case 170 kHz. The result is an impedance matrix containing the resistance, inductance and coupling at the solver frequency. Results of FEM simulations are provided in Table 18.2.

Table 18.2 DC resistance AC resistance inductance coupling

Symbol	Constant width primary	Variable width primary	Secondary
R_{DC} (mΩ)	61.4	59.3	6.06
R_{AC} (mΩ)	148.26	144.1	17.492
L_p (uH)	16.029	16.009	
k	0.96901	0.96931	

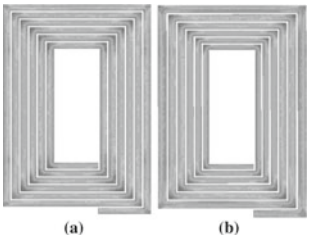

Current density plots for:
(a) constant width;
(b) variable width primary windings

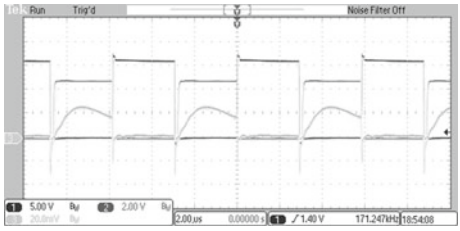

(c) Key waveforms of an experimental half bridge 10W LLC converter with a variable winding planar transformer structure

Fig. 18.3 Design results for constant and variable width primary windings

In order to avoid the saturation of the core a small distributed air gap is introduced. The simulation results from Table 18.2 are performed with a core gap of 0.22 mm. To make a proper comparison between the two winding designs, it is critical that the windings have to be at the same distance to the core gap. If the winding is placed closer to the gap, the AC effects increase due to the magnetic field cutting into the copper.

Following the results of Table 18.2, a 2.8% improvement of the variable width design is noticed in the primary winding resistance at 170 kHz frequency compared to the constant width design. There is a good agreement between the simulated results and Chap. 2.2 theoretical results for the DC resistance. In Fig. 18.3 the current density plots of the primary windings for both designs are presented where almost no difference in current density for the variable width design is noticed, meaning that there are no strangulation points with the variable width turns.

18.3 Intermediate Bus and POL Architectures, Topologies and Control Mechanisms

18.3.1 Intermediate Bus and POL Architectures

The purpose of the intermediate bus converter is to be a buffer between the solar array, battery and point of load converters.

Figure 18.4 shows the relationship between the input stage DC-DC converter and the output stage DC-DC POL. The figure depicts three types of voltage relations between these two: (a) regulated intermediate bus, (b) unregulated intermediate bus and (c) double regulated intermediate bus [9]. In the case of regulated intermediate bus, the input stage converter regulates the bus voltage (Vib) via a feedback loop. The output stage converter operates at fixed parameters (duty cycle and frequency). In the case of unregulated intermediate bus, the input stage converters operate at fixed parameters (duty cycle and frequency) and the output stage converter regulates the load voltage via a feedback loop. In the case of double

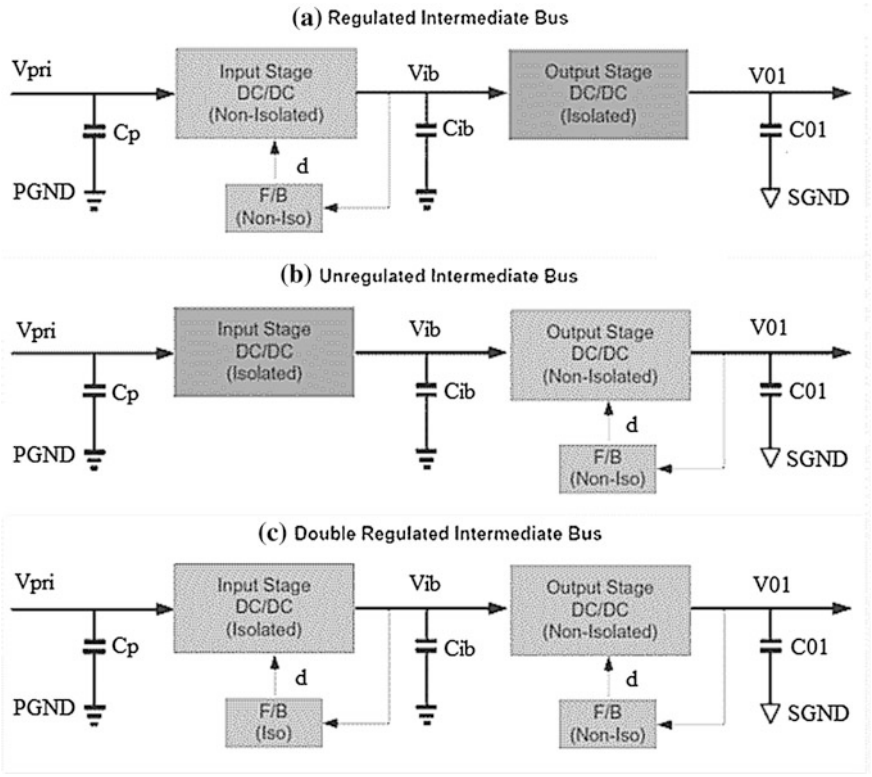

Fig. 18.4 Intermediate Bus and POL architectures

regulated intermediate bus the input stage converter regulates the voltage using a feedback loop and the output stage converter also regulates the load voltage using its own feedback loop. For output voltage requirements of ±10%, the regulated intermediate bus can be used, while the unregulated intermediate bus is capable of ±5% regulation. For a regulation of lower than ±5%, double regulated intermediate bus (DRIBA) is preferred, due to its increased transient capabilities.

Depending on the input voltage range and/or input voltage regulation or quasi-regulation, there are several possible topologies for this type of application and all of them are isolated DC-DC converters. The most used topology is the two Transistor Forward but new cutting edge topologies which obtains higher efficiency include Critical Conduction Flyback and LLC that will be also discussed further.

18.3.2 Two Transistor Forward Converter

The two switch forward converter is chosen as a classical candidate because it is considered to be one of the most reliable converters yet. Its benefits include the following: bulletproof operation (no timing issues or dead time requirements and no chance of shoot-through), no MOSFET body-diode conduction under any condition, no snubber circuitry required, the voltage stress on the main MOSFETs is limited to the maximum supplied voltage and simplicity of operation over a wide range of input voltages and load conditions.

Some of the few drawbacks of the two transistor forward topology are that it requires two transistors and two fast recovery diodes. It also requires a larger transformer and output inductor.

It is falsely stated in many application notes [9, 10] that this topology can't operate in zero-voltage switched (ZVS) mode. ZVS is easily achieved by controlling the amplitude of the primary magnetizing current. Slight modulation in switching frequency enables the control of the magnetizing current. The transfer function equation for the two transistor forward is:

$$V_{out} = Eff \cdot V_{in} \cdot D \cdot N, \tag{18.13}$$

where: V_{out}—the output voltage, Eff—the targeted efficiency, V_{in}—the input voltage, D—converter's duty cycle, N—the transformer turns ratio.

The popular power levels chosen for this converter are in the range of 150 to 750 W. The basic operation is as follows: Fig. 18.5a shows transistors Q1 and Q2, which turn on together transferring energy through the transformer's primary to the secondary. On the secondary side, the forward rectifying diode conducts, transferring energy into the output filter and load.

When transistors Q1 and Q2 are turned off, the transformer magnetizing current flows through the now forward biased diodes D1 and D2 and then back into the source, as shown by Fig. 18.5b. The diodes conduct until all the magnetizing energy in the primary along with energy stored in the leakage inductances is

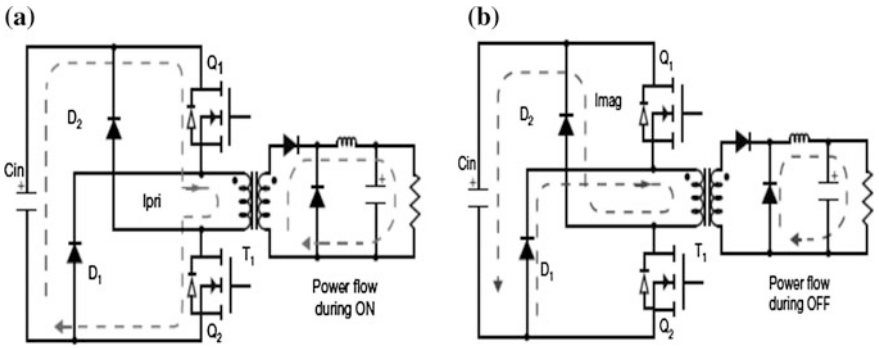

Fig. 18.5 **a** Power transfer stage of operation; **b** Power flow from output cap to power load

returned to the input supply. Since diodes D1 and D2 clamp the input voltage, no snubber circuits are required. On the secondary side, the forward rectifying diode conducts, transferring the output inductor stored energy into the load.

During the non-power delivery cycle of the primary, proper transformer reset time is achieved when the on-time is less than its off-time. As a result, the primary winding itself acts as the reset winding. Having the off-time longer than the on-time, the transformer will always reset. For this reason, the duty cycle of the two switch forward converter does not exceed 50%.

As for any isolated DC-DC converter, a proper design begins with the transformer, which is typically the main source of efficiency loss in the system. In the case of the two switches forward, the full input voltage is applied on the primary winding for a certain amount of time. In this case, the cross-section and core volume of the transformer have to be chosen in such a way to minimize core loss and copper loss. A good transformer design will have similar copper and core loss values. Transformer leakage inductance has to be minimized by winding interleaving techniques since the leakage is decreasing the effective duty cycle.

The output inductor contains in most of the cases only DC current since the AC current amplitude is small. As a result, the inductor flux swing is low and core loss is negligible. Copper losses can be optimized by carefully designing the inductor.

The two primary switches have conduction losses and switching losses. Switching losses are depending on the chosen switching frequency and imposes a limitation in increasing it. The two primary clamping diodes typically exhibit low conduction losses. The rectifier diodes in the secondary side exhibit conduction losses and reverse recovery losses. They can be replaced with synchronous rectifiers which increase the system efficiency but also complicate the driving circuitry. The output capacitors exhibit ESR conduction losses especially when there is a high AC current ripple in the output inductor.

18.3.3 Quasi Resonant Flyback Converter

The classical flyback topology has a fundamental advantage over all other isolated topologies: its ability to operate over large input voltage ranges. This may easily apply to our satellite power system since the solar panel output voltage varies with sunlight, eclipses and temperature. The typical power levels for this converter are in the range of 5 up to 150 W.

The flyback converter operating in continuous conduction mode has several fundamental problems, which are: the leakage inductance voltage spike occurring on the main primary switch, transformer with typically low efficiency due to high AC losses, high switching losses in the main switch and reverse recovery losses in the secondary rectifier. However, the small component count makes this topology very desirable, since the mass and volume, which are key parameters in satellite applications, are lower than for other topologies [11].

Figure 18.6a depicts the flyback converter schematic. To improve the converter's efficiency the converter is operated in discontinuous conduction mode (DCM). This flyback converter is called quasi-resonant flyback or variable frequency flyback or valley switching flyback, and this is largely used in low power switched mode power supply (SMPS) applications such as chargers, adapters and auxiliary supplies. This is also a good candidate for the intermediate bus converter.

The converter stores energy in the primary magnetizing inductance with the main switch is on. In the meantime, output voltage is supplied by the output capacitor and the energy from the secondary winding. When the energy in the secondary winding is depleted, the output voltage is supplied only by the output capacitors. During this period, because the primary switch is off and the secondary rectifier is not conducting, there will be a ringing between the transformer leakage inductance, transformer intra-winding capacitance and the switch's output capacitance, as in Fig. 18.6b.

The voltage across the main switch will experience a minimum valley point, whose minimum value will depend on the flyback reflected voltage. By turning on the main switch at this minimum valley, the flyback is called quasi-resonant or

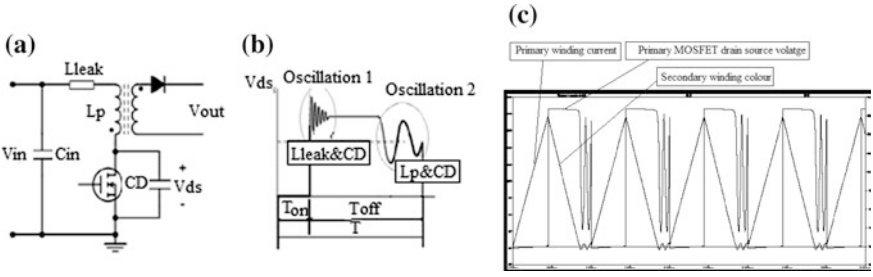

Fig. 18.6 **a** Flyback converter schematic, **b** VDS waveforms of a DCM flyback, **c** Ltspice operation waveforms for V_{in} = 50 V, P_{out} = 50 W

valley switching flyback. To maintain this operation mode, the frequency is adjusted depending on the load.

The transfer function equation of the DCM flyback is:

$$V_{out} = V_{in} \cdot N \cdot D \cdot \sqrt{\frac{R_{load}}{2 \cdot L_p \cdot f_{sw}}}, \tag{18.14}$$

where: V_{out}—the output voltage, V_{in}—the input voltage, N—the transformer turns ratio, D—converter's duty cycle, R_{load}—the converter load resistance, L_p—the primary inductance value, f_{sw}—the converter's switching frequency.

One of the most critical components in any flyback is the transformer design. Since the operation mode is slightly different from any other isolated converter, the transformer acts as a storage device and is delivering power to the output when the main switch is off. The secondary winding is exposed to the magnetic field created by the primary winding, thus having increased AC conduction losses. This applies also to the primary winding being in the magnetic field of the secondary winding, also creating AC conduction losses. The AC losses increase is more significant in the quasi-resonant design.

Minimizing the leakage inductance is a must in any flyback transformer design. This can be achieved by proper winding interleaving. The leakage inductance creates a voltage spike on the main primary switch. This is often dampened by the use of RCD snubbers.

The primary switch exhibits both conduction loss and switching loss. By turning on the switch at the minimum valley voltage, the switching losses decrease. This is one of the main advantages of using a quasi-resonant flyback. The secondary rectifier exhibits conduction losses and reverse recovery losses, the latter being eliminated by operation in quasi-resonant mode. The output capacitor exhibits ESR conduction losses.

Figure 18.7 shows the switching waveforms for a Flyback converter used as an intermediate bus converter.

18.3.4 LLC Converter

Operation at higher switching frequencies reduces the size of passive components such as transformers and filters. Switching losses have been the main obstacle to achieve high frequency operation. Switching losses are directly proportional with switching frequency. Resonant converters have been in the power supply industry for more than 20 years. One of the most successful resonant topology which emerged is the LLC type. Its main advantages are that it obtains Zero Voltage Switching (ZVS) on the primary side switches and Zero Current Switching (ZCS) on the secondary side rectifiers [12]. The typical power levels for the LLC converter can be between 50 W and 1KW.

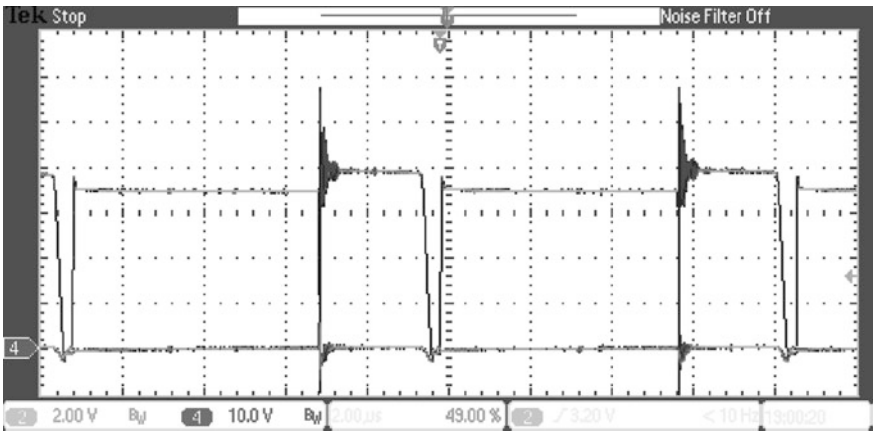

Fig. 18.7 ZVS switching waveforms for critical conduction flyback: CH_4 Mosfet drain, CH_2 Mosfet driving signal

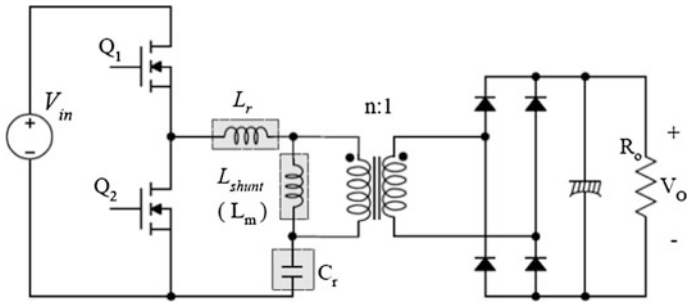

Fig. 18.8 Half-bridge LLC resonant converter

The power supply gain is controlled by changing the switching frequency. The LLC resonant converter contains a resonant network. This network is consisted, as the name implies from two inductors and a capacitor. Figure 18.8 defines a resonant inductor L_r and a shunt inductor L_m and also a resonant capacitance C_r.

The resonant inductor can be the leakage inductance of the transformer, or a discrete inductor, or both in series. The shunt inductor is the magnetizing inductance of the transformer. If the primary side of the converter is used in a half-bridge configuration, the resonant capacitor value is the sum of the two bridge capacitor values. The resonant tank contains two resonant frequencies:

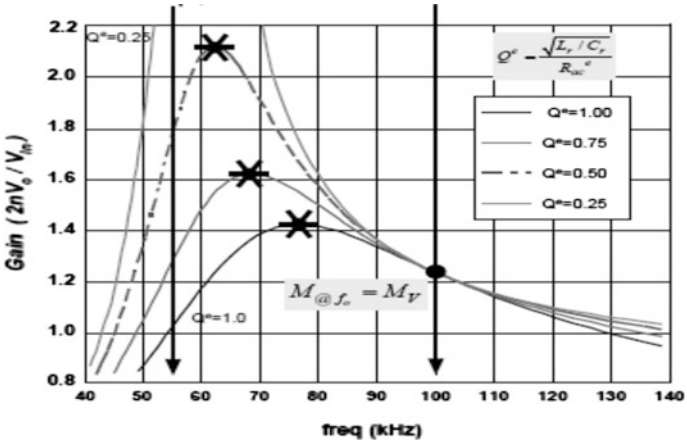

Fig. 18.9 Typical gain curves of LLC resonant converter

– a resonant frequency f_0, defined as:

$$f_0 = \frac{1}{2\pi\sqrt{L_r C_r}} \tag{18.15}$$

– a lower resonant frequency f_p, defined as:

$$f_p = \frac{1}{2\pi\sqrt{L_p C_r}}, \tag{18.16}$$

where L_p is the sum of the shunt inductor and the series inductor, and L_r is the resonant inductor. To maintain ZVS conditions the converter must be designed to operate with a switching frequency higher than fp, ideally f_p + (10–20%) margin.

A particularity of this converter is that by operating around the resonant frequency f0, the gain characteristic is almost independent of the load, as shown in Fig. 18.9 [12].

Analyzing Fig. 18.9, depending on the primary side we can identify conduction losses in switches Q1 and Q2, conduction losses in Lr winding, transformer windings and also in the ESR of the resonant capacitor. The secondary side rectifiers can be diodes or synchronous rectifiers. If operated above the resonant frequency fp, there are theoretically no switching losses, one of the main advantages of this topology. Contrary to other topologies, a larger leakage inductance value will not affect the performance since the leakage inductance value is absorbed in the series inductor.

This topology is a good candidate for an intermediate bus converter because of its load independent constant gain while operated at the resonant frequency f_0. The main drawback of this topology is that the RMS current values in both primary side

and secondary side are higher than typically operated PWM converters and also the peak values of the voltage and currents are higher, thus requiring higher component derating values.

18.3.5 Control Mechanisms of Power Converter Units

Controlling a power DC-DC converter unit is always dependent on the topology, transient needs and other factors required. Control mechanisms can be achieved via analog control, digital control or mixed analog-digital control [13, 14].

Traditionally, analog control was used to generate the drive signals, feedback loop and other auxiliary needs. Some of the main advantages of analog control were the low quiescent power and very fast feedback loops. The disadvantages are the high number of discrete components, higher susceptibility to electrically induced noise and few reconfiguration options. As things evolved, IC manufacturers built integrated analog controllers, which are very good tools in building power supplies. However, they offer little flexibility and their usage is standard.

As things evolved, digital control gained popularity, now being the most used control mechanisms. The advantages are numerous, while the disadvantages are low and decreasing. Advantages come from the fact that there is usually a user-programmable microprocessor core connected to numerous digital and analog peripherals, which offer large flexibility. Such peripherals include high-speed analog-to-digital converters, fast digital and analog comparators, high performance pulse width modulation (PWM) signal generators, which often allows dead time compensation and many other tweaks. Having all those peripherals backed by a microprocessor results in designing fast digital feedback loops, temperature and voltage protection, as well as powerful communication.

Some of the drawbacks of using a microcontroller are that depending on the need for computation power (i.e. how fast the feedback loop needs to be), the current consumption may be higher. Also, for multi-output power supplies, the microcontroller may not have sufficient computation power to drive multiple output, each with its own loop, if we're talking about voltage regulation, or loops if both the voltage and the current needs to be regulated.

Mixed analog and digital control usually incorporates both a user-programmable digital microprocessor and analog circuitry. The microprocessor usually handles communication, faults, temperature measurements, alarms and signal driving, while the analog circuitry provide a fast response feedback loop, with a reference set by the microprocessor. This allows for lower power consumption on the microprocessor (no need to process lot of signals) and very high transient performance of the power supply.

Feedback control mechanisms used vary from the simplest On/Off control, to PI and PID loops, N pole M zero controls, Sliding Mode Controllers and Fuzzy logic. Any of these can be implemented in a microcontroller, with standard C or Assembly programming, or mixed C-ASM. The reason for using mixed C-ASM

coding is: state machines, alarms and communication require usually more complex thinking but are not time critical. For this reason C code (which after compiling, the output is usually less efficient) is a perfect candidate, while feedback loops and cycle by cycle current limiting are written directly in Assembly because of the time constraint. Other advantages in doing this is the fact that though the microcontroller has enough processing power to allow the user to write C-code over the entire firmware, having efficient code allows the possibility of tuning the processor clock down and reduce overall power consumption.

18.4 Adiabatic Point of Load Modern Concept for Space Applications

In thermodynamics, the "adiabatic" term refers to a system that doesn't change (gain or loss) heat with the exterior surroundings. Starting from this definition, an adiabatic point of load technology refers to an ultrahigh efficiency that forces the power converter to virtually produce no heat when processing the power, which is essential in space applications where no atmosphere exists for heating dissipation [15]. Applied in the electrical power systems for the existing satellites whose end-to-end efficiency in payloads doesn't exceed today 65%, this new, modern and of ultrahigh efficiency technology promises to bring the advantages of no heat removal and constant temperature [16].

An illustrated explanation of this adiabatic technology concept is presented in Fig. 18.10a, where the adiabatic region has a slope of minimum 97% efficiency (ideally, at least 98.5%). It can be observed that both cost reduction and efficiency improvement are simultaneously achieved. With an efficiency improvement of only 1.3% the throughout power doubles, as is shown in Fig. 18.10b.

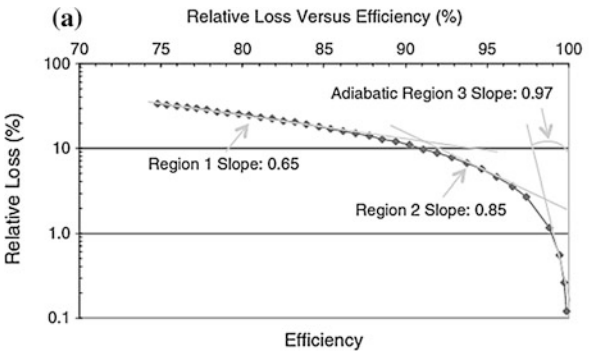

(b)

Efficiency (%)	Efficiency Delta (%) to Cut Loss by a Half
74.78	11.4
80.41	9.0
84.66	7.3
89.38	5.3
92.83	3.7
95.6	1.9
97.4	1.3
98.84	0.6
99.45	0.3

Fig. 18.10 POL with high efficiency intermediate bus converter **a** the definition of the adiabatic region; **b** example of reducing the power loss by a half

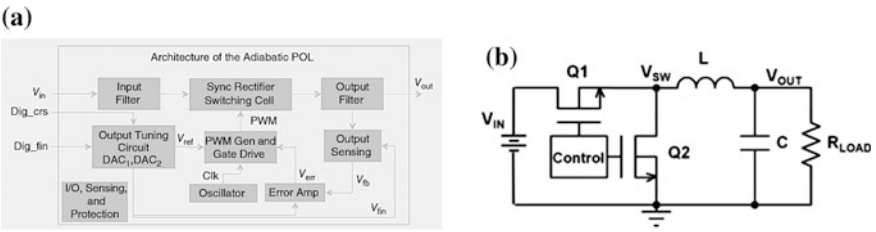

Fig. 18.11 **a** Block diagram of adiabatic POL design; **b** synchronous buck converter (synchronous rectifier)

In Fig. 18.11a the adiabatic POL design block diagram is presented and it can be observed that its overall architecture is similar with the Buck synchronous converter/rectifier, whose electrical diagram results from the basic Buck converter diagram from Fig. 18.11b if diode D1 is replaced with another switch similar to the switch S1, thus significantly reducing losses and optimizing the overall conversion efficiency [17].

Point of Load (POL) or Point of Use (POU) is emerging solutions for applications in which circuits require low voltages of 3.3 V and below. As it was shown above, the most popular POL topology is the Buck converter. Stepping down the voltage from the bus voltage of for example 48 to 1 V or lower will require a very low duty cycle, which will result low converter efficiency. For this reason, to obtain a good power system efficiency the POL must have in front of it an intermediate bus converter as Fig. 18.4c with a double regulated intermediate bus architecture shows. With this type of architecture both the bus converter and the POL converter can reach higher efficiencies and, with both tightly regulated, system's end-to-end efficiency and static and dynamic performances are improved to the level of the needed adiabatic region in Fig. 18.10a.

Typically, the bus voltage for space applications is 12 V. The Buck converter is the most basic SMPS circuit. It is also called a DC transformer without galvanic isolation since it's a non-isolated topology. The Buck topology has several modes of operation: continuous conduction mode, boundary conduction mode and discontinuous conduction mode. Depending on the load current and specific application, the converter can be designed to operate in one or more of these three modes. The Buck converter is widely used in Voltage Regulated Module (VRM) applications, where the output voltage is low and the load current is very high. This is similar the requirements of mission critical power levels. A good part of this proven technology can be borrowed from the VRM technology. For high current applications, the Buck POL will operate in continuous conduction mode and fixed frequency with variable duty cycle. For lower load current and higher voltage applications, the Buck POL will operate in discontinuous conduction mode with variable switching frequency and variable duty cycle.

Figure 18.11b shows synchronous Buck converter's components which are: switches Q1 and Q2 (in the VRM technology, Q2 is placed instead diode D2 of the

classical Buck converter in order to improve efficiency), output filter L and C and input resistance Rload. In the case of synchronized rectification, the main switch and the synchronous rectifier have a complementary drive signal, resulting in the fact that at low duty cycles (for switch Q1), the synchronous rectifier receives most of the load current. The implementation of a synchronous rectifier switch allows the converter to operate in discontinuous conduction mode with a negative rectifier current. This negative current allows the two switches to operate under zero voltage switching mode and eliminate the switching losses. This mode of operation has the drawback of introducing a large AC current ripple in the output inductor L which translates into AC winding inductor losses and increased inductor core loss. This is the reason that for high currents operation in discontinuous mode is less efficient.

Decreasing the size of the POL has been a challenge in the industry for many years, POL efficiency has always been the limiting factor for this. New advancements in semiconductor technologies such as the use of Gallium Nitride (GaN) devices allow the increase of the switching frequency and reduction of the magnetic component size [18, 19]. Low voltage GaN switching devices, which can be employed in the POL are compared by similar silicon device in Table 18.3. These two devices are typical devices specifically designed to be used in POL converters. The GaN switching devices have an advantage over similar silicon devices in terms of parasitic capacitances, which is significantly lower than silicon counterpart.

For the same Drain-to-Source maximum voltage the GaN exhibits a lower conduction resistance. It also exhibits a 40% lower gate charge, which decreases the driving losses. This advantage becomes more significant at a higher switching frequency. The GaN device output capacitance is almost half of the silicon counterpart, meaning that there will be efficiency advantages for the POL in both operating modes. Zero voltage switching is easier to obtain in discontinuous conduction mode because of the lower output capacitance requiring less negative circulating current. In continuous conduction mode the drain-to-source voltage spike on the switching device is lower.

Table 18.3 Silicon versus GaN

	Low voltage silicon BSN012N03LSI	Low voltage GaN EPC2023
V_{DS} (V)	30	30
$R_{DS(on)max}$ (mΩ)	1.6	1.3
I_D (A)	50	60
Size (mm)	3 × 3	6 × 2.3
Q_g (gate charge total) (nC)	37	20
C_{OSS} (output capacitance) (nF)	2.2	1.3
Q_{rr} (reverse recovery charge)	5 nC	0

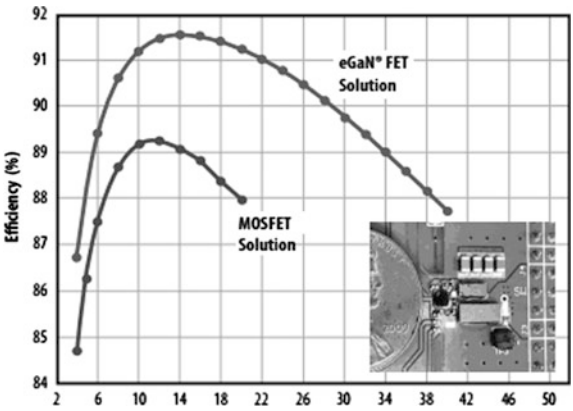

Fig. 18.12 GaN versus MOSFET POL efficiency for a V_{in} = 12 V, V_{out} = 1.2 V, f_{sw} = 1 MHz industrial example

Operation in continuous conduction mode has a fundamental problem in both cases using either rectifying diode or synchronous rectifier because of the reverse recovery losses. In each case this also creates voltage spikes on the switching devices. The main advantage of the GaN switching device is that it experiences zero reverse recovery charge, thus allowing POL operation for high currents at high switching frequencies. The voltage spike amplitude reduction due to the zero reverse recovery charge allows the usage of lower voltage switching devices, which have an inherent lower $R_{DS(ON)}$ and as a result increases efficiency. In Fig. 18.12 we can see power density and efficiency improvements by using GaN transistors instead of conventional silicon ones for a typical POL application running at the switching frequency of 1 MHz. Low voltage GaN devices are being priced at comparable level with the silicone ones which makes them to be taken into account for new designs [20, 21].

Briefly, the trend for POL converters is to decrease the size, increase the efficiency and increase the power density. The ultimate goal is that the converter not to require heat transfer to the surrounding environment. In order for the POL to run in an adiabatic environment, the power dissipation must be controlled, temperatures monitored at all times and considering no air flow, the only possible cooling is done via conduction and radiation.

18.5 Energy Management and Experimental Results

A power system configuration composed by an intermediate bus converter and one or more POL converters must have a governing "brain", which monitors the overall system by knowing exactly each blocks status. This governing function is performed by one or several controllers. In case of multiple controllers, they must be able to establish bidirectional communication between them.

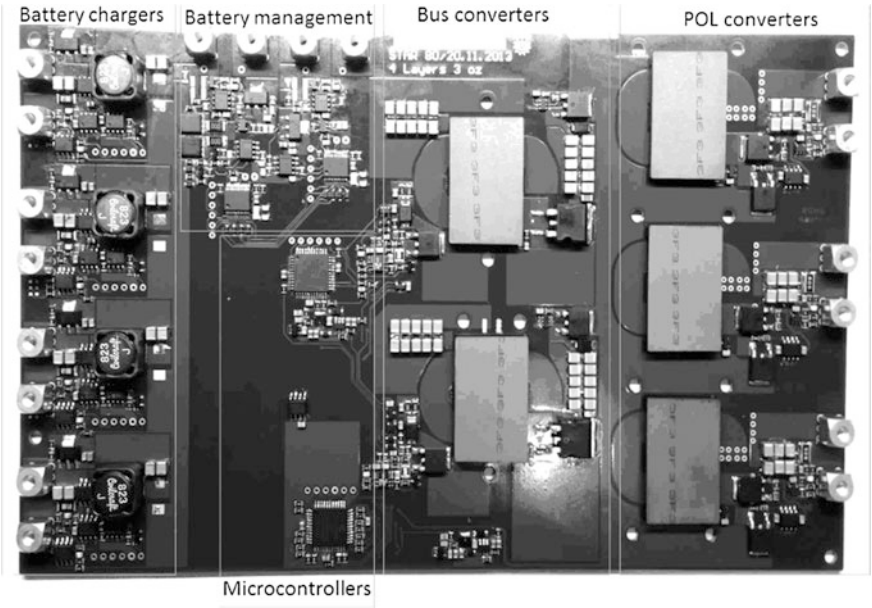

Fig. 18.13 Power management/distribution system for small satellites prototype

In this overall power arrangement there are two or more isolation areas. As already stated before, the intermediate bus converter provides the isolation boundary which is defined by a primary side and a secondary side. The POL is located in the secondary side isolation.

In Fig. 18.13a the power distribution/management system for very small satellites is presented. As also the picture shows, it is composed of four redundant battery charging units (BCU), two battery management units (BMU), two redundant intermediate bus converters, three POL converters and the management unit with two microcontrollers (the primary controller and the secondary controller). The system is designed to have four independent solar panels at its inputs and to supply three galvanic isolated output voltages of 5, 3.3 and 1.2 V. The total combined output power is designed to be 50 W. Also is has a 14.4 ÷ 16.8 V four cell LiIon battery pack connection, which is charged from the solar panels and also supplies the output power when the panels are in shade or malfunctioning. Figures 18.14 and 18.15 describe the software flowchart for the primary side and secondary side controllers. The two intermediate bus converters have two system controllers, one for the primary side and the other for the secondary side. The secondary side controller is also responsible for regulating the voltages on the POL stages. The chosen topology for the intermediate bus converter shown here is the Flyback topology. The Flyback is chosen because of its ability to have a large input voltage range needed for our application and because it has no need for an output inductor and thus saving space on the PCB. The transformers are implemented using planar

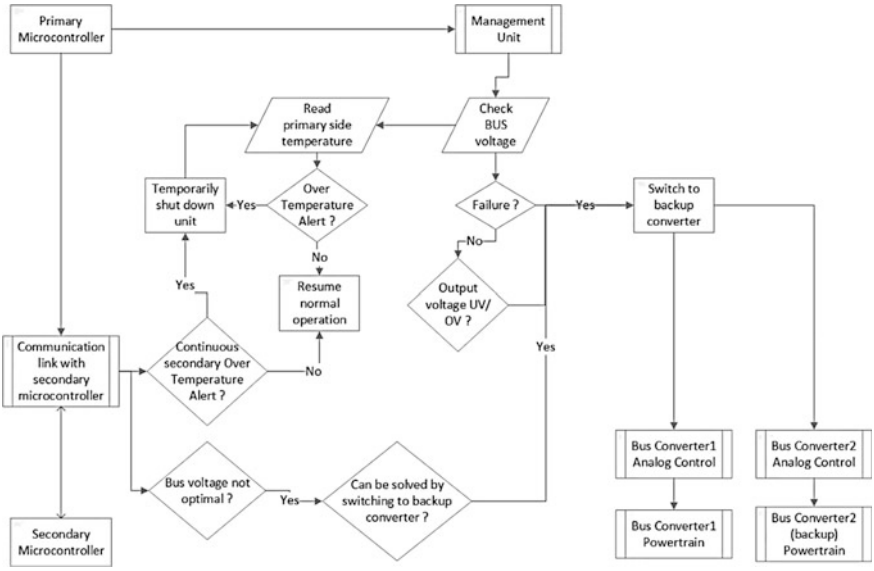

Fig. 18.14 Primary side controller software chart

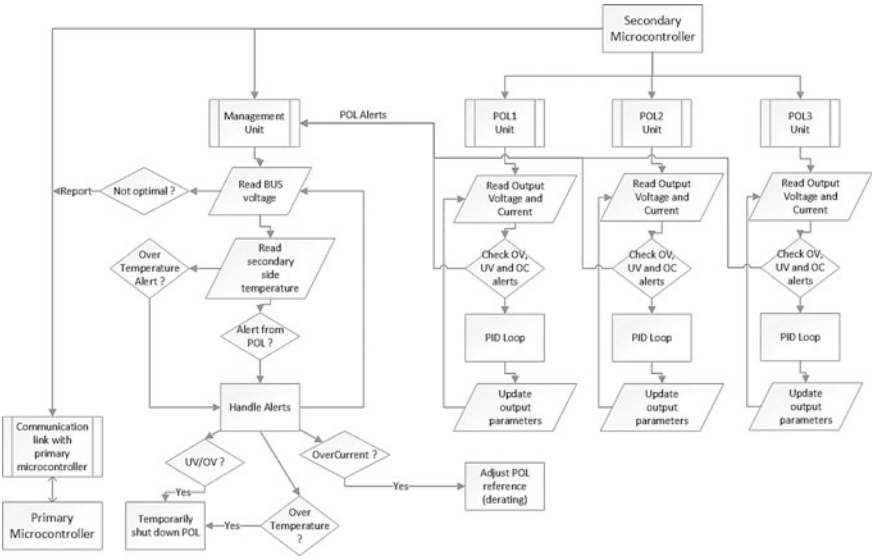

Fig. 18.15 Secondary side controller software chart

magnetic technology, which is more common in military applications and server applications. This was chosen because of inherent cooling capabilities, and better mechanical rigidity, especially in the cases of transportation vibrations. There are two intermediate bus converters for redundancy purposes. Each one has its own analog controller which drives and regulates the output bus voltage. As can be seen in Fig. 18.14, these analog controllers can be turned on and off by the primary system controller. In the same time, this controller can assume the drive and regulation functions, fully replacing the analog control by digital control.

At the end of each Flyback converter there is a protection stage called an ORING stage. This ORING stage technology is borrowed from telecom industry, where multiple DC-DC converters are paralleled into a single bus. The classical approach is for each converter to have an ORING diode. The main drawback of this represents the high power dissipation on the diode. In the latest power systems, this diode has been replaced with a high-side MOSFET switch with low $R_{DS(ON)}$. This switch is controlled by an analog ORING controller, which monitors the switch current and disables the switch if the current becomes negative. A negative current in the switch indicates a converter fault which creates a short circuit path to ground. The basic function of the ORING controller is to disconnect this current path to ground, thus disconnecting and isolating the faulty stage from the bus.

The primary controller also has a temperature monitoring array of sensors for both Flyback intermediate bus converters. Any detection of an abnormal temperature will trigger an internal fault state which decides whether to completely shut down the stage or run it in a power derating mode. The primary controller performs an under voltage and over voltage lockout function in case the bus converter input voltage is outside the accepted specifications.

The primary controller communicates with the secondary controller via a bi-directional digital isolator. Since optoelectronic components are not accepted for mission-critical space applications due to their sensitivity to radiation and fast aging, the chosen isolator with magnetic transformers.

The POL stages, have a regulated input bus voltage of 12 V and output voltages of 5, 3 and 1.8 V. They are digitally controlled and regulated by the secondary side controller. The output current for the 5 V POL is 6 A, for the 3.3 V POL is 9 A and for the 1.8 V output is 10 A.

As depicted in Fig. 18.15, the secondary controller independently reads the output power for each POL and monitors the bus voltage. It also has a temperature monitoring function, buy monitoring the temperature of each POL. The secondary controller can receive fault signals from the primary controller and can control the ORING stages. In the case of an intermediate bus converter fault, the primary controller sends information to the secondary sides which must react and disconnect the faulty stage. This is a redundant protection in case the ORING controller fails to turn off the output switch.

The primary controller can also send to the secondary controller a temperature warning information in the case the intermediate bus converters are getting close to the maximum temperature limit, such as the secondary controller will prepare to go into a power derating mode for the POL loads which allow it. If the POL load does

not allow power derating mode, then the secondary controller will completely shut down the entire POL stage. The secondary controller can send information to the primary side regarding the bus voltage. If the bus voltage is out of the required specification, the secondary controller will send a shutdown command to the primary controller.

One of the most innovative features of the whole system is that the regulated intermediate bus voltage can be adjusted to make the POL converters operating under the most efficient conditions and/or make the Flyback intermediate bus converter run more efficiently. In the scenario of a high load situation for the POLs, with one of the POL stage goes close to the critical operation temperature, and the Flyback stage is in normal operating temperature, the secondary controller will ask the primary controller for a lower bus voltage, decreasing the POL power losses and decreasing the POL temperature. This works both ways, in the case that if the Flyback reaches the critical operating temperature while the POL is in the nominal operating temperature, the primary controller inquires the secondary controller for POL temperature values. If the POL temperatures are in the nominal regions, the primary controller decides to increase the bus voltage, which reduces the Flyback output current, increases its efficiency and inherently lowers the Flyback temperature.

Figure 18.16 shows the intermediate bus converter efficiency curve versus different loading conditions.

The flyback intermediate bus converter operates in critical conduction mode using primary winding feedback. The control method is current mode control. Because of this mode of operation, voltage switching for the main primary side switch can be obtained.

Figure 18.17 shows the efficiency graph of the POL 5 V Vout converter. The three POL converters have the same hardware components, the output voltage is set by the secondary side digital controller. Figure 18.18 shows the efficiency graph of the POL 1V2 Vout converter. Figure 18.19 shows the efficiency graph of the POL 1V2 Vout converter. All three POL's operate in continuous conduction mode with the switching frequency of 250 kHz. The output filter is composed of a planar inductor E32/6/20 core 3F3 material with 1 turn parallelized on 4 layers and six ceramic capacitors 1210 size 22 uF/25 V.

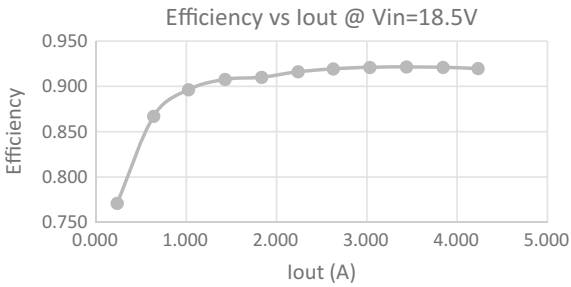

Fig. 18.16 Efficiency graph for intermediate bus converter

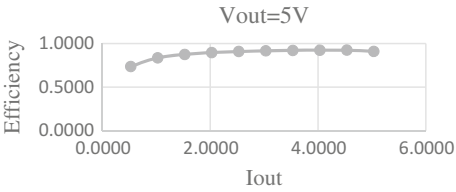

Fig. 18.17 Efficiency graph 5 V POL

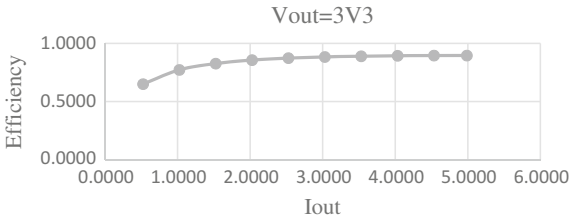

Fig. 18.18 Efficiency graph 3V3 POL

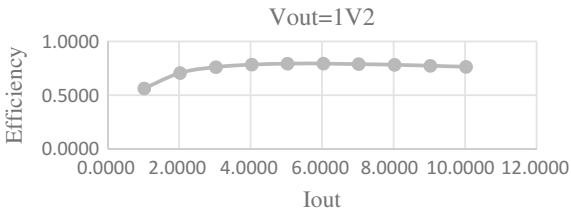

Fig. 18.19 Efficiency graph 1V2 POL

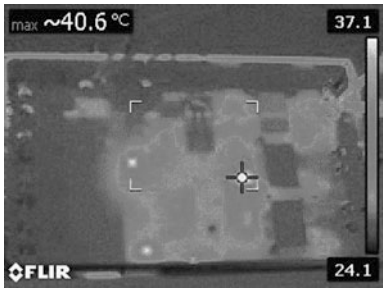

Fig. 18.20 Thermal pictures of the unit

Figure 18.20 shows the thermal imaging of the unit at full load operating conditions. With an ambient temperature of 24° the unit maximum temperature is 40.6° at full load condition. The temperature rise is 16°. The unit is clamped in aluminum housing with gap pad thermal conductive material. The aluminum case extracts heat from the unit in a very efficient way. The components on the PCB are rated to 125 °C and the PCB itself is rated to 150 °C and as a result is way below the maximum temperature of the unit.

Fig. 18.21 Power module testing conditions

Figure 18.21 shows the power module testing conditions. The solar panel and the LiIon battery can be observed. In order to simulate the solar panel in different sunlight conditions a solar array simulator was used.

18.6 Conclusions

Different requirements from conventional power conversion are imposed due to the critical nature of space applications. Any failure will likely trigger a chain of events which may lead to cancelling the mission. Component size restrictions are different from conventional power systems, which, in order to achieve lower end price and higher efficiency, use smaller and more high density and novel parts, which are usually smaller, like smaller resistors and capacitors and ball grid array (BGA) footprints. Especially in space power systems, components have a larger footprint in order to withstand the vibration stress.

In most mission-critical applications there is limited cooling available due to the fact of operation in extreme environments such as the vacuum of space, high altitude, lower or higher pressure and lower or higher temperatures. In such cases, efficiency of the power system is a key parameter in the design. The packaging of the converter is a challenge to design because in the operation in harsh environments the power system needs to be protected from outside elements, but also its inputs and outputs need to be protected with rated connectors. To improve packaging, planar magnetics are the future trend as a replacement for conventional magnetics. The advantages include lower profile, improved cooling, reduced parasitic elements and high repeatability in production. System miniaturization is possible by the use of the planar magnetics and digital control. This feature is very important for power management units designed especially for very small satellites.

The most proven power stage topologies can be imported from conventional power systems. Also the control schemes can be imported from conventional power systems, with an emphasis on parameters monitoring and redundancy. In order to improve converter efficiency new GaN devices can be employed. Intelligent power processing such as intelligent voltage buses help increase the overall power system

efficiency, thus creating much smaller and lighter designs for the electrical power system of the very small satellites.

Acknowledgements This work was supported by a grant of the Romanian National Authority for Scientific Research, Program for research Space Technology and Advanced Research—STAR, project number 80/29.11.2013.

References

1. . http://www.esa.int/Our_Activities/Space_Engineering_Technology/Power_Laboratories
2. Bussarakons T. Thick film hybrid DC-DC converters are standard 'Brick' for satellite power systems. Int Rectifier. http://www.irf.com/product-info/hi-rel/tp-hybridbrick.pdf
3. Dowell PL (2010) Effects of eddy currents in transformer windings. In: IEEE IET proceedings of the institution of electrical engineers, January 2010, vol 113, no 8, pp 1387–1394. ISSN 0020-3270, doi:10.1049/piee.1966.0236
4. Margueron X, Besri A, Lembeye Y, Keradec JP (2010) Current sharing between parallel turns of a planar transformer: prediction and improvement using a circuit simulation software. IEEE Trans Ind Appl 46(3):1064–1071. doi:10.1109/TIA.2010.2046294 0093-9994
5. Prieto R, Garcia O, Cobos JA, Uceda J (2002) Designing inductors at device and converter level. In: IEEE proceedings of the 2002 international symposium on industrial electronics (ISIE 2002), vol 3, pp 987–993. Print ISBN: 0-7803-7369-3, doi:10.1109/ISIE.2002.1025868
6. Xu H, Ngo KDT, Bloom G (1995) Design techniques for planar windings with low resistances. In: IEEE tenth annual proceedings of applied power electronics conference and exposition (APEC 1995), March 1995, vol 2, part 2, pp 533–539. Print ISBN: 0-7803-2482-X, doi:10.1109/APEC.1995.469073
7. Ouyang Z, Thomsen C, Andersen MAE (2012) Optimal design and tradeoffs analysis if planar transformer in high power DC-DC converters. IEEE Trans Ind Electron 59(7):2800–2810. doi:10.1109/TIE.2010.2046005 0278-0046
8. Acero J, Carretero C, Millan I, Lucia O, Alonsoa R, Burdio JM (2011) Analysis and modeling of planar concentric windings forming adaptable-diameter burners for induction heating appliances. In: IEEE transactions on power electronics, May 2011, vol 26, no 5, pp 1546–1558. ISSN: 0885-8993, doi:10.1109/TPEL.2010.2085453
9. Tan D (2014) A review of intermediate bus architecture: a system perspective. IEEE J Emerg Sel Top Power Electron 2(3):363–372. doi:10.1109/JESTPE.2014.2303154 ISSN: 2168-6777
10. Sutto T (2010) 2 switch forward current mode converter. ON semiconductor application note AND8373D. http://www.onsemi.com/pub_link/Collateral/AND8373-D.PDF
11. Saliva AA (2013) Design guide for QR flyback converter. Infineon Technologies North America (INFA) Corporation, January 2013. http://www.mouser.com/pdfdocs/2-9.pdf
12. Fairchild Application Note AN4151 (2014) Half bridge LLC resonant converter design using FSFR-series fairchild power switch (PFS). https://www.fairchildsemi.com/application-notes/AN/AN-4151.pdf
13. Erickson RW, Maksimovic D (2001) Fundamentals of power electronics, 2nd edn. Springer, New York. ISBN -13: 978-1475705591
14. Mohan N, Undeland TM, Robbins WP (2003) Power electronics: converters, applications, and design, 3rd edn. Wiley, USA. ISBN -13: 978-0471226932
15. Tan D (2015) Emerging system applications and technological trends in power electronics. IEEE Power Electron Mag 2(2):38–47
16. Tan D (2015) Power-conversion technology is going adiabatic: adiabatic point-of-load technology for space applications. IEEE Power Electron Mag 2(4):47–53

17. Rashid MH (2014) Power electronics: circuits, devices and applications, 4th edn. Prentice Hall, USA. ISBN -13: 978-0133125900
18. Lidow A, Strydom J, Rooij M, Reusch D (2014) GaN transistors for efficient power conversion, 2nd edn. Wiley, USA. ISBN 978-1-118-84476-2
19. Reusch D, Glaser J (2015) DC-DC conversion handbook: a supplement to GaN transistors for efficient power conversion. Power Conversion Publication. ISBN-10: 0996649204
20. http://epcco.com/epc/Portals/0/epc/documents/briefs/AB006%20eGaN%20FETs%20for%20POL.pdf
21. http://epc-co.com/epc/Applications/DC-DCConversion/PointofLoadConverters.aspx

Chapter 19
Determining the Optimal Battery Model for a Specific Application

Bogdan-Adrian Enache

Abstract Determining the optimal battery model for a specific application is a complex process that must take into account several factors: the type of application, the accuracy required, the degree of complexity, etc. This chapter introduces a new method for determining the optimal model and has its starting point in analyzing the discharge profile, and employs a multi-criteria analysis for processing the experimental data. The method presented is validated experimentally for a $LiFePO_4$ battery subjected to discharge after an Urban Dynamometer Driving Schedule (UDDS) cycle.

Abbreviation and Acronyms

BMS	Battery Management System
DC	Direct Current
LFP	$LiFePO_4$ battery
MCA	Multi-Criteria Analysis
OCV	Open Circuit Voltage
PCB	Protection Circuit Board
RC	Resistance–Capacitor
SoC	State of Charge
SoH	State of Health
UDDS	Urban Dynamometer Driving Schedule

19.1 Introduction

In order to operate, electric vehicles, just like mobile devices, require the energy stored in their batteries. The limitations on the amount of energy that can be stored, as well as the limitations concerning safe operation, restrict the employability of

B.-A. Enache (✉)
Faculty of Electronics, Communications and Computers, University of Pitesti, Pitesti, Romania
e-mail: b0gdan.enache@yahoo.com

N. Bizon et al. (eds.), *Energy Harvesting and Energy Efficiency*, Lecture Notes in Energy 37, DOI 10.1007/978-3-319-49875-1_19

batteries within certain, very strict limits. Battery operation within these limits is the responsibility of the Protection Circuit Board (PCB) that equips the battery. Further developments of the PCB were made in order to extend is applicability not only to safety issues but also to better energy efficiency and so the Battery Management System (BMS) was born.

These devices receive as input the operating parameters of the battery, and based on the logic that they implement, ensure the extraction of the maximum capacity of the battery within the boundaries specified by the manufacturer. Due to the complex processes that occur within the battery, some of these parameters, such as State of Charge (SoC) and State of Health (SoH), cannot be measured directly. However, these characteristics are critical for the energy efficiency of the battery, therefore they must be assessed by a different method. Currently, the most widely used method for determining the SoC and SOH is by approximating them based on a model of the battery operation. By embedding such a model into the BMS a significant improvement in battery capacity during discharge is achieved [1].

The main strategies of developing a functional model of the battery are the electrochemical approach and the approach oriented towards electric circuits, but there are also models that combine elements of both strategies.

The electrochemical models are based on the description of the processes occurring within the battery. They are used to explain the electrochemical phenomena occurring when the electrode interacts with the electrolyte [2]. Therefore they make use of differential equations systems with several unknowns. Using a computer to solve the equation systems gives rise to algebraic loops that need approximation methods to remove them and also to reduce the number of parameters involved. The big advantage of the electrochemical models is their high accuracy. Using such a model in [3] is obtained, for a Li-ion battery, an error smaller than 0.01% to approximate the SoC.

The models based on circuits use electrical and electronic components to describe the behaviour of the battery subjected to discharge. They have as a common source the *Rint* (*elementary*) *model*, which is composed only of a DC voltage source and a resistor set in series. Starting from this, other models have been developed by adding parallel resistor-capacitor branches. The accuracy of the most popular models based on electric circuits is analyzed in [3] which reports for a $LiMn_2O_4$ battery that is subjected to discharge at constant current a maximum relative error in determining the SoC between 0.1 and 0.35%. Unlike the electrochemical models, the models based on electric circuits have lower accuracy, but their easy development and implementation makes them ideal for incorporation into simulation programs.

The analytical models are models that combine properties of the electrochemical models and of the models based on circuits. Their aim is to develop a model that contains a small number of equations and a high accuracy, while at the same time being easy to use in other programs.

Because of the fact that models are being developed along three different directions, choosing the optimal model is a complex issue, which must take into

account many factors, of which the most important are: the scope of the application, the degree of accuracy and the time required to make the model.

In order to develop a BMS for portable devices, where the accuracy of the model used is not the most important parameter, but rather the ability to run in real-time on embedded systems, simple models based on electric circuits are the ideal solution [4, 5].

As far as the applications for electronic devices in which the main factor of interest is displaying the SoC for the user, the models based on electric circuits compete with the analytical ones, as the discriminating factor is their computational complexity.

On the other hand, the sole viable solution for the hybrid vehicles applications designed to reduce fuel consumption, to determine the car performance, or improve the parameters of the batteries, which are usually carried out offline and require high accuracy, are the electrochemical models [3].

The recommendations listed above are general, and are only useful so far as the categorization of the model is concerned, and not for choosing the model itself.

In order to determine the optimal battery model for a specific application a new method based on the analysis of the discharge profile and the use of a multi-criteria analysis (MCA) is presented. This methodology, which is the main contribution of this chapter, was developed for better BMS development and it combines energy efficiency with ease of implementation. The proposed methodology is best suited for Li-Ion batteries which present highly non-linear evolution of the SoC and other parameters.

Li-ion batteries are currently the most common type for power the mobile electronic devices and electric cars. The best known structures of these batteries are: $LiCoO_2$, $LiMn_2O_4$, $LiNiO_2$, $LiNiMnCoO_2$, $LiNiCoAlO_2$, $LiFePO_4$, and they combine high energy density with high power density. Their main disadvantage is related to the flat plateau area from the discharge characteristic which makes very difficult the determination of the SoC [6]. Among these batteries the $LiFePO_4$ (LFP) ones, which use a graphite anode and a cathode made of Li ferrophosphate distinguish them self. The olivine structure of the cathode gives these batteries a high structural and thermodynamic stability, making them the safest Li-based batteries [7]. Besides the advantages of safety and the fact that their structure does not contain rare metals (Ni, Co, Mn, etc.), LFP batteries also present a set of negative aspects as compared to the rest of Li-Ion batteries. The most important of them are the low energy density, the low electrical potential (3.2–3.3 V compared to 3.6–3.7 V that is typical for Li-Ion batteries) and the strongly non-linear discharge characteristic.

The next of the chapter is organized as follows: Sects. 19.2–19.4 describe the most known types of modeling strategies—electrochemical, analytical and circuit based followed by the proposed screening process for determining the optimal model for a specific application and a case study to validate it.

19.2 Electrochemical Models

The electrochemical models describe the behaviour of batteries based on the chemical processes that occur between the electrodes and the electrolyte. They use a set of differential equations to represent, in time, the processes of ion diffusion, transportation, reduction, oxidation, and distribution, and the side effects occurring in the battery. Solving these equations yields the time evolution of the battery voltage and current.

The complexity of the chemical processes determines the complexity of the model, and thus the number of differential equations needed for it.

There are several electrochemical models, which, starting from the lumped model which needs only two equations, evolve towards the very complex models that require up to six equations and more than 50 parameters in order to describe the behaviour of the battery.

19.2.1 The Lumped Model

The lumped model was one of the first models that described the processes that take place in the battery with a less complex chemical structure, such as lead-acid batteries or some Ni-MH batteries.

This model is based on the Butler-Vormer equations and the Nerst theory, and considers the spatial distribution of the chemical elements between the two electrodes as uniform.

In this model the Open Circuit Voltage (OCV) generated by the electrochemical processes is given by the Nerst equation [3]:

$$\Phi(t) = \Phi^0 - \frac{RT}{nF} \ln\left(\prod_k \left(m_k(t)\gamma_k\right)^{\nu_k}\right) \tag{19.1}$$

where:

- $\Phi(t)$—the potential of an electrode [V];
- Φ^0—the electromotive force under standard conditions [V];
- R—the universal gas constant;
- T—temperature [K];
- F—Faraday's constant [C/mol];
- k—number of participants in the reaction;
- m—molarity;
- γ—the activity coefficient;
- ν—stoichiometric ratio

To determine the current density of the battery the Butler-Vormer equation is used [2]:

$$J(t) = J_0\left[e^{\frac{\alpha F}{RT}\eta(t)} - e^{\frac{(1-\alpha)F}{RT}\eta(t)}\right] \tag{19.2}$$

where:

- J_0—density of transfer current;
- α—transfer coefficient;
- η—polarization.

The advantage of this model is that it uses only two simple equations, which are easy to integrate in a simulation software. Thus, a model was developed for a Ni-MH cell, which allowed simulating its behavior in a matter of milliseconds by using the existing computers [4].

The main disadvantage of the lumped model is that the equations that it uses are insufficient to describe the complex processes taking place in the modern batteries, which use advanced materials such as Li-ion, Li-Po, metal-air, etc. To model such batteries a new class of models has been developed, which have as a starting point the porous electrode theory. Among these the best known model is the Doyle-Fuller-Newman model which is presented next.

19.2.2 The Doyle–Fuller–Newman Model

The Doyle-Fuller-Newman model describes in detail the electrochemical processes of ion diffusion, transport and distribution that take place into a Li-ion battery. The structure of a Li-ion cell—Fig. 19.1, consists of an anode and a cathode made from a porous material, which are isolated by a separator, the whole assemblage being immersed in the electrolyte.

When the battery is charged, the *Li* ions occupy the interstitial space within the anode. As the battery discharges, the *Li* ions leave the anode and enter the electrolyte. From there they pass through the separator and reach the cathode. This migration of ions ends when they reach the cathode and occupy an interstitial space within it. When *Li* ions leave the anode, an electron is released into the external circuit, generating power. When that electron reaches the cathode, it allows a *Li* ion to occupy a position inside it. Charging retraces the *Li* ions path, yet backwards, and now the cell receives power from the external circuit cell instead of delivering electricity.

The Doyle-Fuller-Newman is also known as the 1D model because it considers the dynamic processes as taking place only along one axis (the horizontal axis—*x*). This approximation is made because the length of a cell structure along the *x*-axis is

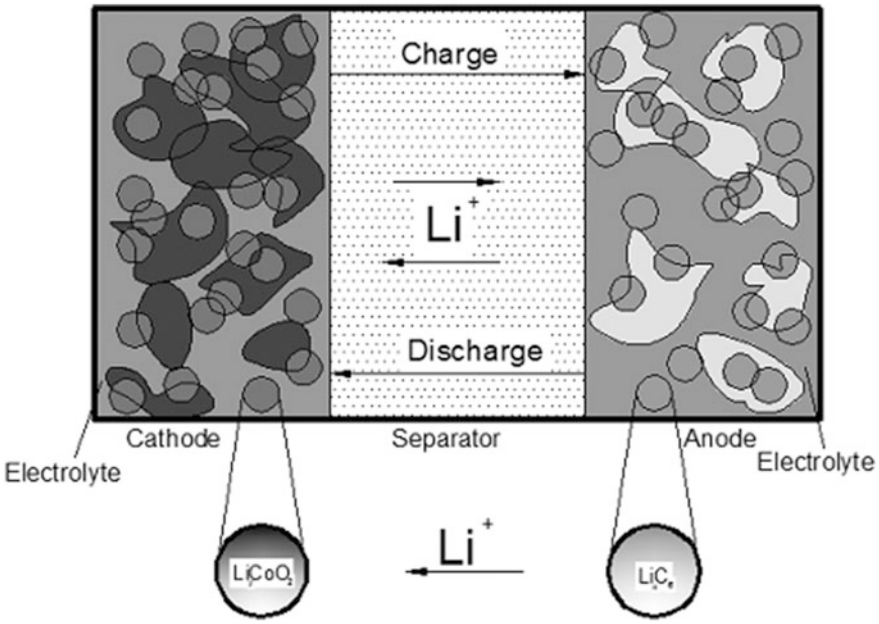

Fig. 19.1 Structure of a Li-Ion cell [2]

much smaller (of the order of 100 μm) than the length of the structure for the other axes (ranging up to 100,000 μm) [3].

The model uses a set of differential equations to describe the linear diffusion of *Li* ions in the electrolyte and the solid material of the electrodes, as well as the spatial distribution of the electrochemical processes generated as part of that process. These equations are obtained from Fick's diffusion law (for *Li* ion concentration), Ohm's law (for electric potential distribution) and the Nerst and Butler-Vormer equations [8]. The coefficients occurring in these equations are listed in Table 19.1.

The 1D model is based on the diffusion of *Li* ions in the solid material of the electrodes. This diffusion occurs at each point of the anode and the cathode, and is modelled by the following equation, where the particles taking part in the reaction are considered to be spherical [9].

$$\frac{\partial c_{1,j}}{\partial t}(r,t) = \frac{d_{1,j}}{r^2}\frac{\partial}{\partial r}\left(r^2\frac{\partial c_{1,j}}{\partial r}(r,t)\right) \tag{19.3}$$

Table 19.1 Symbols used for the Doyle–Fuller–Newman model

Symbol	Name	U.M.
L_n	Thickness of the anode	m
L_s	Thickness of the separator	m
L_p	Thickness of the cathode	m
R_n	Radius of anode particles	m
R_p	Radius of cathode particles	m
t^+	Transfer number	–
b	Brugman's number	–
d_2	Diffusivity of solution	m^2s^{-1}
ε_{2n}	Fractional volume of the anode solution	–
ε_{2s}	Fractional volume of the separator solution	–
ε_{2p}	Fractional volume of the cathode solution	–
d_{1n}	Diffusivity of anode solid material	m^2s^{-1}
d_{1p}	Diffusivity of cathode solid material	m^2s^{-1}
k_n	Anode reaction rate	$(Am^{-2})\ (mol\ m^{-3})^{1+\alpha}$
k_p	Cathode reaction rate	$(Am^{-2})\ (mol\ m^{-3})^{1+\alpha}$
R_{SEI}	Thickness of the anode layer	m
c_2	Concentration of the initial solution	$mol\ m^{-3}$
u_{nref}	Anode balance potential	V
u_{pref}	Cathode balance potential	V
k	Solution conductivity	Ωm

On the other hand, the concentration of *Li* ions in the electrolyte—$c_2(x,t)$, depends on the current density J and is described by Fick's law [9]:

$$\varepsilon_2 \frac{\partial c_2}{\partial t}(x,t) = \frac{\partial}{\partial x}\left(d_2^{eff}\frac{\partial c_2}{\partial t}(x,t)\right) + \frac{1-t^+}{F}J(x,t) \tag{19.4}$$

The current density J is determined by the potential difference between the electrolyte solution and the solid material of the electrodes, and is, according to the Butler-Vormer relationship [9]:

$$J(\mathrm{x},t) = a_j i_{0,j}\left[e^{\frac{\alpha_{a,j}F}{RT}\eta_j(\mathrm{x},t)} - e^{-\frac{\alpha_{c,j}F}{RT}\eta_j(\mathrm{x},t)}\right] \tag{19.5}$$

$$i_{0,j} = k_j\left(c_{1,j}^{\max} - c_{1,j}^{S}\right)^{\alpha_{a,j}}\left(c_{1,j}^{S}\right)^{\alpha_{c,j}}(c_2)^{\alpha_{a,j}}, j = n,p \tag{19.6}$$

The electrochemical potential of the two electrodes, including both the solid material and the electrolyte solution, is described mathematically by the relations [9]:

$$\begin{cases} \eta_p(x,t) = \phi_1(x,t) - \phi_2(x,t) - u_{pref}(x,t) \\ \eta_n(x,t) = \phi_1(x,t) - \phi_2(x,t) - u_{nref}(x,t) - \frac{J(x,t)}{a_n}R_{SEI} \end{cases} \tag{19.7}$$

Considering Ohm's law, the potential for each component of the electrodes can be determined by means of the relationships [9]:

$$\frac{\partial}{\partial x}\left(\sigma_j^{eff}\frac{\partial \phi_{1,j}}{\partial x}(x,t)\right) - J(x,t) = 0 \tag{19.8}$$

$$\frac{\partial}{\partial x}\left(k^{eff}\frac{\partial \phi_2}{\partial x}(x,t)\right) + J(x,t) + \frac{\partial}{\partial x}\left(k_D\frac{\partial}{\partial x}\ln(c_2(x,t))\right) = 0 \tag{19.9}$$

The differential equations system (19.3)–(19.9) represents the 1D model for a cell Li-ion cell that is both in the process of discharging and in the process of recharging.

The traditional methods for solving this equations system are based on the finite difference technique, which consists in dividing the x axis into equal intervals that are small enough to allow estimation of derivatives using Taylor series.

Another way to process it is by linearization and solving the equations using the BAND subroutine [10]. This subroutine is coded in COBOL and solves nonlinear of equations systems with partial derivatives. The subroutine underlay the development of the DUALFOIL software, which is used for modelling and simulation of complex-structure batteries.

19.2.3 DUALFOIL

DUALFOIL is a free software, coded in FORTRAN, which enables modelling and simulation of such batteries as Lithium-metal, Li-ion, Na-ion and Ni-MH.

To be used, the program requires an input file with the specific parameters of the battery being modelled. The user must enter in this file, in addition to the battery discharge profile, no less than 50 parameters concerning its geometrical and electrochemical properties. Among them are the thickness and porosity of the electrodes, the initial temperature, salt concentration in the electrolyte, heat dissipation capacity for the entire battery, diffusion coefficient, etc. [10].

After running, the program produces four output files. The main file contains the values for the most important parameters: time, current, voltage and battery temperature. The remaining files contain more detailed reports about the battery operating mode; the most important being the file that describes the evolution of internal resistance.

In order to be used, the DUALFOIL program requires detailed knowledge about the battery to be modelled, which is not always accessible to the average user. But once this obstacle has been overcome, the results of the modelling are of high fidelity, and are often used as benchmarks for determining the accuracy of other models.

The electrochemical models are based on a linear equations system that describe the electrochemical phenomena that takes place inside the batteries. To solve this

system, a whole range of techniques of simplification and approximation are used, which do not significantly affect the accuracy of the model, but do not reduce its complexity, either. Electrochemical models generally have a high accuracy, yet they require long periods of time for simulation and detailed knowledge about the electrochemical structure of the batteries that are being modelled. For this reason they cannot be incorporated into other simulation systems that include other functional elements apart from batteries.

To facilitate incorporation of the battery model within a more general simulation system electrochemical models have been abandoned for models whose accuracy is smaller, while also being less complex. These models were grouped into two classes: analytical models, and models based on electric circuits.

19.3 Analytical Models

Analytical models describe the behaviour of the battery at a higher level of abstraction than electrochemical models. They have been developed from experimental tests performed on the battery, and the obtained data were processed by curve fitting techniques. The great advantage of these models is that they manage to describe the behaviour of the battery using a small number of equations. The best known analytical models are the Shepherd model and the Peukert model which are presented next.

19.3.1 The Peukert Model (Peukert's Law)

Wilhelm Peukert studied the behaviour of lead-acid batteries subjected to constant current discharge. Following these tests, he noticed that only one equation is sufficient to determine the remaining battery capacity for a discharge current:

$$C = I^k \cdot t \tag{19.10}$$

where:

- C—battery capacity, expressed in Ah;
- I—discharging current;
- t—discharge time, in hours;
- k—calibration coefficient.

Equation 19.10 is known as Peukert's law, and was developed to model the behaviour of the battery for different discharge currents.

When a battery is subjected to discharge using increasingly higher constant currents, it was found that the battery internal resistance increases and the discharged battery capacity (up to the cutoff voltage) decreases. To compensate for

these losses Peukert introduced the calibration coefficient k, also known as Peukert's coefficient.

The value of Peukert's coefficient is determined experimentally using two different battery discharge curves. If we consider that the battery is discharged in time t_1 for the current I_1, and in t_2 for the current I_2, then, applying Eq. (19.10), one gets:

$$\left.\begin{aligned} C &= I_1^k \cdot t_1 \\ C &= I_2^k \cdot t_2 \end{aligned}\right\} \Rightarrow I_1^k \cdot t_1 = I_2^k \cdot t_2 \Rightarrow \left(\frac{I_1}{I_2}\right)^k = \frac{t_2}{t_1} \Rightarrow$$
$$k \cdot \ln\left(\frac{I_1}{I_2}\right) = \ln\frac{t_2}{t_1} \Rightarrow k = \frac{\ln\frac{t_2}{t_1}}{\ln\left(\frac{I_1}{I_2}\right)} \tag{19.11}$$

Introducing the calibration coefficient was only a partial solution for determining the capacity discharged from the battery. It has been experimentally proven that, in a battery subjected to discharge under a high value current, even after the cutoff voltage is reached, the available capacity it is not zero [11]. This remaining capacity is caused by the decrease of the active centers number in the active substance at the cathode and the rapid increase in the resistance for the interaction between the anode and the electrolyte [12, 13].

Similarly, it was demonstrated experimentally that the Peukert model can only be applied to batteries that are subjected to discharge at constant current and constant temperature. In many real situations, however, the battery discharge is done using varying currents within an extended temperature range. In such circumstances, the Peukert model usually approximates a smaller capacity for the battery [11].

A first attempt to adapt the Peukert model, when the discharging current is variable, involves using an effective pseudo-current. Thus the discharge alternating current is discretized in several areas where its value can be considered constant; and for those areas the value of the pseudo-current (I_{eff}) is calculated, using the relationship:

$$I_{eff} = I \cdot \left(\frac{I}{I_{nom}}\right)^{k-1} \tag{19.12}$$

where I is the constant discharge current, I_{nom} is the rated discharge current supplied by the manufacturer (usually, a battery discharge time of 20 h).

In this situation the total discharged capacity (C_d) from the battery is determined for each constant current range (Δt) as:

$$C_d = \sum \left(I_{eff} \cdot \Delta t\right) \tag{19.13}$$

This method is generally accepted as an improvement on the Peukert model [14] for variable currents; however its accuracy is limited because it neglects the temperature effects over the discharge.

Another way to improve the Peukert model proposes an equation that includes the effects of both a variable current and the temperature variation. Accordingly, the capacity discharged from the battery is defined as:

$$\Delta C_d = f(I, T) \tag{19.14}$$

Considering the least favorable case, when the discharging temperature drops and the current increases, in order to describe the behaviour of the variable discharge current this relationship is used:

$$f(I) = \left(\frac{I}{I_{nom}}\right)^{\alpha} \tag{19.15}$$

where α is a constant that depends on the type of the calibration coefficient.

To describe the behaviour of the temperature within the discharge process, a function similar to that presented in (19.15) is used.

$$f(T) = \left(\frac{T_{nom}}{T}\right)^{\beta} \tag{19.16}$$

where: T_{nom} is the rated discharge temperature, T is the temperature in the discharge process, and β is a coefficient that depends on the battery technology and the battery configuration.

Considering the relations (19.15) and (19.16), an improved Peukert model is given by:

$$\Delta C_d = \gamma \cdot \left(\frac{I}{I_{nom}}\right)^{\alpha} \cdot \left(\frac{T_{nom}}{T}\right)^{\beta} \tag{19.17}$$

where γ is a coefficient that compensates the combined effect of α and β coefficients.

This model has been verified experimentally, and it was shown to have an error of less than 5% for an extended range of temperature and discharge currents [14].

The Peukert model is one of the simplest and most enduring models developed to simulate battery behaviour. Although it has undergone some changes over time, it remains a model with a limited degree of accuracy, which is used, in particular, to deal with batteries with a simple structure. For batteries that involve more complex phenomena in the process of discharge, the Peukert model is not sufficient. For such batteries a different model that combines ease of use with high accuracy, namely the Shepherd model is used.

19.3.2 The Shepherd Model

The Shepherd model was developed to optimize the capacity/weight ratio of the batteries used by the US Navy. To achieve this objective it was considered necessary to develop a model that could express the dependence of the output voltage of the battery for a specific the discharge [15].

Developing the model was done according to the following hypotheses:

- The anode and cathode have porous active materials;
- The electrolyte and the electrodes are homogeneous;
- The electrodes are parallel;
- The current density is evenly distributed between the two electrodes;
- The distance between the electrodes is small compared with their dimensions (width, length);
- The temperature is constant;
- Internal resistance is constant;
- The battery is discharged at a constant current.

After formulating the hypotheses, the development of the model passed on obtaining the discharge curves for different types of batteries: Ni-Cd, silver-zinc-alkaline; Air-zinc-alkaline, lead-acid, etc. On this basis Shepherd noted that any discharge feature presents three distinct areas which are presented in Fig. 19.2 and are:

- The initial area;
- The zone determined by the polarization effects;
- The zone determined by internal resistance;

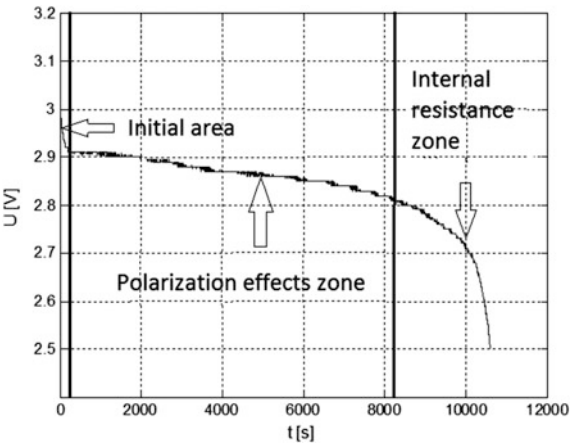

Fig. 19.2 The discharge zones for a $LiFePO_4$ battery

After establishing the discharge zones, Shepherd approximated their evolution by a series of curves with known equations. As a result of this process, it was determined that the equation that best models the discharge behavior of the battery is:

$$V_{batt} = E_0 - K \cdot \left[Q / \left(Q - \int idt \right) \right] \cdot i - R_0 \cdot i \tag{19.18}$$

where:

- V_{batt}—output voltage of the battery (V);
- E_0—open circuit voltage (V);
- K—polarization coefficient (Ω);
- Q—battery capacity (Ah);
- i—discharge current (A)
- R_0—battery internal resistance (Ω).

This relationship is known as the Shepherd model. It presents a nonlinear term $K \cdot \left[Q / \left(Q - \int idt \right) \right]$ that models the terminal voltage variation in accordance with the magnitude of the discharge current. This behaviour is specific to real batteries, but this term generates an infinite loop and instability in simulation [16].

For the Shepherd model to be usable in simulations software, the algebraic loop must be removed. The models obtained in this way are known as simplified Shepherd models, and the most representative such model is described by the relation [17]:

$$V_{batt} = E_0 - K \cdot [Q / (Q - i \cdot t)] + A \cdot \exp(-B \cdot it) \tag{19.19}$$

where:

- A—the amplitude at the end of zone 1 (V);
- B—the inverse value of the capacity discharged at the end of zone 2 (Ah^{-1}).

The Shepherd model has the great advantage of incorporating, into a single equation, the dependence of output voltage for a discharge current. This makes it easy to use in a complex simulation system that also includes other operation equations for the components involved.

As regards the simulation systems that use electrical and electronic components, the Shepherd model, and by extension analytical models, cannot be used, so a new category of models was developed specifically for these systems, i.e. models based on electric circuits which are presented next.

19.4 Models Based on Electric Circuits

The models based on circuits describe the electrochemical phenomena that occur as part of the batteries, using only electrical and electronic components. They typically use voltage sources, resistors and capacitors to model the variation of the output voltage for a specific discharge current and SoC.

The complexity of the system is given, in general, by the number of components used in the model. The simplest systems use only a voltage source and a resistor, and the most complex ones use in addition one or more parallel resistor—capacitor branches.

19.4.1 The Elementary (Rint) Model

The simplest circuit model used to describe the behaviour of a battery consists of a voltage source whose value is equal to the OCV of the battery (E_0) and a resistance whose value is equal to the internal resistance of the battery (R_0)—Fig. 19.3.

If a load is connected to the terminals of that circuit, it will produce a current in the circuit which, according to Kirchhoff's second theorem, will have the expression:

$$I = \frac{E_0 - V_{batt}}{R_0 + R_L} \tag{19.20}$$

where V_{batt} is the output voltage, and R_L is the load resistance.

The emergence of the discharge current will lead to a lower battery capacity, and consequently to a output voltage drop. To model this behaviour it is necessary that both the value of the supply voltage and the value of the internal resistance should change in concordance with the battery SoC. This being the case, the easiest method for determining the remaining battery capacity consists in integrating the

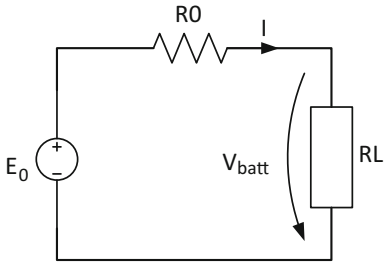

Fig. 19.3 The elementary (Rint) model

discharge current over time. Thus, by integrating Eq. (19.20) one gets the variation of the SoC for a specific discharge current:

$$SOC(t) = SOC(t_0) - \frac{1}{Q_{NOM}} \int_{t_0}^{t} I(t)dt \tag{19.21}$$

where:

- $SOC(t)$—the battery charge status at a given time t;
- $SOC(t_0)$—the battery charge status at the beginning of the discharge;
- Q_{NOM}—rated capacity of the battery;
- I—discharge current.

In those specific cases where the battery charge state is very well determined, the discharge current has very low variance, and the discharge time is also short, the elementary model is sufficient to accurately model the behaviour of the battery.

The elementary model considers the battery to be an ideal voltage source whose value depends only on the discharge current and SoC, but it fails to consider more complex phenomena such as polarization or hysteresis, and therefore in the more complex simulations its accuracy is limited.

A way for increasing the elementary model's accuracy in incorporating a number of nonlinear elements to reproduce the more complex phenomena occurring in the battery. One of these models is the Thévenin model.

19.4.2 The Thévenin Model

It is a circuit-based model, which extends the elementary model by adding a parallel group consisting of a resistor and a capacitor (an RC branch)—Fig. 19.4.

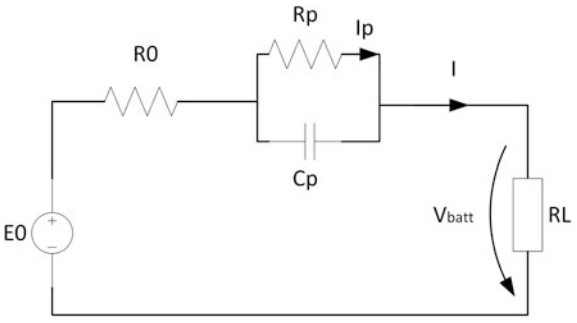

Fig. 19.4 The Thévenin model

Applying Kirchhoff's second theorem for the Thévenin, one gets:

$$V_{batt} = E_0 - R_0 \cdot I - R_p \cdot I_p \tag{19.22}$$

where R_p is the polarization resistance and I_p is the polarization current.

The polarization current is obtained by applying Kirchhoff's first theorem to the circuit node and taking into account the expression of the current on the polarization capacitor C_p side:

$$\frac{dI_p}{dt} = \frac{(I - I_p)}{\tau} \tag{19.23}$$

where $\tau = R_p C_p$ is the time constant of the circuit.

A discrete solution of the Eq. (19.23) is [18]:

$$I_{p,i} = \left(1 - \frac{1 - \exp(-\Delta t/\tau)}{-\Delta t/\tau}\right) \cdot I_i + \left(1 - \frac{1 - \exp(-\Delta t/\tau)}{-\Delta t/\tau}\right) \cdot I_{i-1} + \exp(-\Delta t/\tau) \cdot I_{p,i-1} \tag{19.24}$$

Keeping the same discretization pace and applying the solution provided by Eq. (19.24) in the Eq. (19.22), the equation for the Thévenin model is obtained in a discrete form:

$$V_{batt,i} = E_0 - R_0 \cdot I_i - R_p \cdot I_{p,i} \tag{19.25}$$

This Eq. (19.25) is the basis for determining the values of the components used in the model. The main techniques for extracting the parameters of the model are based on the analysis of a discharge pulse or approximation and errors minimizing strategies.

The Thévenin model is able, by adding the RC branch, to model both polarization effects and the effects of the loss of capacity due to the high current discharge [3]. From this point of view it manages to describe some of the complex processes that occur within the battery without appealing to complicated differential equations.

The Thévenin model combines the electrochemical effects occurring into the batteries with the ease of use and easy integration into simulation systems, which makes it a model often used both by battery manufacturers and developers of systems for the automotive industry.

19.4.3 The R-C Network Model

It is a model that extends the Thévenin model by adding several parallel resistance–capacitor branches—Fig. 19.5. The number of RC branches models the transitory behaviour of the battery through a truncated exponential series. They determine, in fact, the resolution of the system response for various input signals.

For a real battery there are no exponential series that can entirely model its behaviour, therefore the number of RC branches must be chosen in such a way as to best approximate the behaviour of the battery for a particular discharge profile [18].

By applying Kirchhoff's first theorem to each node of the RC networks and taking into account that the voltage on an RC branch is the same for both the capacitor and the resistor, one can obtain the differential equation of the system:

$$\begin{bmatrix} \dot{V}_{C1} \\ \dot{V}_{C2} \\ \vdots \\ \dot{V}_{Cn} \end{bmatrix} = \begin{bmatrix} -\frac{1}{R_1 C_1} & 0 & \dots & 0 \\ 0 & -\frac{1}{R_2 C_2} & \dots & 0 \\ 0 & 0 & \dots & -\frac{1}{R_n C_n} \end{bmatrix} \cdot \begin{bmatrix} V_{C1} \\ V_{C2} \\ \vdots \\ V_{Cn} \end{bmatrix} + \begin{bmatrix} \frac{1}{C_1} \\ \frac{1}{C_2} \\ \vdots \\ \frac{1}{C_n} \end{bmatrix} \cdot i \qquad (19.26)$$

where V_{C1}, V_{C2}, ... V_{Cn} represent the voltages over the branches RC_1, RC_2, ... RC_n, R_1, R_2, ... R_n—the resistances in the RC branches, C_1, C_2, ... C_n—the capacity of the capacitors of the RC branches, and i the discharge current.

By solving the Eq. (19.26), and considering Kirchhoff's second theorem, the equation of the RC network model is obtained:

$$V_{batt} = E_0 - R_0 \cdot I - V_{C1} - V_{C2} - \cdots - V_{Cn} \qquad (19.27)$$

where E_0 is the OCV who dependents on SoC, and R_0 the internal resistance.

The parameters to be determined for the use of this model are: E_0 function of SoC, R_1, R_2, … R_n respectively C_1, C_2, … C_n.

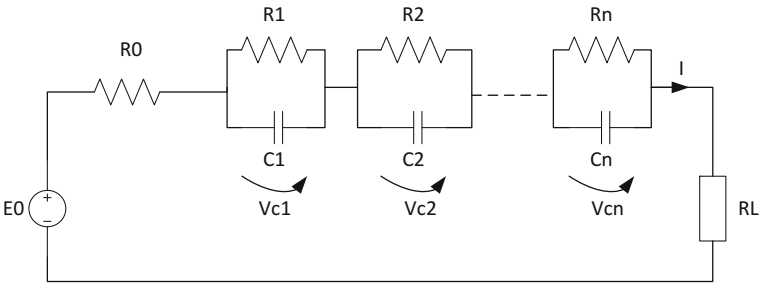

Fig. 19.5 The RC network model

19.5 Determining the Optimal Battery Model for a Specific Application

Determining the optimal battery model for a specific application is actually a problem of establishing a compromise between accurately approximating the experimental data and the complexity of the model. In general, the complexity of the model is limited by the computational resources and the correlation of the phenomena occurring inside the battery with the number of elements that are part of it [19].

Another indispensable factor that needs to be taken into account when determining the optimal model is the nature of the discharge profile. As a result of experimental measurements carried out in [20] it is shown that in discharge profiles involving rapid current changes, the response of the system is determined by the component with the lowest time constant.

In general the most common discharge profiles is the constant current discharge [21, 22] or slow variation pulses [23]. For this case, the determination of the optimal model is done by analyzing the response of the system to a discharge impulse at 10% of the SoC [21]. This method of analysis cannot be applied in the case of complex profiles that include rapid variations of the discharge current.

Taking into account all of the above, next is presented a novel method for determining the optimal battery model for a specific application. This method comprises of two phases: a discharge profile analysis and a data processing stage for choosing the model that combines best approximation of the experimental data with the minimum of resources used.

In the first stage from the discharge profile are extracted the areas that have rapid variations of the discharge current and the areas where the discharge current is constant, namely plateau areas. Since a single model should best approximate both areas, the less favorable ones are extracted. These areas are the area where the variation of the discharge current occurs within the shortest period of time, and the area where the plateau discharge has the longest period. For those areas the response speed of the models undergoing analysis will be determined.

In the second stage the experimental data previously obtained are processed by a MCA and the optimal model is determined.

MCA is a tool for comparison and ranking of the different results, even when using multiple evaluation criteria [24]. It operates with several concepts, of which the most important are: the option, the criteria, the performance matrix, the score and weight.

The **options** are items that are subject to comparison or hierarchy. Of these, after applying the MCA, the best solution (option) is chosen according to certain criteria.

A **criteria** is the measure according to which the options are assessed. Each criteria measures a relevant aspect of the option, and should not depend on any other criteria.

Systematization of data, as part of the MCA, is done by using the **performance matrix**. Each row of the matrix represents option, and each column includes an

evaluation criteria. The values that are recorded in each cell represent the performance level of an option for a particular evaluation criteria.

The **score** (the number of **points**) represents the value of the consequences generated by each option. They are usually standardized for a scale between 0 and 100, where the best option gets 100, and the remaining options get values proportional to their performance.

The **weights** represent a percentage values assigned to each criteria in order to highlight its importance. The sum of the weights must add up to 100%.

In the next section a case study which involve determining the optimal model for a LFP battery subjected to discharge after the Urban Dynamometer Driving Schedule (UDDS) cycle is presented. This study has the main goal of establishing the best suited model to be incorporated into a BMS for a LFP battery. The model has to combine ease of implementation with energy efficiency.

The characteristics of the LFP cell used are:

- Rated voltage: 3.3 V
- Rated discharge current: 0.7 A
- Rated capacity: 1400 mAh for the rated discharge current
- Cut off voltage: 2.5 V
- Maximum allowable discharge current: 2.1 A.

The UDDS discharge cycle—Fig. 19.6, was chosen because of its high complexity [25] and also because it is part of the basic tests aimed to determine the characteristics of the batteries that equip electric and hybrid cars in Europe and America, alongside other test such as: European Driving Cycle, Extra Urban Driving Cycle, Highway Fuel Economy Test, New York City Cycle, Urban Dynamometer Driving Schedule.

To determine the optimal model for the LFP cell subjected to discharge after the UDDS cycle only those models which include the variation of the output voltage with the discharge current, and which can be incorporated in a BMS will be

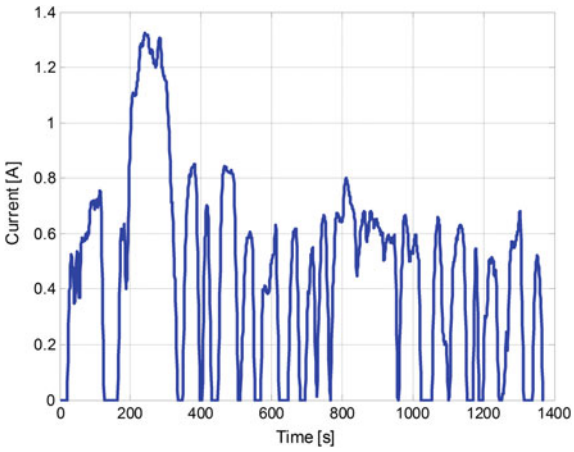

Fig. 19.6 The UDDS discharge cycle

Table 19.2 The parameters of the Shepherd model

	E_{FULL} (V)	E_{EXP} (V)	Q_{EXP} (Ah)	E_{NOM} (V)	Q_{NOM} (Ah)
Shepherd	3.430	3.409	0.068	3.301	1.120

analyzed. Therefore, the following models were chosen: Shepherd, Thévenin, second, third and fourth RC network.

Determining the parameters used in these models was based on experimental tests carried out in accordance with the procedures prescribed in the USABC [26], and PNGV [27, 28], manuals. The determined parameters are presented in Tables 19.2 and 19.3.

In accordance with the method proposed, in the first stage the UDDS discharge cycle is analyzed, and the most representative areas of rapid change and plateau are extracted—Fig. 19.7a. These areas are number from P1 to P5 for the plateau areas and from R1 to R6 for the rapid change ones, after this they are organized according to their duration. The longest plateau and the shortest rapid change areas are chosen which, in this case, are P3 and R2. From these areas a new discharge profile is constructed—Fig. 19.7b.

This profile is applied to the selected models and their response speed for the two areas is calculated—Fig. 19.8.

The second stage of the proposed methodology is dedicated to data analysis. Now the MCA for the five models is constructed as follows:

Options: The Shepherd model, the Thévenin model, the RC network model of order II, III and IV;

Criteria: The response speed of the models for the new discharge profile (for both areas P3 and R2) and the number of parameters needed for the modelling (to reduce the complexity of the models).

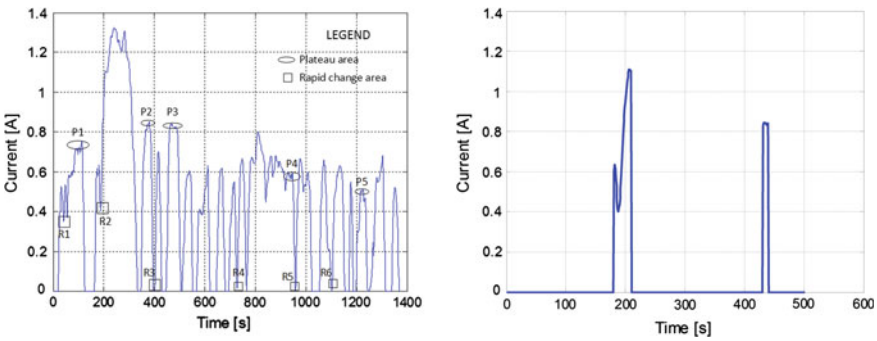

(a) Determining the areas of interest

(b) The new discharge profile

Fig. 19.7 Analysis of the UDDS discharge cycle

Table 19.3 The parameters of the models based on electric circuits

	E_0 (V)	R_0 (Ω)	R_1 (Ω)	C_1 (F)	R_2 (Ω)	C_2 (F)	R_3 (Ω)	C_3 (F)	R_4 (Ω)	C_4 (F)
Thévenin	3.313	0.131	0.053	337.1	–	–	–	–	–	–
Second order RC	3.313	0.131	0.038	257.5	0.014	549.4	–	–	–	–
Third order RC	3.313	0.131	0.038	257.5	0.005	549.4	0.008	549.4	–	–
Fourth order RC	3.313	0.131	0.038	257.5	0.005	549.4	0.003	549.4	0.004	549.4

Weights: Response rates for both areas get a 45% weight, and the number of model parameters a 10% weight [29].

The values of each option for the following three criteria are (Tables 19.4 and 19.5):

Table 19.4 Values of the options for the three criteria of the MCA

	P3 speed (V/s)	R2 speed (V/s)	No. of parameters
Shepherd	0.002973	0.000007	5
Thévenin	0.010944	0.017025	4
Second order RC	0.011295	0.025271	6
Third order RC	0.011383	0.02605	8
Fourth order RC	0.011446	0.026482	10

Table 19.5 The performance matrix of the MCA

	Score speed of the model	Score mean relative error	Score no. of parameters	Total
Shepherd	11.68725	0.0118947	8	19.69915
Thévenin	43.02662	28.929813	10	81.95643
Second order RC	44.40408	42.942079	6.66	94.00616
Third order RC	44.7495	44.264512	5	94.01401
Fourth order RC	45	45	4	94

Through the standardization of these values and applying the weights, the performance matrix of the MCA is obtained.

Analyzing the scores in the performance matrix, it can be noticed that the four models based on electric circuits are very similar in terms of performance, while the Shepherd model does not perform so well for this discharge profile.

Even though the fourth order RC network has the highest score regarding performance, it fails to compensate the large number of parameters used, so ends up on the third place with a total score of 94 points. Even if the score difference between the first two models is very small, **the third order RC network model**, which obtained the best score, i.e. 94.01, is the optimal model for a LFP cell subjected to discharge after the UDDS cycle, as it manages to achieve the best compromise between approximating the experimental data and the number of parameters required for modelling.

In order to validate the proposed method, we compared the data obtained from the five models subjected to discharge after the UDDS cycle to the data obtained from a LFP cell subjected to discharge after the same test—Fig. 19.9.

Once all data has been processed, the mean and maximum relative errors generated by the five models were counted. The most significant errors were reported

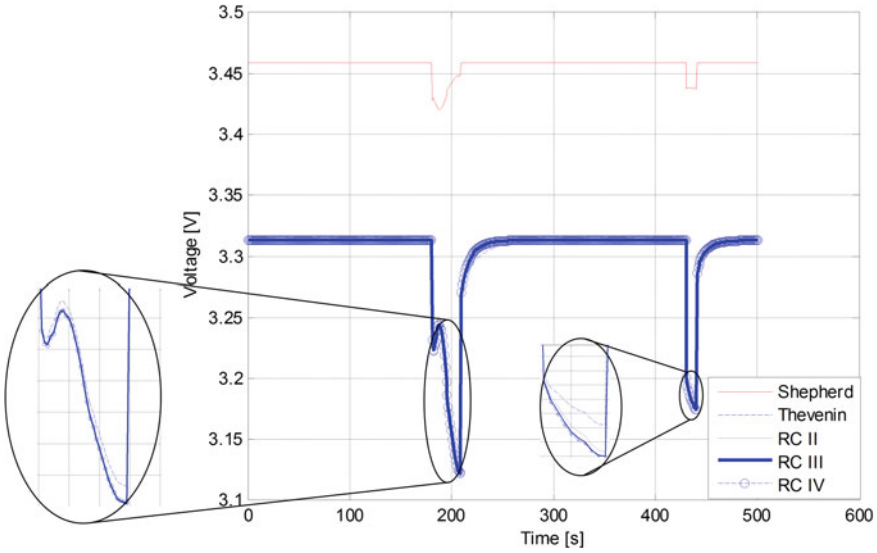

Fig. 19.8 Determining the response speed of the five models

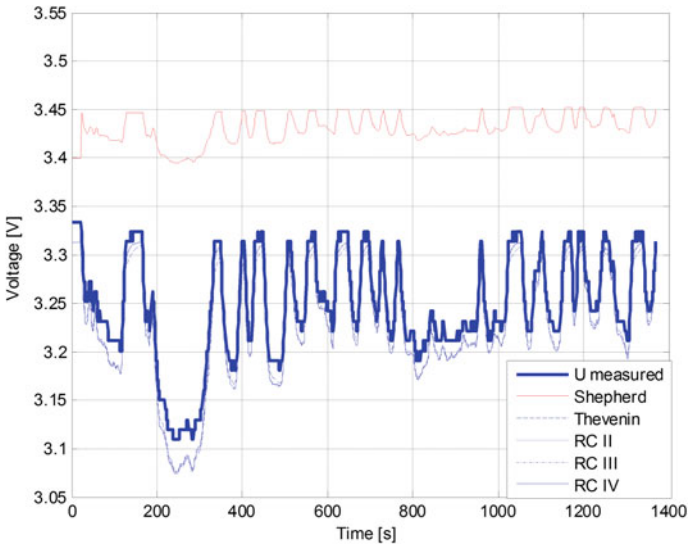

Fig. 19.9 Validating the proposed methodology

for the Shepherd model, i.e. 5.64% for the mean relative error, and 9.25% for the maximum relative error, respectively. The models based on electric circuits came within a much narrower error range, i.e. 0.53–0.57% for the mean relative error, and 1.30–1.40% for the maximum relative error, respectively. As expected the fourth

order RC network model produces the smallest errors 0.53 and 1.30% respectively, but its large number of parameters and the close performance of the other two models makes him the third choice. The third and second order RC network models have almost the same mean error of 0.55%, but the difference in the maximum error i.e. 1.34% for the third order RC network and 1.37% for the second order RC network makes the third order RC network model the best choice for this application. The results obtained from the real data comparison are very similar with the ones from the proposed methodology and so the method is validated.

19.6 Conclusions

Battery modelling is a complex area where there is still no universally valid constant. Choosing the right model is be based on several parameters, out of which the most important ones are: the range of application, the accuracy and the model complexity.

The main modeling techniques are involve electrochemical phenomena, electrical and electronic circuits or analytic approximation techniques.

The electrochemical models are based on a linear system of equations that describe the electrochemical phenomena that occur within the batteries. Solving this system require a range of techniques for approximation and reduction, which do not significantly affect the accuracy of the model, but do not significantly reduce its complexity either.

In general, the electrochemical models have high accuracy, but require large simulation periods of time and detailed knowledge about the electrochemical structures of the batteries being modelled.

The analytical models describe the behaviour of the battery at a higher abstraction level than do the electrochemical models. They have been developed from experimental tests performed on the batteries, on which curve fitting techniques were applied. The great advantage of these models is that they manage to describe the behaviour of the battery using a small number of equations. The accuracy of these models is smaller than that of the electrochemical models, but they are more suitable for incorporation into the simulation systems and other systems.

The models based on electrical circuits do not represent the internal structure of the battery, but they rather replicate its behavior by using different electrical components. They typically use voltage sources, resistors and capacitors to model the variation of the output voltage for a specific discharge profile and SoC. They have a lower degree of accuracy, but are the easiest to integrate into the simulation systems and BMSs, which makes them attractive both for battery manufacturers and developers of systems for the automotive industry.

For applications that involve rapid discharge current variations, and also periods of stability, such as the UDDS discharge profile, after the research conducted it was determined that the optimal model for an LFP cell is the **third order RC network**

model. This model was chosen from a wide range of models based on electric circuits and analytical models, using a new test methodology that was validated experimentally.

References

1. Chiasserini C, Rao RR (2001) Energy efficient battery management. IEEE J Sel Areas Commun 19(7):1235–1245
2. Pattipati BR, Sankavaram C, Pattipati KR (2011) System identification and estimation framework for pivotal automotive battery management system characteristics. IEEE Trans Sys Man Cybern Part C 11:869–884
3. Seaman A, Dao TS, McPhee J (2014) A survey of mathematics-based equivalent-circuit and electrochemical battery models for hybrid and electric vehicle simulation. J Power Sour 256:410–423
4. Wua B, Mohammedb M, Brighamb D, Elderb R, White RE (2001) A non-isothermal model of a nickel—metal hydride cell. J Power Sour 101(2):149–157
5. Suleiman A-S, Dennis D (2004) Rapid test and non-linear model characterisation of solid-state lithium-ion batteries. J Power Sour 130(1–2):266–274
6. Kim MJ, Peng HB, Lin C-C, Stamos E, Tran D (2005) Testing, modeling, and control of a fuel cell hybrid vehicle. In: ACC Conference, Portland, OR, United States, vol 6. Article number FrA14.3, pp 3859–3864
7. Enache B, Lefter E, Cepișcă C (2014) Autonomous vehicles: intelligent transport systems and smart technologies, Chap. 15. Batteries for electrical vehicles: a review. Nova Science Publishers Inc., pp 323–345
8. Fuller TF, Doyle M, Newman J (1994) Simulation and optimization of the dual lithium ion insertion cell. J Electrochem Soc 141(1):1–10
9. Forman JC, Moura SJ, Stein JL, Fathy HK (2012) Genetic identification and fisher identifiability analysis of the Doyle–Fuller–Newman model from experimental cycling of a $LiFePO_4$ cell. J Power Sour 210:263–275
10. Albertus P, Newman J (2014) Introduction to Dualfoil 5.0. http://www.cchem.berkeley.edu/jsngrp/fortran_files/Intro_Dualfoil5.pdf. Accessed 29 May 2014
11. Doerffel D, Suleiman A-S (2006) A critical review of using the peukert equation for determining the remaining capacity of lead-acid and lithium-ion batteries. J Power Sour 155:395–400
12. Pavlov D, Petkova G (2002) Phenomena that limit the capacity of the positive lead acid battery plates: I. The charge potential transient as an indicator of positive plate state of charge and state of health. J Electrochem Soc 149:A644–A653
13. Pavlov D, Petkova G (2002) Phenomena that limit the capacity of the positive lead acid battery plates: II. Electrochemical impedance spectroscopy and mechanism of discharge of the plate. J Electrochem Soc 149:A654–A661
14. Hausmann A, Depcik C (2013) Expanding the peukert equation for battery capacity modeling through inclusion of a temperature dependency. J Power Sour 235:148–158
15. Shepherd CM (1965) Design of primary and secondary cells II. An equation describing battery discharge. J Electrochem Soc 112:657–664
16. Tremblay O, Dessaint LA, Dekkiche AI (2007) A generic battery model for the dynamic simulation of hybrid electric vehicles. In: VPPC conference, pp 284–289
17. Enache B, Lefter E, Stoica C (2013) Comparative study for generic battery models used for electric vehicles. In: Proceedings of the 8th international symposium on advanced topics in electrical engineering, pp 1–6

18. Li J, Mazzola MS (2013) Accurate battery pack modeling for automotive applications. J Power Sour 237:215–228
19. Huria T, Ceraolo M, Gazzarri J, Jackey R (2012) High fidelity electrical model with thermal dependence for characterization and simulation of high power lithium battery cells. In: IEVC conference, pp 1–8
20. Wang L, Cheng Y, Zou J (2014) Battery available power prediction of hybrid electric vehicle based on improved dynamic matrix control algorithms. J Power Sour 261:337–347
21. Jackey R, Saginaw M, Gazzarri J, Huria T, Ceraolo M (2013) Battery model parameter estimation using a layered technique: an example using a lithium iron phosphate cell. https://www.mathworks.com/tagteam/76117_SAE%203013%20-%20Battery%20Estimation%20Layered%20Technique.pdf. Accessed 01 Sept 2015
22. Verbrugge B, Heremans Y (2009) Modelling the RESS: describing electrical parameters of batteries and electric double-layer capacitors through measurements. World EVJ 3
23. Hariharan SK, Kumar VS (2013) A nonlinear equivalent circuit model for lithium ion cells. J Power Sour 222:210–217
24. Lefter E, Enache B, Mara I, Goia C (2015) Hybridization of trolleybuses—means for increasing the transports flexibility and reduction of the pollution. UPB Sci Bull Ser C 77 (3):293–304
25. Enache B, Constantinescu LM, Alexandru ME (2015) A $LiFePO_4$ battery discharge simulator for EV applications—part 2: developing the battery simulator. In: Proceedings of the 9th international symposium on advanced topics in electrical engineering, pp 883–888
26. USCAR (1996) USABC electric vehicle battery test procedures manual, revision 2
27. PNGV (2001) PNGV battery test manual, revision 3
28. Duong T (2000) USABC and PNGV test procedures. J Power Sour 89:244–248
29. Enache B, Constantinescu LM, Alexandru ME (2015) A $LiFePO_4$ battery discharge simulator for EV applications—part 1: determining the optimal circuit based battery model. In: Proceedings of the 9th international symposium on advanced topics in electrical engineering, pp 877–882
30. Pistoia G (2014) Lithium-ion batteries advances and application, Chap. 4. In: Hudak N (ed) Nanostructured electrode materials for lithium-ion batteries. Elsevier, pp 57–82

Chapter 20
Electrical Energy Consumption Forecasting to Improve Energy Efficiency of Water Distribution Systems

Gheorghe Grigoras

Abstract The energy management problem is essential in optimal planning and operation of water distribution systems. This problem involves establishing the operation schedule for all water hydrophore stations from the system. One of the available policies for improving energy efficiency is related to the decrease of electricity consumption. This supposes two important aspects: the upgrading of the water distribution system and use of software packages order to ease the decision making process. Two approaches based on clustering and decision trees are proposed for electrical energy consumption forecasting in the water distribution systems. The comparative studies were realized using a database of 85 urban water hydrophore stations belonging to a Romanian water distribution company. Based on these results, it can be considered that the new proposed approaches have the ability to constitute an IT infrastructure which can be actively used for improving energy efficiency in water distribution systems.

Keywords Electrical energy consumption · Clustering · Decision trees · Hydrophore stations · Water distribution system

Abbreviation and Acronyms

AI	Artificial Intelligence
ANN	Artificial Neural Networks
CART	Classification and Regression Trees
EP	Evolutionary Programming
FT	Fuzzy Techniques
RLP	Representative Loading Profiles
SGI	Silhouette Global Index
MAPE	Mean Absolute Percentage Error
WF	Daily Water Flow

G. Grigoras (✉)
Department of Power System, Faculty of Electrical Engineering,
"Gheorghe Asachi" Technical University of Iasi,
Bd. Dimitrie Mangeron, No. 21-23, 700050 Iasi, Romania
e-mail: ggrigor@tuiasi.ro

N. Bizon et al. (eds.), *Energy Harvesting and Energy Efficiency*,
Lecture Notes in Energy 37, DOI 10.1007/978-3-319-49875-1_20

PG Pressure Growth
W Daily Electrical Energy Consumption

20.1 Energy Efficiency of Water Distribution Systems

The linkage between two important components of our life, namely water and energy, sometimes called the water-energy nexus, is increasingly tighter due to massive demand for both water and energy. Water is used in electrical energy production and electrical energy is necessary to extract, treat and distribute water and to clean the waste water.

These aspects explain the water-energy nexus, such that both components must be addressed together in an efficiency energy policy [1]. Even if there is a relationship between the two components, these have been considered and managed independently until recently.

In planning or operating water supply systems, traditionally the electrical energy consumptions were mostly neglected or given little importance [2, 3]. The interdependency between these two important components is shown in Fig. 20.1 [4].

These interdependencies must be considered, because the constraints of one resource introduce constraints in the other. For example, the droughts and heat waves can lead to water constraints that, subsequently, can become constraints in the hydropower sector. In the same way, the outages from power systems can represent constraints in the water and wastewater sectors [3, 5].

High energy amounts are needed for pumping water, treating the water to drinking quality, distribution of water, pumping and treating wastewater. Thus, obtaining potable water and cleaning wastewater using less electrical energy amount should represent an important target for water companies. For example, there are countries where energy used for water treatment is of about 3% of the nation's electricity use (in USA and UK). In some European countries, Sweden for example, the energy amount is approximately 1%. However, there are countries

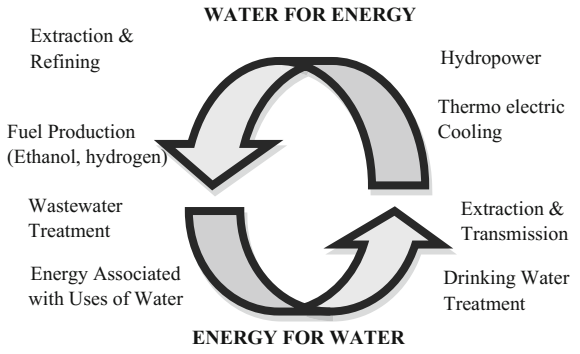

Fig. 20.1 The water-energy nexus [4]

with a big percent, around 10% (for example Israel) [1, 6]. From the entire chain, water pumping requires the highest energy amount.

In this moment, some countries have already launched nation-wide energy efficiency programs in water supply systems. For example, in the USA, in California region, energy efficiency must increase by 20% according to the California Water Plan. A similar percentage was approved in China and Sweden, where the wastewater treatment energy saving target is set for at least 20–30% from the total electrical energy requirement [1].

In the context of energy efficiency, the Watergy concept appeared. The term "Watergy" was coined by the Alliance to Save Energy in order to describe the strong link between water and energy in urban water distribution systems [7, 8].

In a statement given in the Alliance to Save Energy report [8] it is stated that between 2 and 3% of the total world electricity consumption is used for the pumping and treatment of water used by residential and industrial consumers.

For the water supply companies, these costs with consumed energy are the largest expenditure. These costs can reach up to 65% of the annual operating budget of a water supply company [9]. Also, water losses can augment the total cost. These losses may reach high levels in cities from countries where investments in water supply systems are very small. The examples can include countries from Latin America (Mexico, Brazil) or India where the losses are in the range of 40–50% [8].

The major steps involved in cities with clean water supply are presented in Fig. 20.2 [10]. It can be observed that in each step the electrical energy consumption is significant.

The electrical energy consumption from water supply systems is influenced by factors such as: topographical factors, geographical factors (water sources and consumers location), technical factors (pipe dimensions and configurations, rated powers of the pumps), treatment standards, and consumption factors (consumers' number, consumers' types, and consumption category). This varies from city to city, depending on the factors described above [7–9, 11–15].

Other factors that can also significantly affect electrical energy consumption depend on operational strategies and technology choices at national level [14].

An analysis of Fig. 20.2 can lead to the discovery of the technical factors that lead to a high electrical energy consumption: pump stations poor design, installation or maintenance, old pipes with high head loss, bottlenecks in the supply networks, excessive supply pressure, or inefficient operation strategies of various supply facilities [9, 11, 16–23].

There are many solutions for energy-saving in water supply systems, which do not require huge investment: from decreasing the volume of water pumps (e.g., adjusting pressure zone boundaries) to reducing the price of energy (e.g., avoiding peak hour pumping and making effective use of storage tanks) or increasing pump efficiency (e.g., ensuring that pumps are operating near their best efficiency point). These solutions can recover their costs in a time period ranging from a few months to 3 years [19–24].

In addition to these technical solutions, the companies can implement modern solutions based on the supervisory, control, and acquisition data systems. These

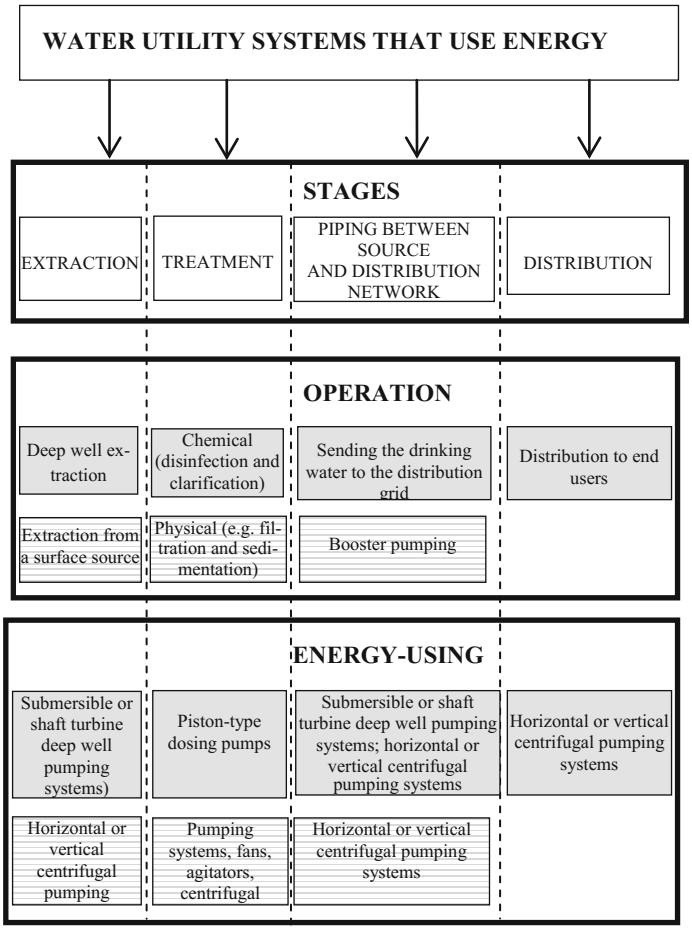

Fig. 20.2 Water utility system that use energy [10]

solutions use integrated information systems, able to realize complex monitoring and automation functions, implemented through customized software packages. Also, the SCADA systems can provide an efficient energy consumption management and can improve all activities from water supply systems. The motivation for introducing such systems is due the following factors [9, 17–23].

- the structure of the water supply systems became increasingly complex due to rising demands and the diversity of water sources;
- an aging infrastructure that leads to high operating costs;
- the availability and reliability of capable hardware components and software packages.

The energy efficiency policies in water supply systems must take account both of technical aspects which lead to infrastructure upgrades and information aspects that enable the supervisory and control of all activities through SCADA systems.

Energy efficiency policies correlated with of electricity prices growth have stimulated water supply companies, to find solutions to minimize their electrical energy consumption. An electrical energy consumption forecast with small errors can guarantee an efficient management plan leading to water supply of the customers at all times with minimum energy cost, considering the various technical constraints (reservoir levels, water pressure in the distribution system, water quality, and supply restrictions). Because in electricity markets, the price of electricity can change hourly, the water supply companies could move a part from the daily electrical energy consumption from a certain hour to other hours when the price is lower. But to achieve this target the water companies must have accurate electricity consumption forecasts. If the errors are high, they can lead to purchasing a supplementary energy amount with a high price from the day-ahead market or the intra-day market.

For electrical energy consumption forecasting, many methods were proposed in the literature. These methods are based mainly on classical approaches: heuristic, linear regression, or similar day. From these, the heuristic approach leads to the smallest errors (between 2.5 and 3%). In order to apply this type of method, a significant input database is required, with measurements: weather forecast, day type (working or weekend), knowledge of future events, and other historical operational data.

Out of these methods, few are taking into account the technical characteristics of the water hydrophore stations and the uncertainties that may exist in the system due to lack of measurements. The higher uncertainty degree leads to lower quality decisions made by the human operator. Therefore, the attempts to reduce uncertainty must be well substantiated. However, even with the reduction of the information uncertainty, considerable efforts and expenses are necessary. Thus, the targets of the forecasting process are to determine those parameters and characteristics which influence most the results and to improve the quality of the corresponding models and the relevant information.

In order to consider all these factors, the Artificial Intelligence (AI) techniques based on decision trees and clustering techniques are proposed for the electrical energy consumption forecasting in water distribution systems. These approaches are original because, to the author's best knowledge, no other methods proposed previously in the literature use decision trees or clustering for electricity consumption forecasting in water distribution systems. A comparative study using a database that contains records from 85 urban hydrophore stations belonging to a water distribution company from Romania will be presented. Using these approaches, the forecasting errors of the electrical energy consumption are better (approximately 1%) than the ones currently expected by water companies (approximately 3%). Thus, the results obtained demonstrate the ability of the proposed approaches to become an important step in ensuring an efficient management in the water distribution systems.

The remainder of this chapter is organized as follows. Section 20.2 presents a short review of AI techniques. Section 20.3 presents the implementation details of the proposed methods and the results of their testing on a real water distribution system from Romania. Section 20.4 contains the concluding remarks.

20.2 AI Techniques in Electrical Energy Consumption Forecasting

20.2.1 General Aspects

Today, information technology has drastically changed education, the nature of work, society, and decision-making processes all over, among other things. More information is becoming available, faster than ever before. The changing face of information technology and communication are proof that the economy, and in particular the utilities systems sector (power, water, gas, etc.), have entered a new era of fundamental change. The impact is being felt in the market, in the control and operation of the power, water or gas networks. Under these circumstances of momentous change, AI has the potential to play a more important role [25–27].

The main AI applications developed worldwide in the last years are:

- Load/energy forecasting,
- Optimal flow,
- Operating and expansion planning,
- Tariff selection,
- Alarm processing and fault diagnosis,
- Consumption control (power, water, gas, etc.).

The most used AI techniques are: Neural Networks, Fuzzy Logic, or Evolutionary programming. Other techniques based on machine learning are also used for classification and prediction. From these, the Decision Trees and Clustering algorithms are considered the most popular approaches. In the following, a summary of some theoretical issues relates to the AI techniques are presented.

20.2.2 Artificial Neural Networks

Artificial Neural Networks (ANN) are used increasingly in modelling and controlling industrial processes, gaining momentum in recent years in front of the conventional methods. Also called connectionist networks, ANNs reproduce certain functions of the human brain by simulating a model of the brain which is as yet extremely simplified. Because they are able to generalize linear statistic methods, ANNs are extremely well adapted for solving shape recognition problems, for

which they give excellent results. Much of this interest has come about with the successful of real-word applications of ANNs and their ability to learn [26].

ANNs, as universal approximators, can give a systematic approach to the modelling of industrial processes, especially in those complex processes where solving the operation equations is very difficult using conventional mathematical methods. The most widely used ANN is the Multilayer Perceptron with the associated back propagation error learning, for minimizing the observed sum of squared errors over a given set of data.

In the literature excellent results were obtained using RNAs in some technical areas, but there have been also some problems that could not be successfully resolved using these techniques. From a recent analysis of applications in electric systems the main conclusions are:

- ANNs are extremely well developed to forecasting short-term consumption, especially if their architecture is optimized (for example, by using genetic algorithms);
- encouraging results have been obtained in modelling and controlling production units, alarm processing, and distribution networks control;
- ANNs are not the best choice for problems concerning network safety, production plan research and electrical networks planning.

The success in industrial process modelling can be firstly represented by the ability to extract information about the model structure and the relationships between its input and output data from trained network. Thus, these can become very important in validation of the models and the optimization and control of process. Furthermore, when the model of the process is not known, the objective is to learn as much about the system, and the obtained information to be used in the analysis of the process and in determining the disturbing factors that affect it.

20.2.3 Fuzzy Techniques

The fuzzy techniques (FT) were presented for the first time in the mid of the 60s by L. A. Zadeh. They had a huge success and have been used immediately in various fields. The broad development of mathematical theory, especially in areas of Possibility Theory, Fuzzy Control, ANN, and Pattern Recognition provided the basis for resolving different problems. Today, these techniques are implemented in many software packages and hardware components [25–28].

The advantage of these techniques is represented by the ability to work and perform calculations with uncertainties. These uncertainties can result from human observations based on descriptions and abstract information obtained by modelling the process. A classification of the uncertainty sources and the mathematical models corresponding to these is shown in Fig. 20.3.

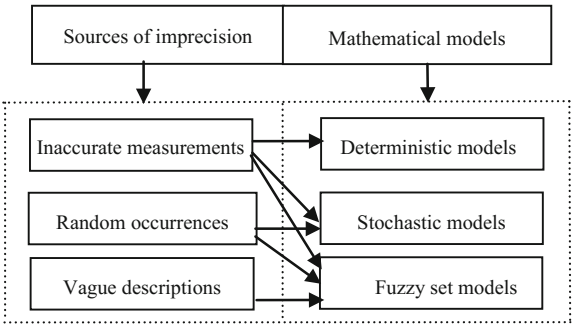

Fig. 20.3 Mathematical models for imprecision [28]

If for the first two sources of imprecision (inaccurate measurements, random events) appropriate mathematical models have been determined, it's not the same for the last source of imprecision (description language), although we use everyday expressions such as "the energy consumption is small/big" etc. Most linguistic descriptions such as Small, Medium, and High are fuzzy in nature. These vague descriptions are part of modelling process and the algorithm.

The decision maker must make the difference between the various linguistic classes, e.g., when these classify the operation regimes of the supervised system according to certain operational characteristics [25–28]. The linguistic description is a part of the modelling process and the operators/experts' language. The experts' knowledge is usually translated in natural language. Therefore, it requires a way of encoding and manipulating knowledge expressed in natural language. This approach could be based on the use of linguistic variables and nuanced sets. Moreover, the experts' knowledge is affected by the ambiguity and imprecision of the natural language. The fuzzy techniques try to resolve these problems through a coherent modelling of the uncertainty, while providing the possibility to operate with such models.

The fuzzy sets are conceptually linked to the uncertain intrinsic properties of the model. A fuzzy set presents the following:

- an area that represents the fuzzy population;
- the semantic representation associated fuzzy population;
- a function that defines the degree of membership of an element from the fuzzy population to the set.

Unlike bivalent logic, in which membership degree of an element to the set can have two values, in fuzzy logic it can have any real value in the [0, 1] range.

The major advantage of this logic is that it operates with sets which by definition are characterized by continue and normal membership functions.

Fuzzy logic can be used with success in real applications, where there are many uncertainties in mathematical models (both in the objective function and constraints). But, these uncertainties can be modelled using the FTs. Designed to work with uncertain data, the fuzzy techniques can be applied in most industry sectors

process control. Thus, the control and regulation of industrial processes are areas where fuzzy techniques found a breeding ground for their application.

20.2.4 Evolutionary Programming

Evolutionary programming (EP) searches an optimal solution by evaluating a set of candidate solutions, over a number of generations or iterations. In each iteration, another set is formed, starting from the existing set, using the mutation operator. Thus, a new solution is obtained, by disturbing each element of the existing solution by a random value. The optimality degree of o each candidate solution or individual is measured by its fitness, which can be defined based on the objective function of the problem. In this case, if a competition scheme is used, the individuals in each population compete with each other. The winning individuals will form a resultant set, which is regarded as the next generation [26].

The optimization process must be conducted so that the competitive scheme should favour the survival of the better solutions.

20.2.5 Decision Trees

Machine learning represents an important AI research domain. This is due to the following two aspects:

- the ability to learn represents a characteristic of an intelligent behaviour;
- the understanding of the intelligence should be done through the understanding of the learning model [29].

In the last years, the approach based on decision trees (DTs) was used increasingly in resolving classification and prediction problems. DTs use a flow chart-like tree structure. From the view point of data-mining tools, decision trees

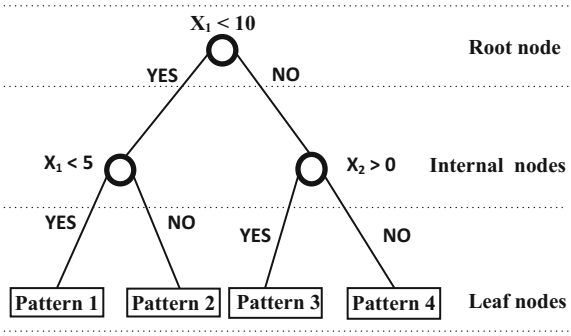

Fig. 20.4 The structure of a decision tree

can extract useful information contained in large databases, which can be used in decision-making processes.

A decision tree can have three nodes categories: root, internal, and leaf. The structure of a decision tree can be seen in Fig. 20.4.

If a decision tree is viewed as a logical model, this can indicate a relationship between a target variable and a set of predictor variables [29, 30]. The classification process will take place in function by separation rules relating to the numerical or categorical values of the explanatory variables. Each node will have proper classification rules derived from a mathematical process that will minimize the impurity of the resulting nodes, using the available learning set. Using these classification rules, the leaf nodes will be finally reached [30, 31]. But, for the leaf nodes, the separation rules are not applied just like internal nodes. With the help of these nodes, the probability of each obtained pattern can be estimated. From the structure of a decision tree it can observed that the root and internal nodes indicate a binary split test on an attribute. The classification process depends mainly by first node (root) that contains all learning set.

Also, the leaf nodes represent the results of the classification process so that they are labelled as targets. From the point of view of the algorithm, in order to generate a decision tree, two steps should be covered, namely learning and classification [30]. These steps are shown in Fig. 20.5. The available data must be divided in two sets: the first set (the learning set) is used in the learning process in order to build the structure of the tree, while the second set (the testing set) has the role to assess the generalization capability of the tree using new input data. The sizes of the two sets are different and depend on the number of elements from the database. The

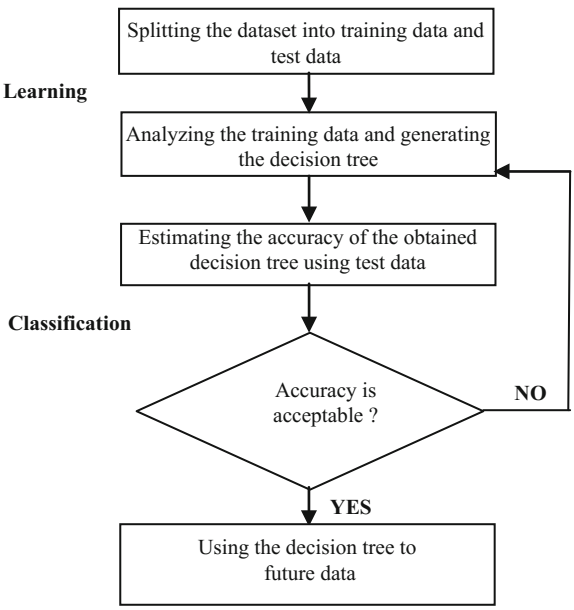

Fig. 20.5 The flow-chart of decision tree generation [30]

ratio between the two sets can vary between 90/10 and 60/40%. In the literature, the most used method used to generate a decision tree is Classification and Regression Trees (CART) method [32, 33].

This method uses the data recorded in a database during a period of time to construct the structure of the decision tree. Also, a number of patterns must be introduced from the beginning of the learning process. These patterns can be obtained using various techniques (for example, clustering techniques).

Finally, the information resulted from the learning and classification processes can be arranged in a matrix named confusion matrix [34, 35]. Based on this matrix, the performance of the classification process can be assessed.

20.2.6 Clustering Techniques

Clustering techniques are based on the arranging/organization of an objects/elements set into groups (clusters) with similar characteristics. With the help of these techniques, information can be extracted easily from large databases, such that the decision maker understands the existing relationships between recorded data.

In the clustering process, there are some important steps which the decision maker should take into account. The steps are presented in Fig. 20.6 [25, 36, 37].

Feature selection In this step, the relevant characteristics corresponding to the elements/objects from the database will be chosen for the clustering process.

Clustering algorithm According to the choice of the clustering algorithm, the elements/objects from the database can be separated either into clearly defined groups, either into fuzzy groups, where each element has a varying degree of membership to each resulted group.

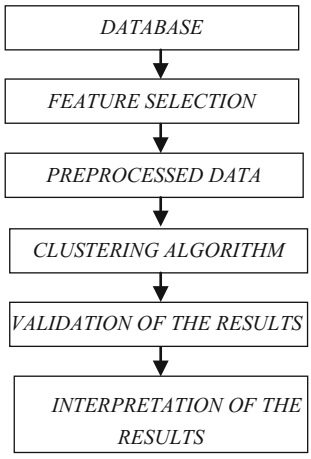

Fig. 20.6 The steps of a clustering process [37]

Validation of the results In this step, an evaluation of the clustering process is made. Usually, an optimization criterion is used. This analysis must be objective and it is performed to determine if the results are grouped as accurately as possible.

Interpretation of the results The decision maker will compare the obtained results with other methods. In accordance with the benchmarking, it will reach a conclusion and it will take a decision.

In literature, two clustering methods categories were developed: hierarchical clustering and *K*-means clustering.

Hierarchical clustering In the hierarchical clustering, two type of methods can be identified: agglomerative methods, which perform a succession of unifications of the n elements from the initial database into clusters, and divisive methods, which separate the n elements gradually into finer clusters. The agglomerative techniques are easier to implement. The clustering process can be interpreted through a two dimensional diagram (dendrogram). This explains the unifications/splits which take place in each step.

The hierarchical clustering can be used for databases with a number up to several hundred elements. The methods from this category are differentiated by how the similarity between clusters is evaluated. The similarity is determined by computing the Euclidean distance. Single linkage clustering (connectedness or minimum method), complete linkage clustering (diameter or maximum method), average linkage clustering, and the centroid method can be used.

K-means clustering In this method, the elements are grouped in K clusters (K is a positive integer number, introduced a priori) based on the similar characteristics of the elements from the database. Initially, the c_k centroids of each cluster $C_k \subset S$ (the set of clusters), $k = 1, \ldots, K$, are chosen randomly. An element x_i will be assigned to a centroid c_k if the distance between them $d(x_i, c_k)$ is the minimum of all distances between this element, x_i, and the other centroids. The algorithm has as objective the minimization of a squared error function.

The objective function E will minimize the distance between each element and the centroid of the cluster to which the element will be assigned.

$$\min(E) = \min\left(\sum_{k=1}^{K}\sum_{x\in C_k} d\left(x^i, c_k\right)\right) \tag{20.1}$$

where:

c_k—represents the centroid of cluster C_k ($c = \{c_1, \ldots, c_k\}$, $C = \{C_1, \ldots, C_K\}$, $C_k \subset S$, $k = \{1, \ldots, K\}$);
$d(x_i, c_k)$ is the Euclidean distance computed between the element $x_i \in S$, $i = 1, \ldots, N$, and the centroid c_k

In the first step, a set of K centroids will be initiated randomly. Then, the algorithm tries to assign each element from the dataset to a cluster when distance between it and the centroid is the shortest. Further, the new positions for centroids

will be recomputed. The iterative process will stop when the positions of centroids will not change. After that, the decision maker will verify the validation of the obtained results.

The validation and evaluation of the results must highlight the quality of the clustering process. This quality will be evaluated through an analysis that will consider the clusters' density, sizes and, separation degrees. In the literature, the main approaches used for the cluster validation are [38]:

- *external tests*—the results obtained in the clustering process will be compared with the results obtained using other databases.
- *internal tests*—the quality of clustering process is evaluated based on the input data to validate the division mode of the clusters.
- *relative tests*—the final results are compared using the same clustering algorithm, but with different parameters.

The most used tests in clustering analysis are the internal ones. Many of these are based on a Silhouette Global Index (*SGI*). In the determination of this index, the following silhouette widths will be evaluated successively: for each sample, for each cluster, and for the entire database. The last width represents the average silhouette that will be used for validation. Also, with its help, the optimal number of clusters will be determined.

$$SGI = \frac{1}{K}\sum_{k=1}^{K} S_{C_k} \tag{20.2}$$

where:

S_{Ck}—the silhouette width for cluster C_k. This is evaluated with the formula:

$$S_{C_k} = \frac{1}{n_j}\sum_{i=1}^{n_j} s_i \tag{20.3}$$

s_i—the silhouette width for i-sample. It can be calculated with the formula:

$$s_i = \frac{b_i - a_i}{\max\{b_i, a_i\}} \tag{20.4}$$

a_i—the average distance between the element i and elements of the same sample j;
b_i—the minimum average distance between the element i and elements in class closest to class j.

An interpretation of the Silhouette Global Index is given in [39, 40]:

- 0.71–1.0: The formed structure is strong. The results can be trusted.
- 0.5–0.7: An acceptable structure of the clusters was obtained.

- 0.26–0.5: The obtained structure is very poor. Low confidence degree.
- <0.25: The degree of confidence in results is zero. No structure exists.

Data validity represents the most important step in clustering analysis. Based on its results, the decision maker can assess the confidence degree in the relationships established between the input data.

20.3 Electrical Energy Consumption Forecasting in Water Distribution Systems

20.3.1 Clustering-Based Approach

In this section, an extension of the clustering based profiling techniques in the area of water distribution systems for electricity consumption forecasting is presented. The *K*-means clustering algorithm will be used for determining the representative loading profiles (RLP) of hydrophore stations, and these, together with a statistical approach will forecast the electrical energy consumption from the water distribution systems [41, 42].

By knowing the loading profiles of the hydrophore stations, the distribution companies can forecast easily the water demand for a certain zone. Based on this forecast, these can establish the best energy efficiency strategies. The load profiling can represent a more realistic approach for energy consumption forecasting because the loads are not monitored in all hydrophore stations at each hour. Thus, a representative loading profile will be attached for each hydrophore station, determined based on the different operation conditions (season, type of day, types of supplied consumers, energy consumption, water consumption etc.). The sampling interval can be 10, 15, 30 or 60 min. In these conditions, the loading profiles can have 144, 96, 48 or 24 load values. The forecasted profile of a hydrophore station is obtained using a representative loading profile and its daily (monthly, yearly, depending the case) electric energy consumption.

20.3.1.1 Load Profiling for Water Hydrophore Stations

In the profiling process, the clustering techniques can be used for grouping the loading profiles recorded in hydrohpore stations (in various measurement campaigns) in coherent clusters based on their the similarities. Finally, a representative loading profile will be attached to each cluster. This profile is achieved if all loading profiles belonging to the respective cluster are averaged.

Each RLP is represented by a vector $x_i = \{x_{ih}, h = 1, \ldots, T\}$ for $i = 1, \ldots, K$, and the comprehensive set of RLPs is contained in the set $P = \{x_i, \mathrm{i} = 1, \ldots, K\}$. The time scale along the day is partitioned into T time intervals of duration Δt_h, for $h = 1, \ldots, T$. Hourly values are used in this chapter. The variables used in the

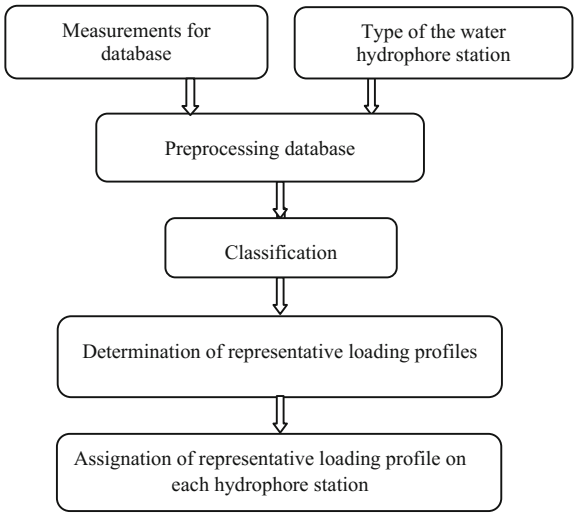

Fig. 20.7 The flow-chart for obtaining of the representative load profiles [41]

calculations are assumed to be represented as constant (average) values within each time interval. The clustering process generates K clusters corresponding the hydrophore stations. In the final step, each hydrophore station will have a RLP attached, based on its loading characteristics. All steps of the algorithm are presented in Fig. 20.7 [41]. Each step will be detailed in the following.

Measurements After the measurement campaigns performed in each hydrophore station from the water distribution system during a certain time period (day, month, season, or year), a set of loading profiles will be obtained. The profiles can have a certain number of values, according to the used sampling step. After that, all loading profiles will be collected into a database.

Data cleaning and pre-processing Due to the following factors: measurements carried out over a long period of time, high number of recorded data, and a spread of the hydrophore stations on a large geographical area, the recorded data can be affected by communication errors and failures of the measurement equipment. These problems will impact the quality of recorded data. In order to remove the missing or irregular values from the database of, data pre-processing is required.

Classification In the classification process, the clustering methods will be used. Because the database can have a high number of profiles, the best suited algorithm is K-means. In order to use this algorithm, an important aspect is represented by the normalization of the loading profiles before starting the clustering process. A suitable factor is the energy consumption over the analysed time. This factor is used because each hydrophore station has an energy meter with classical measurement technology.

Determination of RLPs For each cluster, a representative loading profile will be determined by averaging all its assigned profiles. This profile will characterize the

operation regime of all hydrophore stations from a certain cluster from hourly load and energy consumption viewpoints.

Assignation For the characteristic regime of a hydrophore station, a representative loading profile will be assigned.

20.3.1.2 Electrical Load and Energy Consumption Forecasting

The electrical load and energy consumption forecasting of a water distribution system can be made with an improved simulation method which uses the representative loading profiles of the hydrophore stations. The method can be used if the following assumptions are considered [41, 42]:

- the hourly average load is approximately proportional to the electrical energy consumption. This load represents a cluster of hydrophore stations from a water distribution system during the analysed time period.
- the hourly average loads have a normal statistical distribution.

If these assumptions are satisfied, the hourly load in a water distribution system can be forecasted with:

$$P_h^S = \sum_{i=1}^{K} n_i W_{av}^{C_i} p_h^{C_i} + \sqrt{\sum_{i=1}^{K} n_i \left(W_{av}^{C_i} \sigma_h^{C_i}\right)^2}, (\text{kW}),\ h = 1, \ldots, 24 \qquad (20.5)$$

where:

P_h^S—the forecasted load at the hour $h = 1, \ldots, 24$, (kW);
K—the number of clusters resulted from the clustering process for the hydrophore stations;
n_i—the number of the hydrophore stations from cluster C_i;
W_{av}^{Ci}—the daily average energy consumption of the hydrophore stations belonging to cluster C_i, $i = 1, \ldots, K$, (kWh);
p_h^{Ci}—the average hourly loading factor of the hydrophore stations belonging to cluster C_i, (kW/kWh);
σ_h^{Ci}—the standard deviation of the load from hydrophore stations belonging to cluster C_i, (kW/kWh).

The hourly loads from a particular hydrophore station can be estimated with the help of the loading factors p_h^{Ci} belonging the cluster C_i which contains the station, and of the real energy consumption recorded in that station. For the electrical energy consumption forecast, the following equation can be used:

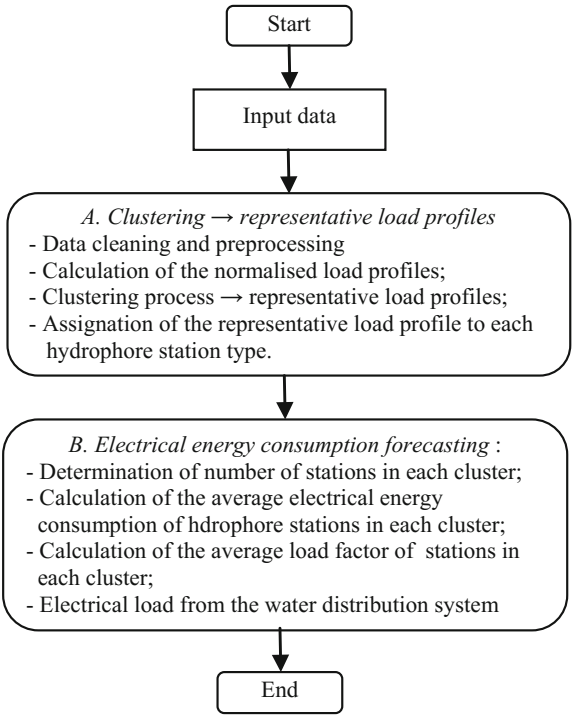

Fig. 20.8 The flow-chart of the proposed algorithm

$$W^S = \sum_{h=1}^{T} P_h^S, \ (kWh) \tag{20.6}$$

20.3.1.3 The Electrical Energy Consumption Forecasting Algorithm

The algorithm adopts a two stage procedure presented in Fig. 20.8:

- the use of a clustering technique (*K*-means method) in the first stage to deal with the time evolution of (normalized) electrical load patterns and to determine a subset of representative load profiles to be processed in the second stage. At each iteration, the clustering outcomes simplify the process of selecting a relatively small number of profiles corresponding to the hydrophore stations;
- the use of load simulation in the second stage. This approach is based on a statistical method which assumes that the hourly loads have a normal statistical distribution.

A. Determination of Representative Load Profiles

The electrical energy consumption is used in the normalization process of the characteristic loading profiles. This normalization factor is used because each hydrophore station has measurement meters that record continuously the electrical energy consumption. In the next step, the algorithm will determine the optimal numbers of clusters with the *K*-means clustering and an internal test that uses the silhouette global index to validate the classification. Subsequently, the representative loading profiles (RLP) will be obtained through an averaging process of all normalized profiles inside each cluster. In the final step, the representative loading profiles will be assigned to all hydrophore stations based on their type.

B. The Electrical Load Forecasting

Using information from the clustering process (hourly average values, average energy consumption and standard deviation of the distribution of load for each hydrophore station from the cluster C_i, $i = 1, \ldots, K$ and Eq. 20.5, the hourly loads of the analyzed water distribution system will be obtained.

The forecast accuracy depends on the accuracy of information recorded in the database. If the real value of the load is known, the forecasting error can be assessed using the mean absolute percentage error (MAPE):

$$MAPE = \frac{\sum_{h=1}^{T} \frac{\left|P^S_{h,real} - P^S_{h,f}\right|}{P^S_{h,real}}}{T} \cdot 100 \tag{20.7}$$

In Eq. 20.7, the variables $P^S_{h,real}$ and $P^S_{h,f}$ are the real and forecasted values for the load of a water distribution system at the hour h.

MAPE is a dimensionless quantity. This can highlight the comparison with other results obtained using other databases in order to establish the accuracy of the algorithm.

Table 20.1 The technical data of hydrophore stations

Type	Number of stations	Rated power (kW)	Rated water flow (m^3/h)
I	3	3 × 2.2	24
II	6	4 × 2.2	32
III	11	4 × 4	64
IV	13	3 × 5.5	96
V	33	4 × 5.5	128
VI	7	4 × 7.5	128

20.3.1.4 Results

The proposed method was tested to forecast the electrical energy consumption in a real water distribution system with $N = 85$ hydrophore stations. For each hydrophore station, the technical characteristics and the load patterns are known. The technical data is presented in Table 20.1.

The primary characteristics of a water distribution station are: the daily water flow, the pressure growth, the number and nominal power of force pumps located in these distribution substations. The stations are equipped with 3 or 4 pumps working in parallel, with rated powers in the 2.2–7.7 kW range. The input data used in the analysis is based on a measurements campaign performed during a year. The recorded parameters are represented by the consumed active power, the water flow, and the pressure of the water in repression and aspiration zones of the pumps in each hydrophore station, recorded using a 5 min sampling rate.

In the pre-processing step, 12 water hydrophore stations were eliminated due to missing technical characteristics (the daily water flow, pressure growth and rated powers of force pumps located in the stations). Then, the remaining data was recorded in a database for each of the remaining stations (73 stations).

In the analysis, one of the technical characteristic used in the clustering process is the pressure growth of the water. This parameter represents the difference between the pressures of the water in the repression and aspiration zones of the pumps:

$$\Delta p = p_{rep} - p_{asp} \tag{20.8}$$

where:

p_{rep}—the pressure of the water in the repression zone of the pumps;
p_{asp}—the pressure of the water in the aspiration zone of the pumps.

The consumed active powers are represented by loading profiles of the water hydrophore stations. The profiles were analysed only for the day when the maximum load in the water distribution system was registered. The time interval is defined by taking hourly steps within a day, that is, $T = 24$ and $\Delta t_h = 1$ h.

In the first step of the clustering process, normalization is applied to all loading profiles from the database, using the daily electrical energy consumption as normalizing factor.

Table 20.2 Clustering process results

Cluster	Stations		Type of stations						W_{med}
	(no.)	(%)	I	II	III	IV	V	VI	(kWh)
C_1	8	12.33	3	5	1	–	–	–	28.58
C_2	24	32.88	–	–	4	2	11	7	41.42
C_3	41	54.79	–	1	6	11	22	–	32.35
Total	73	100	3	1	11	13	33	7	34.11

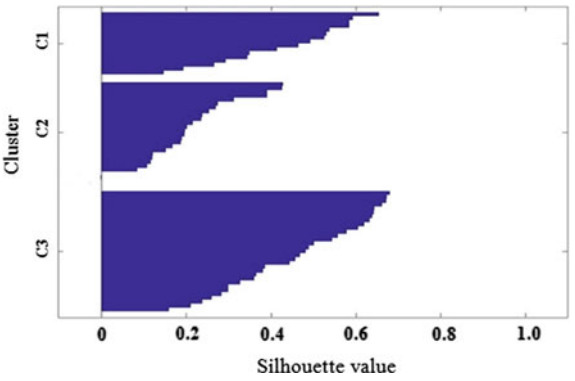

Fig. 20.9 The silhouette plot for $K_{opt} = 3$

In the next step, the maximum number of clusters will be determined using formula:

$$(K_{max} = \sqrt{N} \approx 9) \tag{20.9}$$

Further, the *K*-means algorithm will be applied successively for *K* varying in the range between 2 and K_{max} in order to determine the optimal number of clusters (K_{opt}). For each result, an internal test based on the silhouette global index (*SGI*) will verify the classification quality. The optimal solution will correspond to the classification that will obtain the highest value for the silhouette global coefficient. In our case, K_{opt} is 3 (*SGI* = 0.52).

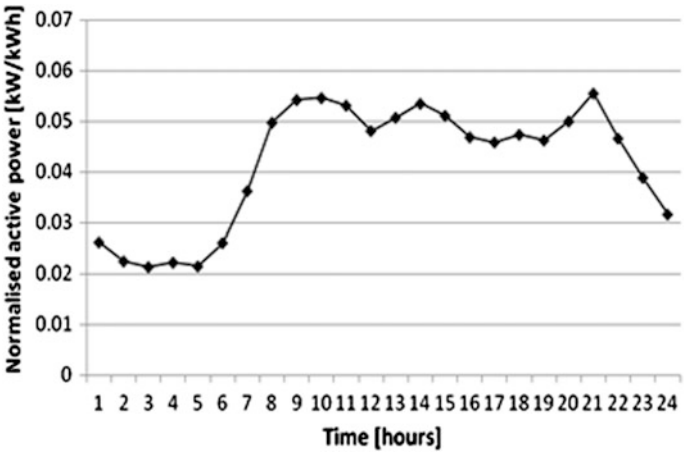

Fig. 20.10 Representative load profile for C_1

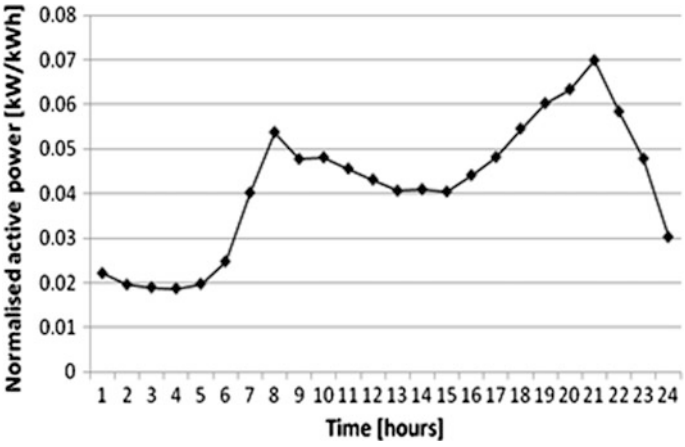

Fig. 20.11 Representative load profile for C_2

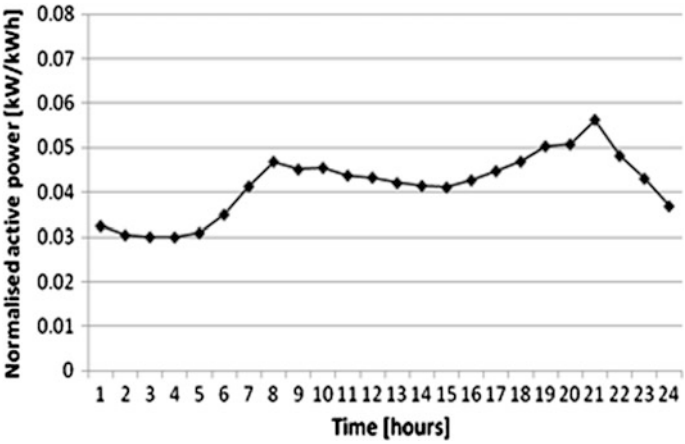

Fig. 20.12 Representative load profile for C_3

The representation of the silhouette coefficient in the optimal variant is given in Fig. 20.9. The results of the first stage of the clustering procedure are presented in Table 20.2.

The analysis of the results highlights that the clusters C_2 and C_3 include a high number of loading profiles (approximately 88%). This emphasizes that the majority of the hydrophore stations have a similar operation mode. Concerning the technical characteristics, the stations from cluster C_1 have a rated power lower than 8.8 kW, and the stations from clusters C_2 and C_3 have a higher rated power, between 16 and 30 kW. In the final step of the clustering process, RLPs will be built using the

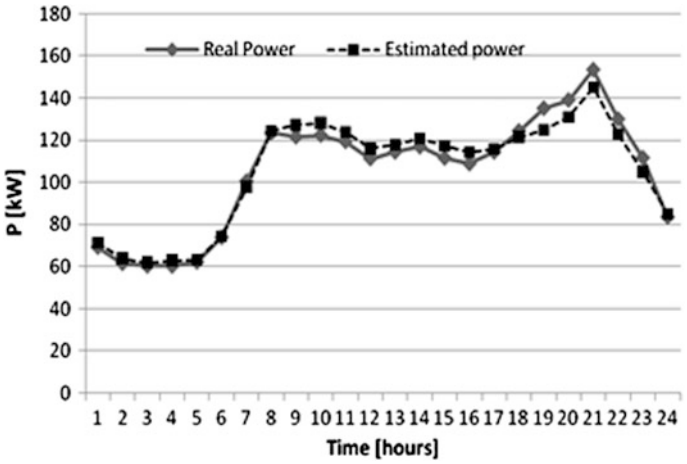

Fig. 20.13 The forecasted and real loads

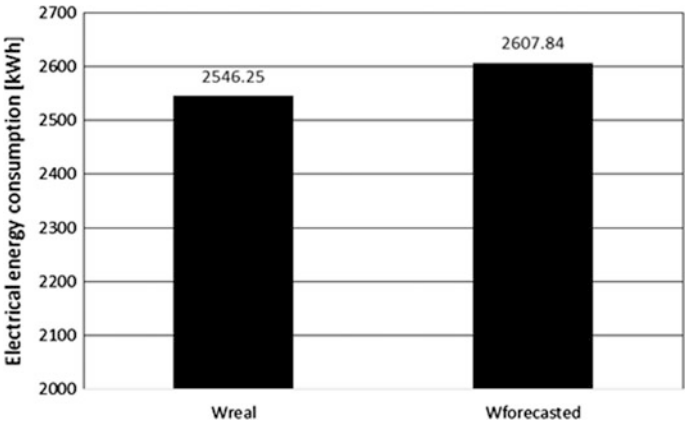

Fig. 20.14 The real and forecasted electrical energy consumption

averaging method of the normalized loading profiles. The representative loading profiles are plotted in Figs. 20.10, 20.11 and 20.12.

In the second stage of the study, the total load in the water distribution system at each hour $h = 1, \ldots, 24$ will be computed considering the results from the clustering process (Table 20.2) and the reasoning presented in Sect. 20.3.1.2. The forecasted and real values are plotted in Fig. 20.13. The forecasting errors have the following values: maximum error—4.79%, minimum error—1.37%, and mean absolute percentage error—3.11%. Finally, the electrical energy consumption was forecasted using Eq. 20.6 and the results are presented in Fig. 20.14. The forecasting error obtained with the proposed approach is 2.42%. This value can be

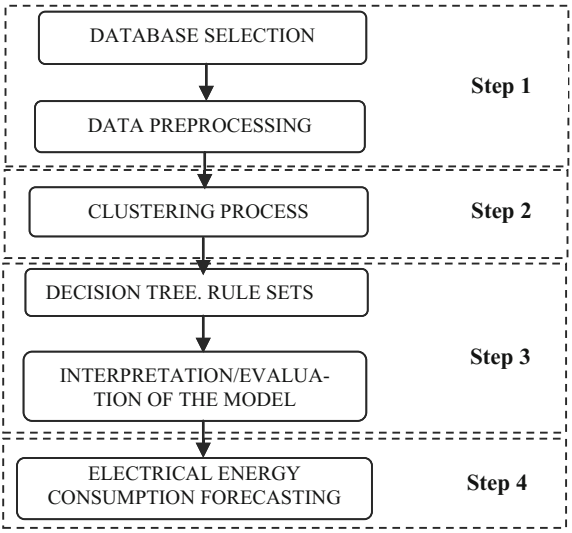

Fig. 20.15 The flow-chart of the proposed method

considered small, if the arbitrary inherent behaviour of the consumers in a water distribution system is taken into account.

20.3.2 Decision Trees-Based Approach

20.3.2.1 The Electrical Energy Consumption Forecasting Algorithm

In this section, a decision trees-based methodology for the daily electrical energy consumption forecasting of a water distribution system is presented. The algorithm consists of four steps, as presented in Fig. 20.15.

Firstly, a database of possible primary variables which characterize the behaviour of the water hydrophore stations from the analysed system is built. The choice of primary variables is based on the decision maker's experience. The chosen variables are: the daily water flow, pressure growth and rated powers of the pumps located in the stations. In this step, data preprocessing is also performed. This aspect is very important because preprocessing detects/corrects/removes improper data. In the following step, the water hydrophore stations will be classified based on their daily water flow, pressure growth, and electrical energy consumption, using the clustering techniques. The *K*-means algorithm will be used in the clustering process to obtain a finite number of significant patterns with similar behaviour.

The third step refers to building the decision tree. This tree will explain the behaviour of each station with regard to the variables chosen in the second step. Thus, by entering the significant variables that explain the technical and operational characteristics of the water hydrophore stations, based on the rules that

characterize the structure of the decision tree, the daily electrical energy consumption will be forecasted. The decision tree will be verified and validated using a test set.

In the fourth step, the daily electrical energy consumption forecasting in the water distribution system is made using a statistical approach which must satisfy the assumptions made in Sect. 20.3.1.2. The used expression in the proposed approach is:

$$W^S = \sum_{i-1}^{K} n_i W_{med}^{C_i} + \sqrt{\sum_{i=1}^{K} n_i \left(\sigma_W^{C_i}\right)^2} \tag{20.10}$$

where:

W^S—the daily electrical energy consumption of the water distribution system, (kWh);
n_i—the number of the hydrophore stations from cluster C_i;
W_{med}^{Ci}—the daily average energy consumption of the hydrophore stations belonging a cluster C_i, (kWh);
σ_w^{Ci}—the standard deviation of daily energy consumption of the hydrophore stations from the cluster C_i, (kWh);
K—the total number of clusters.

20.3.2.2 Results

The proposed methodology was applied on same database with 85 water hydrophore stations presented in Sect. 20.3.1.4. The daily electrical energy consumption is the target variable and the technical characteristics are the input variables. Thus, the technical variables (the daily water flow, pressure growth, and rated powers of force pumps) were recorded for each hydrophore station. In the pre-processing step, 12 water hydrophore stations were removed due to some incorrect data corresponding to the daily water flow or electrical energy consumption. Then, the data for each of the remaining stations (73 stations) were stored in a database

For generating the decision tree, CART method is used. In the first CART stage, the number of patterns must be known. The patterns can be obtained with the clustering techniques. Using these techniques, a more precise model was obtained that, has ability to adapt easily to any other input data set.

The hydrophore stations were classified in five significant clusters (patterns) by their daily water flow (*WF*), pressure growth (*PG*) and daily electrical energy consumption (*W*) on the basis of the *K*-means clustering algorithm. The representation of these clusters (patterns) is given in Fig. 20.16. Table 20.3 presents the statistical parameters (average and standard deviation) for each input variable corresponding to all clusters.

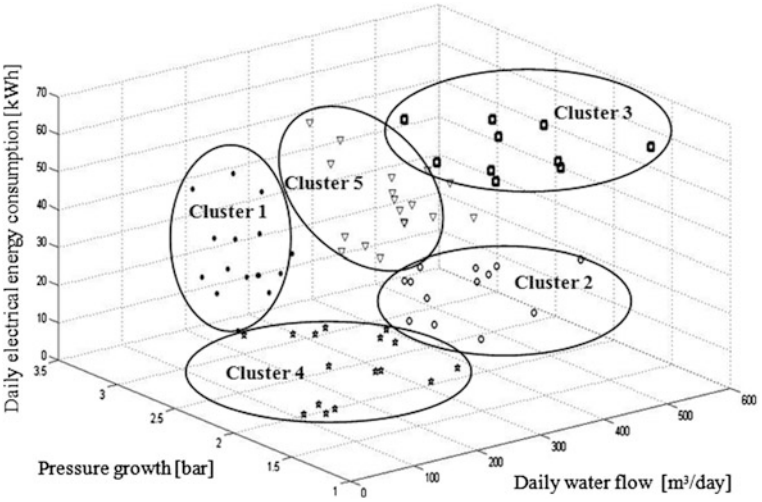

Fig. 20.16 The grouping of the the water hydrophore stations

Table 20.3 The results of the clustering process

Cluster	Number of stations	Daily water flow (m^3/day)		Pressure growth (bar)		Daily electrical energy consumption (kWh)	
		m	σ	m	σ	m	σ
1	16	166.97	39.27	2.83	0.27	29.73	7.19
2	14	314.00	58.68	1.71	0.25	29.20	5.14
3	10	463.37	44.08	2.40	0.22	54.72	5.54
4	15	143.37	59.33	1.78	0.30	14.86	4.52
5	18	329.13	43.07	2.46	0.26	41.90	6.92

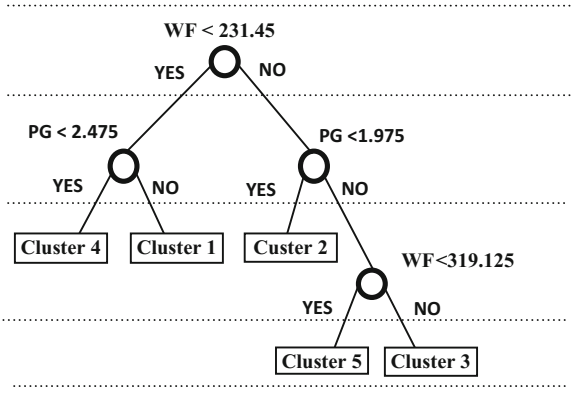

Fig. 20.17 The structure of the decision tree

Table 20.4 Rule set corresponding to decision tree

Rule 1	IF WF < 231.4 and PG < 2.47 THEN W—Cluster 4
Rule 2	IF WF < 231.4 and PG > 2.47 THEN W—Cluster 1
Rule 3	IF WF > 231.4 and PG < 1.97 THEN W—Cluster 2
Rule 4	IF WF > 231.4 and PG > 1.97 and WF < 391.12 THEN W—Cluster 5
Rule 5	IF WF > 231.4 and PG > 1.97 THEN W—Cluster 3

Table 20.5 The Confusion Matrix for the classification process (learning database)

Actual		Classified					Correctness rate
		Cluster 1	Cluster 2	Cluster 3	Cluster 4	Cluster 5	
Cluster 1	10	10	0	0	0	0	1.000
Cluster 2	13	0	11	0	1	1	0.846
Cluster 3	2	0	0	2	0	0	1.000
Cluster 4	15	0	0	0	15	0	1.000
Cluster 5	10	0	0	1	0	9	0.900

In the next stage, the algorithm uses 2/3 of the database for learning (50 water hydrophore stations) and of the 1/3 of database (23 water hydrophore stations) for testing. The structure of the decision tree corresponding to the learning database is shown in Fig. 20.17. The internal nodes have test rules for one of the variables (PG or WF) and the leaf nodes represent the final results of the decisions taken.

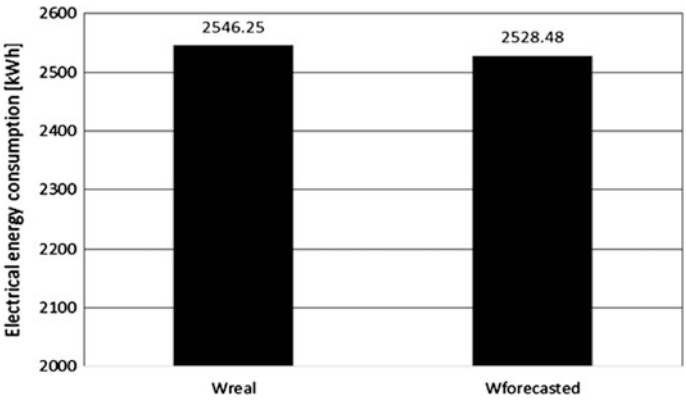

Fig. 20.18 The real and forecasted electrical energy consumption

Table 20.6 The Confusion Matrix for the classification process (test database)

Actual		Classified					Correctness rate
		Cluster 1	Cluster 2	Cluster 3	Cluster 4	Cluster 5	
Cluster 1	5	5	0	0	0	1	1.000
Cluster 2	2	0	2	0	0	0	0.846
Cluster 3	7	0	0	7	0	0	1.000
Cluster 4	1	0	0	0	1	0	1.000
Cluster 5	8	0	0	0	0	8	1.000

The rule set that characterizes the decision tree obtained is presented in Table 20.4. The confusion matrix corresponding to the classification process, for the learning database, is presented in Table 20.5.

The analysis of data from Table 20.5 indicated that all stations from Clusters 1, 3, and 4 were classified correctly, and only 4 stations (3 stations from Cluster 2 and 1 station from Cluster 5) were misclassified. Thus, it can be seen that for the learning database, the accuracy rate is 0.94.

This decision tree structure was verified on the test database. The results are presented in Table 20.6, corresponding to the confusion matrix. Only one station from Cluster 1 was misclassified, so that the accuracy rate is 0.96.

In the final stage, using information from the classification process (Table 20.3 and Eq. 20.10) the daily electrical energy consumption in the analysed water distribution system was obtained, as in Fig. 20.18. The forecasting error is 0.7% (17.77 kWh), which is better than the expected one by water companies (2–3%) [43].

20.4 Conclusions

A proper evaluation of the existing linkage between the two important components from human life (water and energy) can lead to saving both money and resources by water distribution companies. The investigation methods, which take in account the aspects of the two components, can lead to increasing energy efficiency in order to minimize electricity consumption in water distribution systems.

In this study, two approaches based on AI techniques (clustering and decision trees) for forecasting the amount of energy consumed in water use are presented. These approaches are tested on a real water distribution system from Romania.

The first approach is based on two stages in which the *K*-means clustering algorithm and a load simulation technique are exploited the electrical energy consumption forecasting. The *K*-means clustering algorithm was used in the profiling process to obtain the representative loading profiles of the hydrophore stations. The electrical energy consumption was forecasted using statistical techniques. The mean absolute percentage error in the forecasting process was 2.42%.

The second approach is based on a set of input data processed through the *K*-means clustering algorithm, and then on a decision tree through with which the daily electrical energy consumption for one or more hydrophore stations, depending on some input variables (the water flow and the pressure of the water in repression and aspiration zones of the pumps) was estimated with a very good accuracy. The forecasting error for electrical energy consumption was 0.7%.

Using these approaches, the forecasting errors of the electrical energy consumption are very close or even better than the ones expected by water companies (between 2 and 3%).

In both case studies, the results obtained demonstrate the utility of the AI techniques in resolving problems in water distribution systems operation. The solutions proposed can improve decision making, in order to ensure an efficient management in the water distribution systems.

References

1. Olsson G (2012) Water and energy nexus. In: Encyclopaedia of sustainability science and technology. Springer, New York
2. World Economic Forum. Energy vision update. Thirsty energy: water and energy in the 21st century. http://www3.weforum.org/docs/WEF_WaterAndEnergy21stCentury_Report.pdf
3. Stillwell A, King C, Webber M, Duncan I, Hardberger A. Energy-water nexus in Texas. Environmental defense fund. http://www.circleofblue.org/waternews/wp-content/uploads/2010/08/9479_Energy-WaterNexusinTexasApr20091.pdf
4. World Energy Council. Water for energy. https://www.worldenergy.org/wp-content/uploads/2012/10/PUB_Water_For_Energy_2010_WEC.pdf
5. Martin Delgad A (2012) Water footprint of electric power generation: modeling its use and analyzing options for a water-scarce future. Master of Science in Technology and Policy Thesis, Massachusetts Institute of Technology
6. Farley J, Gaddis E (2007) An ecological economic assessment. In: Restoring natural capital: science, business and practice. Island Press, Washington D.C.
7. European Commission. Directorate General for Environment. http://ec.europa.eu/environment/water/index_en.htm
8. Alliance to Save Energy. What watergy involves. https://www.ase.org/resources/what-watergy-involves
9. Boulos PF, Wu Z, Orr, CH, Moore M, Hsiung P, Thomas D (2001) Optimal pump operation of water distribution systems using genetic algorithms. In: American water works association distribution system symposium
10. Barry JA. Watergy: energy and water efficiency in municipal water supply and wastewater treatment cost-effective savings of water and energy.
11. Anton A, Perju S (2004) Monitoring the main parameters of a water supply pumping station over ten years. In: 6th International conference on hydraulic machinery and hydrodynamics
12. Goldstein R, Smith W. Water and sustainability: U.S. electricity consumption for water supply & treatment—the next half century. http://www.epri.com/abstracts/Pages/ProductAbstract.aspx?ProductId=000000000001006787
13. House L. Water supply related electricity demand in California. http://drrc.lbl.gov/publications/water-supply-related-electricity

14. Kenway SJ, Priestley A, Cook S, Seo S, Inman M, Gregory A, Hall M. Energy use in the provision and consumption of urban water in Australia and New Zealand. https://publications.csiro.au/rpr/download?pid=csiro:EP116078&dsid=DS1
15. Pulido-Calvo I, Gutiérrez-Estrada JC (2011) Selection and operation of pumping stations of water distribution systems. Environ Res J 5(3):1–20
16. Cutore P, Campisano A, Kapelan Z, Modica C, Savic D (2008) Probabilistic prediction of urban water consumption using the SCEM-UA algorithm. Urban Water J 5(2):125–132
17. Feldman K (2009) Aspects of energy efficiency in water distribution systems. In: 5th IWA Water Loss Reduction Specialist Conference, pp 85–89
18. Ionescu GC, Ionescu DS (2005) The optimization of energy consumption in water supply systems. Acta Electrotehnica 46(4):191–194
19. Grigoras G, Istrate M (2011) An efficient clustering method in evaluation of the electric energy consumption from water hydrophore stations. Int Rev Model Simul 4(2):813–818
20. Sârbu I (1997) Energetic optimization of the water distribution systems. Publishing House of the Romanian Academy, Bucharest
21. Szychta L (2006) Energy consumption of water pumping for selected control systems. Electr Power Qual Util J 12(1):67–73
22. Wagner J, Shamir U, Marks D (1988) Water distribution reliability: analytical methods. J Water Resourc Plann Manage 114(3):253–275
23. Zessler U, Shamir U (1989) Optimal operation of water distribution systems. J Water Resourc Plann Manage 115(6):735–751
24. Magadan M, Rivas J (2011) The impact of energy consumption on the benefit functions of enterprises: proposal of an energy efficiency indicator. Environ Eng Manage J 10(12): 1831–1834
25. Cartina G, Grigoras G, Bobric EC (2005) Clustering techniques in fuzzy modelling, Application in power systems. Venus Publishing House, Iasi
26. Bobric EC, Cartina G, Grigoras G (2009) Fuzzy technique used for energy loss determination in medium and low voltage networks. Electron Electr Eng 90(2):95–98
27. Cartina G (2000) Artificial intelligence modelling techniques in power system control. Model Optim Mach Build Field 1(7):254–257
28. Steitz T, Haubrich HJ, Bovy A (1993) Reliability evaluation of power distribution systems with local generation using fuzzy sets. In: 11th power systems computation conference, Avignon, France
29. Quinlan JR (1986) Induction of decision trees. Mach Learn 1(1):81–106
30. Yu Z, Haghighat F, Fung BCM, Hiroshi Y (2010) A decision tree method for building energy demand modelling. Energy Build 42(10):1637–1646
31. Olaru C, Wehenkel L (2003) A complete fuzzy decision tree technique. Fuzzy Sets Syst 138(2):221–254
32. Timofeev R (2004) Classification and regression trees (CART): theory and applications. Master's thesis, Humboldt University, Berlin
33. Loh WY (2008) Classification and regression tree methods. In: Encyclopaedia of statistics in quality and reliability. Wiley, pp 315–323
34. Lu X, Yang Z, Dong A (2005) Electricity market price spike forecast with data mining techniques. Electr Power Syst Res 73(1):19–29
35. Reston JC, Affonso CM, Oliveira RCL (2009) Pricing analysis in the Brazilian energy market: a decision tree approach. In: 2009 IEEE Power Tech, Bucharest
36. Razaee MR, Lelieveldt BPF, Reiber JHC (1998) A new cluster validity index for the fuzzy C-means. Pattern Recogn Lett 19(3/4):237–246
37. Halkidi M, Batistakis Y, Vazirgiannis M (2001) On clustering validation techniques. J Intell Inf Syst 17(2/3):107–145
38. Gordon AD (1999) Classification, 2nd edn. Chapman & Hall, NewYork
39. Rousseeuw PJ (1987) Silhouettes: a graphical aid to the interpretation and validation of cluster analysis. J Comput Appl Math 20:53–65

40. Istrate M, Grigoras G (2010) Energy consumption estimation in water distribution systems using fuzzy techniques. Environ Eng Manage J 9(2):249–256
41. Grigoras G, Istrate M, Scarlatache F (2013) Electrical energy consumption estimation in water distribution systems using a clustering based method. In: 6th international conference on electronics, computers and artificial intelligence
42. Grigoras G (2014) Assessment of electrical load in water distribution systems using representative load profiles-based method. Adv Elect Eng 2014:1–10
43. Jentgen L, Kidder H, Hill R, Conrad S. Water consumption forecasting to improve energy efficiency. http://www.waterrf.org/PublicReportLibrary/91189.pdf

Chapter 21
Flow Control Devices for Wind Turbines

Iñigo Aramendia, Unai Fernandez-Gamiz, Jose Antonio Ramos-Hernanz, Javier Sancho, Jose Manuel Lopez-Guede and Ekaitz Zulueta

Abstract The following chapter provides an overview about available knowledge, references and investigations on the active and passive flow control devices, initially developed for aeronautic industry that are currently being investigated and introduced on wind turbines. The main goal pursued with the introduction of these devices is to delay the boundary layer separation and enhance/suppress turbulences. The aim is to achieve a lift enhancement, drag reduction or flow-induced noise reduction among other parameters. However, achieving these goals present some issues, because the improvement of one of these parameters may suppose an undesired effect in another. For this reason it is necessary to study in detail each one of these devices, their operating concept, applications and their main advantages and drawbacks. Depending on the flow control nature, devices can be classified as actives or passives. Passive techniques allow to improve the performance of the

I. Aramendia (✉) · U. Fernandez-Gamiz · J. Sancho
Department of Nuclear Engineering and Fluid Mechanics,
University of the Basque Country, Nieves Cano 12,
01006 Vitoria-Gasteiz, Araba, Spain
e-mail: inigo.aramendia@ehu.eus

U. Fernandez-Gamiz
e-mail: unai.fernandez@ehu.eus

J. Sancho
e-mail: javier.sancho@ehu.eus

J.A. Ramos-Hernanz
Department of Electrical Engineering, University of the Basque Country,
Nieves Cano 12, 01006 Vitoria-Gasteiz, Araba, Spain
e-mail: josean.ramos@ehu.eus

J.M. Lopez-Guede · E. Zulueta
Department of Systems Engineering and Automatics,
University of the Basque Country, Nieves Cano 12, 01006 Vitoria-Gasteiz,
Araba, Spain
e-mail: jm.lopez@ehu.eus

E. Zulueta
e-mail: ekaitz.zulueta@ehu.eus

N. Bizon et al. (eds.), *Energy Harvesting and Energy Efficiency*,
Lecture Notes in Energy 37, DOI 10.1007/978-3-319-49875-1_21

wind turbines without external energy expenditure whereas active techniques require external energy for their activation. There are a lot of devices and in this chapter there have been compiled some of the most important ones, both passives devices (Vortex Generators, Microtabs, Spoilers, Fences, Serrated trailing edge) and actives devices (Trailing edge flaps, Air Jet Vortex Generators, Synthetic Jets).

Keywords Wind turbine · Flow control · Passive devices · Active devices · Cost of energy · Energy efficiency

Abbreviation and Acronyms

AcVG	Actuator Vortex Generator
AFC	Active Flow Control
AJVG	Air Jet Vortex Generator
CFD	Computational Fluid Dynamics
COE	Cost of Energy
DS	Delay Stall
DOF	Degree of Freedom
DTU	Danmarks Tekniske Universitet
EWEA	Energy Wind Energy Association
FEM	Finite Element Method
VG	Vortex Generator
LE	Leading Edge
MC	Mid Chord
MDO	Multidisciplinary Design Optimization
NREL	National Renewable Energy Laboratory
O&M	Operation and Maintenance
RANS	Reynolds Averaged Navier Stokes
RWT	Reference Wind Turbine
SST	Shear Stress Transport
TE	Trailing Edge
PVGJ	Pulsed Vortex Generator Jet
E_C	Kinetic Energy
ρ	Density
t	Time
C_L	Lift Coefficient
C_D	Drag Coefficient
A	Area
v	Velocity
α	Angle of Attack
c	Chord
b	Span
h	Height

21.1 Introduction

Nowadays, the depletion of global fossil fuel reserves, the environmental concerning and energy security after recent accidents as happened in Fukushima nuclear plant in Japan in 2011, has served to focus attention on the development of ecologically compatible and renewable energy sources. Besides, the power demand is also increasing more and more through new emergent economies as China, Brazil or India.

At this point, the optimization of renewable power systems (wind, solar thermal, biomass, etc.) is a key point to be able to compete in energy production and cost against the traditional energies. Wind energy becomes in a promising technology able to provide a large portion of the power requirements in many countries of the world. Wind turbines are a practical way to capture and convert the kinetic energy of the atmospheric air to either mechanic or, consequently, electrical energy.

According to EWEA [1] (European Wind Energy Association) wind power is the generating technology with the highest rate for new installations in 2014, representing the 43.7% of total power capacity, an increment of 12% in relation to 2013. Since 2000, 29.4% of new capacity installed in Europe has been wind power, 56.2% renewables and 91.1% renewables and gas combined.

The total wind power generating capacity has been increasing continuously, not only in Europe but worldwide for the last 15 years [2], as it can be seen in Fig. 21.1.

In 2015, China was the country which led the wind capacity installed, with almost a half of the total 63.000 MW, followed by the USA and Germany. 12.105 MW of the global amount capacity until 2015 corresponds to offshore installations being UK, Germany and Denmark the countries with more wind capacity installed of this type (5061, 3295 and 1271 MW respectively).

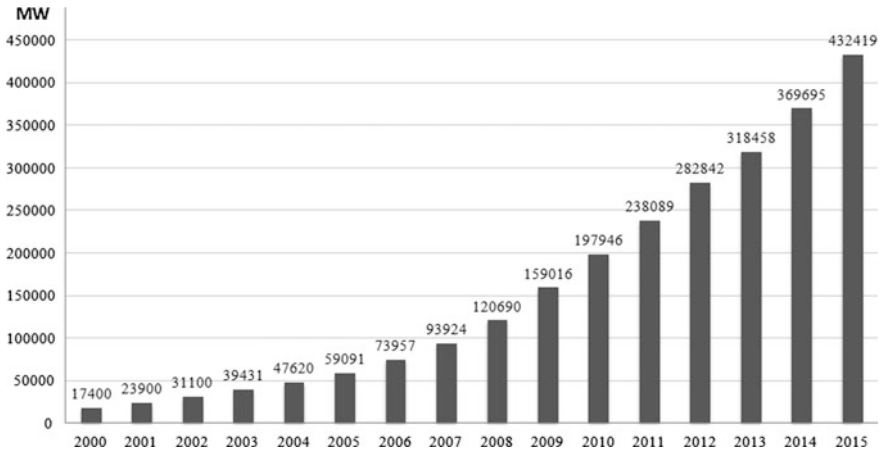

Fig. 21.1 Global cumulative installed wind capacity 2000–2015

However, even though the wind cost of energy has decreased in the last decade, a high initial investment is yet required, so it is necessary to improve its lifetime and efficiency in order to keep it economically viable.

There are several research fields to achieve this goal. Development of new materials which allow to reduce the structure weight or new blade designs just to reduce the fatigue loads and increase the aerodynamic performance of the rotors, are some of them. CFD simulations become a very interesting tool to study the behavior of this new improvements and their impact in wind turbines.

The considerable growth of wind turbines size and weight in the last years has made it impossible to control as they were controlled 30 years ago. Rotors of 120 m are now a reality. Johnson et al. [3] compiled some of the most important load control techniques that could be used in wind turbines to assure a safe and optimal operation under a variety of atmospheric conditions. They include blades made of soft, flexible materials that change shape in response to wind speed or aerodynamic loads, aerodynamically-shaped rotating towers, flexible rotor systems with hinged blades and other advanced control systems.

The higher the size of a wind turbine the higher the structural and fatigue loads. By researching and working in new and innovative load control techniques a decrease of these excessive loads could be achieved, which affect the rotor and other key components of the turbine. Loads on wind turbines are normally divided into extreme structural loads and fatigue loads. Reducing these fatigue loads is a main goal, which can reduce the maintenance costs and improve the reliability of wind turbines.

21.2 Wind Turbine Improvement Goals

The improvements of wind turbines present 3 key points [4]:

1. Setting upper bounds on and limiting the torque and power experienced by the drive train, mainly the low-speed shaft.
2. Minimize the fatigue life extraction from the rotor drive train and other structural components due to changes in wind direction, speed (including gusts), and turbulence, as well as start-stop cycles of the wind turbine.
3. Maximize the energy production.

The cost of energy (COE) [5] plays an important role inside this last key point, in order to maintain this kind of energy as a viable alternative in economic terms with traditional or other renewable energies. There are three independent variables to calculate its value as we can see in (Eq. 21.1): the total energy captured by the turbine and the costs related with the turbine (capital cost) and with the operation and maintenance (O&M) works.

$$\text{COE} = \frac{\text{Lifetime Energy Captured}}{\text{Capital Cost} + \text{O\&M Costs}} \tag{21.1}$$

The loads, directly related with the second key point, can be separated into aerodynamics and structural loads. The relative velocities around the blade sections, as a result of horizontal or vertical wind shear, turbulences and yaw and tilt misalignment, influence the aerodynamic loads on the rotor. The gravitational forces can also play a role producing periodic structural loads in the rotor blades. Control systems should be able to reduce and minimize the variation of these aerodynamic loads or to add damping to the structural nodes.

First of all, it is essential to know the relationship between the wind speed and the normalized power in a wind turbine. There are four different operating regions, as shown in Fig. 21.2, which define the power curve.

In Region 1, the wind speed is not enough to power generation. In Region 2, which lies between the cut-in velocity ($V_{cut\text{-}in}$) and rated velocity (V_{rated}), the generator works under the rated power. In Region 3, the power output is limited by the turbine. This happens when there is enough wind intensity for the turbine to reach its rated output power. The Region 4 corresponds to higher wind speed, which could shut down the turbine and even cause damage in the blades or structure of the wind turbine, with the resulting impact on maintenance costs.

The curve which separates the regions 1 and 2 shows a basic law about generation of power, where the power is directly related to the wind speed cubed. (See Fig. 21.3).

Air volume to the rotor:

$$V = A \cdot v \cdot t \tag{21.2}$$

Kinetic energy contribution from the air to the rotor:

$$E_C = \frac{1}{2} \cdot dAv \cdot t \cdot v^2 \tag{21.3}$$

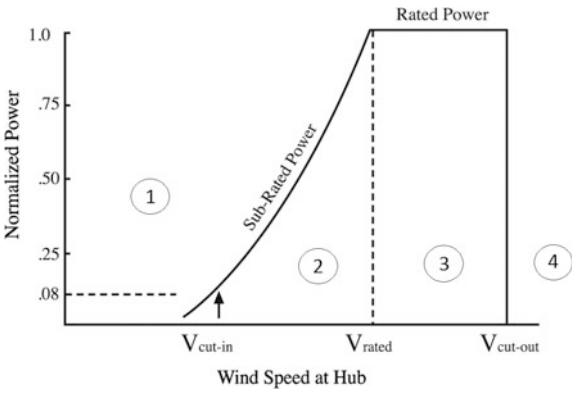

Fig. 21.2 Power curve of a wind turbine [3]

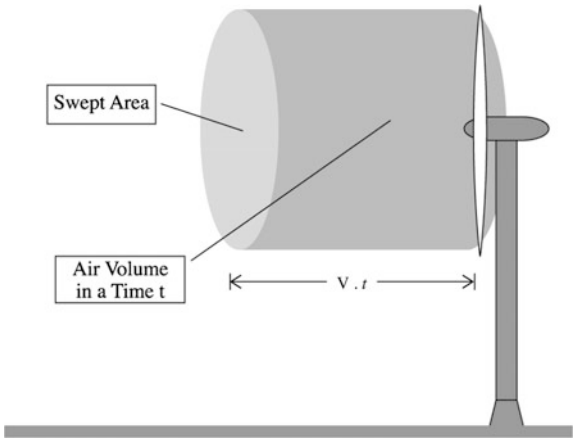

Fig. 21.3 Air volume to the rotor

Delivered power to the rotor:

$$E_C = \frac{1}{2} \cdot dA \cdot v^3 \tag{21.4}$$

21.3 Flow Control Devices Classification

Through the last decades many different flow control devices have been developed. Most of them were created for aeronautical issues and this was its first research field and application. Nowadays researchers are working to optimize and introduce this type of devices in wind turbines. Wood [6] developed a four layer scheme which allows to classify the different concepts that are part of all flow control devices (See Fig. 21.4).

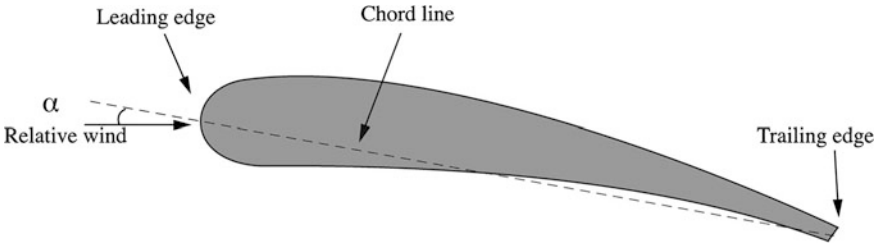

Fig. 21.4 Section and main components of an airfoil

1st Layer
According to the technique:

1. Geometric device (G): Modify the geometry and airfoil shape and thereby the airflow about it.
2. Fluidic device (F): Change the flow about the blade section by either adding air into or subtracting air from external flow.

2nd Layer
Depending on where the device is set:

1. Near the leading edge (LE).
2. Near the trailing edge (TE).
3. In the mid-chord (MC).

3rd Layer
Depending on how the device adjusts the lift curve, flow control devices modify the lift curve of an airfoil in two different ways (See Fig. 21.5).

1. Shifting the curve up (increasing lift) or down (reducing lift). (See Fig. 21.5b).
2. Extending the lift curve of the airfoil to stall at a higher angle of attack (α). (See Fig. 21.5a).

To alleviate loads successfully, it is indispensable the device to be able to reduce the generated lift. With a first watching to Fig. 21.5, it can be seen that delaying stall (DS) only increases lift at high angles of attack. For that reason devices based on DS concept would not be considered as a good alternative for load mitigation. Nevertheless, a suggestion presented by Corten [7] provides a different way of using this type of devices to mitigate turbine loads. Their main purpose is to include them to an existent profile to increase C_{Lmax} and, consequently, to delay stall. In Fig. 21.6 we can see an example with passive vortex generator (VG).

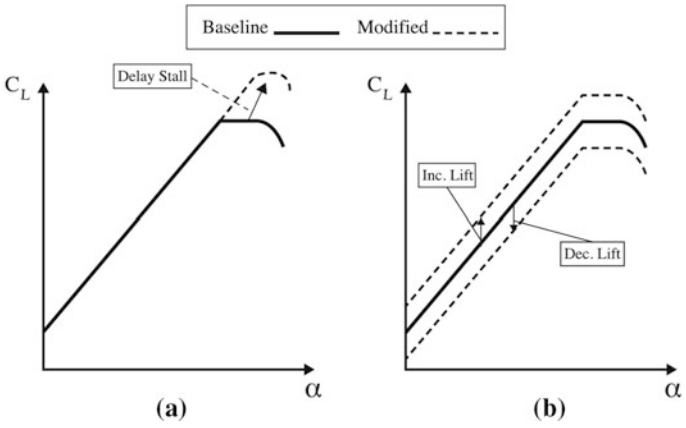

Fig. 21.5 Lift curve variation based on C_L and α [3]

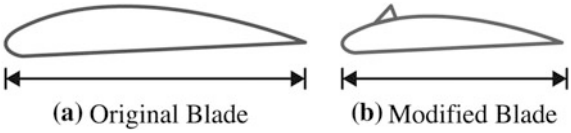

Fig. 21.6 **a** Original airfoil and **b** redesign airfoil with a VG for a same lift generation [3]

It is known that lift force is defined by the (Eq. 21.5):

$$F_L = C_{L\max} \cdot \frac{1}{2} \cdot \rho \cdot A \cdot v^2 \tag{21.5}$$

where (ρ) is air density in kg/m^3, (A) is airfoil area in m^2 and (v) is the air velocity over the blade in m/s. C_{Lmax} is the maximum lift coefficient.

The idea presented by Corten was to redesign the blade in order that the maximum sectional lift of a blade with a DS device matches that of the original blade without a DS device. Figure 21.6 illustrates the difference in chord length between both designs. Density and velocity around the blades would be equal at similar conditions. So, if C_{Lmax} is increased by the effect of the DS device, the chord (c) could be reduced an equivalent quantity according to the lift force equation, as it can be seen in (Eqs. 21.6 and 21.7).

Without a DS device

$$\mathrm{F_L} = \mathrm{C_{Lmax}} \cdot \frac{1}{2} \cdot \rho \cdot \mathrm{A} \cdot \mathrm{v}^2 = \mathrm{C_{Lmax}} \cdot \frac{1}{2} \cdot \rho \cdot (\mathrm{c} \cdot \mathrm{b}) \cdot \mathrm{v}^2 \tag{21.6}$$

With a DS device

$$F_L = C_{L\max} \uparrow \cdot \frac{1}{2} \cdot \rho \cdot A \downarrow \cdot v^2 = C_{L\max} \cdot \frac{1}{2} \cdot \rho \cdot (c \downarrow \cdot b) \cdot v^2 \tag{21.7}$$

where (c) is the chord of the blade, in meters, and (b) is the span of the blade in meters as well.

4th Layer

Depending on device working conditions, we can classify them as steady or unsteady devices (if the position of a device varies with time about a nominal setting or not). For instance, a TE flap system is considered a steady device because it changes its position to produce a sequence of steady state conditions.

21.4 Types of Devices

Depending on their operating principle they can be classified as actives or passives. This chapter is going to describe some of the main devices in each category.

(1) Passive control

(a) Vortex Generators.
(b) Microtabs.
(c) Serrated trailing edge.
(d) Fences.
(e) Spoilers.

(2) Active control

(a) Trailing-edge flaps.
(b) Synthetic jets.
(c) Air Jet Vortex Generators.

Passive control techniques represent an improvement in the turbine's efficiency and in loads reduction without external energy consumption. Active control techniques, instead, require external energy or a secondary power source. Even though, further investigations must be carried on to make sure that this raise in energy output can balance the external energy necessary for load control together with the increase in turbine capital and O&M costs.

Johnson et al. [3] made an analysis and discussed 15 different devices for wind turbine control. Some of them are still being tested on full-scale turbines.

21.4.1 Passive Control Systems

21.4.1.1 Vortex Generators

A Vortex Generator (VG) is a passive flow control device which modifies the boundary layer fluid motion bringing momentum from the outer flow region into the inner flow region of the wall bounded flow. Its main goal is to delay the flow separation and increase the maximum lift coefficient C_{Lmax}. VGs are designed to re-energize the boundary layer by inducing momentum transfer between the free stream velocity and the near wall region. The boundary layer separation begins when the portion of boundary layer closest to the wall or leading edge reverses in flow direction. (See Fig. 21.7). The separation is where the shear stress is null or close to under stall conditions.

Initially introduced by Taylor [8] VGs have been investigated for more than fifty years for a wide range of applications in aerodynamics and airplane wings. They are small vanes, usually triangular or rectangular, inclined at an angle to the incoming flow and placed as close as possible of the leading edge. They are generally assembled in a spanwise on the suction side of the blade and present the advantage that they can be added as a post-production fix to blades that do not perform as expect. Its height is usually similar to the boundary layer thickness.

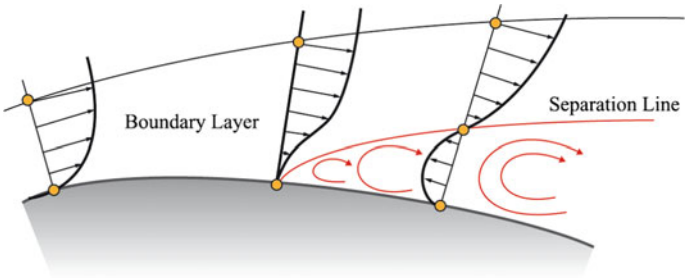

Fig. 21.7 Boundary layer separation and velocity profile with an adverse pressure gradient

Fernandez-Gamiz et al. [9] studied the behavior of a rectangular VG on a flat plane and the streamwise vortices produced by them to investigate how the physics of the wake behind VGs in a negligible streamwise pressure gradient flow can be reproduced in CFD simulations and their accuracy in comparison with experimental observations. (See Fig. 21.8).

Pearcey [10] noted that the vane type VG can be set in two basic ways, as shown in Fig. 21.9.

1. Co-rotating array: the vortices which are shed are all of the same rotational direction.
2. Counter-rotation array: the rotational sense of the vortices alternate along the array.

Godard and Stanislas [11] demonstrated that VGs work most efficiently when creating counter-rotating vortices and their geometry is triangular.

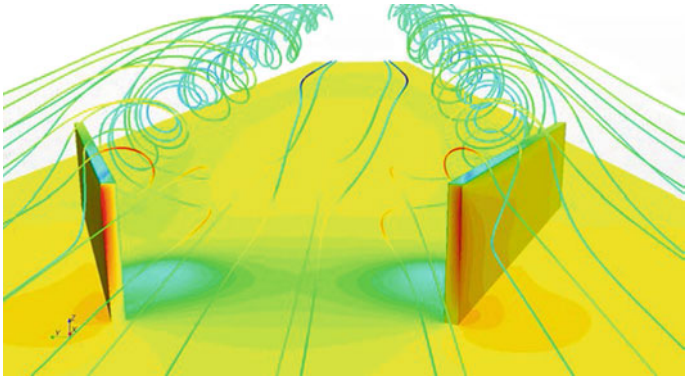

Fig. 21.8 Streamlines on a flat plane with Vortex Generators (Fernandez-Gamiz [9])

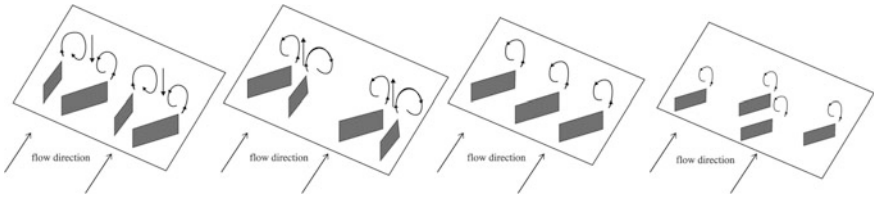

Fig. 21.9 Pairs of VGs generating co-rotating and counter-rotating vortices

In order to study the impact of VGs on wind turbines, to optimize their position and distribution, CFD tools can be used. However, modelling a fully-meshed profile with VGs becomes prohibitively expensive because of its small size (VGs height are usually equal to the boundary layer thickness). This great number of cells in the simulation becomes a trouble in computation time and therefore, in costs.

An alternative way of modeling VGs in CFD is to model the influence of the vortex generator on the boundary layer using body forces and boundary conditions generated by them. In that way, Bender et al. [12] presented the BAY model for simulating the vane vortex generators without the necessity of defining the VG geometry in the mesh. Later, Jirasek [13] introduced a new version of this model, called jBAY model, based on the lifting force theory.

Fernandez-Gamiz et al. [14] presented a detailed comparison between four different models of VGs on a flat plane. The first one is based on the traditional mesh-resolved VG. The second one, called Actuator Vortex Generator Model (AcVG), based on [12] provides an efficient method for CFD simulations of flows with VG's. The third one is an experimental model (Velte et al. [15]) based in experimental data, where measurements were carried out in a low speed closed-circuit wind tunnel. The fourth model is the analytical model of the primary vortex based on the helical structure of longitudinal embedded vortex. Following the same idea, Zamorano et al. [16] studied the evolution of the wake downstream a rectangular VG at different incidence angles. Øye [17] and Miller [18] compared, on a 1 MW wind turbine, the measured power curves with VGs and without them. Although they used quite rough methods for the VGs design optimization, both studies showed that, in these cases, VGs on average increased the output power for nearly all winds.

These devices present some important advantages, such as their small size, that allows to distribute a big number of them along the profile. They are also replaceable with no trouble in an inexpensive and uncomplicated way and they have the possibility to add them once the aerodynamic profile is built. On the other hand, their main disadvantage is the drag increases (C_D) that involve the implantation of this device, an undesirable feature for this kind of applications. Great care is also need to be taken in their blade integration not to deteriorate the performance of the wind turbine or the aeroelastic conditions.

Case Study: DTU 10 MW Reference Wind Turbine

The DTU 10 MW RWT (Reference Wind Turbine) is part of the Light Rotor Project [19]. Initiated as a cooperation of DTU Wind Energy and Vestas, its main goal is to create the design basis for next generation wind turbines of 10 MW (See Table 21.1).

The purpose of this design is [20]:

1. To achieve a design in a sequential multidisciplinary design optimization process.
2. To obtain a high-quality aerodynamic performance with lower weight.
3. To achieve a high-detail design for a complete comparison of both aero-elastic as well as high fidelity aerodynamic and structural tools.
4. To provide a openly available design basis for next generation of wind turbines.

In this project the manufacturing process is not considered, so the design does not provide a design to that end. Therefore, the purpose is not to provide a design of a complete wind turbine but of the rotor.

DTU Wind Energy developed some codes used in the design of DTU 10 MW RWT.

1. HAWC2 (Horizontal Axis Wind turbine simulation Code 2nd generation). An aeroelastic code proposed for calculating wind turbine response in time domain.
2. HAWCstab2: (Aero-servo-elastic stability tool for wind turbines).
3. BECAS. Determines cross section stiffness properties using FEM.
4. HAWTOPT (Wind turbine optimization software).
5. EllipSys2D/3D. A multiblock finite volume discretization of the incompressible of RANS equations.

Table 21.1 Key parameters of the DTU 10 MW RWT [20]

Description	Value
Rating	10 MW
Rotor orientation, configuration	Upwind, 3 blades
Control	Variable speed, collective pitch
Drive train	Medium speed, multiple stage gearbox
Rotor, hub diameter	178.3, 5.6 m
Hub height	119 m
Cut-in, rate, cut-out wind speed	4, 11.4, 25 m/s
Rated tip speed	90 m/s
Overhang, shaft tilt, pre-cone	7.07 m, 5º, 2.5º
Pre-bend	3 m
Rotor mass	229 tons (each blade ~41 tons)
Nacelle mass	446 tons
Tower mass	605 tons

ABAQUS and XFOIL were used as well for the structural design (FEM computations) and airfoil characteristics respectively.

Recently, Troldborg et al. [21] presented a case study of the DTU 10 MW RWT, making a CFD comparison with and without VGs installed on the inboard part of the blades. A personalized version of the BAY model, previously mentioned, was used in order to overcome the computational cost of simulating a blade with a large number of this type of devices on it. Forty VG pairs are distribute on each blade and were setting up in counter-rotation distribution. A grid sensitivity study was performed, with five different configurations, to check out that the model calculates the lift with precision on all grids.

The EllipSys3D flow solver was implemented which solves, in a steady state mode, the incompressible finite volume Reynolds-Averaged Navier-Stokes (RANS) equations. A fully developed turbulent boundary layer on the blade surface was assumed using the k-ω Shear SST Model [22, 23].

Figure 21.10 illustrates the rotor surface mesh, together with the VGs region as can be seen with a little more detail in the second picture, corresponding to 8 cells per VG pair and for a height of the first boundary layer of 2×10^{-6} m in order to obtain a y+ < 2.

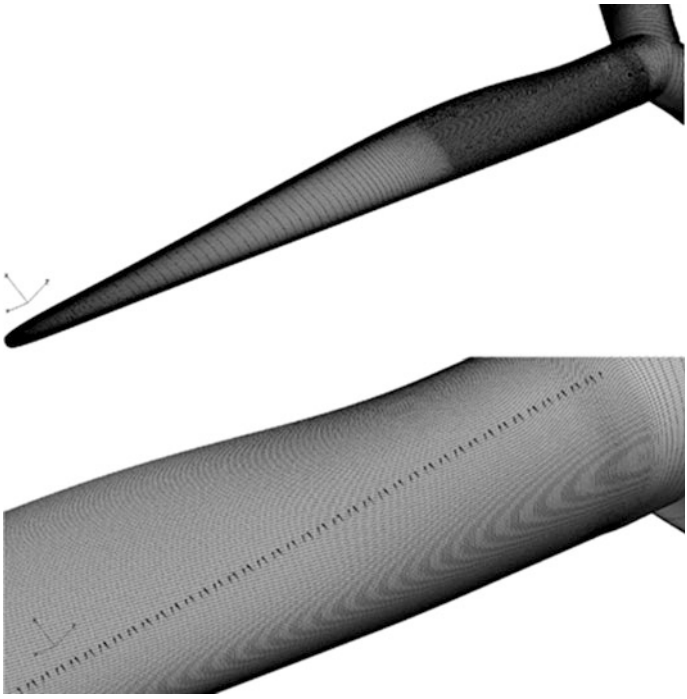

Fig. 21.10 Surface mesh for the DTU 10 MW RWT [21]

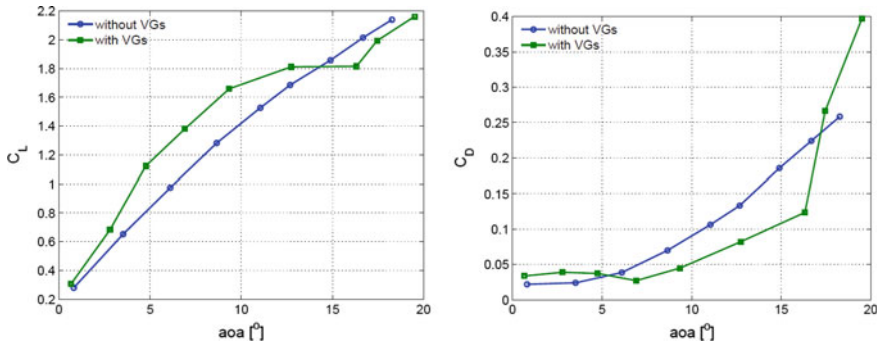

Fig. 21.11 Lift and drag polars for the section at r = 24 m (airfoil thickness 41%) [21]

The results of the simulations, in a blade with VGs, showed an increase in both tangential and normal forces at the inboard part of the blade. At the outer part of the blade, however, a slight reduction in both forces was appreciated in the case with VGs installed. The power improvement caused by the VGs is 0.51% in the best scenario studied corresponding to a wind speed of 10 m/s. Figure 21.11 shows the lift and drag curves with and without VGs at a radial position r = 24 m. It can be seen how the VGs increase the lift for a broad series of angles of attack but, on the other hand, involve a more abrupt stall which finally causes a higher drag and a lower lift.

The simulations showed a good adjustment between CFD results and wind tunnel experiments, so the 8 grid cells per VG pair can be considered enough to capture the effect of them.

21.4.1.2 Microtabs

The microtabs consist on small tabs situated near the TE of an airfoil, which projects perpendicular to the surface of the airfoil a few percent of the chord length (1–2% c) corresponding to the boundary layer thickness.

The small movement of these microtabs jets the flow in the boundary layer away from the blade's surface, bringing a recirculation zone behind the tab, as can be observed in Fig. 21.12 affects the aerodynamics shifting the point of flow separation and, therefore, providing changes in lift. Lift improvement is obtained by deploying the microtab downwards (on the pressure side) and lift reduction is obtained by deploying the microtab upwards (on the suction side).

Van Dam [25] has made multiple studies and investigations into this topic, including CFD simulations and wind-tunnel experiments in order to determine their optimal distribution height and location. The results provided, as previous studies, that the best place to situate the lower surface tab with respect to lift and drag was around 95% c with a height of 1% c and around 90% c for the upper surface tab.

They present some appealing features for wind turbine control applications:

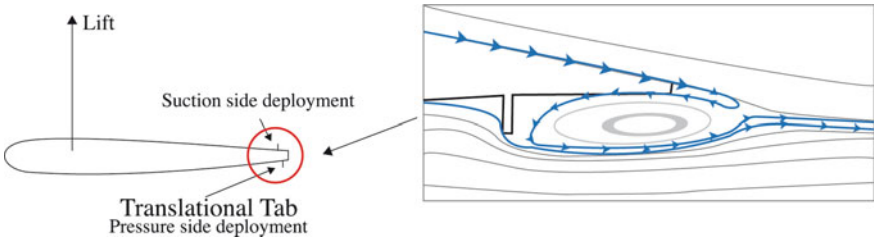

Fig. 21.12 Microtab concept and zoom of streamlines around a trailing-edge region during tab pressure side deployment (Chow and Van Dam) [24]

1. Small size.
2. Low power requirements for its activation.
3. Simplicity of the design (low cost).
4. They can be installed without significant changes in the actual techniques to manufacture the profiles.

Case Study: New Design of a Microtab Deployment Mechanism

The existing microtab device system described before presents two main drawbacks (See Fig. 21.13):

1. The insufficient tab height when it is fully-deployed.
2. The actuating mechanism which causes stiction during tab deployment.

Tsai et al. [26] presented recently and innovative design to improve the microtabs performance. The new microtab system is based on a four-bar linkage that overcomes the two disadvantages previously mentioned and providing:

1. An increase of the maximum tab height in relation to the existing microtab system. From 1 to 1.7% c.
2. A higher stability due to the four-bar linkage mechanism.

The four-bar linkage mechanism has four links and pivot joints (See Fig. 21.14); and therefore a DOF = 1. The degree of freedom (DOF) of a mechanism, i.e. the number of independent moves it has, is defined by Gruebler's equation:

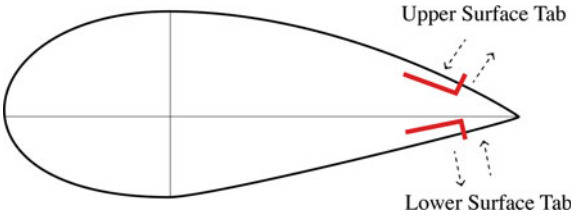

Fig. 21.13 Existing microtab actuation system [26]

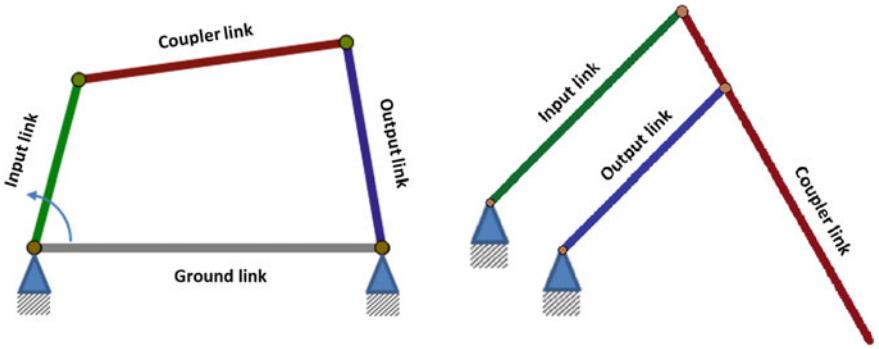

Fig. 21.14 Four-bar linkage scheme and the new scheme which is used for the microtab

$$DOF = 3(N - 1) - 2M \tag{21.8}$$

where M is the number of pivot joints and N is the number of links.

The input link is connected to an actuator which is the responsible for controlling the movement of the system, retracting or extending the microtab. Due to the space limitations in the trailing edge, the microtab cannot be positioned normal to the lower surface but a tilting angle is required. The steadiness and reliability improvement is achieved using five links (three input links and two output links) instead of the lever arm which is used in the existing microtabs.

In normal conditions, this new microtab will describes a curved trajectory throughout its deployment and retraction. To avoid that and to remain a simple straight line motion the actuator input bar is transformed into a V-shape. The measurements of the links and their angles, the stroke length and the slot length were also calculated as well as the force of the actuator.

21.4.1.3 Serrated Trailing Edge

Wind turbine noise is one of the main issues for the widespread use of wind energy. The sources of aerodynamic noise can be divided into [27]:

1. *Airfoil self-noise*: is produced by the blade in an undisturbed inflow and it is caused due to the interaction between an airfoil blade and the turbulence produced in its own boundary layer and near wake. Self-noise can be tonal or broadband in character and may be caused by several mechanisms, such as laminar boundary-layer vortex-shedding noise, turbulent boundary-layer/trailing edge interaction noise (trailing-edge noise), blade tip noise or trailing-edge bluntness noise.
2. *Inflow-turbulence noise*: it depends on the atmospheric conditions and it is caused by the interaction of upstream atmospheric turbulence with the blade.

Originally, the aerodynamic surfaces of wind turbine blades have sharp or moderately blunt trailing edges from which the wake is shed. The shedding of the wake and the confluence of flow from the pressure and suction sides of the profile are sources of aerodynamic noise, and increased drag and reduced lift. It has long been recognized that airfoil trailing edge noise may be reduced by modifying the trailing edge geometry so that the efficiency by which vorticity is scattered into sound is reduced. One alternative to resolve this trouble was patented by Siemens [28] and consists in a flexible serrated trailing edge, also known as Dino Tail, shown in Fig. 21.15.

Over the years, the characteristics and properties of airfoil noise have been studied extensively in both theoretical and experimental investigations. Both inflow turbulence and self-noise mechanisms were considered and dependence on parameters such as flow speed, angle of attack or radiation direction was studied by Howe [29]. About experimental studies, Oerlemans et al. [30] carried out different investigations where they tested the noise reduction in NACA 64418 airfoil and in blades of 2.3 MW wind turbine.

As an added aerodynamic profile, it presents the advantage of creating a customized geometry profile for each device according to the operating conditions in which it is located (See Fig. 21.16).

21.4.1.4 Fences

Fences, a system patented in 2009, consist in fin-like vertical surfaces attached to the upper surfaces of the wing that are used to control the airflow [31]. Their purpose is to disrupt the spanwise airflow, protecting the outboard wing section from a developing inboard stall. So, keeping the outboard section from stalling,

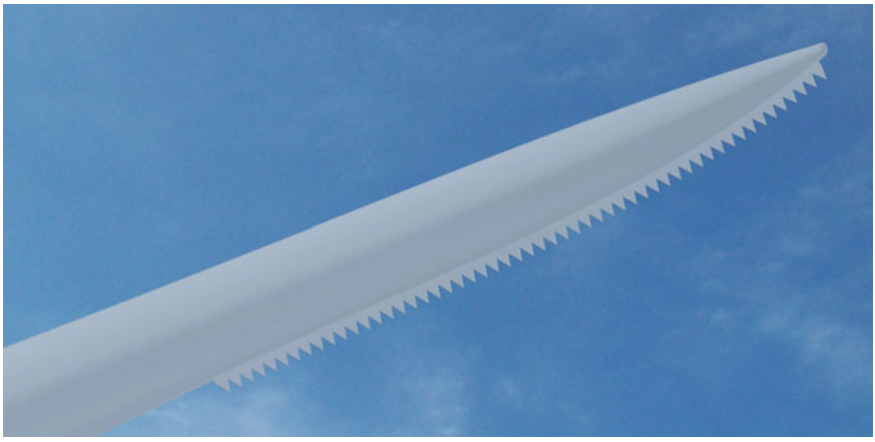

Fig. 21.15 Wind turbine blade with serrated trailing edge device

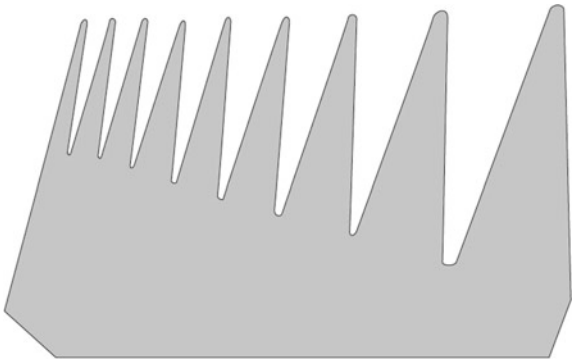

Fig. 21.16 Sawtooth trailing-edge serrations

aileron effectiveness is maintained during a stall, enabling the pilot to keep the aircraft level and exit the stall safety.

On straight wing airplanes they control the airflow in the flap area and on swept wing airplanes they prevent the accumulation of air toward the tip at high angles of attack placing them at about two-thirds of the way out towards the wing tip. In both cases, they give better slow speed handling and stall characteristics (See Fig. 21.17).

On wind turbines, the airflow also spreads in spanwise direction of the blades. This airflow generate adverse consequences in wind turbines performance, particularly because contribute to the separation of the main airflow of the blade surface, and therefore, reduce the rotor blade lift.

In order to fix that problem a fence is placed (See Fig. 21.18) extending through the entire blade surface in chord-wise direction, to prevent the creation of these airflows. This barrier or wall delay this effect by preventing the spanwise flow from moving too far along the wing and gaining speed.

The extent to which the fence is able to prevent these airflows is directly related to the fence height. However, the higher the height, the higher the weight, besides the fact that it affects to other aerodynamic characteristics of the blade, as the lift. So, it comes to choose a fence design that does not get worse the blade qualities, even though does not remove the spanwise airflow completely.

The required height and length of the particular planar element and the optimal position of this element on the suction side of the rotor blade inherently varies with the distance from the rotor axis of rotation, the blade contour depth, the rotor width, the most likely speed of the incident airflow, etc. So, the best configuration is determined empirically.

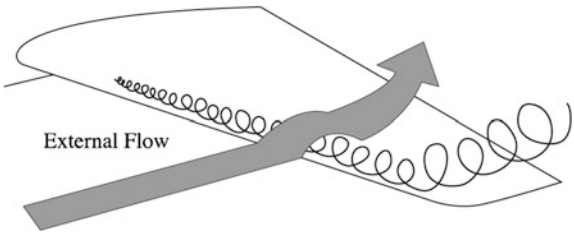

Fig. 21.17 Spanwise airflow through the blade

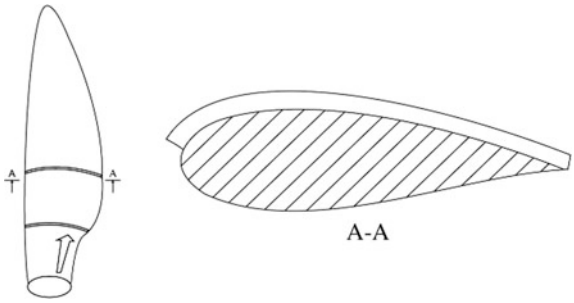

Fig. 21.18 Sketch of wind turbine blade with a fence installed and its section A-A [31]

Chow and Van Dam [32] made a fence height study with an NREL 5-MW blade of 63 m span. The fence height study was made at the same constant spanwise location or maximum chord location, at 13.7 m from the blade baseline. Figure 21.19 illustrates the percent change in power and thrust for different fence heights, for a free stream velocity of 11 m/s and rotor speed of 11.89RPM. It can be appreciated a nearly constant difference between power and thrust for large fence heights ($h_{fence} > 5\%c_{max}$) and the maximum power values for heights between 1 and $2.5\%c_{max}$. The thrust and power curves are very pronounced for small fence heights ($h_{fence} < 3\%c_{max}$). At the spanwise position of $2\%c_{max}$ is located the most favorable fence height, with a power increase of 0.67% and a thrust increase of 0.34% (See Fig. 21.19).

The previous study was made at the same constant spanwise location or maximum chord location; so now a fence location study is needed in order to determine the optimal place where it should be located. Fence locations from 9.2 through 15.7 m are studied in 0.5 m increments with a fence height of $10\%c_{max}$. The free

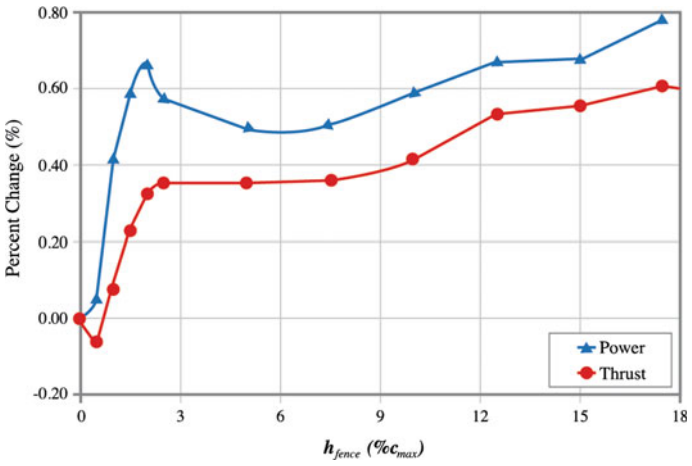

Fig. 21.19 Percent change in rotor power and thrust for different fence heights relative to the baseline NREL 5 MW blade (Chow and Van Dam [32])

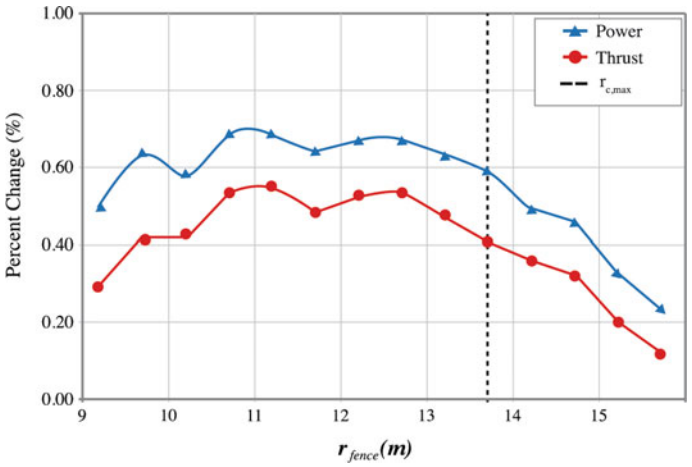

Fig. 21.20 Percent change in rotor power and thrust for various fences located at various spanwise fence locations relative to the baseline NREL 5 MW blade (Chow and Van Dam [32])

stream wind and rotor speeds remain constant as in the previous study (11 m/s and 11.89RPM, respectively). Figure 21.20 illustrates the thrust and power curves and their relation, almost constant over the entire range of spanwise locations studied, with a relatively larger increment in power capture of 0.15% in comparison to thrust. The effectiveness of the fences clearly gets worse when fences are located further and further outboard beyond maximum chord.

21.4.1.5 Spoilers

In general terms, the shape of a wind turbine blade can be defined in three regions (See Fig. 21.21)

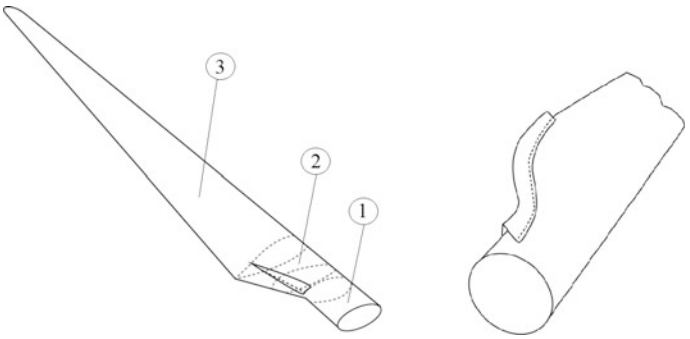

Fig. 21.21 Regions of a wind turbine blade with a spoiler device [33]

1. The nearest region to the hub (circular section).
2. The transition region between the circular section and the airfoil region.
3. The airfoil region.

The root and transition region, because of their section, do not help to the energy production of the wind turbine and even decreases it due to drag. These sections of wind turbines often work in stall situations, especially at high wind speeds. Therefore it is desirable a mechanism, such as spoilers [33], to increase the lift on these conditions (and not to stop) and for increasing the power generated by the turbine. The spoiler is assembled in the inboard part of the blade, i.e. the part nearest the hub, and particularly to the transition region of the blade, as shown in Fig. 21.22. A realistic estimate of the potential performance improvement is 1–1.5% of annual energy yield compared to conventional wind turbine blades without such spoilers. This provides a substantial economic benefit compared to the additional manufacturing costs related to the manufacturing of blades with such spoilers. However, this device presents a main disadvantage for its application in wind turbines against aerodynamics, the fact that the blades must work with higher angles of incidence.

21.4.2 Active Control Systems

21.4.2.1 Traditional Trailing-Edge Flaps

Before coming as a candidate for wind turbine control, traditional trailing-edge flaps were used previously with good results in aircraft load control. The National Renewable Energy Laboratory (NREL) began and carried out their investigations throughout the 1990s in order to improve wind turbines performance with this type of active control system.

The trailing-edge flaps vary the airfoil camber. The lift and the camber line, which is a measure of the amount of airfoil curvature, are directly related. The more curve the camber line is, the more lift the airfoil will generate. So, deploying the flap on the pressure side a lift increase is obtained and deploying it on the suction side a lift reduction is obtained.

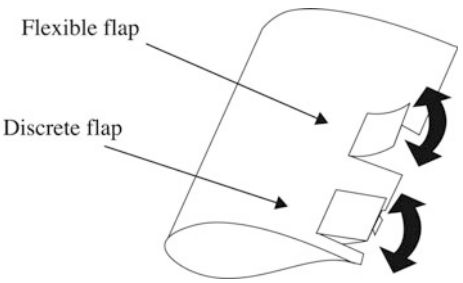

Fig. 21.22 Airfoil with discrete flap and flexible flap

They can be assembled in two ways: either as discrete flaps or flexible flaps (See Fig. 21.22).

1. *Discrete trailing-edge flap*: Conventionally used in aircraft, also known as ailerons are assembled in the blade (hinged) and require a moment over the hinge to achieve the required position. They provide good results in terms of power regulation and load alleviation. The development cost to integrate them in the blade should not be high considering all the background experience with this type of device in aviation.
2. *Flexible trailing-edge flap*: Their addition into the wind turbine blade is similar than discrete flaps. However, in this case there is no need for implementing rotating shafts mounted at the sides of the flaps. Therefore it is possible to produce the flexible flaps in modules which are attached to the blade only via a single connecting surface.

Its application in wind turbines presents some drawbacks, such as the size and weight that can reach the device and the mechanical actuators necessaries for its deployment. The aero-acoustic noise during operation and the energy required for deployment are some pending parameters to improve for its application.

21.4.2.2 Air Jet Vortex Generators

The air jet vortex generator (AJVG) was first suggested by Wallis et al. [34], where circular jets issuing from a surface (airfoil) were used to produce "persistent velocity" for the purpose of delaying turbulent separation. It was discovered that a normal jet issuing into the free stream would produce a pair weak counter-rotating vortices that would pass downstream. Wallis chose a cross-stream jet that was angled at a pitch angle of 45° to the airfoil surface. The vortex remains embedded in the boundary layer over the airfoil and entrains high-momentum air from the undisturbed flow into the boundary layer. This process helps mitigate boundary layer separation and leads to an increase in C_{Lmax} and angle of attack at stall α_{stall} (See Fig. 21.23).

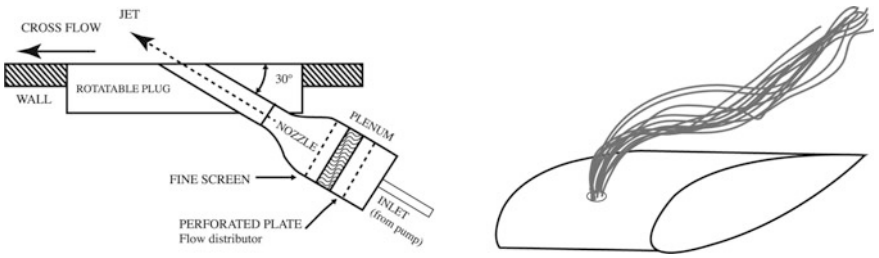

Fig. 21.23 Schematic of AJVG actuator with a pitch angle of 30° and streamlines representation in a wind turbine blade [3]

Johnston and Nishi [35], in 1990, studied more in detail the AJVG choosing a number of simple cases to assess the effects of the vortices. However, there was a problem in this study with the measurement system because the scale of the vortex compared to the size of the hole-probe (used to derive the vorticity in the cross-flow plane) and the sampling grid was quite small. Consequently, it was not possible to sample the vorticity in the region where the vortex was close to the wall, so too much information of the vortex was lost.

A study by Compton and Johnston [36] in 1992 showed that, even for the strongest case tested, the air-jet was qualitatively compared with the vortex produced from a VG but the dissipation of the vorticity takes place at a much greater rate for the AJVG.

Lately, investigations with pulsed vortex generator jets (PVGJ), which are placed in the leading edge, have been gaining interest because they are more effective in delaying stall due to two factors mainly:

1. The improved vorticity production related with the impulsively started jet flow.
2. The reduction in mass flow compared to steady jets due to the reduced duty cycle.

The AJVG presents some interesting characteristics for wind turbine applications. One of the most important is its wide controllability, which allows to modify the parameters of vortex generation according to the circumstances. Its location in the leading edge makes it easy to install, however, it requires the installation of compressed air lines and determine how much air would be necessary and its power expenditure. Other factor that must be taken into account is to maintain the exit ports free of outside influences (insects, dirt or ice).

21.4.2.3 Synthetic Jets

Initially investigated by James et al. [37] in 1996, this type of active flow control creates streamwise vortex similar to those created by PVGJ but with a significant difference, a synthetic jet adds momentum to airflow without adding mass. A conventional jet sucks in air, accelerates this air, and exhausts the air out of a different opening, maintaining airflow. In contrast, a synthetic jet alternates sucking in and blowing out air through the same opening at high frequencies. One method for creating this jet is to use a piezoelectric diaphragm to act as the oscillating membrane. When this membrane oscillates, it sends puffs of air through the cavity and out of a small surface hole. Figure 21.24 illustrates the operating principle of this type of active control device.

Pechlivanoglou [38] summarized the main characteristics of synthetic jets, their mechanical structure, integration, costs and reliability. They are usually located at 10–20% c (close to the leading edge) and can be installed at any angle to the aerodynamic surface. In this case there would not be any problem in terms of space to integrate the synthetic jets. Another factor to be taken into account about their

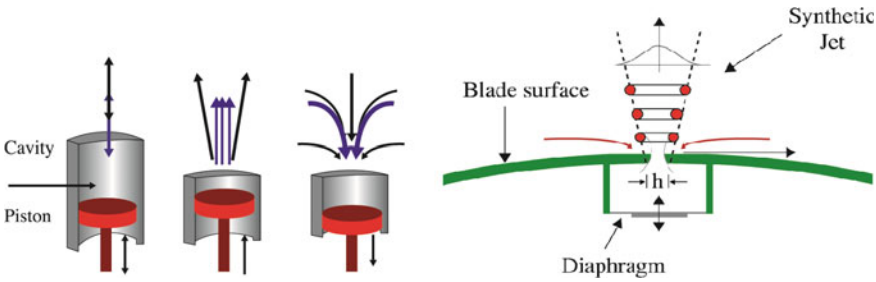

Fig. 21.24 Synthetic jet production principle

integration in wind turbine blades is the structural consequences of the surface discontinuities caused by the synthetic jet slots/holes. The most possible solution to mitigate this trouble would be the integration of additional parts in the blade structure and consequently, changing the laminate structure of the blade.

The existence of synthetic jet mechanisms inside the blade structure increases the complexity of the blade as well as the required maintenance effort. For this reason the flow control mechanisms (individual or integrated in inserted units) should be removable and replaceable in such a way that their maintenance and replacement is fast and cost effective.

Numerous investigations, experimental [39] and numerical [40] have supported the efficiency of this device in aerodynamics achieving significant maximum lift increases, about 29%, and delaying boundary layer separation.

21.5 Energy Efficiency of Active and Passive Flow Control Devices

The cost of electricity generated by wind turbines depends on the location of the wind farm, i.e. the number of full load hours per year. In low wind areas the costs ranges from 0.05 to 0.07 €/kWh and at windy coastal areas the costs ranges from 0.09 to 0.11 €/kWh [41]. A place at the highest point possible and away from obstructions (forests, towers, rocky outcrops) corresponds to the best location for a wind turbine, where the wind can concentrate and get higher speeds.

Currently, it is not easy to quantify in terms of profits the improvement of these flow control devices because it depends on many variables such as the size and weight of each wind turbine or the wind speed average over the year. In terms of lift enhancement, active control devices, in general, present better results than passive control devices, and therefore to improve the energy efficiency of wind turbines, even though they are more costly to integrate in the blades and to maintenance.

Pechlivanoglou [38], with his experimental investigations in large wind tunnel facilities testing different flow control devices, could check the advantages and

disadvantages that present each device in costs (development, integration, maintenance, operation) and therefore get some preliminary conclusions about the cost of energy and their efficiency.

21.6 Conclusion

The wind-power sector is growing rapidly and shows evidences that it will continue in that way in the following years. The growth of this industry becomes in an increase in the size of wind turbines, which leads to an increase in fatigue and structural loads that the system have to support. This may also lead to higher O&M costs to maintain the structure lifetime. The active and passive flow control devices are presented as a solution to these problems. Small size and lightweight are some of their main characteristics and can offset turbulent wind loads. Improvements in these types of devices can increase the life-cycle of wind turbines, power production, system performance and reduce the COE. This decrease in COE would allow to increase the competitiveness in price against traditional sources or other renewable alternatives. The purpose of this chapter was not to make a direct comparison between the different types of devices, reach a conclusion or make a recommendation to choose one device or another. The goal was just to present to the reader a review of today's research in this field that could make major contributions to improve wind turbine control in the next years.

Acknowledgements I would like to take the opportunity to thank Dr. Unai Fernandez Gamiz, from Nuclear Engineering and Fluid Mechanics Department of University of the Basque Country of Vitoria-Gasteiz, for his support for the performance of this chapter, and his willingness to share bibliography, time and knowledge. This work was supported by both the Government of the Basque Country and the University of the Basque Country UPV/EHU through the SAIOTEK (S-PE11UN112) and EHU12/26 research programs, respectively.

References

1. The European Wind Energy Association (EWEA) (2015) Wind in power: European statistics. http://www.ewea.org/fileadmin/files/library/publications/statistics/EWEA-Annual-Statistics-2014.pdf
2. The Global Wind Energy Council (GWEC) (2015) Global wind statistics 2015. http://www.gwec.net/wp-content/uploads/vip/GWEC-PRstats-2015_LR_corrected.pdf
3. Johnson SJ, Van Dam CP, Berg DE (2008) Active load control techniques for wind turbines. Sandia National Laboratories. http://windpower.sandia.gov/other/084809.pdf. doi:10.2172/943932
4. Committee on Assessment of Research Needs for Wind Turbine Rotor Materials Technology (1991) Assessment of research needs for wind turbine rotor materials technology. National Academy Press, Washington

5. Poore R, Lettenmaier T (2003) Alternative design study report: WindPACT advanced wind turbine drive train designs study. National Renewable Energy Laboratory. http://www.nrel.gov/docs/fy03osti/33196.pdf. doi:10.2172/15004456
6. Wood RM (2002) A discussion of aerodynamic control effectors (ACEs) for unmanned air vehicles (UAVs). Paper presented at AIAA's 1st technical conference and workshop on unmanned aerospace vehicle, systems, technologies and operations, Portsmouth, 20–23 May 2002. doi:10.2514/6.2002-3494
7. Corten GP (2007) Vortex blades, oral presentation, WindPower 2007, Los Angeles
8. Taylor HD (1947) The elimination of diffuser separation by vortex generators. United Aircraft Corporation Report No. R-4012-3
9. Fernandez-Gamiz U, Velte CM, Réthoré PE, Sørensen NN, Egusquiza E (2016) Testing of self-similarity and helical symmetry in vortex generator flow simulations. Wind Energy 19 (6):1043–1052. doi:10.1002/we.1882
10. Pearcey HH (1961) Introduction to shock induced separation and its prevention by design and boundary layer control. In: Lachmann GV (ed) Boundary layer and flow control. Its principles and applications, vol 2. Pergamon Press, Oxford, pp 1170–1355. doi:10.1016/B978-1-4832-1323-1.50021-X
11. Godard G, Stanislas M (2006) Control of a decelerated boundary layer. Part 1: optimization of passive vortex generators. Aerosp Sci Technol 10(3):181–191. doi:10.1016/j.ast.2005.11.007
12. Bender EE, Anderson BH, Yagle PJ (1999) Vortex generator modeling for Navier-Stokes codes. In: 3rd ASME/JSME joint fluids engineering conference, San Francisco, 18–23 July 1999
13. Jirásek A (2005) Vortex-generator model and its application to flow control. J Aircr 42 (6):1486–1491. doi:10.2514/1.12220
14. Fernandez-Gamiz U, Réthoré PE, Sørensen NN, Velte CM, Zahle F, Egusquiza E (2012) Comparison of four different models of vortex generators. In: Proceedings of EWEA 2012—European wind energy conference & exhibition. European Wind Energy Association (EWEA)
15. Velte CM, Okulov VL, Hansen MOL (2011) Alteration of helical vortex core without change in flow topology. Phys Fluids 23(5):051707. doi:10.1063/1.3592800
16. Zamorano-Rey G, Garro B, Fernandez-Gamiz U, Zulueta-Guerrero E (2015) A computational study of the variation of the incidence angle in a vortex generator. DYNA New Technol 2 (1):1–13. doi:10.6036/NT7357
17. Øye S (1995) The effect of vortex generators on the performance of the ELKRAFT 1000 kW turbine. In: 9th IEA symposium on aerodynamics of wind turbines, Stockholm
18. Miller GE (1984) Comparative performance tests on the Mod-2, 2.5-MW wind turbine with and without vortex generators. In: DOE/NASA workshop on horizontal axis wind turbine technology, Cleveland
19. Bak C, Bitsche R, Yde A, Kim T, Hansen MH, Zahle F, Gaunaa M, Blasques JPAA, Døssing M, Wedel H, Jens J, Behrens T (2012) Light rotor: the 10-MW reference wind turbine. In: Proceedings of EWEA 2012—European wind energy conference & exhibition. European wind energy association (EWEA)
20. Bak C, Zahle F, Bitsche R, Kim T, Yde A, Henriksen LC, Hansen MH, Blasques JPAA, Gaunaa M, Natarajan A (2013) The DTU 10-MW reference wind turbine, Danish Wind Power Research, Fredericia, 27 May 2013
21. Troldborg N, Zahle F, Sørensen N (2015) Simulation of a MW rotor equipped with vortex generators using CFD and an actuator shape model. In: 53rd AIAA aerospace sciences meeting, AIAA SciTech. doi:10.2514/6.2015-1035
22. Wilcox DC (2006) Turbulence modeling for CFD. DCW Industries, La Cañada
23. Menter FR (1993) Zonal two equation k-ω turbulence models for aerodynamic flows. AIAA J. paper 93-2906. doi:10.2514/6.1993-2906
24. Chow R, Van Dam CP (2006) Unsteady computational investigations of deploying load control microtabs. J Aircr 43(5):1458–1469. doi:10.2514/1.22562

25. Yen DT, Van Dam CP, Bräuchle F, Smith RL, Collins, SD (2000) Active load control and lift enhancement using MEM translational tabs. In: Proceedings of the fluids conference and exhibit, Denver, 19–22 June 2000. doi:10.2514/6.2000-2242
26. Tsai KC, Pan CT, Cooperman AM, Johnson SJ, Van Dam CP (2015) An innovative design of a microtab deployment mechanism for active aerodynamic load control. Energies 8(6):5885–5897. doi:10.3390/en8065885
27. Oerlemans S, Fisher M, Maeder T, Kögler K (2009) Reduction of wind turbine noise using optimized airfoils and trailing-edge serrations. AIAA J 47(6):1470–1481. doi:10.2514/1.38888
28. Stiesdal H, Enevoldsen PB (2003) Flexible serrated trailing edge for wind turbine rotor blade. European Patent Office, EP 1 314 885 B1, 28 May 2003
29. Howe M (1991) Noise produced by a sawtooth trailing edge. J Acoust Soc Am 90(1):482–487. doi:10.1121/1.401273
30. Oerlemans S, Schepers J, Guidati G, Wagner, S (2001) Experimental demonstration of wind turbine noise reduction through optimized airfoil shape and trailing-edge serrations. In: Proceedings of the European wind energy conference and exhibition, Copenhagen, 2–6 July 2001
31. Quell P, Petsche M (2009) Rotor blade for a wind power station. US Patent 7,585,157 B2, 8 Sept 2009
32. Chow R, Van Dam CP (2011) Inboard stall and separation mitigation techniques on wind turbine rotors. In: 49th AIAA aerospace sciences meeting including the new horizons forum and aerospace exposition, Orlando, 4–7 January 2011. doi:10.2514/6.2011-152
33. Lenz K, Fuglsang P (2008) Wind turbine having a spoiler with effective separation of airflow. European Patent Office, EP 2 141 358 A1, 12 Dec 2008
34. Wallis RA (1960) A preliminary note on a modified type of air jet for boundary layer control. Aeronautical Research Council, Current-Paper 513, London
35. Johnston J, Nishi M (1990) Vortex generator jets–a means for passive and active control of boundary layer separation. AIAA J 28(6):989–994. doi:10.2514/3.25155
36. Compton DA, Johnston JP (1992) Streamwise vortex production by pitched and skewed jets in a turbulent boundary layer. AIAA J 30(3):640–647. doi:10.2514/3.10967
37. James RD, Jacobs JW, Glezer A (1996) A round turbulent jet produced by an oscillating diaphragm. Phys Fluids 8(9):2484–2495. doi:10.1063/1.869040
38. Pechlivanoglou G (2013) Passive and active flow control solutions for wind turbine blades. Dissertation, Technische Universitat Berlin
39. Seifert A, Bachar T, Koss D, Shepshelovich M, Wygnanski I (1993) Oscillatory blowing: a tool to delay boundary-layer separation. AIAA J 31(11):2052–2060. doi:10.2514/3.49121
40. Donovan JF, Kral LD, Cary AW (1998) Active flow control applied to an airfoil. In: 36th AIAA aerospace sciences meeting and exhibit, Reno, Nevada. doi:10.2514/6.1998-210
41. Krohn S, Morthorst PE, Awerbuch S (2009) The economics of wind energy, a report by the European wind energy association. http://www.ewea.org/fileadmin/files/library/publications/reports/Economics_of_Wind_Energy.pdf

Index

N. Bizon et al. (eds.), *Energy Harvesting and Energy Efficiency*,
Lecture Notes in Energy 37, DOI 10.1007/978-3-319-49875-1